Development of Small Molecules Targeting GPCRs (PAR2 and LPA1) for Potential Use in Cancer Diagnosis and Therapy

A Thesis Presented to the Faculty of Graduate Studies of Lakehead University

By

Yang Mao

In partial fulfillment of the requirements for the degree of Doctor of Philosophy in Chemistry and Materials Science.

Lakehead University

Thunder Bay, Ontario, Canada, May 2025

Abstract

Lung cancer continues to be the leading cause of cancer-related mortality for both men and women worldwide. Over the past two decades, advancements in prevention, screening, and treatment have contributed to reducing the overall cancer burden in Canada, though challenges remain. Molecular imaging, particularly PET imaging, employs radionuclide-labeled tracers to non-invasively diagnose diseases by visualizing biochemical processes *in vivo*. The success of PET imaging depends on radiopharmaceuticals targeting relevant receptors. G protein-coupled receptors (GPCRs) constitute the largest gene family in the human genome, regulating various cellular functions, with their dysregulation implicated in numerous diseases, including cancer. Protease-activated receptor 2 (PAR2) and lysophosphatidic acid receptor 1 (LPA1), both GPCRs, are overexpressed in lung cancer and play critical roles in tumor progression and metastasis, making them promising targets for cancer diagnosis and therapy. This thesis focuses on design, synthesis, and evaluation of small molecules that targeting PAR2 and LPA1 for potential use in cancer diagnosis and therapy.

Abnormal activation of PAR2 initiates downstream signaling pathways that promote cancer progression and tumor metastasis in various cancer types. Studies have shown that PAR2 is significantly overexpressed, up to 16-fold, in lung cancer tissues. Chapter 2 presents the design and organic synthesis of novel PAR2 ligands (total of 35 compounds), based on AZ3451, a previously reported potent and selective PAR2 antagonist. Collaborators from Western University evaluated all compounds for functional activity by assessing PAR2-dependent calcium signaling and β-arrestin1/2 recruitment. Based on the functional activity assay, structural modifications of AZ3451 are expected to yield novel biased PAR2 negative allosteric modulators (NAMs). Further assessment of all the compounds for bias in PAR2 mediated mini-G protein recruitment to evaluate all compounds for their therapeutic potential is under way. Among these compounds, a fluorine-containing compound, P1c, was selected as the candidate with an EC_{50} value of 16.8 nM (n=1) and 1.2nM (n=1), determined through β-arrestin 1 and 2 recruitment in a trypsin-induced assay. To facilitate the development of ^{18}F-radiolabeled compounds targeting PAR2, a precursor SPIAd iodonium (III) ylide was synthesized and characterized. Ongoing efforts focus on investigating the optimal reaction conditions for ^{18}F-radiolabeling.

LPA1 has been identified as being overexpressed in various cancers, particularly in lung cancer, where its activation promotes cell migration and invasion. Chapter 3 presents two series of design and synthesis of novel LPA1 antagonists with total 23 compounds. The synthetic scheme of first series is derived from the previously reported potent and selective LPA1 antagonist, RO6842262. The second series is derived from compound 12f, an anti-metastatic agent previously reported by our group. The core structure of this series was identified through scaffold hopping and molecular docking studies. All final compounds have been fully characterized, and their biological activity is currently being evaluated using cAMP and wound healing assays. Notably, compound L22p in the second series exhibited an IC_{50} value of 1.36 nM (n=1) in cAMP assay, indicating strong antagonistic activity against LPA1. This suggest that the novel scaffold holds promise as a potent LPA1 antagonist. Given the high expression of LPA1 in cancer, the candidate compound described in Chapter 3 will be converted into an iodo-compound, which will then react with SPIAd to generate iodonium (III) ylide precursors. These precursors will subsequently undergo treatment with fluorine-18 ions, followed by hydrolysis, to yield the radiolabeled final compounds.

Acknowledgements

Over the past six years, it has been a great pleasure to join Lakehead University and become a member of the Department of Chemistry. Here, I encountered excellent faculty and professors. Firstly, I would like to thank my supervisor, Dr. Jinqiang Hou. I truly appreciate him for leading and guiding me into the field of medicinal chemistry and providing significant help in my studies. He willingly shared his study and research experiences with us, always bringing us together and forming an incredible, cohesive team.

Secondly, I am extremely grateful to my committee members—Dr. Campbell, Dr. Gottardo, and Dr. Jiang—for their time and scientific advice over the years. I thank Dr. Campbell for teaching the medicinal chemistry class, providing radiosynthesis training, and sharing many chemicals with me; I thank Dr. Gottardo for teaching the organic synthesis class and sharing many chemicals; and I thank Dr. Jiang for teaching the carbohydrate chemistry class and sharing the lab and equipment, which greatly facilitated my synthetic work.

I also extend heartfelt thanks to the Chemistry Department and Graduate Studies of Lakehead University, the Thunder Bay Regional Health Research Institute, and the Cyclotron and Radiopharmacy Program for providing me with the capacity to conduct this research. I thank the technicians—Debbie Puumala, Brad Miller, and Michael Sorokopud—for all their time and support. I also thank the program coordinators, Dr. Magajna and Dr. Mawhinney, for their time and endless support during every semester and milestone of this journey.

I further extend my gratitude to my collaborating professor. I thank Dr. Ramachandran for conducting various biological assays on my compounds since my MSc thesis and for providing many helpful suggestions regarding my abstract and presentation. I also thank Dr. Thu for testing, assessing, and organizing the biological data for my compounds—this was very thoughtful. This research would not have been possible without the help and support of these knowledgeable, kind, and generous mentors.

I thank my wonderful group members for sharing this scientific journey with me: Dr. Wenjie Liu, Dr. Dong Zhao, Dr. Taylor P.A. Hari, Dr. Guillem Dayer, Antal H. Kovacs, Austin Hopkins, Alanna Wade, Catherine Jiang, Kate Muzyka, Jessica Lorentson, Julio Lopez, Qianqian Wang, and Jonas Olsen. I especially thank Dr. Liu for advising me on molecular docking and Dr. Zhao for answering many questions regarding scientific careers and helping me evaluate the compounds.

Lastly, I can never thank my family enough for their constant support, especially my parents and parents-in-law, who have always been there for me. I also wish to thank my lovely wife, Rui Zhu, for willingly following me to the coldest place. I always say that she deserves half of this medal—after all, while I earned my PhD, she earned a diploma. I also wish to thank my dear children—my son, Ryan Mao, and my daughter, Emma Mao—who provided me with much motivation during my graduate studies.

Dedication

This thesis is dedicated to my family, especially my father, whose unwavering support and encouragement have been my greatest motivation throughout this journey.
This work is also dedicated to all those affected by cancer - may this research serve as a small step toward earlier diagnosis and better treatment options. And, one day, a cure.

Table of Contents

Abstract II

Acknowledgements III

Dedication IV

List of Abbreviations and Symbols XII

Chapter 1 1

Introduction 1

1.1 Cancer 2

1.1.1 Overview of Cancer 2

Figure 1.1 Hallmarks of cancer. 2

Figure 1.2. Distribution of leading causes of death in Canada from 2020 to 2023. 3

1.1.2 Lung Cancer 4

Table 1.1. The difference of SCLC and NSCLC. 4

Figure 1.3. Location and ratios of lung cancer. 6

1.1.3 Cancer and Molecular Imaging 6

1.2 Positron emission tomography (PET) 7

1.2.1 PET Imaging Agent Development from Bench to Bedside 7

Figure 1.4. Development of PET imaging agent - from bench to bedside. 8

Figure 1.5. PET imaging: how it works. 9

Table 1.2. Characteristics of commonly used positron emitting radionuclides. 10

Figure 1.6. Production of ^{18}F. Cycltron-accelerated protons are bombarded on oxygen-18 enriched water. 11

Figure 1.7. Nucleophilic ^{18}F-Fluorination. 12

1.2.4 [^{18}F]FDG PET/CT for Cancer Diagnosis 13

Figure 1.8. The images of PET/CT scan. 13

1.3 G protein-coupled receptors (GPCRs) 14

1.3.1 What are GPCRs? 14

Figure 1.9. The classes of GPCRs consist of seven-transmembrane proteins located in the cell membrane. 15

1.3.2 Known [^{18}F]-labeled PET Imaging Agents Targeting GPCRs 16

Figure 1.10. The structure of selected [^{18}F]-labeled radiopharmaceuticals. 17

1.4 Overview of Research Project 18

Chapter Two 20

Design, synthesis and evaluation of small molecule ligands targeting Protease-activated Receptor 2 (PAR2) as potential diagnostic and therapeutic agents 20

2.1 Introduction 21

2.1.1 Protease-Activated Receptors (PARs) Family 21

Figure 2.1. The activation feature of most of the GPCRs and PARs. 21

2.1.2 Structural Features and Activation Mechanisms of PARs 22

Figure 2.2. The structure of PARs. Schematic (blue) and folded (green). 22

Figure 2.3. PARs activation mediated desensitization, internalization and resensitization mechanisms. 23

2.1.3 Overview of PAR2 Signaling Pathway 24

Figure 2.4. PAR2-mediated downstream signal transduction pathways. 26

2.1.4 PAR2 Knockout Mouse Model for Human Diseases 27

Table. 2.1 Summary of PAR2 related disease models and effect of PAR2 knockout (K/O). 27

2.1.5 PAR2 in Lung Cancer 28

Figure 2.5. Diagram of the mechanism of PAR2 antagonism in Osimertinib resistance. 29

2.1.6 Known PAR2 Ligands 29

Figure 2.6. Synthetic tethered ligand (TL)-mimicking peptides primarily bind to the extracellular loop 2 (ECL2) 30

Figure 2.7. Structure of GB110, a peptidomimetic agonist with 0.28uM EC_{50} in intracellular Ca2+ release in HT29 cells. 31

2.1.7 MSc Study 34

Figure 2.8. **A**. The structure of AZ3451. **B**. The allosteric antagonist AZ3451 binding in the pockets of PAR2. The benzimidazole nitrogen forms a hydrogen bond with Tyr210, highlighted with a green dotted line. 35

Scheme 2.1. The synthetic scheme for AZ3451 analogues. 36

Figure 2.9. A molecular modeling study was conducted to present the structure of AZ3451 and four types of potential conformational isomers. 37

Scheme 2.2. Proposed radiolabeling scheme with SPIAd ylides. 38

Figure 2.10. The structure of AZ3451 and derivates with R1-3 group. 38

2.2 Results and discussion 38

2.2.1 PhD study - Optimizing Synthetic Conditions.....38

Scheme 2.3. Optimizing the reaction condition.....40

2.2.2 Ligand Design.....40

Figure 2.11. AZ3451 analogues with R_1 group.....41

2.2.3 The Library of AZ3451 Analogues.....42

Figure 2.12. Building blocks of R1 group.....43

Figure 2.13. ^{13}C-NMR spectrum of compound P1i 44

Figure 2.14. Ligand-receptor interaction for analogues P2a. AZ3451 is colored in red, analogues P2a is colored in white. The key hydrogen bond for both compounds is conserved and colored in green. The key residues highlighted in yellow.....45

2.2.4 Synthesis and Characterization of the Two Series of AZ3451 Derivatives 46

Figure 2.15. Structure of AZ3451 derivatives with R2 and R3 groups.....46

Scheme 2.4. The synthetic schemes of two series of AZ3451 derivates. 47

2.3 Biological Evaluation.....48

Figure 2.16. Specific TM and ICL helices contribute to distinct G protein coupling. 48

Table 2.3. Summary of BRET assay results (β-arrestin 1&2) of R1 group. 49

Table 2.4. Summary of BRET assay results (β-arrestin 1&2) of R2-3 group. 52

Table 2.5. Summary of Ca^{2+} signaling assay results of partial compounds 53

Figure 2.17. Probe dependence of AZ3451 analogs. 55

Figure 2.18. AZ3451 analogs show biased activity. 56

2.4 Radiolabel approach.....57

2.4.1 Select the Candidate Compound for Radiolabeling Study.....57

Figure 2.19. Reported structure of [^{18}F]29.....57

Figure 2.20. Structure of compound P1c and proposed radiopharmaceutical.....58

2.4.2 ^{18}F-Radiolabeling Method 58

Figure 2.21.....59

Scheme 2.5. A-C. Synthesis of SPIAd auxiliary/precursors.....60

2.5 Experimental Procedures and Results.....61

2.5.1 General Information of Organic Synthesis.....61

2.5.3 Methodology of Molecular Docking Study 62

2.5.4 Experimental Procedures 63

Chapter Three 83

Design, Synthesis, and Evaluation of Novel Lysophosphatidic Acid Receptor 1 (LPA1)-Targeting Small Molecules as Therapeutic and Diagnostic Agents 83

3.1 Introduction 84

3.1.1 Lysophosphatidic Acid (LPA) 84

Figure 3.1. LPA intracellular and extracellular production and degradation. X in the structure is represented hydrophilic head group. 85

3.1.2 Lysophosphatidic Acid 1 Receptor (LPAR1) 86

Figure 3.2. LPA1 receptor downstream signaling and signaling intermediates. 87

3.1.3 The Role and Function of LPA1 in Disease 88

Table 3.1. Physiological and Pathological Roles of LPA1 88

3.1.4 The Role of LPA1 Receptor in Lung Cancer 90

Figure 3.3. Signalling pathways involved in A549 cell proliferation and migration induced by LPA. 90

Figure 3.4. A. The pathway of LPA receptor antagonists is to block the activation of the receptor, thus blocking the initiation of signaling. 91

3.1.5 Known LPA1 Ligands 92

Figure 3.5. Lipid-based (A) LPA1 agonists and Lipid-based (B) LPA1 antagonists. 93

Figure 3.6. Selected non-lipid LPA1 antagonists - Ki16425 derivatives and RO6842262 derivatives. 95

Figure 3.7. Reported structures of SAR-100842, ONO-7300243, and ONO-0300302. 97

3.2 Results and discussion 98

3.2.1 First Series - Structural Optimization and Synthesis of RO6842262 Analogues 98

Scheme 3.1 A. Structure of RO6842262 and analogue L9x. 99

Scheme 3.2. A - Unwanted reaction and structure of compounds L3a, Lb, and Lc. 101

Scheme 3.3 A - Optimized synthetic scheme of RO6842262 analogues 103

Figure 3.8. Structure of desired compound L6 and undesired compoundL6a. 104

Figure 3.9. 1-D selective NMR irradiation spectrum of compound L6. It was dissolved in chloroform-d. 105

Figure 3.10. **A**. Structure of ester compound L8x (colored in red), undesired hydrolyzed compounds, L8' (colored in orange), L8'' (colored in blue) and desired hydrolyzed compound, L9x (colored in green). **B**. HPLC-MS monitoring the reaction mixture after 2 hours. **C**. HPLC-MS monitoring the reaction mixture after 10 hours. Pink color is impurity during hydrolysis reaction. **Note:** Alternative hydrolysis conditions were only tested using other bases (e.g., LiOH); acid hydrolysis conditions were not examined due to time constraints. 106

Scheme 3.4. Synthetic scheme of analogue L12y. Commercially available chemical - L7y: 4-fluorobenzoic acid. 107

3.2.2 Synthesis of L9x Derivatives via the Mitsunobu Reaction 108

Scheme 3.5. Proposed synthetic scheme employing the Mitsunobu reaction (from compound L7 to L14). 109

3.2.3 Second Series – Employing Scaffold Hopping Strategy on Compound 12f for Developing Novel LPA1 Antagonists 110

Figure 3.11. Development of a triazolo pyrimidine compound from compound 12f using scaffold hopping. 111

Figure 3.12. A - Structure of compound 12f and L22s. B - Docking result of 12f, colored in white. C - Docking result of L22s, colored in green. 112

Scheme 3.6. Synthetic scheme and building blocks (L-a to L-u) with amino group of compounds L22a to L22u. 113

Figure 3.13. Building blocks of R_4 group. L-u colored in blue. 114

Figure 3.14. Structure of desired L17 and undesired L17' regio-isomers. 116

Figure 3.15. 1-D selective NMR of compound L18. 117

Figure 3.16. A - VT-NMR spectra of compound L22p. 118

Figure 3.17. Structure of compound 12f, L22s, and L25d. 119

Scheme 3.7. Synthetic scheme and building blocks with alcohol group of compounds L23a to L23e. 120

3.3 Biological Evaluation of the 2nd Series of Ligands 120

Figure 3.18. cAMP assay results using compound L22j, L22p, and L22s. 121

3.5 Inspired by BMS-986278: Integration with the Second Series for Third Series 122

Figure 3.20. Structure of BMS-986020, 986020a, and BMS-986278. 123

Figure 3.21. Representative structure of third-series compound L33i - Inspired by BMS-986278. 123

Scheme 3.11. A. Synthetic scheme for preparation of compound L37. B. Synthetic scheme for preparation of compound L33i, m, p, and t. 124

3.6 Experimental procedure and Results 125

3.6.1 Molecular Docking Study 125

3.6.2 General Information of Organic Synthesis 126

3.6.3 Experimental Procedure and Results for the First Series Compounds 126

3.6.4 Experimental Procedure and Results for the Third Series Compounds 161

Chapter Four 165

Conclusions and Future Work 165

4.1 Conclusions 166

Figure 4.1. Radioligand [^{18}F]P1c holds the potential for precision imaging in cancer diagnosis. 167

Figure 4.2. L22p holds promise as a LPA1 antagonist with anti-metastatic potential. 167

4.2 Future Work 168

4.2.1 Development of Novel Biased Ligands for PAR2 168

Figure 4.3. Structure of P8 and P14 derivatives with several examples of building blocks (R1). 169

4.2.2 Biological evaluation of novel LPA1 antagonists *in vitro* assays 169

4.2.3 Employing the Boc Group for Amide Protection 169

Scheme 4.1. Proposed synthetic scheme with Boc group for radiolabeling. 170

4.2.4 Modification of the Synthetic Scheme for Efficient ^{18}F-Labeling in 2nd Series 171

Figure 4.4. Chemical structures of reported LPA1 radiotracer. 171

Scheme 4.2. A – 172

Scheme 4.3. (A) Hypothetical Boc-protected reaction of compound L27d with the R6 building block. (B) Proposed structure of Iodo-compound (L28) incorporating the R6 building block. 173

Scheme 4.4. Proposed radiolabeling scheme to produce ^{18}F-labeled compounds: production of the iodonium ylide species and subsequent one-pot reaction with ^{18}F and LiOH to yield the final 'hot' compound. 174

Reference 175

Appendix A - Characterization Data of Chapter 2 190

Results of Mass Spectroscopy and HPLC purity 190

Spectrum of Proton-NMR (^{1}H-NMR) 210

Appendix B - Characterization Data of Chapter 3 and Chapter 4 222

Results of Mass Spectroscopy and HPLC purity 222

Appendix C 282

Dose-response curve of β-arrestin 1-Trypsin 282

Dose-response curve of β-arrestin 2-Trypsin 283

Dose-response curve of β-arrestin 1- SLIGRL-HN_2 285

Dose-response curve of β-arrestin 2- SLIGRL-HN_2 287

Dose-response curve of calcium signaling assay (Trypsin-induced) 289

Dose-response curve of calcium signaling assay (SLIGRL-induced) 290

List of Abbreviations and Symbols

Ana-HPLC	Analytical High-performance liquid chromatography
ADDP	1,1′-(Azodicarbonyl)dipiperidine
cAMP	cyclic adenosine monophosphate
$CDCl_3$	Chloroform-d
$CHCl_3$	Chloroform
DCM (CH_2Cl_2)	Methylene chloride
DEAD	Diethyl azodicarboxylate
DMSO-d6	(Methyl sulfoxide)-d6
DIAD	Diisopropyl azodicarboxylate
DPPA	Diphenylphosphoryl azide
ECL	Extracellular loop
ERK	Extracellular signal-regulated kinase
EtOAc	Ethyl acetate
FDG	18F-fluorodeoxyglucose
FLIPR	Fluorescent imaging plate reader
GDP	Guanosine diphosphate
GPCR	G-protein-coupled receptor
GTP	Guanosine triphosphate
HPLC	High-performance liquid chromatography
IC_{50}	Half-maximal inhibitory concentration
IP3	Inositol 1,4,5-triphosphate
K_{222}	Krypto fix $_{222}$
K_D	Dissociation constant

LiOH	Lithium hydroxide
LPA	Lysophosphatidic acid
MAPK	Mitogen-activated protein kinase
mCPBA	meta-Chloroperoxybenzoic acid
MeOH	Methanol
MRI	Magnetic resonance imaging
MS	Mass spectrometry
MW	Microwave
m/z	Mass-to-charge ratio
NMR	Nuclear magnetic resonance
NaOH	Sodium hydroxide
PARs	Protease-activated receptors
PET	Positron-emission tomography
PLA	Phospholipase A
Prep-HPLC	Preparative High-performance liquid chromatography
RBF	Round-bottomed flask
SCIDY	Spirocyclic iodonium ylide
SPECT	Single-photon emission computed tomography
SPIAd	Spiroadamantyl-1,3-dioxane-4,6-dione
TFA	Trifluoroacetic acid
TGF-β1	Transforming growth factor beta 1
THF	Tetrahydrofuran
TLC	Thin-layer chromatography
TMD	Transmembrane receptor Doma

Chapter 1

Introduction

1.1 Cancer

1.1.1 Overview of Cancer

Cancer is a complex and multifaceted disease that remains a leading cause of death worldwide, deeply affecting human health and society[1]. According to the National Cancer Institute (NCI), cancer is a disease of uncontrolled proliferation by transformed cells that evolve under natural selection, influenced by genetic, epigenetic, and microenvironmental factors[2]. As presented in **Figure 1.1**, cancer cells exhibit several distinct biological characteristics that differentiate them from normal cells[3].

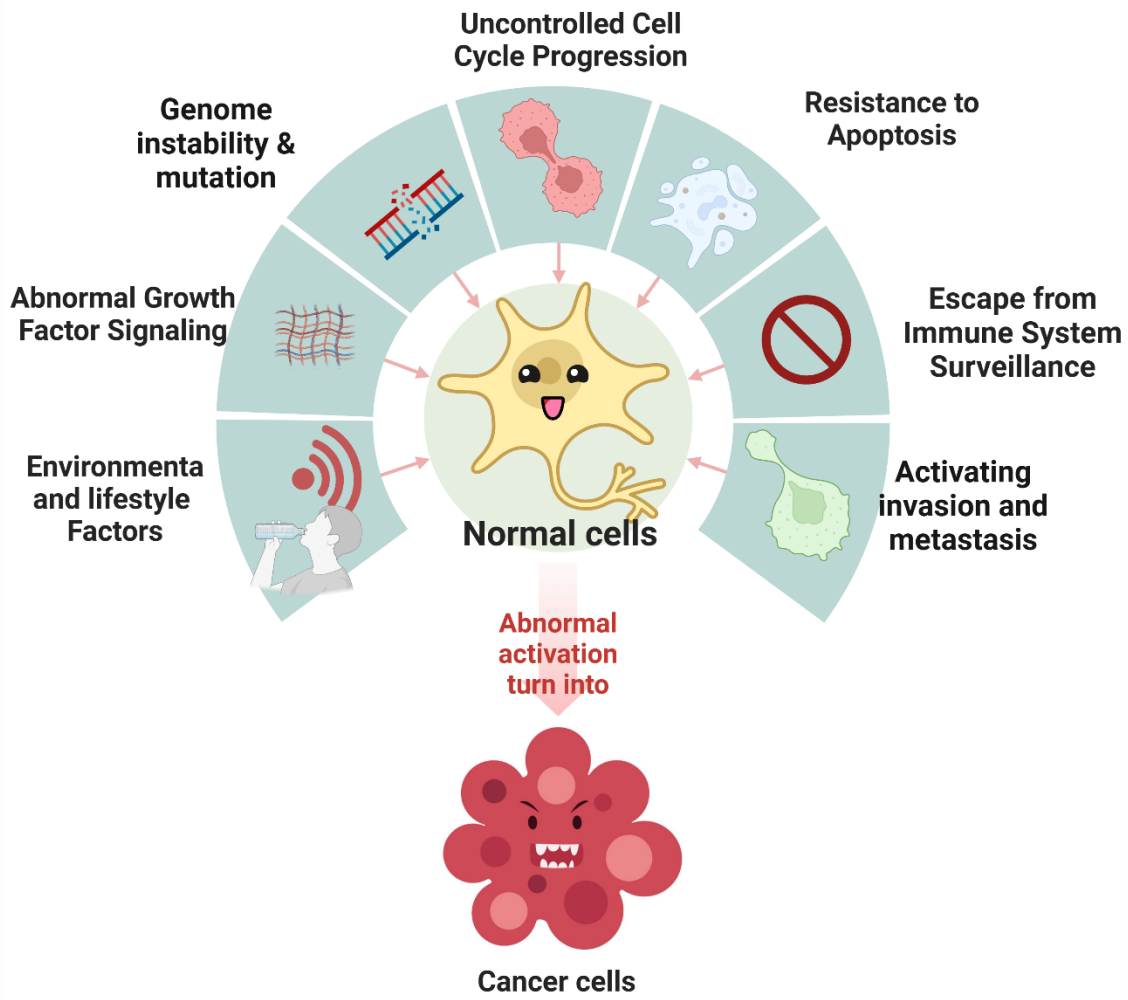

Figure 1.1 Hallmarks of cancer. Cancer cells bypass regulatory signals, evade apoptosis, and accumulate mutations that drive tumor progression[3]. Metabolic pathways are reprogrammed to sustain rapid growth, while angiogenesis ensures oxygen and nutrient supply. Cancer cells invade surrounding tissues, metastasize to distant organs, and evade immune surveillance, enabling continued proliferation.

These mutations disrupt the regulatory processes governing cellular growth and death, enabling mutated cells to proliferate indefinitely under certain conditions, as observed in HeLa cells[3,4]. A hallmark of cancer cells is their loss of adhesion molecules, which normally anchor cells within tissues[2,3]. This loss facilitates metastasis, the spread of cancer to other parts of the body through the blood or lymphatic systems[2,5]. Metastasis is a major contributor to cancer-related mortality, as it disrupts the function of vital organs and complicates treatment[3,6]. In Canada, cancer significantly impacts individuals and the healthcare system[7]. According to Canadian Cancer Statistics, approximately 40% of Canadians will receive a cancer diagnosis during their lifetime[7,8]. In 2024, an estimated 240,000 Canadians are expected to be diagnosed with cancer, with 90,000 deaths projected[7–9]. Even during the COVID-19 pandemic (2020–2023), cancer claimed around 82,000 lives annually, making it the country's leading cause of death (**Fig. 1.2**)[7].

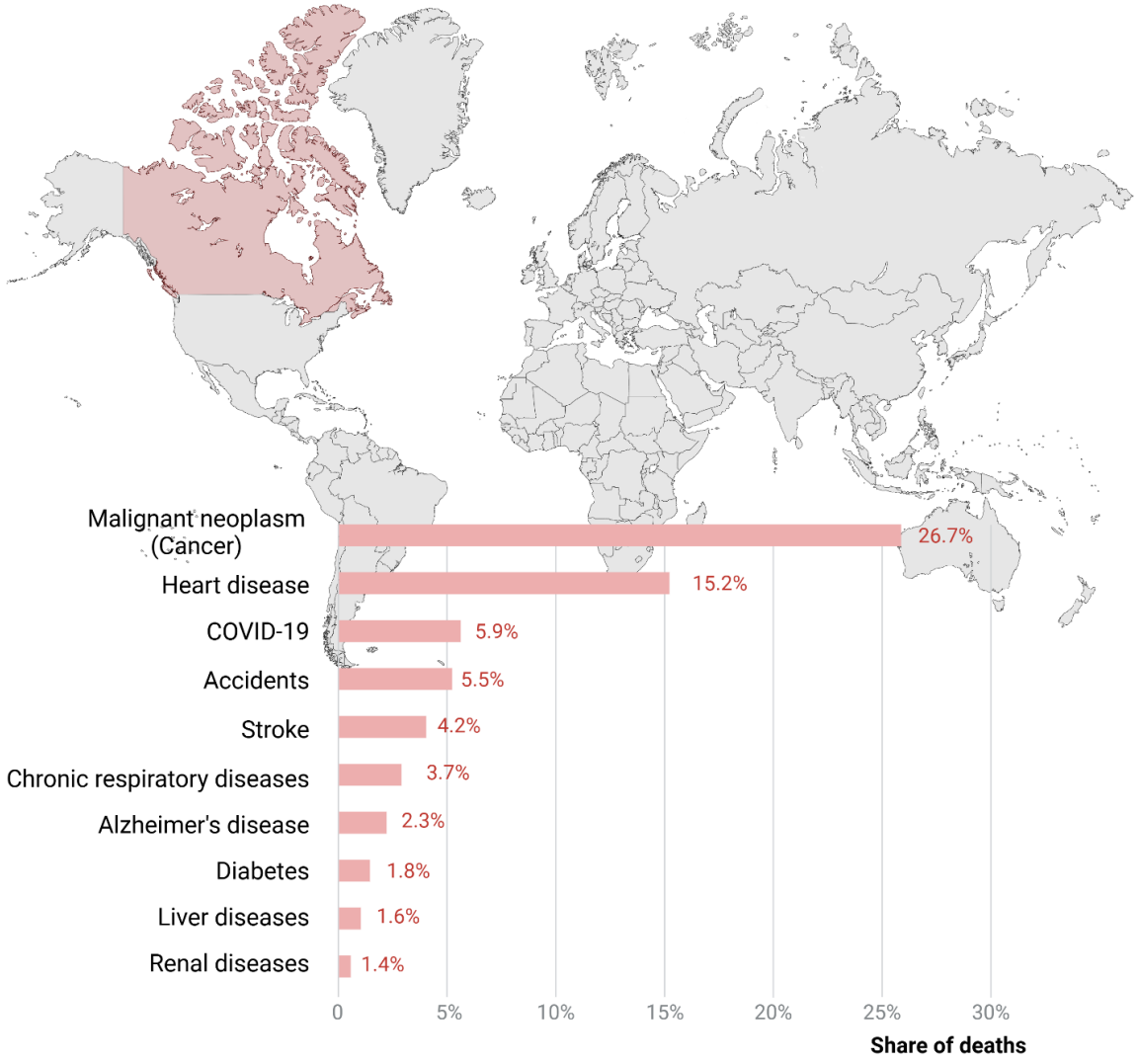

Figure 1.2. Distribution of leading causes of death in Canada from 2020 to 2023.

Malignant tumors accounted for 26.7% of all deaths during this period, exceeding the combined mortality from the next three leading causes of death[7]. As Canada's population grows and ages, the number of cancer cases and deaths continues to rise[8]. Additionally, cancer cells exhibit remarkable adaptability, evolving to evade the body's immune responses and resist therapeutic interventions[3,10]. This ability to adapt complicates efforts to control and eradicate the disease[10].

1.1.2 Lung Cancer

Lung cancer is a malignant disease originating in the respiratory epithelium and remains the leading cause of cancer-related deaths worldwide, with over 2.2 million new cases and nearly 1.8 million deaths annually[1,11]. In Canada, lung cancer is the most diagnosed cancer and the leading cause of cancer-related deaths among both men and women, with the mortality even larger than the combined of breast, colorectal, and prostate cancers[7,8]. Early symptoms, such as mild cough, fatigue, or chest pain, are often subtle and easily misdiagnosed, resulting in a high percentage of late-stage diagnoses[11,12]. Approximately 70% of patients are diagnosed in the middle to advanced stages of the disease, when regional or distant spread significantly limits treatment options[7,8,13]. Over 50% of patients die within one year of diagnosis, and the five-year survival rate is only about 17%[713].

The widespread use of cigarettes as the predominant tobacco product in the 20th century contributed to a significant rise in lung cancer incidence[12,13]. Smoking is the primary risk factor for lung cancer and is responsible for at least 80% of lung cancer deaths[13]. Clinically, lung cancer is classified into small cell lung cancer (SCLC), accounting for about 15% of cases, and non-small cell lung cancer (NSCLC), which represents approximately 85% of cases (**Table 1.1**)[14–16].

Table 1.1. The difference of SCLC and NSCLC.

Type	SCLC	NSCLC
Proportion	~15%	~85%
Growth and spread	Rapid and early metastasis	Slow and late metastasis
Molecular characteristics	Tumor Protein p53(TP53), (Retinoblastoma 1) RB1 mutations, Myelocytomatosis	(Epidermal Growth Factor Receptor) EGFR, Anaplastic Lymphoma Kinase (ALK), (Kirsten Rat Sarcoma Viral Oncogene Homolog) KRAS mutations

	oncogene (MYC) amplification	
Histological differences	Small, round or oval cells, and dense nuclear chromatin	Adenocarcinoma, squamous cell, and large cell carcinoma
Staging	Limited and extensive stage	Staged using the tumor, node, and metastasis system
Treatment	Chemotherapy, radiation, immunotherapy	Surgery, targeted therapy, immunotherapy
Prognosis	Poor – median survival 7-16 months	Variable – widely based on stage, early-stage patients have better outcomes with therapy

NSCLC is further divided into three subtypes: adenocarcinoma, squamous cell carcinoma, and large cell carcinoma[17]. The location of these types of lung cancer is summarized in the table below (**Fig. 1.3**)[17,18]. Large cell carcinoma represents approximately ~5% of lung cancers[11,17]. This subtype lacks squamous or glandular differentiation and is often diagnosed by exclusion[11,17]. It frequently begins in the central part of the lungs and may spread to nearby lymph nodes, the chest wall, and distant organs. Large cell carcinoma is strongly associated with smoking[11,17,18].

Squamous cell carcinoma accounts for about ~25% of lung cancers and originates from squamous cells in the airway epithelium of the bronchial tubes, typically in the central regions of the lungs. Like large cell carcinoma, it is closely linked to cigarette smoking[11,17,18].

Adenocarcinoma is the most common lung cancer subtype, comprising ~55% of cases[17,18]. It arises from small airway epithelial cells and mucus-secreting alveolar cells[17,18]. Unlike other subtypes, adenocarcinoma is prevalent among both smokers and non-smokers, affecting men and women of all ages[12,17,18]. It usually occurs in the lung periphery, which may be related to changes in cigarette design that encourage deeper inhalation[12,16]. Advances in imaging technology and earlier detection have improved diagnosis rates for adenocarcinoma[19,20]. Compared to other lung cancer subtypes, it grows relatively slowly, making early detection and targeted treatments critical for improving patient outcomes[14,19].

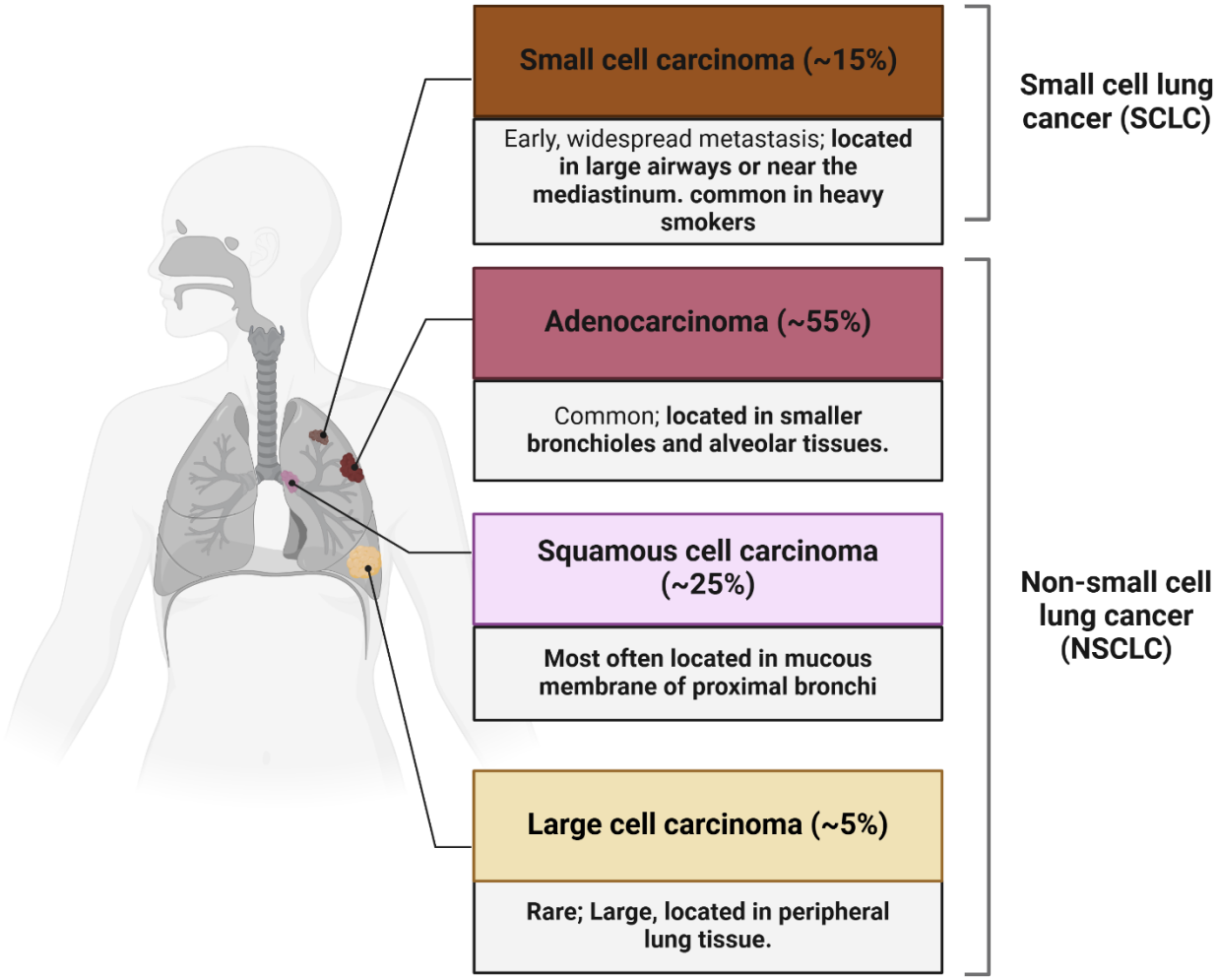

Figure 1.3. Location and ratios of lung cancer.

1.1.3 Cancer and Molecular Imaging

Encouragingly, overall cancer death rates decreased by an average of 0.8% per year from 2010 to 2020 in many regions[1,13]. Improvements in cancer survival rates are attributed to three main factors: enhanced prevention strategies, more effective screening programs, and advancements in clinical treatments[6,15,21]. Screening aims to detect cancer at an early stage, often before symptoms appear, increasing the likelihood of successful treatment[15,21]. Common screening and diagnostic tools include blood tests, DNA analysis, and medical imaging techniques[15,21].

Medical imaging is an important component of modern medicine, including X-ray, ultrasound, computed tomography (CT), and magnetic resonance imaging (MRI), enabling the noninvasive visualization of internal structures within the human body[6,22]. It has revolutionized disease monitoring and diagnosis by providing detailed anatomical information[6]. However, these techniques are unable to reveal dynamic biological processes occurring at the cellular and molecular levels[22].

This limitation is addressed by molecular imaging[19,23,24]. Over the past few decades, significant technical advancements in image quantification have transformed how researchers and physicians understand biological systems and diagnose diseases, specifically by visualizing and measuring molecular and cellular activities in living organisms[19,23,24].

Certain medical imaging technologies can be adapted into molecular imaging techniques with appropriate modifications[19,24,25]. Transforming medical imaging technologies into molecular imaging requires introducing target-specific probes or agents that interact with molecular targets[26,27]. For example, ultrasound employs targeted contrast agents to highlight specific tissues or processes, MRI can be enhanced with molecular probes to visualize functional activity, and fluorescence and bioluminescence enable real-time tracking of biological processes in preclinical models[20,23,28].

Nuclear imaging is a special modality in molecular imaging, producing images by detecting radiation from the body after a radiotracer (radiopharmaceutical) is given to the patient[29–31]. In the early 20th century, researchers relied on devices like Geiger counters to measure the biodistribution of radioactive substances in the body[26,31]. These tools, while groundbreaking at the time, provided only crude, point-by-point measurements and lacked the ability to produce detailed images due to the absence of imaging systems[26,32]. Significant progress came in 1950 when Benedict Cassen developed the rectilinear scanner, the first imaging device capable of creating two-dimensional representations of radiotracer distributions[26,33]. By 1956, advancements in the scanner's photographic components greatly improved the resolution and sensitivity of imaging instruments, marking a pivotal moment in nuclear medical imaging[26]. The two most common nuclear imaging techniques are Single Photon Emission Computed Tomography (SPECT) and Positron Emission Tomography (PET)[33]. In SPECT, the radionuclides are gamma-emitting isotopes that emit single photons directly, whereas in PET, the radionuclides are positron-emitting isotopes that undergo beta-plus decay[33].

1.2 Positron emission tomography (PET)

1.2.1 PET Imaging Agent Development from Bench to Bedside

The key steps in the design and characterization of PET imaging agents are outlined in **Figure 1.4**[20,33,34].

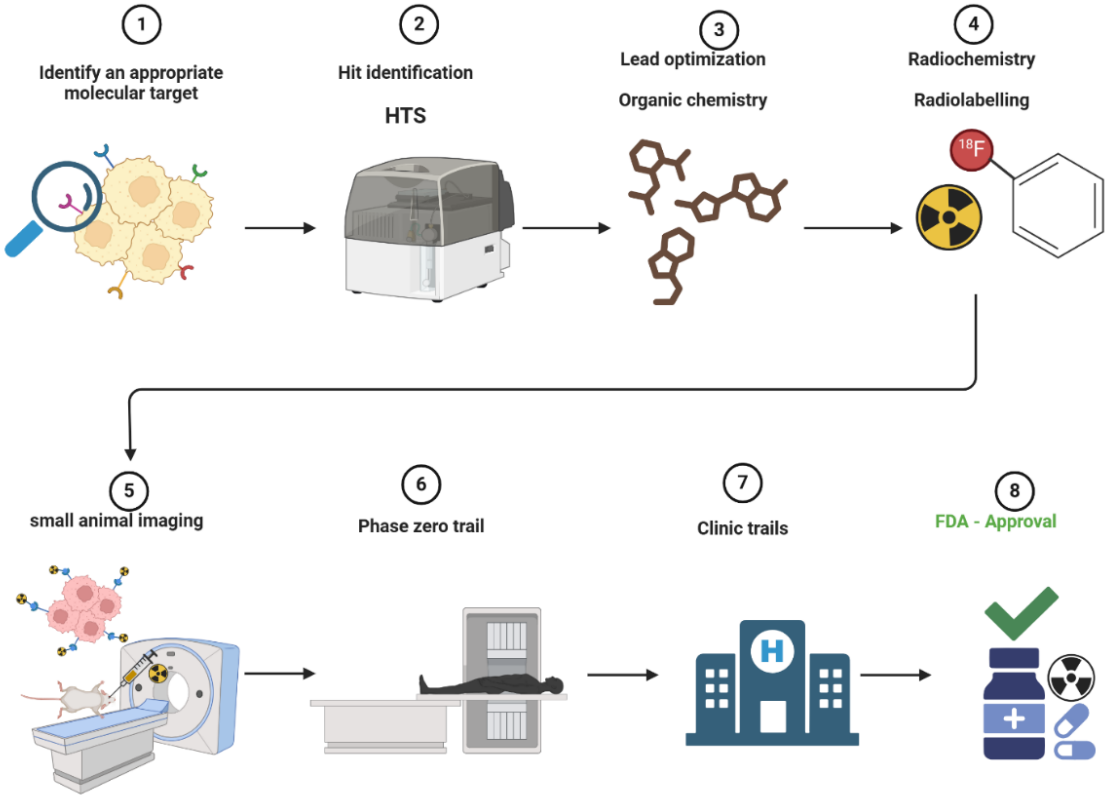

Figure 1.4. Development of PET imaging agent - from bench to bedside.

In Step 1, the goal of target identification is to find a biomarker associated with the disease of interest. Biomarkers can serve as indicators of the physiological state of the disease and may include proteins or nucleic acids[20,35]. Once a promising target is identified, Step 2 involves hit identification, which aims to discover compounds that interact effectively with the target[20,35]. This is achieved through high-throughput screening (HTS), a method used to rapidly evaluate large compound libraries[20,36]. Step 3 focuses on lead optimization, where advanced organic synthesis techniques are used to optimize compounds[20,35]. This process aims to enhance their potency, solubility, and pharmacokinetic properties while minimizing side effects, thereby improving their drug-like characteristics[20,37]. Optimized lead compounds (candidates) then undergo *in vitro* testing to confirm their biological functions[38,39]. In Step 4, radiochemistry combines radionuclides with candidate compounds to produce PET imaging agent[35,40]. Compounds with the highest binding affinity from Step 3-4 are radiolabeled to produce PET tracers, which will be injected and evaluated in small-animal models that replicate human diseases (Step 5)[35,40]. PET imaging studies assess the target specificity and biodistribution of these radiotracers *in vivo*[31,35]. Using small animal models is a critical step before translating these compounds into clinical practice[35]. Eventually, in Steps 6 to 8, these tracers are evaluated

in clinical trials, where their safety, efficacy, and imaging accuracy are assessed[35,41]. Once proven successful, they can be submitted for regulatory approval and introduced to the market[35,36].

1.2.2 How PET Imaging Work

PET is a highly sensitive, non-invasive, three-dimensional nuclear imaging technique that visualizes and monitors physiological and biochemical processes in the body[40,42,43]. Known as 'functional imaging,' it is particularly valuable for assessing metabolic activity in tissues and organs[40,44]. This makes PET a critical tool for diagnosing various conditions, such as evaluating brain activity, assessing cardiac performance, and detecting and characterizing tumors, including monitoring their response to treatment[31,40,45]. The mechanism of PET imaging is summarized in **Figure 1.5**[46].

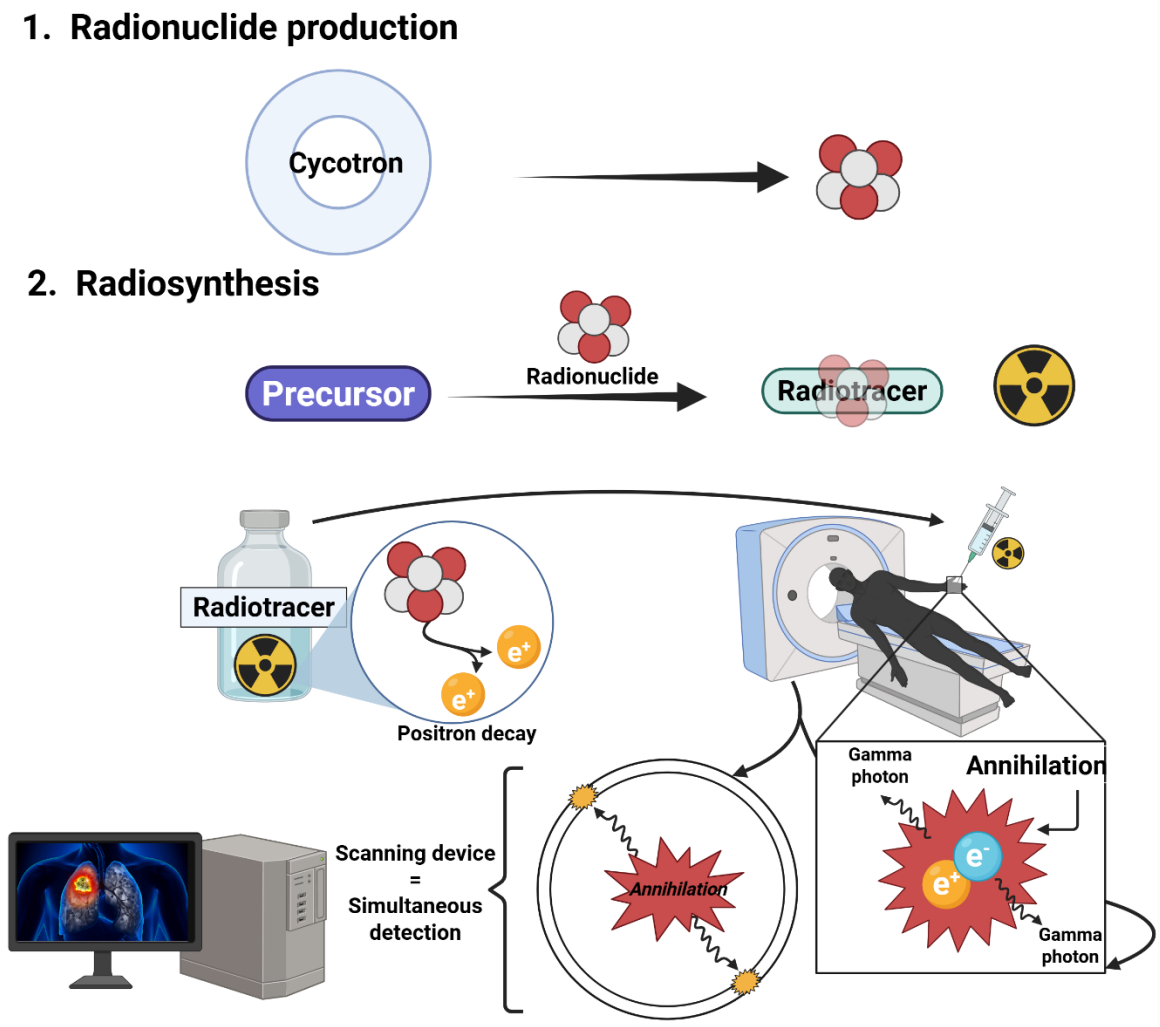

Figure 1.5. PET imaging: how it works.

PET imaging involves administering a radiopharmaceutical tagged with a radioactive isotope that binds to a specific biological target, acting as a biomarker[44,46]. Radionuclides are produced using specialized facilities, such as cyclotrons or generators, depending on their production requirements[26,46]. These radionuclides are chemically incorporated into molecules through radiosynthetic reactions to yield the desired radiotracer[46,47]. After injection into the body, the radiotracer accumulates preferentially in the target tissue[29,46]. The radionuclide undergoes β+ decay, emitting a positron that collides with an electron, resulting in annihilation[33,46]. This process produces two photons, each with an energy of 511 keV, traveling in nearly opposite directions[31,46]. These photons are detected by ring-shaped detectors, and the data is used to reconstruct an image that maps the distribution of the radiotracer within the body[46,48]. This imaging provides critical insights into physiological processes occurring in the patient[46].

The most common radioisotopes for the PET imaging modality include ^{11}C (half-life = 20.3 minutes), ^{18}F (half-life = 109.8 minutes), ^{13}N (half-life = 9.97 minutes), ^{64}Cu (half-life = 12.7 hours) and ^{68}Ga (half-life = 67.8 minutes)[46,49]. Nuclear properties of commonly used short-lived radionuclides are presented in **Table 1.2**[46,50].

Table 1.2. Characteristics of commonly used positron emitting radionuclides.

Isotope	Half-life	Mode of decay	Common source
^{82}Rb	1.3 min	β^+ (95%)	Generator
^{15}O	2 min	β^+ (100%)	Cyclotron
^{13}N	10 min	β^+ (100%)	Cyclotron
^{11}C	20.4 min	β^+ (100%)	Cyclotron
^{68}Ga	67.7 min	β^+ (89%)	Generator
^{18}F	109.8 min	β^+ (97%)	Cyclotron
^{64}Cu	12.7 h	β^+ (17%)	Cyclotron

Among the various existing positron-emitting nuclides, fluorine-18 (^{18}F) is the most used radionuclide for PET imaging[48]. ^{18}F is ideal for routine PET imaging due to its excellent characteristics over other nuclides[46,48]. For example, ^{18}F is efficiently produced in high quantities by cyclotrons, a type of particle accelerator that generates charged particles in the ion chamber. (**Fig. 1.6**)[30,46]. It decays via a high β+-emission with a branching ratio of ~97%,

and its nearly 120-minutes half-life allows multistep radiosynthesis, access to a broad variety of PET radiotracer precursors and short-distance transport[51]. ^{18}F has a relatively low maximum positron energy (635KeV), giving it a short positron range, which favorably increases the spatial resolution limits of PET to ~1 mm[51,52]. Moreover, the medium-length half-life also has the benefit of clearing from the body quickly[46,52].

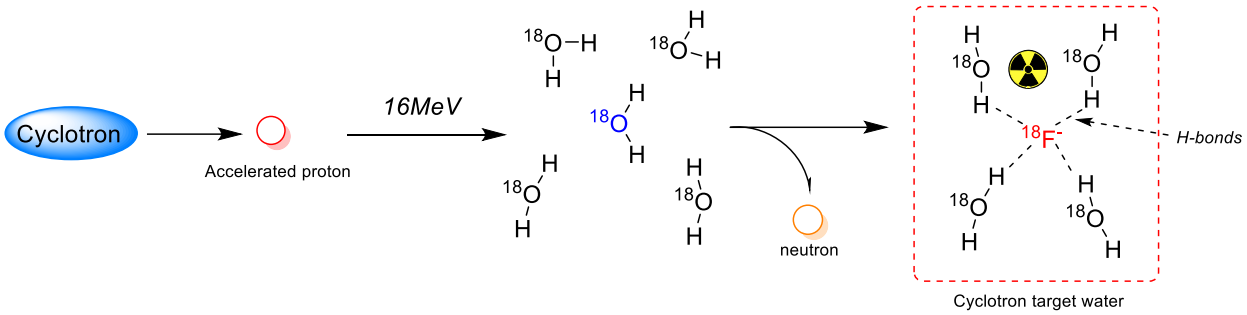

Figure 1.6. Production of ^{18}F. Cycltron-accelerated protons are bombarded on oxygen-18 enriched water.

1.2.3 ^{18}F-Radiofluornation

Fluorine, due to its unique physical and chemical properties, serves as a bio-isostere for hydrogen, carbonyl, sulfonyl, and cyanide groups[53,54]. In drug design, fluorine is frequently incorporated into small molecules to block sites susceptible to oxidative metabolism, thereby enhancing the metabolic stability of compounds and prolonging their action *in vivo*[51,52]. Additionally, the greater lipophilicity of fluorine compared to hydrogen improves the membrane permeability of compounds, reduces the generation of active metabolites, minimizes enzyme-mediated metabolism, and enhances drug potency and bioavailability[51,52,55].

In radiochemistry, the strategies for introducing ^{18}F differ significantly from those in conventional organic chemistry due to the decay characteristics of this radionuclide[53,56]. Because ^{18}F has a short half-life (~110 minutes), radiosynthesis reactions must be rapid (typically completed within 30 minutes) to maximize radiochemical yield and minimize decay losses[53,54]. Furthermore, severe precautions are required to ensure radiation safety during these processes[53,54]. The radiolabeling process of introducing fluorine-18 can be categorized into direct and indirect radiolabeling, while the chemical mechanisms can involve electrophilic or nucleophilic labeling[53,54,57]. The most frequently used method for alkyl [^{18}F] is nucleophilic substitution labeling[54,57]. This method involves replacing a leaving group with [^{18}F] and is widely used for synthesizing radiotracers[54]. Based on the different labeling mechanisms (S_N2

and S_NAr) and substrate reactvity, introducing [$^{18}F^-$] can be accomplished through both aliphatic and aromatic nucleophilic substitution (**Fig. 1.7**)[53,54].

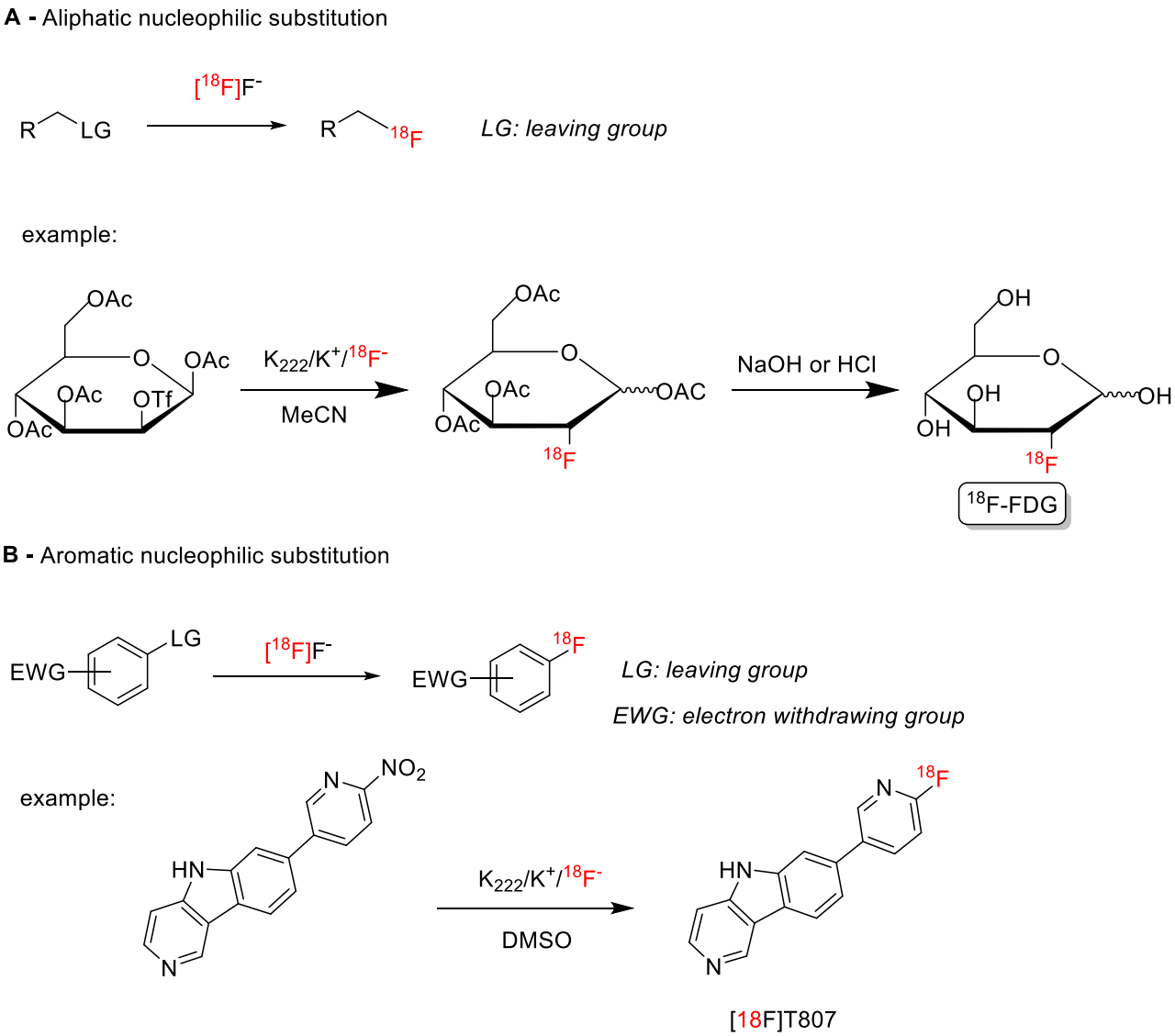

Figure 1.7. Nucleophilic ^{18}F-Fluorination.

An important example of aliphatic nucleophilic [^{18}F]-labeling is the production of [^{18}F]FDG[24,45,58]. In fluorinated compounds, compared with sp^3, the C-F bond strength is higher in sp^2 because sp^2 hybridized carbons have a higher s-character (33%) than sp^3 hybridized carbons (25%), leading to sp^2 C-F bonds being generally more stable than sp^3 C-F bonds[51,52,55]. In ^{18}F-labeled aromatic compounds, sp^2 C-^{18}F bonds also show higher stability than sp^3 C-^{18}F bonds, making them less prone to defluorination during metabolic processes *in vivo*[51,52]. However, introducing [^{18}F] into aromatic compounds is challenging due to the poor reactivity of non-activated aromatic rings[51,52,59]. Strategies and approaches to address this challenge in the thesis are further discussed in **Chapters 2 and 3**.

1.2.4 [^{18}F]FDG PET/CT for Cancer Diagnosis

The most used radiotracer in PET imaging is [^{18}F] Fluorodeoxyglucose ([^{18}F]FDG)[43,45]. Since its development in 1976, FDG-PET has become a cornerstone of clinical oncology, used in the diagnosis and evaluation of over 80% of cancers[24,58]. The biological basis for [^{18}F]FDG in cancer imaging is the Warburg effect, a metabolic adaptation in cancer cells that favors aerobic glycolysis over oxidative phosphorylation (aerobic respiration)[24,35]. This shift allows cancer cells to rapidly divide and proliferate[35,43]. Although aerobic glycolysis is less efficient at producing ATP compared to aerobic respiration, it supports cancer cells by generating biosynthetic precursors needed for growth[43,45].

To compensate for this inefficiency, cancer cells consume significantly more glucose than normal cells[45]. Since [^{18}F]FDG is a glucose analogue, it is taken up and accumulates in cancer cells due to their heightened glucose metabolism[45]. PET scans detect this accumulation, creating detailed three-dimensional images of radiotracer distribution that reflect metabolic activity[43]. These images are used to diagnose and evaluate cancer by highlighting areas of abnormal glucose uptake[43,45].

Clinically, hybrid imaging techniques such as PET/MRI, PET/CT, and SPECT/CT are increasingly used to combine the strengths of different imaging modalities[60]. For example, PET/CT integrates the functional imaging capability of PET, which highlights metabolic activity, with the anatomical detail provided by CT, enabling a more comprehensive assessment of disease (**Fig. 1.8**)[61,62].

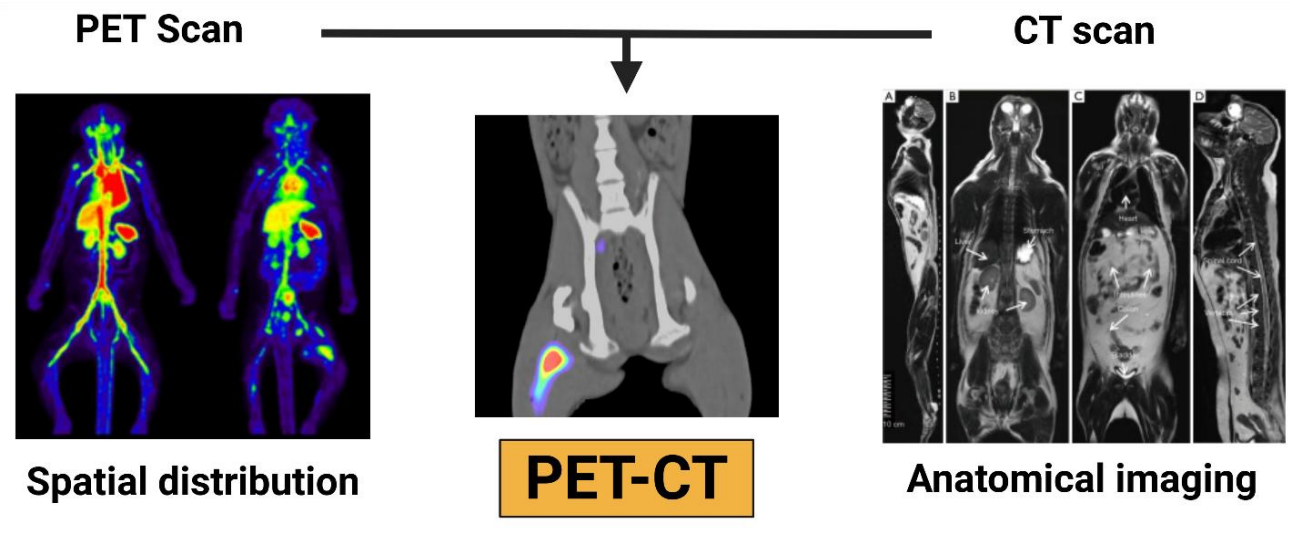

Figure 1.8. The images of PET/CT scan.

[^{18}F]FDG accumulates in cancer cells due to their elevated glucose metabolism, enabling PET/CT scans to generate detailed three-dimensional images of radiotracer distribution[43,61]. These images reveal areas of abnormal metabolic activity associated with cancer[63]. However, [^{18}F]FDG has notable limitations, particularly in breast cancer, where its specificity is challenged by uptake in non-malignant tissues, such as inflammatory or fatty tissues, leading to potential false positives[61,64,65]. High [^{18}F]FDG uptake may result from inflammatory or tumorous conditions and can also accumulate in fatty tissue rather than mammary tumors, leading to false positives and reduced staging accuracy[61,64]. Similarly, [^{18}F]FDG has limitations in diagnosing lung cancer, particularly in patients with infectious diseases[64,66]. Early-stage lung cancer can be difficult to detect due to metabolic overlaps with other lung conditions, and high [^{18}F]FDG uptake may result from infections such as tuberculosis or sarcoidosis rather than malignancy[64,66]. Therefore, there is an urgent need for diagnostic and therapeutic tools with greater accuracy to improve the clinical use of radiotracers.

1.3 G protein-coupled receptors (GPCRs)

1.3.1 What are GPCRs?

A successful PET imaging agent is a validated radiopharmaceutical that targets a biologically relevant receptor[67]. A receptor is a protein that triggers a biological response when activated by its specific ligand[68]. G protein-coupled receptors (GPCRs) are the largest family of membrane proteins, encoded by approximately 1000 genes in the human genome[69]. GPCRs mediate signal transduction by responding to diverse stimuli, including photons, ions, neurotransmitters, peptides, odorants, and small molecules such as hormones and lipids[69,70]. GPCRs are classified into four main classes, Class A (rhodopsin-like), Class B (secretin-like), Class C (metabotropic glutamate/pheromone receptors), and Class F (Frizzled/Smoothened) based on sequence homology, ligand binding, and structural characteristics[70,71]. Specifically, compared with other classes, Class A encompasses the largest group, including rhodopsin, adrenergic receptors, and dopamine receptors (**Fig. 1.9**)[71,72].

Structural characteristics of GPCRs share a conserved core of seven transmembrane α-helices connected by extracellular and intracellular loops[71,72]. The extracellular regions, including the N-terminus and loops, interact with diverse ligands, such as neurotransmitters, hormones, and peptides, facilitating receptor activation[72,73]. The intracellular regions, particularly the C-terminus and intracellular loops, engage signaling proteins like G proteins, β-arrestins, and kinases, driving downstream signaling pathways[73,74]. Recent advancements in structural

biology, particularly X-ray crystallography and cryo-electron microscopy (cryo-EM), have provided high-resolution insights into GPCR conformational dynamics, revealing how ligand binding stabilizes active or inactive receptor states[73,74].

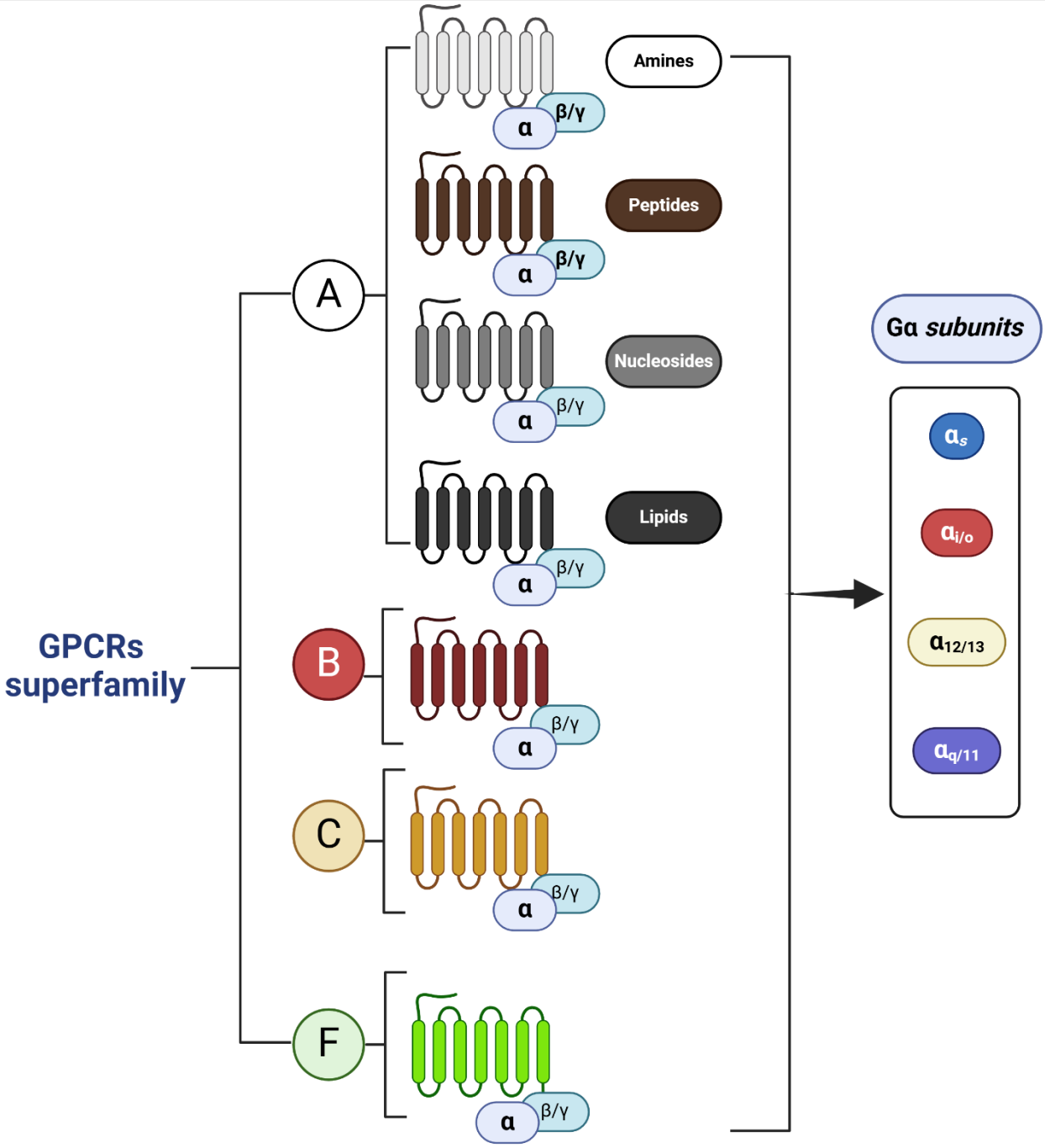

Figure 1.9. The classes of GPCRs consist of seven-transmembrane proteins located in the cell membrane. G proteins are made up of alpha (α), beta (β), and gamma (γ) subunits.

GPCRs regulate an incredible range of bodily functions and exhibit two classifications of signaling mechanisms: G protein-dependent and G protein-independent[73–75]. In the canonical pathway, activated GPCRs engage heterotrimeric G proteins, which consist of three subunits:

Gα, Gβ, and Gγ[74]. The type of Gα subunit determines the specific signaling cascade initiated[75]. For instance, G_s activates adenylate cyclase, increasing cyclic AMP (cAMP) levels and stimulating protein kinase A (PKA), which regulates numerous cellular responses[75]. $G_{i/o}$ inhibits adenylate cyclase, reducing cAMP levels and downregulating related pathways[75]. $G_{q/11}$ activates phospholipase C (PLC), generating second messengers' inositol trisphosphate (IP3) and diacylglycerol (DAG), which mobilize intracellular calcium and activate protein kinase C (PKC), respectively. $G_{12/13}$ interacts with Rho GTPases, modulating cytoskeletal remodeling and promoting cell migration[74–76]. GPCRs also utilize β-arrestin-dependent pathways, representing a G protein-independent signaling mechanism. β-arrestins regulate receptor desensitization, so called 'uncoupling' from G proteins, and mediate receptor internalization into endosomes, where they can influence receptor recycling or degradation[36,76]. Moreover, β-arrestins act as scaffolds for additional signaling cascades, such as the mitogen-activated protein kinase/extracellular signal-regulated kinase (MAPK/ERK) pathway[36,76].

In 2012, the significance of GPCRs in physiology and medicine was highlighted by the Nobel Prize in Chemistry, awarded to Robert Lefkowitz and Brian Kobilka for their breakthrough of research on GPCR structure and function[77]. Their work provided a molecular-level understanding of how GPCRs transmit signals, paving the way for the development of targeted therapies[77,78]. These therapies have revolutionized the treatment of various diseases, including neurological conditions, cardiovascular disorders, and cancer[69,79]. This achievement firmly establishes the central role of GPCRs in drug discovery[79]. Today, GPCRs remain at the forefront of medical research, offering immense potential for advancing therapeutic innovation and improving patient therapeutic outcomes[36,79,80].

GPCRs are one of the most successful therapeutic targets in modern medicine, with approximately 34% of U.S. FDA-approved drugs targeting this receptor family[36,80]. These drugs address conditions such as cardiovascular diseases, mood disorders, pain management, diabetes, and cancer[36].

1.3.2 Known [^{18}F]-labeled PET Imaging Agents Targeting GPCRs

Although GPCRs are highly successful drug targets, with many approved therapies based on this receptor family, no [^{18}F]-labeled PET imaging agents targeting GPCRs have received FDA approval to date[40,81,82]. Most [^{18}F]-labeled radiotracers remain in research or preclinical study phases[81]. Examples include [^{18}F]Fallypride, [18F]KSS3, [^{18}F]FV45, and [^{18}F]5e and [^{18}F]5b (**Fig. 1.10**)[50,59,83–85].

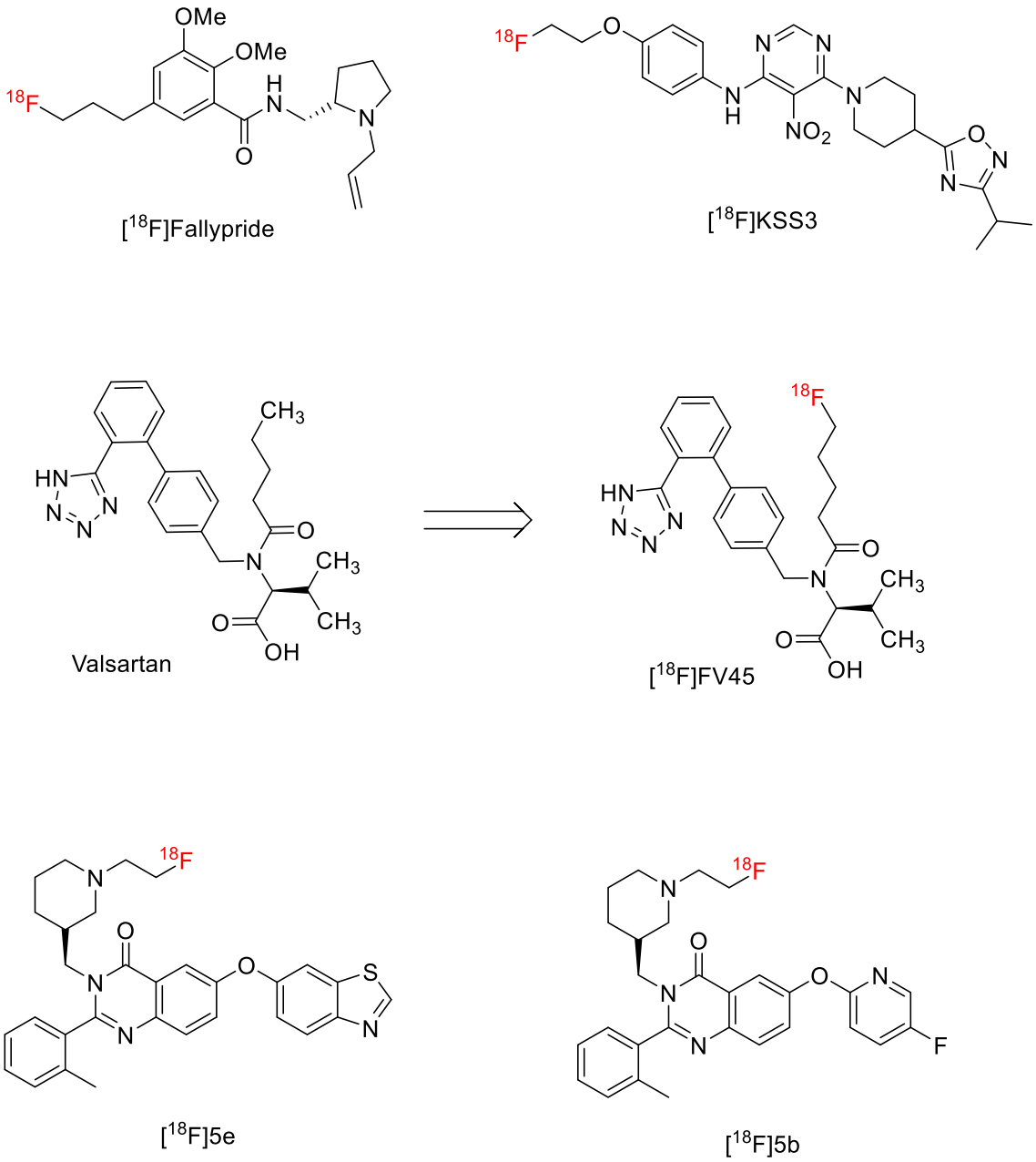

Figure 1.10. The structure of selected [^{18}F]-labeled radiotracers.

Huhtala's group reported [^{18}F]Fallypride, a radiolabeled dopamine D2/D3 receptor antagonist primarily used for neuroimaging[50]. Its high affinity and selectivity allow for visualization of dopamine receptor distribution in the brain[50]. Widely used in preclinical and clinical studies, [^{18}F]Fallypride has applications in studying neurodegenerative and psychiatric disorders, including Parkinson's disease, schizophrenia, and Huntington's disease[50].

Solingapuram Sai's group reported the first PET imaging ligand for GPR119, [^{18}F]KSS3, which is involved in glucose metabolism and diabetes regulation[86]. Preclinical studies demonstrated its high specificity and significant uptake in GPR119-expressing tissues, such as

the liver, confirming its potential to visualize and quantify GPR119 activity[86]. This makes [^{18}F]KSS3 a valuable tool for evaluating glucose homeostasis and GPR119-targeted therapies[86].

Decker's group developed a new 18F-labeled PET tracer, [^{18}F]FV45, it derived from the clinically used AT1 antagonist *valsartan*. [^{18}F]FV45 targeting the angiotensin II type 1 receptor (AT1R), a key GPCR in the renin−angiotensin system (RAS)[84]. Preclinical studies showed significant uptake in the kidneys, reflecting AT1R expression, and blocking studies confirmed its target selectivity[84]. [^{18}F]FV45 holds promise for imaging cardiovascular and inflammatory diseases, as well as potential applications in oncology[84].

Dr. Len Luyt's group reported two fluorine-labeled quinazolinone derivatives, [^{18}F]5e and [^{18}F]5b, targeting the growth hormone secretagogue receptor type 1a (GHS-R1a), also known as the ghrelin receptor[85,87]. With low nanomolar binding affinity, both compounds were [^{18}F] radiolabeled with high purity and demonstrated promising results in murine cancer models[85,87]. These findings suggest their potential for non-invasive imaging of ghrelin receptor expression in cancers where GHSR is differentially expressed[85].

1.4 Overview of Research Project

Positron emission tomography (PET) imaging utilizes positron-emitting radionuclides labeled to molecular tracers to visualize biochemical and physiological processes *in vivo*, enabling non-invasive disease diagnosis[35]. This technique is widely applied in imaging the brain, heart, and cancer[35]. Protease-Activated Receptor 2 (PAR2) and Lysophosphatidic Acid Receptor 1 (LPA1) are G protein-coupled receptors (GPCRs) expressed on the cell membrane[88,89]. Studies indicate that elevated expression of PAR2 and LPA1 is associated with various cancers, including breast, prostate, and lung cancer[90–92]. Notably, PAR2 expression correlates with cancer staging and progression and is linked to tumor metastasis[41,93,94]. Similarly, LPA1 overexpression is observed in aggressive cancers, where its activation enhances cell migration and invasion[89,90]. PAR2 activation also promotes pro-inflammatory signaling, angiogenesis, and resistance to apoptosis, contributing to an aggressive tumor phenotype[95,96]. Likewise, LPA1 activation supports tumor cell proliferation, survival, and metastasis through downstream signaling[97,98]. Armed with this knowledge, the purpose of this thesis is to focus on developing novel small molecules targeting PAR2 and LPA1 as potential PET imaging agents for lung cancer diagnosis and evaluating these compounds for their therapeutic potential for lung cancer treatment[11,14].

More specifically, the first two years of my studies involved expanding the array of PAR2 antagonists based on a lead compound, AZ3451[99]. Four different series of AZ3451 derivates

were designed, and a total of 15 compounds, were synthesized. All the compounds were fully characterized by Mass Spectrometry (MS), Proton-NMR (^{1}H -NMR), and achieved 95% purity as confirmed by HPLC-MS. Collaborator Dr. Rithwik Ramachandran from University of Western Ontario (UWO) performed functional assays to evaluate all compounds for their therapeutic potential. They assessed the functional activity of these compounds by measuring PAR2-dependent calcium signaling, β-arrestin1/2 recruitment, and Mini-G protein coupling. A para-fluorine containing compound was selected as the candidate for radiolabelling studies to introduce ^{18}F into the candidate compound. A site-specific and one-step radiolabelling method that introduces ^{18}F into molecules was performed, called Spirocyclic Iodonium Ylide (SCIDY) technology[46,57,100]. The corresponding precursor—SPIAd iodonium (III) ylide—was synthesized and characterized. A one-step fluorination reaction with fluorine-19 using the SPIAd precursor and Tetrabutylammonium fluoride (TBAF) was successful. Subsequent studies focus on optimizing the reaction conditions for ^{18}F-radiolabeling.

In the last two years, this research has focused on developing novel small molecules targeting LPA1 through three different series of structural modifications. The first series is based on RO6842262[101]; two triazole derivatives compounds were synthesized, characterized, and evaluated *in vitro* using the cAMP and wound healing assay by Dr. Zhao in our group. In the second series, the core structure was identified through scaffold hopping and molecular docking studies[102,103]. 23 compounds were synthesized; among them, 18 compounds were fully characterized by mass spectrometry and ^{1}H -NMR, achieving 95% purity as confirmed by HPLC. These compounds are currently being evaluated in our group using cAMP and wound healing assays. The core structure of the third series takes BMS-986278 as an example and combines it with the second series[104]. The synthetic scheme is designed, and four important intermediates are synthesized. The candidate compound from these three series of LPA1 antagonists will be selected for radiolabeling with ^{18}F using SPIAd iodonium (III) ylide. The long-term objective will involve radioligand binding assays for the candidate compound. Finally, the lead imaging agent will then be evaluated *in vitro* and *in vivo* using small animal models of lung cancer.

Chapter Two

Design, synthesis and evaluation of small molecule ligands targeting Protease-activated Receptor 2 (PAR2) as potential diagnostic and therapeutic agents

2.1 Introduction

2.1.1 Protease-Activated Receptors (PARs) Family

From the mid-1960s to the early 1980s, the mitogenic actions of serine proteases, such as thrombin and trypsin, at the cell membrane were noticed and recognized[105–107]. In the 1990s, the receptors responsible for the actions of these proteases, known as protease-activated receptors (PARs), were discovered[107,108]. The PAR family consists of four members: PAR1 to PAR4, and they all belong to the GPCR superfamily[107,108]. PARs are membrane-spanning cell surface proteins, characterized by seven transmembrane domains, and their activation pathways are like those of other GPCRs[106,109]. However, unlike other GPCRs, PARs are not activated by binding a soluble ligand. Instead, they are activated by proteases, primarily serine proteases (**Fig. 2.1**)[109].

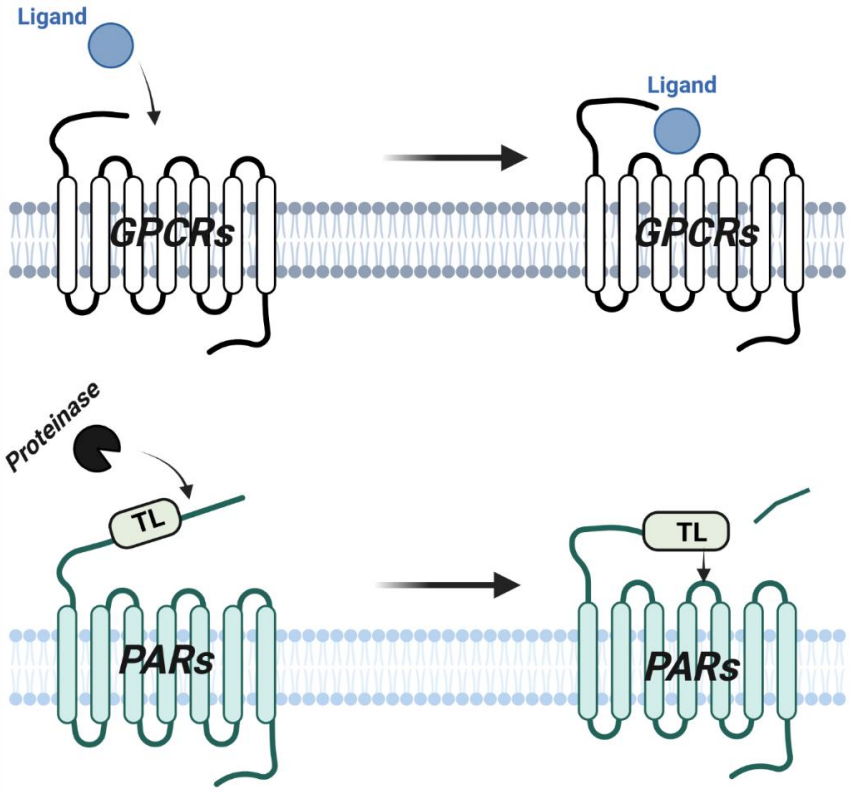

Figure 2.1. The activation feature of most of the GPCRs and PARs.

In the inactive state, PARs have an amino terminus (N-terminal) that 'masks' the ligand[106]. In the active state, this ligand is exposed after a specific protease cleaves the N-terminal portion, creating a newly formed N-terminal known as a tethered ligand (TL)[106,109]. The new TL can then interact with the activation domain on the receptor to initiate receptor activation (**Fig. 2.1**)[106,109].

2.1.2 Structural Features and Activation Mechanisms of PARs

In 2017, the crystal structures of two PAR members, PAR1 and PAR2, were determined, confirming the presence of intramolecular interactions and structural features of the PAR family[99]. PARs span the membrane seven times with alpha-helical segments (TM1-7) and feature three intracellular loops (ICL1-3) and three extracellular loops (ECL1-3)[99,110]. A conserved disulfide bond (red line in **Fig. 2.2**) between ECL2 and TM3 contributes to structural stability, a common feature in all GPCRs[99,110,111]. Proteolytic cleavage of PARs results in the irreversible removal of the N-terminal, exposing the tethered ligand (TL), which then binds to the ECL2 domain[99,111]. This interaction initiates conformational changes and downstream signaling[108]. The TM domains are crucial for ligand binding and conformational changes[108]. Specifically, for PAR1, TL binding triggers changes in TM3 and TM6. For PAR2, the changes primarily occur in TM6, with TM7 stabilizing the receptor's active conformation[99,108]. In PAR4, TM3 and TM5 are often involved in ligand binding and the stabilization of the active state. There are fewer studies on how specific TM domains are involved in PAR3[106,109,112].

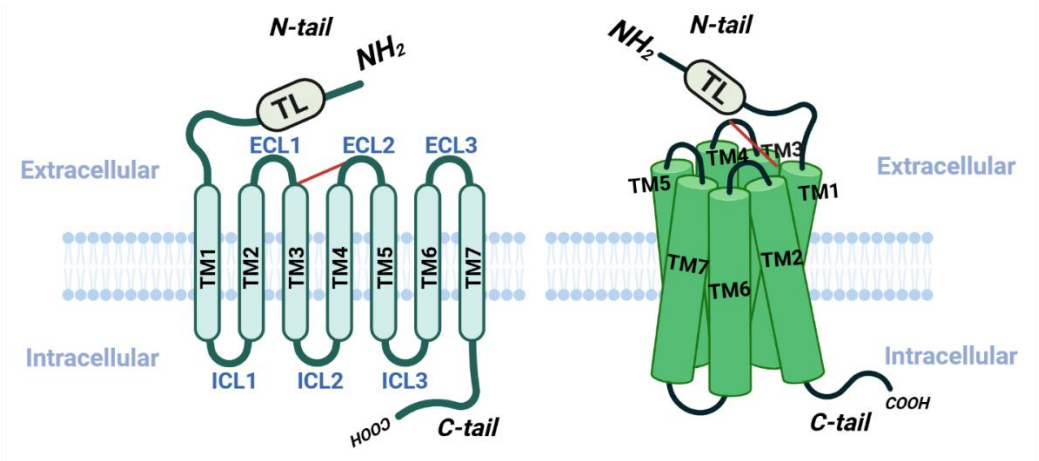

Figure 2.2. The structure of PARs. Schematic (blue) and folded (green).

The PAR activation mediated desensitization, internalization and recycling mechanisms PARs are shown in **Figure 2.3**[106,108,109]. Upon activation, PARs interact with G-proteins by binding guanosine triphosphate (GTP) and guanosine diphosphate (GDP)[106,108]. The G-proteins are heterotrimeric, consisting of α-, β-, and γ-subunits. The α- and γ-subunits are membrane-anchored, while the β-subunit forms a complex with the γ-subunit, known as a heterodimer[106,109]. Based on the type of α subunit, G-proteins can be classified into four major types (Gαi, Gαs, $G\alpha_{12/13}$, and Gαq), each associated with distinct signaling pathways and physiological roles[106,109]. For example, $G_{\alpha i}$ inhibits cyclic adenosine monophosphate (cAMP), modulating pain, heart rate, and immune cell migration. $G_{\alpha q}$ activates phospholipase C,

increasing calcium signaling, which influences inflammation and vasoconstriction. $G_{\alpha 12/13}$ activates RhoA, regulating cytoskeletal remodeling, thereby driving vascular remodeling, fibrosis, and blood-brain barrier integrity.

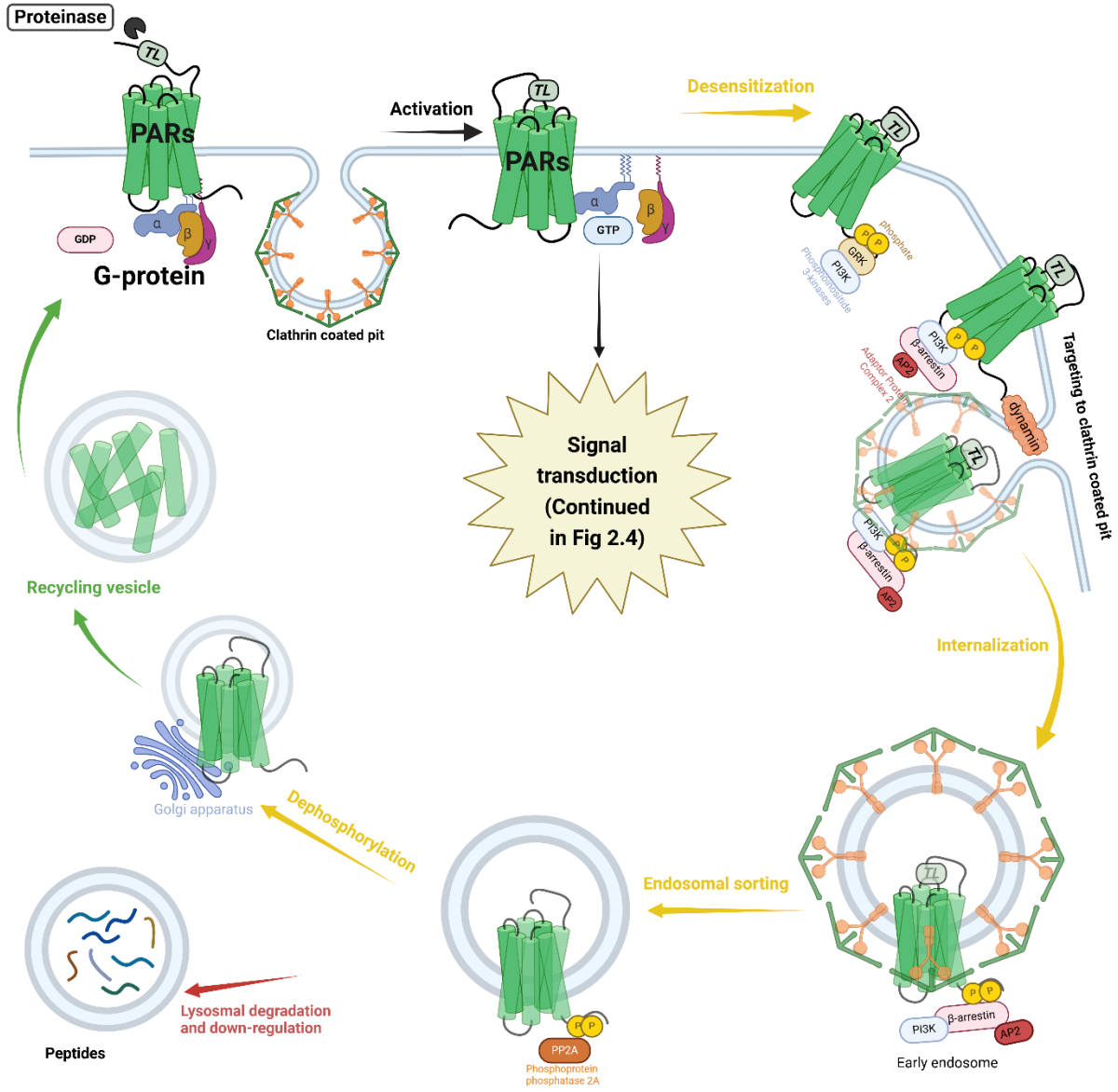

Figure 2.3. PARs activation mediated desensitization, internalization and resensitization mechanisms. Following ligand binding, PARs rapidly couple to signaling effectors (Gα, Gβ/γ, or β-arrestin) to activate intracellular signaling cascades. Termination of PAR signaling involves phosphorylation by GRKs or protein kinase C (PKC) and subsequent β-arrestin binding, leading to receptor desensitization, clathrin-mediated internalization or endocytosis, dephosphorylation by protein phosphatases, and either receptor reinsertion into the membrane or lysosomal degradation.

During the "resting" state, the α-subunit is bound to GDP. Once ligand binding causes a conformational change, it transforms into the "awakening" state, allowing the α-subunit to exchange GDP for GTP and dissociate from the β/γ complex[108]. The activated α-subunit then regulates a membrane-bound protein, catalyzing the production of a second messenger[108,113]. This conformational change can also lead to intracellular phosphorylation of PAR by GPCR kinases (GRKs) or protein kinase C (PKC)[113,114]. The phosphorylated receptor binds with high affinity to β-arrestin-1 and β-arrestin-2, facilitating signal desensitization, PAR internalization, and targeting to lysosomes for recycling and degradation (yellow, green, and red arrow in **Fig. 2.3**)[106,109].

2.1.3 Overview of PAR2 Signaling Pathway

There are four known PARs, designated PAR1, PAR2, PAR3, and PAR4, mainly activated by serine protease[106,108]. In contrast with PAR1, PAR3, and PAR4 are associated with thrombosis, PAR2 is associated with trypsin[99]. While the other three PAR member are primarily linked to inflammatory disease, PAR2 has a distinct role, particularly in cancer progression, which is the focus of our research project[35]. As part of the PAR2 activation feature, upon proteolytic cleavage, trypsin recognizes a substrate sequence (Ser-Leu-Ile-Gly-Lys-Val-SLIGKV- in human, and Ser-Leu-Ile-Gly-Lys-Val SLIGRL- in rat) on the N-terminus located in the extracellular domain[106,108]. A new N-terminus sequence, such as SLIGKV-, is revealed as a tethered ligand that folds back to interact and bind with the ECL2 in the receptor's orthosteric binding pocket, initiating the activated state of PAR2. ECL2 is crucial for guiding the tethered ligand to its binding site and stabilizing ligand interactions[106,108]. Some literature demonstrates that small molecules can act as agonists and directly activate the receptor[106,109]. Additionally, certain peptide sequences mimicking the tethered ligand can also activate the receptor. Existing studies on signal transduction following PAR2 activation focus on three main intracellular pathways (**Fig. 2.4**)[109,113,115].

The PLC−Ca^{2+}−PKC−MAPK cascade, primarily mediated by Gq/11 proteins, plays an important role in inflammation, pain sensitization, and cancer progression[116–118]. Upon activation, phospholipase C (PLC) hydrolyzes phosphatidylinositol 4,5-bisphosphate (PIP_2), generating inositol triphosphate (IP_3) and diacylglycerol (DAG)[117,119]. IP_3 triggers the release of intracellular Ca^{2+}, while DAG activates protein kinase C (PKC)[119]. This cascade ultimately leads to the phosphorylation of mitogen-activated protein kinases (MAPKs), such as extracellular signal-regulated kinase (ERK), driving cell proliferation and inflammatory

responses[117,119]. Dysregulation of this pathway is implicated in inflammatory disease, neuropathic pain, and tumor metastasis in breast, lung, and colorectal cancers[117,119].

The MAPK−JNK−p53 cascade, regulated by Gi/o proteins, acts as a 'double-edged sword', promoting either cell survival or apoptosis[116,118]. C-Jun N-terminal kinase (JNK) phosphorylates c-Jun protein, forming the activator protein-1 (AP-1) transcription factor, which enhances inflammation and tumor growth[117,120]. Consistent JNK activation can lead to neuronal apoptosis, exacerbating neurodegeneration. Conversely, JNK stabilizes p53, causing cell cycle arrest and apoptosis[121]. This pathway influences cancer progression and suppression, fibrosis in liver, lung, and kidney diseases, and neurodegenerative disorders like Alzheimer's and Parkinson's disease[116,121].

The MAPK−JNK−STAT3 cascade, mediated by Gi/o and G12/13 proteins or β-arrestin, plays a key role in chronic inflammation, immune diseases, and cancer metastasis[117]. Upon activation, STAT3 is phosphorylated and translocated into the nucleus, where it regulates immune responses, inflammation, and tumor progression[122]. Aberrant STAT3 signaling contributes to conditions such as colitis, multiple sclerosis, and fibrosis[123]. Additionally, it promotes tumor cell survival, angiogenesis, and immune evasion in gastric, liver, and pancreatic cancers[88,123].

PAR2 signaling through the β-arrestin scaffolding protein activates key downstream pathways, including RhoA (Ras homolog family member A), phosphoinositide 3-kinase (PI3K)/Akt, Src kinase, and extracellular signal-regulated kinases 1 and 2 (ERK1/2)[88,124]. This β-arrestin-mediated signaling is important in cell migration, survival, and receptor desensitization, contributing to cancer progression, inflammation, and cardiovascular disorders[124,125]. In the cardiovascular system, β-arrestin regulates vascular smooth muscle contraction and endothelial function, linking it to diseases such as hypertension and atherosclerosis[124,125]. Additionally, the role of β-arrestin in ERK1/2 activation is implicated in both neuroprotection and neurodegeneration, impacting disorders such as stroke and neuroinflammatory diseases[126,127].

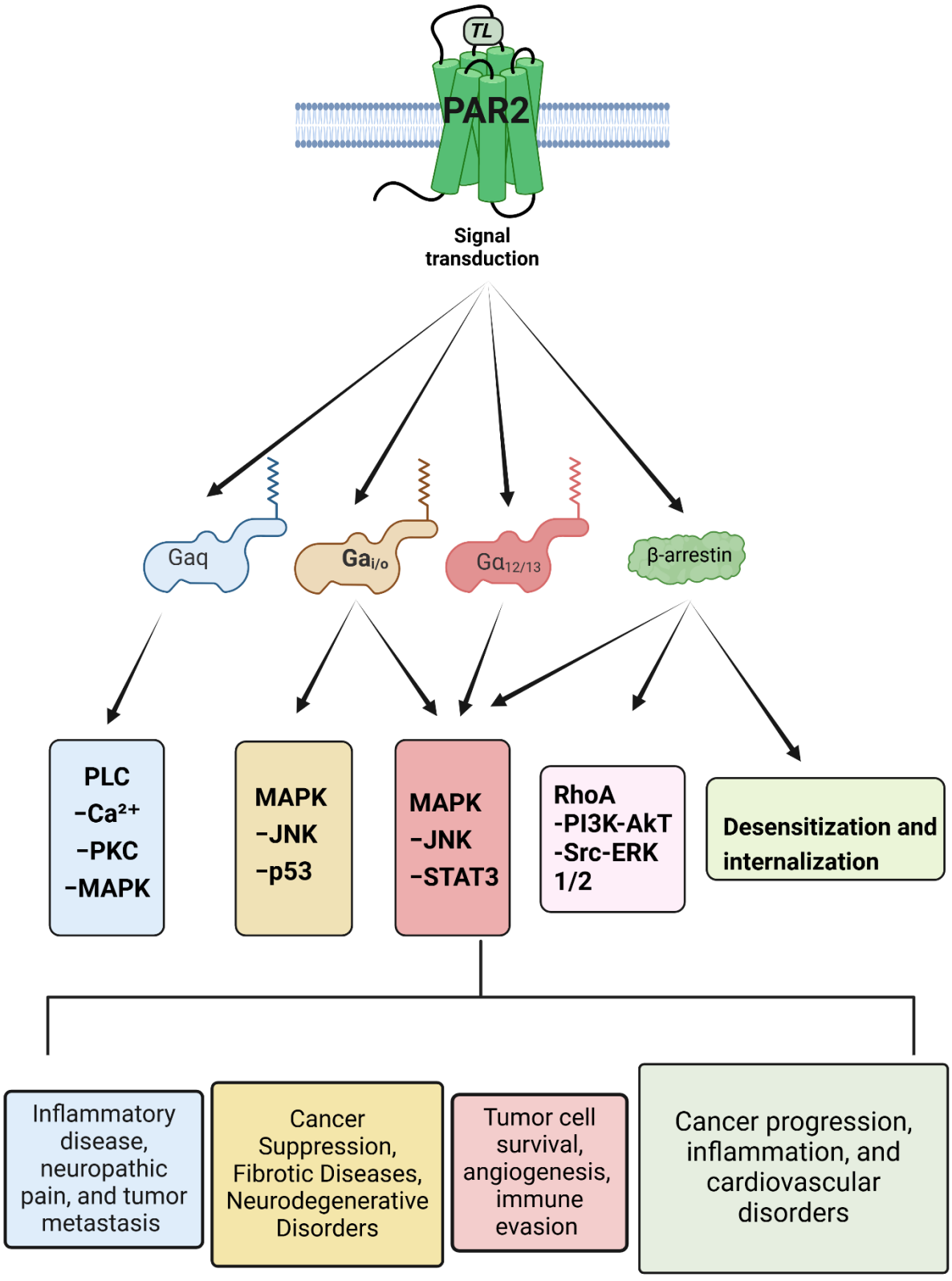

Figure 2.4. PAR2-mediated downstream signal transduction pathways. These pathways regulate diverse cellular functions and disease processes.

2.1.4 PAR2 Knockout Mouse Model for Human Diseases

PAR2 is widely expressed in many cell types, including, but not limited to, endothelial and smooth muscle cells in the cardiovascular, immune, and central nervous systems[119]. Physiologically, PAR2 is mainly involved in inflammation, cell migration, and the functioning of tissue metabolism[41,96,128]. The physiological functions of PAR2 activation have been widely studied using PAR2 knockout (K/O) mouse models, as detailed in **Table 2.1**, the disease models that involve comparisons between wild-type and PAR2 knockout mice[94,114]. Studies have demonstrated that inhibiting PAR2 can alleviate inflammation, pain, metabolic dysfunction, and tumor progression, highlighting its relevance in treating various diseases[94,114]. Targeting and blocking PAR2 activity could have potential diagnostic and therapeutic applications for these human diseases[67,129,130].

Table. 2.1 Summary of PAR2 related disease models and effect of PAR2 knockout (K/O).

Disease Model	**PAR2 Function**	**Therapeutic Effects of PAR2 antagonism/knock out**
Arthritis	PAR2 contributes to joint inflammation, cartilage degradation, and synovial hyperplasia.	PAR2 K/O reduces joint swelling, cartilage erosion, and synovitis, improving mobility and reducing pain.
Dermatitis	PAR2 increases skin inflammation through mast cell degranulation and cytokine release.	PAR2 K/O reduces edema, inflammatory cell infiltration, and cytokine levels in the skin, alleviating dermatitis symptoms.
Asthma	PAR2 activation worsens airway inflammation, enhances eosinophil recruitment, and increases hyperresponsiveness.	PAR2 knockout (K/O) reduces airway hyperreactivity, mucus hypersecretion, and eosinophilic inflammation, suggesting a protective effect against asthma.
Colonic Inflammation (HT29)	PAR2 activation induces apoptosis and cytokine production in epithelial cells.	PAR2 siRNA reduces inflammation-induced apoptosis and cytokine release in HT29 cells, helping to protect epithelial integrity.

Cancer Pain	PAR2 activation sensitizes nociceptors, increasing pain perception in cancer.	PAR2 K/O inhibits hyperalgesia caused by tumor-related factors, alleviating in pain models of cancer.
Hyperalgesia	PAR2 drives nociceptive pain by activating proteases in peripheral sensory neurons.	PAR2 K/O reduces thermal and mechanical hyperalgesia, improving pain thresholds in models of inflammation and injury
Mammary Tumor	PAR2 enhances tumor invasion, metastasis, and tumor microenvironment remodeling.	PAR2 K/O delays tumor development, reduces metastasis, and inhibits cancer cell proliferation.
Retinal Angiogenesis	PAR2 induces pathological angiogenesis via VEGF and endothelial cell activation.	PAR2 K/O reduces neovascularization and vascular leakage in retinal models, helping to prevent vision impairment.

2.1.5 PAR2 in Lung Cancer

Numerous studies have shown that PAR2 promotes lung adenocarcinoma progression through the activation of both G protein-dependent and G protein-independent pathways, as well as EGFR (Epidermal Growth Factor Receptor) activation[131–133]. PAR2 signaling via Gαq, Gαi, and Gα12/13 subunits activates PLC and downstream MAPK/ERK pathways, enhancing tumor cell proliferation and survival[119,128,134]. PAR2 engages β-arrestin scaffolding, sustaining ERK signaling, facilitating cytoskeletal reorganization, and promoting cell migration and invasion[119,131,135]. The interaction between PAR2 and EGFR amplifies tumorigenic signaling that drives angiogenesis, proliferation, and metastasis in lung adenocarcinoma[131,135].

Furthermore, Jiang *et al*. first discovered that blocking PAR2 can reverse drug resistance in NSCLC (**Fig. 2.5**)[136]. One example, osimertinib is a medication used to treat NSCLC[137,138]. It is a third-generation EGFR tyrosine kinase inhibitor (EGFR-TKI)[137,138]. In osimertinib-resistant cells, elevated PAR2 expression activates the β-arrestin-ERK signaling pathway, leading to EGFR activation, which drives downstream processes such as epithelial-mesenchymal transition (EMT)[137–139]. PAR2 inhibition disrupts this signaling cascade, suppressing ERK activation, and attenuating ERK-mediated EMT expression[137–139]. Their studies suggested that PAR2 could be a drug target for osimertinib resistance, and PAR2 inhibition is a promising strategy beneficial for the clinical treatment of NSCLC patients[137–139].

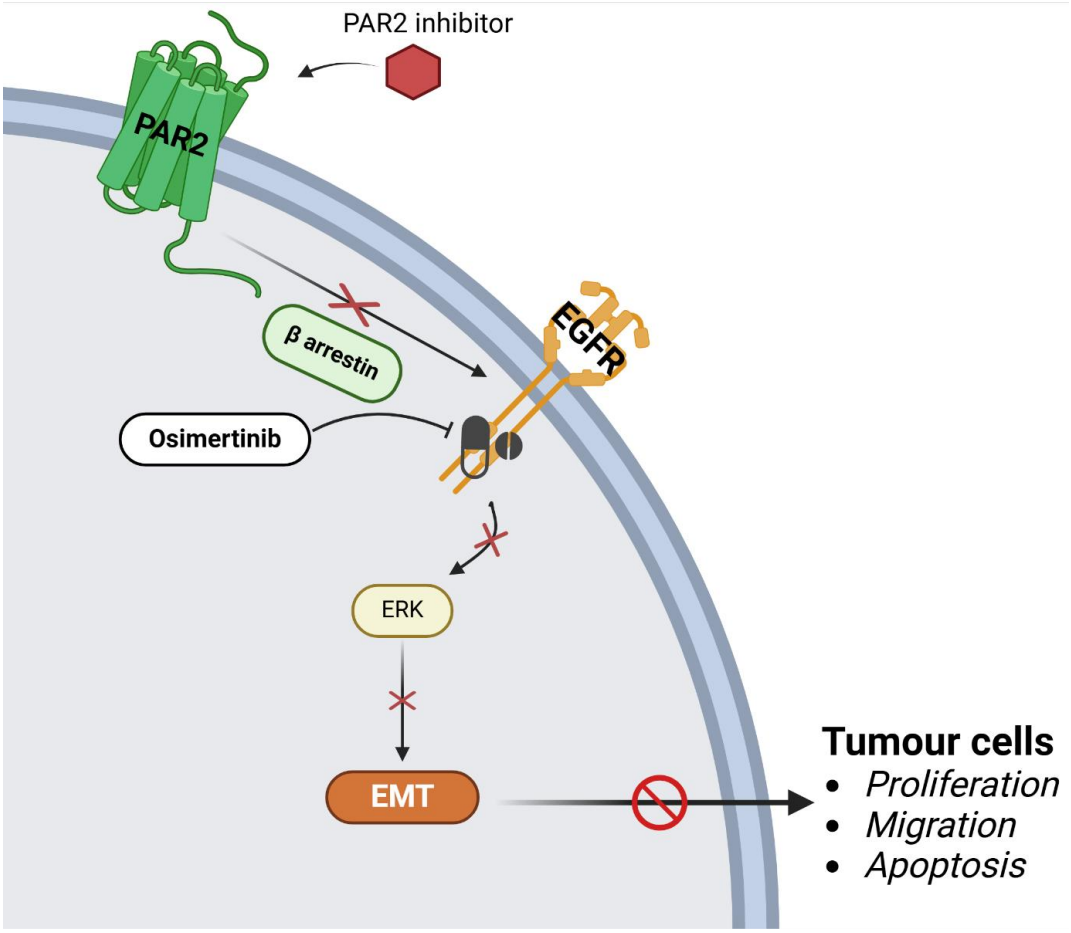

Figure 2.5. Diagram of the mechanism of PAR2 antagonism in Osimertinib resistance.

2.1.6 Known PAR2 Ligands

Since the discovery of PAR2 in the 1990s, numerous studies have focused on developing effective PAR2 ligands[67]. These include a diverse range of molecules such as endogenous proteases, peptides, small molecules, antibodies, and peptidomimetics[67,106,109]. These ligands are designed to either activate or inhibit PAR2, mediating distinct downstream pathways[106,109]. Among them, peptide-based compounds and small molecules have emerged as the most prominent classes (**Fig. 2.6**)[106,108].

In drug development, early investigations into ligands targeting related receptors often focus on designing compounds that mimic the action of natural agonists[109,140]. These efforts aim to replicate the physiological effects of endogenous ligands by activating the receptor, triggering the same downstream signaling pathways[106,109]. This approach is based on the principle that understanding and emulating the natural activation process can provide a foundation for developing therapeutic agents that enhance or restore normal receptor function[109,141]. By identifying and refining these mimetic compounds, researchers can develop drugs that

specifically target receptors involved in various diseases, offering precise and effective treatment options[92,129,141].

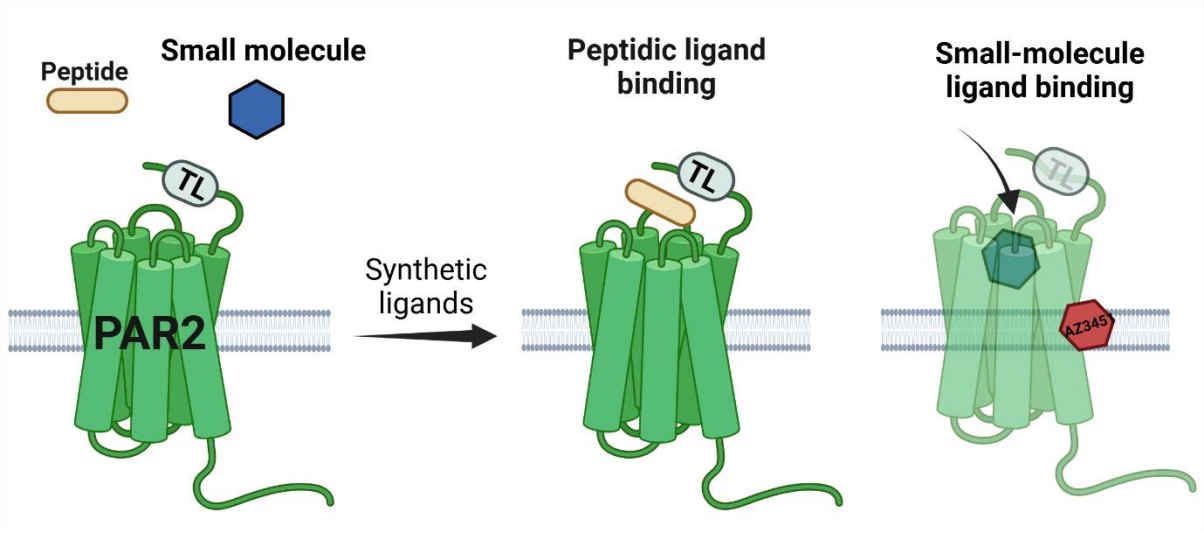

Figure 2.6. Synthetic tethered ligand (TL)-mimicking peptides primarily bind to the extracellular loop 2 (ECL2), while small-molecule ligands interact with specific residues within the transmembrane helices bundle (certain antagonists, such as AZ3451, bind to extracellular regions outside the helix bundle).

Research on peptide-based PAR2 agonists has facilitated the development of PAR2 antagonists by revealing critical mechanisms of receptor activation and ligand-receptor interactions[119,129,142]. Synthetic peptide agonists, such as SLIGRL-NH_2, helped identify the tethered ligand sequence and key structural motifs required for PAR2 activation[142,143]. This understanding enabled the design of peptide-based antagonists, like FSLLRY-NH_2 and LSIGRL-NH_2, which mimic the tethered ligand structure but compete with proteases or activating peptides to block receptor activation[109,143]. These antagonists demonstrated the potential to inhibit PAR2 signaling, particularly in protease-driven systems[109].

Building further on this foundation, the structural insights gained from peptide agonists guided the development of more stable and selective small-molecule antagonists[92,109]. Compounds such as ENMD-1068 were designed to overcome the limitations of peptide-based approaches, including poor bioavailability and receptor specificity[144,145]. Interestingly, a small molecule agonist equipotent to the PAR2 synthetic peptide agonist, GB110, led to the development of two antagonists (GB83 and GB88), bridging the gap between peptide and small-molecule ligands (**Fig. 2.7**)[146,147].

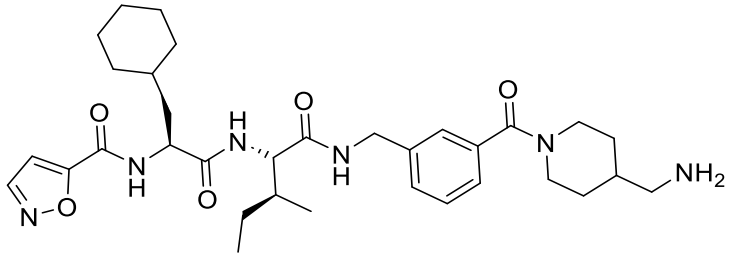

GB 110
EC_{50}~0.28uM

Figure 2.7. Structure of GB110, a peptidomimetic agonist with 0.28uM EC_{50} in intracellular Ca2+ release in HT29 cells.

In designing a novel PAR2-targeting small molecule antagonist, the literature on PAR2-specific ligands in the past two decades was reviewed, summarized, and listed in **Table 2.2**.

Table 2.2. Comprehensive list of selected-known PAR2 antagonist *in vitro* and *in vivo* activity.

Antagonist	*In Vitro / In Vivo* Activity
ENMD-1068[145] IC_{50} ~ 10mM selective PAR2 antagonist 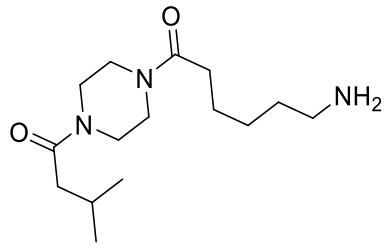	*In vitro*: Weakly inhibits PAR2 signaling by targeting trypsin-induced cleavage. *In vivo*: Reduces joint swelling in arthritis models through protease inhibition.
GB83[141] IC_{50} ~ 2uM Competitive PAR2 antagonist 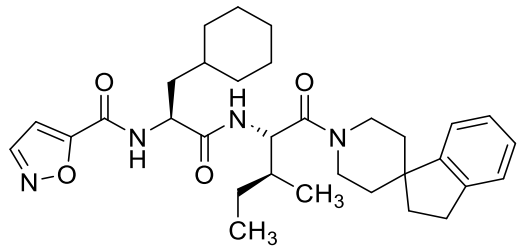	*In vitro*: Suppresses PAR2 calcium signaling and downstream inflammatory responses in cell models.

GB88[92] IC_{50} ~ 2-10uM Full PAR2 antagonist 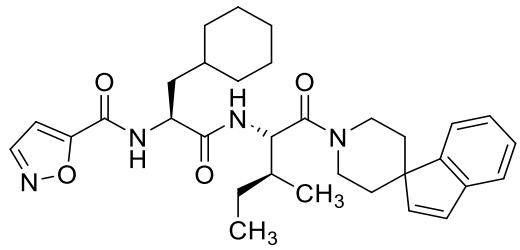	*In vitro*: Inhibits calcium mobilization and cytokine release. *In vivo*: Reduces inflammation in arthritis and colitis by selectively dampening pro-inflammatory signaling.
I-191[148] IC_{50} ~ 10–100 nM (calcium flux, ERK signaling) Negative allosteric modulator of PAR2 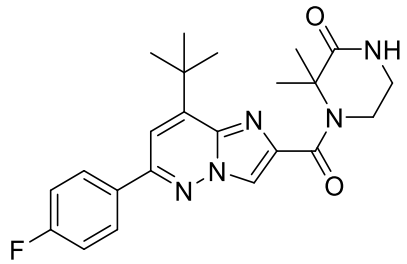	*In vitro*: Suppresses calcium signaling and cytokine secretion. *In vivo*: Reduces inflammatory cytokine release and cancer cell migration by interfering with ERK signaling.
AZ8838[99] IC_{50} ~500nM~5uM Negative allosteric modulator of PAR2 Competitive orthosteric PAR2 antagonist 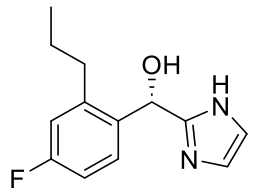	*In vitro*: Inhibits calcium flux, β-arrestin recruitment, and ERK phosphorylation. *In vivo*: Reduces paw swelling and inflammation in rat models.

AZ3451[99] IC_{50} ~ 23nM (calcium flux) Negative allosteric modulator of PAR2 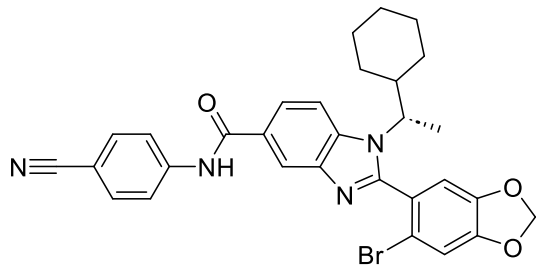	*In vitro*: Blocks peptide-induced calcium flux, IP_1 production, and ERK phosphorylation. *In vivo*: Reduces inflammation in rat paw edema models.
I-287[93] IC_{50} 45-500 nM (calcium flux, RhoA activation) Negative allosteric modulator of PAR2 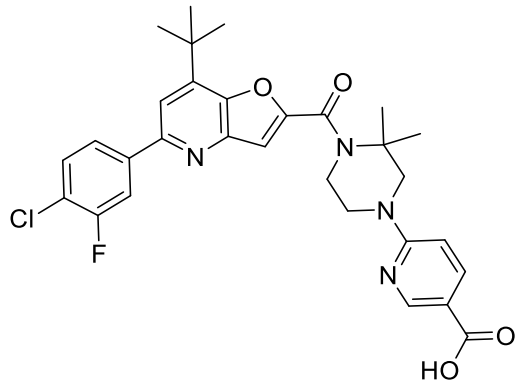	*In vitro*: Reduces IL-8 secretion and inflammation-associated calcium signaling. *In vivo*: Suppresses inflammatory response in paw edema models.

ENMD-1068, a piperazine derivative, was the first non-peptidic small molecule PAR2 antagonist reported by NeoPharm in 2010[144,145]. It is a weak and slightly selective PAR2 antagonist at millimolar concentrations, requiring very large doses to attenuate several PAR2-mediated physiological responses[109]. It is selective for PAR2 over other PARs *in vitro*, but its low potency likely limits *in vivo* selectivity[144,145]. Subsequently, GB83 and GB88 were developed by Alexander's group at the University of Queensland, focusing on PAR2's role in inflammation and disease[141]. GB83 and GB88 share a similar chemical structure, with the key difference being the unsaturated carbon chain attached to the N-terminal group. GB88 features a fully saturated N-terminal carbon chain, which alters its binding dynamics to enable

interaction with an allosteric site on PAR2, acting as a full antagonist that blocks receptor activation regardless of agonist concentration[109,141].

In 2017, Cheng *et al.* at AstraZeneca Pharma revealed the crystal structures of PAR2 and reported two novel antagonists, AZ8838 (an imidazole derivative) and AZ3451 (a benzimidazole derivative)[99,149]. Subsequent studies characterized both as potent negative allosteric modulators (NAMs) of PAR2, inhibiting activation by preventing conformational changes in the receptor.AZ8838 binds to a deeply buried allosteric pocket near the extracellular surface of PAR2, while AZ3451 binds to a lipid-facing hydrophobic pocket outside the transmembrane domain[149,150]. AZ3451 is a highly lipophilic ligand. It exhibits potent inhibition with an IC_{50} of ~23nM and has shown anti-inflammatory effects in a rat post-traumatic osteoarthritis model[149].

More recently, two additional PAR2 NAMs, I-191 and I-287, were published[93,148]. Although similarly named, they were developed by different organizations: I-191 by Vertex Pharmaceuticals and I-287 by Paraza Pharma. I-191 inhibits PAR2-mediated calcium signaling, ERK phosphorylation, pro-inflammatory cytokine release, and cAMP accumulation in the human colorectal adenocarcinoma cell line HT29[148]. I-287, characterized as a biased ligand, selectively inhibits Gq and G12/13 signaling pathways while avoiding Gi/o and β-arrestin signaling[93]. It effectively targets inflammatory pathways in paw edema models, reducing inflammation while preserving other receptor functions[93].

2.1.7 MSc Study

My previous MSc research project, the development of novel small molecule targeting PAR2, started in 2019[35]. Given that the first two years of my PhD study was a continuation of the research from my MSc thesis, a brief introduction to my MSc project is presented in this section.

Initial efforts focused on modifying AZ3451; it is a novel, potent (IC_{50} ~23 nM in calcium flux assays), and selective PAR2 antagonist. The structure of AZ3451 is studied into four parts for ligand design: all the analogs share the benzimidazole core. The first series focuses on the R1 position, the aryl amide tail, which is colored in blue. The second series is the R2 group labeled in red, the cyclohexyl substituent. The third series is the R3 group labeled in yellow, the bromoaryl fragment (**Fig. 2.8-A**)[35,99]. Crystallographic studies indicate that AZ3451 binds to an allosteric site outside the helical bundle of PAR2 (**Fig. 2.8-B**)[99,149].

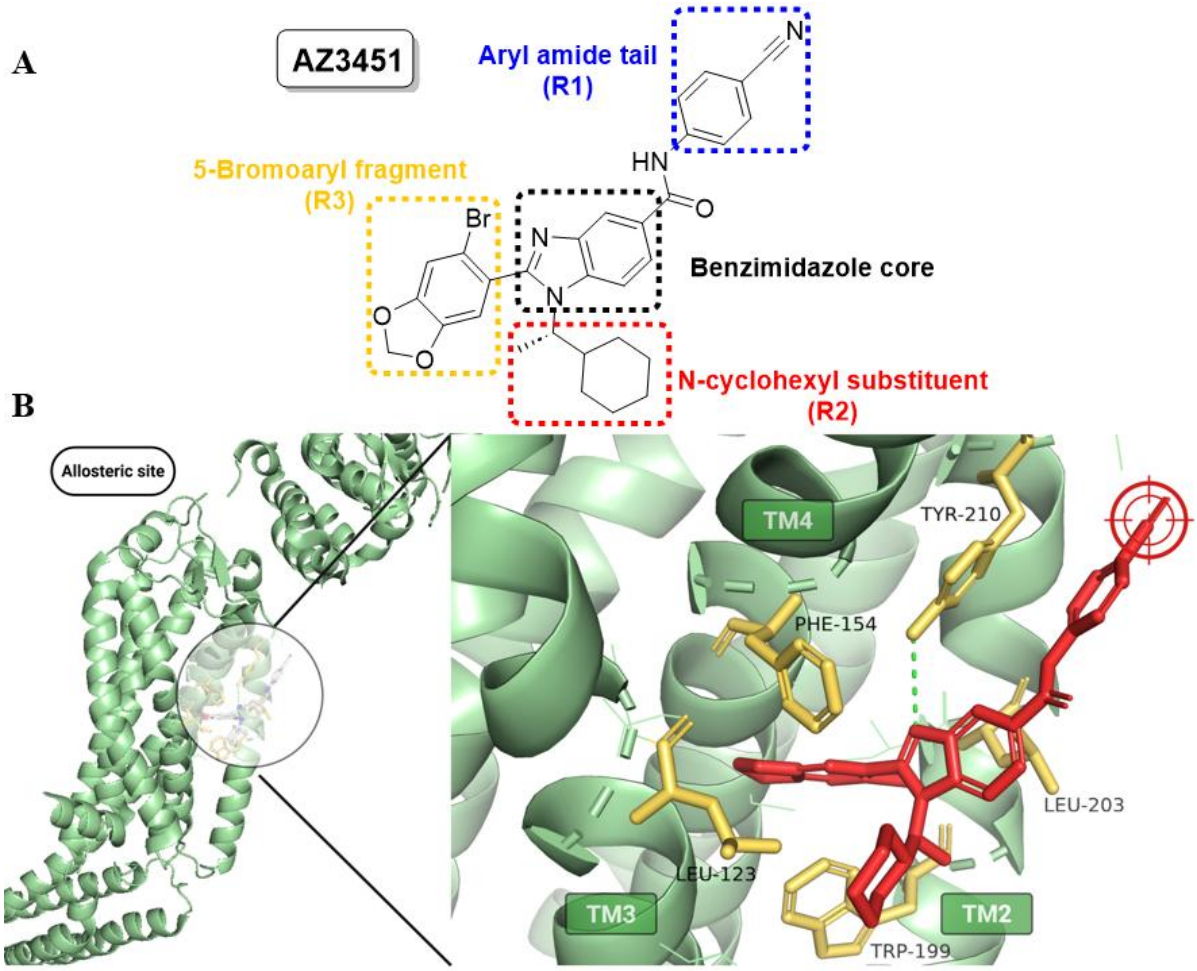

Figure 2.8. **A**. The structure of AZ3451. **B**. The allosteric antagonist AZ3451 binding in the pockets of PAR2. The benzimidazole nitrogen forms a hydrogen bond with Tyr210, highlighted with a green dotted line.

The mechanism of antagonism by AZ3451 is not fully explored; the most plausible mechanism is that this ligand restricts the conformational rearrangement (most like is between TM2, TM3, and TM4) of helical bundle upon PAR2 activation[149]. And molecular docking studies were performed to investigate the binding mode of AZ3451[99]. The detailed discussion of ligand - receptor interaction can be found in my MSc thesis[35]. Importantly, the aromatic ring of the benzonitrile moiety interacts with Try210 through π-π stacking interactions, while this benzonitrile is solvent-exposed and can be readily modified through amide bind coupling in the last step[99]. Therefore, the benzonitrile group can be seen as an access point to introduce new functional groups with variable properties to yield AZ3451 analogues (an arrow indicated in **Fig. 2.8-B**)[35,99].

The synthetic scheme initially executed for the synthesis of AZ3451 was adapted from that reported by Cheng *et al.* with some small modifications (**Scheme 2.1**), the detailed methodology can be found in **Chapter 2.5** (Experimental Procedure)[35,99].

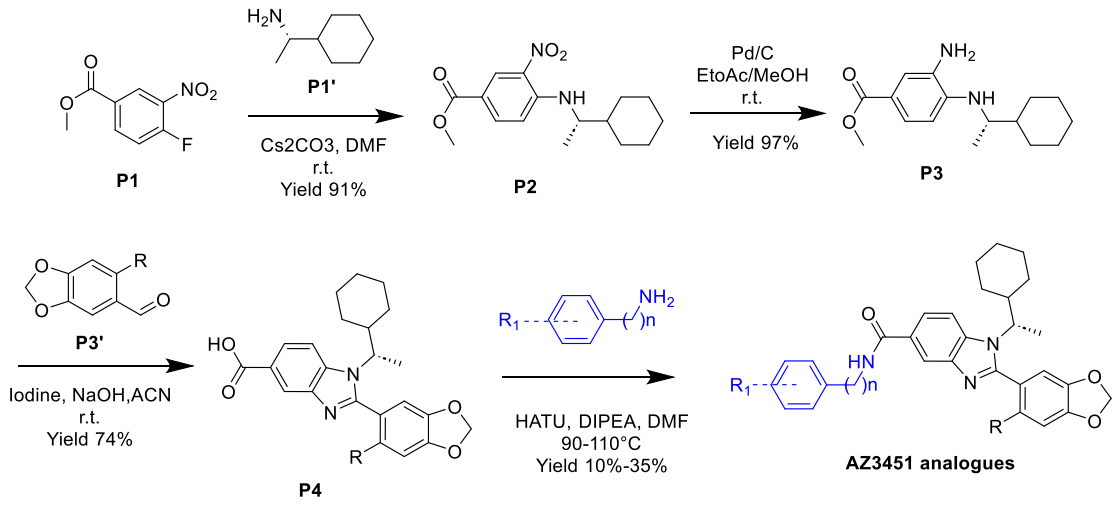

Commercial available chemicals - *P1: Methyl 4-fluoro-3-nitrobenzoate P1': (R)-(−)-1-Cyclohexylethylamine P3': 6-bromobenzo-d-1,3-dioxole-5-carbaldehyde*

Scheme 2.1. The synthetic scheme for AZ3451 analogues. Compound P1, P1', and P3' are commercially available[35]. To enhance clarity and consistency throughout this chapter, all compounds are labeled with a prefix "P" (representing *PAR2*), such as P1, P2, and P3.

Following **Scheme 2.1**, I synthesized and characterized the reference compound and 15 analogues of AZ3451 (structures are presented in **Chapter 2.2**)[35]. Molecular docking using AutoDock Vina and Discovery Studio was performed to predict and visualize the ligand-receptor interactions for all 15 compounds, and they all displayed similar binding modes compared to AZ3451[35,103].

A key finding during my MSc studies was the identification of a conformational isomer issue in AZ3451 and its analogs. (**Fig. 2.9**)[35]. Moreover, based on the proton NMR (^{1}H-NMR) and variable temperature NMR (VT-NMR) spectra, multiple potential conformational isomers exist for AZ3451[35]. These isomers are produced during the cyclization step (the proposed mechanism is in my MSc thesis) and cannot be separated or purified using conventional SiO_2 chromatography or even preparative HPLC.

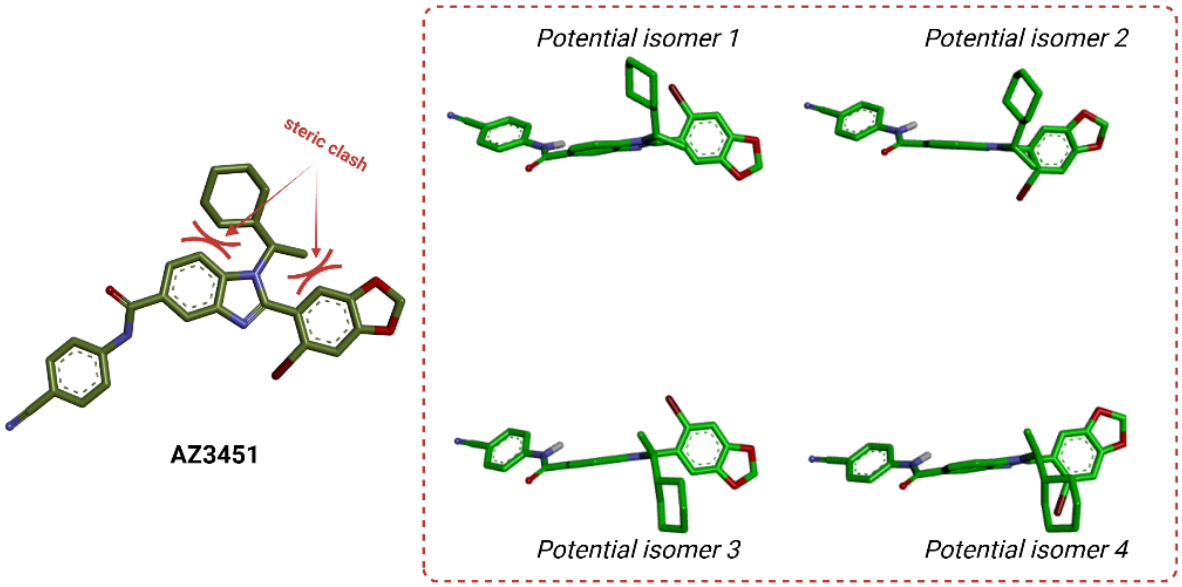

Figure 2.9. A molecular modeling study was conducted to present the structure of AZ3451 and four types of potential conformational isomers. The carbon-carbon bond between the imidazole and aromatic ring of 1,3-benzodioxole cannot freely rotate by 180 degrees. Also, steric hindrance from the methyl group (connected to the methylcyclohexane) affects the protons in the carbon atom connected to the two oxygen atoms in 1,3-benzodioxole[35].

Collaborators from Western University evaluated all the analogues for functional activity to PAR2 (detailed information is presented in **Chapter 2.3**). Data from functional assays are used to select a candidate for ^{18}F-radiolabeling. During my MSc studies, the corresponding precursor and radiolabeling scheme were proposed (**Scheme 2.2**)[35].

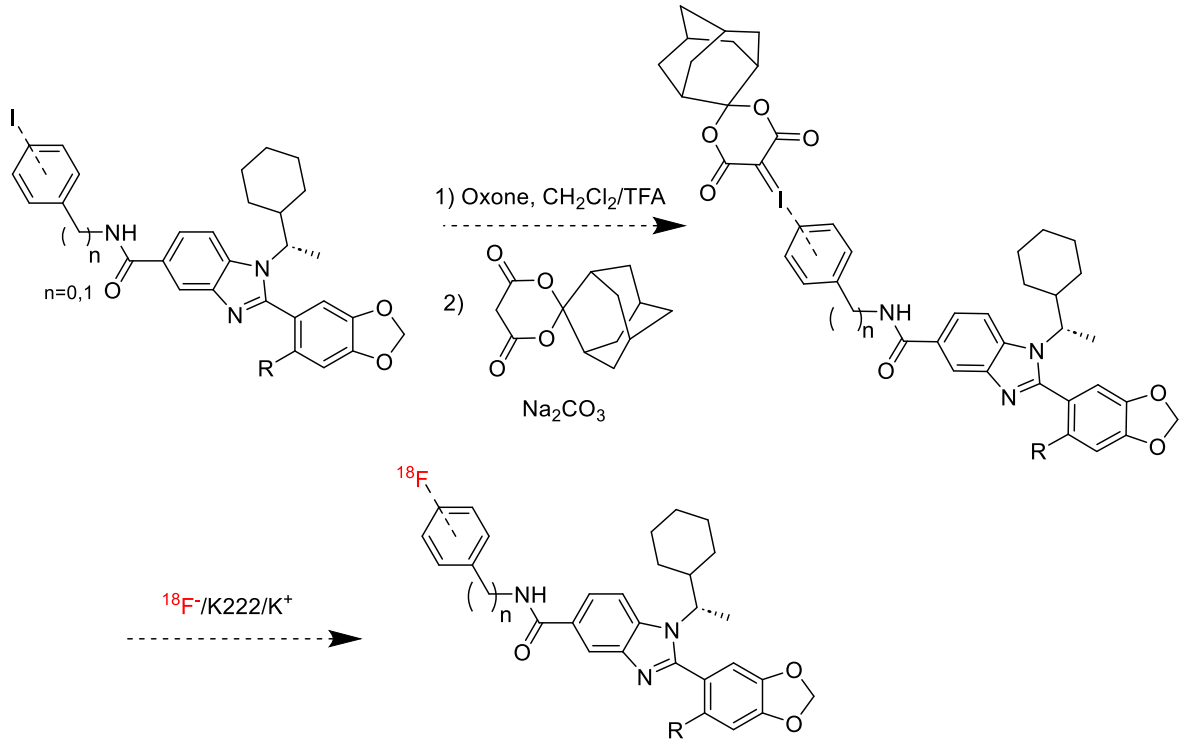

Scheme 2.2. Proposed radiolabeling scheme with SPIAd ylides.

Furthermore, the structure of two different generations of AZ3451 derivates (R_2-R_3) and corresponding synthetic scheme were proposed (**Fig. 2.10**)[35].

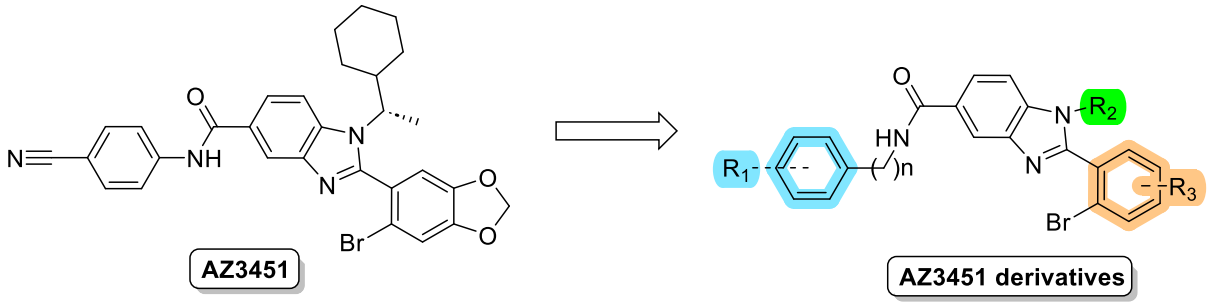

Figure 2.10. The structure of AZ3451 and derivates with R1-3 group.

2.2 Results and discussion

2.2.1 PhD study - Optimizing Synthetic Conditions

This journey continued through my PhD study in 2021. The further studies focused on introducing additional building blocks (R_1 group) to expand the library of AZ3451 analogues through optimizing the reaction condition of the last step (amide bond formation). During the MSc study, it was found that the yield of the last step is around 7% - 12% due to most of selected building blocks containing electron-withdrawing group (EWG). It can indeed impact

the efficiency of amide bond formation by reducing the nucleophilicity of the amine group of selected building blocks. For example, the reference compound containing cyanide group and the yield of last step is 7%.

The use of thionyl chloride ($SOCl_2$) is an improved method for amide bond formation. Using $SOCl_2$ to convert the carboxylic acid into an acid chloride, which is significantly more reactive than carboxylic acids, makes the amide bond formation more efficient, even in the presence of EWG[151,152]. The yields of the corresponding $SOCl_2$ involved final compound were improved to 15%-18% (**Scheme 2.3-A**).

Microwave-assisted synthesis is an efficient technique widely used in organic and medicinal chemistry[153,154]. As an electromagnetic irradiation, microwave irradiation interacts efficiently with polar bonds such as carboxylic acids through dipolar polarization[153,154]. The electromagnetic waves in the microwave frequency range cause dipolar carboxylic acids to rapidly rotate and vibrate, aligning with the oscillating field[155]. This molecular motion generates heat through dielectric heating effects, leading to rapid heating and enhancing the possibility of effective molecular collisions[155]. Additionally, microwave irradiation lowers the activation energy of the reaction, enabling faster intermediate formation[155]. These intermediates then undergo nucleophilic attack by an amine, forming the desired amide bond[155]. By combining thionyl chloride under microwave conditions, the yield of the final step is significantly improved to over 35% (**Scheme 2.3-B and C**).

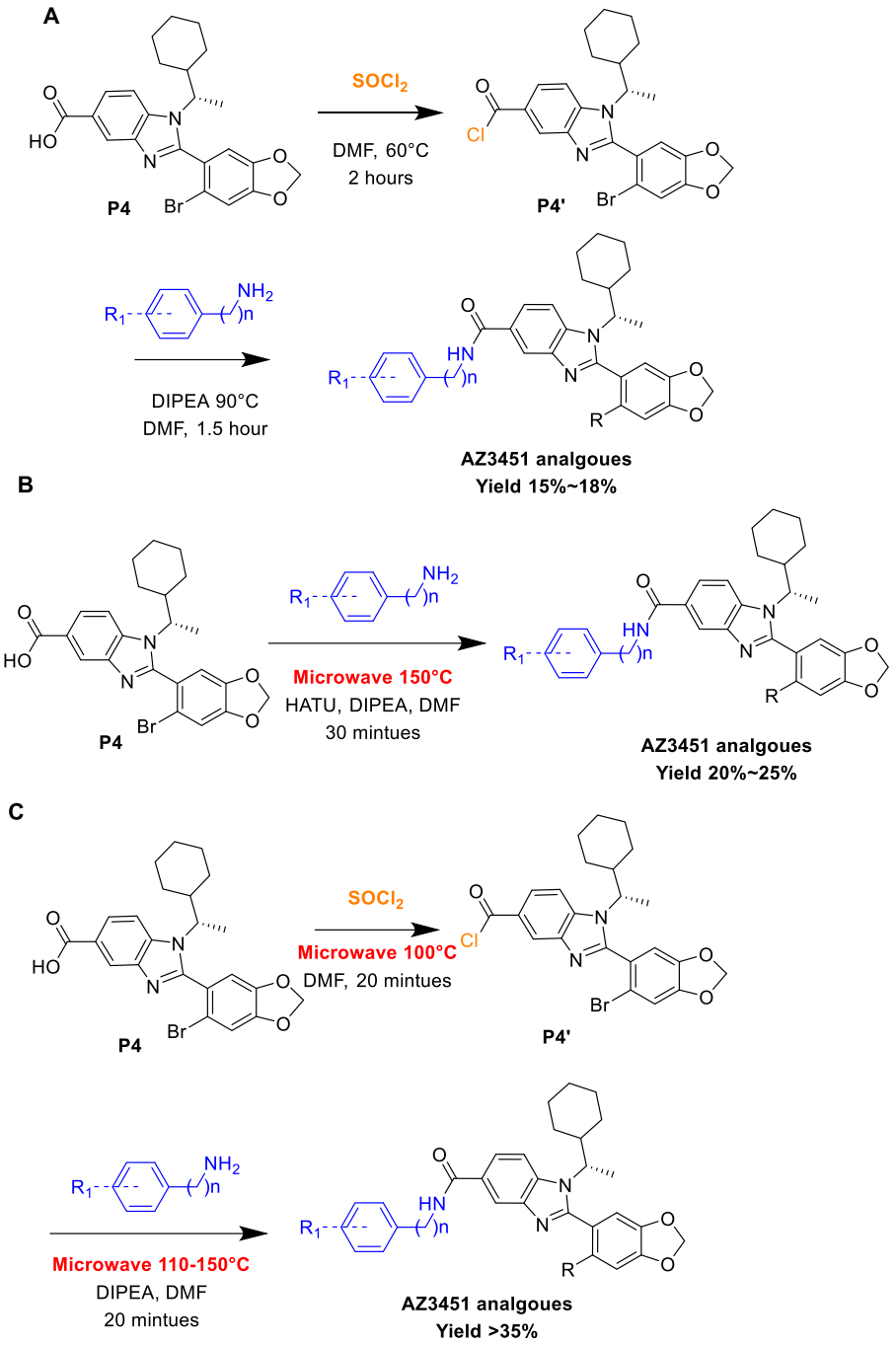

Scheme 2.3. Optimizing the reaction condition by introducing thionyl chloride (A), microwave assisted synthesis (B), and combination of thionyl chloride and microwave assisted (C).

2.2.2 Ligand Design

In drug design, a structural moiety of a starting compound is replaced by other groups to improve the molecule's properties, such as binding affinity, functional activity, and Absorption, Distribution, Metabolism, Excretion, and Toxicity (ADMET)[156,157]. Although AZ3451 is of particular interest due to its high potency and selectivity, developing AZ3451 analogues with

modified functional groups may lead to novel ligands exhibiting functional selectivity (biased signaling) at PAR2.

As shown in **Figure 2.8-B**, the benzonitrile group of AZ3451 does not strongly interact with the receptor[67]. In addition, the cyanide group raises potential pharmacokinetic and safety concerns, including possible metabolic release of cyanide and limited aqueous solubility, which may impair systemic exposure. Therefore, the benzonitrile group serves as a breakthrough point for introducing an aromatic substituent, allowing the analogues to form stronger interactions with the receptor. Our first round of structural optimization will focus on the R_1 group as shown in **Figure 2.11**.

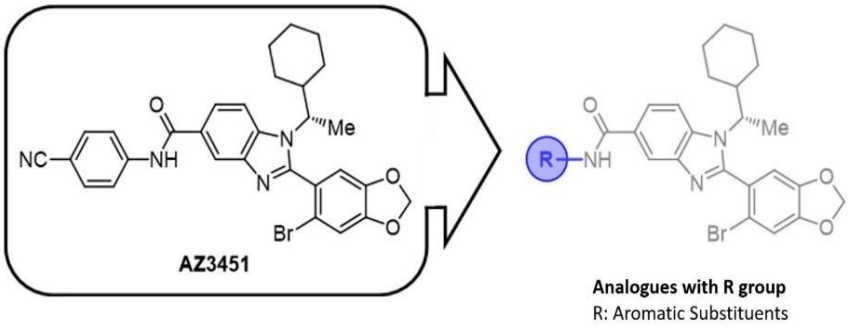

Figure 2.11. AZ3451 analogues with R_1 group.

Halogens (X = F, Cl, Br, and I) are widely used substituents in medicinal chemistry because they enhance ligand properties[158,159]. Introducing halogen atoms into a ligand can form additional stable interactions through halogen bonds, thereby enhancing binding affinity between the ligand and the target protein[158]. Halogen bonds being 'orthogonal' to hydrogen bonds means they do not disrupt existing critical interactions like hydrogen bonding or hydrophobic interactions[158]. Instead, they complement these interactions and further stabilize the binding[158]. For example, bromine and iodine, due to their larger atomic sizes and stronger polarizability, can form specific halogen bonds with key protein residues, enhancing the stability of the ligand-protein complex without interfering with existing hydrogen bonds[158,160]. Fluorine (F) is particularly important in medicinal chemistry[51,52]. Introducing F into a compound increases lipophilicity, favoring hydrophobic binding sites within membranes[55,56]. From a pharmacological perspective, the stable carbon-fluorine bond protects the aromatic ring, allowing fluorinated compounds to delay drug metabolism in the body[51,52,55]. Additionally, given our focus on using ^{18}F to label candidate compounds, the corresponding 'cold' compound is essential for developing a PET imaging agent[54,56,161].

Heterocyclic compounds can participate in a variety of molecular interactions, including acting

as hydrogen bond donors or acceptors, and exhibiting van der Waals forces and hydrophobic interactions[162,163]. These interactions enable heterocyclic compounds to bind to receptors in several ways[162]. Introducing heterocycles to bioactive compounds provides functional groups that can be modified to optimize solubility, lipophilicity, and polarity[162,163]. Additionally, heterocycles come in a variety of shapes and sizes, allowing them to fit the different binding pockets of receptors[92,162]. Heterocyclic aromatic compounds, such as pyridine, have been introduced in this thesis. Unlike a benzene ring, pyridine is a unique aromatic ring[162,163]. The lone pair of its nitrogen atom does not overlap with the π-system of the aromatic ring, contributing to the basicity of pyridine[162,163]. Due to its weak basicity, pyridine can be used to improve the water solubility of drugs[162]. More importantly, in the context of the structure-activity relationship (SAR), varying the position of the fluorine and nitrogen atoms of the pyridine moiety at the *ortho*, *meta*, and *para* positions on the aromatic ring offers significant opportunities for exploration[51,52,164]. Fluorine, due to its high electronegativity and small size, enhances binding affinity, metabolic stability, and membrane permeability[51,52]. The nitrogen atom of the pyridine ring contributes additional interactions through hydrogen bonding with the target protein[163]. This positional variation allows for a systematic exploration of how these substitutions influence the biological activity and selectivity of the compounds[51,163,164].

Furthermore, by adding a bulky group to the ligand, like n-biphenyl and n-phenoxy phenyl, and quinazolinone derivatives, the metabolic stability of ligand will be increased[165,166]. This is because the bulky groups are used as a shield, which is a known steric hindrance[165]. This effect is used to control the selectivity of ligands, potentially enhancing ligand-receptor interactions and avoiding side effects[165]. Our latest synthesized analogues focus on two design strategies: replacing the cyanide group with a bio-isostere and introducing a group to mimic the cyanide group. The first strategy aims to retain the electronic and steric properties of the cyanide group while potentially improving pharmacokinetic profiles by using a bio-isostere[167,168]. The second strategy involves introducing functional groups that mimic the behavior of the cyanide group to enable similar interactions with the biological target[169]. These approaches aim to preserve or enhance the biological activity and selectivity of the compounds[35,169].

2.2.3 The Library of AZ3451 Analogues

A library of 32 AZ3451 analogues was constructed, and to comprehensively explore the structure-activity relationship (SAR) within this library, 15 compounds synthesized during my MSc research were also included (colored in blue in **Fig. 2.12**) [35].

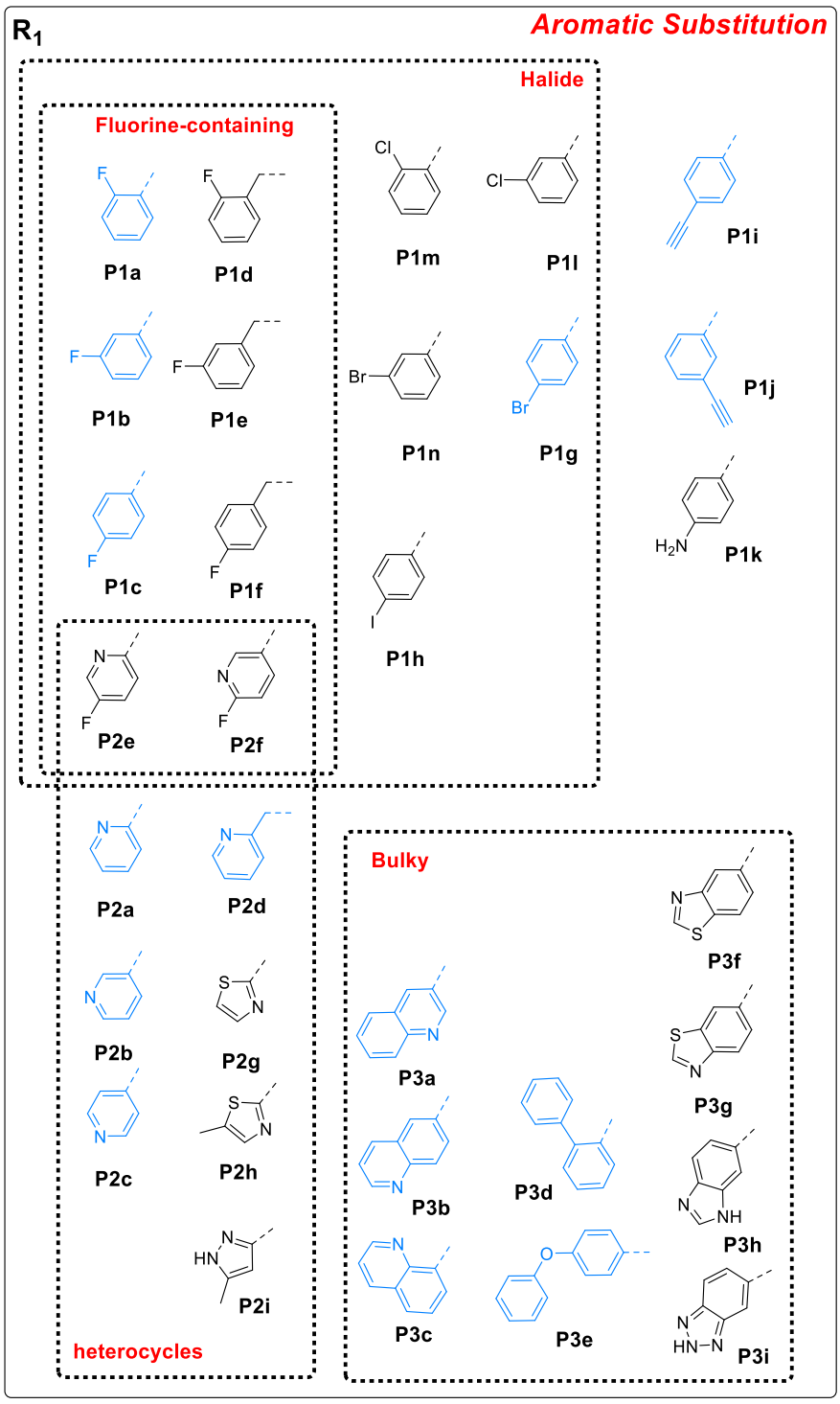

Figure 2.12. Building blocks of R1 group. The analogues synthesized during my PhD study are black (17), and the analogues synthesized during my MSc study are coloured in blue (15).

The introduced building blocks can be categorized into four smaller groups. These analogs were summarized into the following four categories: halide, fluorine-containing, bulky, and heterocyclic substitutions, as presented in **Figure 2.12**. The first library was designed with a diverse set of building blocks at the R1 position, varying in position, electronics, and steric

properties, to see how these differences impact biological activity in the SAR study. For example, P1a to c aimed to modulate the electronic density of the aromatic ring. The heterocyclic groups, such as P2g and P3g, were selected as they may provide additional hydrogen bonding opportunities and enhance binding specificity. Bulky P3d offered increased conformational constraints, improving stability in the binding pocket. Their synthesis follows a process like AZ3451, with detailed procedures outlined in **Chapter 2.4**.

The purities of the 32 analogues were tested by HPLC using a solvent system of water and acetonitrile, and all met the 95% purity requirement for biological assays. Biological assays are conducted for all analogues, except P1m, P1n, and P2i due to time constraints. The biological evaluation data is further discussed in **Chapter 2.3**. The structures of all AZ3451 analogues are in **Chapter 2.4**, the data and spectra from MS, HPLC, and ^{1}H-NMR are available in **Appendix A**.

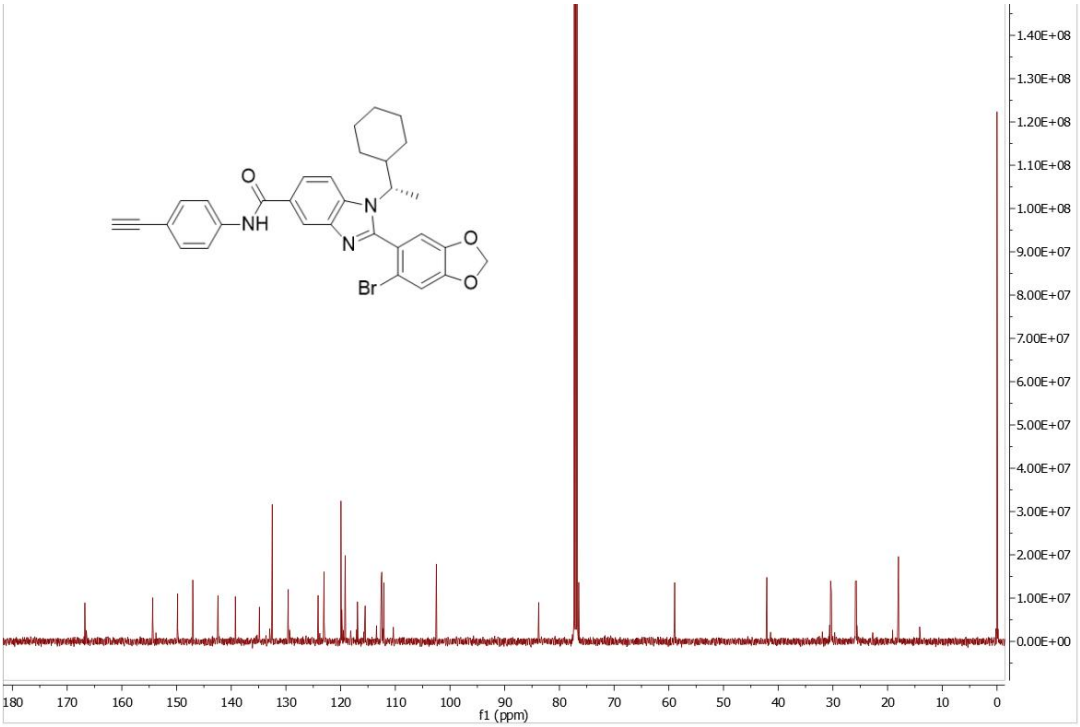

Figure 2.13. ^{13}C-NMR spectrum of compound P1i.

^{13}C-NMR are not available due to the conformational isomer issues, which leads to an apparent increase in the number of carbons signals and complicates spectral interpretation. As a representative case, the ^{13}C NMR spectrum of compound P1i was selected to illustrate this issue. As shown in **Figure 2.13**, ^{13}C-NMR characterization of flexible molecules is challenging due to the presence of conformational isomers. While such isomers are clearly observed in structural analysis, their potential impact on the biological activity of AZ3451 remains

unknown, as the existing literature does not provide a clear discussion or evaluation of this issue.

Molecular docking studies were performed for all analogues[103]. Compound P2a was selected for molecular docking studies and compared to AZ3451, following the methodology previously reported in the literature. Molecular docking studies were performed using the crystal structure of PAR2 to investigate the binding mode of AZ3451 and analog P2a. As shown in **Figure 2.14,** the top-ranked binding modes of P2a and AZ3451 were superimposed to compare their binding orientations within PAR2 [35]. Both compounds were found to occupy the same allosteric pocket located on the outer surface of the TM domain. This hydrophobic pocket is formed by several key residues including Try210, Phe154, Leu203, Leu23, and Trp199, consistent with the binding site reported in the literature[99]. The docking alignment suggests that compound P2a preserves key binding interactions and may function via a similar mechanism. In summary, these two molecules overlapped relatively favorably, with only minor differences in their positions. This suggests that the two structures are likely to share a similar functional profile, which is promising for the modification of novel AZ3451 analogues[35]. The methodology of molecular docking study for compound P2a is available in **Chapter 2.5.3**.

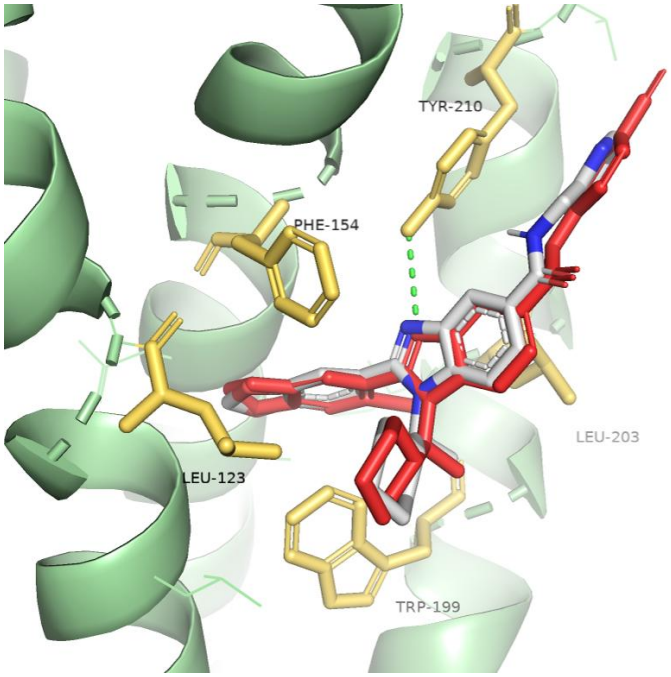

Figure 2.14. Ligand-receptor interaction for analogues P2a. AZ3451 is colored in red, analogues P2a is colored in white. The key hydrogen bond for both compounds is conserved and colored in green. The key residues highlighted in yellow.

2.2.4 Synthesis and Characterization of the Two Series of AZ3451 Derivatives

To fully explore the structural potential of AZ3451 for bias signalling activity, the cyanide group (-CN) was retained and the two other structural positions – R2 and R3 – were systematically modified (**Fig. 2.15)**.

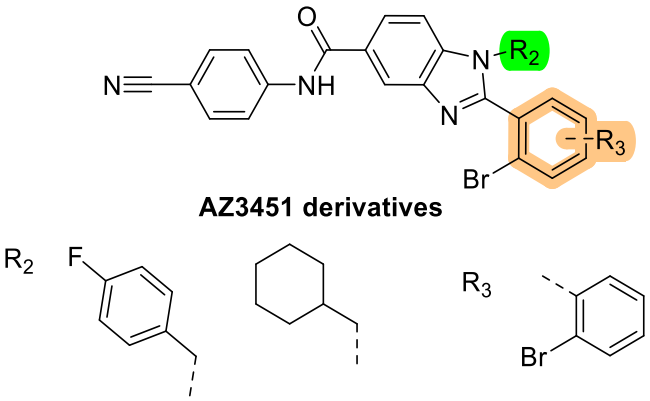

Figure 2.15. Structure of AZ3451 derivatives with R2 and R3 groups.

Three representative compounds from two series of AZ3451 derivatives were synthesized **(Scheme 2.4)**. The modification in **Scheme 2.4-A** is that (*S*)-(+)-1-cyclohexylethanamine was replaced by 4-fluorobenzylamine. The main idea behind this aromatic ring replacement is that the aromatic ring may enhance the π-π stacking interactions with residues in the binding pocket. Additionally, the fluorine atom in 4-fluorobenzylamine has the potential to yield a novel PET imaging agent. In **Scheme 2.4-B**, (*S*)-(+)-1-cyclohexylethanamine was replaced by cyclohexylmethanamine. The purpose of this modification is to investigate the conformational isomer. Compound P12 can serve as a control group compared to AZ3451 in biological assays. Without the methyl group connected to methylcyclohexane, the carbon-carbon bond between the imidazole and the aromatic ring of 1,3-benzodioxole can freely rotate. This is confirmed by the ^{1}H-NMR of P12. Based on the NMR spectra, no conformational isomers are present in the final product. The modifications for **Scheme 2.4-C** involved replacing the 1,3-benzodioxole with a bromine substituent by a benzene ring with a bromine substituent. Molecular docking studies of P14 were conducted, and they indicated that there were hydrophobic interactions between the 1,3-benzodioxole moiety and several residues. Therefore, making this moiety of the molecule more hydrophobic may potentially improve its binding interactions with PAR2 and help compound P14 fit into the hydrophobic pocket of PAR2.

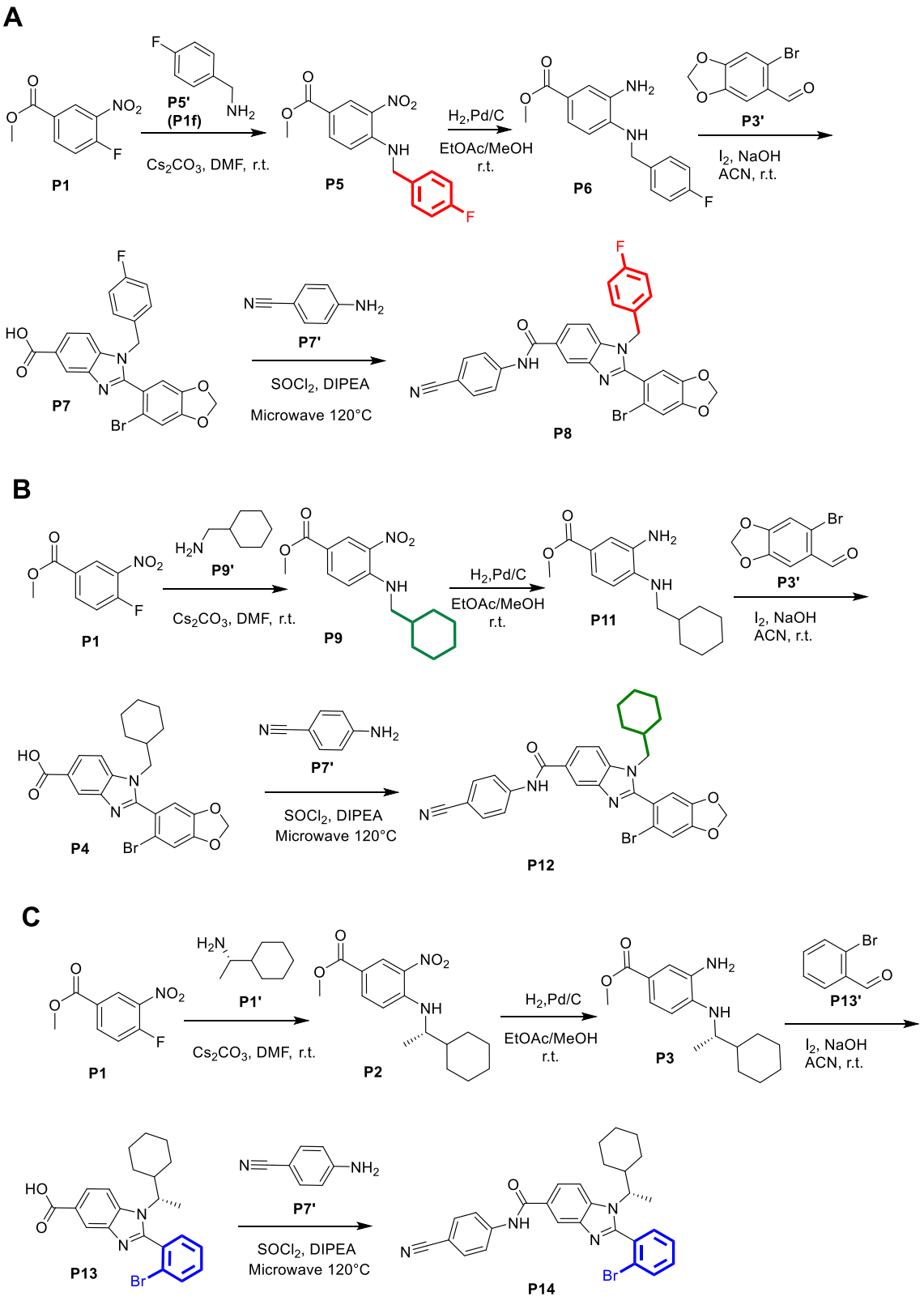

Scheme 2.4. The synthetic schemes of two series of AZ3451 derivates. The main differences among the three representative compounds are colored in red, green, and blue. Commercially available chemicals - P5':(4-fluorophenyl) methanamine P7' 4-aminobenzonitrile P9': cyclohexylmethanamine P13':2-bromobenzaldehyde

2.3 Biological Evaluation

GPCRs, including PAR2, are dynamic proteins. Ligand binding induces conformational changes, meaning the receptor does not function as a simple on/off switch but instead mediates complex signaling cascades with multiple downstream pathways[70,79]. As shown in **Figure 2.16**, PAR2 engages in complex signaling cascades through multiple downstream pathways[79,170]. Several studies demonstrate that specific transmembrane (TM) helices and intracellular loops (ICL) contribute to distinct G protein coupling[109,170].

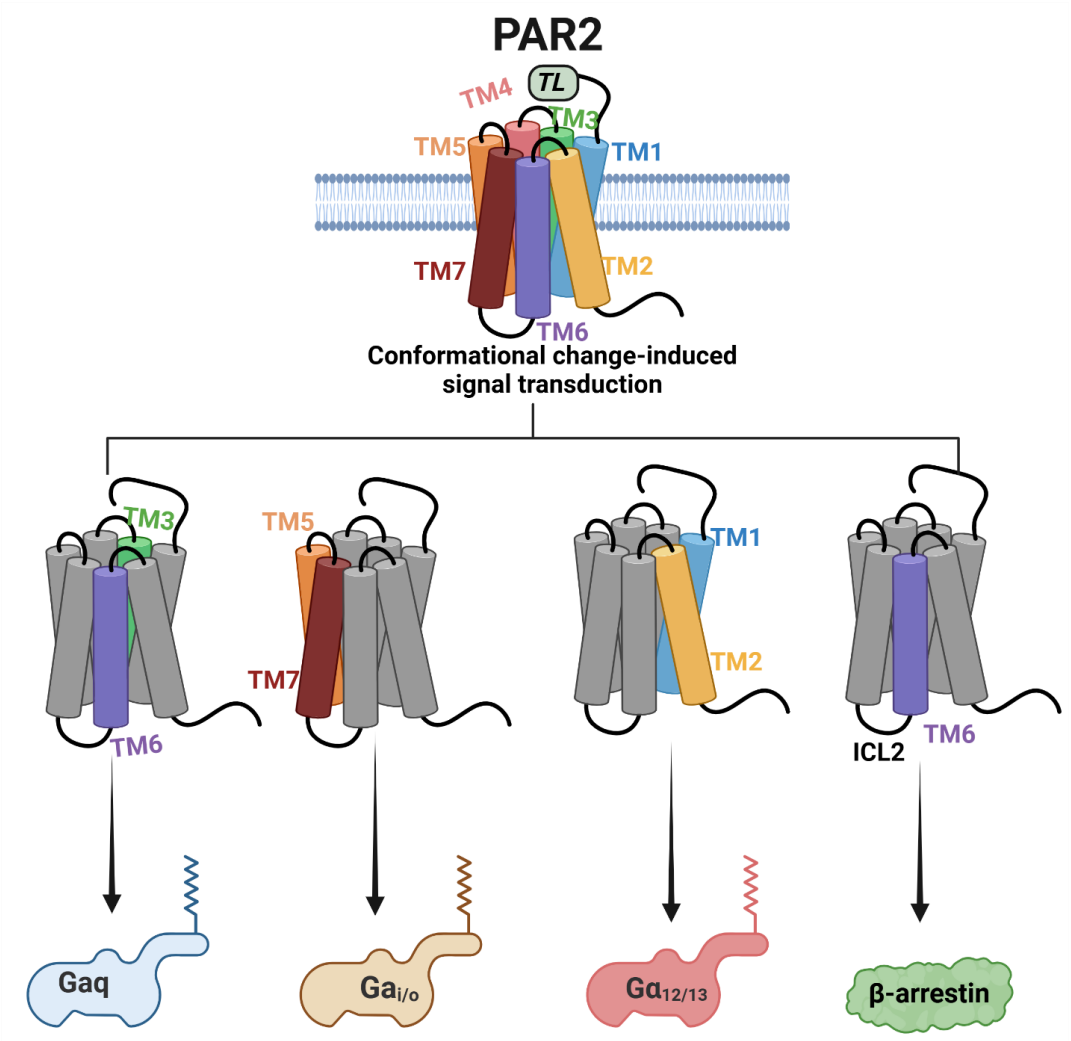

Figure 2.16. Specific TM and ICL helices contribute to distinct G protein coupling. Gαq activation is primarily mediated by rearrangements in TM3 and TM6. Gαi/o coupling is primarily mediated by TM5 and TM7. Gα12/13 engagement is influenced by TM1 and TM2. β-arrestin recruitment is primarily mediated by TM6 and ICL2.

PAR2 plays important roles in cell tissues in both health and disease, with its activation influencing various physiological and pathological processes[96,109]. In healthy tissues, PAR2

activation by peptides contributes to protective wound healing, normal vascular function, and immune regulation[88,96]. However, in pathological conditions, trypsin-mediated PAR2 activation is often linked to inflammation, fibrosis, and cancer progression[96]. In tumors, PAR2 is frequently overactivated by tumor-associated proteases, exacerbating disease[96].

Our collaborator, Dr. Rithwik Ramachandran's group at the Western University, is interested in developing pathway-selective PAR2 inhibitors that offer therapeutic advantages by selectively blocking pathological signaling while preserving beneficial physiological responses[93,109]. To evaluate the functional activity of our compounds, they conducted several biological assays[93]. One is the trypsin- and agonist peptide-induced Gαq/11-mediated calcium (Ca^{2+}) signaling assay. Another is the trypsin- and agonist peptide-induced β-arrestin 1/2 recruitment assay. Due to the time constraint, the results of the β-arrestin 1/2 recruitment assays for all compounds and the calcium signaling assay for partial compounds are summarized in **Tables 2.3–2.5**, and the dose-response curves are available in **Appendix C**.

Table 2.3. Summary of BRET assay results (β-arrestin 1&2) of R1 group. The results of β-arrestin 1 are colored in blue and β-arrestin 2 are colored in green.

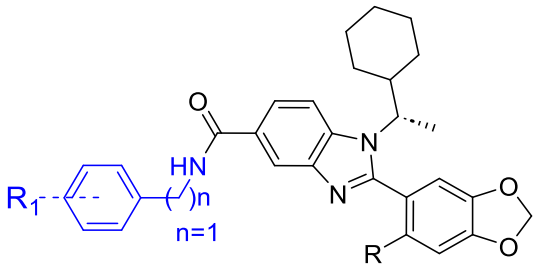

Compound	R_1	EC_{50}/nM (vs Trypsin) (β-arrestin 1 / 2) (n=1)	EC_{50} /nM (vs SLIGRL-NH_2) (β-arrestin 1 / 2) (n=1)
AZ3451		24.9 / >1000	31.9 / 126.7
P1a	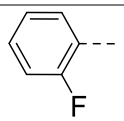	41.6 / 3.8	64.7 / 44.7
P1b	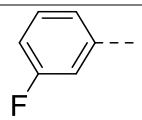	55.1 / 31.8	>1000 / 28.1

Compound	R_1	EC_{50}/nM (vs Trypsin) (β-arrestin 1 / 2)	EC_{50} /nM (vs SLIGRL-NH_2) (β-arrestin 1 / 2)
P1c	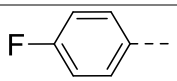	16.8 / 1.2	14.6 / 22.4
P1d	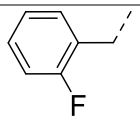	>1000 / 30.5	36.1 / 29.5
P1e	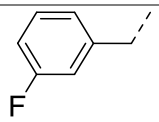	45.7 / 40.0	140.2 / 92.2
P1f	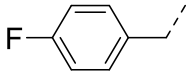	75.2 / 218.9	16.4 / 55.7
P1g	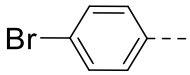	24.9 / 404.2	697.5 / 2.1
P1h	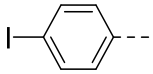	69.1 / 34.4	37.2 / 19.8
P1i	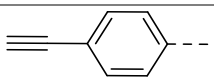	38.8 / 23.8	44.5 / 13.6
P1j	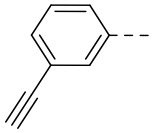	17.2 / 51.4	9.1 / 3.7
P1k	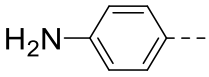	328.8 / >1000	19.9 / 15.6
P1l	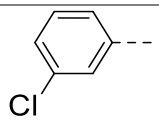	80.8 / 65.6	208.1 / 67.4
P2a	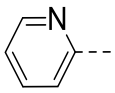	144.2 / 40.2	22.9 / 28.2
P2b	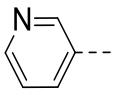	20.2 / 75.3	321.5 / 78.4

Compound	R_1	EC_{50}/nM (vs Trypsin) (β-arrestin 1 / 2)	EC_{50} /nM (vs SLIGRL-NH_2) (β-arrestin 1 / 2)
P2c	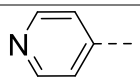	22.0 / 84.7	>1000 / >1000
P2d	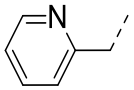	23.4 / 65.0	57.5 / 1.1
P2e	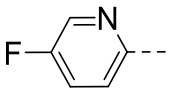	175.0 / 674.5	22.4 / 15.9
P2f	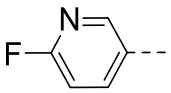	44.3 / >1000	27.7 / 233.7
P2g		58.3 / 76.5	553.8 / 270.1
P2h	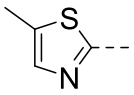	33.0 / 122.6	83.3 / 147.1
P3a	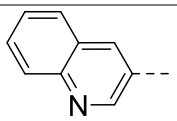	48.6 / 81.2	24.4 / 24.8
P3b	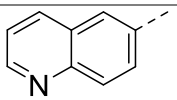	13.6 / 64.8	30.6 / 68.0
P3c	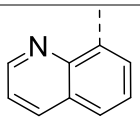	3.4 / 26.2	10.9 / 22.0
P3d	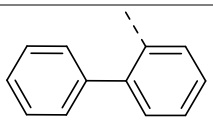	34.4 / 56.3	10.5 / 52.8
P3e	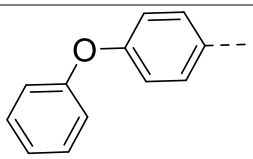	50.1 / 65.4	1.5 / 3.3

P3f	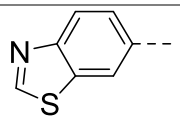	23.8 / 73.3	87.9 / 133.9
P3g	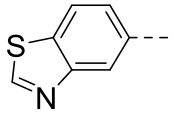	57.9 / 112.7	>1000 / >1000
P3h	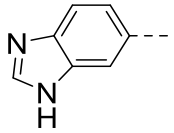	104.3 / 429.9	58.7 / 69.2
P3i	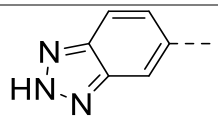	44.3 / 134.4	762.9 / >1000

Note: The presented data were obtained from a single experiment, and follow-up testing to validate the results is currently ongoing.

Table 2.4. Summary of BRET assay results (β-arrestin 1&2) of R2-3 group. The results of β-arrestin 1 are colored in blue and β-arrestin 2 are colored in green.

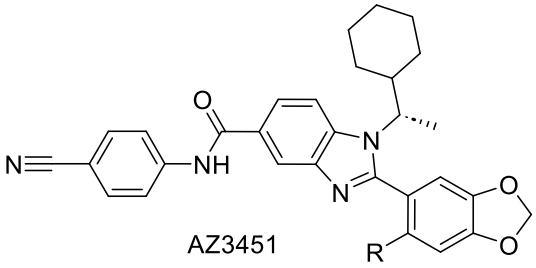

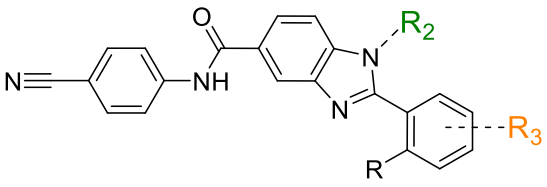

Compound	Building blcok	EC_{50}/nM (vs Trypsin) (β-arrestin 1 / 2) (n=1)	EC_{50} /nM (vs SLIGRL-NH_2) (β-arrestin 1 / 2) (n=1)
P8 (R_2)	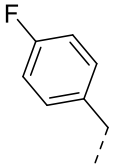	174.3 / 61.8	>1000 / > 1000

P12 (R_2)	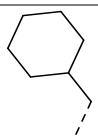	44.8 / 92.3	70.2 / 101.9
P14 (R3)	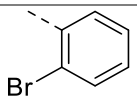	83.9 / 151.8	17.6 / 18.7

Note: The presented data were obtained from a single experiment, and follow-up testing to validate the results is currently ongoing.

Table 2.5. Summary of Ca^{2+} signaling assay results of partial compounds

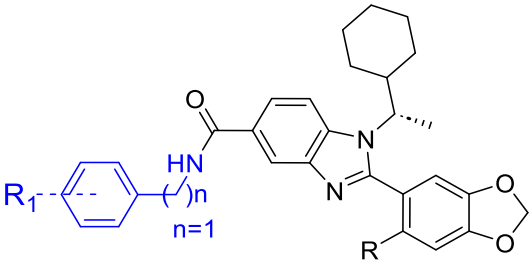

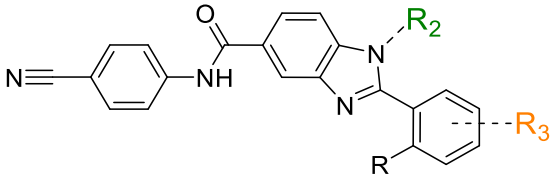

Compound	Building block (R_1, R_2, and R_3)	IC_{50} /nM (vs Trypsin) (n=1)	IC_{50} /nM (vs SLIGRL-NH_2) (n=1)
AZ3451		**2.2**	**3.1**
P1a	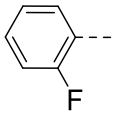	**>2uM**	**210.7**
P1b	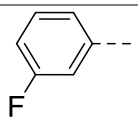	**1122.2**	**338.3**
P1c	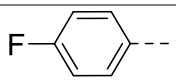	**123.6**	**222.1**
P1d	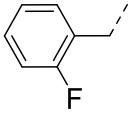	**239.6**	**>2uM**
P1e	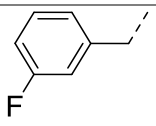	**>2uM**	**>2uM**

P1f	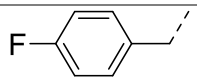	**>2uM**	**281.5**
P1g	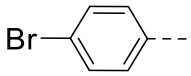	**310.4**	**674.1**
P2b	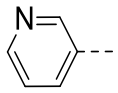	**>2uM**	**622.8**
P2c	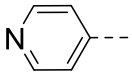	**6.3**	**6.4**
P3a	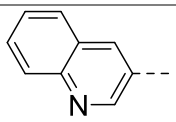	**1246.1**	**273.5**
P3b	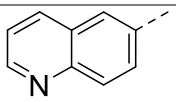	**>2uM**	**249.5**
P3f	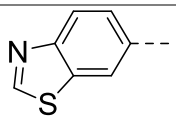	**242.3**	**350.9**
P3g	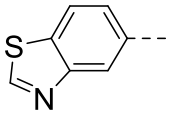	**>2uM**	**284.5**
P8 (R_2)	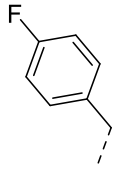	**>2uM**	**>2uM**
P12 (R_2)	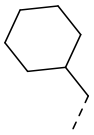	**>2uM**	**338.4**
P14 (R_3)	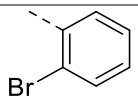	**>2uM**	**>2uM**

Note: The presented data were obtained from a single experiment, and follow-up testing to validate the results is currently ongoing.

Unlike AZ3451 (a pan-inhibitor)[93], some compounds demonstrate probe dependence (Trypsin vs. SLIGRL-NH2) in β-arrestin 1/2 recruitment assays, the results as shown in **Figure 2.17**.

For example, compounds P1b, P3g, and P3i demonstrate probe dependence, acting as potent inhibitors of trypsin-induced β-arrestin 1/2 recruitment, while being less active against SLIGRL-NH_2-induced β-arrestin 1/2 recruitment (**Fig. 2.17-A**). Conversely, compounds P1k, P2e, and P2f are potent inhibitors of SLIGRL-NH_2-induced β-arrestin 1/2 recruitment but are inactive in trypsin-induced β-arrestin 1/2 recruitment (**Fig. 2.17-B**). These findings highlight probe dependence among the AZ3451 analogues, demonstrating their ligand-specific inhibitory profiles[93].

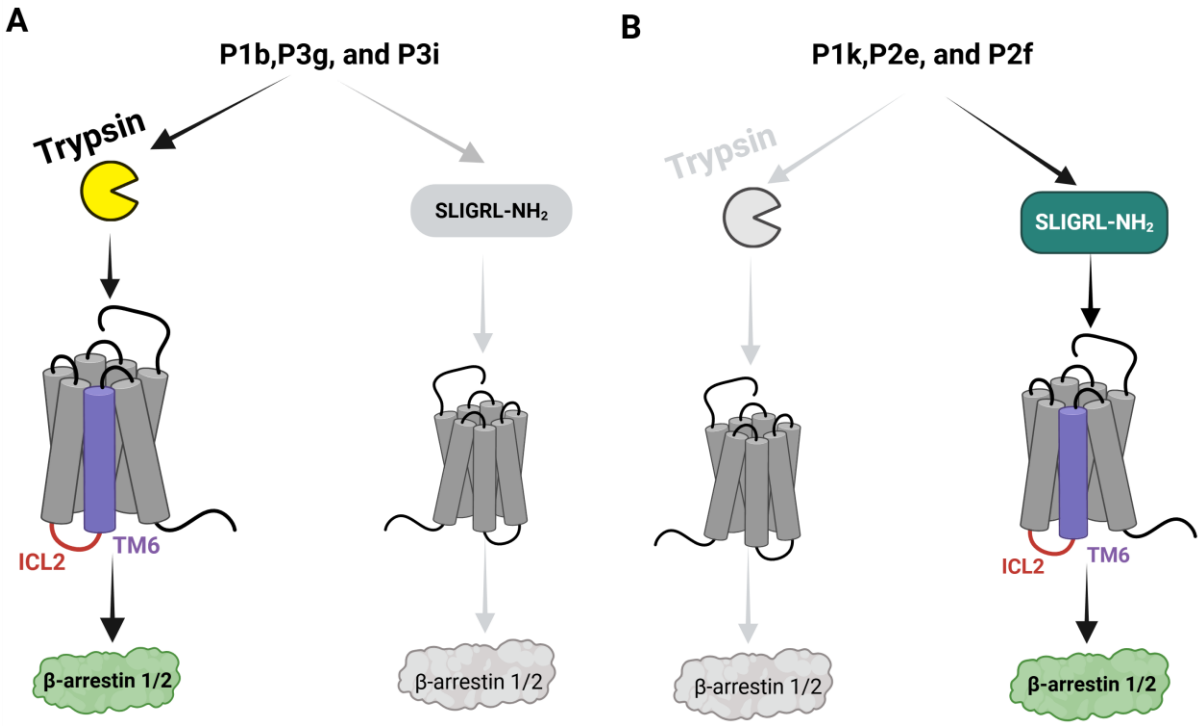

Figure 2.17. Probe dependence of AZ3451 analogs. **A** - Compound P1b, P3g, and P3i can inhibit trypsin-induced β-arrestin 1/2 recruitment assays. **B** - Compound P1k, P2e, and P2f can inhibit peptide-induced β-arrestin 1/2 recruitment assays.

Studies applied Ca^{2+} signaling and β-arrestin 1&2 recruitment assays reveal that certain AZ3451 analogues exhibit potential biased activity, as shown in **Figure 2.18**. In **Figure 2.18-A**, compound P2c is a weak inhibitor of SLIGRL-NH_2-induced β-arrestin 1&2 recruitment and is completely inactive against trypsin-activated β-arrestin 1&2 recruitment assay. However, P2c is equipotent to AZ3451 in both trypsin-induced and SLIGRL-NH_2-induced Ca^{2+} release assays, indicating a preference for calcium signaling over β-arrestin recruitment. In contrast, **Figure 2.18-B,** compound P1e exhibits balanced potent for both trypsin- and SLIGRL-NH_2-induced β-arrestin 1&2 recruitment but is a weak inhibitor in the Ca^{2+} release assay, suggesting

a bias toward β-arrestin signaling. Notably, structural modifications at the R2 and R3 positions of AZ3451 also influence biased activity. Compounds P8 and P14 exhibit balanced potent in both trypsin- and SLIGRL-NH_2-induced β-arrestin 1&2 recruitment assays, but they act as weak inhibitors in Ca^{2+} signaling assays, further reinforcing a β-arrestin-biased profile. These findings suggest that structural modifications to the cyclohexyl or benzodioxole group of AZ3451 could lead to the development of novel biased PAR2 inhibitors, selectively modulating distinct signaling pathways[93,171].

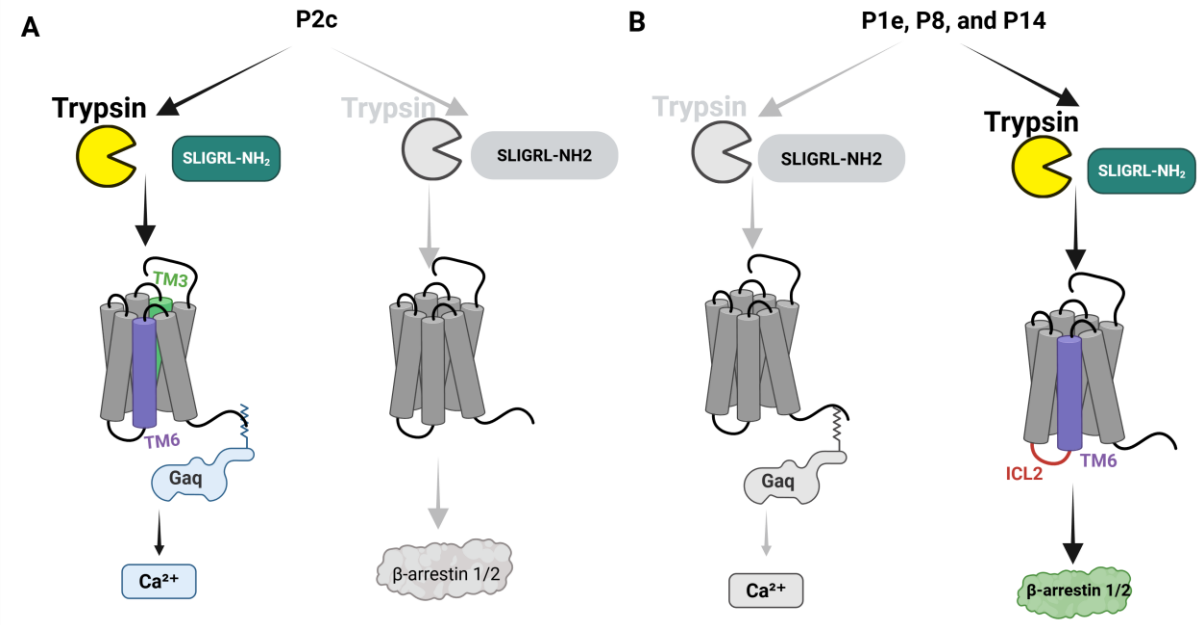

Figure 2.18. AZ3451 analogs show biased activity. A - Compound P2c is potent in the Ca^{2+} signaling assay but shows weak activity in the β-arrestin 1&2 recruitment assay. B - Compound P1e, P8, and P14 are potent in the β-arrestin 1&2 recruitment assay but inactive in the calcium signaling assay.

Given that different ligands can induce distinct PAR2 conformations, the biological evaluation of functional activity provides key insights into probe dependence and biased signaling, helping identify compounds capable of selectively modulating PAR2 pathways[92,93]. These assays confirmed that the compounds not only bind to PAR2 but also exhibit specific functional activity.

2.4 Radiolabel approach

2.4.1 Select the Candidate Compound for Radiolabeling Study

In 2003, Jin *et al.* provides early evidence for the involvement of PAR2 in lung adenocarcinoma, particularly in alveolar capillary endothelial cell proliferation and tumor angiogenesis[172]. Using microdissected tissues from 20 patients with lung adenocarcinomas, their study showed that PAR2 mRNA expression was elevated 16-fold in tumor alveolar walls compared to normal alveolar walls[172]. Subsequent research groups have also confirmed the high expression of PAR2 in lung cancer[121,139]. Given this significant overexpression, there is an urgent need to develop small-molecule PET imaging agents targeting PAR2 for lung cancer diagnosis.

To date, no small-molecule PET imaging agents targeting PAR2 have been reported[142,173]. The only existing PAR2-targeting PET imaging agent is a peptide derivative, [^{18}F]29, developed and published by Dr.Len Luyt's group in 2023 (**Fig. 2.19**)[142].

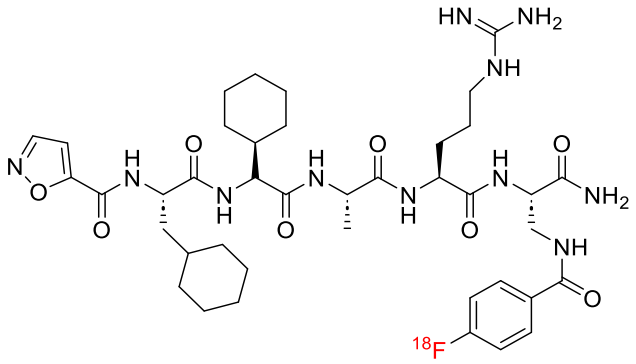

Figure 2.19. Reported structure of [^{18}F]29.

Although this peptide demonstrates high potency and specificity for PAR2, peptide-based tracers often face challenges such as rapid enzymatic degradation and limited metabolic stability, which can limit their clinical utility[174,175]. Therefore, based on biological results of functional activity of the array of PAR2 antagonists, compound P1c was selected as a candidate for radiolabeling studies (**Fig. 2.20**). It was determined that this compound has an IC_{50} value of 123.6 nM in the trypsin-induced calcium signaling assay and 222.1 nM in the peptide-induced calcium signaling assay. Moreover, compound P1c shows potency in both the trypsin-induced (EC_{50} of 16.8 nM for β-arrestin 1 and 1.2 nM for β-arrestin 2) and peptide-induced (EC_{50} of 14.6 nM for β-arrestin 1 and 22.4 nM for β-arrestin 2) β-arrestin recruitment assays. Although compound P1c was not evaluated using direct PAR2 binding assays (e.g., radioligand binding assays), its functional activity was validated through calcium signaling and β-arrestin 1/2

recruitment assays. These assays are widely accepted in GPCR drug discovery for assessing receptor activation and downstream signaling. β-arrestin recruitment assays provide insights into ligand-receptor interactions and biased signaling and have been shown in many studies to correlate with ligand binding affinity to PAR2, especially when high potency is observed[176]. Therefore, the strong β-arrestin responses of compound P1c support a potent and specific interaction with PAR2.

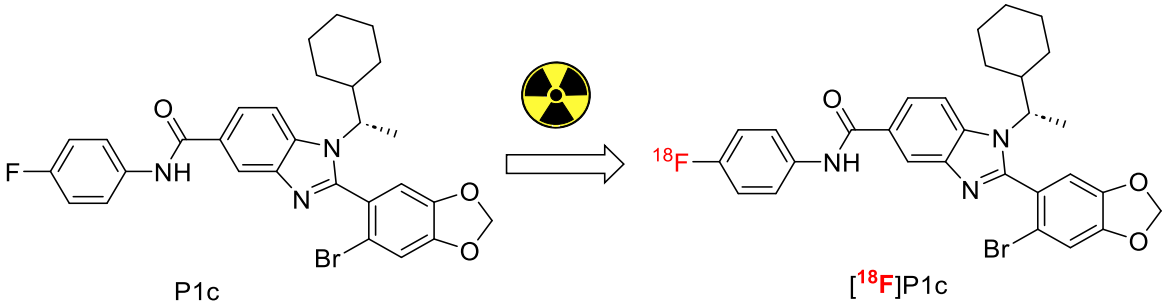

Figure 2.20. Structure of compound P1c and proposed radiotracer.

2.4.2 ^{18}F-Radiolabeling Method

Fluorination reactions used in organic chemistry are not suitable for radio-fluorination due to their long reaction times, harsh conditions, and limited substrate scopes[46]. In radiochemistry, introducing fluorine-18 into substrates relies on intermediates that accommodate the half-life while providing mild and selective fluorination[46,53,57]. Aromatic [^{18}F]-labeling remains technically challenging due to the low reactivity of non-activated aryl substrates. To address this, the Spirocyclic Iodonium Ylide (SCIDY) strategy was selected, as it has been demonstrated to enable efficient and regioselective [^{18}F]-incorporation into aromatic systems under mild conditions. Given the limited number of alternative methods suitable for direct arene labeling, and due to time constraints, other precursors or labeling strategies were not explored. The SCIDY method, originally developed by Vasdev and Liang's group in 2014, provides a one-step, site-specific approach that is well-suited for radiolabeling electron-neutral or electron-rich arenes, making it an appropriate choice for this study[57,100]. SCIDY technology is based on hypervalent iodine (III) species and is designed to achieve regioselective radio-fluorination[100,177]. Its defining feature is a spirocyclic scaffold that stabilizes the iodine (III) center and facilitates reductive elimination of [^{18}F] to form carbon-fluorine bonds (**Fig. 2.21**)[177]. This mechanism avoids common issues encountered with diaryliodonium salts, such as low regioselectivity and competing byproduct formation[177]. SCIDY operates by forming a highly reactive iodine (III)-fluoride intermediate, which undergoes nucleophilic attack by [^{18}F],

followed by reductive elimination to produce the desired [^{18}F]-radiotracer[100,177,178]. The electronic and steric properties of the auxiliary groups attached to the spirocyclic structure enhance selectivity and minimize potential side reactions[177].

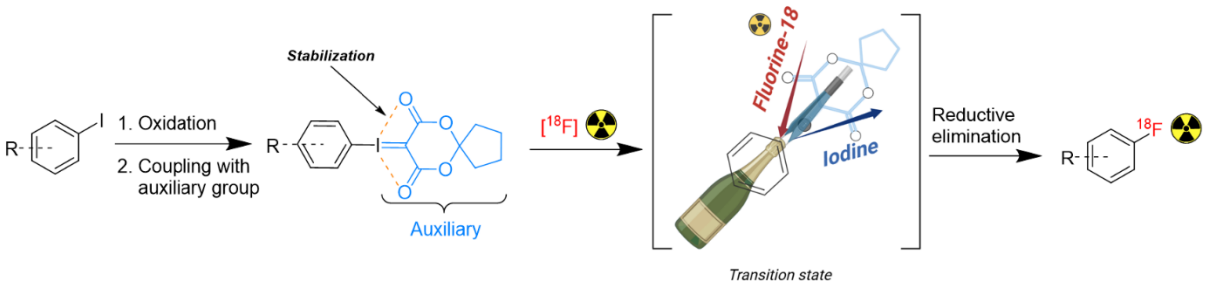

Figure 2.21. NMR and X-ray crystallography studies demonstrate that the iodine–oxygen bond (highlighted in orange) within the spirocyclic auxiliary group contributes to the overall stability of the SCIDY precursor[100]. During the transition state, the auxiliary group adopts a conformation that facilitates the departure of iodine and the incorporation of fluorine-18, likely by stabilizing the hypervalent iodine (III)-fluoride intermediate. This conformational effect has been likened to a 'pincer', due to its ability to position the reacting groups favorably for reductive elimination.

In 2016, the second-generation SCIDY auxiliary group, spiroadamantyl-1,3-dioxane-4,6-dione (SPIAd), was reported by the same group[177]. SPIAd is an air and temperature stable compound that can be purified in high yields, making it more practical for bench work (**Scheme 2.5-A**)[177]. This method has been demonstrated to work efficiently with various electron-rich and sterically hindered substrates[57,177]. Based on the advancements reported by Vasdev and Liang's group, SPIAd-mediated SCIDY technology is an attractive and promising approach for [^{18}F]-radiolabeling[57]. In this thesis, SCIDY is used to radiolabel compound P1c with fluorine-18 (**Scheme 2.5 B-D**).

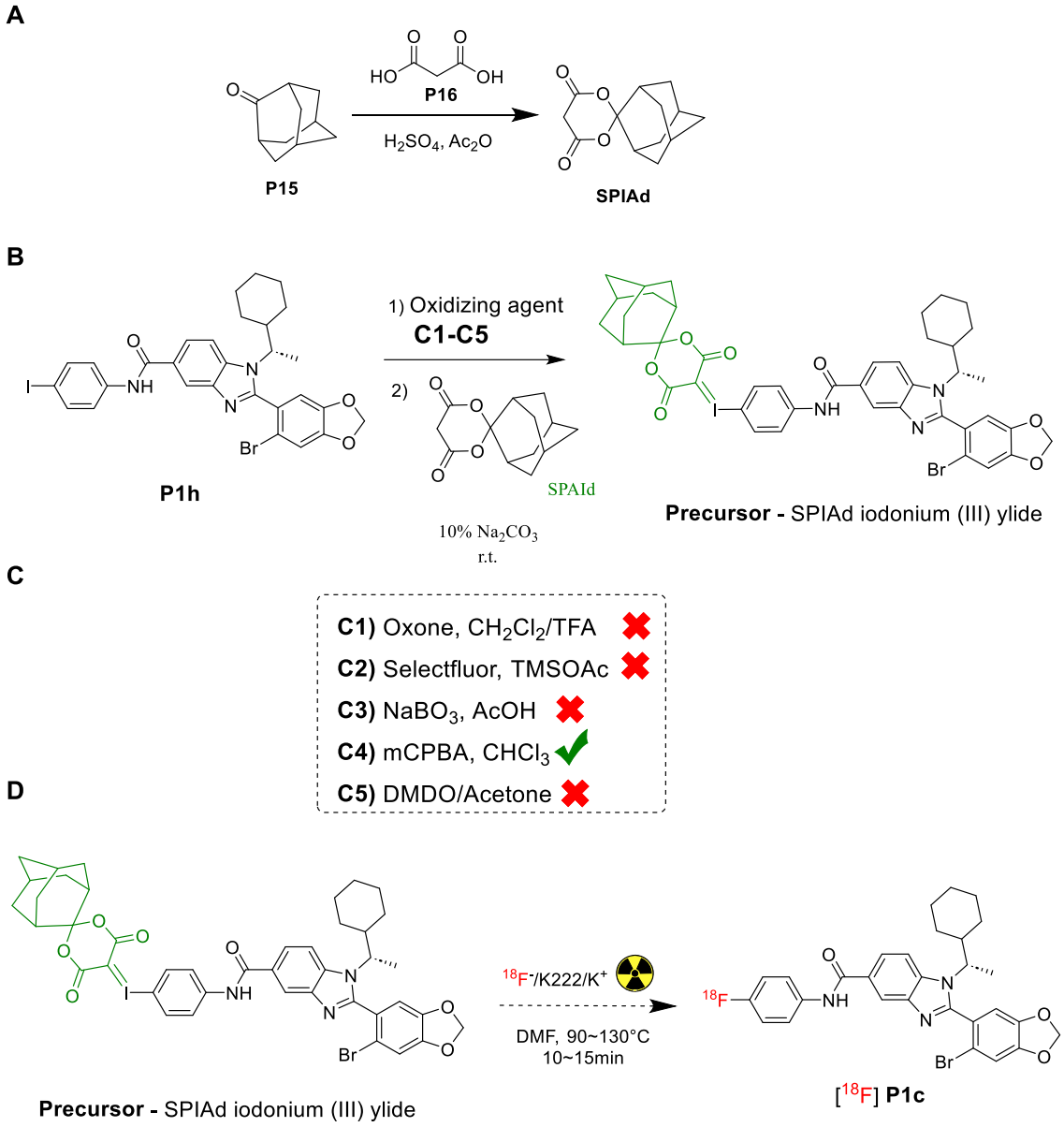

Commercial avaiable chemicals *- P15: Malonic acid P16: acetic anhydride*

Scheme 2.5. A-C. Synthesis of SPIAd auxiliary/precursors. D. Proposed radiolabeling scheme to produce 18F-labeled compound.

The group explored six oxidative conditions with corresponding oxidizing agents and solvents for precursor synthesis, each offering distinct advantages[57,179]. Due to the relatively complex parent structure of compound P1c, Oxone and Selectfluor were initially employed to generate the desired precursor. However, the outcomes did not meet expectations. Based on literature reports, 3-chloroperoxybenzoic acid (mCPBA) and sodium perborate ($NaBO_3$) have demonstrated effectiveness in oxidizing simpler substrates[179]. Therefore, an attempt was made to use these two oxidizing agents to oxidize compound P1h. The results showed that while

mCPBA successfully oxidized the compound, the yield was low (~10%). Subsequently, DMDO (dimethyldioxirane) was tested to see if it would improve the yield, but the results were again unsatisfactory.

Precursor SPIAd iodonium (III) ylide was characterized by using ^{1}H-NMR, MS, and HPLC; the data can be found in **Chapter 2.3**. Furthermore, to assess the feasibility of fluorine-18 incorporation, a one-step fluorination reaction was first performed using fluoride-19, provided as Tetrabutylammonium fluoride (TBAF), with the SPIAd iodonium (III) ylide precursor under non-radioactive conditions (**Scheme 2.6**).

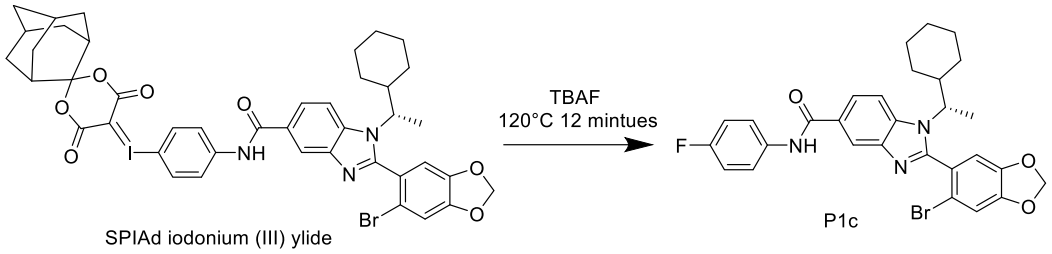

Scheme 2.6. A one-step fluorination reaction to yield compound P1c via TBAF.

Finally, this precursor undergoes radio-fluorination, where the SPIAd reacts with nucleophilic [^{18}F] to yield the final compound (radiotracer)[179]. The radiolabeling step is performed using automated synthesis in a GE Tracerlab FXFN radio-synthesis module. Current investigations focus on optimizing reaction conditions for fluorine-18 radiolabeling. So far, [^{18}F]-radiolabeling has been attempted with reaction temperatures of 90 and 130°C and reaction times at 10 and 15 minutes. The current investigation focuses on finding the optimal reaction conditions for [^{18}F]-radiolabeling.

2.5 Experimental Procedures

2.5.1 General Information of Organic Synthesis

All reagents are available and were obtained from Sigma-Aldrich, Fisher Scientific, Oakwood Chemicals, and AA blocks chemicals. NMR spectra were obtained on a 500 Hz Bruker NMR Instrument Chloroform-d or DMSO-d6 with the chemical shifts referenced to solvent signals. Chemical shifts are reported as parts per million (ppm) downfield from internal TMS in appropriate organic solutions. Peak multiplicities are expressed as follows: s, singlet; d, doublet; dd, doublet of doublet; t, triplet; br s, broad singlet; m, multiplet. NMR and mass spectra were run on isolated intermediates and final products and are consistent with the proposed structures.

Chromatographic purification was conducted using a silica gel (SiO_2) column. Four elution gradients were performed: Type A - gradient from 10 to 30% EtOAc in hexanes; Type B - gradient from 20 to 50% EtOAc in hexanes; Type C - gradient from 5 to 10% MeOH in DCM; Type D - gradient from 10 to 15% MeOH in DCM. Purification by preparative High-performance liquid chromatography (HPLC/MS) was done on a Waters LC-MS system by using a Waters Symmetry column (C18, 5 uM, 19 mm diameter, 150 mm length). The solvent system was used with a mixture of water and acetonitrile or methanol with 1% formic acid (gradient from 5% to 95%). The purities of compounds for biological tests were assessed by analytical LC-MS on a UV detector system using conditions as the following: column, XSELECT CSH C18 5 μm 4.6x150 mm; solvent A, water 0.1% formic acid; solvent B, acetonitrile 0.1% formic acid; flow rate, 0.8 mL/min; gradient, from 5 to 95% solvent B.

2.5.2 Methodology of Biological Evaluations

Calcium mobilization assay: HEK293 cells loaded with the Fluo4-NW calcium indicator were incubated with test compounds (300 to 0.3 nM) for 30 minutes at room temperature before monitoring PAR2-activated Ca^{2+} mobilization in response to submaximal doses of trypsin and the PAR2-activating peptide, SLIGRL-NH2, on a FlexStation III microplate reader (Molecular Devices).

β-arrestin 1 and 2 recruitment: A Bioluminescence Resonance Energy Transfer (BRET) assay was conducted in HEK293 cells transfected with YFP-tagged hPAR2 and Rluc-tagged β-arrestin 1 or 2. Forty-eight hours post-transfection, cells were treated with trypsin (300 to 3 nM) or SLIGRL-NH2 (300 to 3 μM) for 20 minutes at room temperature in the presence or absence of a submaximal dose (1 μM) of the tested compounds. β-arrestin 1 and 2 recruitment (increase in BRET ratio) was monitored in the presence of the Rluc substrate, Coelenterazine-H (5 μM), on a Mithras LB940 microplate reader (Berthold).

2.5.3 Methodology of Molecular Docking Study

The receptor structure was derived from the crystal structure of PAR2 (PDB ID: 5NDZ) and converted to PDBQT format using AutoDockTools 1.5.6. The ligand structure of P2a was prepared and energy-minimized using DS Viewer 3.5. Docking simulations were carried out using AutoDock Vina.

The docking grid was centered at coordinates (x = 3.825, y = 9.886, z = 49.486) with dimensions set to 20 × 20 × 28 $Å^3$, fully encompassing the allosteric binding site identified in

the crystal structure. The number of binding modes was set to 10, and the exhaustiveness parameter was set to 100 to increase search accuracy. All other parameters were maintained at their default values. Docking results were analyzed using PyMOL and Discovery Studio Visualizer to assess binding poses and key ligand–receptor interactions.

All figures were created with ***BioRender.com***.

2.5.4 Organic Synthesis

Synthesis of (S)-methyl 4-((1-cyclohexylethyl) amino)-3-nitrobenzoate. (Compound P2)

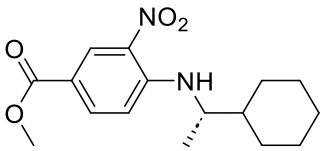

To a 250 mL round-bottom flask equipped with a stir bar was added methyl 4-fluoro-3-nitrobenzoate (1000 mg, 5.02 mmol), and caesium carbonate (3271.1 mg, 10.04 mmol). To this reaction mixture, (S)-cyclohexyl ethylamine (766.13 mg, 6.024 mmol) was added via a syringe. DMF (20 mL) was added to the round-bottomed flask, sealed with a rubber septum and allowed to stir for two hours at room temperature. The resulting orange/yellow-coloured mixture was then checked by TLC 1:3 EtOAc: hexane. The reaction mixture was diluted with 100 mL of EtOAc and extracted with 200mL of saturated NH_4Cl solution. The aqueous layer was separated, extracted 2 times with EtOAC. The combined organic layers were dried over Na_2SO_4 and filtered. The solvent was then removed under reduced pressure by rotary evaporation. The crude product was then prepared for flash silica gel chromatography. Column type A was used to elute the purified product, (S)-methyl 4-((1-cyclohexylethyl) amino)-3-nitrobenzoate. A 1401 mg (91% yield) of pure product was obtained. ^1H NMR (500 MHz, $CDCl_3$) δ 8.83 (s, 1H), 8.48 (d, 1H), 8.01 (m, 1H), 3.90 (s, 3H), 2.01 (m, 1H), 1.55 (m, 3H), 1.47 (m, 1H), 1.15(m, 9H), 0.64 (m, 1H) MS m/z: for Chemical Formula: $C_{16}H_{22}N_2O_4$, LC-MS $[M + H]^+$ =307.12 (calcd.) 306.4 (found).

Synthesis of (S)-methyl 3-amino-4-((1-cyclohexylethyl) aminobenzoate. (Compound P3)

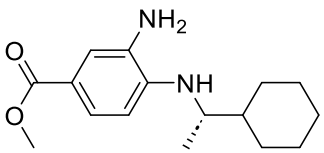

(S)-methyl 4-((1-cyclohexylethyl) amino)-3-nitrobenzoate (1401 mg, 4.57 mmol) was added to a 250 mL round-bottom flask. Pd/C catalyst (Palladium content 10%, 40 mg, 0.37 mmol) was added into the flask via spatula along with a stir bar. A 1:1 EtOAc: MeOH solution (12 mL) was added and then sealed with a rubber septum. The air within the flask was removed under vacuum and refilled twice with H_2 by balloon. With the H_2-filled balloon still attached, the reaction was then allowed to stir for 8 hours at room temperature. The reaction was checked for completion by TLC (1:3 EtOAc: Hexane) and then filtered through a layer of diatomaceous earth washed with high volumes of EtOAc. The resulting light grey colour liquid was then concentrated under pressure by rotary evaporation and further dried in a desiccator to afford the desired product as a light green solid. 1262 mg (97% yield) was obtained, and this product was used directly without further purification in the next step. ^{1}H NMR (500 MHz, $CDCl_3$) δ 7.57 (m, 1H), 7.41 (s, 1H), 6.55 (s, 1H), 3.87 (s, 3H), 2.04 (m, 1H), 1.35 (m, 3H), 1.51 (m, 1H), 1.13 (m, 9H), 0.67 (m, 1H) MS m/z: for Chemical Formula: $C_{16}H_{24}N_2O_2$, LC-MS $[M + H]^+$ =276.18 (calcd.) 275.9 (found).

Synthesis of (S)-2-(6-bromobenzo[d] [1,3] dioxol-5-yl)-1-(1-cyclohexylethyl)-1H-benzo[d]imidazole-5-carboxylic acid. (Compound P4)

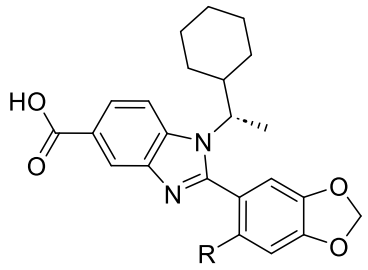

To a 250 mL round-bottomed flask was added (S)-methyl 3-amino-4-((1-cyclohexylethyl) aminobenzoate (1262 mg, 4.45 mmol) and iodine (2259.2 mg, 8.9 mmol). Sodium hydroxide pellets (1779.4 mg, 44.5 mmol), followed by 6-bromobenzo-d-1,3-dioxole-5-carbaldehyde (823.3 mg, 4.45 mmol) was added to the flask. A stir bar was added and the reagents dissolved in acetonitrile (12 mL). The round-bottom flask was sealed with a rubber septum. The flask was flushed with Argon. After sonication, the flask was stirred for 6 hours at room temperature under argon gas. This reaction was checked by TLC (1:3 EtOAc: Hexane and 1:1 EtOAc: Hexane). The reaction mixture was a smooth, shaded brown sand-like solution. The reaction mixture was acidified to pH 2-3 using a 2M HCl solution. The crude product was concentrated via rotary evaporation to yield a dark/brown oil. The residue was redissolved in EtOAc (100 mL, sonicated) and poured into a 500mL separatory funnel. Saturated NaCl solution (150 mL)

was added, followed by distilled water (100 mL). Three extractions of aqueous layers were performed, adding 30mL of EtOAc each time. The combined organic layers were dried over Na_2SO_4, filtered, washed using EtOAc, and concentrated under reduced pressure by rotary evaporation. The sample was then prepared for a flash silica chromatography column. The crude product in silica was then added to the column and was washed with hexane. Column A was initially used, which was switched to column B. A 1902 mg (81% yield) was obtained. MS m/z: for Chemical Formula: $C_{23}H_{23}BrN_2O_4$, LC-MS $[M + H]^+ = 470.08$ (calcd.) 471.1 (found). ^{1}H NMR (500 MHz, DMSO) δ 12.79 (s, 1H), 8.26 (s, 1H), 7.90 – 7.86 (m, 2H), 7.44 (d, 1H), 7.12 (s, 1H), 6.26 – 6.19 (m, 2H), 3.75 (m, 1H), 2.16 – 1.99 (m, 1H), 1.87 (m, 1H), 1.70 (m, 3H), 1.62 – 1.42 (m, 3H), 1.29 – 1.13 (m, 1H), 1.07 – 0.75 (m, 4H), 0.68 – 0.49 (m, 1H).

General synthetic method for AZ3451 and its derivatives.

Original synthetic method: To a 100 mL round-bottom flask was added compound P4 (100 mg, 0.206 mmol), HATU (158 mg, 0.412 mmol), DIPEA (53.2 mg, 0.412 mmol), and DMF (5 mL). This was stirred at room temperature for 1 hour, followed by the addition of the specific amine (1.2 equivalent). The reaction was then heated to 110°C for 5 hours and monitored by TLC. The reaction mixture was diluted with 200 mL of DI water and 100 mL of saturated NaCl solution in a 500 mL separatory funnel. The aqueous layer was washed twice with EtOAc (60 mL). The combined organic layers were dried over Na_2SO_4, filtered, and concentrated under reduced pressure by rotary evaporation. A crude mixture was obtained and prepared for flash silica gel column chromatography or preparative HPLC (prep-HPLC).

Optimal synthetic method: Compound P4 (100 mg, 0.206 mmol) was dissolved in DMF, then thionyl chloride ($SOCl_2$) (0.416 mmol). The reaction mixture was irradiated in the microwave at 100°C for 30 minutes. After cooling to room temperature, excess thionyl chloride was removed under vacuum to give the crude aryl chloride. The specific amine was then added to the intermediate (aryl chloride) with DIPEA (53.2 mg, 0.412 mmol) and DMF (2.5 mL). The reaction mixture was irradiated in the microwave at 110-150°C for 20 minutes. The combined organic layers were dried with Na_2SO_4, filtered, and the solvent was removed under reduced pressure. The compound was purified by prep-HPLC with a gradient from 60% to 95% acetonitrile (0.1 % formic acid) in water.

Synthesis of (S)-2-(6-bromobenzo[d] [1,3] dioxol-5-yl)-N-(4-cyanophenyl)-1-(1-cyclohexylethyl)-1Hbenzo[d]imidazole-5-carboxamide (AZ3451).

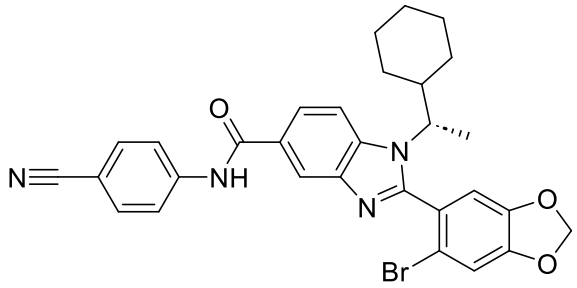

4-Aminobenzonitrile (36.5 mg, 0.412 mmol) was added into the round-bottom flask (RBF) and heated to 120°C under microwave irradiation for 30 minutes. The reaction mixture was monitored by TLC (1:3 EtOAc: Hexane and 1:12 MeOH: DCM plus one drop of NH_4OH).

After extraction, filtration, and concentration, a light-brown, oil-like material was obtained and purified for the first on silica gel (1:5 EtOAc:Hexane), which was later switched to 1:3 EtOAc:Hexane as the final eluent. The residue was purified further using flash silica gel column chromatography (eluent gradient, 5 % Method in DCM). A light brown solid product 48.8 mg (yield – 41 %) was obtained. Chemical Formula: $C_{30}H_{27}BrN_4O_3$. LC-MS $[M + H]^+$ = 573.1 (calcd.) 573.16 (found.). Molecular Weight: 571.48. ^1H NMR (500 MHz, DMSO) δ 10.67 (s, 1H), 8.42 – 8.36 (m, 1H), 8.08 – 8.02 (m, 2H), 7.96 (m, 1H), 7.86 (m, 3H), 7.46 (m, 1H), 7.25 – 7.10 (m, 1H), 6.26 – 6.20 (m, 2H), 3.87 – 3.68 (m, 1H), 2.14 – 2.03 (m, 1H), 1.90 (m, 1H), 1.72 (m, 3H), 1.63 (dm 1H), 1.58 – 1.43 (m, 2H), 1.26 (m, 1H), 1.07 – 0.76 (m, 4H), 0.59 (m, 1H). Purity testing by HPLC (Acquisition method 65%-95% Acetonitrile 20 minutes) t_R = 16.7 minutes. Purity=98%.

Synthesis of (S)-2-(6-bromobenzo-1,3-dioxol-5-yl)-1-(1-cyclohexylethyl)-N-(4-fluorophenyl)-1H-benzo[d]imidazole-5-carboxamide. (Compound P1c)

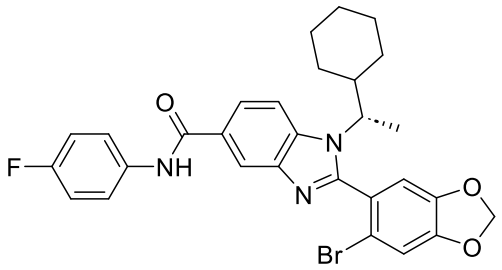

The method is similar for the preparation of AZ3451 was used except replacing the building block with 4-Fluoroaniline (36.5 mg, 0.412 mmol). The reaction condition is conventional heating (100 °C), reaction time is 5 hours. The residue was purified using flash silica gel column chromatography (eluent gradient, 5% Method in DCM). A light-yellow solid product-

61mg (yield - 43.6 %) was obtained. Chemical Formula: $C_{29}H_{27}BrFN_3O_3$ Molecular Weight: 564.46. LC-MS $[M + H]^+$ = 566.1 (calcd.) 566.2 (found). ^1H NMR (500 MHz, $CDCl_3$) δ 9.46 (m, 1H), 8.48 (m, 1H), 7.91 (m, 1H), 7.68 – 7.62 (m, 2H), 7.60 (m, 1H), 7.02 – 6.93 (m, 2H), 6.70 – 6.56 (m, 1H), 6.08 – 5.98 (m, 2H), 3.85 – 3.64 (m, 1H), 1.98 (m, 1H), 1.89 (m, 1H), 1.71 (m, 3H), 1.62 – 1.46 (m, 3H), 1.41 – 1.18 (m, 1H), 1.13 – 0.74 (m, 4H), 0.71 – 0.47 (m, 1H). Purity testing by HPLC (Acquisition method 75%-95% Acetonitrile 20 minutes) t_R = 16.6 minutes. Purity=98%.

Synthesis of (S)-2-(6-bromobenzo-1,3-dioxol-5-yl)-1-(1-cyclohexylethyl)-N-(2-fluorobenzyl)-1H-benzo[d]imidazole-5-carboxamide. (Compound P1d)

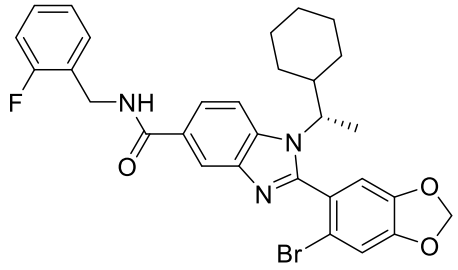

The method is similar for the preparation of AZ3451 was used except replacing the building block with 2-Fluorobenzylamine (53 mg, 0.41 mmol). The reaction condition was run under conventional heating (100°C), reaction time is 4 hours. The residue was purified using flash silica gel column chromatography (eluent gradient, 5% Method in DCM). A white solid product-81mg (yield – 45 %) was obtained. ^1H NMR (500 MHz, $CDCl_3$) δ 8.18 (m, 1H), 7.83 (m, 1H), 7.61 (m, 1H), 7.44 (m, 1H), 7.19 – 6.99 (m, 3H), 6.97 – 6.86 (m, 1H), 6.77 (m, 1H), 6.10 (d, 2H), 4.73 (m, 2H), 3.90 – 3.69 (m, 1H), 2.03 (m, 1H), 1.92 (m, 1H), 1.75 (m, 3H), 1.57 (m, 3H), 1.22 (m, 1H), 1.09 – 0.78 (m, 4H), 0.73 – 0.52 (m, 1H). Chemical Formula: $C_{30}H_{29}BrFN_3O_3$. LC-MS $[M + H]^+$ =580.1 (calcd.) 580.2 (found.). Purity testing by HPLC (Acquisition method - 75%-95% Acetonitrile 12 minutes) t_R = 15.2 minutes. Purity=97%.

Synthesis of (S)-2-(6-bromobenzo-1,3-dioxol-5-yl)-1-(1-cyclohexylethyl)-N-(3-fluorobenzyl)-1H-benzo[d]imidazole-5-carboxamide. (Compound P1e)

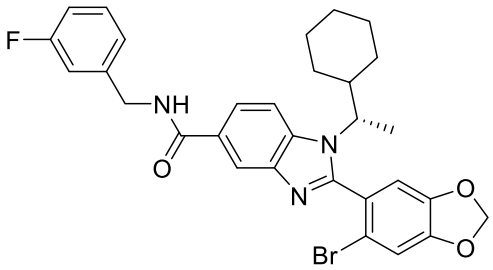

The method is similar for the preparation of AZ3451 was used except replacing the building block with 3-Fluorobenzylamine (55 mg, 0.411 mmol). The reaction condition is conventional heating (100°C), reaction time is 4 hours. The residue was purified using flash silica gel column chromatography (eluent gradient, 5% Method in DCM). A white solid product-83mg (Yield - 46%) was obtained. ^{1}H NMR (500 MHz, $CDCl_3$) δ 8.20 (m, 1H), 7.86 (m, 1H), 7.62 (m, 1H), 7.32 – 7.25 (m, 1H), 7.19 – 7.04 (m, 2H), 6.96 (m, 1H), 6.88 (s, 1H), 6.84 – 6.71 (m, 1H), 6.10 (d, 2H), 4.72 – 4.63 (d, 2H), 3.90 – 3.70 (m, 1H), 2.04 (m, 1H), 1.92 (m, 1H), 1.76 (m, 3H), 1.58 (m, 3H), 1.42 – 1.19 (m, 1H), 1.10 – 0.79 (m, 4H), 0.64 (m, 1H). Chemical Formula: $C_{30}H_{29}BrFN_3O_3$. LC-MS $[M + H]^+$ =580.1 (calcd.) 580.2 (found.). Purity testing by HPLC (Acquisition method - 75%-95% Acetonitrile 10 minutes) t_R = 15.8 minutes. Purity=99%.

Synthesis of (S)-2-(6-bromobenzo-1,3-dioxol-5-yl)-1-(1-cyclohexylethyl)-N-(4-fluorobenzyl)-1H-benzo[d]imidazole-5-carboxamide. (Compound P1f)

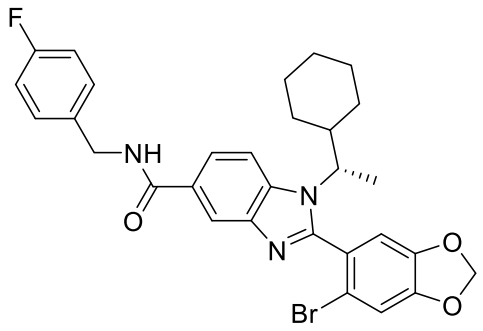

The method is similar for the preparation of AZ3451 was used except replacing the building block with 4-Fluorobenzylamine (53 mg, 0.41 mmol). And the reaction time was changed to 90 minutes under microwave irradiation (120℃). The residue was purified using flash silica gel column chromatography (eluent gradient, 5% Method in DCM). A light-brown solid product-80mg (yield – 44 %) was obtained. ^{1}H NMR (500 MHz, $CDCl_3$) δ 8.17 (m, 1H), 7.84 (m, 1H), 7.61 (m, 1H), 7.33 (m, 2H), 7.14 (m, 1H), 7.01 (m, 2H), 6.89 – 6.70 (m, 1H), 6.09 (d, 2H), 4.64 (d, 2H), 3.90 – 3.71 (m, 1H), 2.03 (m, 1H), 1.92 (m, 1H), 1.75 (m, 3H), 1.64 – 1.49 (m, 3H), 1.24 (m, 1H), 1.17 – 0.78 (m, 4H), 0.63 (m, 1H). Chemical Formula: $C_{30}H_{29}BrFN_3O_3$. LC-MS $[M + H]^+$ =580.1 (calcd.) 580.4 (found.) Purity testing by HPLC (Acquisition method - 65%-95% Acetonitrile 10 minutes) t_R = 9.9 minutes. Purity=97%.

Synthesis of (S)-2-(6-bromobenzo[d] [1,3] dioxol-5-yl)-1-(1-cyclohexylethyl)-N-(4-iodophenyl)-1H-benzo[d]imidazole-5-carboxamide (Compound P1h)

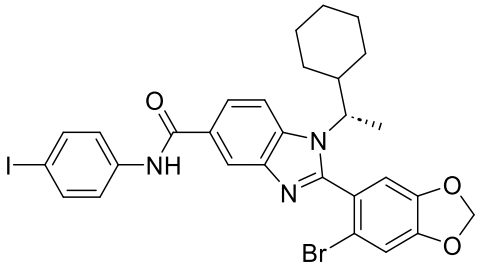

The method is similar for the preparation of AZ3451 except replacing the building block with 4-iodoaniline (351 mg, 1.63 mmol) and different reaction condition. The reaction mixture was run under the microwave at 120°C for 30 minutes. The combined organic layers were dried with Na_2SO_4 and filtered, and the solvent was removed under reduced pressure, and the residue was purified using flash silica gel column chromatography (eluent gradient, 3% Method in DCM). A light-yellow solid product was obtained in 37.3% yield (266mg). HPLC-MS (Waters), Chemical Formula: $C_{29}H_{27}BrIN_3O$. Molecular Weight: 672.36. LC-MS $[M + H]^+$ = 674.1(calcd.) 674.2(found). ^1H NMR (500 MHz, $CDCl_3$) δ 8.87 (d, *J* = 89.1 Hz, 1H), 8.39 (d, *J* = 19.3 Hz, 1H), 7.90 (m, *J* = 16.8, 8.5 Hz, 1H), 7.62 (d, *J* = 8.0 Hz, 2H), 7.49 (d, *J* = 8.3 Hz, 2H), 7.12 – 6.99 (m, 1H), 6.78 – 6.63 (m, 1H), 6.08 (d, *J* = 8.9 Hz, 2H), 3.76 (m, *J* = 37.1, 30.1 Hz, 1H), 2.13 – 1.97 (m, 1H), 1.91 (d, *J* = 12.6 Hz, 1H), 1.72 (m, *J* = 12.5 Hz, 3H), 1.56 (d, *J* = 22.5 Hz, 3H), 1.24 (d, *J* = 15.2 Hz, 1H), 0.88 (m, *J* = 26.6, 24.0, 11.6 Hz, 4H), 0.61 (m, *J* = 33.7, 11.9 Hz, 1H). Purity testing by HPLC (Acquisition method - 75%-95% Acetonitrile 10 minutes) t_R = 14.7 minutes. Purity=95%.

Synthesis of (S)-N-(4-aminophenyl)-2-(6-bromobenzo[d] [1,3] dioxol-5-yl)-1-(1-cyclohexylethyl)-1H-benzo[d]imidazole-5-carboxamide (Compound P1k)

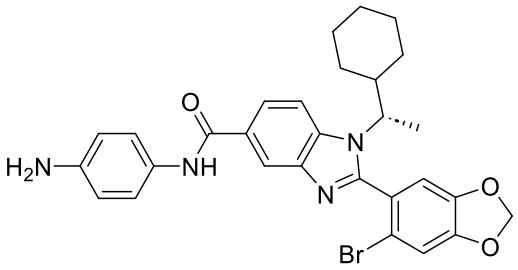

The method is similar for the preparation of AZ3451 except replacing the building block with P-phenylenediamine (54 mg, 0.31 mmol) and different reaction condition. The reaction mixture was run under the microwave at 120°C for 30 minutes. The combined organic layers were dried with Na_2SO_4 and filtered, and the solvent was removed under reduced pressure. The residue was purified using flash silica gel column chromatography (eluent gradient, 5% Method in

DCM). The final compound was further purified by prep-HPLC with a gradient from 65% to 95% acetonitrile (0.1% formic acid) in water. A light-yellow solid product-50mg (36.6%) was obtained. Chemical Formula: $C_{29}H_{29}BrN_4O_3$. Molecular Weight: 561.48. LC-MS $[M + H]^+$ = 563.1 (calcd.) 563.2 (found). ^{1}H NMR (500 MHz, $CDCl_3$) δ 8.27 (m, *J* = 7.1 Hz, 1H), 8.03 (d, *J* = 15.8 Hz, 1H), 7.91 – 7.86 (m, 1H), 7.64 (m, *J* = 12.1, 8.7 Hz, 1H), 7.44 (d, *J* = 8.6 Hz, 2H), 7.13 (d, *J* = 35.5 Hz, 1H), 6.89 – 6.73 (m, 1H), 6.72 – 6.68 (m, 2H), 6.10 (m, *J* = 16.9, 1.1 Hz, 2H), 3.81 (m, *J* = 17.3, 13.8, 10.4, 6.9 Hz, 1H), 2.05 (m, *J* = 34.0, 11.1 Hz, 1H), 1.93 (d, *J* = 12.6 Hz, 1H), 1.76 (m, *J* = 10.6 Hz, 3H), 1.58 (m, *J* = 17.1, 10.1 Hz, 3H), 1.29 – 1.22 (m, 1H), 1.09 – 0.81 (m, 4H), 0.63 (m, *J* = 21.5, 12.7, 10.8 Hz, 1H). A yellow solid product - 27mg was obtained (Yield – 23.3%). Purity testing by HPLC (Acquisition method 65%-95% Acetonitrile 20 minutes) t_R = 16.7 minutes. Purity=98 %.

Synthesis of (S)-2-(6-bromobenzo[d] [1,3] dioxol-5-yl)-N-(3-chlorophenyl)-1-(1-cyclohexylethyl)-1H-benzo[d]imidazole-5-carboxamide (Compound P1l)

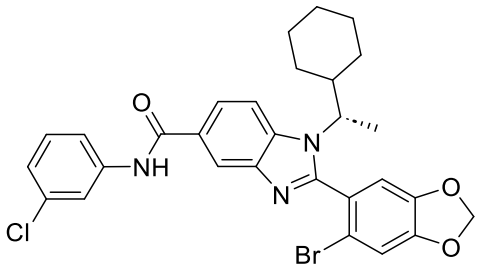

The method is similar for the preparation of AZ3451 except replacing the building block by 3-choloaniline (40 mg, 0.31 mmol) and different reaction condition. The reaction mixture was run under microwave irradiation at 120°C for 30 minutes. The combined organic layers were dried with Na_2SO_4 and filtered, and the solvent was removed under reduced pressure. The residue was purified using flash silica gel column chromatography (eluent gradient, 3% Method in DCM). The final compound was further purified by prep-HPLC with a gradient from 65% to 95% acetonitrile (0.1% formic acid) in water. A light-grey solid product-66mg (yield-36.6%) was obtained. Chemical Formula: $C_{29}H_{27}BrClN_3O_3$. Molecular Weight: 580.91. LC-MS $[M + H]^+$ = 582.12 (calcd.) 582.23 (found). ^{1}H NMR (500 MHz, $CDCl_3$) δ 9.22 (m, *J* = 63.5 Hz, 1H), 8.45 (m, *J* = 22.9 Hz, 1H), 7.89 (m, *J* = 18.9, 10.9 Hz, 2H), 7.62 (m, *J* = 8.2 Hz, 1H), 7.50 (m, *J* = 11.7 Hz, 1H), 7.07 (m, *J* = 8.3 Hz, 1H), 6.98 (s, 1H), 6.75 – 6.62 (m, 1H), 6.06 (m, *J* = 30.5 Hz, 2H), 3.77 (d, *J* = 56.9 Hz, 1H), 2.08 – 1.85 (m, 2H), 1.70 (m, *J* = 5.7 Hz, 3H), 1.62 – 1.48 (m, 3H), 1.23 (m, *J* = 13.7 Hz, 1H), 1.12 – 0.77 (m, 4H), 0.59 (m, *J* = 24.0, 11.6 Hz, 1H). A

white solid product was obtained in 30.3% yield (36mg). Purity testing by HPLC (Acquisition method 65%-95% Acetonitrile 20 minutes) t_R = 17.9 minutes. Purity=98%.

Synthesis of (S)-2-(6-bromobenzo[d] [1,3] dioxol-5-yl)-N-(2-chlorophenyl)-1-(1-cyclohexylethyl)-1H-benzo[d]imidazole-5-carboxamide (Compound P1m)

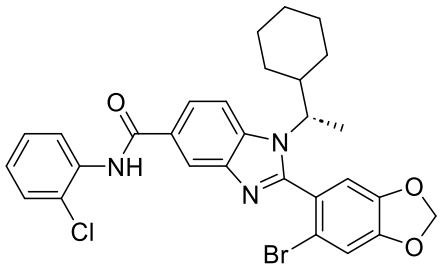

The method is similar for the preparation of AZ3451 except replacing the building block by 2-choloaniline (40mg, 0.31mmol) and different reaction condition. The reaction mixture was run under microwave irradiation at 120°C for 30 minutes. The combined organic layers were dried with Na_2SO_4 and filtered, and the solvent was removed under reduced pressure. The residue was purified using flash silica gel column chromatography (eluent gradient, 3% Method in DCM). The final compound was further purified by prep-HPLC with a gradient from 65% to 95% acetonitrile (0.1% formic acid) in water. A light-grey solid product-69mg (yiled-38.6%) was obtained. Chemical Formula: $C_{29}H_{27}BrClN_3O_3$. Molecular Weight: 580.91. LC-MS $[M + H]^+$ = 582.12 (calcd.) 582.21 (found). ^{1}H NMR (500 MHz, $CDCl_3$) δ 8.65 – 8.57 (m, 2H), 8.37 (d, 1H), 7.94 (d, 1H), 7.72 (d, 1H), 7.43 (d, 1H), 7.34 (d, 1H), 7.15 (s, 1H), 6.93 (s, 1H), 6.12 (d, 2H), 3.86 (m, 1H), 2.09 – 1.91 (m, 2H), 1.78 (m, 3H), 1.62 (m, 2H), 1.26 (m, 2H), 1.12 – 0.85 (m, 4H), 0.62 (d, *J* = 12.2 Hz, 1H). Purity testing by HPLC (Acquisition method 65%-95% Acetonitrile 20 minutes) t_R = 18.1 minutes. Purity=98%.

Synthesis of (S)-2-(6-bromobenzo-1,3-dioxol-5-yl)-N-(3-bromophenyl)-1-(1-cyclohexylethyl)-1H-benzo[d]imidazole-5-carboxamide. (Compound P1n)

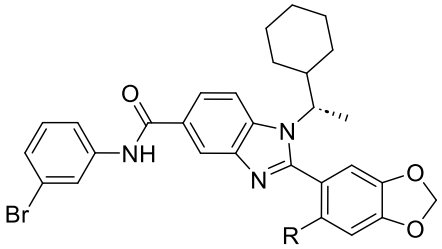

The method is similar for the preparation of AZ3451 was used except replacing the building block with 3-Bromoaniline (82.6 mg, 0.477 mmol). The reaction time was changed to 30 minutes under microwave irradiation (120℃). The residue was purified using flash silica gel column chromatography (eluent gradient, 5% Method in DCM). A white-yellow solid product-57mg (yield-36.6%) was obtained. Chemical Formula: $C_{29}H_{27}Br_2N_3O_3$. Molecular Weight: 625.36. LC-MS $[M + H]^+$ = 626.1 (calcd.) 626.3 (found). ^1H NMR (500 MHz, $CDCl_3$) δ 8.25 (s, 1H), 7.99 (d, 2H), 7.89 (s, 1H), 7.69 (d, 1H), 7.55 (s, 1H), 7.13 (d, 2H), 6.90 (s, 1H), 6.12 (d, 2H), 3.81 – 3.72 (m, 1H), 1.77 (m, 3H), 1.63 (m, 4H), 1.25 (m, 3H), 0.88 (m, 4H).Purity testing by HPLC (Acquisition method 65%-95% Acetonitrile 20 minutes) t_R = 13.5 minutes. Purity=97%.

Synthesis of (S)-2-(6-bromobenzo[d][1,3] dioxol-5-yl)-1-(1-cyclohexylethyl)-N-(5-fluoropyridin-2-yl)-1H-benzo[d]imidazole-5-carboxamide. (Compound P2e)

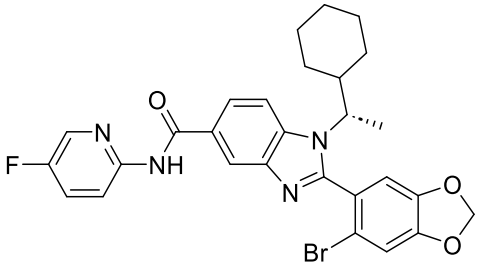

Compound P4 (100 mg, 0.206 mmol) was dissolved in DMF, then thionyl chloride (SOCl2) (0.416mmol). The reaction mixture was run under the microwave at 100°C for 30 minutes. After cooling to room temperature, excess thionyl chloride is removed under vacuum to give the crude aryl chloride. Separately, 2-Amino-5-fluoropyridine (35mg, 0.31mmol) was added into the intermediate (aryl chloride) with DIPEA (53.2 mg, 0.412 mmol) and DMF (2.5ml), The reaction mixture was run under the microwave at 120°C for 20 minutes. The combined organic layers were dried with Na_2SO_4 and filtered, and the solvent was removed under reduced pressure. The residue was purified using flash silica gel column chromatography (eluent gradient, 25% EtOAc in Hexanes). The final compound was further purified by prep-HPLC

with a gradient from 65% to 95% acetonitrile (0.1% formic acid) in water. A white solid product-58mg (yield-38.6%) was obtained. Chemical Formula: $C_{28}H_{26}BrFN_4O_3$. Molecular Weight: 565.44. LC-MS $[M + H]^+$ = 567.1 (calcd.) 567.2 (found). ^{1}H NMR (500 MHz, $CDCl_3$) δ 8.66 (s, 1H), 8.46 (m, *J* = 9.1, 4.1 Hz, 1H), 8.35 (m, *J* = 11.7 Hz, 1H), 7.92 – 7.88 (m, 1H), 7.68 (m, *J* = 14.6, 8.7 Hz, 1H), 7.54 – 7.48 (m, 1H), 7.18 (d, *J* = 35.6 Hz, 1H), 6.85 (d, *J* = 75.1 Hz, 1H), 6.12 (d, *J* = 16.0 Hz, 2H), 3.80 (m, *J* = 10.3, 7.0 Hz, 1H), 1.99 (m, *J* = 45.4, 12.1 Hz, 2H), 1.78 (m, *J* = 6.9 Hz, 3H), 1.62 (m, *J* = 7.1 Hz, 3H), 1.27 (m, *J* = 13.0 Hz, 1H), 0.97 (m, *J* = 52.6, 22.9, 12.1 Hz, 4H), 0.62 (m, *J* = 12.0 Hz, 1H). Purity testing by HPLC (Acquisition method 65%-95% Acetonitrile 20 minutes) t_R = 16.4 minutes. Purity=95%.

Synthesis of (S)-2-(6-bromobenzo[d][1,3] dioxol-5-yl)-1-(1-cyclohexylethyl)-N-(6-fluoropyridin-3-yl)-1H-benzo[d]imidazole-5-carboxamide. (Compound P2f)

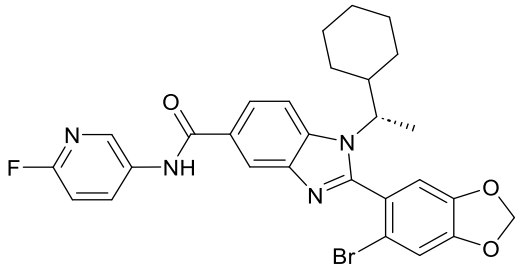

The method is similar for the preparation of compound P2e except replacing the building block with 5-Amino-2-fluoropyridine (35.6 mg, 0.31 mmol). The residue was purified using flash silica gel column chromatography (eluent gradient, 25% EtOAc in Hexanes). The final compound was further purified by prep-HPLC with a gradient from 65% to 95% acetonitrile (0.1% formic acid) in water. A white solid product-56mg (yield-37.6%) was obtained. Chemical Formula: $C_{28}H_{26}BrFN_4O_3$. Molecular Weight: 565.44. LC-MS $[M + H]^+$ = 567.1 (calcd.) 567.2 (found). ^{1}H NMR (500 MHz, $CDCl_3$) δ 10.54 – 10.35 (s, 1H), 8.65 (m, *J* = 21.3 Hz, 1H), 8.43 (m, *J* = 47.0, 1.6 Hz, 1H), 8.31 – 8.19 (m, 1H), 7.94 (m, *J* = 29.8, 8.6, 1.5 Hz, 1H), 7.60 (m, *J* = 8.6, 2.7 Hz, 1H), 6.95 – 6.88 (m, 1H), 6.84 (m, *J* = 6.5, 3.2 Hz, 1H), 6.61 – 6.52 (m, 1H), 6.04 (m, *J* = 15.5, 1.3 Hz, 2H), 3.82 – 3.61 (m, 1H), 2.01 – 1.84 (m, 2H), 1.74 (d, *J* = 13.6 Hz, 1H), 1.65 – 1.57 (m, 3H), 1.51 (m, *J* = 10.9 Hz, 2H), 1.23 – 1.17 (m, 1H), 1.06 – 0.75 (m, 4H), 0.69 – 0.48 (m, 1H). Purity testing by HPLC (Acquisition method 65%-95% Acetonitrile 20 minutes) t_R = 15.5 minutes. Purity=97%.

Synthesis of (S)-2-(6-bromobenzo [1,3] dioxol-5-yl)-1-(1-cyclohexylethyl)-N-(thiazol-2-yl)-1H-benzo[d]imidazole-5-carboxamide. (Compound P2g)

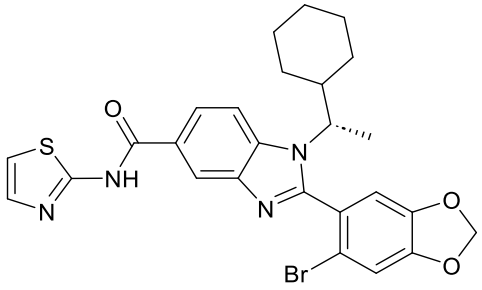

The method is similar for the preparation of compound P2e except replacing the building block with 2-Aminoarhiazole (32 mg, 0.309 mmol). The combined organic layers were dried with Na_2SO_4 and filtered, and the solvent was removed under reduced pressure. The residue was purified using flash silica gel column chromatography (eluent gradient, 25% EtOAc in Hexanes). The final compound was further purified by prep-HPLC with a gradient from 65% to 95% acetonitrile (0.1% formic acid) in water. A white solid product-48mg (yield-35.6%) was obtained. Chemical Formula: $C_{26}H_{25}BrN_4O_3S$. Molecular Weight: 553.48. LC-MS $[M + H]^+$ = 555.1 (calcd.) 554.9 (found). ^1H NMR (500 MHz, $CDCl_3$) δ 8.54 (m, *J* = 16.7 Hz, 1H), 8.00 – 7.95 (m, 1H), 7.68 (m, *J* = 9.3 Hz, 1H), 7.29 (m, *J* = 3.6 Hz, 1H), 7.14 (m, *J* = 33.8 Hz, 1H), 6.94 (m, *J* = 4.2 Hz, 1H), 6.84 (m, *J* = 63.6 Hz, 1H), 6.15 – 6.07 (m, 2H), 3.94 – 3.75 (m, 1H), 2.08 – 1.91 (m, 2H), 1.77 (m, *J* = 9.8 Hz, 3H), 1.59 (m, *J* = 26.9, 9.0 Hz, 3H), 1.32 – 1.17 (m, 1H), 1.12 – 0.79 (m, 4H), 0.76 – 0.56 (m, 1H). Purity testing by HPLC (Acquisition method 65%-95% Acetonitrile 20 minutes) t_R = 16.4 minutes. Purity=99%.

Synthesis of (S)-2-(6-bromobenzo [1,3] dioxol-5-yl)-1-(1-cyclohexylethyl)-N-(5-methylthiazol-2-yl)-1H-benzo[d]imidazole-5-carboxamide. (Compound P2h)

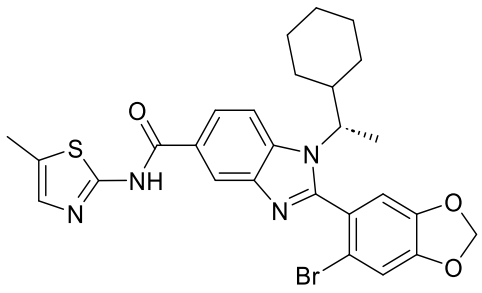

The method is similar for the preparation of compound P2e except replacing the building block with 2-Amino-5-methylthiazole (35mg, 0.309mmol). The combined organic layers were dried with Na_2SO_4 and filtered, and the solvent was removed under reduced pressure. The residue was purified using flash silica gel column chromatography (eluent gradient, 20% EtOAc in Hexanes). The final compound was further purified by prep-HPLC with a gradient from 65% to 95% acetonitrile (0.1% formic acid) in water. A white solid product-49mg (yield-36%) was

obtained. Chemical Formula: $C_{27}H_{27}BrN_4O_3S$. Molecular Weight: 567.50. LC-MS $[M + H]^+$ = 569.1 (calcd.) 569.2 (found). ^1H NMR (500 MHz, $CDCl_3$) δ 8.50 (m, *J* = 18.7 Hz, 1H), 7.99 – 7.92 (m, 1H), 7.68 (m, *J* = 13.2, 8.6 Hz, 1H), 7.15 (m, *J* = 32.5 Hz, 1H), 6.93 – 6.76 (m, 2H), 6.11 (m, *J* = 20.5, 1.2 Hz, 2H), 3.94 – 3.74 (m, 1H), 2.37 (m, *J* = 0.9 Hz, 3H), 2.09 – 1.92 (m, 2H), 1.77 (m, *J* = 6.9 Hz, 3H), 1.59 (m, *J* = 26.3, 9.1 Hz, 3H), 1.32 – 1.20 (m, 1H), 1.11 – 0.55 (m, 5H). Purity testing by HPLC (Acquisition method 65%-95% Acetonitrile 20 minutes) t_R = 16.5 minutes. Purity=97%.

Synthesis of (S)-2-(6-bromobenzo[d][1,3]dioxol-5-yl)-1-(1-cyclohexylethyl)-N-(5-methyl-1H-pyrazol-3-yl)-1H-benzo[d]imidazole-5-carboxamide. (Compound P2i)

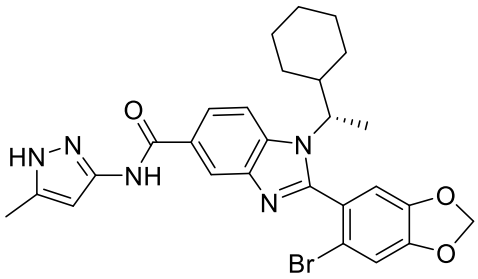

The method is similar for the preparation of compound P2e except replacing the building block with 5-methyl-1H-pyrazol-3-amine (31 mg, 0.309 mmol). The combined organic layers were dried with Na_2SO_4 and filtered, and the solvent was removed under reduced pressure. The residue was purified using flash silica gel column chromatography (eluent gradient, 20-30% EtOAc in Hexanes). The final compound was further purified by prep-HPLC with a gradient from 65% to 95% acetonitrile (0.1% formic acid) in water. A white solid product-39mg (yield-34%) was obtained. Chemical Formula: $C_{27}H_{28}BrN_5O_3$. Molecular Weight: 550.46 LC-MS $[M + H]^+$ = 550.12 (calcd.) 550.21 (found). Purity testing by HPLC (Acquisition method 75%-95% Acetonitrile 20 minutes) t_R = 5.4 minutes. Purity=96%.

Synthesis of (S)-N-(benzo[d]thiazol-6-yl)-2-(6-bromobenzo[d][1,3] dioxol-5-yl)-1-(1-cyclohexylethyl)-1H-benzo[d]imidazole-5-carboxamide. (Compound P3f)

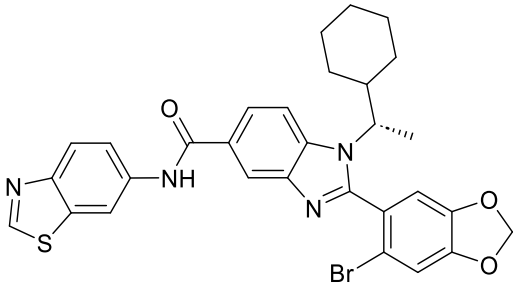

The method is similar for the preparation of compound P2e except replacing the building block with 6-Aminobenzothiazole (47.7 mg, 0.31 mmol). The combined organic layers were dried with Na_2SO_4 and filtered, and the solvent was removed under reduced pressure. The residue was purified using flash silica gel column chromatography (eluent gradient, 20-30% EtOAc in Hexanes). A light brown solid product was obtained in 36.8% yield (45 mg). Chemical Formula: $C_{30}H_{27}BrN_4O_3S$. ^{1}H NMR (500 MHz, $CDCl_3$) δ 9.69 (m, *J* = 90.4 Hz, 1H), 8.93 (s, 1H), 8.69 (s, 1H), 8.56 (m, *J* = 28.2 Hz, 1H), 8.05 – 7.92 (m, 2H), 7.67 – 7.58 (m, 2H), 6.91 (m, *J* = 41.4 Hz, 1H), 6.70 – 6.58 (m, 1H), 5.98 (d, *J* = 11.3 Hz, 1H), 5.79 (d, *J* = 28.3 Hz, 1H), 3.85 – 3.64 (m, 1H), 1.94 (m, *J* = 48.4, 11.4 Hz, 2H), 1.74 (m, *J* = 15.3 Hz, 3H), 1.63 – 1.48 (m, 3H), 1.25 (m, *J* = 17.3, 9.8 Hz, 1H), 1.15 – 0.76 (m, 4H), 0.59 (m, *J* = 35.6, 11.7 Hz, 1H). LC-MS $[M + H]^+$ = 605.1 (cacld.) 605.2 (found). Purity testing by HPLC (Acquisition method 65%-95% Acetonitrile 20 minutes) t_R = 15.7 minutes. Purity=98%.

Synthesis of (S)-N-(benzo[d]thiazol-5-yl)-2-(6-bromobenzo[d][1,3] dioxol-5-yl)-1-(1-cyclohexylethyl)-1H-benzo[d]imidazole-5-carboxamide. (Compound P3g)

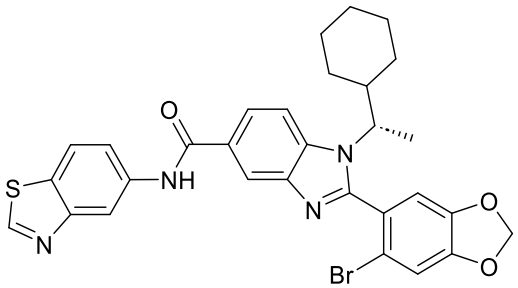

The method is similar for the preparation of compound P2e except replacing the building block with 1,3-benzothiazol-5-amine (47.7 mg, 0.309 mmol). The combined organic layers were dried with Na_2SO_4 and filtered, and the solvent was removed under reduced pressure. The residue was purified using flash silica gel column chromatography (eluent gradient, 20-30% EtOAc in Hexanes). A light brown solid product was obtained in 38.6% yield (49 mg). $C_{30}H_{27}BrN_4O_3S$. ^{1}H NMR (500 MHz, $CDCl_3$) δ 9.45 (m, *J* = 48.1 Hz, 1H), 9.00 (m, *J* = 4.4 Hz, 1H), 8.54 (m, *J* = 19.3, 7.6 Hz, 2H), 8.00 – 7.94 (m, 1H), 7.87 (m, *J* = 6.6 Hz, 2H), 7.63 (m, *J*

= 8.6, 4.6 Hz, 1H), 6.94 (m, *J* = 49.8 Hz, 1H), 6.74 – 6.60 (m, 1H), 6.03 – 5.86 (m, 2H), 3.76 (m, *J* = 24.3, 10.5, 6.9 Hz, 1H), 2.03 (m, *J* = 33.3, 16.5, 7.4 Hz, 1H), 1.90 (m, *J* = 12.7 Hz, 1H), 1.72 (m, *J* = 23.7, 10.3 Hz, 3H), 1.63 – 1.47 (m, 3H), 1.23 (m, *J* = 12.9, 5.8 Hz, 1H), 1.07 – 0.76 (m, 4H), 0.59 (m, *J* = 20.1, 11.2, 10.1 Hz, 1H). HPLC-MS (Waters), t_R = 15.5 minutes. LC-MS $[M + H]^+$ = 605.1 (cacld.) 605.2 (found). Purity testing by HPLC (Acquisition method 65%-95% Acetonitrile 20 minutes) t_R = 15.4 minutes. Purity=95%.

Synthesis of (S)-N-(1H-benzo[d]imidazol-6-yl)-2-(6-bromobenzo[d][1,3] dioxol-5-yl)-1-(1-cyclohexylethyl)-1H-benzo[d]imidazole-5-carboxamide. (Compound P3h)

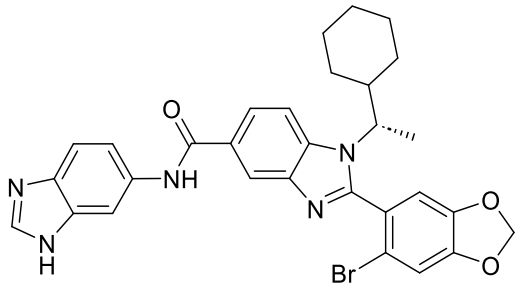

The method is similar for the preparation of compound P2e except replacing the building block with 5-Aminobenzimidazole (42 mg, 0.309 mmol). The combined organic layers were dried with Na_2SO_4 and filtered, and the solvent was removed under reduced pressure. The residue was purified using flash silica gel column chromatography (eluent gradient, 20-30% EtOAc in Hexanes). A light brown solid product was obtained in 39.6% yield (47 mg). Chemical Formula: $C_{30}H_{28}BrN_5O_3$. ^{1}H NMR (500 MHz, $CDCl_3$) δ 9.53 (s, 1H), 8.49 (s, 1H), 8.15 (s, 1H), 7.92 (s, 2H), 7.56 (m, *J* = 17.9 Hz, 1H), 7.47 (s, 1H), 7.32 (s, 1H), 7.06 – 6.92 (m, 1H), 6.72 (m, *J* = 71.7 Hz, 1H), 5.99 (m, *J* = 37.4 Hz, 2H), 3.75 (m, *J* = 42.6 Hz, 1H), 2.05 – 1.83 (m, 2H), 1.78 – 1.64 (m, 3H), 1.58 – 1.45 (m, 3H), 1.24 (m, *J* = 20.5, 6.7 Hz, 1H), 0.87 (m, *J* = 77.2, 20.6 Hz, 4H), 0.54 (m, *J* = 9.6 Hz, 1H). LC-MS $[M + H]^+$ = 588.1 (calcd.) 588.2 (found). Purity testing by HPLC (Acquisition method 65%-95% Acetonitrile 20 minutes) t_R = 10.8 minutes. Purity=96%.

Synthesis of (S)-N-(2H-benzo[d][1,2,3] triazol-5-yl)-2-(6-bromobenzo[d][1,3]dioxol-5-yl)-1-(1-cyclohexylethyl)-1H-benzo[d]imidazole-5-carboxamide. (Compound P3i)

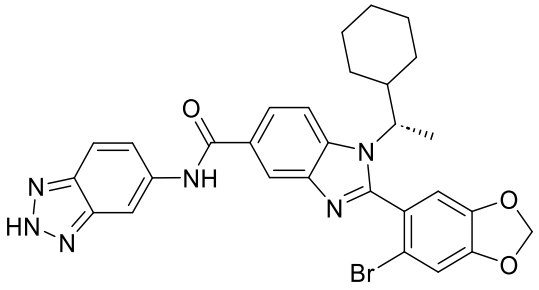

The method is similar for the preparation of compound P2e except replacing the building block with 5-Aminobenzotriazole (42 mg, 0.31 mmol). The combined organic layers were dried with Na_2SO_4 and filtered, and the solvent was removed under reduced pressure. The residue was purified using flash silica gel column chromatography (eluent gradient, 20-30% EtOAc in Hexanes). The final compound was further purified by prep-HPLC with a gradient from 65% to 95% acetonitrile (0.1% formic acid) in water. A light brown solid product was obtained in 32% yield (41mg). Chemical Formula: $C_{29}H_{27}BrN_6O_3$. ^{1}H NMR (500 MHz, $CDCl_3$) δ 8.61 (m, *J* = 51.2 Hz, 2H), 8.02 (s, 1H), 7.80 (s, 1H), 7.65 – 7.41 (m, 2H), 6.91 – 6.56 (m, 2H), 5.84 (m, *J* = 86.0 Hz, 2H), 3.74 (m, *J* = 38.9 Hz, 1H), 2.00 (m, *J* = 25.1 Hz, 1H), 1.87 (m, *J* = 4.0 Hz, 1H), 1.68 (m, *J* = 19.3 Hz, 3H), 1.54 (m, *J* = 33.4 Hz, 3H), 1.22 (m, *J* = 20.4 Hz, 1H), 1.09 – 0.75 (m, 4H), 0.54 (m, 1H). LCMS LC-MS $[M + H]^+$ = 589.1 (calcd.) 589.2 (found). Purity testing by HPLC (Acquisition method 65%-95% Acetonitrile 20 minutes) t_R = 13.9 minutes. Purity=97%.

Synthesis of 2-(6-bromobenzo[d][1,3] dioxol-5-yl)-N-(4-cyanophenyl)-1-(4-fluorobenzyl)-1H-benzo[d]imidazole-5-carboxamide. (Compound P8)

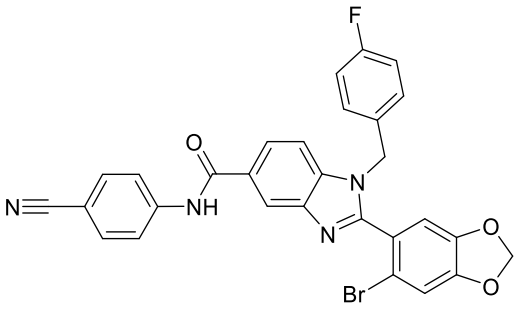

The method is similar for the preparation of AZ3451 in **Scheme 2.1**, except (S)-1-cyclohexylethan-1-amine was replaced by (4-fluorophenyl) methanamine (79 mg, 0.63 mmol) to make compound P5 in **Scheme 2.4**. Purification with similar method by the crude product

was purified by flash silica chromatography with an elution gradient 1:5 EtOAc: Hexane. The final compound was further purified by prep-HPLC with a gradient from 65% to 95% acetonitrile (0.1% formic acid) in water. A light grey solid product was obtained in 46% yield (72 mg). Chemical Formula: $C_{29}H_{18}BrFN_4O_3$. ^{1}H NMR (500 MHz, $CDCl_3$) δ 9.38 (s, 1H), 8.51 (s, 1H), 7.91 (m, *J* = 7.8 Hz, 1H), 7.84 (m, *J* = 8.0 Hz, 2H), 7.60 (d, *J* = 8.0 Hz, 2H), 7.31 (d, *J* = 7.5 Hz, 1H), 6.93 (d, *J* = 5.9 Hz, 4H), 6.66 (s, 1H), 6.04 (s, 2H), 5.19 (s, 2H). LC-MS $[M + H]^+$ = 570.1 (calcd.) 570.2 (found). Purity testing by HPLC (Acquisition method 65%-95% Acetonitrile 20 minutes) t_R = 14.4 minutes. Purity=96%.

Synthesis of 2-(6-bromobenzo[d][1,3] dioxol-5-yl)-N-(4-cyanophenyl)-1-(cyclohexylmethyl)-1H-benzo[d]imidazole-5-carboxamide. (Compound P12)

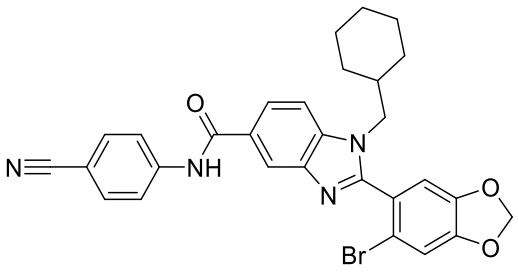

The method similar for the preparation of AZ3451 in **Scheme 2.1**, except (S)-1-cyclohexylethan-1-amine was replaced by cyclohexylmethanamine (72 mg, 0.63 mmol) to compound P11 in **Scheme 2.4**. Purification with similar method by the crude product was purified by flash silica chromatography with an elution gradient 1:10 EtOAc: Hexane. And then, the column solvent system was changed to 1:5 EtOAc: Hexane. The final compound was further purified by prep-HPLC with a gradient from 65% to 95% acetonitrile (0.1% formic acid) in water. A white solid product was obtained in 41.1% yield (47 mg). Chemical Formula: $C_{29}H_{25}BrN_4O_3$. ^{1}H NMR (500 MHz, $CDCl_3$) δ 8.39 (s, 1H), 7.96 (m, *J* = 8.5, 1.6 Hz, 1H), 7.84 (d, *J* = 8.7 Hz, 2H), 7.64 (d, *J* = 8.6 Hz, 2H), 7.51 (m, *J* = 8.5 Hz, 1H), 7.05 (s, 1H), 6.84 (s, 1H), 6.09 (s, 2H), 3.81 (m, *J* = 65.6 Hz, 2H), 1.25 (m, 3H), 1.09 (m, 2H), 0.86 (m, *J* = 17.3, 6.4 Hz, 6H). LC-MS $[M + H]^+$ = 559.1 (calcd.) 559.2 (found). Purity testing by HPLC (Acquisition method 65%-95% Acetonitrile 20 minutes) t_R = 16.2 minutes. Purity=95%.

Synthesis of (S)-2-(2-bromophenyl)-1-(1-cyclohexylethyl)-1H-benzoimidazole-5-carboxylic acid. (Compound P14)

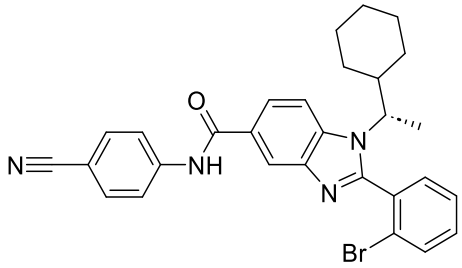

The method is similar for the preparation of AZ3451 in **Scheme 2.1**, except that 6-bromobenzo-d-1,3-dioxole-5-carbaldehyde was replaced by 2-Bromobenzaldehyde to make compound P9 in **Scheme 2.4**. Purification with similar method by the crude product was purified by flash silica chromatography with an elution gradient 1:5 EtOAc: Hexane. And then, the column solvent system was changed to 1:3 EtOAc: Hexane. The final compound was further purified by prep-HPLC with a gradient from 65% to 95% acetonitrile (0.1% formic acid) in water. A dark-brown solid product of 104 mg (45%) was obtained. ^{1}H NMR (500 MHz, $CDCl_3$) δ 8.59 (m, 1H), 8.34 (m, 1H), 7.91 (m, *J* = 7.9 Hz, 1H), 7.82 (m, *J* = 7.8 Hz, 2H), 7.67 (m, *J* = 27.6, 8.5 Hz, 4H), 7.47 – 7.36 (m, 3H), 3.79 (d, *J* = 66.2 Hz, 1H), 2.10 – 1.86 (m, 2H), 1.76 (m, *J* = 6.0 Hz, 4H), 1.56 – 1.48 (m, 2H), 1.25 (m, 1H), 0.89 (m, *J* = 96.8, 12.1 Hz, 4H), 0.58 (m, 1H). LC-MS $[M + H]^+$ = 529.1 (calcd.) 529.2 (found). Purity testing by HPLC (Acquisition method 65%-95% Acetonitrile 20 minutes) t_R = 17.1 minutes. Purity=96%.

Synthesis of compound spiroadamantyl-1,3-dioxane-4,6-dione (SPIAd).

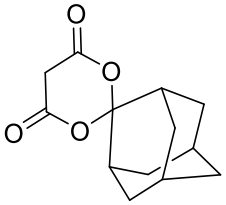

The compound was made according to literature procedures with some modifications. Malonic acid (5.0 g, 48 mmol) and acetic anhydride (4.8 mL) were measured and added into a round-bottom flask with conc. H_2SO_4 (0.2 mL). The reaction mixture was heated with stirring to 60 °C for 20 minutes. Cool the reaction mixture to room temperature (25°C) and 2-adamantanone (4.0 g, 48 mmol) was added to the mixture for 30 min via a glass addition funnel at an approximate rate of one liquid drop per 15–20 second. Stir the reaction mixture for 24 h at room temperature under an argon balloon. When completed, remove the volatiles by rotary evaporation under vacuum. Resolubilize the mixture in ethyl acetate (500 mL), wash the

organic solution with DI water (5 × 100 mL) and brine (300 mL), and dry over anhydrous $MgSO_4$ (20 g) for 20 minutes. Concentrate the crude product, re-disperse, and grind carefully in ethyl acetate and diethyl ether (120 mL, 1:1) until just a small amount of white solid can be observed. Filter the above solution quickly over a silica gel pad (5-cm thickness) and concentrate the filtration. Precipitate the crude product in diethyl ether and hexanes (90 mL, 3:2 (vol/vol)) in a freezer (−20°C) for 5 hours. Grind carefully and filter to yield 3.8 g (57%) of a white solid. Chemical Formula: $C_{13}H_{16}O_4$. ^{1}H NMR (500 MHz, $CDCl_3$) δ 3.61 (s, 1H), 3.61 (s, 1H), 2.17 (d, *J* = 32.3 Hz, 3H), 2.17 (d, *J* = 32.3 Hz, 3H), 1.92 (s, 1H), 1.92 (s, 1H), 1.79 (d, *J* = 27.9 Hz, 3H), 1.79 (d, *J* = 27.9 Hz, 3H).

Synthesis of precursor.

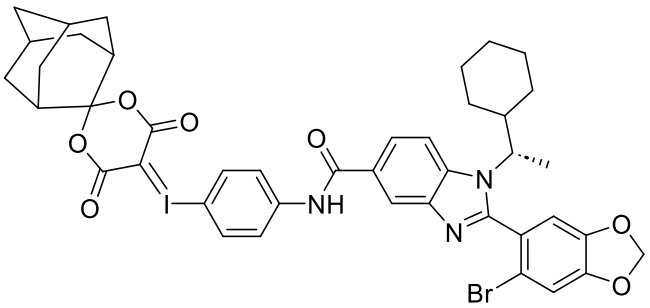

This procedure is based on literature reports. mCPBA (232 mg, 1.35 mmol) was added to a solution of aryl iodide - compound 1h (300 mg, 0.45 mmol) in chloroform (10 mL). The reaction mixture was stirred at room temperature for 4 hours until full conversion of the starting material was determined by TLC plate in 1:1 EtOAc: Hexanes solvent system. The reaction mixture was concentrated in vacuo to yield a dry, white residue. Then EtOH (25 mL) was added to the mixture to dissolved white residue. A solution of SPIAd in 10% Na_2CO_3 (aq) (w/v, 10mL) was added to the reaction mixture. The mixture was then stirred at room temperature for another 4 hours. The mixture was then dried in a freezer dryer to remove the water. Obtained a dry, light-yellow powder-like crude product. The crude product was then dissolved with chloroform and filtered. The solvent was removed under reduced pressure by rotary evaporation. The crude product was purified by prep-HPLC with a gradient from 65% acetonitrile in water (0.1% formic acid). It was dried to give the precursor 29mg in 17% yield. HPLC−MS (Waters) method: 65% of acetonitrile in water (0.1% formic acid), 20 min run, t_R (min) 14.4. Chemical

Formula: $C_{42}H_{41}BrIN_3O_7$. ^{1}H NMR (500 MHz, $CDCl_3$) δ 8.38 (s, 1H), 7.94 (m, *J* = 8.2 Hz, 1H), 7.66 (m, *J* = 24.8, 8.5 Hz, 3H), 7.52 (m, *J* = 8.2 Hz, 2H), 7.11 (m, *J* = 29.9 Hz, 1H), 6.80 (m, *J* = 64.0 Hz, 1H), 6.11 (m, *J* = 13.5 Hz, 2H), 3.81 (m, *J* = 32.1 Hz, 1H), 2.55 (s, 1H), 2.35 (s, 1H), 2.17 (m, *J* = 12.3 Hz, 2H), 2.04 (m, *J* = 42.2, 12.0 Hz, 4H), 1.94 (s, 3H), 1.80 (m, *J* = 47.9, 9.8 Hz, 8H), 1.59 (m, *J* = 37.9 Hz, 3H), 1.25 (s, 1H), 0.94 (m, *J* = 42.8, 23.4, 12.2 Hz, 4H), 0.62 (m, *J* = 25.5 Hz, 1H). LC-MS $[M + H]^+$ = 908.12 (calcd.) 908.06 (found). Purity testing by HPLC (Acquisition method 75%-95% Acetonitrile 20 minutes) t_R = 17.3 minutes. Purity=98%.

Chapter Three

Design, Synthesis, and Evaluation of Novel Lysophosphatidic Acid Receptor 1 (LPA1)-Targeting Small Molecules as Therapeutic and Diagnostic Agents

3.1 Introduction

3.1.1 Lysophosphatidic Acid (LPA)

Lysophosphatidic acid (LPA) is a small (relatively low molecular weight) but highly significant bioactive lipid, widely recognized for its role in cellular signaling[181–183]. However, in the 1960s, early studies thought LPA as a minor metabolite involved in membrane phospholipid biosynthesis[181]. At that time, its biological significance was unclear, and its role as a signaling molecule was not recognized yet[181]. Over the next three decades, numerous studies demonstrated that LPA could function as a signaling molecule[181,183,184]. By the 1990s, LPA was firmly established as a potent signaling molecule influencing diverse cellular processes such as proliferation, survival, cytoskeletal reorganization, and calcium influx[183,184]. A key breakthrough in LPA research came in 1996 with the cloning and characterization of the first LPA receptor, LPAR1 or LPA1[98,185]. Initially named "ventricular zone gene-1" due to its expression in the neurogenic regions of the embryonic brain, LPA1 was identified as a member of the G protein-coupled receptors (GPCRs) family[181,186]. This discovery highlighted LPA's role as an extracellular signaling molecule. Following this, two additional receptors, LPA2 and LPA3, were identified[181,186]. These three receptors were further subdivided into the "endothelial differentiation gene" (EDG) family due to their significant sequence homology[187,188]. Later, three more related receptors, LPA4-LPA6, were discovered and classified into the Purinergic receptor P2, subtype Y (P2Y) receptor family[181,189].

LPA is present both intracellularly and extracellularly, with different production pathways depending on the involved enzymes and substrates (**Fig. 3.1**)[89,190]. Given that LPA1 belongs to the GPCR family located in the cell membrane, extracellular production is the primary pathway for LPA signaling through the LPA1 receptor[181,190].

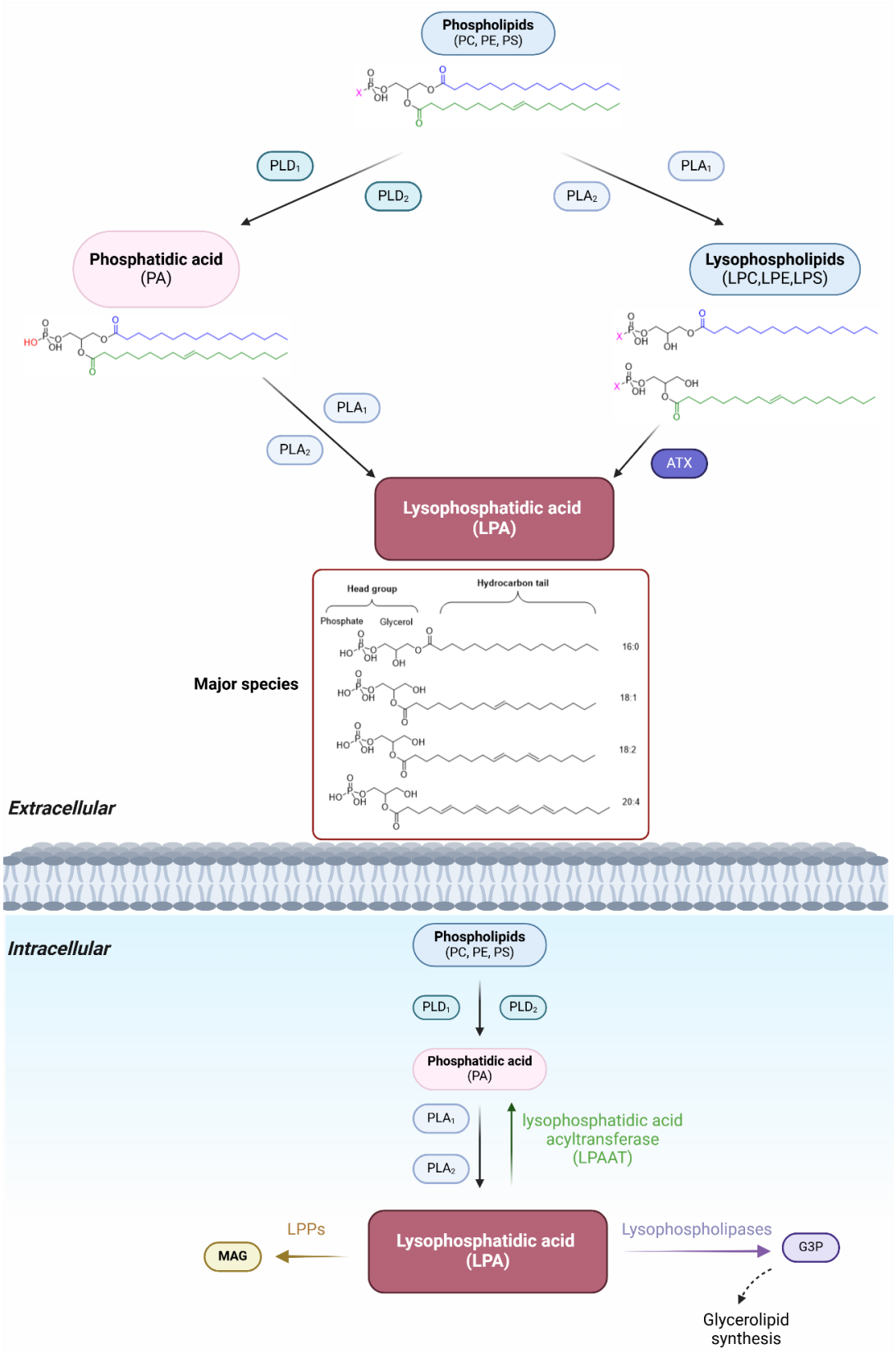

Figure 3.1. LPA intracellular and extracellular production and degradation. X in the structure is represented hydrophilic head group.

Extracellularly, LPA can be produced via two mechanisms: an independent mechanism and an autotaxin (ATX)-dependent mechanism[183,189]. In independent mechanisms, phospholipids are converted into phosphatidic acid (PA) by phospholipase D (PLD), and PA is then deacylated by phospholipase A enzymes (PLA1 and PLA2) to produce LPA[34,89,190]. In the ATX-dependent mechanism, phospholipids are hydrolyzed into lysophospholipids (such as lysophosphatidylcholine [LPC], lysophosphatidylethanolamine [LPE], and lysophosphatidylserine [LPS]) by PLA1 and PLA2, followed by cleavage by ATX to produce LPA[89,191].

In circulation, enzymes also regulate LPA degradation through three pathways. The first involves lipid phosphate phosphatases (LPPs), which dephosphorylate LPA to monoacylglycerol (MAG)[185,192]. The second pathway involves LPA acyltransferase (LPAAT), which catalyzes the conversion of LPA to PA[190,192]. The third pathway converts LPA into glycerol-3-phosphate (G3P) by phospholipase[190]. Also, most studies indicate that the intracellular pathway of LPA (synthesis and degradation) serves only as an intermediate step in glycerolipid synthesis and not as an extracellular signaling pathway[190,193].

All LPA molecules are characterized by a phosphate group (the head group) attached to a glycerol backbone, which is linked to a single aliphatic chain of varied length and saturation (the hydrocarbon tail)[184,194]. The terms "16:0," "18:0," and "18:1" describe the fatty acid chain's length and degree of unsaturation in an LPA molecule[89,194]. Specifically, 18:1-LPA, oleoyl-LPA (1-acyl-2-hydroxy-sn-glycero-3-phosphate), is the commonly used experimental reagent for activating LPA receptors in research[181]. With its monounsaturated fatty acid chain, this species is a standard ligand for investigating LPA1-mediated signaling pathways[181].

3.1.2 Lysophosphatidic Acid 1 Receptor (LPAR1)

Lysophosphatidic acid (LPA) receptors, including LPAR1 to LPAR6 (or LPA1 for shorts), belong to the GPCR family and are involved in various physiological and pathological processes, including cancer, fibrosis, and inflammation[181,185]. LPA1, the first lysophosphatidic acid receptor to be discovered, is the most studied in the LPA family[98,195]. It shares over 50% sequence similarity with LPA2 and LPA3 but less than 20% with LPA4 to LPA6[181]. This sequence similarity reflects critical regions for ligand binding and receptor activation, while differences enable unique functional roles in cellular signaling[181,196].

LPA1 is strongly implicated in various human diseases, particularly lung diseases such as idiopathic pulmonary fibrosis (IPF), chronic obstructive pulmonary disease (COPD), and acute

lung injury (ALI)[185,197,198]. Aberrant activation of LPA1 promotes the progression of these diseases by dysregulating cellular signaling pathways[185,188]. In LPA receptor family, LPA1 is considered the primary receptor involved in lung fibrosis and serves as a key therapeutic target, with other LPA receptors contributing to fibrotic mechanisms to a lesser extent[188,194]. The first crystal structure of human LPA1 receptor in complex with three antagonists was published in 2015[196]. This study provided detailed insights into the receptor's structure and interactions with antagonist compounds, offering a foundation for understanding ligand access to the LPA1 binding pocket and its implications for receptor function[185,196]. LPA receptors couple with all four Gα proteins (G12/13, Gq/11, Gi/o, and Gs), initiating various signaling cascades[190]. LPA1 has been shown to couple with Gi, Gq, and G12/13 proteins[190]. These pathways, summarized in **Figure 3.2**, involve several distinct classes of heterotrimeric G proteins, leading to diverse downstream signaling and cellular activities[115,190,192].

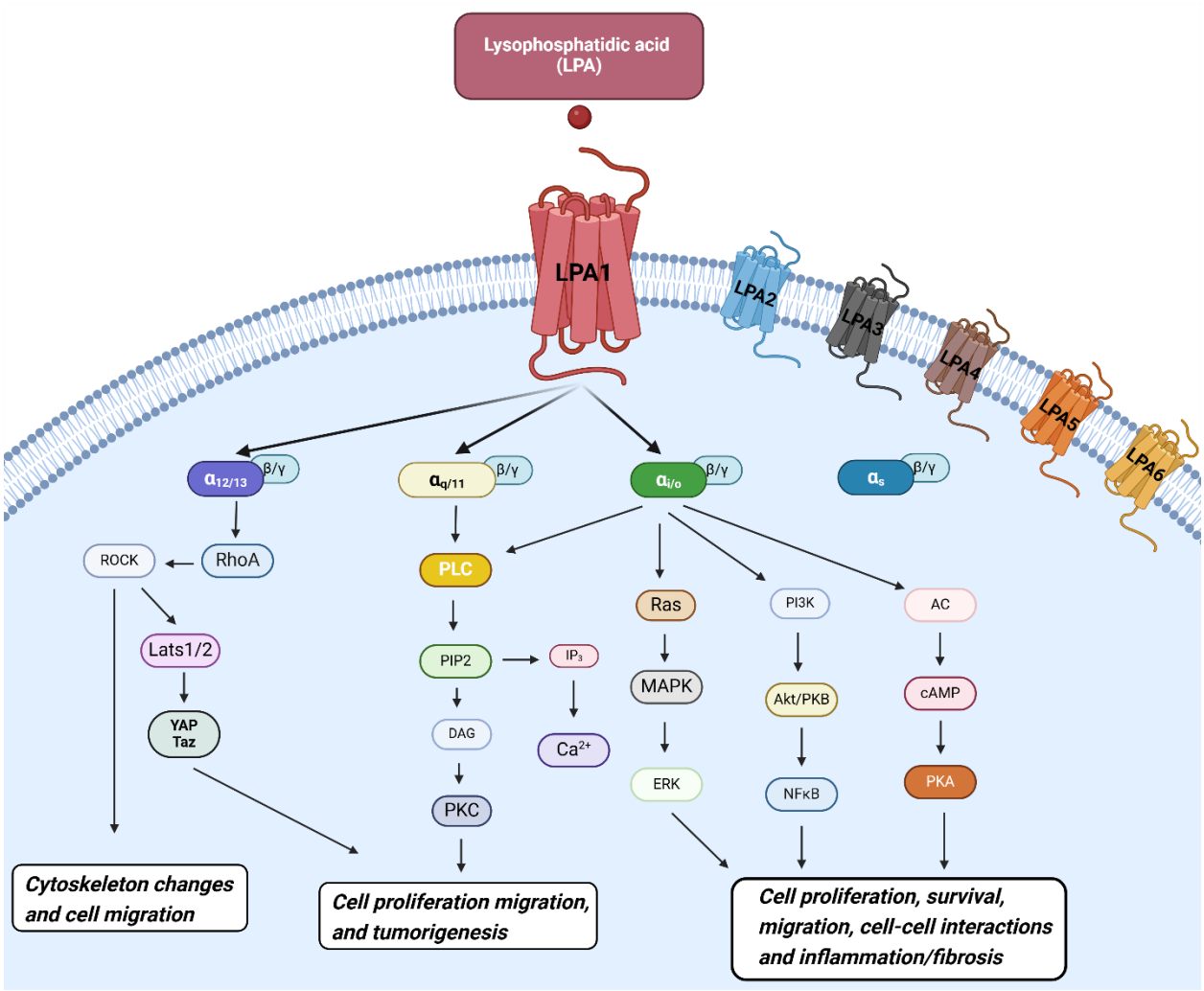

Figure 3.2. LPA1 receptor downstream signaling and signaling intermediates.

Coupling with Gi/o allows LPA1 to activate the PI3K/Akt pathway, promoting cell survival and proliferation while inhibiting apoptosis[185,190]. This pathway is crucial in cancer progression, supporting tumor growth and resistance to cell death[183,185]. Interaction with G12/13 activates RhoA, a small GTPase regulating cytoskeletal dynamics and stress fiber formation via the Rho-associated protein kinase (ROCK) pathway[183]. This signaling is central to cell motility, invasion, and fibroblast recruitment, essential in both metastatic cancer and fibrotic tissue development[183]. Coupling to Gq/11 activates phospholipase C (PLC), generating inositol trisphosphate (IP3) and diacylglycerol (DAG), leading to calcium release and protein kinase C (PKC) activation[185]. These events stimulate the MAPK/ERK pathway, promoting cellular proliferation and survival[185].

3.1.3 The Role and Function of LPA1 in Disease

Numerous studies demonstrate LPA1 is widely expressed in several organs, including the brain, uterus, testis, lung, small intestine, heart, stomach, kidney, spleen, thymus, placenta, and skeletal muscle[190,192]. It mediates a wide range of cellular processes and is linked to numerous disease states[190]. The physiological and pathological roles of the LPA1 receptor are summarizing in **Table 3.1**[189,190].

Table 3.1. Physiological and Pathological Roles of LPA1.

Role	Physiological Functions of LPA1	Pathological Implications of LPA1
Neural and skeletal development	Regulates neural differentiation, axon guidance, and synapse formation. Facilitates cell migration for skeletal development.	Dysregulated signaling can lead to developmental abnormalities, such as impaired neural connectivity and skeletal distortions.
Lung Fibrosis	Facilitates tissue repair after minor lung injuries by promoting controlled fibroblast activity.	Leads to excessive fibroblast recruitment, differentiation, and extracellular matrix deposition, causing progressive scarring and compromised lung function.
Vascular System	Enhances endothelial survival and vascular integrity, supporting normal angiogenesis and vascular remodeling.	Induces pathological angiogenesis and vascular remodeling, contributing to hypertension and atherosclerosis.
Immune Response	Regulates immune cell trafficking and activation to support wound healing and defense mechanisms.	Promotes chronic inflammation in fibrotic diseases, atherosclerosis, and rheumatoid arthritis.

Cancer	Maintains tissue homeostasis and cellular signaling under normal conditions.	Promotes tumor progression and metastasis in lung, breast, and ovarian cancers. Enhances tumor-associated angiogenesis.
Pain	Modulates the feeling of pain and inflammatory responses.	Increases pain sensitivity and contributes to chronic conditions, including neuropathic and inflammatory pain.
Metabolism	Regulates lipid and glucose metabolism under normal physiological conditions.	Dysregulation is linked to obesity, metabolic syndrome, and related complications.
Nervous System	Facilitates neuronal survival, axonal growth, and cytoskeletal organization during development. Supports synaptic plasticity.	Drives heightened pain sensitivity in neuropathic and inflammatory pain and contributes to neurodegenerative conditions.

Under normal conditions, LPA1 regulates the development and maintenance of tissues and organs[189]. It supports neural differentiation, axonal growth, and synaptic formation, essential for brain function[192]. LPA1 also regulates the migration and differentiation of various cells, such as mesenchymal cells, contributing to skeletal development and tissue organization[190]. In maintaining vascular health, LPA1 promotes endothelial cell survival, preserves blood vessel integrity, and supports the formation and repair of blood vessels[189]. In the nervous system, it promotes neuronal survival, synaptic plasticity, and facilitates neuronal growth and organization[189,193]. LPA1 contributes to immune system regulation by helping recruit and activate immune cells like macrophages and T cells, crucial for responding to injuries and infections[193]. Additionally, LPA1 supports metabolic processes by regulating lipid and glucose metabolism, aiding in systemic energy balance[193].

However, dysregulation of LPA1 becomes a significant driver of disease[189]. In lung fibrosis, it promotes fibroblast recruitment and activation, leading to excessive extracellular matrix deposition, tissue scarring, and loss of lung function[199]. In the vascular system, LPA1 contributes to abnormal blood vessel growth and remodeling, or pathological angiogenesis, key features of conditions like atherosclerosis and hypertension[189]. In cancer, LPA1 enhances tumor cell migration, invasion, and survival, playing a critical role in the progression of aggressive cancers such as lung, breast, and ovarian[125,186,200]. It also contributes to the tumor microenvironment by promoting angiogenesis, providing tumors with the necessary oxygen and nutrients for growth and metastasis[201]. In the nervous system, dysregulated LPA1 signaling is implicated in neuropathic and inflammatory pain conditions, where elevated activation

amplifies pain sensitivity, aggravating chronic pain syndromes[98]. In the immune system, pathological LPA1 signaling promotes chronic inflammation, contributing to diseases such as rheumatoid arthritis and fibrotic disorders[198,202]. Moreover, dysregulation in metabolic pathways is associated with obesity and metabolic syndrome, highlighting its broader systemic implications in pathological states[202].

In summary, the LPA1 receptor is crucial for maintaining normal biological processes, and its dysregulation drives disease progression[202]. Its significant pathological characteristics make LPA1 become a promising drug target for treating human diseases such as inflammation and cancer[203].

3.1.4 The Role of LPA1 Receptor in Lung Cancer

The A549 cell line is a widely used human lung carcinoma model [204,205]. Studies have demonstrated that LPA is overexpressed and induces A549 cell migration, proliferation, and colony formation through the LPA1 receptor, which is coupled to the Gi protein [186,206]. LPA1 signaling drives proliferation and migration through key pathways, as shown in **Figure 3.3**[198,205].

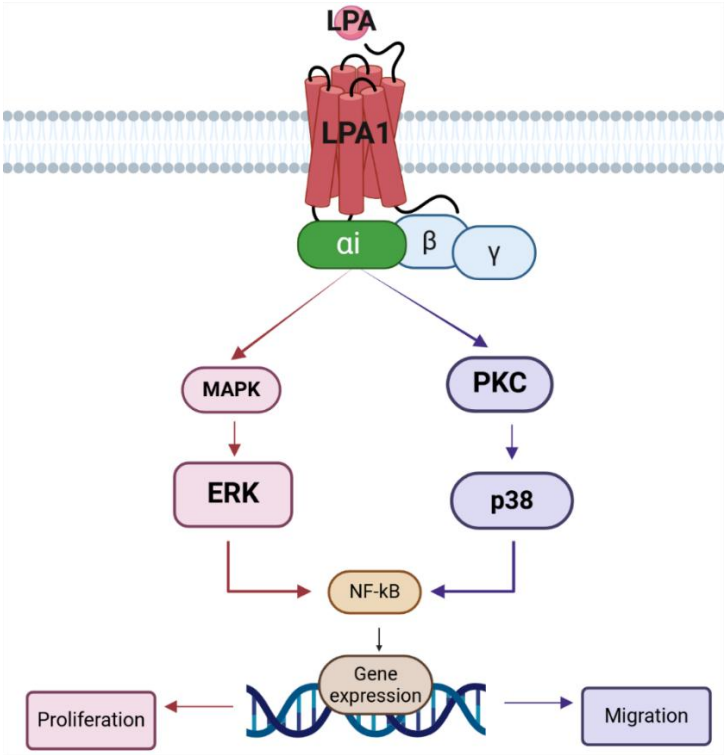

Figure 3.3. Signalling pathways involved in A549 cell proliferation and migration induced by LPA.

The MAPK/ERK pathway promotes cell cycle progression by facilitating the G_1 phase (gap 1) to S phase (synthesis) transition, which regulates the expression of cyclins and cyclin-dependent kinases (CDKs) necessary for DNA replication and cell division[198,207]. In cancer, this transition becomes dysregulated, leading to enhanced proliferation 'energized' by overactive LPA1 signaling[198,205]. The LPA/LPA1/G_i /$ERK_{1/2}$/NF-κB signaling pathway is involved in lung cancer cell proliferation[208]. Meanwhile, the LPA/LPA1/G_i/PKC/p38/NF-κB signaling pathway is involved in lung cancer cell migration[208]. Additionally, PKC signaling contributes specifically to migration by regulating cellular motility[204].

Beyond the LPA1 receptor, several studies using preclinical models and clinical samples from lung carcinoma patients reveal the role of the ATX/LPA axis in lung cancer progression, providing new therapeutic development strategies targeting the LPA signaling pathway (red dotted circle in **Fig. 3.4-B**)[201,207].

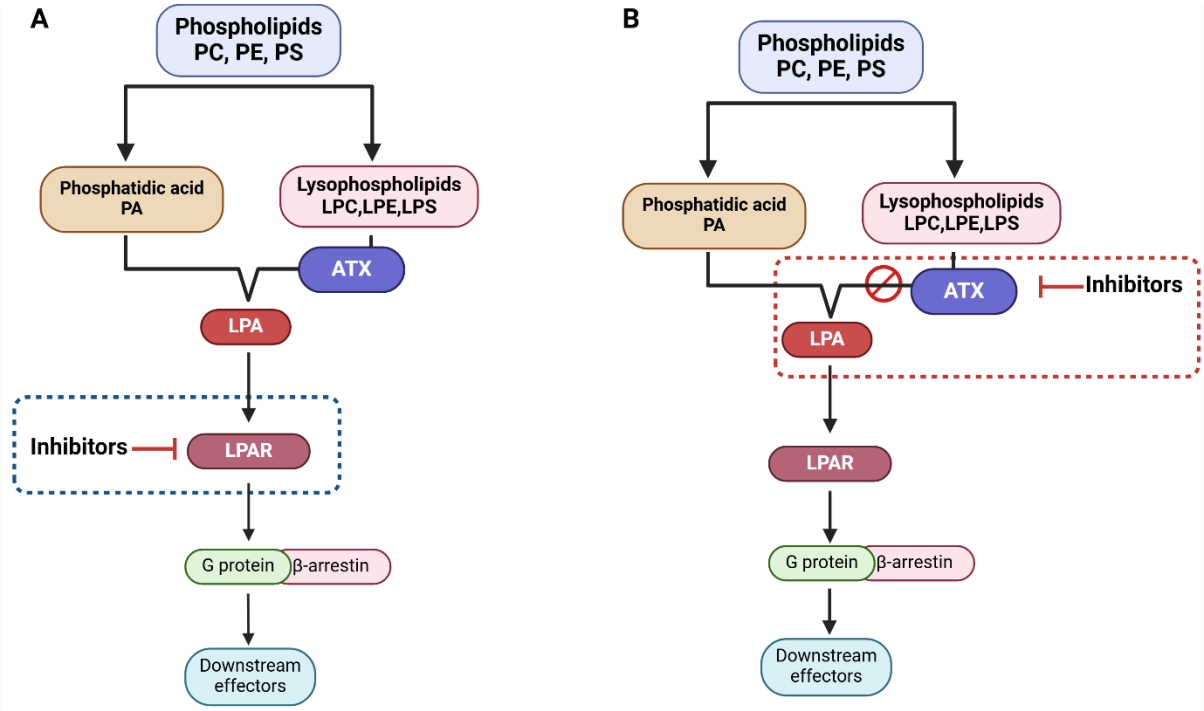

Figure 3.4. A. The pathway of LPA receptor antagonists is to block the activation of the receptor, thus blocking the initiation of signaling. **B.** The potential therapeutic development strategies target the LPA signaling pathway by using ATX inhibitors to reduce the level of LPA and attenuate LPAR activation, thereby preventing the initiation of downstream signaling.

ATX, encoded by the ectonucleotide pyrophosphatase/phosphodiesterase 2 (ENPP2) gene, is a secreted glycoprotein present in biological fluids[207]. ATX catalyzes the conversion of LPC to LPA, providing a continuous source of LPA in the tumor microenvironment[207]. While LPA

can also be produced through the hydrolysis of PA by PLA1/2, research indicates that ATX is the primary enzyme responsible for extracellular LPA production, particularly in tumor conditions[201,207]. Studies have demonstrated that raised levels of ATX are frequently observed in lung cancer tissues and patient serum, which correlates with increased LPA production in the tumor microenvironment[207]. Similar observations have also been validated in two widely used lung cancer animal models[193,201].

Elevated ATX levels in lung cancer tissues correlate with increased LPA production, which sustains and amplifies LPA receptor activation[201]. Binding of LPA to its receptors (LPA1–LPA6) activates downstream pathways such as MAPK/ERK and Rho/ROCK, promoting cell survival, proliferation, and migration[193]. The axis also facilitates epithelial-to-mesenchymal transition (EMT), enabling cancer cells to acquire invasive and metastatic traits[191]. Additionally, the ATX/LPA axis enhances angiogenesis by inducing VEGF expression via LPA receptor activation and modulates the tumor microenvironment by increasing vascular permeability and promoting the recruitment of inflammatory cells, thereby supporting tumor progression[191].

Several known ATX inhibitors, such as PF-8380, S32826, and IOA-289, have demonstrated efficacy in preclinical models by reducing LPA levels and attenuating disease progression[207,209,210]. IOA-289 was developed for treating cancers associated with fibrosis[210].

3.1.5 Known LPA1 Ligands

Given the importance of the LPA1 receptor in various pathologies, potent and selective ligands are crucial to exploring its potential as a therapeutic target[211,212]. While numerous LPA1-targeting compounds have been investigated, no drugs targeting the LPA1 receptor have been approved by the U.S. Food and Drug Administration (FDA) to date [212]. Several LPA1 antagonists, such as BMS-986278 and SAR100842 (structure presented in **Fig. 3.6** and **3.7**), have advanced to clinical trials for fibrotic diseases, but their clinical efficacy remains under evaluation. [182,212]. This highlights the need for continued advancements in drug discovery to fully realize the therapeutic potential of LPA1 in managing human diseases, including cancer.[212]. Notably, numerous novel LPA1 ligands, including both lipid and nonlipid agonists and antagonists, have been discovered in recent years, demonstrating promising efficacy in preclinical studies. To facilitate the development of a novel small-molecule compound targeting LPA1, research articles spanning two decades on LPA1-specific antagonists were reviewed.

Like most ligand development strategies, the approach of designing ligands for a specific receptor often begins with its natural agonist. This strategy has also been applied to develop potent ligands for the LPA1 receptor. [184]. Initial studies on LPA1 antagonist development were conducted by making minor modifications to 18:1 LPA[184]. In 1994, Sugiura's group reported the first LPA-based agonist, NAEPA (N-acyl ethanolamide phosphoric acid (2-[(9Z)-octadec-9-enoylamino] ethyl dihydrogen phosphate)[89,184]. It was synthesized by replacing the glycerol in LPA with ethanolamine and was characterized as an LPA mimetic with an EC_{50} of around 40 nM in human platelet aggregation (**Fig. 3.5**)[89,184].

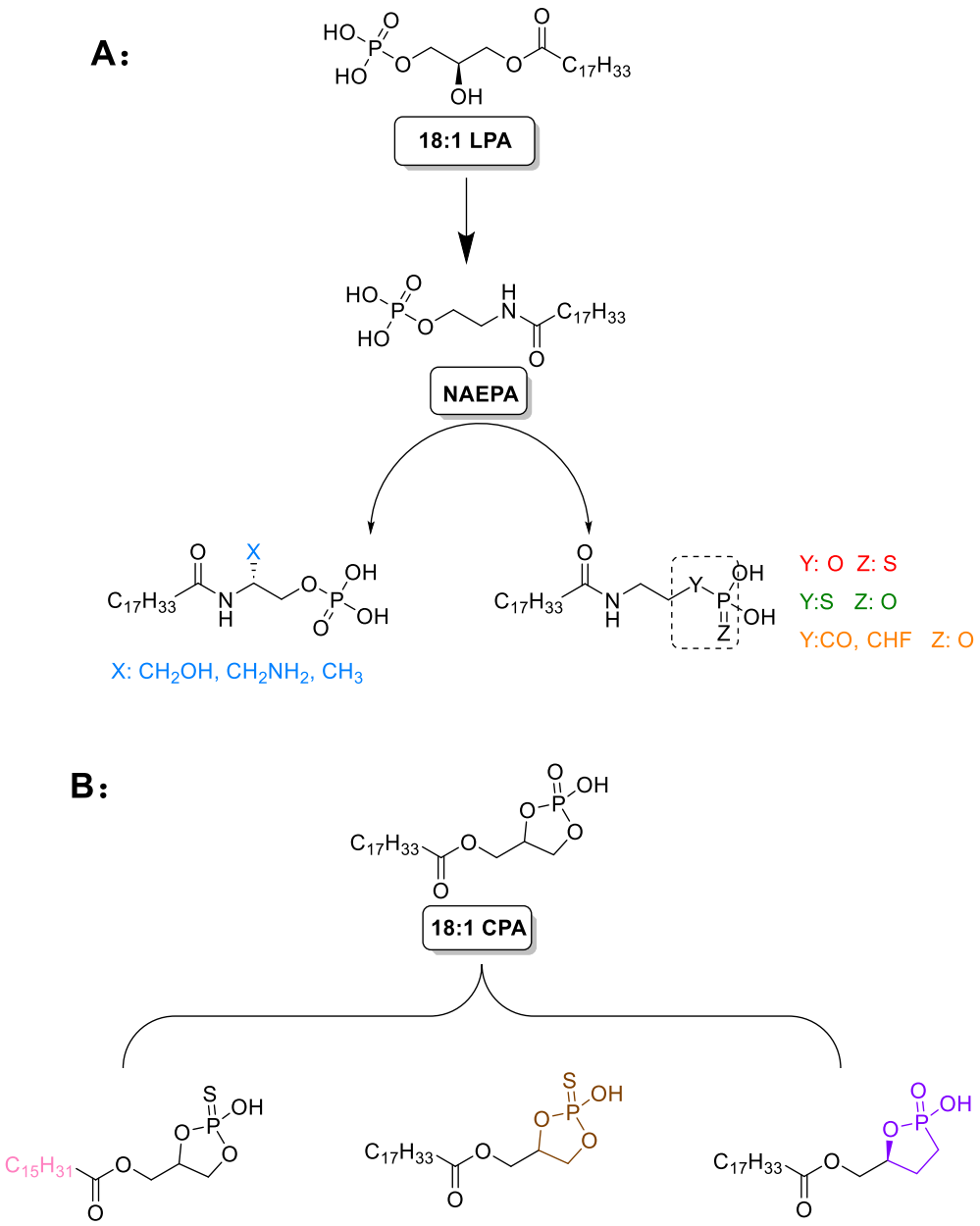

Figure 3.5. Lipid-based (A) LPA1 agonists and Lipid-based (B) LPA1 antagonists.

Using NAEPA as a lead compound, several modifications were made to obtain a series of NAEPA analogues, such as 2-substituted, replacements of the phosphorothioate, and the phosphate/phosphonate group[184].

Furthermore, lipid-based LPA1 antagonists, such as derivatives of cyclic phosphatidic acid (CPA), have been reported[184,213]. CPA is a naturally occurring analogue of LPA in which an oxaphospholane ring is formed by the sn-2 hydroxy group and the sn-3 phosphate group[213]. Based on CPA's structure, Xu's group reported a series of three CPA analogues with selectivity for LPA1 and LPA3[213].

Although lipid-based analogues demonstrated good potency as LPA receptor antagonists and selectivity for LPA1, the phosphonate functional groups and lipid alkyl chain posed challenges for achieving sufficient bioavailability[203]. The binding pocket of the LPA1 receptor is primarily hydrophobic, naturally accommodating lipid-based ligands like LPA[202]. However, hydrophilic regions near the pocket entrance are crucial for interacting with polar functional groups of ligands[202]. The high hydrophobicity of lipid-based compounds may lead to challenges in drug development, such as poor solubility and non-specific interactions[184,202]. Therefore, recent studies have moved focus from synthesizing lipid-based LPA analogues to small molecule compounds with increased hydrophilicity[184,202].

In 2003, Ki16425, a non-lipid compound, was reported as one of the first three small molecule-based LPA1 antagonists (blue dotted circle in **Fig. 3.6**)[214]. It was identified from Kirin Brewery's compound library[214]. The structure of Ki16425, contained a carboxylic acid and a carbamate core of aminoisoxazole[214]. Although Ki1645 shows moderately potent antagonism of LPA1 in calcium mobilization assays (IC_{50}~0.34 μM), the core of structure inspired numerous structural modifications by different research groups and pharmaceutical companies, leading to the development of many potent and selective LPA1 antagonists, some of which have even advanced to clinical trials[104,215,216]. Later, Komachi *et al.* adapted from enantiomers of (R)-Ki16425 and reported a methyl ester derivative of Ki16425, Ki16198. While the potency and selectivity of Ki16198 haven't changed much compared with Ki16425, it prevented cancer cell migration and invasion *in vitro*, such as pancreatic cancer[89].

Several research groups and organizations have made continuous efforts to synthesize derivatives of Ki16425, including a series of analogues developed by Amira Pharmaceutical: AM095, AM966, and BMS-986020 (**Fig. 3.6**)[89,184]. Compared to Ki16425, the major structural modification involved adding a phenyl group to replace the sulfur atom and shortening the long

aliphatic chain (AM095 and AM966)[184,202]. BMS-986020 features a cyclopropane group next to the carboxylic acid position[202]. AM095 and AM966 showed high potency and selectivity for LPA1, with IC_{50} values in the low nanomolar range (AM095: ~25 nM, AM966: ~17 nM)[184,202]. While BMS-986020 has moderate potency (IC_{50}: ~300 nM), its biphenyl and cyclopropane structure inspired further studies[184].

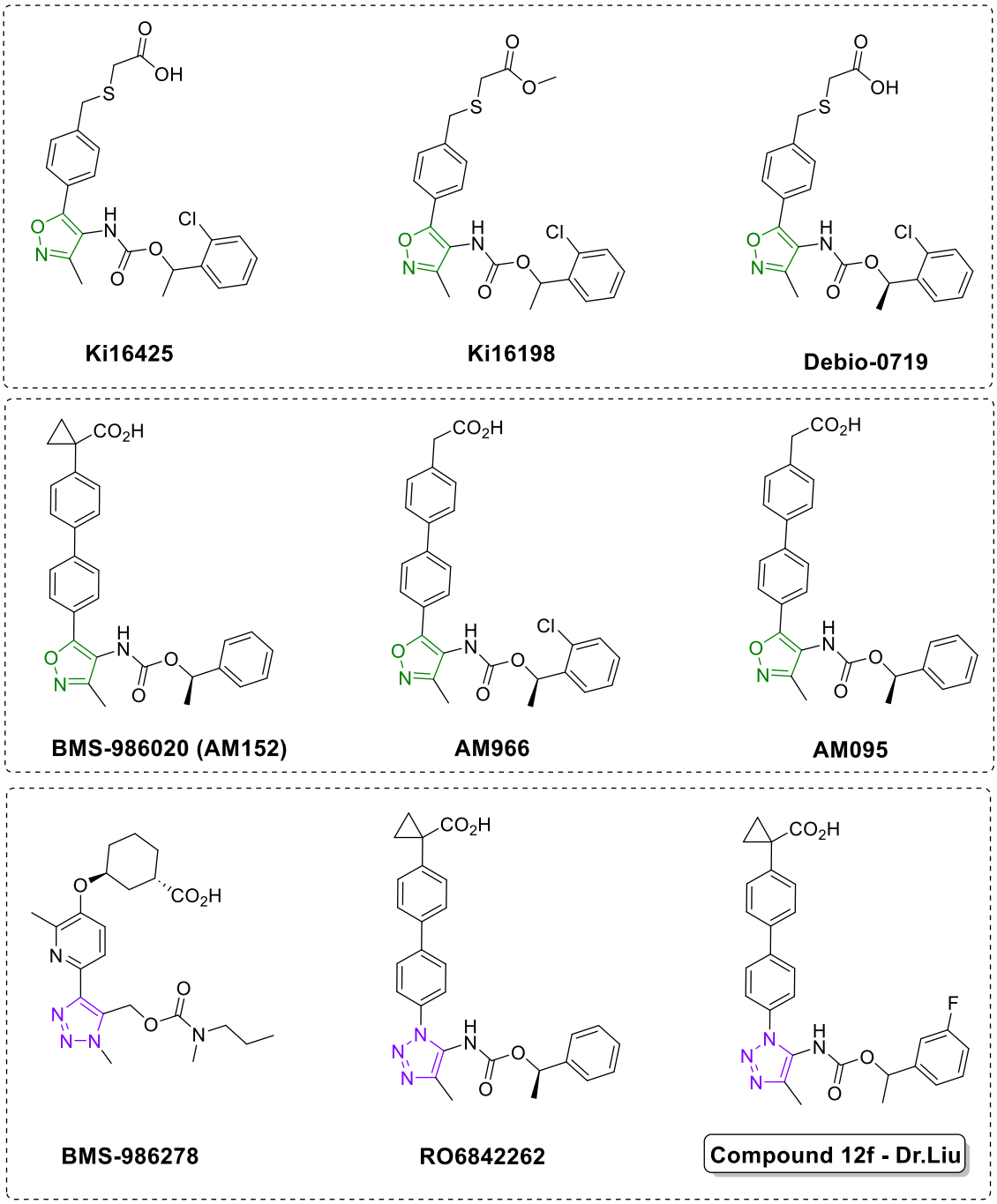

Figure 3.6. Selected non-lipid LPA1 antagonists - Ki16425 derivatives and RO6842262 derivatives.

In 2012, Qian *et al.* published a novel LPA1 antagonist, RO6842262, displaying great potency (IC_{50}: 25 nM) and high LPA1 selectivity (compared to LPA3 IC_{50}: ~30 μM) in calcium flux assays[101]. RO6842262 is structurally like BMS-986020, except the isoxazole core replaced by a triazole[97]. This modification enhanced performance of RO6842262 in decreasing LPA-induced cell proliferation and contraction in lung fibroblasts[101].

The development of LPA1 antagonists has significantly advanced the treatment of lung fibrosis, with compounds such as Ki16425, AM095, RO6842262, and BMS-986278 providing critical insights into LPA1 receptor inhibition[101,104]. Notably, BMS-986278, a second-generation LPA_1 antagonist, is currently in phase 2 clinical development for the treatment of idiopathic pulmonary fibrosis (IPF)[60]. It has demonstrated significant efficacy by reducing the rate of lung function decline, with patients showing improved outcomes compared to those receiving placebo[104,217]. In October 2023, the FDA granted it breakthrough therapy designation. The pharmaceutical company (Bristol Myers Squibb) is planning to evaluate the safety and efficacy of BMS-986278 with a global phase 3 program for IPF[218].

Recent studies demonstrate that lung fibrosis and lung cancer share several key LPA1-mediated signaling pathways[186,188,204]. In both disease conditions, LPA1 signaling promotes cell migration, proliferation, and survival[199]. In lung fibrosis, LPA1 drives fibroblast recruitment, extracellular matrix deposition, and scarring, while in lung cancer, it facilitates tumor cell migration, metastasis, and growth[199]. These overlapping mechanisms strongly suggest that LPA1 antagonism could inhibit cancer progression, motivating continued efforts to develop more potent and selective LPA1 antagonists for lung cancer treatment.

In 2024, Dr. Liu from our group reported a new and potent RO6842262 analog, compound 12f[90]. It demonstrates strong inhibitory activity in both cAMP assays (IC_{50} = 16.0 nM) and calcium mobilization assays (IC_{50} = 18.4 nM)[90]. In vitro functional studies demonstrated that compound 12f effectively inhibits LPA-induced survival, migration, and invasion of MDA-MB-231, a triple-negative breast cancer (TNBC) cell line, in a dose-dependent manner, without inducing apoptosis or cytotoxicity[90]. These results suggest that 12f could be used as an anti-metastatic drug in cancer treatment[90]. Given that RO6842262 was initially reported as an antifibrotic LPA1 antagonist, our findings demonstrate the potential of RO6842262 derivatives as a foundation for developing novel LPA1 antagonists for cancer treatment[101].

Beyond the molecular scaffold of biaryl and triazole moieties, several novel and potent LPA1 antagonists have been reported recently. In 2016, Terakado *et al.* from Ono Pharmaceutical

Co., Ltd. published their discovery of a novel LPA1-selective compound, ONO-7300243 (**Fig. 3.7**), which was optimized from a high-throughput screening (HTS) campaign[219]. The compound was potent and selective for LPA_1 (IC_{50} = 160 nM), with markedly reduced activity against LPA_2 (IC_{50} = 8,600 nM) and LPA_3 (IC_{50} > 10,000 nM)[219].

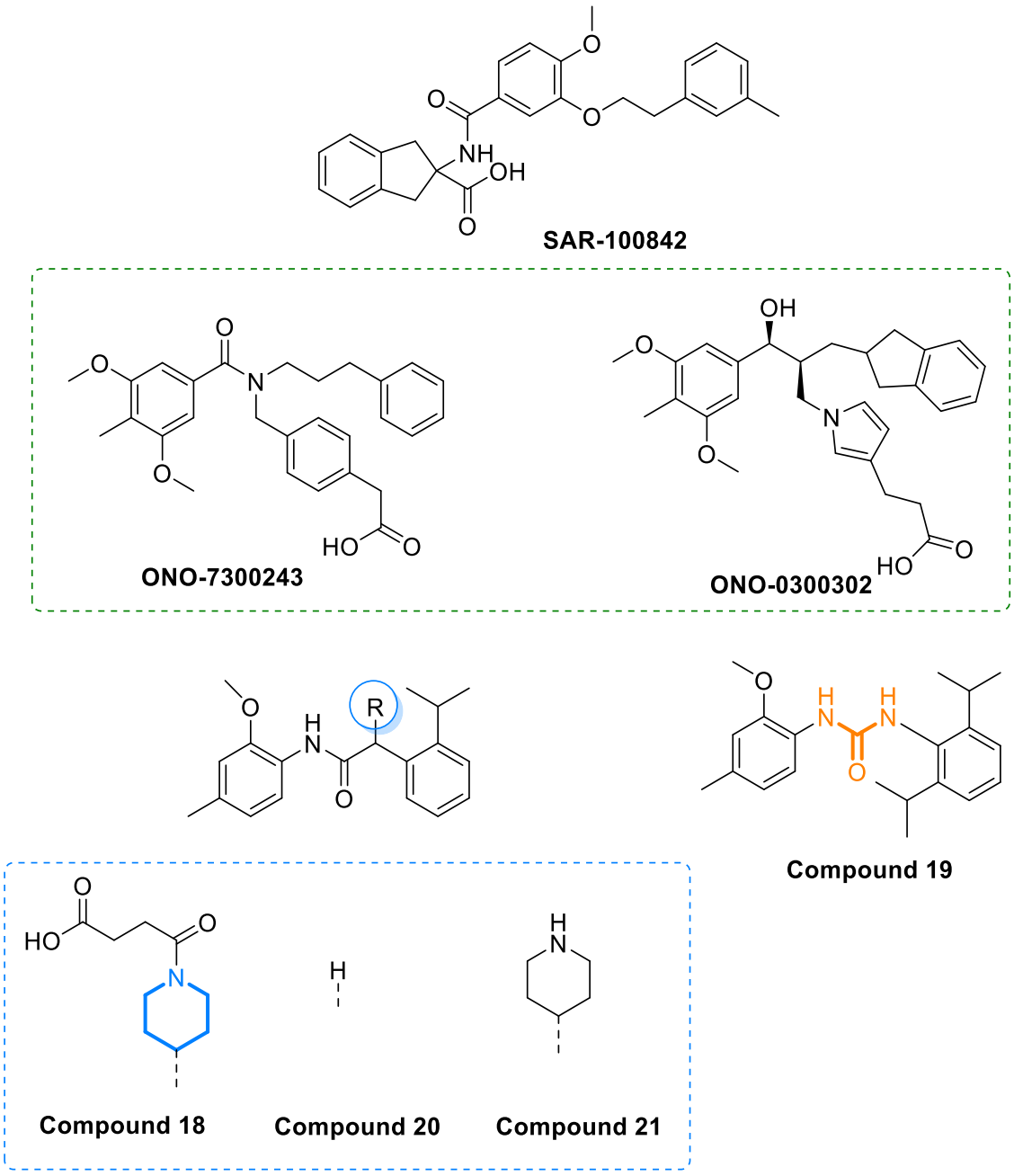

Figure 3.7. Reported structures of SAR-100842, ONO-7300243, and ONO-0300302. Reported structures with R group of compounds 18, 20, and 21. Reported structure of compound 19 (a urea derivative).

ONO-7300243 demonstrated therapeutic efficacy in a rat intraurethral pressure model induced by LPA, supporting its potential pharmacological relevance[219]. Further optimization led to the development of ONO-0300302 (**Fig. 3.7**), which exhibited substantially improved potency (IC_{50} = 0.16 nM) in a calcium assay after a 24-hour incubation period[219]. However, the selectivity of ONO-0300302 for LPA1 over other LPA receptors was not explicitly reported in the available literature[219].

Moreover, in 2024, Lescop *et al*. from Idorsia Pharmaceuticals, Ltd. reported the discovery of three novel LPA1 antagonists (blue dotted circle in **Fig. 3.7**)[220]. Among them, piperidine-derived compound 18 (IC_{50} = 3.3 nM) was identified as a potent, orally active, and selective LPA1 antagonist[220]. This compound was optimized from the urea derivative compound 19 through medicinal chemistry efforts to enhance its potency and metabolic stability[220]. In preclinical models, compound 18 effectively inhibited LPA-induced vascular leakage in a mouse model, significantly reducing Evans blue extravasation (vascular permeability assay) in a dose-dependent manner for up to 16 hours post-administration[220].

3.2 Results and discussion

3.2.1 First Series - Structural Optimization and Synthesis of RO6842262 Analogues

RO6842262 (RO), initially developed by Qian *et al.* at Hoffmann-La Roche Pharma for pulmonary fibrosis treatment, has been selected as a model compound for developing novel LPA1-targeting antagonists due to its high potency and selectivity[101,221]. The mechanism of RO6842262 is that this ligand competitively binds to the orthosteric site of the LPA1 receptor, thereby blocking LPA-mediated receptor activation. Therefore, given that lung fibrosis and lung cancer share much of the LPA1 signaling pathway, modifying RO to create novel LPA1 antagonists shows promise for treating lung cancer driven by LPA1 signaling[98,209]. The structure of RO was divided into three main components to guide ligand design in this chapter (**Scheme 3.1-A**). All analogs retain the triazole–phenyl core, while structural modifications focus primarily on the carbamate tail and the carboxylic acid fragment. As presented in **Scheme 3.1-A,** the first series of structures modification of RO analogs. Compared with RO, the N and O positions in the carbamate group were switched, and the synthetic route was optimized to generate the first series of ligand designs, compound L9x.

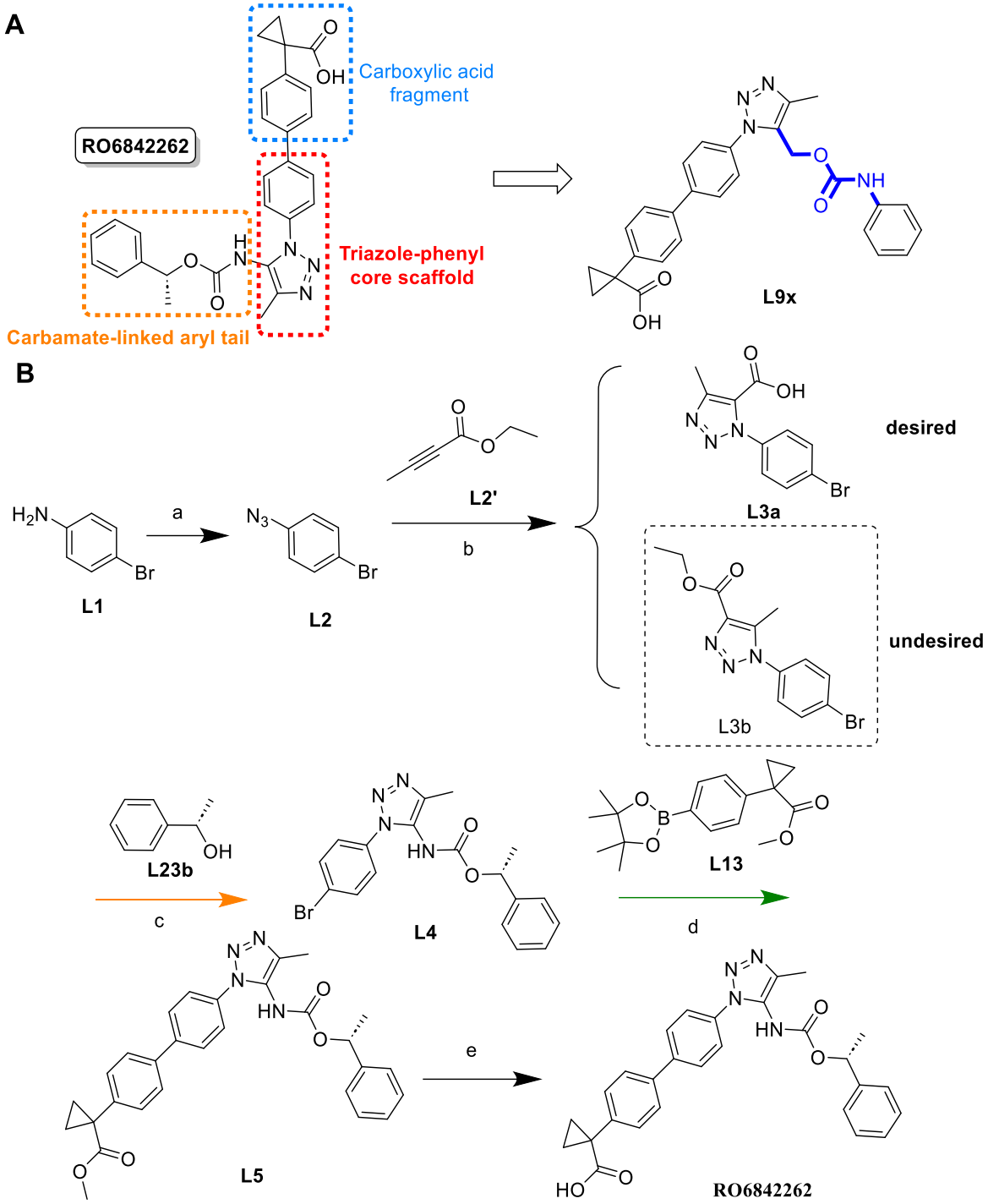

Scheme 3.1 A. Structure of RO6842262 and analogue L9x. The core structural difference is colored, RO6842262 is red and L9 is blue. **B**. Reported synthetic scheme of RO6842262. Desired (L3a) and undesired (L3b) regioisomers of the triazole cyclization reaction. Reaction condition: (a) 4N HCl, $NaNO_2$, NaN_3, H_2O, 0˚C, 22 hrs; (b) anhydrous toluene, Argon, 130˚C, 6hrs (c) TEA, DPPA, anhydrous toluene, Argon, 80˚C, 8hrs; (d) Na_2CO_3, $Pd(dppf)Cl_2$, dioxane, H_2O, Argon, 80˚C, 12 hrs; (e) NaOH, H_2O, ethanol, THF, overnight, rt. To enhance clarity and

consistency throughout this chapter, all compounds are labeled with a prefix "L" (representing *LPA1*), such as L1, L2, and L3.

After reviewing the original synthetic scheme of RO6842262, it became evident that optimization was necessary to address two key challenges[221]. The first challenge was the formation of regioisomers during the triazole cyclization reaction, highlighting the need to refine this step to improve selectivity and yield[101,221]. As described in the original literature, the reported synthetic scheme of RO6842262 is displayed in **Scheme 3.1-B**[101]. The initial triazole cycloaddition reaction was carried out uncatalyzed and performed under conventional heating[101]. This leads to cycloaddition between the azide and alkyne groups to produce the triazole ring[101]. The issue is a lack of regioselectivity (desired compound L3a and undesired compound L3b), resulting in low yield (<10%) and time-consuming purification due to the distribution of triazole group substituents as presented in **Scheme 1-B**[101].

Given the high expression of LPA1 in cancer, this characteristic can be utilized for cancer diagnosis. Therefore, the synthetic route was adjusted to facilitate the incorporation of iodonium ylide precursors for PET imaging[221]. The second challenge is to exchange the sequence of the Curtius rearrangement reaction (orange arrow in **Scheme 3.1-B**) and the Suzuki-Miyaura cross-coupling reaction (green arrow in **Scheme 3.1-B**)[101,221]. As presented in **Chapter 2.4**, for the synthesis of SPAId iodonium (III) ylide precursor, the intermediate of the candidate compound must first be converted into an iodo-compound, which subsequently reacts with SPAId to serve as the precursor for ^{18}F-radiolabeling[177]. Given that Suzuki coupling reactivity follows the order iodine **(I) >>** bromine **(Br)** for the electrophilic partner, the iodine will compete with bromine (compound Lb) to react with the boronic ester building block, leading to the formation of an undesired side product, compound Lc (**Scheme 3.2-A**)[57,222]. As a result, compound Lc is unable to react with SPAId to generate the desired precursor for radiolabeling[177].

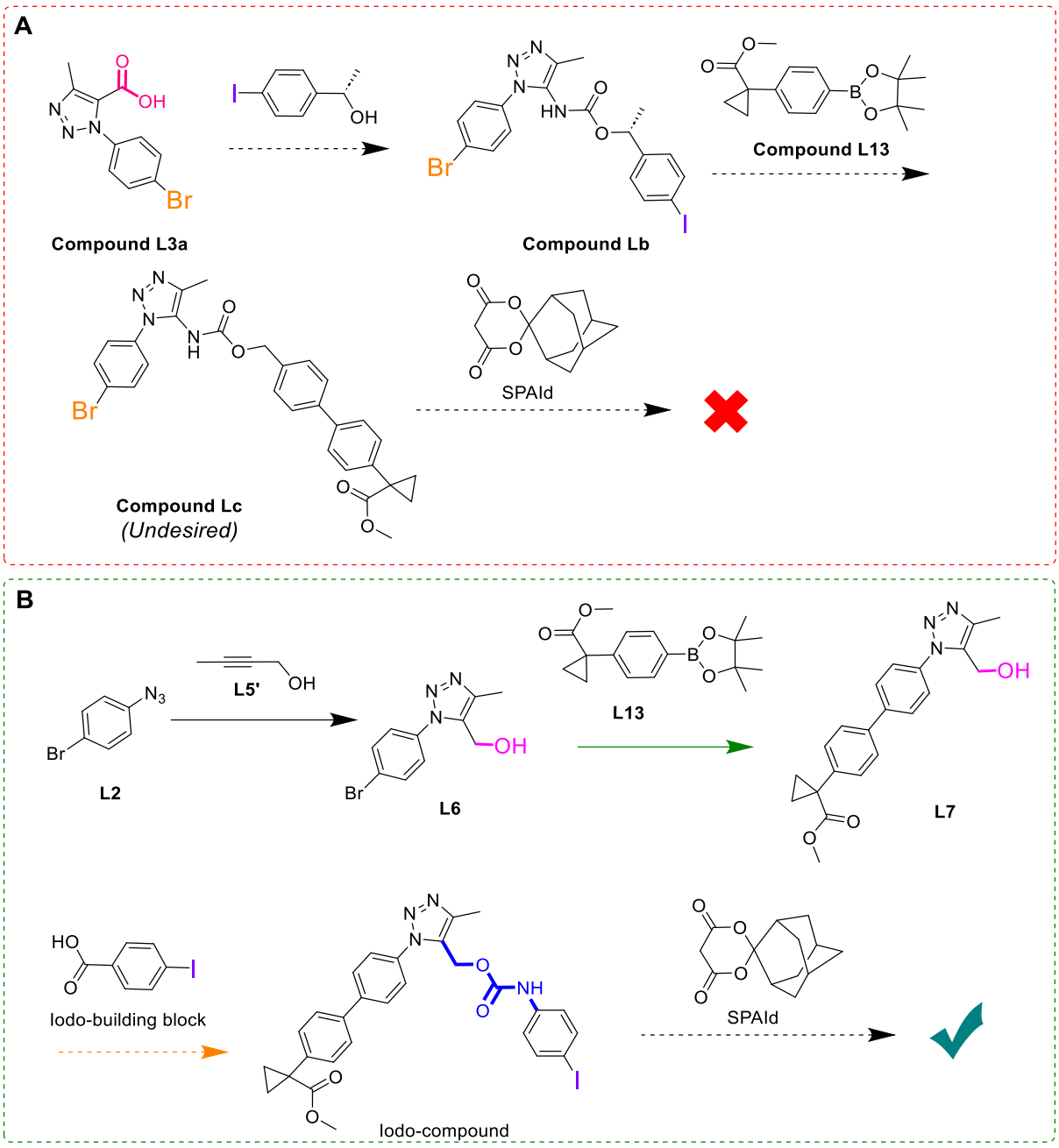

Scheme 3.2. A - Unwanted reaction and structure of compounds L3a, Lb, and Lc. **B** - Proposed scheme for synthesis of iodo-compound.

The optimized synthetic scheme is outlined in **Scheme 3.2-B**[221]. The scheme incorporates a newly optimized triazole cyclization step, with the most significant change being the rearrangement of the sequence of the Curtius rearrangement reaction and the Suzuki-Miyaura cross-coupling reaction[101,221]. This modification involves shifting the incorporation of the iodo-building block (via the Curtius rearrangement) to the penultimate step[221]. This adjustment was necessary because the SPAId building block is unstable under the high-temperature and prolonged reaction conditions[177]. Therefore, it is preferable to introduce the SPAId building

block as late as possible in the synthetic scheme[179]. Additionally, replacing the ester building block (compound L2') with an alcohol building block (compound L5') for the reaction with compound L2 results in the formation of an alcohol (compound L6) rather than a carboxylic acid moiety (compound L3a). This change leads to a rearrangement of the nitrogen and oxygen atoms within the carbamate moiety formed during the Curtius rearrangement[221].

The optimized synthetic scheme is presented in **Scheme 3.3-A**[221]. The boronic ester building block, L13, remains incorporated and was synthesized exactly according to the three-step procedure outlined in the patent related to the synthesis of RO6842262(**Scheme 3.3-B**)[223]. The first step, which is the synthesis of L2 through the formation of a diazonium intermediate that is substituted by azide, is the same as in **Scheme 3.1-B**[223]. The second step is the optimized triazole cyclization reaction to form L6[221]. The reaction conditions were extensively investigated, with multiple parameters and variations explored to optimize this step[221,224–226]. Through these efforts, the use of the ruthenium complex catalyst, Cp*RuCl (COD), was found to provide near-complete regioselectivity for the formation of the desired 1,5-regioisomer, L6, when the alkyne group contained a propargylic alcohol substituent[224,225]. However, initial yields were relatively low when using conventional heating, as compared to values reported in the literature[225,226]. This limitation was successfully addressed by implementing a microwave reactor, which significantly improved the reaction yield[227]. The reaction begins with the addition of a small amount of Cp*RuCl (COD) catalyst to a microwave reaction vial, then adding anhydrous toluene, followed by L5' via syringe, and then adding L2 into the reactant mixture[227]. The order in which the reactants are added is also important; the azide must be added after the alkyne [225–227]. This sequence ensures that the alkyne first coordinates with the ruthenium catalyst, stabilizing the catalytic complex and facilitating selective activation of the azide[224,225]. If the azide were added before the alkyne, it could interact prematurely with the ruthenium center, potentially leading to unwanted side reactions or even deactivate the catalyst[225,226]. The reaction was then placed in the microwave reactor and mixed at 60˚C under ~15 W of microwave radiation[224]. This approach significantly improved reaction efficiency, increasing yields from 10% to 45% while reducing reaction time from 12 hours to 1 hour[221].

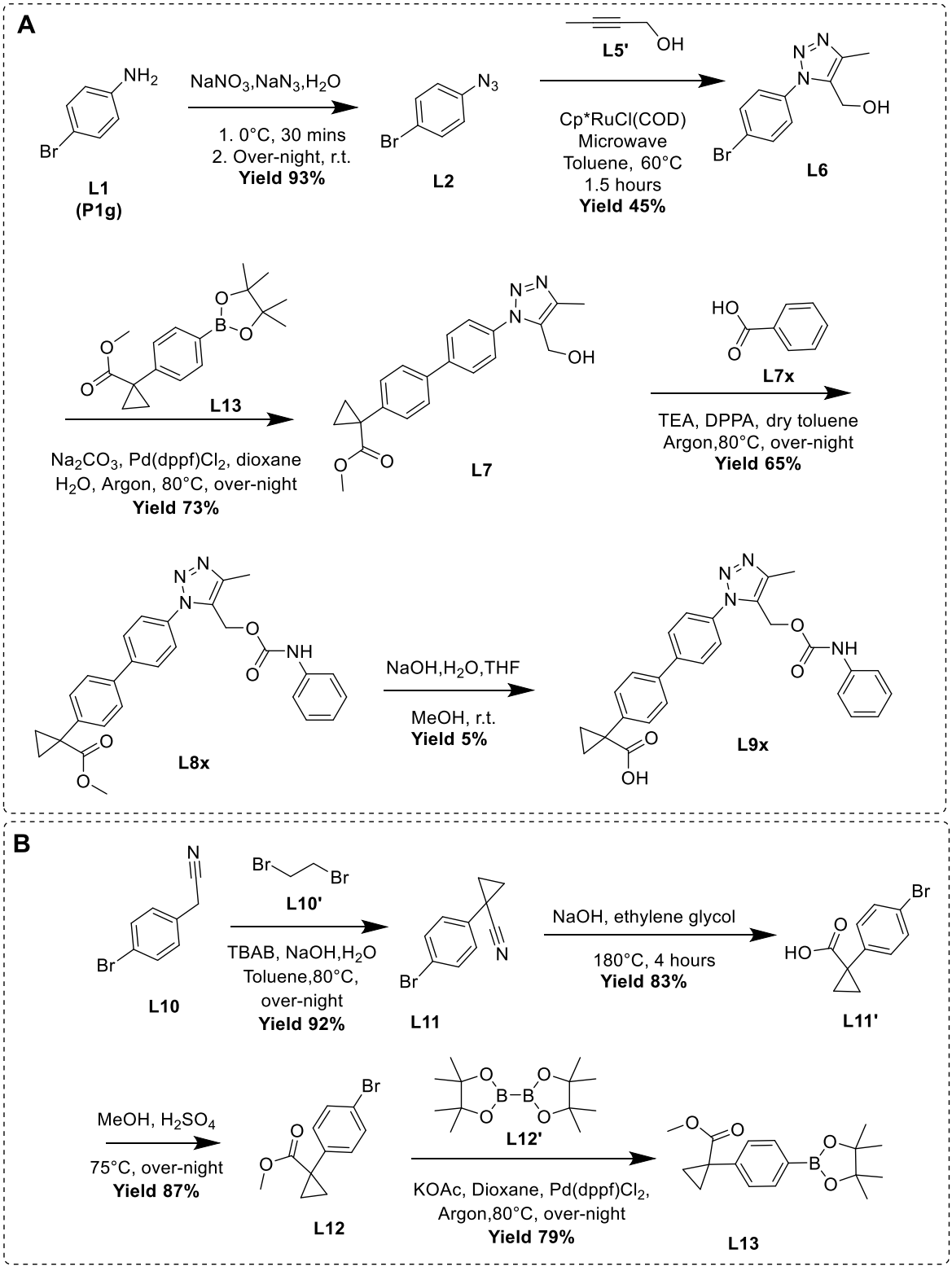

Scheme 3.3 A - Optimized synthetic scheme of RO6842262 analogues. Building block P1g in Chapter 2 acts as starting material L1 in this scheme. **B** - Synthetic scheme of boronic ester, L13 (methyl-containing boronic ester). Commercially available chemical - L5': but-2-yn-1-ol, L7x: benzoic acid, L10: 2-(4-bromophenyl) acetonitrile, L10': 1,2-dibromoethane, L12': Bis(pinacolato)diboron.

By employing the Cp*RuCl(COD) catalyst and managing the proper order of reagent addition, this method effectively avoids the formation of the undesired regioisomer (Compound L6a in **Figure 3.8**) during the cycloaddition reaction[221]. The detailed experimental procedure for this reaction step, including extraction, filtration, and purification, can be found in **Chapter 3.5.2**.

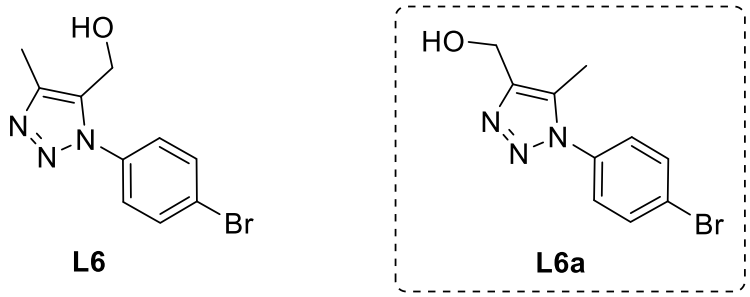

Figure 3.8. Structure of desired compound L6 and undesired compoundL6a.

Compound L6 was characteristized through HPLC-MS and ^{1}H-NMR. To investigate and confirm the desired structure of L6, a 1-dimensional selective NMR Overhauser Effect (NOE) experiment is employed (as shown in **Fig 3.9**)[228]. The protons with a chemical shift of 2.46 ppm correspond to the methyl group, while the protons at a chemical shift of 4.69 ppm correspond to the methylene group that connects to the hydroxyl group. **Figure 3.9** displays a signal (an upside-down peak) at a chemical shift around 7.63 ppm in the spectrum of freq: 4.693 ppm, while no signal is observed at the same chemical shift in the spectrum of freq: 2.465 ppm. This signal confirms the formation of the desired regioisomer during the triazole cyclization reaction.

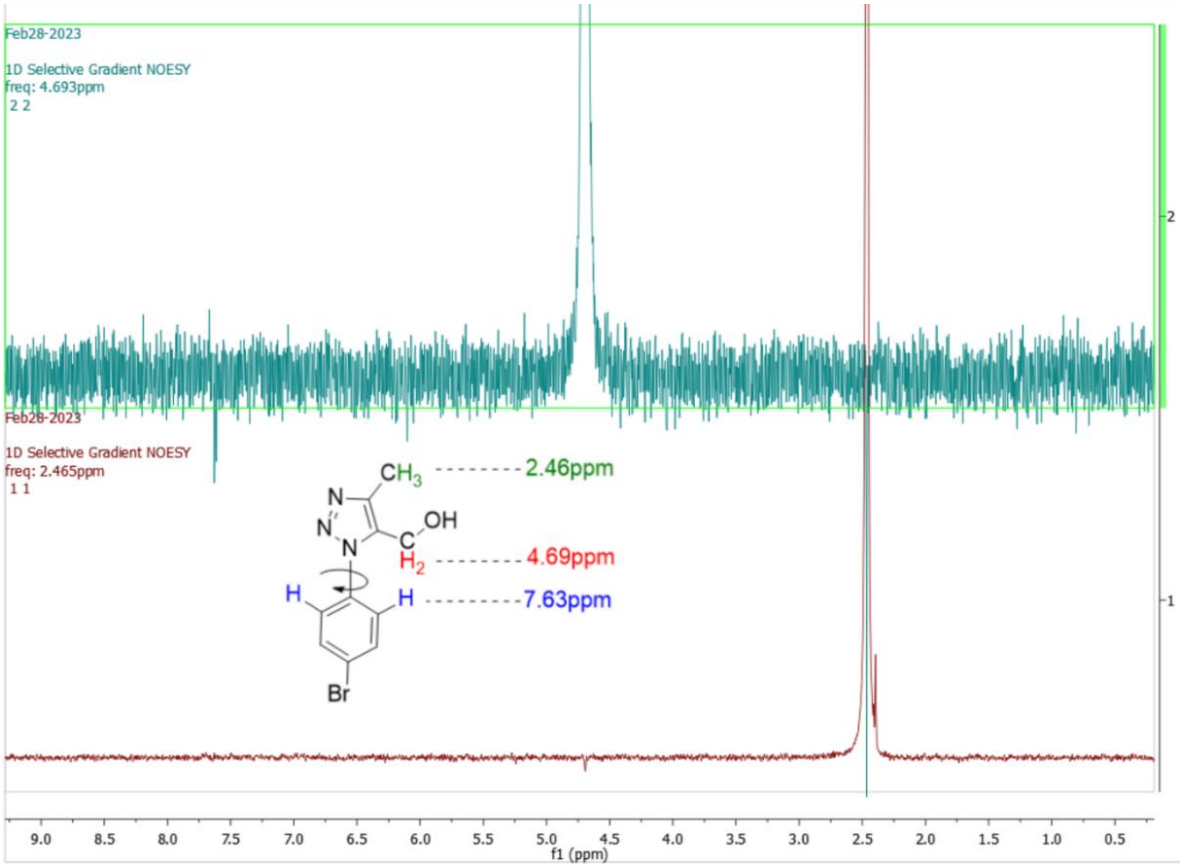

Figure 3.9. 1-D selective NOE spectrum of compound L6. It was dissolved in chloroform-d. **Note:** This inverted peak indicates a nuclear Overhauser effect between the irradiated methylene proton (colored in red)and a nearby aromatic proton (colored in blue). The upside-down appearance results from the phase behavior in NOE difference spectroscopy, where positive NOEs are displayed as negative signals in subtraction mode.

Compounds L7 and L8 were subsequently synthesized through Suzuki cross-coupling and Curtius rearrangement reactions, and both were characterized by HPLC-MS and ^{1}H-NMR. The experimental procedure and results data are available in **Chapter 3.5.2**. The most challenging step is the last step, hydrolysis reaction. The ester group (adjacent to the cyclopropane group) is expected to hydrolyze into the carboxylic acid, forming the final compound L9. However, the carbamate bond is unexpectedly broken, resulting in three compounds: L8', L8'', and L9, as shown in **Figure 3.10-A**. If the hydrolysis reaction continues overnight (more than 10 hours), the carbamate bond of the final compound L9 continues to break, and compound L8'' becomes the sole product.

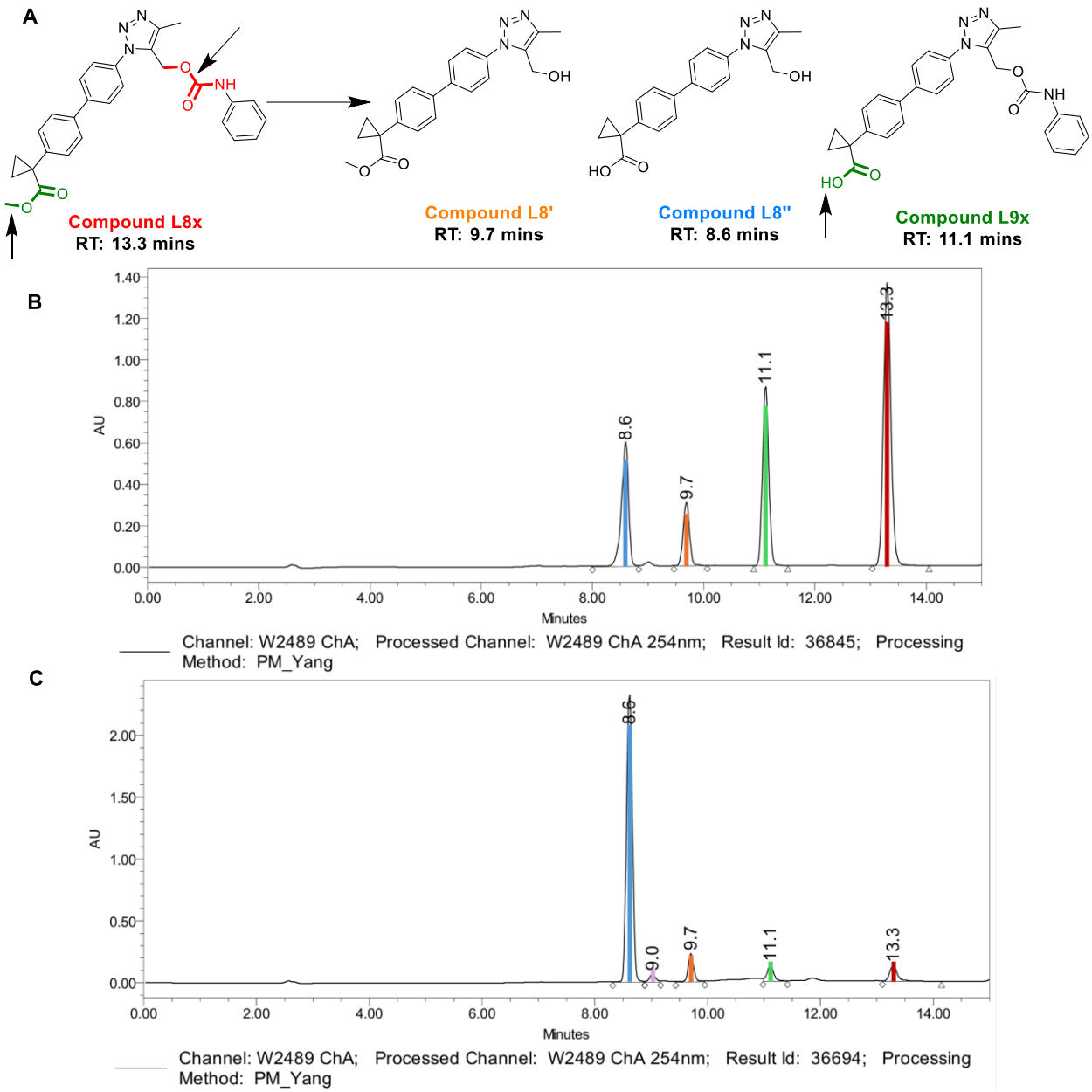

Figure 3.10. **A**. Structure of ester compound L8x (colored in red), undesired hydrolyzed compounds, L8' (colored in orange), L8'' (colored in blue) and desired hydrolyzed compound, L9x (colored in green). **B**. HPLC-MS monitoring the reaction mixture after 2 hours. **C**. HPLC-MS monitoring the reaction mixture after 10 hours. Pink color is impurity during hydrolysis reaction. **Note:** Alternative hydrolysis conditions were only tested using other bases (e.g., LiOH); acid hydrolysis conditions were not examined due to time constraints.

This finding has been monitored and investigated using HPLC-MS, with each compound showing a specific retention time in Analytical-HPLC (ana-HPLC) (**Fig.3.10-B** and **C**). It has been confirmed by ^{1}H-NMR after each compound was purified by preparative HPLC using an acetonitrile/water eluent gradient. While analogue L9x was eventually purified using

preparative HPLC (prep-HPLC), this unexpected hydrolysis issue caused significant product loss, with the yield of the final step being less than 5%. The experimental results and data are available in **Chapter 3.4.2** and **Appendix B**.

Furthermore, given that elevated LPA expression has been observed in lung cancer cells, such as A549 cell line[204,207]. Fluorine-19 was incorporated into the structure of RO6842262 analogues to explore their potential for PET imaging applications in lung cancer diagnosis. A fluorine-containing analogue, L12y, was synthesized and characterized using the same synthetic procedure during the same period (**Scheme 3.4**). The hydrolysis issue resulted in a yield of less than 5% for L12y. The detailed experimental procedure and results of analogues L9x and L12y are available in **Chapter 3.5.2**. Substitutions at the para positions with fluorine atoms, serving as a 'cold' compound, will facilitate the development of ^{18}F-labeled radiotracers for PET imaging studies. Our group has conducted a preliminary biological evaluation of analogue L9x and L12y, including cAMP and wound healing assays.

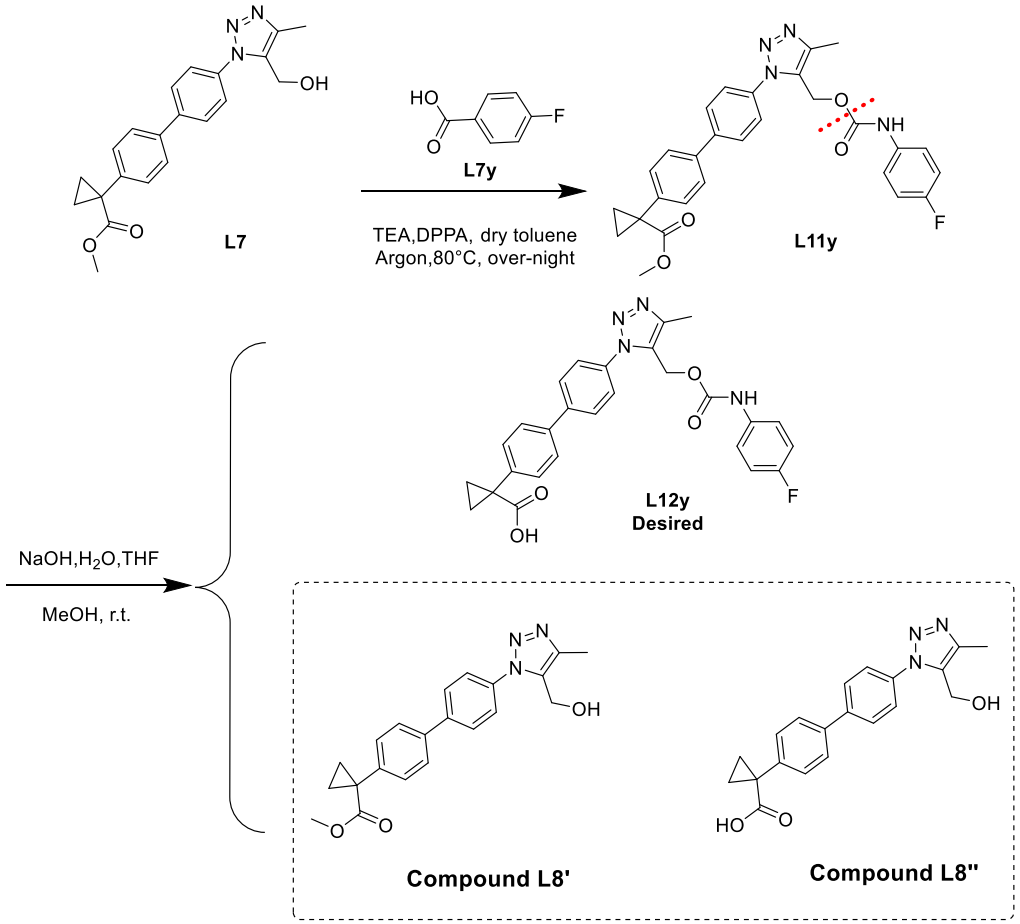

Scheme 3.4. Synthetic scheme of analogue L12y. Commercially available chemical - L7y: 4-fluorobenzoic acid.

3.2.2 Synthesis of L9x Derivatives via the Mitsunobu Reaction

While the Curtius rearrangement is efficient for transforming acyl azides into isocyanates and subsequently into carbamates, the hydrolysis of carbamate and ester groups was a recurring issue, the multi-functional group hydrolysis resulting in unwanted side products and decreased yields. To address this issue in the synthesis of the target compound, the Mitsunobu reaction was employed as an alternative strategy[229]. This allowed the transfer of the carbamate group to the ether group, effectively avoiding hydrolysis issues. The optimized reaction conditions included the use of diethyl azodicarboxylate (DEAD) or diisopropyl azodicarboxylate (DIAD) as azodicarboxylates in combination with triphenylphosphine (PPh_3) under mild condition, such as room temperature that around 25℃ [229].

The Mitsunobu reaction employing the optimized synthetic scheme is presented in **Scheme 3.5**. In the initial attempts, the experimental results consistently showed the formation of the side product L14' rather than the desired compound L14. This issue arises from the self-reactivity of compound L7, which reacts with itself instead of the intended building block L13. The underlying mechanism involves the dual role of L7 as both an electrophile and a nucleophile. The phosphonium intermediate, generated from the interaction of PPh_3 and DEAD, reacts with the alcohol group of L7 to activate it by converting it into a phosphonium salt, a good leaving group[230–232]. The alcohol group of another L7 molecule then acts as the nucleophile, attacking the activated alcohol and displacing the leaving group, resulting in the formation of the side product L14'.

Two primary factors may cause to this issue. First, if the concentration of L7 is higher than that of the intended building block L13, the possibility of self-reaction increases significantly[231]. Second, compared with compound L13, the larger steric size of compound L7 introduces significant steric hindrance, which may block L13 from approaching L7's reactive sites[231]. This steric hindrance could prevent L13 from effectively reacting with L7, favoring the self-reactivity of L7 instead[231].

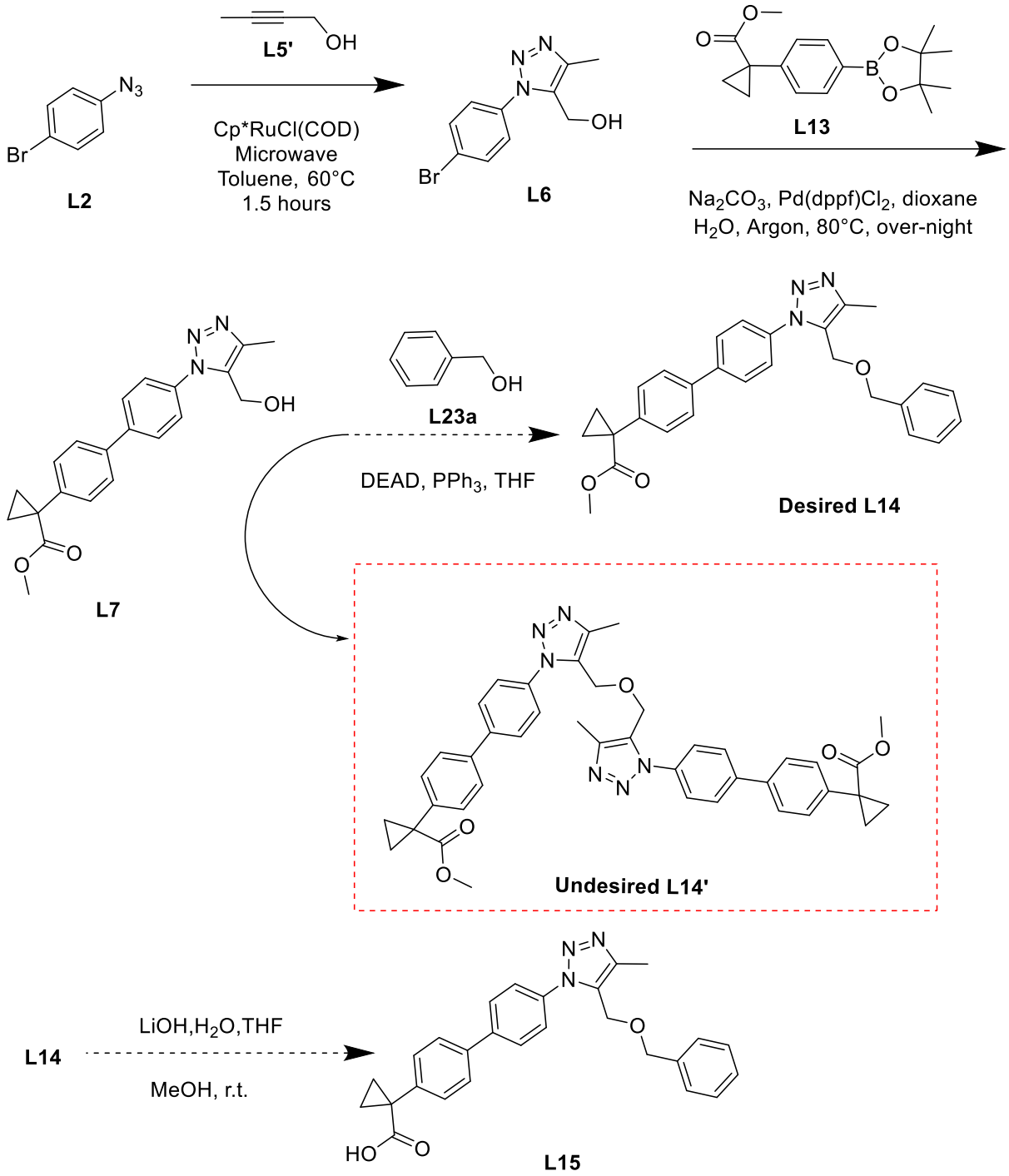

Scheme 3.5. Proposed synthetic scheme employing the Mitsunobu reaction (from compound L7 to L14). Commercially available chemical - L23a: Benzyl alcohol

To address this issue, several optimizations are under investigation. For example, using an excess of L13 relative to L7 can increase the probability of the target reaction[230]. Lowering the reaction temperature, such as using an ice bath, may enhance the possibility of the desired reaction between L7 and L13[230,232]. While low-temperature reactions cannot affect steric hindrance, it can slow the rate of side reactions and improving reaction selectivity, suppressing

L7's self-reactivity, thereby increasing the opportunities for L7 to react with L13 and form the desired product[230]. Additionally, the choice of azodicarboxylates, such as DIAD or dimethyl azodicarboxylate (DMAD), may influence the competition between the desired reaction and side reactions[231].

3.2.3 Second Series – Employing Scaffold Hopping Strategy on Compound 12f for Developing Novel LPA1 Antagonists

Scaffold hopping is a medicinal chemistry strategy used to explore alternative molecular scaffolds while preserving or enhancing the desired biological activity of a well-characterized drug molecule[102,233,234]. This approach involves identifying novel core structures through bioisosteric replacements, replicating key molecular interactions with the biological target[233,234]. Scaffold hopping aims to develop drug candidates with improved pharmacological properties, such as potency, selectivity, stability, or solubility, while addressing limitations of the original scaffold[102,233]. By employing this strategy, drug discovery can be accelerated by providing alternative starting points based on proven chemical compounds, facilitating the development of safer and more effective therapeutics[102,233]. Scaffold hopping has been successfully applied in numerous drug discovery projects and fosters innovation by uncovering structurally diverse scaffolds with similar biological activities, thereby expanding opportunities for therapeutic development[233,234].

While the modifications shown in **Scheme 3.3-A** rearrange the position of the nitrogen and oxygen atoms in the carbamate moiety, and **Scheme 3.5** resolves the hydrolysis issue by employing the ethyl ether group (Mitsunobu reaction), the resulting core structure in both schemes still retains long and flexible chains[235,236]. This flexibility can potentially disrupt the bioactive conformation of the molecule, reducing its binding affinity within the orthosteric binding pocket of LPA1[235,236].

Building upon the strategy of addressing the hydrolysis issue, where the carbamate group undergoes cleavage, one commonly employed approach in scaffold hopping is the introduction of a ring structure to increase stability[102,233]. Given that compound 12f has demonstrated promising potential in cancer treatment, it was selected as a reference for designing novel LPA1 antagonists in the second series[235]. As shown in **Figure 3.11**, scaffold hopping resulting in a ring closure upon compound 12f and replacing its triazole carbamate core for a triazole pyrimidine core to generate a novel structural LPA1 antagonist, referred to as the triazolo pyrimidine compound[235,237]. This modification not only resolve the potential multi-functional

group hydrolysis problem but also locks the molecule into a more rigid and stable bioactive conformation[235,237]. By stabilizing the interaction with the orthosteric binding pocket of LPA1, this novel core structure holds the potential to preserve or enhance antagonistic activity[235,237]. Molecular docking studies further support the hypothesis that this scaffold modification improves binding stability and receptor interactions[103,237,238].

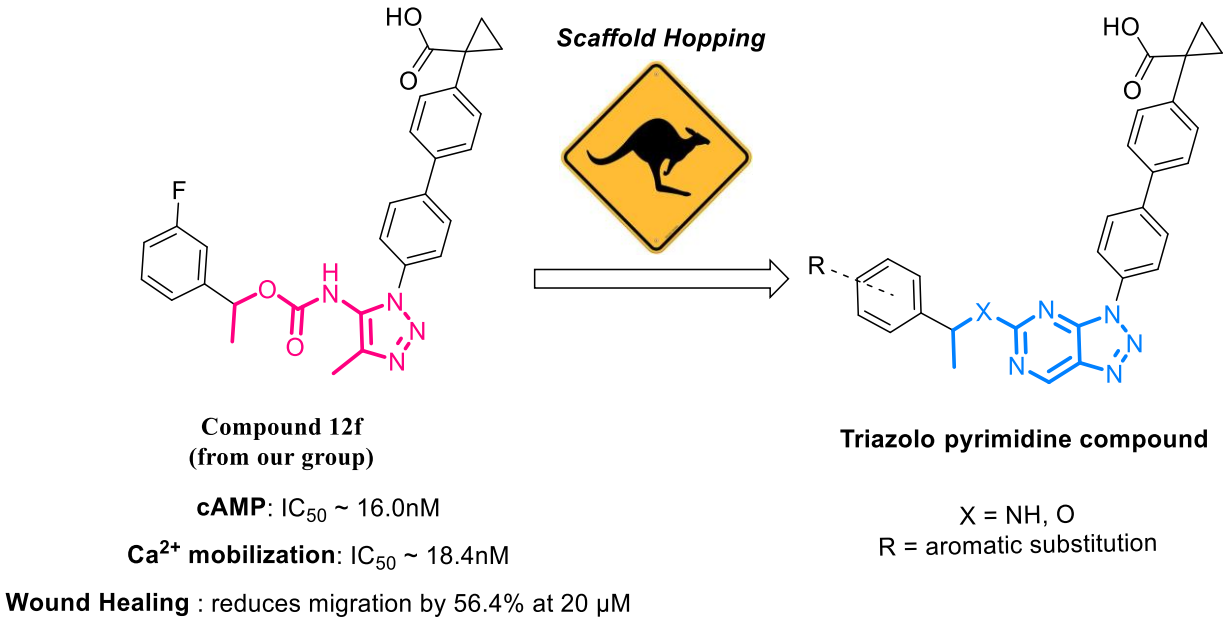

Figure 3.11. Development of a triazolo pyrimidine compound from compound 12f using scaffold hopping. The "X" represents the building blocks are two categories, amine and alcohol group.

To compare the triazolo pyrimidine scaffold to that of compound 12f, molecular docking computation was performed using the crystal structure of the LPA1 receptor [103,196]. Compound L22s was selected for molecular docking studies and compared to compound 12f, following the methodology previously reported in the literature (**Fig 3.12-A**)[237]. Compound-12f was reported to bind to the orthosteric site (endogenous ligand-binding pocket), several ligand-receptor interactions are presented in **Figure 3.12-B**[90]. Using AutoDock Vina, numerous binding modes were predicted for both compound 12f and analogue L22s[103]. The top-ranked pose of 12f was extracted for subsequent comparison with L22s. As shown in **Figure 3.12-B and C**, the docking study demonstrated that RO6842262 and L22j were found to bind to the orthosteric binding pocket of LPA1 in a similar fashion, with only minor differences in molecular position[237]. The methodology of molecular docking study for compound L22s is available in **Chapter 3.6.1**.

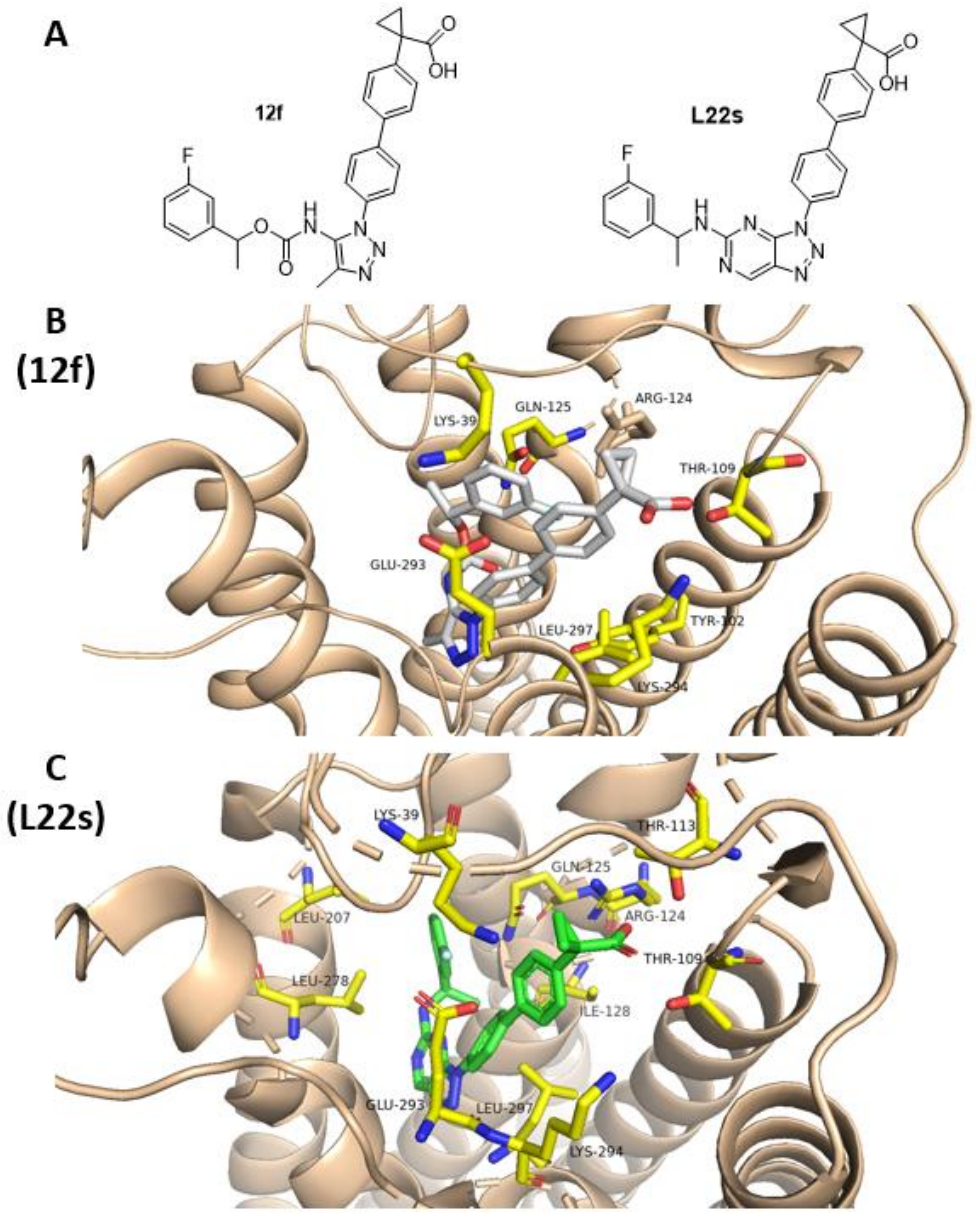

Figure 3.12. A - Structure of compound 12f and L22s. B - Docking result of 12f, colored in white. C - Docking result of L22s, colored in green. Docking results of compound 12f and L22s in the orthosteric binding pocket of LPA1. The LPA1 receptor is colored in wheat, and the interacting residues are colored in yellow.

In summary, hydrogen bonding was evident between Thr-109, Arg-124, and the carboxylic acid functional group, and several pi-anion and pi-alkyl interactions (Lys-39, Gln-125, Glu-293, Leu-297, and Lys-294) were conserved[237]. An additional hydrogen bond interaction was predicted between Leu-278 and the pyrimidine moiety for the new scaffold[237]. Additionally, two interactions were present with residues Leu207 and Ile128, which were not observed in compound 12f. These may indicate a higher degree of stabilizing interactions between LPA1

and L22s[237]. This suggests that the two scaffolds are likely to share a similar functional profile, which is promising for the novel scaffold.

Given the interest in synthesizing the novel scaffold, several patents and relevant literature were reviewed to design the synthetic scheme and experimental procedure[237,239]. The synthetic scheme, as shown in **Scheme 3.6**, comprises a six-step synthesis using commercially available reagents, the boronic ester building block L13 remains incorporate in penultimate step[237,239].

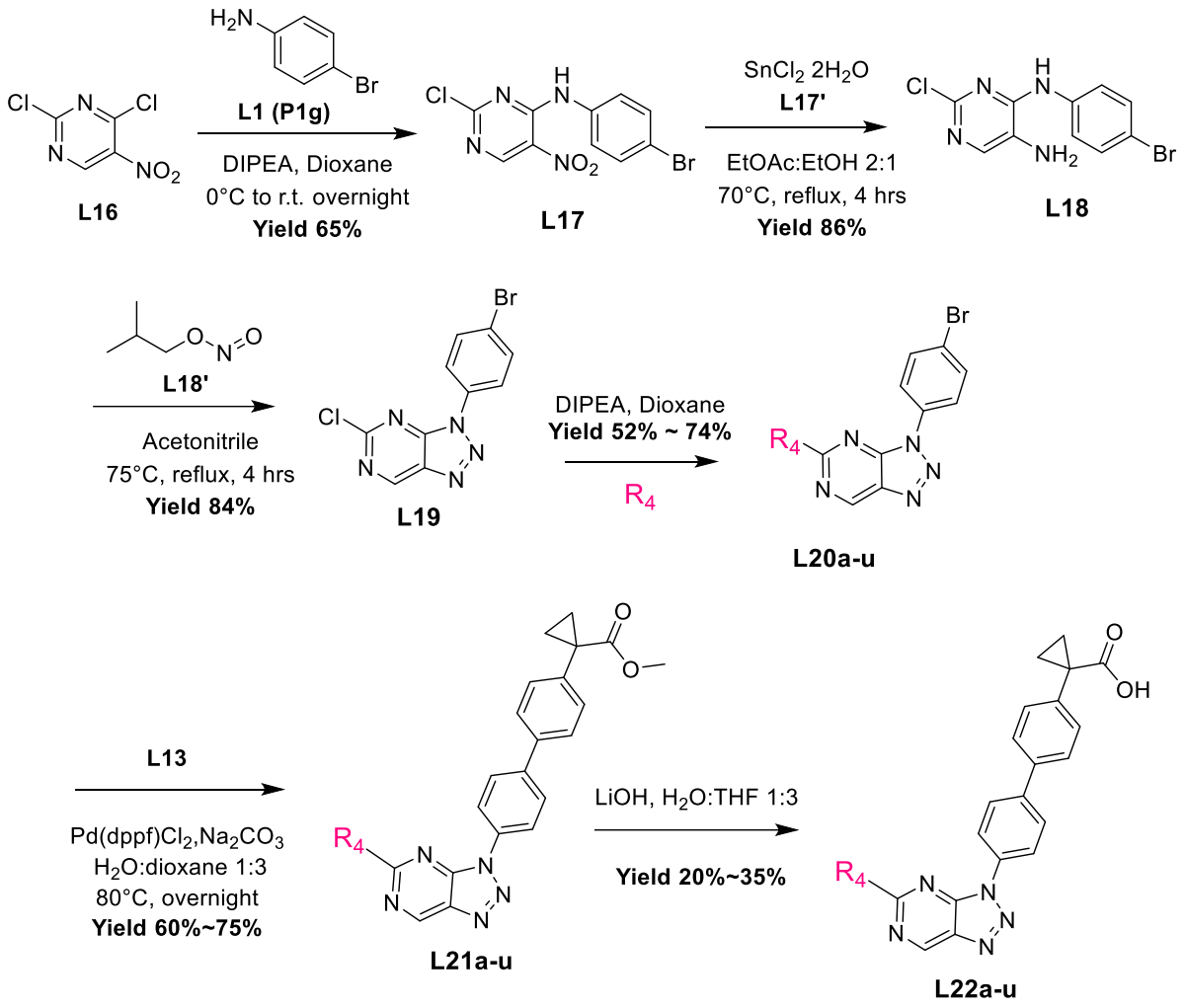

Scheme 3.6. Synthetic scheme and building blocks (L-a to L-u) with amino group of compounds L22a to L22u. Commercially available chemical – L16: 2,4-dichloro-5-nitropyrimidine L17': Tin (II) chloride dihydrate.

To fully investigate the SAR between ligands and the LPA1 receptor in this thesis, 22 diverse building blocks were proposed and synthesized, including L-u, which was also categorized for SAR discussion (**Fig 3.13**).

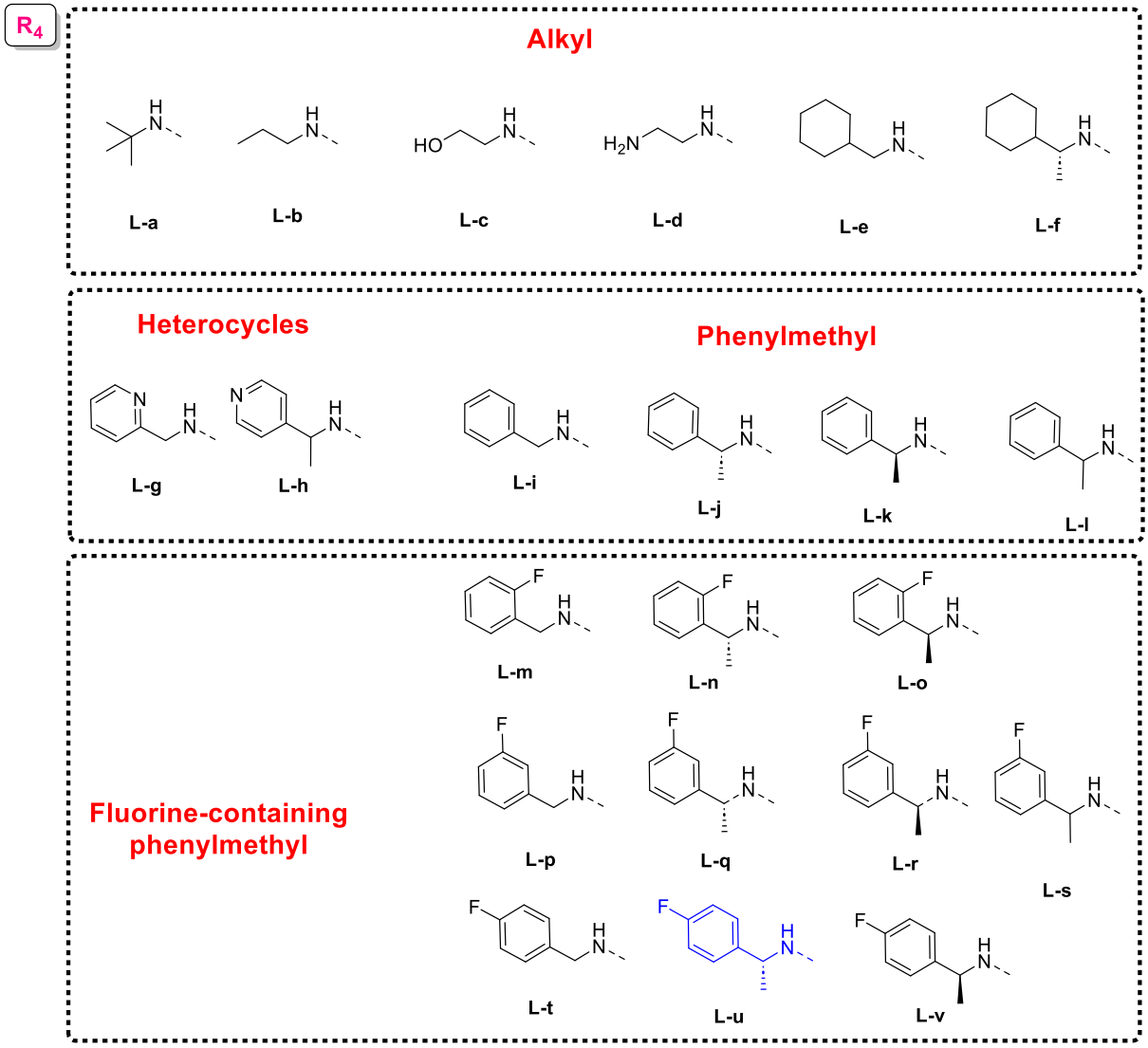

Figure 3.13. Building blocks of R_4 group. L-u colored in blue. Alkyl groups (L-a to L-f) varied in size and polarity to evaluate the contribution of steric bulk, hydrophobic interactions, and potential hydrogen bonding. Heterocycles (L-g, L-h) introduced nitrogen-containing aromatic rings to probe possible π–π stacking and polar interactions. Phenylmethyl derivatives (L-i to L-l) were employed to assess how aromatic substituents influence binding affinity through π–π interactions. Stereoisomers (e.g., L-j, L-k) were included to investigate the effect of chirality on receptor recognition. Fluorine-containing phenylmethyl groups (L-m to L-v) were prioritized for their ability to enhance lipophilicity, metabolic stability, and electronic modulation. Fluorine atoms can fine-tune molecular recognition by influencing dipole interactions and altering the electronic density of the aromatic ring. *Para*, *ortho*, and *meta*-substituted analogs (e.g., L-t, L-u) were designed to examine potential effects on receptor selectivity and in *vivo* pharmacokinetics.

Among these, compound L22u was synthesized in our group by Austin Hopkins[237] (colored in blue in **Fig 3.13**). Of the 22 compounds (a-v), 18 are characterized by HPLC-MS and ^{1}H-NMR. The experimental procedures and results are detailed in **Chapter 3.5.3**, and all the data are available in **Appendix B** (Due to routine maintenance of the HPLC-MS system during that period, the mass spectrometry (MS) data for a few intermediate products were not obtained).

These building blocks (R4) are categorized into four main types: alkylate, heterocycles, phenylmethyl, and fluorine-containing phenylmethyl groups. Incorporating these groups into the scaffold was achieved via nucleophilic aromatic substitution (S_NAr) reactions in step four of the synthetic scheme[237]. The LPA1 binding pocket, predominantly hydrophobic, provides an opportunity for enhancing hydrophobic interactions by replacing aromatic groups with alkyl groups[196]. The R4 groups focus on replacing various aromatic substitutions, as well as a few alkyl groups. The aromatic group expected to promote favorable π-π stacking interactions, while some small non-polar alkyl groups are designed to enhance hydrophobic interactions. Additionally, fluorine-containing groups are designed to increase lipophilicity and improve binding affinity. For example, compounds L22a-d take full advantage of this strategy to improve binding affinity[196,237]. Specifically, four amine-containing building blocks (L22i-L22l) were used to investigate the role of stereochemistry and methyl substitution in ligand-receptor interactions[237,240]. The fluorine-containing phenylmethyl series, with substitutions at ortho, meta, and para positions, allows for a detailed analysis of optimal substituent placement, as well as determining the best position for ^{18}F-labeling study[98,237]. Control compounds (L22m, p, and t) were included to evaluate the importance of methyl groups in the context of fluorine-containing compounds[237]. Future work will expand this array with novel functional groups, including bulky groups, to further explore steric effects and binding affinity.

The first reaction is a S_NAr reaction in which the chlorine atom that is adjacent to the nitro group is replaced by 4-bromoaniline; a slight excess of the weak base, N, N-diisopropylethylamine (DIPEA), is used to neutralize the formed hydrochloric acid[239]. This reaction is started at 0ºC and warmed up to room temperature to enhance the selectivity for the indicated position[239]. Due to the two possible positions of chloride in the starting material, L16, the formation of compound L17' as an undesired regioisomer occurs during the reaction (**Fig. 3.14**)[239]. Based on the reaction mechanism and experimental observations, extending the reaction time in an ice bath to 6 hours has been found to effectively reduce the formation of L17'[239]. While prolonging the ice-bath reaction time does not alter the reaction mechanism, it allows the reaction system to favor the kinetically controlled pathway, thereby minimizing side

reactions that lead to the undesired regioisomer and significantly improving the yield of the desired product, L17 (yield >65%)[239].

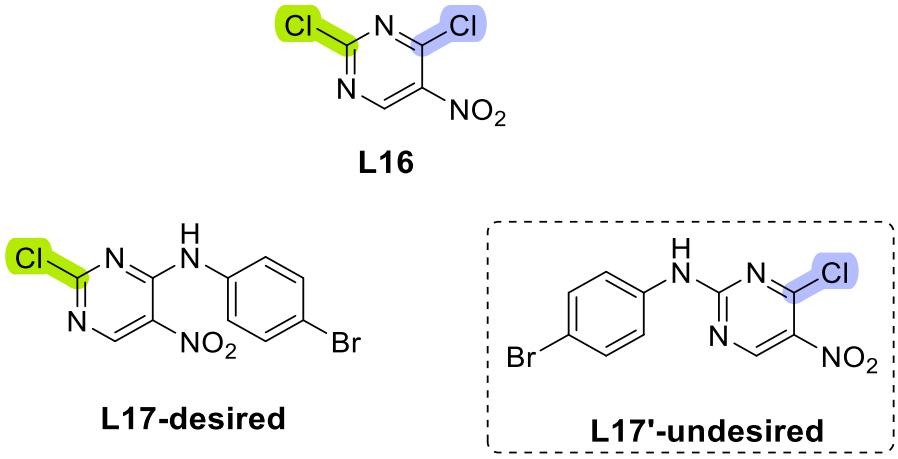

Figure 3.14. Structure of desired L17 and undesired L17' regio-isomers.

The desired structure of L17 was characterized by HPLC-MS and ^{1}H-NMR, and confirmed by 1-D selective NMR of compound L18, as shown in **Figure 3.15**[228]. The two upside-down peaks indicate interactions with the "blue" amino group, confirming that the desired regioisomer is formed in the first step[228].

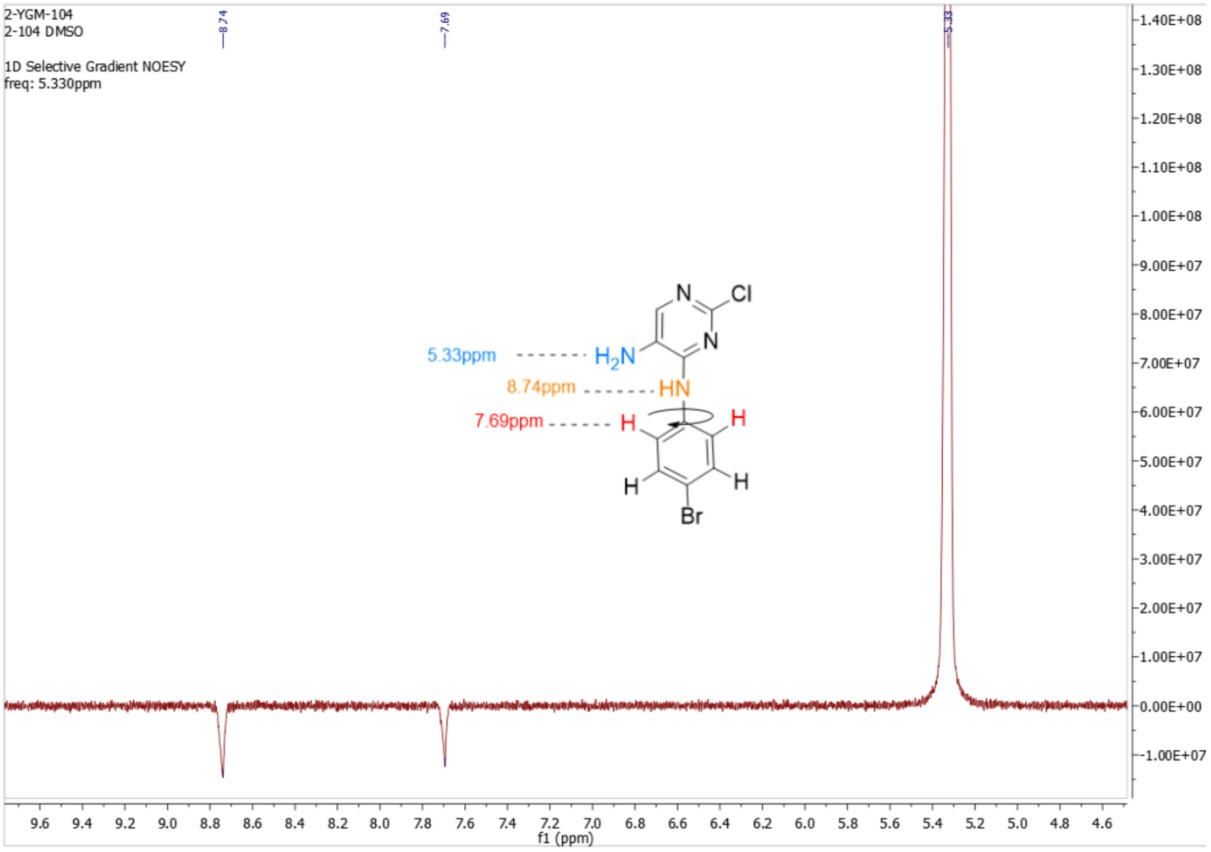

Figure 3.15. 1-D selective NMR of compound L18. Compound L18 was dissolved in DMSO-d, and a selective scan at 5.33 ppm, corresponding to the amino group (colored in blue), revealed two upside-down peaks at 7.69 ppm (colored in red) and 8.74 ppm (colored in orange), corresponding to the proton of the amino group attached to the benzene ring and the two protons in the benzene ring.

The following is a cyclization reaction, where the primary and secondary amine groups in L18 are converted into a triazole ring using an alkyl nitrite at elevated temperature[241]. This step forms a bicyclical system in L19, establishing the core structure required for subsequent modifications. The next step involves a S_NAr reaction. A selected nucleophilic building block (a-u) replaces the remaining chlorine substituent on the pyrimidine ring of L19[237]. This reaction is facilitated by DIPEA, which neutralizes the acid byproduct, yielding L20a-u[237]. Subsequently, compound L13 incorporated through a Suzuki coupling reaction using a palladium catalyst producing the ester-intermediate (L21a-u) for the final step[223]. Then the ester group is hydrolyzed to a carboxylic acid using lithium hydroxide (LiOH) in a 1:3 mixture of water (H_2O) and tetrahydrofuran (THF)[223]. The reaction is followed by an acid work-up to yield the final products (L22a-u)[223]. The detailed experimental procedures and results of all the intermediates and final compounds can be found in **Chapter 3.5.3**, and the characterization data are available in **Appendix B.**

Upon reviewing the proton-NMR spectra of the final compounds, some peaks displayed shoulder peaks adjacent to the main signal. To determine whether these were conformational isomers rather than impurities, variable temperature NMR (VT-NMR) was performed on select compounds, including L22p[242]. Compound L22p was dissolved in chloroform-d and tested in ^1H -NMR with three different temperatures: 25°C, 50°C, and 100°C, as shown in **Figure 3.16-A**[242]. Based on the NMR spectra, as temperature increased, the side peaks merged with the main peak, indicating faster conformational exchange. The red-cycle highlighted bond is rotationally restricted, likely due to extended π-conjugation, resulting in slow-exchanging conformers observed in the NMR spectrum (**Fig. 3.16-B**). This supports the interpretation that the additional minor peaks arise from conformational isomers rather than impurities.

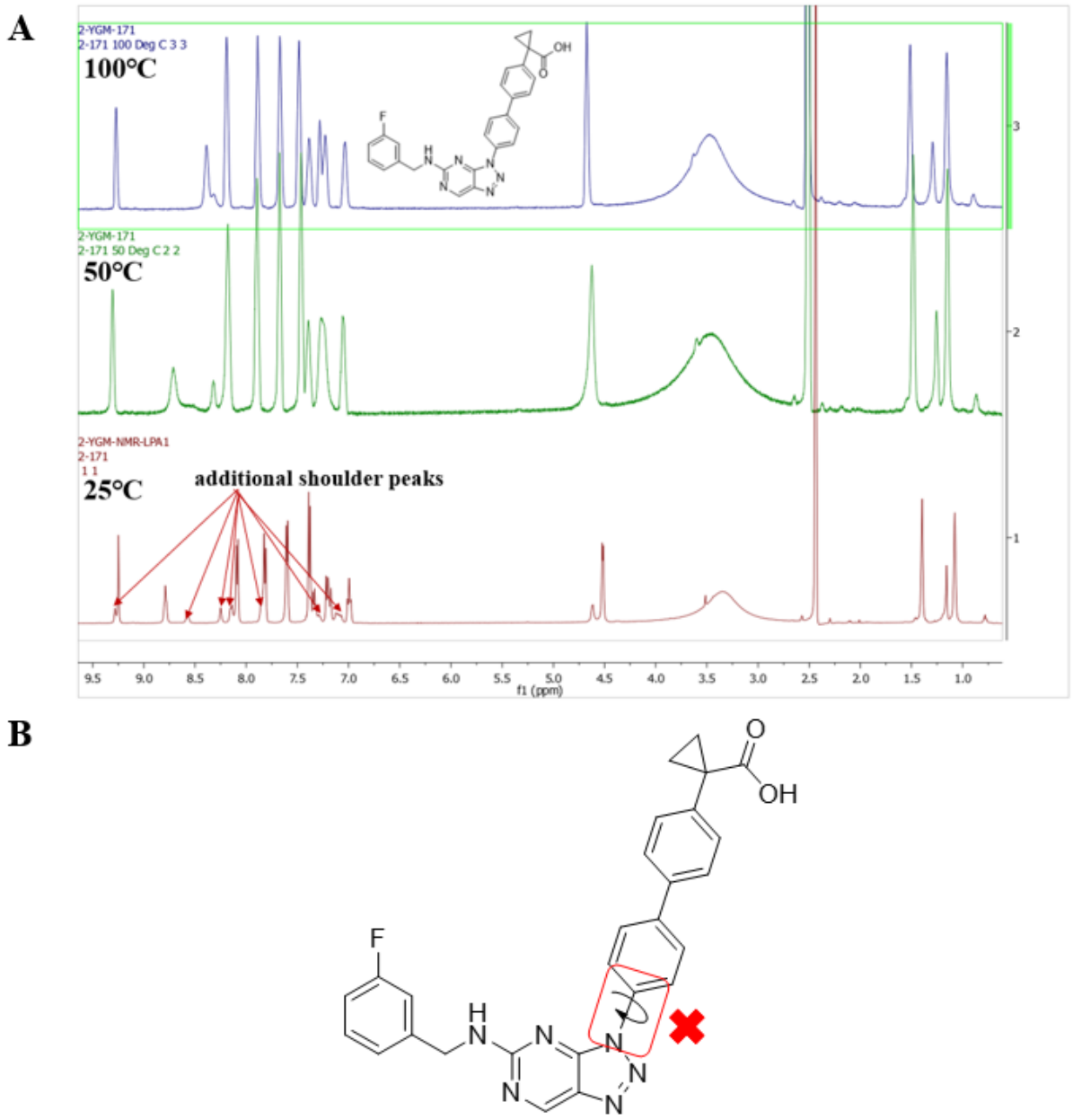

Figure 3.16. A - VT-NMR spectra of compound L22p. The compound was tested in ^{1}H-NMR with 25℃ (colored in red), 50℃ (colored in green), and 100℃ (colored in purple). The side peaks are indicated by red arrows in the 25°C spectrum. B - Restricted rotation between the triazole and aryl rings due to extended π-conjugation.

As shown in **Figure 3.17**, compared with the building block 1-(3-fluorophenyl) ethan-1-amine (L20s), the building block 1-(3-fluorophenyl) ethan-1-ol (L23d) is embedded in the structure of compound 12f. Using this substituent for the novel scaffold would allow for an unambiguous comparison between the two scaffolds[101,237].

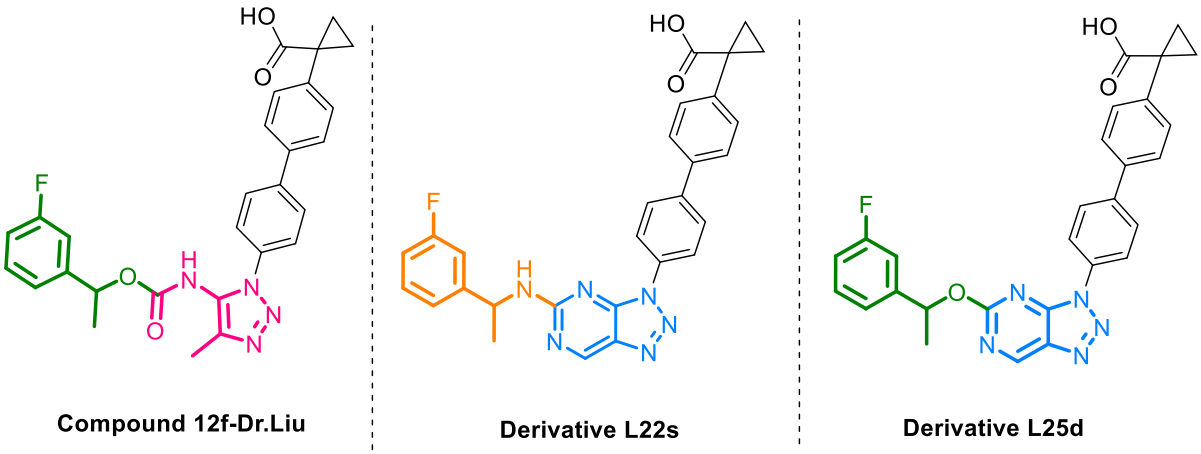

Figure 3.17. Structure of compound 12f, L22s, and L25d.

The alcohol group is introduced to the synthetic system as shown in **Scheme 3.7**, and five intermediates with R5 group (L23a-e) were synthetized.

Introducing an alcohol group in S_NAr reactions often requires harsher conditions compared to an amino group[243]. The oxygen atom of the alcohol group is more electronegative, which reduces the nucleophilicity of its lone pair, making it less reactive[243]. Several bases, solvents, and conditions were tested. Employing sodium hydride (NaH) in combination with microwave assistance was found to improve the yield[244]. However, NaH's high reactivity and the associated safety concerns necessitate cautious handling and strict control[244]. As a result, alternative and safer reaction conditions are currently under investigation.

Due to the alcohol group being less reactive in S_NAr reactions and time constraint, L25a is only one final compound synthesized in **Scheme 3.7**. The experimental procedure, results, and MS data of all the intermediates can be found in **Chapter 3.5.3** and **Appendix B**.

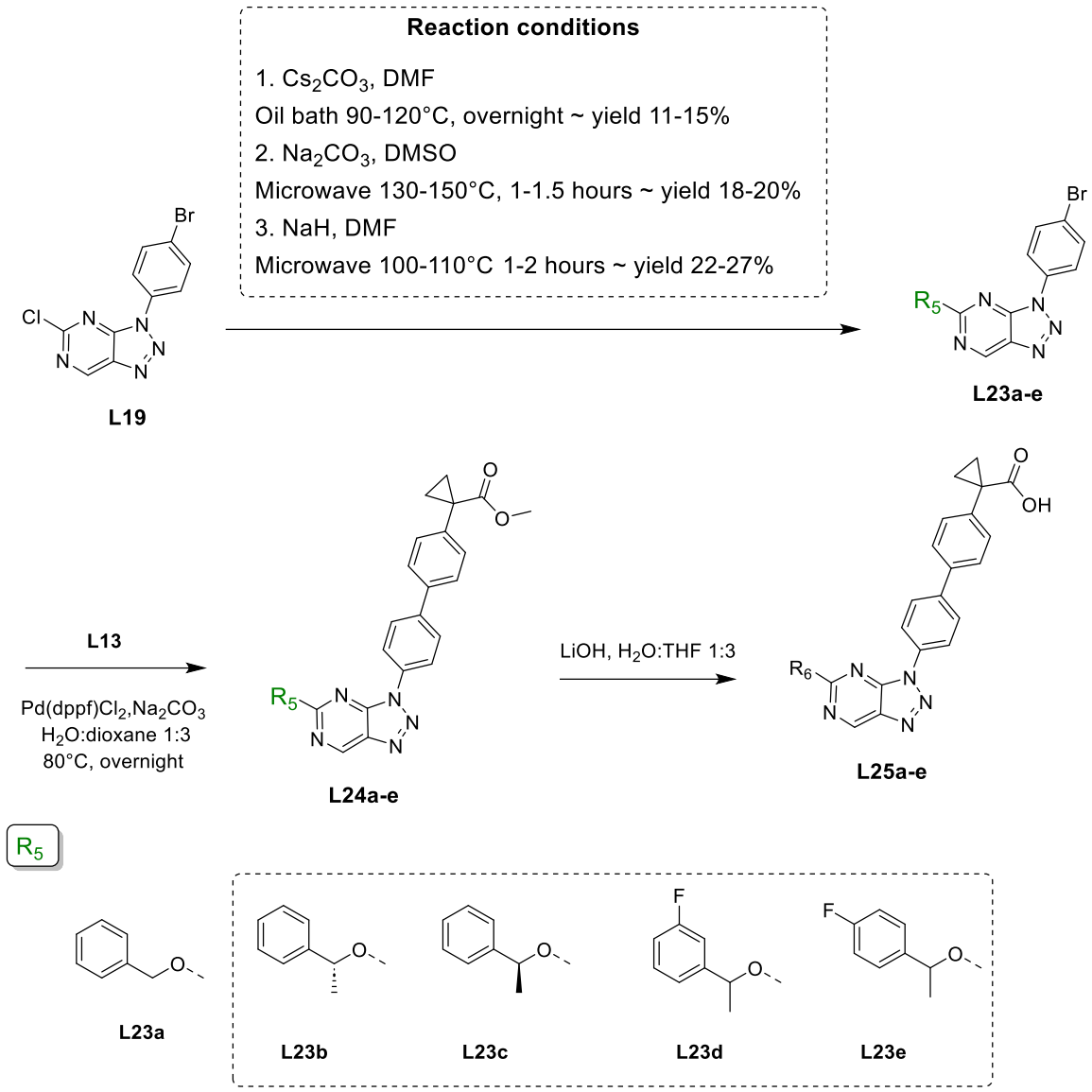

Scheme 3.7. Synthetic scheme and building blocks with alcohol group of compounds L23a to L23e.

3.3 Biological Evaluation of the 2nd Series of Ligands

In our group, Dr. Zhao initially performed a cAMP assay to test compounds L22j, L22p, and L22s. The results from this assay are summarized by the concentration-response curve shown in **Figure 3.18**.

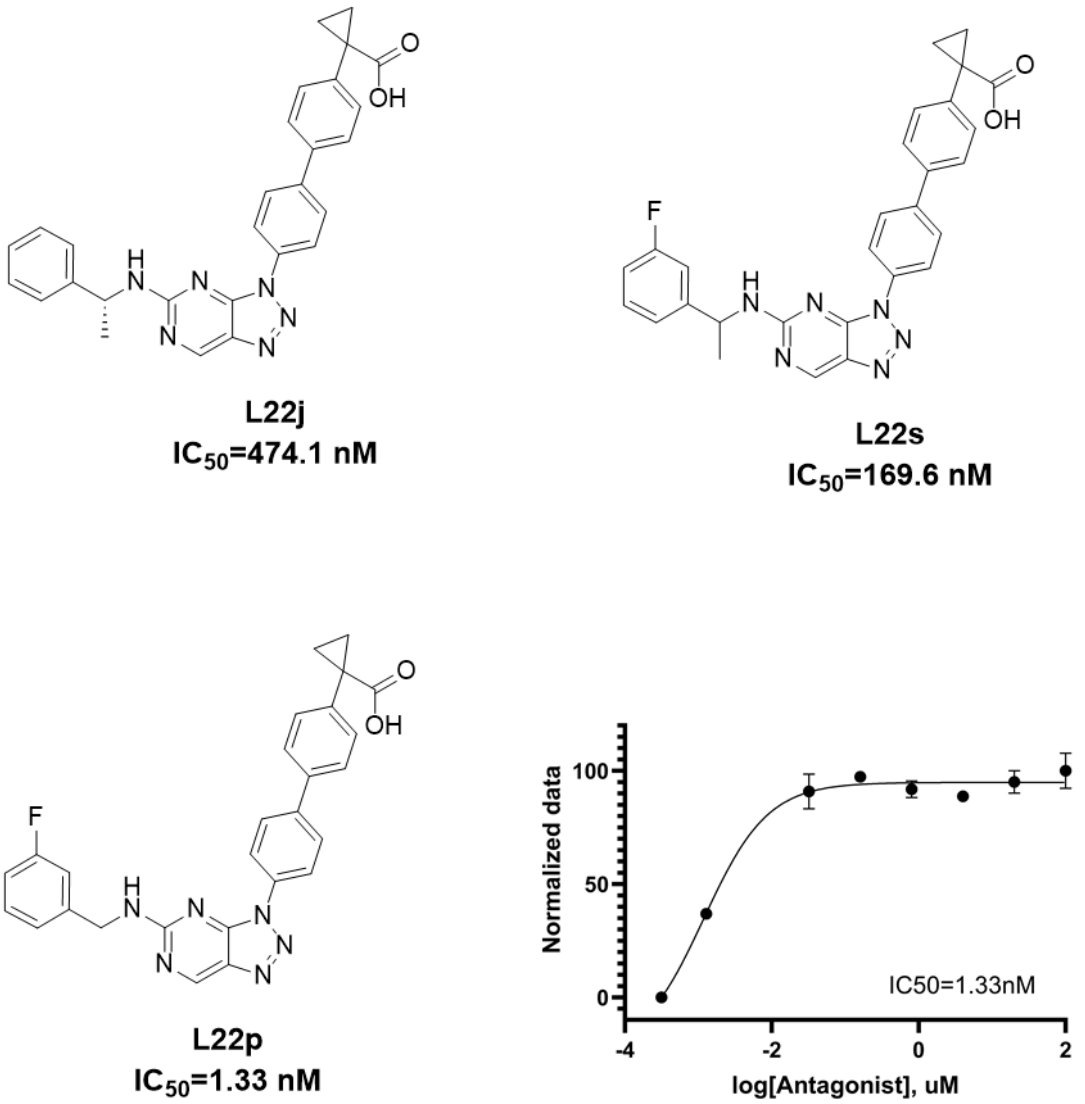

Figure 3.18. cAMP assay results using compound L22j, L22p, and L22s.

As shown in **Figures 3.1** and **3.2**, LPA1 activation by 18:1 LPA leads to a suppression of intracellular cAMP production through Gi signaling[199,211]. The three tested compounds were evaluated in an *in vitro* cAMP assay using a Chinese hamster ovary (CHO) cell line overexpressing LPA1[209,245]. The cAMP-Glo luminescence assay was used to quantify intracellular cAMP levels, where increased cAMP production resulted in decreased luminescence[209]. IC_{50} values were calculated using a three-parameter logistic fit in GraphPad Prism. Based on these data, compound L22p revealed a potent IC_{50} value of 1.33 nM, indicating strong antagonistic activity at LPA1. This demonstrates that the novel scaffold holds promise as an LPA1 antagonist and could also exhibit a high level of antagonistic activity. The remaining compounds are also being tested with the cAMP assay in our group. The results will guide the design of future optimizations through structure-activity relationship (SAR) studies to enhance potency and selectivity.

3.5 Inspired by BMS-986278: Integration with the Second Series for Third Series

In 2021, Cheng *et al*. from Bristol Myers Squibb Pharma. introduced BMS-986278 (**Fig. 4.2)**, a second-generation LPA1 antagonist designed for progressive pulmonary fibrosis (PPF) treatment[60,215,248]. This drug builds upon its predecessor, BMS-986020, initially developed for idiopathic pulmonary fibrosis (IPF)[60]. Despite BMS-986020's success in reducing lung function decline during Phase 2 clinical trials, its development was terminated due to hepatobiliary toxicity, attributed to off-target effects specific to its chemical structure (inactive amino-isoxazole 986020a in **Fig 3.20**)[215,217]. The significant structural improvement from BMS-986020 to BMS-986278 is replacement of the biphenyl and cyclopropane moiety with a 3-oxycyclohexyl acid group (colored in red in **Fig. 3.20**)[60]. This modification enhances the compound's metabolic stability and minimizes transporter inhibition, thereby addressing toxicity issues[60]. Currently, the U.S. FDA has granted BMS-986278 fast-track designation and orphan drug designation[248]. The Pharma. is continuing the development of BMS-986278 with the global Phase 3 ALOFT program for PPF and IPF[215,217].

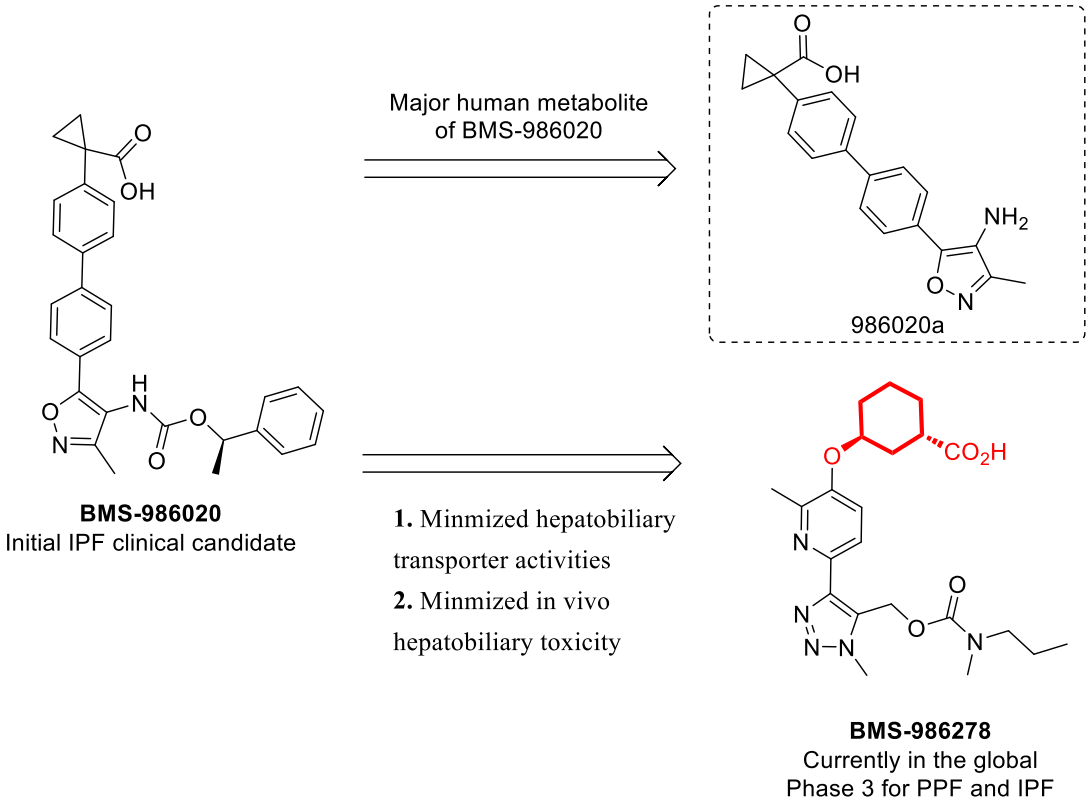

Figure 3.20. Structure of BMS-986020, 986020a, and BMS-986278.

This section aims to further refine the structural framework of LPA1 antagonists and is inspired by BMS-986278, a 3-oxycyclohexyl acid group was incorporated into the second series, which forms the foundation for the development of the third series[60]. While hepatobiliary toxicity is not a hallmark of lung cancer, many cancer drugs are metabolized or excreted through hepatobiliary transport pathways[11,18,215]. Moreover, studies have demonstrated the involvement of LPA1 signaling and liver processes in tumorigenesis, fibrosis, and drug metabolism, further linking these pathways to disease progression and drug action[11,204]. More importantly, from a drug development perspective, safety and efficacy are primary factors in designing effective cancer treatments[198,204]. The structural refinement of the third series avoids safety concerns and enhances its potential to serve as a novel class of potent LPA1 antagonists. Therefore, the third series hold promise for therapeutic applications in lung cancer by balancing pharmacological effectiveness with patient safety.

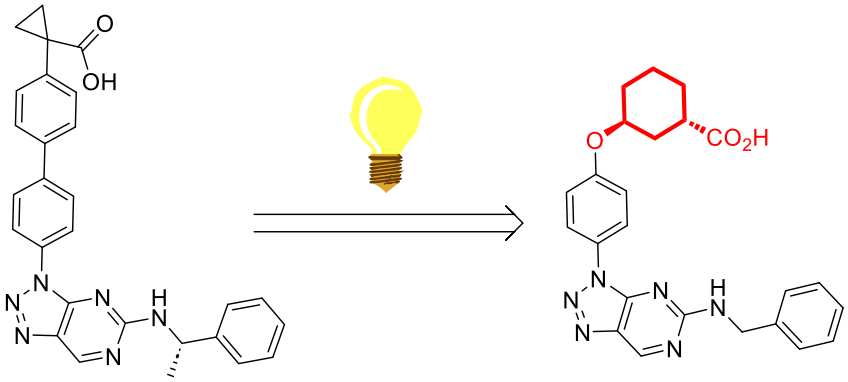

Compound L22j
2nd series

Compound L33i
3rd series

Figure 3.21. Representative structure of third-series compound L33i - Inspired by BMS-986278.

Due to the multi-racemic nature of the 3-oxycyclohexyl acid group, the building blocks selected for the third series are designed to minimize racemization[60]. This approach has the potential to enhance binding affinity and selectivity for targeting LPA1[60]. A rational synthetic scheme was designed after the ligand design components were decided. **Scheme 3.11** displays the synthetic scheme; the key side product in **Scheme 3.11-A** is adapted from Cheng *et al.* with some modifications[60]. **Scheme 3.11-B** presents a total four-step synthesis and adapted from Cheng *et al.* with some modifications as well[60]. There are a total of four intermediates that have

synthesized and characterized (L31i, m, p, and t), the experimental procedure, results and data are available in **Chapter 3.6.4** and **Appendix B**.

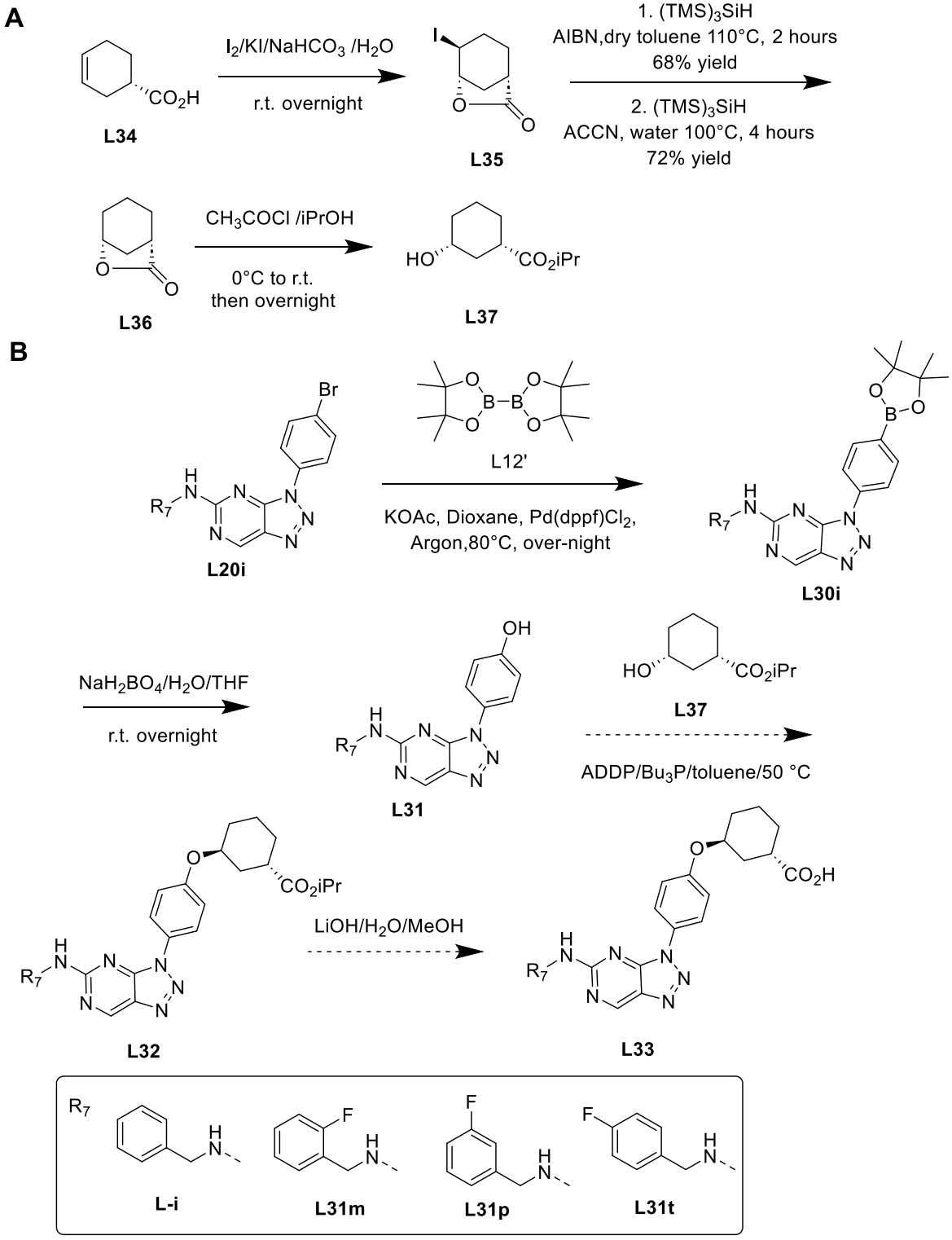

Scheme 3.11. A. Synthetic scheme for preparation of compound L37. B. Synthetic scheme for preparation of compound L33i, m, p, and t. Commercially available chemical L34: (S)-cyclohex-3-enecarboxylic acid

The key product - cyclohexyl ester building block, (3R)-hydroxycyclohexyl (1S)-isopropyl ester intermediate L37 is synthesized in three steps are shown in **Scheme 3.11-A**[60]. The synthetic sequence begins with the iodolactonization of the commercially available chemical (S)-3-cyclohexene carboxylic acid, L34, where the carboxylic acid reacts with iodine to form the iodolactone intermediate L35[60]. Given that this step involves an iodine atom in the intermediate, it leads to a subsequent deiodination reaction. The deiodination of L35 is carried out using trimethylsilyl hydride ($(TMS)_3SiH$) as the reducing agent[249]. This process removes the iodine atom and forms the lactone compound L36, which features a cyclic ester functional group[60]. Finally, the lactone L36 undergoes a ring-opening reaction mediated by acetyl chloride[60]. This step converts the cyclic ester into the linear ester, yielding the target compound, (3R)-hydroxycyclohexyl (1S)-isopropyl ester, compound L37.

The main steps for synthesizing the third series of products are shown shown in **Scheme 3.11-B**, the first step is a Miyaura borylation reaction, involving the $Pd(dppf)Cl_2$ catalyzed cross-coupling of bis(pinacolato)diboron and the boroarene group of L20i to produce the pinacol arylboronate L30i[241]. The catalyst undergoes a redox cycle in which it coordinates and activates the boroarene and bis(pinacolato)diboron to produce the coupled product[241]. Conversion of the pinacol arylboronate to the corresponding hydroxyphenyl triazole L31i was achieved via hydrolysis of the pinacol arylboronate intermediate with sodium hydrogen carbonate[97,241]. A Mitsunobu reaction will perform on the hydroxyphenyl triazole pyrimidine intermediate L31i and the 3-(R)-hydroxycyclohexyl ester L37 to produce the trans-(3S,1S)-phenyloxycyclohexyl ester L32i[60]. Subsequent ester hydrolysis of L32i will deliver the triazole pyrimidine oxycyclohexyl acid L33i[60].

The (3R)-hydroxycyclohexyl (1S)-isopropyl ester building block L37 was successfully synthesized. Current synthetic efforts are focused on obtaining the trans-(3S,1S)-pyridyloxycyclohexyl ester intermediate L32 via a Mitsunobu reaction.

3.6 Experimental Procedure

3.6.1 Molecular Docking Study

The crystal structure of human LPA_1 (**PDB ID: 4z36**) was used as the docking receptor. Receptor and ligand structures were prepared using AutoDockTools. The ligand structures were energy-minimized and converted to PDBQT format using DS Viewer 3.5. Docking simulations were carried out using AutoDock Vina.

The docking grid box was centered at (x = –3.0, y = –25.5, z = 53.5) with dimensions of 26 × 26 × 26 Å³ to fully cover the ligand-binding site. The number of output binding modes was set to 50, and all other docking parameters were left at default values. The docking poses were visualized and analyzed using PyMOL and Discovery Studio Visualizer to evaluate binding orientation and key ligand–receptor interactions.

3.6.2 General Information of Organic Synthesis

All solvents and chemicals used were reagent grade and purchased from commercial manufacturers. The purity and characterization of compounds were determined using a combination of HPLC, TLC, and NMR analyses. Where possible, spectral data were compared with reference data from the literature. Chromatographic purification was performed using silica gel column chromatography. Preparative high-performance liquid chromatography (HPLC/MS) purification was conducted on a Waters LC-MS system equipped with a Waters Symmetry column (C18, 5 µm, 19 mm diameter, 150 mm length).

The purities of compounds intended for biological testing were assessed by analytical LC-MS on a UV detector system under the following conditions: column, XSELECT CSH C18 (5 µm, 4.6 x 150 mm); solvent A, water with 0.1% formic acid; solvent B, acetonitrile with 0.1% formic acid; flow rate, 0.8 mL/min; gradient, 5% to 95% solvent B.

^{1}H NMR spectra were recorded on a 500 MHz Bruker NMR spectrometer, with chemical shifts reported in parts per million (ppm) relative to internal TMS in appropriate organic solvents. Peak multiplicities are designated as follows: s (singlet), d (doublet), dd (doublet of doublets), t (triplet), and m (multiplet). NMR and mass spectra were obtained for isolated intermediate and final products, with data consistent with the proposed structures.

All figures were created with ***BioRender.com.***

3.6.3 Experimental Procedure for the First Series Compounds

Synthesis of 1-Azido-4-bromobenzene (L2)

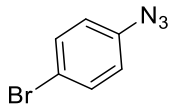

4-Bromoaniline (6.19 g, 35.98 mmol) was added into a 250 mL RBF with 4N HCl (45 mL, prepared by combining 14.8 mL of concentrated HCl with 45 mL of water) with a magnetic stir bar. The mixture was stirred and cooled to 0˚C using an ice bath. A solution of $NaNO_2$

(2.77 g, 40.15 mmol) was prepared separately in 7 mL of water. The solution was added dropwise to the RBF over the course of 30 minutes. Next, NaN_3 (2.83 g, 45.53 mmol) was added portion-wise to the RBF, with foaming observed in the reaction mixture upon addition. The reaction mixture was then removed from the ice bath and allowed to slowly warm to room temperature, then continued to mix at room temperature for 21 hrs. The reaction mixture was then mixed with EtOAc (50 mL) to extract the organic layer. The organic layer was then dried over Na_2SO_4, then vacuum filtered washing with EtOAc. The resulting solution was concentrated in rotovap, followed by high vacuum to give L2 as a dark brown oil (6.82 g, 99.2% yield). Chemical Formula: $C_6H_4BrN_3$. ^{1}H NMR (500 MHz, $CDCl_3$) δ 7.46 (d, J = 8.7 Hz, 2H), 6.90 (d, J = 8.7 Hz, 2H).

Synthesis of 1-(4-bromophenyl)-4-methyl-1H-1,2,3-triazol-5-yl] methanol (L6)

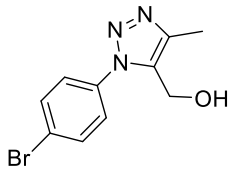

A small scoop of Cp*RuCl(COD) catalyst (5 mg, 0.01 mmol)was added to a 100 ml microwave reaction RBF with a magnetic stir bar. The flask was capped and flushed with Ar three times. Anhydrous toluene (5 mL) was added via syringe. Next, but-2-yn-1 ol (L5') (35 mg, 0.55 mmol) was added by syringe to the mixture. Finally, 1-azido-4 bromobenzene L2 (100 mg, 0.51 mmol) was added by syringe. The reaction vessel was placed in the microwave reactor, still under Ar, and sealed. The reaction proceeded at 60˚C under ~15 MW of microwave irradiation for 0.5 hr. The reaction mixture was concentrated, diluted in EtOAc and absorbed onto silica gel. The crude product was purified through flash column chromatography (eluent gradient, 30% EtOAc in hexanes) to yield L6 as a dark crystal (57 mg, 43% yield). Chemical Formula: $C_{10}H_{10}BrN_3O$. Molecular Weight: 268.11. LC-MS, $[M + H]^+$ = 268.01 (calcd.) 268.08 (found). ^{1}H NMR (500 MHz, $CDCl_3$) δ 7.67 (d, 2H), 7.60 (d, 2H), 4.67 (s, 2H), 2.44 (s, 3H).

Synthesis of methyl 1-(4'-(5-(hydroxymethyl)-4-methyl-1H-1,2,3-triazol-1-yl)-[1,1'-biphenyl]-4-yl) cyclopropane-1-carboxylate (L7)

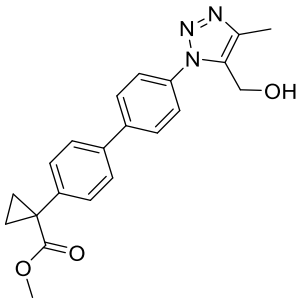

200 mg (0.75 mmol) of 1-(4-bromophenyl)-4-methyl-1H-1,2,3-triazol-5-yl]methanol (L6) and 278 mg (0.8mmol) of Ethyl 1-(4-(4,4,5,5-tetramethyl-1,3,2-dioxaborolan-2 yl)phenyl)cyclopropane-1-carboxylate (L13) were mixed together with Na_2CO_3 (167mg, 1.58 mmol) in a solution of dioxane (10 mL) and water (3.5mL) in a 100 mL three neck RBF with a magnetic stir bar. To this solution was added Pd(dppf)Cl_2 (55mg, 0.12mmol). A condenser was attached, and all openings were sealed with septa. A needle was used to bubble the reaction mixture with the contents of an Ar filled balloon, with a second needle used to allow air to escape (degassing). Next, the vessel was flushed three times with Ar. The reaction mixture was refluxed at 80 ˚C for 12 hrs under Ar. The resulting mixture was diluted with EtOAc (40mL), then washed with water followed by brine. The organic layer was concentrated and dissolved in EtOAc followed by absorption onto silica gel. The crude product was purified through flash column chromatography (eluent gradient, 30-50% EtOAc in hexanes). Product fractions were concentrated in the rotovap and under high vacuum to yield L7 (136mg, 52% of yield) as a white powder. Chemical Formula: $C_{21}H_{21}N_3O_3$. Molecular Weight: 363.42. LC-MS, $[M + H]^+$ = 364.17 (calcd.) 364.20 (found). ^{1}H NMR (500 MHz, $CDCl_3$) δ 7.74 (s, 4H), 7.58 (d, *J* = 8.3 Hz, 2H), 7.46 (d, *J* = 8.2 Hz,2H), 4.73 (d, *J* = 5.5 Hz, 2H), 3.67 (s, 3H), 2.47 (s, *J* = 6.2 Hz, 2H), 1.66 (q, *J* = 4.0 Hz, 2H), 1.25 (q, *J* = 7.0, 4.0 Hz, 2H).

Synthesis of methyl 1-(4'-(4-methyl-5-(((phenylcarbamoyl)oxy) methyl)-1H-1,2,3-triazol-1-yl)-[1,1'-biphenyl]-4-yl) cyclopropane-1-carboxylate (L8x)

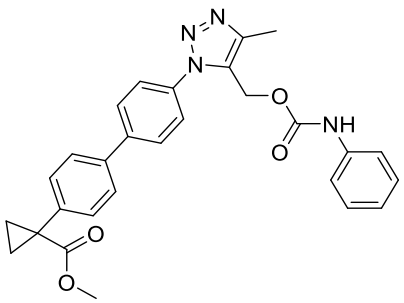

methyl 1-(4'-(4-methyl-5-(((phenylcarbamoyl)oxy) methyl)-1H-1,2,3-triazol-1-yl)-[1,1'-biphenyl]-4-yl) cyclopropane-1-carboxylate (L7) (130 mg, 0.36mmol) was added into anhydrous toluene (10 mL) in a 100 mL RBF with a magnetic stir bar. To this solution was added Benzoic acid (101mg, 0.72mmol), TEA (80mg, 0.4mmol), and DPPA (150 mg, 0.6mmol). Next a condenser was attached to the RBF and a septum was used to seal the opening. The vessel was flushed with Ar three times, and the reaction was refluxed under Ar for 8 hrs. The reaction mixture was diluted in EtOAc (30 mL), then the solution was washed with brine. The organic layer was separated and dried over $MgSO_4$, followed by filtration and concentration. The crude product was dissolved in DCM and absorbed onto silica gel for flash column chromatography purification (eluent gradient, 30-40% EtOAc in hexanes). Product fractions were concentrated in the rotovap and under high vacuum to yield L8 (125mg, 70% of yield) as a light-yellow powder. Chemical Formula: $C_{28}H_{26}N_4O_4$ Molecular Weight: 482.54. LC-MS, $[M + H]^+$ = 483.20 (calcd.) 483.28 (found). ^1H NMR (500 MHz, $CDCl_3$) δ 7.70 (s, 2H), 7.54 (d, *J* = 7.9 Hz, 4H), 7.44 (s, 4H), 7.33 (s, 2H), 7.10 (s, 1H), 5.20 (s, 2H), 3.66 (s, 3H), 2.47 (s, 3H), 1.65 (s, 2H), 1.23 (s, 2H).

Synthesis of 1-(4'-(4-methyl-5-(((phenylcarbamoyl)oxy) methyl)-1H-1,2,3-triazol-1-yl)-[1,1'-biphenyl]-4-yl) cyclopropane-1-carboxylic acid (L9x)

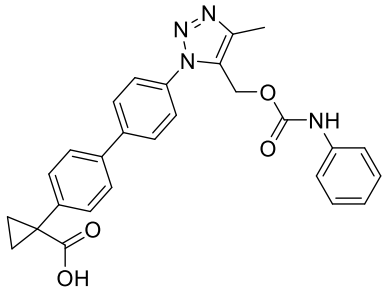

Compound L8 (103 mg, 0.2 mmol) was dissolved in 12 mL of a prepared 1:3 mixture of H_2O: THF. Lithium hydroxide pellets (LiOH) (23 mg, 1 mmol) were added to the solution, and the solution was stirred for 6 hrs. The mixture was partitioned between EtOAc and brine, and the organic phase was separated, dried over Na_2SO_4, filtered, and concentrated. The crude was purified by ACN/Water (65% / 35%) in prep-HPLC to provide the final compound L9x. (6 mg, yield: 4%). Chemical Formula: $C_{27}H_{24}N_4O_4$. Molecular Weight: 468.51. LC-MS, $[M + H]^+$ = 469.19 (calcd.) 469.21 (found). ^1H NMR (500 MHz, DMSO) δ 9.72 (s, 1H), 7.83 (s, 2H), 7.66 (s, 2H), 7.60 (s, 2H), 7.37 (s, 4H), 7.20 (s, 2H), 6.93 (s, 1H), 5.18 (s, 2H), 2.35 (s, 3H), 1.40 (s, 2H), 1.09 (s, 2H). Purity testing by HPLC (Acquisition method 75%-95% Acetonitrile 20 minutes) t_R = 14.5 minutes. Purity=98%.

Synthesis of methyl 1-(4'-(5-((((4-fluorophenyl) carbamoyl) oxy) methyl)-4-methyl-1H-1,2,3-triazol-1-yl)-[1,1'-biphenyl]-4-yl) cyclopropane-1-carboxylate (L11y)

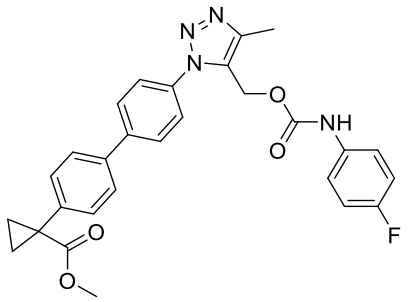

methyl 1-(4'-(4-methyl-5-(((phenylcarbamoyl)oxy) methyl)-1H-1,2,3-triazol-1-yl)-[1,1'-biphenyl]-4-yl) cyclopropane-1-carboxylate (L7) (200 mg, 0.56 mmol) was added into anhydrous toluene (15 mL) in a 100 mL RBF with a magnetic stir bar. To this solution was added 4-fluorobenzoic acid (145 mg, 1.33 mmol), TEA (142 mg, 1.41 mmol), and DPPA (235 mg, 0.76 mmol), as well as a scoop of molecular sieve. Next a condenser was attached to the RBF and a septum was used to seal the opening. The vessel was flushed with Ar three times, and the reaction was refluxed under Ar for 6 hrs. The reaction mixture was diluted in EtOAc (50 mL), then the solution was washed with brine. The organic layer was separated and dried over $MgSO_4$, followed by filtration and concentration. The crude product was diluted with DCM and absorbed onto silica gel for subsequent purification through flash column chromatography (eluent gradient, 15% EtOAc in hexanes) to yield L11y (193 mg, 71% of yield). Chemical Formula: $C_{28}H_{25}FN_4O4$. Molecular Weight: 500.53. LC-MS, $[M + H]^+$ = 501.19 (calcd.) 501.17 (found). ^1H NMR (500 MHz, $CDCl_3$) δ 7.69 (d, *J* = 8.4 Hz, 2H), 7.52 (d, *J* = 8.4, 1.9 Hz, H), 7.43 (d, *J* = 8.2 Hz, 2H), 7.38 (s, 2H), 7.03 (t, 2H), 5.19 (s, 2H), 3.66 (s, 2H), 2.46 (s, 3H), 1.66 (q, *J* = 4.2 Hz, 2H), 1.23 (q, *J* =4.2 Hz, 2H). Purity testing by HPLC (Acquisition method 65%-95% Acetonitrile 20 minutes) t_R = 14.5 minutes. Purity=98%.

Synthesis of 1-(4'-(5-((((4-fluorophenyl) carbamoyl) oxy) methyl)-4-methyl-1H-1,2,3-triazol-1-yl)-[1,1'-biphenyl]-4-yl) cyclopropane-1-carboxylic acid (L12y)

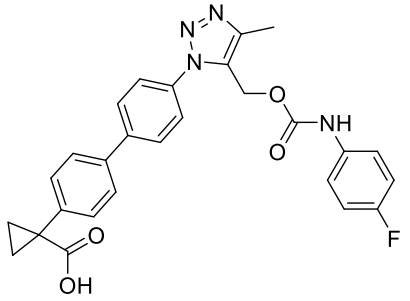

Compound L11y (57 mg, 0.0325 mmol) was dissolved in 2 mL of a prepared 1:3 mixture of H_2O: THF. Lithium hydroxide pellets (LiOH) (20 mg, 0.709 mmol) were added to the solution, and the solution was stirred for overnight. The mixture was partitioned between EtOAc and brine, and the organic phase was separated, dried over Na_2SO_4, filtered, and concentrated. The residue was dissolved in a mixture of HPLC-grade acetonitrile (ACN) with 0.1% formic acid. The crude was purified by ACN/Water (65% / 35%) in prep-HPLC to provide the final compound L12y (13 mg, 4% of yield). Chemical Formula: $C_{27}H_{23}FN_4O_4$. Molecular Weight: 486.50. LC-MS, $[M + H]^+$ = 487.18 (calcd.) 487.20 (found). ^{1}H NMR (500 MHz, DMSO) δ 12.36 (s, 1H), 9.76 (s, 1H), 7.83 (d, *J* = 8.4 Hz, 2H), 7.63 (dd, 4H), 7.38 (d, *J* = 8.1 Hz, 4H), 7.04 (t, *J* = 8.7 Hz, 2H), 5.18 (s, 2H), 2.35 (s, 3H), 1.40 (s, 2H), 1.09 (s, 2H). Purity testing by HPLC (Acquisition method 75%-95% Acetonitrile 20 minutes) t_R = 11.1 minutes. Purity=98%.

Synthesis of side product - 1-(4-Bromophenyl) cyclopropane-1-carbonitrile (L11)

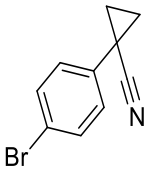

NaOH (12.35 g, 308.75 mmol) was added to water (6 mL) in a 250 mL RBF with a stir bar and was sonicated to form a solution. This was followed by addition of toluene (50 mL), then 4-bromophenylacetonitrile (6.00 g, 30.60 mmol) and TBAB (0.51 g, 1.58 mmol). After mixing, 1,2-dibromoethane (4 mL, 46.26 mmol) was added dropwise over 30 minutes. The reaction was left to stir closed to room temperature for 14 hrs. After this, the mixture was extracted with ether (30 mL) and concentrated to form a red oil. The crude product was diluted with DCM and absorbed onto silica gel for subsequent purification through flash column chromatography (eluent gradient, 5% EtOAc in hexanes) to yield L11 as an orange/red crystal (5.22 g, 70% yield). Chemical Formula: $C_{10}H_8BrN$. Molecular Weight: 222.08 ^{1}H NMR (500 MHz, $CDCl_3$) δ 7.47 (d, 2H), 7.18 – 7.15 (d, 2H), 1.74 (dd, *J* = 5.3 Hz, 2H), 1.38 (dd, *J* = 5.3 Hz, 2H).

Synthesis of Ethyl 1-(4-bromophenyl) cyclopropane-1-carboxylate (L12)

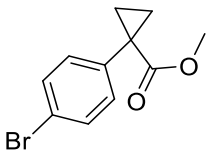

1-(4-Bromophenyl) cyclopropane-1-carbonitrile L11 (3.05 g, 13.73 mmol) and NaOH (2.31 g, 57.75 mmol) are mixed into ethylene glycol (43 mL) in a 250 mL RBF with a magnetic stir

bar. The reaction was heated to 180˚C and mixed for 5 hrs. The mixture was poured over water and acidified with concentrated HCl to yield a brown precipitate. The precipitate was gravity filtered over 2 hrs, being initially rinsed with HCl acidified water. The precipitate was dried under high vacuum. The crude material was added to methanol (30 mL) with sulphuric acid (0.41 mL) in a 100 mL RBF with a magnetic stir bar. The reaction was heated to 70 ˚C and stirred overnight. The reaction mixture was then extracted with EtOAc (25 mL), and the organic layer was washed with water followed by brine. The organic layer was dried over Na_2SO_4 and vacuum filtered, then concentrated to yield L12 as a dark golden-brown oil (1.00g, 83% yield). Chemical Formula: $C_{11}H_{11}BrO_2$. Molecular Weight: 255.11. ^{1}H NMR (500 MHz, $CDCl_3$) δ 7.44 – 7.42 (d, 2H), 7.22 – 7.20 (d, 2H), 3.62 (s, 2H), 1.61 (dd, *J* = 4.0 Hz, 2H), 1.16 (dd, *J* = 4.0 Hz, 2H).

Synthesis of Ethyl 1-(4-(4,4,5,5-tetramethyl-1,3,2-dioxaborolan-2 yl) phenyl) cyclopropane-1-carboxylate (L13)

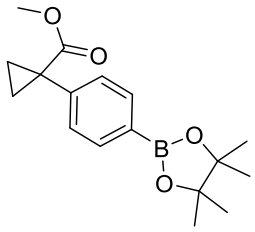

Ethyl 1-(4-bromophenyl) cyclopropane-1-carboxylate (L12) (2.51 g, 9.33 mmol), KOAc (1.85 g, 18.85 mmol), bis(pinacolato)diboron (2.58 g, 10.16 mmol) and Pd(dppf)Cl2 (0.32 g, 0.44 mmol) were combined in anhydrous dioxane (21 mL) in a 150 mL two-neck RBF with a magnetic stir bar. A condenser was attached to the RBF and the vessel was sealed at all openings with septa. The reaction mixture was bubbled with the contents of an Argon (Ar) filled balloon, delivered through a needle and vented with a different needle. The vessel was then flushed with Ar three times. The reaction was heated to 80˚C under Ar protection overnight. The reaction mixture was filtered using a diatomaceous earth (Celite) filter aid to remove the Pd(dppf)Cl_2. The filtrate was partitioned between EtOAc, and water and the organic layer was isolated and washed with brine, then concentrated down. The crude product was then dissolved in DCM and absorbed onto silica gel for subsequent purification through flash column chromatography (eluent gradient, 3-5% EtOAc in hexanes). The product was concentrated in the rotovap and dried under high vacuum to yield L13 as a white crystal (1.8 g, 61% yield). Chemical Formula: $C_{17}H_{23}BO_4$. Molecular Weight: 302.18. LC-MS, $[M + H]^+$ = 303.18 (calcd.) 303.32 (found). ^{1}H NMR (500 MHz, $CDCl_3$) δ 7.70 (d, *J* = 8.1 Hz, 2H), 7.28

(d, 2H), 3.55 (s, J = 3.1 Hz, 3H), 1.53 (dd, J = 4.0 Hz, 2H), 1.26 (s, 12H), 1.12 (dd, J = 4.0 Hz, 2H).

Synthesis of compound - Methyl 1-(4'-(5-(((4-fluorobenzyl) oxy) methyl)-4-methyl-1H-1,2,3-triazol-1-yl)-[1,1'-biphenyl]-4-yl) cyclopropane-1-carboxylate (L14)

In a 100 mL round-bottom flask (RBF) with a stir bar, PPh_3 (15 mg, 0.2 mmol) was added to a solution of L7 (58 mg, 0.16 mmol) and benzyl alcohol (L23a) (55 mg, 0.32 mmol) in THF (8.0 mL). The mixture was cooled in an ice-water bath, then treated slowly with DEAD (0.5 mL, 2.1 mmol). The mixture was allowed to reach room temperature while stirring overnight. The reaction mixture was monitored with HPLC-MS every 3 hrs. The desired compound, L14, didn't appear; however, the undesired compound, **L14'**, was found. Compound **L14'** - Chemical Formula: $C_{43}H_{42}N_6O_5$. Molecular Weight: 722.85. LC-MS, $[M + H]^+$ = 723.33 (calcd.) 723.34 (found).

3.6.3 Experimental procedure and results for the second series compounds

Synthesis of N-(4-bromophenyl)-2-chloro-5-nitropyrimidin-4-amine (L17)

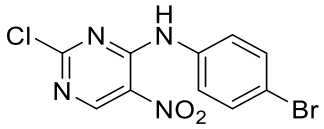

A 0ºC solution of 4-bromoaniline (1893 mg, 11 mmol) in 1,4-dioxane (30 mL) was prepared using an ice bath. To this solution was slowly added 2,4-dichloro-5-nitropyrimidine (1940 mg, 10 mmol), shortly followed by the slow addition of N, N-diisopropylethylamine (1422 mg, 11 mmol) via syringe. The reaction mixture was allowed to warm to room temperature and then stirred for 1 hr. The reaction mixture was diluted with ethyl acetate and extracted with brine. The separated organic phase was dried over sodium sulfate, filtered, and evaporated. The residue was adsorbed to silica and purified using flash silica gel column chromatography (eluent gradient, 10-20% EtOAc in hexanes) to afford Compound L17 (2610 mg, yield: 81%). Chemical Formula: $C_{10}H_6BrClN_4O_2$. Molecular Weight: 329.54. ^{1}H NMR (500 MHz, $CDCl_3$) δ 9.20 (s, 1H), 7.58 (d, J = 8.8 Hz, 2H), 7.53 (d, J = 8.9 Hz, 2H).

Synthesis of N4-94-bromophenyl)-2-chloropyrimidine-4,5-diamine (L18)

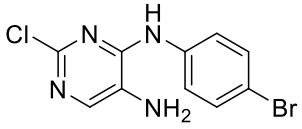

Compound L17 (2610 mg, 8.03 mmol) was dissolved in a 1:2 mixture of EtOH:EtOAc (60 mL) and the reflux condenser was set up. $SnCl_2 \bullet 2H_2O$ (5151 mg, 22.83 mmol) was weighed and slowly added to the stirring flask, and the reaction was heated to 70ºC. The reaction was stirred for 3 hrs. After cooling to room temperature, a saturated solution of sodium carbonate was prepared and added to the reaction mixture. The basified solution was filtered through a pad of Celite, washed with EtOAc, dried over sodium sulfate, and evaporated. The residue was adsorbed to silica and purified using flash silica gel column chromatography (eluent gradient, 30-50% EtOAc in hexanes) to afford Compound L18 (1511 mg, 66% of yield). Chemical Formula: $C_{10}H_8BrClN_4$. Molecular Weight: 299.56. ^{1}H NMR (500 MHz, $CDCl_3$) δ 7.87 (s, 1H), 7.52 (d, *J* = 8.8 Hz, 2H), 7.49 (d, *J* = 8.9 Hz, 2H).

Synthesis of 3-(4-bromophenyl)-5-chloro-3H- [1,2,3] triazolo[4,5-d] pyrimidine (L19)

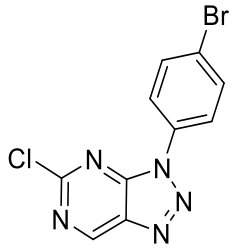

To Compound L18 (1630 mg, 5.41 mmol) was added acetonitrile (25 mL), and a reflux condenser was set up. The solution was heated to 70ºC and isobutyl nitrite (L18') was slowly added via syringe. The reaction was allowed to continue for 16 hrs and then slowly cooled to room temperature. EtOAc (50 mL) was added to the room temperature solution, after which it was further cooled to -20ºC. Orange-brown crystals formed and were collected by filtration and washed with cold EtOAc and cold hexane. This recrystallization process was repeated a total of three times. The collected crystals were desiccated to give Compound L19 (1401 mg, yield: 83%). Chemical Formula: $C_{10}H_5BrClN_5$. Molecular Weight: 310.54 ^{1}H NMR (500 MHz, $CDCl_3$) δ 9.49 (s, 1H), 8.16 (d, *J* = 8.5 Hz, 2H), 7.77 (d, *J* = 8.5 Hz, 2H).

Synthesis of Compounds L20a-L22a

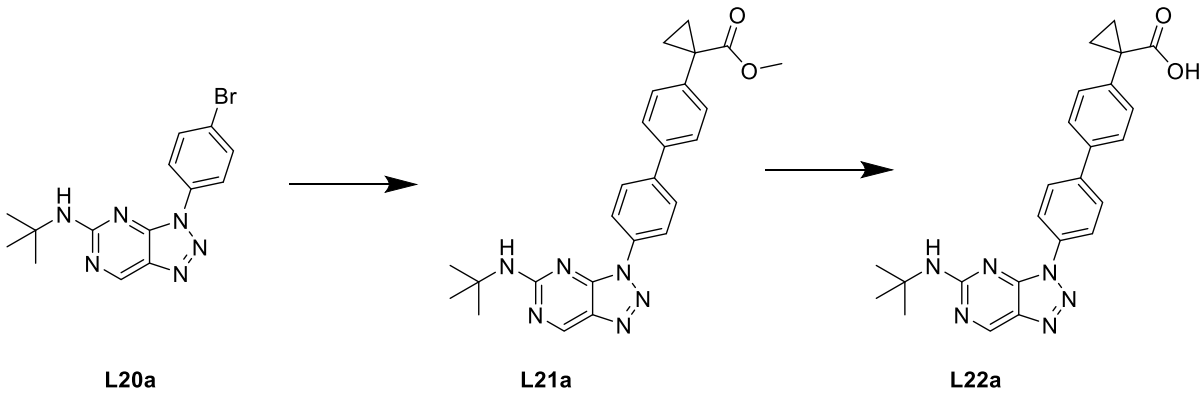

Synthesis of Compound - 3-(4-bromophenyl)-N-(tert-butyl)-3H- [1,2,3] triazolo[4,5-d] pyrimidin-5-amine (L20a)

Compound L19 (127 mg, 0.40 mmol) was dissolved in 1,4-dioxane (5 mL), and to this solution was added 2-methylpropan-2-amine (55 mg, 0.40 mmol) and N, N-diisopropylethylamine (57 mg, 0.44 mmol) via syringe in short succession. The reaction was stirred for 16 hrs and then diluted with EtOAc (30 mL). A series of brine extractions were performed, and the separated organic layer was dried over sodium sulfate, washed with EtOAc, and filtered. The filtrate was concentrated and desiccated. The dried residue was adsorbed to silica and purified using flash silica gel column chromatography (eluent gradient, 10-15% EtOAc in hexanes) to afford Compound L20a. Chemical Formula: $C_{14}H_{15}BrN_6$. Molecular Weight: 347.22. ^{1}H NMR (500 MHz, $CDCl_3$) δ 9.06 (s, 1H), 8.18 (d, *J* = 8.4 Hz, 2H), 7.70 (d, *J* = 8.4 Hz, 2H), 5.74 (s, 1H), 1.53 (s, 9H).

Synthesis of Compound - Methyl 1-(4'-(5-(tert-butylamino)-3H- [1,2,3] triazolo[4,5-d] pyrimidin-3-yl)-[1,1'-biphenyl]-4-yl) cyclopropane-1-carboxylate (L21a)

Compound L20a (101 mg, 0.24 mmol) was dissolved in 8 mL of a 1:3 mixture of H2O:1,4-dioxane and the reflux condenser was prepared. The solution was heated to 80ºC, and Na_2CO_3 (54 mg, 0.515 mmol) was added to the solution. Compound L13 (99 mg, 0.31 mmol) was added to the solution, quickly followed by the addition of $Pd(dppf)Cl_2$ (18 mg, 10 mol%). The solution was bubbled with argon and then stirred for 10 hrs. The mixture was cooled and then filtered through diatomaceous earth and partitioned between EtOAc and brine. The organic phase was separated, dried over Na_2SO_4, filtered, and concentrated. The dried residue was adsorbed to silica and purified using flash silica gel column chromatography (eluent gradient, 5-10% EtOAc in hexanes) to afford Compound L21a. Chemical Formula: $C_{25}H_{26}N_6O_2$.

Molecular Weight: 442.52. LC-MS, $[M + H]^+$ = 443.22 (calcd.) 443.32 (found). ^{1}H NMR (500 MHz, $CDCl_3$) δ 9.08 (s, 1H), 8.33 (d, *J* = 8.4 Hz, 2H), 7.79 (d, *J* = 8.4 Hz, 2H), 7.62 (d, *J* = 7.9 Hz, 2H), 7.46 (d, *J* = 7.9 Hz, 2H), 5.72 (s, 1H), 3.67 (s, 3H), 1.66 (q, 2H), 1.55 (s, 9H), 1.25 (q, 2H).

Compounds - 1-(4'-(5-(tert-butylamino)-3H- [1,2,3] triazolo[4,5-d] pyrimidin-3-yl)-[1,1'-biphenyl]-4-yl) cyclopropane-1-carboxylic acid (L22a)

Compound 21a (25 mg, 0.05 mmol) was dissolved in 2 mL of a prepared 1:3 mixture of H_2O: THF. Lithium hydroxide pellets (LiOH) (21 mg, 0.72 mmol) were added to the solution, and the solution was stirred overnight. The mixture was partitioned between EtOAc and brine, and the organic phase was separated, dried over Na_2SO_4, filtered, and concentrated. The crude product was purified through flash column chromatography (eluent gradient, 30% EtOAc in hexanes) to provide the final compound L22a. A white solid product was obtained in 31% yield (26 mg). Chemical Formula: $C_{24}H_{24}N_6O_2$. Molecular Weight: 428.50. LC-MS, $[M + H]^+$ = 429.20 (calcd.) 429.39 (found). ^{1}H NMR (500 MHz, DMSO) δ 9.32 (s, 1H), 8.31 (d, *J* = 8.3 Hz, 2H), 8.00 (d, *J* = 7.8 Hz, 2H), 7.76 (d, *J* = 7.8 Hz, 2H), 7.50 (d, *J* = 8.3 Hz, 2H), 1.53 (s, 9H), 1.36 – 1.32 (m, 2H), 0.88 (m, 2H). Purity testing by HPLC (Acquisition method 65%-95% Acetonitrile 20 minutes) t_R = 10.9 minutes. Purity=98%.

Synthesis of Compounds L20b-L22b

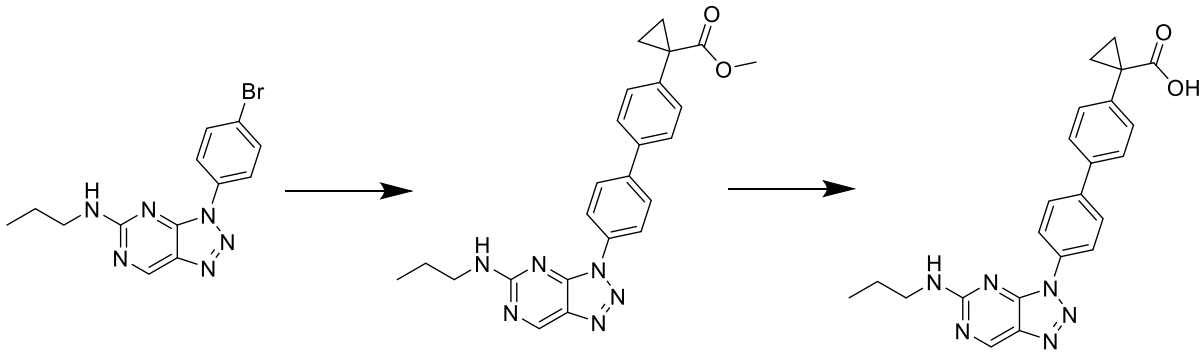

L20b **L21b** **L22b**

Synthesis of Compound - 3-(4-bromophenyl)-N-propyl-3H- [1,2,3] triazolo[4,5-d] pyrimidin-5-amine (L20b)

Compound **L20b** was prepared using the same procedures as L20a, but propan-1-amine was used in place of 2-methylpropan-2-amine. Chemical Formula: $C_{13}H_{13}BrN_6$. Molecular Weight: 333.19. ^{1}H NMR (500 MHz, $CDCl_3$) δ 9.07 (s, 1H), 8.20 (d, *J* = 8.3 Hz, 2H), 7.69 (d, *J* = 8.3

Hz, 2H), 5.80 (s, 1H), 3.49 (d, *J* = 6.5 Hz, 2H), 1.72 (m, *J* = 7.0 Hz, 2H), 1.03 (t, *J* = 7.4 Hz, 3H).

Synthesis of Compound - Methyl 1-(4'-(5-(propylamino)-3H- [1,2,3] triazolo[4,5-d] pyrimidin-3-yl)-[1,1'-biphenyl]-4-yl) cyclopropane-1-carboxylate (L21b)

L21b was prepared using the same procedures as L21a. Chemical Formula: $C_{24}H_{24}N_6O_2$. Molecular Weight: 428.50. ^{1}H NMR (500 MHz, $CDCl_3$) δ 9.09 (s, 1H), 8.35 (d, *J* = 8.3 Hz, 2H), 7.79 (d, *J* = 8.3 Hz, 2H), 7.61 (d, *J* = 7.8 Hz, 2H), 7.46 (d, *J* = 7.8 Hz, 2H), 5.70 (s, 1H), 3.67 (s, 3H), 3.53 (q, 2H), 1.74 (m, 2H), 1.66 (q, 2H), 1.25 (q, 3H), 1.05 (t, 3H).

Synthesis of Compound - 1-(4'-(5-(propylamino)-3H- [1,2,3] triazolo[4,5-d] pyrimidin-3-yl)-[1,1'-biphenyl]-4-yl) cyclopropane-1-carboxylic acid (L22b)

L22b was prepared using the same procedures as L22a. The crude product was purified through flash column chromatography (eluent gradient, 30% EtOAc in hexanes) to provide the final compound L22a. A white solid product was obtained in 33% yield (28mg). Chemical Formula: $C_{23}H_{22}N_6O_2$. Molecular Weight: 414.47 LC-MS, $[M + H]^+$ = 415.19 (calcd.) 415.39 (found). ^{1}H NMR (500 MHz, DMSO) δ 12.38 (s, 1H), 9.30 (s, 1H), 8.29 (d, *J* = 8.3 Hz, 1H), 8.26 – 8.21 (m, 1H), 7.94 (d, *J* = 7.8 Hz, 2H), 7.70 (d, *J* = 7.8 Hz, 2H), 7.46 (d, *J* = 8.3 Hz, 2H), 3.38 – 3.34 (q, 2H), 1.50 (q, *J* = 6.3, 3.8 Hz, 2H), 1.24 (t, 2H), 1.20 (q, *J* = 6.3, 3.7 Hz, 2H), 0.96 (t, *J* = 7.3 Hz, 3H). Purity testing by HPLC (Acquisition method 75%-95% Acetonitrile 20 minutes) t_R = 8.5 minutes. Purity=96%.

Synthesis of Compounds L20c-L22c

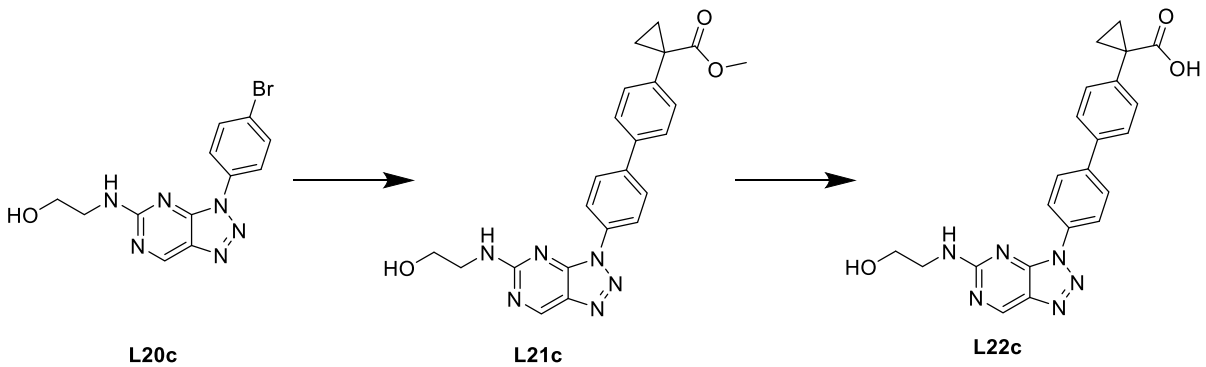

L20c L21c L22c

Synthesis of Compound - 2-((3-(4-bromophenyl)-3H- [1,2,3] triazolo[4,5-d] pyrimidin-5-yl) amino) ethan-1-ol (L20c)

Compound **L20c** was prepared using the same procedures as L20a, but 2-aminoethan-1-ol was used in place of 2-methylpropan-2-amine. Chemical Formula: $C_{12}H_{11}BrN_6O$. Molecular Weight: 335.17. ^{1}H NMR (500 MHz, $CDCl_3$) δ 9.12 (s, 1H), 8.13 (d, *J* = 8.3 Hz, 2H), 7.70 (d, *J* = 8.3 Hz, 2H), 6.05 (s, 1H), 3.92 (d, *J* = 5.0 Hz, 2H), 3.74 (d, *J* = 5.0 Hz, 2H).

Synthesis of Compound - Methyl 1-(4'-(5-((2-hydroxyethyl) amino)-3H- [1,2,3] triazolo[4,5-d] pyrimidin-3-yl)-[1,1'-biphenyl]-4-yl) cyclopropane-1-carboxylate (L21c)

L21c was prepared using the same procedures as L21a. Chemical Formula: $C_{23}H_{22}N_6O_3$. Molecular Weight: 430.47. ^{1}H NMR (500 MHz, $CDCl_3$) δ 9.13 (s, 1H), 8.26 (d, *J* = 8.2 Hz, 2H), 7.79 (d, *J* = 8.2 Hz, 2H), 7.60 (d, *J* = 7.7 Hz, 2H), 7.46 (d, *J* = 7.7 Hz, 2H), 6.13 (s, 1H), 3.93 (q, 2H), 3.76 (q, 2H), 3.67 (s, 3H), 1.66 (q, 2H), 1.26 (q, 2H).

Synthesis of Compound **L22c** - 1-(4'-(5-((2-hydroxyethyl) amino)-3H- [1,2,3] triazolo[4,5-d] pyrimidin-3-yl)-[1,1'-biphenyl]-4-yl) cyclopropane-1-carboxylic acid

L22c was prepared using the same procedures as L22a. The crude product was purified through flash column chromatography (eluent gradient, 30% EtOAc in hexanes) to provide the final compound L22a. A white solid product was obtained in 35% yield (29mg). The product needs further purification. Chemical Formula: $C_{22}H_{20}N_6O_3$. Molecular Weight: 416.44. LC-MS, $[M + H]^+$ = 417.17 (calcd.) 417.23 (found). ^{1}H NMR (500 MHz, DMSO) δ 9.28 (s, 1H), 8.27 (d, *J* = 7.7 2H), 8.09 (s, 1H), 7.95 (d, *J* = 8.0 Hz, 2H), 7.70 (d, *J* = 7.7 Hz, 2H), 7.45 (d, *J* = 8.0 Hz, 2H), 3.66 – 3.63 (t, 2H), 3.51 – 3.48 (t, 2H), 1.48 (q, *J* = 2.4 Hz, 2H), 1.19 (q, *J* = 2.4 Hz, 2H).

Synthesis of Compounds L20d

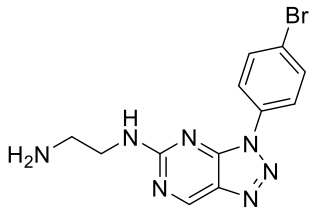

Synthesis of Compound - N1-(3-(4-bromophenyl)-3H- [1,2,3] triazolo[4,5-d] pyrimidin-5-yl) ethane-1,2-diamine (L20d)

Compounds **L20d** was prepared using the same procedures as L20a, but ethane-1,2-diamine was used in place of 2-methylpropan-2-amine. Chemical Formula: $C_{12}H_{12}BrN_7$. Molecular Weight: 334.18. LC-MS, $[M + H]^+$ = 336.04 (calcd.) 336.07 (found).

Synthesis of Compounds L20e-L22e

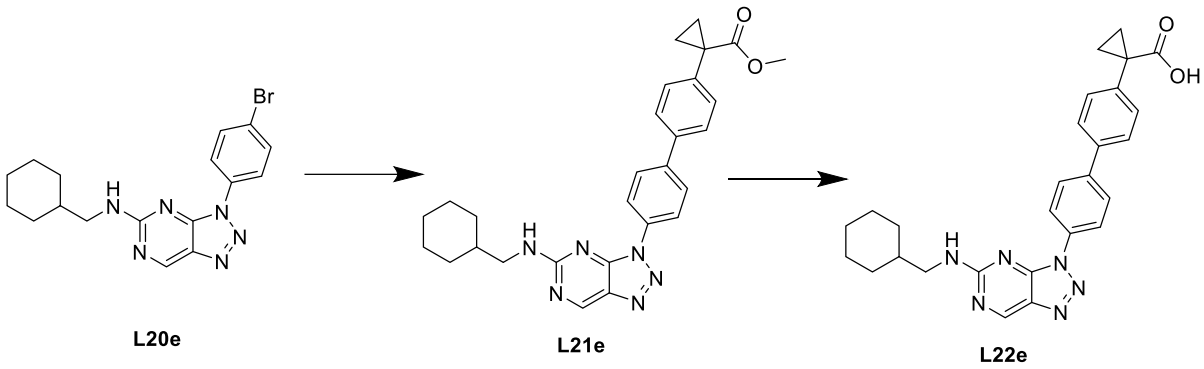

Synthesis of Compound - 3-(4-bromophenyl)-N-(cyclohexylmethyl)-3H-[1,2,3] triazolo[4,5-d]pyrimidin-5-amine (L20e)

L20e was prepared using the same procedures as L20a, but cyclohexylmethanamine was used in place of 2-methylpropan-2-amine. Chemical Formula: $C_{17}H_{19}BrN_6$. Molecular Weight: 387.29. ^{1}H NMR (500 MHz, $CDCl_3$) δ 9.10 (d, 1H), 8.21 (d, *J* = 8.2 Hz, 2H), 7.69 (d, *J* = 8.2 Hz, 2H), 5.84 (s, 1H), 3.37 (s, 2H), 1.81 (m, 7H), 1.29 (d, 1H), 1.20 (m, 1H), 1.06 (m, 2H).

Synthesis of Compound - Methyl 1-(4'-(5-((cyclohexylmethyl)amino)-3H-[1,2,3] triazolo[4,5-d] pyrimidin-3-yl)-[1,1'-biphenyl]-4-yl) cyclopropane-1-carboxylate (L21e)

L21e was prepared using the same procedures as L21a. Chemical Formula: $C_{28}H_{30}N_6O_2$. Molecular Weight: 482.59. LC-MS, $[M + H]^+$ = 483.25 (calcd.) 483.40 (found). ^{1}H NMR (500 MHz, $CDCl_3$) δ 9.07 (s, 1H), 8.35 (d, *J* = 8.4 Hz, 2H), 7.79 (d, *J* = 8.4 Hz, 3H), 7.61 (d, *J* = 7.8 Hz, 2H), 7.46 (d, *J* = 7.8 Hz, 2H), 5.76 (s, 1H), 3.67 (s, 3H), 3.41 (s, 2H), 1.85 (d, *J* = 12.2 Hz, 2H), 1.77 (d, *J* = 12.2 Hz, 2H), 1.67 (m, 4H), 1.27 (m, 5H), 1.06 (d, 2H).

Synthesis of Compound - 1-(4'-(5-((cyclohexylmethyl)amino)-3H- [1,2,3] triazolo[4,5-d] pyrimidin-3-yl)-[1,1'-biphenyl]-4-yl) cyclopropane-1-carboxylic acid (L22e)

L22e was prepared using the same procedures as L22a. The crude was purified by ACN/Water (65% / 35%) in prep-HPLC to provide the final compound. A light-yellow powder product was obtained in 23% yield (21mg). Chemical Formula: $C_{27}H_{28}N_6O_2$. Molecular Weight: 468.56. LC-MS, $[M + H]^+$ = 469.24 (calcd.) 469.41 (found). ^{1}H NMR (500 MHz, DMSO) δ 9.33 (d, 1H), 8.33 (d, *J* = 8.5 Hz, 2H), 7.97 (d, *J* = 7.7 Hz, 2H), 7.74 (d, *J* = 7.7 Hz, 2H), 7.51 (d, *J* = 8.5 Hz, 2H), 3.30 (d, 2H), 1.86 – 1.52 (m, 10H), 1.30 – 1.18 (m, 5H). Purity testing by HPLC (Acquisition method 75%-95% Acetonitrile 20 minutes) t_R = 9.5 minutes. Purity=99%.

Synthesis of Compounds L20f-L22f

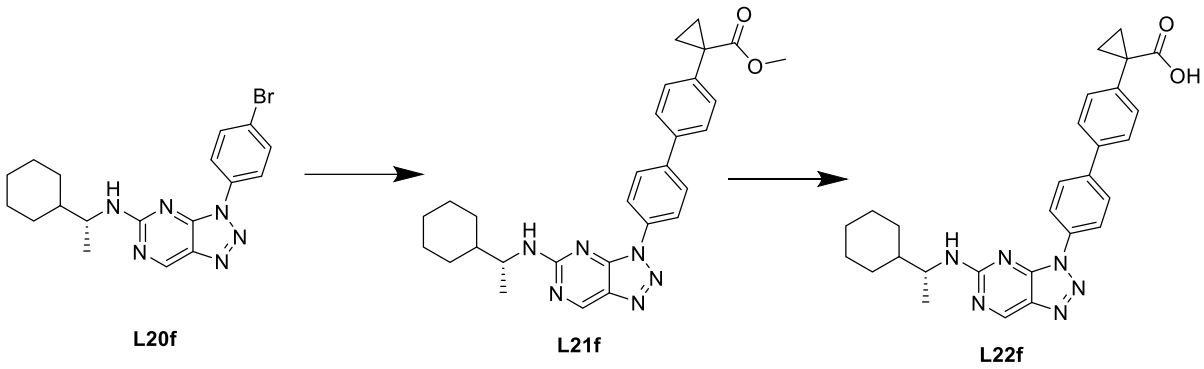

Synthesis of Compound - (R)-3-(4-bromophenyl)-N-(1-cyclohexylethyl)-3H- [1,2,3] triazolo[4,5-d] pyrimidin-5-amine (L20f)

L20f was prepared using the same procedures as L20a, but (R)-1-cyclohexylethan-1-amine was used in place of 2-methylpropan-2-amine. Chemical Formula: $C_{18}H_{21}BrN_6$. Molecular Weight: 401.31. ^{1}H NMR (500 MHz, $CDCl_3$) δ 9.09 (s, 1H), 8.18 (d,*J* = 8.4 Hz, 2H), 7.69 (d, *J* = 8.4 Hz, 2H), 5.66 (s, 1H), 4.04 (s, 1H), 1.81 (m, 4H), 1.64 (m, 3H), 1.24 (d, 3H), 1.12 (m, 4H).

Synthesis of Compound - Methyl (R)-1-(4'-(5-((1-cyclohexylethyl) amino)-3H- [1,2,3] triazolo[4,5-d] pyrimidin-3-yl)-[1,1'-biphenyl]-4-yl) cyclopropane-1-carboxylate (L21f)

L21f was prepared using the same procedures as L21a. Chemical Formula: $C_{29}H_{32}N_6O_2$. Molecular Weight: 496.62. LC-MS, $[M + H]^+$ = 497.27 (calcd.) 497.34 (found). ^{1}H NMR (500 MHz, $CDCl_3$) δ 9.06 (s, 1H), 8.32 (d, *J* = 8.4 Hz, 2H), 7.78 (d, *J* = 8.4 Hz, 2H), 7.61 (d, *J* = 7.7 Hz, 2H), 7.46 (d, *J* = 7.7 Hz, 2H), 5.60 (s, 1H), 4.12 (m, 1H), 3.67 (s, 3H), 1.86 (d, 1H), 1.78 (d, 3H), 1.75 (m, 3H), 1.25 (m, 8H), 1.12 (m, 3H).

Synthesis of Compound - (R)-1-(4'-(5-((1-cyclohexylethyl) amino)-3H- [1,2,3] triazolo[4,5-d] pyrimidin-3-yl)-[1,1'-biphenyl]-4-yl) cyclopropane-1-carboxylic acid (L22f)

L22f was prepared using the same procedures as L22a. The crude was purified by ACN/Water (65% / 35%) in prep-HPLC to provide the final compound. A yellow solid product was obtained in 22% yield (23mg). Chemical Formula: $C_{28}H_{30}N_6O_2$. Molecular Weight: 482.59. LC-MS, $[M + H]^+$ = 483.25 (calcd.) 483.41 (found). ^{1}H NMR (500 MHz, DMSO) δ 9.28 (s, 1H), 8.30 (d, *J* = 7.9 Hz, 2H), 7.96 (d, *J* = 8.4 Hz, 3H), 7.74 (d, *J* = 8.4 Hz, 2H), 7.50 (d, *J* = 7.9 Hz, 2H), 4.02 – 3.95 (m, 2H), 1.84 – 1.73 (m, 4H), 1.56 (m, 4H), 1.26 – 1.20 (m, 7H), 0.89

(d, J = 6.9 Hz, 3H). Purity testing by HPLC (Acquisition method 65%-95% Acetonitrile 20 minutes) t_R = 13.3 minutes. Purity=98%.

Synthesis of Compounds L20g-L22g

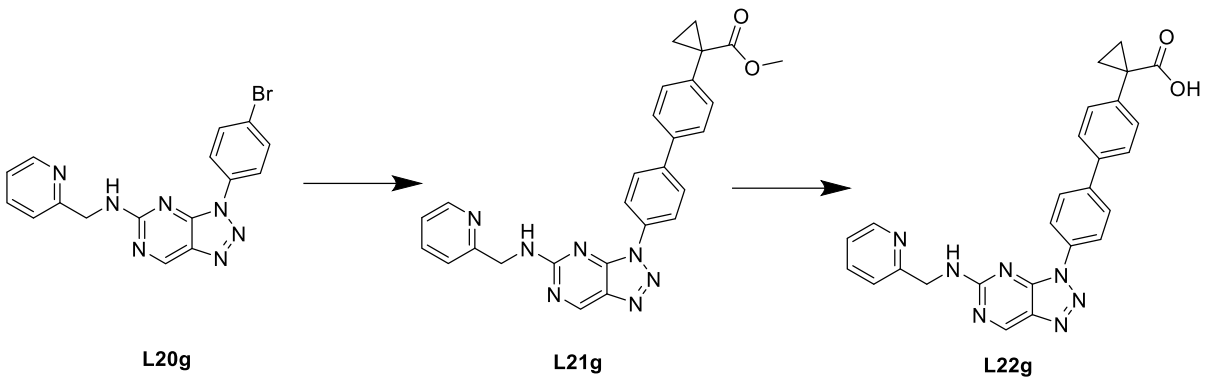

Synthesis of Compound - 3-(4-bromophenyl)-N-(pyridin-2-ylmethyl)-3H- [1,2,3] triazolo[4,5-d] pyrimidin-5-amine (L20g)

L20g was prepared using the same procedures as L20a, but pyridin-2-ylmethanamine was used in place of 2-methylpropan-2-amine. Chemical Formula: $C_{16}H_{12}BrN_7$. Molecular Weight: 382.23. ^{1}H NMR (500 MHz, $CDCl_3$) δ 9.14 (s, 1H), 8.62 (d, 1H), 8.15 (d, 2H), 7.68 (d, 3H), 7.36 (d, 1H), 7.23 (t, 1H), 6.89 (s, 1H), 4.83 (s, 2H).

Synthesis of Compound - Methyl 1-(4'-(5-((pyridin-2-ylmethyl) amino)-3H- [1,2,3] triazolo[4,5-d] pyrimidin-3-yl)-[1,1'-biphenyl]-4-yl) cyclopropane-1-carboxylate (L21g)

L21g was prepared using the same procedures as L21a. Chemical Formula: $C_{27}H_{23}N_7O_2$. Molecular Weight: 477.53. LC-MS, $[M + H]^+$ = 478.20 (calcd.) 478.29 (found).

Synthesis of Compound - 1-(4'-(5-((pyridin-2-ylmethyl) amino)-3H- [1,2,3] triazolo[4,5-d] pyrimidin-3-yl)-[1,1'-biphenyl]-4-yl) cyclopropane-1-carboxylic acid (L22g)

L22g was prepared using the same procedures as L22a. The crude product was purified through flash column chromatography (eluent gradient, 30% EtOAc in hexanes) to provide the final compound. The product needs further purficaiton. Chemical Formula: $C_{26}H_{21}N_7O_2$. Molecular Weight: 463.50. LC-MS, $[M + H]^+$ = 464.18 (calcd.) 464.29 (found).

Synthesis of Compounds L20h-L22h

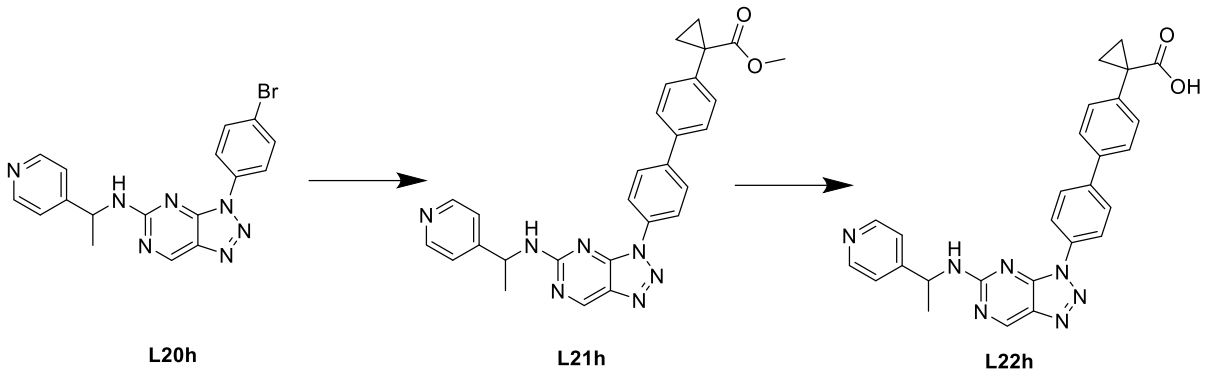

Synthesis of Compound - 3-(4-bromophenyl)-N-(1-(pyridin-4-yl) ethyl)-3H-[1,2,3] triazolo[4,5-d] pyrimidin-5-amine (L20h)

L20h was prepared using the same procedures as L20a, but 1-(pyridin-4-yl) ethan-1-amine was used in place of 2-methylpropan-2-amine. Chemical Formula: $C_{17}H_{14}BrN_7$. Molecular Weight: 396.25. LC-MS, $[M + H]^+$ = 398.06 (calcd.) 398.13 (found). ^{1}H NMR (500 MHz, $CDCl_3$) δ 9.12 (s, 1H), 8.60 (d, *J* = 8.3 Hz, 2H), 7.83 (s, 2H), 7.61 (s, 2H), 7.32 (d, *J* = 8.3 Hz, 2H), 6.04 (s, 1H), 5.02 (s, 1H), 1.63 (d, *J* = 7.0 Hz, 3H).

Synthesis of Compound - Methyl 1-(4'-(5-((1-(pyridin-4-yl) ethyl) amino)-3H- [1,2,3] triazolo[4,5-d] pyrimidin-3-yl)-[1,1'-biphenyl]-4-yl) cyclopropane-1-carboxylate (L21h)

L21h was prepared using the same procedures as L21a. Chemical Formula: $C_{28}H_{25}N_7O_2$. Molecular Weight: 491.56. LC-MS, $[M + H]^+$ = 492.21 (calcd.) 492.30 (found). ^{1}H NMR (500 MHz, $CDCl_3$) δ 9.13 (d, 1H), 8.61 (d, *J* = 8.4 Hz, 2H), 7.98 (d, 1H), 7.68 (m, *J* = 8.0 Hz, 2H), 7.60 (d, *J* = 8.4 Hz, 2H), 7.47 (d, 3H), 7.36 (d, *J* = 8.0 Hz, 2H), 6.12 (s, 1H), 5.06 (s, 1H), 3.68 (s, 3H), 1.67 (m, 2H), 1.64 (d, 3H), 1.27 (m, 2H).

Synthesis of Compound - 1-(4'-(5-((1-(pyridin-4-yl) ethyl) amino)-3H- [1,2,3] triazolo[4,5-d] pyrimidin-3-yl)-[1,1'-biphenyl]-4-yl) cyclopropane-1-carboxylic acid (L22h)

L22h was prepared using the same procedures as L22a. The crude was purified by ACN/Water (65% / 35%) in prep-HPLC to provide the final compound. A white solid product was obtained in 34% yield (30mg). Chemical Formula: $C_{27}H_{23}N_7O_2$. Molecular Weight: 477.53. LC-MS, $[M + H]^+$ = 478.20 (calcd.) 478.29 (found). ^{1}H NMR (500 MHz, DMSO) δ 12.38 (s, 1H), 9.31 (d, 1H), 8.91 (d, 1H), 8.55 (d, *J* = 7.9 Hz, 2H), 8.06 (d, *J* = 8.3 Hz, 2H), 7.89 (d, *J* = 8.3 Hz, 2H), 7.70 (d, *J* = 7.9 Hz, 2H), 7.47 (d, 2H), 7.08 (d, 1H), 6.83 (d, 2H), 5.03 (q, 1H), 1.57 (q, 2H),

1.53 (d, J = 7.2 Hz, 3H), 1.20 (q, 2H). Purity testing by HPLC (Acquisition method 65%-95% Acetonitrile 20 minutes) t_R = 10.7 minutes. Purity=99%.

Synthesis of Compounds L20i-L22i

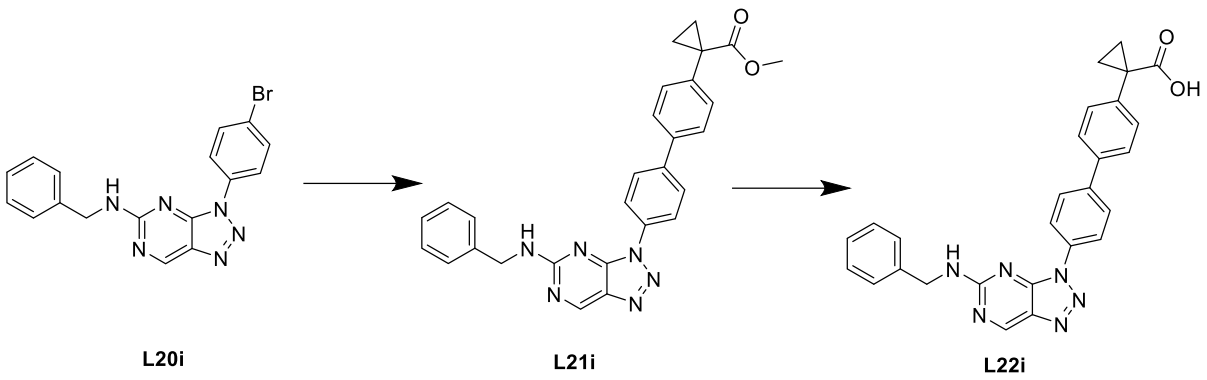

Synthesis of Compound - N-benzyl-3-(4-bromophenyl)-3H-[1,2,3] triazolo[4,5-d]pyrimidin-5-amine (L20i)

L20i was prepared using the same procedures as L20a, but phenylmethanamine was used in place of 2-methylpropan-2-amine. Chemical Formula: $C_{17}H_{13}BrN_6$. Molecular Weight: 381.24. LC-MS, $[M + H]^+$ = 383.04 (calcd.) 383.17 (found). ^{1}H NMR (500 MHz, $CDCl_3$) δ 9.10 (s, 1H), 8.10 (d, J = 8.5 Hz, 2H), 7.66 (d, J = 8.5 Hz, 2H), 7.38 (m, 4H), 7.31 (d, 1H), 6.14 (s, 1H), 4.71 (s, 2H).

Synthesis of Compound - Methyl 1-(4'-(5-(benzylamino)-3H- [1,2,3] triazolo[4,5-d] pyrimidin-3-yl)-[1,1'-biphenyl]-4-yl) cyclopropane-1-carboxylate (L21i)

L21i was prepared using the same procedures as L21a. Chemical Formula: $C_{28}H_{24}N_6O_2$. Molecular Weight: 476.54. LC-MS, $[M + H]^+$ = 477.20 (calcd.) 477.22 (found). ^{1}H NMR (500 MHz, $CDCl_3$) δ 9.12 (s, 1H), 8.26 (d, J = 8.5 Hz, 2H), 7.76 (d, J = 8.5 Hz, 2H), 7.60 (d, J = 8.0 Hz, 2H), 7.46 (d, J = 8.0 Hz, 2H), 7.42 (s, 2H), 7.38 (t, J = 7.4 Hz, 2H), 7.31 (t, J = 7.4 Hz, 1H), 4.75 (s, 2H), 3.67 (s, 3H), 1.66 (q, J = 4.0 Hz, 2H), 1.25 (q, J = 4.0 Hz, 2H).

Synthesis of Compound - 1-(4'-(5-(benzylamino)-3H- [1,2,3] triazolo[4,5-d] pyrimidin-3-yl)-[1,1'-biphenyl]-4-yl) cyclopropane-1-carboxylic acid (L22i)

L22i was prepared using the same procedures as L22a. The crude was purified by ACN/Water (65% / 35%) in prep-HPLC to provide the final compound. A white powder product was obtained in 35% yield (31mg). Chemical Formula: $C_{27}H_{22}N_6O_2$. Molecular Weight: 462.51. LC-MS, $[M + H]^+$ = 463.19 (calcd.) 463.25 (found). ^{1}H NMR (500 MHz, DMSO) δ 9.35 (s,

1H), 8.89 (s, 1H), 8.23 (d, *J* = 8.3 Hz, 2H), 7.96 (d, *J* = 8.3 Hz, 2H), 7.75 (d, *J* = 8.0 Hz, 2H), 7.54 – 7.48 (m, 4H), 7.42 (d, *J* = 8.0 Hz, 2H), 7.29 (t, *J* = 7.1 Hz, 1H), 4.63 (s, 2H), 1.58 (m, 2H), 1.25 (m, 2H). Purity testing by HPLC (Acquisition method 65%-95% Acetonitrile 20 minutes) t_R = 16.4 minutes. Purity=95%.

Synthesis of Compounds L20j-L22j

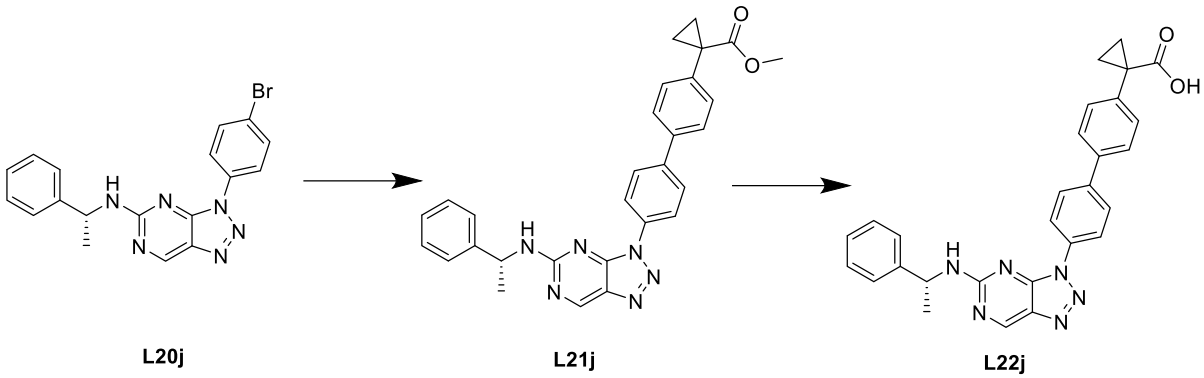

Synthesis of Compound - (R)-3-(4-bromophenyl)-N-(1-phenylethyl)-3H- [1,2,3] triazolo[4,5-d] pyrimidin-5-amine (L20j)

L20j was prepared using the same procedures as L20a, but (R)-1-phenylethan-1-amine was used in place of 2-methylpropan-2-amine. Chemical Formula: $C_{18}H_{15}BrN6$. Molecular Weight: 395.26. LC-MS, $[M + H]^+$ = 397.06 (calcd.) 397.17 (found). ^1H NMR (500 MHz, $CDCl_3$) δ 9.08 (s, 1H), 7.95 (d, *J* = 7.5 Hz, 2H), 7.62 (d, 2H), 7.42 (d, *J* = 7.5 Hz, 2H), 7.37 (t, 2H), 7.28 (d, 1H), 6.08 (s, 1H), 5.06 (s, 1H), 1.63 (d, 3H).

Synthesis of Compound - Methyl (R)-1-(4'-(5-((1-phenylethyl) amino)-3H- [1,2,3] triazolo[4,5-d] pyrimidin-3-yl)-[1,1'-biphenyl]-4-yl) cyclopropane-1-carboxylate (L21j)

L21j was prepared using the same procedures as L21a. Chemical Formula: $C_{29}H_{26}N_6O_2$. Molecular Weight: 490.57. LC-MS, $[M + H]^+$ = 491.22 (calcd.) 491.30 (found). ^1H NMR (500 MHz, $CDCl_3$) δ 9.10 (s, 1H), 8.12 (d, *J* = 7.6 Hz, 2H), 7.72 (d, *J* = 8.1 Hz, 2H), 7.61 (d, *J* = 8.1 Hz, 2H), 7.46 (m, 4H), 7.38 (t, *J* = 7.6 Hz, 2H), 7.28 (d, 1H), 6.04 (s, 1H), 5.13 (s, 1H), 3.68 (s, 3H), 1.67 (q, *J* = 4.0 Hz, 2H), 1.64 (d, *J* = 6.9 Hz, 3H), 1.26 (q, *J* = 4.0 Hz, 2H).

Synthesis of Compound - (R)-1-(4'-(5-((1-phenylethyl) amino)-3H- [1,2,3] triazolo[4,5-d] pyrimidin-3-yl)-[1,1'-biphenyl]-4-yl) cyclopropane-1-carboxylic acid (L22j)

L22j was prepared using the same procedures as L22a. The crude was purified by ACN/Water (65% / 35%) in prep-HPLC to provide the final compound. A white solid product was obtained

in 36% yield (27mg). Chemical Formula: $C_{28}H_{24}N_6O_2$. Molecular Weight: 476.54. LC-MS, $[M + H]^+$ = 477.20 (calcd.) 477.22 (found). ^{1}H NMR (500 MHz, DMSO) δ 9.22 (s, 1H), 8.77 (d, 1H), 8.06 (d, *J* = 8.4 Hz, 2H), 7.83 (d, *J* = 8.4 Hz, 2H), 7.62 (d, 2H), 7.40 (m, 4H), 7.29 (t, *J* = 7.5 Hz, 2H), 7.13 (t, *J* = 7.5 Hz, 1H), 5.00 – 4.95 (m, 1H), 1.45 (d, *J* = 6.9 Hz, 3H), 1.40 (m, 2H), 1.09 (m, 2H). Purity testing by HPLC (Acquisition method 75%-95% Acetonitrile 20 minutes) t_R = 9.7 minutes. Purity=95%.

Synthesis of Compounds L20k-L22k

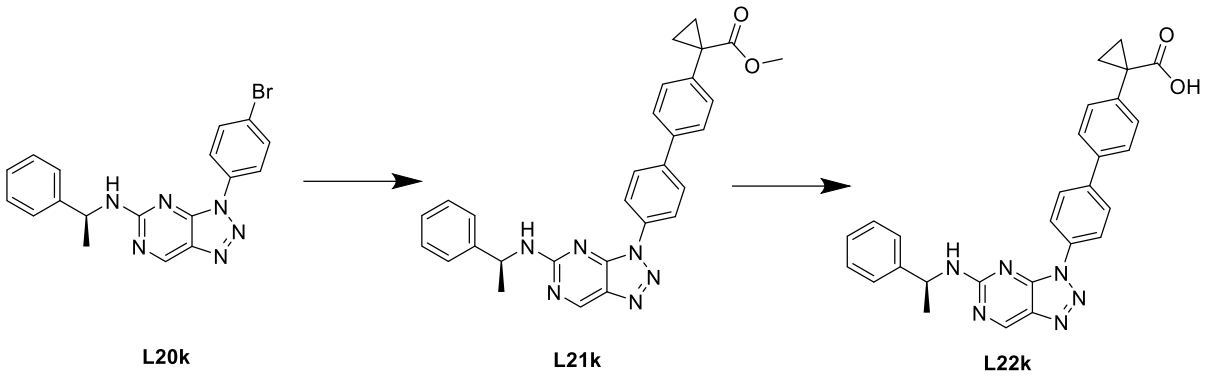

Synthesis of Compound - (S)-3-(4-bromophenyl)-N-(1-phenylethyl)-3H- [1,2,3] triazolo[4,5-d] pyrimidin-5-amine (L20k)

L20k was prepared using the same procedures as L20a, but (S)-1-phenylethan-1-amine was used in place of 2-methylpropan-2-amine. Chemical Formula: $C_{18}H_{15}BrN6$. Molecular Weight: 395.26. LC-MS, $[M + H]^+$ = 397.06 (calcd.) 397.09 (found). ^{1}H NMR (500 MHz, $CDCl_3$) δ 9.09 (s, 1H), 7.95 (d, *J* = 7.5 Hz, 2H), 7.62 (d, 2H), 7.42 (d, *J* = 7.5 Hz, 2H), 7.37 (t, 2H), 7.28 (d, 1H), 6.06 (s, 1H), 5.06 (s, 1H), 1.63 (d, 3H).

Synthesis of Compound - Methyl (S)-1-(4'-(5-((1-phenylethyl) amino)-3H- [1,2,3] triazolo[4,5-d] pyrimidin-3-yl)-[1,1'-biphenyl]-4-yl) cyclopropane-1-carboxylate (L21k)

L21k was prepared using the same procedures as L21a. Chemical Formula: $C_{29}H_{26}N_6O_2$. Molecular Weight: 490.57. LC-MS, $[M + H]^+$ = 491.22 (calcd.) 491.23 (found). ^{1}H NMR (500 MHz, $CDCl_3$) δ 9.10 (s, 1H), 8.13 (d, *J* = 7.5 Hz, 2H), 7.72 (d, *J* = 8.1 Hz, 2H), 7.61 (d, *J* = 8.1 Hz, 2H), 7.46 (m, 4H), 7.38 (t, *J* = 7.5 Hz, 2H), 7.28 (t, 1H), 6.03 (s, 1H), 5.12 (s, 1H), 3.68 (s, 3H), 1.67 (q, *J* = 4.1 Hz, 2H), 1.64 (d, *J* = 6.9 Hz, 3H), 1.26 (q, *J* = 4.1 Hz, 2H).

Synthesis of Compound - (S)-1-(4'-(5-((1-phenylethyl) amino)-3H- [1,2,3] triazolo[4,5-d] pyrimidin-3-yl)-[1,1'-biphenyl]-4-yl) cyclopropane-1-carboxylic acid (L22k)

L22k was prepared using the same procedures as L22a. The crude was purified by ACN/Water (65% / 35%) in prep-HPLC to provide the final compound. A grey solid product was obtained in 37% yield (29mg). Chemical Formula: $C_{28}H_{24}N_6O_2$. Molecular Weight: 476.54. LC-MS, $[M + H]^+$ = 477.20 (calcd.) 477.34 (found). ^{1}H NMR (500 MHz, DMSO) δ 9.22 (s, 1H), 8.77 (d, 1H), 8.06 (d, *J* = 8.3 Hz, 2H), 7.83 (d, *J* = 8.3 Hz, 2H), 7.63 (d, *J* = 7.8 Hz, 2H), 7.40 (t, 4H), 7.28 (d, *J* = 7.8 Hz, 2H), 7.13 (t, 1H), 5.01 – 4.95 (m, 1H), 1.45 (d, *J* = 6.9 Hz, 3H), 1.41 (s, 2H), 1.10 (s, 2H). Purity testing by HPLC (Acquisition method 65%-95% Acetonitrile 20 minutes) t_R = 16.1 minutes. Purity=98%.

Synthesis of Compounds L20l-L22l

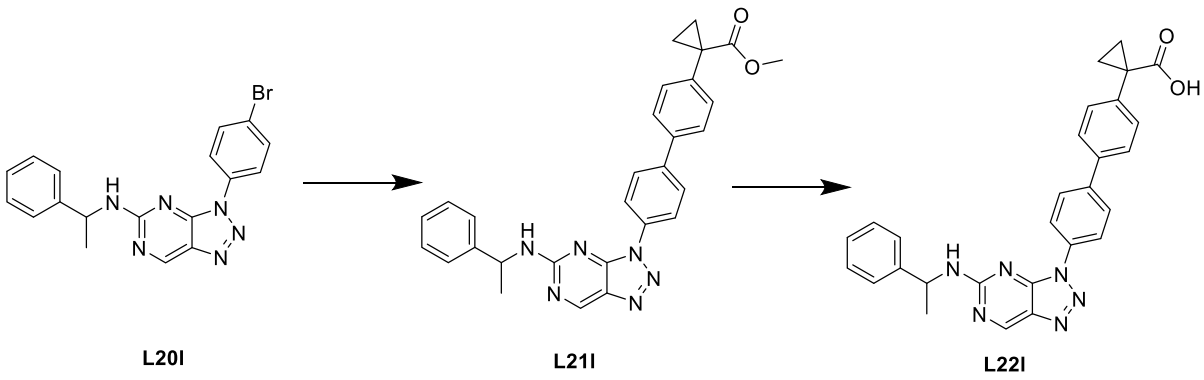

Synthesis of Compound - 3-(4-bromophenyl)-N-(1-phenylethyl)-3H-[1,2,3] triazolo[4,5-d] pyrimidin-5-amine (L20l)

L20l was prepared using the same procedures as L20a, but 1-phenylethan-1-amine was used in place of 2-methylpropan-2-amine. Chemical Formula: $C_{18}H_{15}BrN6$. Molecular Weight: 395.26. ^{1}H NMR (500 MHz, $CDCl_3$) δ 9.09 (s, 1H), 7.95 (d, *J* = 8.0 Hz, 2H), 7.62 (d, *J* = 8.0 Hz, 2H), 7.39 (m, 4H), 7.28 (d, 1H), 6.06 (s, 1H), 5.06 (s, 1H), 1.63 (d, 3H).

Synthesis of Compound - Methyl 1-(4'-(5-((1-phenylethyl) amino)-3H- [1,2,3] triazolo[4,5-d] pyrimidin-3-yl)-[1,1'-biphenyl]-4-yl) cyclopropane-1-carboxylate (L21l)

L21l was prepared using the same procedures as L21a. Chemical Formula: $C_{29}H_{26}N_6O_2$. Molecular Weight: 490.57. LC-MS, $[M + H]^+$ = 491.2 (calcd.) 491.34 (found). ^{1}H NMR (500 MHz, $CDCl_3$) δ 9.10 (s, 1H), 8.13 (s, *J* = 7.5 Hz, 2H), 7.72 (d, *J* = 7.9 Hz, 2H), 7.61 (d, *J* = 7.9 Hz, 2H), 7.46 (m, 4H), 7.38 (t, *J* = 7.5 Hz, 2H), 7.28 (d, *J* = 7.3 Hz, 1H), 6.05 (s, 1H), 5.12 (s, 1H), 3.67 (s, 3H), 1.67 (q, *J* = 4.0 Hz, 2H), 1.64 (d, *J* = 6.9 Hz, 3H), 1.26 (q, *J* = 4.0 Hz, 2H).

Synthesis of Compound - 1-(4'-(5-((1-phenylethyl) amino)-3H- [1,2,3] triazolo[4,5-d] pyrimidin-3-yl)-[1,1'-biphenyl]-4-yl) cyclopropane-1-carboxylic acid (L22l)

L22l was prepared using the same procedures as L22a. The crude product was purified through flash column chromatography (eluent gradient, 20% EtOAc in hexanes) to provide the final compound. The product needs further purification. Chemical Formula: $C_{28}H_{24}N_6O_2$. Molecular Weight: 476.54. LC-MS, $[M + H]^+$ = 477.20 (calcd.) 477.33 (found). ^{1}H NMR (500 MHz, DMSO) δ 12.38 (s, 1H), 9.30 (s, 1H), 8.84 (d, 1H), 8.17 (d, *J* = 8.3 Hz, 2H), 7.91 (d, *J* = 8.3 Hz, 3H), 7.71 (d, *J* = 7.4 Hz, 2H), 7.48 (t, 4H), 7.37 (t, *J* = 7.4 Hz, 2H), 7.21 (t, 1H), 5.09 – 5.00 (m, 1H), 1.53 (d, *J* = 7.2 Hz, 3H), 1.51 (m, *J* = 2.1 Hz, 2H), 1.21 (m, *J* = 2.1 Hz, 2H).

Synthesis of Compounds L20m-L22m

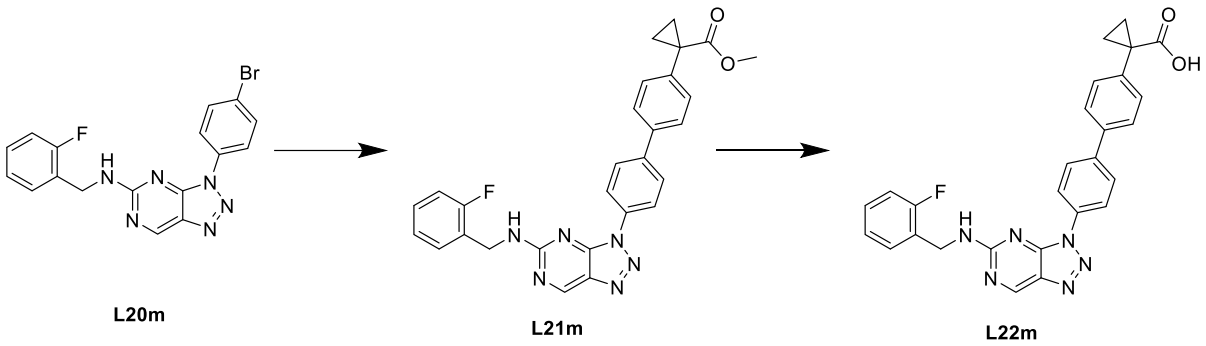

L20m L21m L22m

Synthesis of Compound - 3-(4-bromophenyl)-N-(2-fluorobenzyl)-3H-[1,2,3] triazolo[4,5-d] pyrimidin-5-amine (L20m)

L20m was prepared using the same procedures as L20a, but (2-fluorophenyl) methanamine was used in place of 2-methylpropan-2-amine. Chemical Formula: $C_{17}H_{12}BrFN_6$. Molecular Weight: 399.23. ^{1}H NMR (500 MHz, $CDCl_3$) δ 9.10 (s, 1H), 8.14 (d, *J* = 8.7 Hz, 2H), 7.69 (d, *J* = 8.7 Hz, 2H), 7.42 (t, 1H), 7.28 (d, 1H), 7.10 (d, 2H), 4.77 (s, 2H).

Synthesis of Compound - Methyl 1-(4'-(5-((2-fluorobenzyl) amino)-3H- [1,2,3] triazolo[4,5-d] pyrimidin-3-yl)-[1,1'-biphenyl]-4-yl) cyclopropane-1-carboxylate (L21m)

L21m was prepared using the same procedures as L21a. Chemical Formula: $C_{28}H_{23}FN_6O_2$. Molecular Weight: 494.53. LC-MS, $[M + H]^+$ = 495.19 (calcd.) 495.26 (found). ^{1}H NMR (500 MHz, $CDCl_3$) δ 9.12 (s, 1H), 8.28 (d, *J* = 8.0 Hz, 2H), 7.78 (d, *J* = 8.0 Hz, 2H), 7.62 (d, *J* = 7.6 Hz, 2H), 7.46 (d, 3H), 7.29 (t, 1H), 7.10 (d, *J* = 7.6 Hz, 2H), 6.10 (s, 1H), 4.80 (s, 2H), 3.67 (s, 3H), 1.67 (q, *J* = 4.1 Hz, 2H), 1.24 (q, *J* = 4.1 Hz, 2H).

Synthesis of Compound - 1-(4'-(5-((2-fluorobenzyl) amino)-3H- [1,2,3] triazolo[4,5-d] pyrimidin-3-yl)-[1,1'-biphenyl]-4-yl) cyclopropane-1-carboxylic acid (L22m)

L22m was prepared using the same procedures as L22a. The crude product was purified through flash column chromatography (eluent gradient, 20% EtOAc in hexanes) to provide the final compound. A white solid product was obtained in 39% yield (32mg). Chemical Formula: $C_{27}H_{21}FN_6O_2$. Molecular Weight: 480.50. LC-MS, $[M + H]^+$ = 481.18 (calcd.) 481.25 (found). ^{1}H NMR (500 MHz, DMSO) δ 9.36 (s, 1H), 8.24 (d, *J* = 8.1 Hz, 2H), 7.96 (d, *J* = 8.0 Hz, 2H), 7.75 (d, *J* = 8.1 Hz, 2H), 7.51 (d, *J* = 8.0 Hz, 2H), 7.42 (d, 1H), 7.38 – 7.28 (m, 2H), 7.22 (t, 1H), 4.72 (s, 2H), 1.58 (q, 2H), 1.33 (q, 2H). Purity testing by HPLC (Acquisition method 65%-95% Acetonitrile 20 minutes) t_R = 11.8 minutes. Purity=94%.

Synthesis of Compounds L20n-L22n

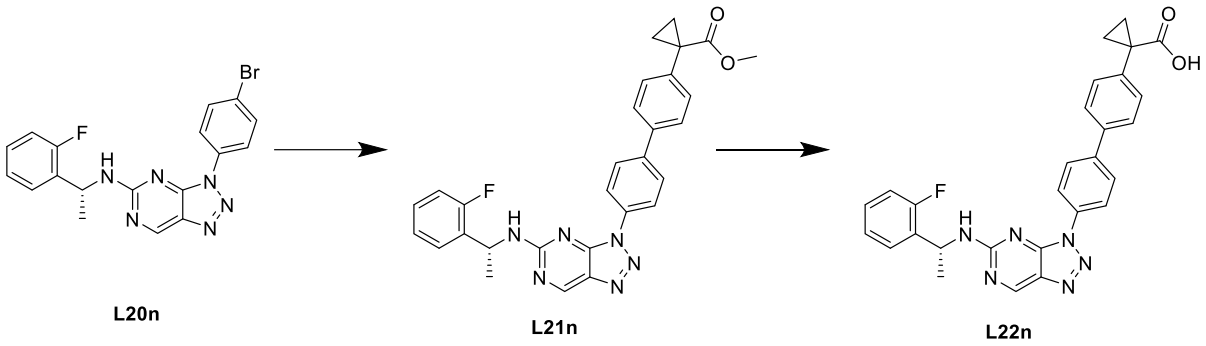

Synthesis of Compound - (R)-3-(4-bromophenyl)-N-(1-(2-fluorophenyl) ethyl)-3H-[1,2,3] triazolo[4,5-d] pyrimidin-5-amine (L20n)

L20n was prepared using the same procedures as L20a, but (R)-1-(2-fluorophenyl) ethan-1-amine was used in place of 2-methylpropan-2-amine. Chemical Formula: $C_{18}H_{14}BrFN_6$. Molecular Weight: 413.25. ^{1}H NMR (500 MHz, $CDCl_3$) δ 9.08 (s, 1H), 8.04 (d, *J* = 8.3 Hz, 2H), 7.64 (d, *J* = 8.3 Hz, 2H), 7.38 (t, 1H), 7.23 (d, 1H), 7.10 (d, 2H), 6.34 (s, 1H), 5.39 (s, 1H), 1.65 (d, 3H).

Synthesis of Compound - Methyl (R)-1-(4'-(5-((1-(2-fluorophenyl) ethyl) amino)-3H-[1,2,3] triazolo[4,5-d] pyrimidin-3-yl)-[1,1'-biphenyl]-4-yl) cyclopropane-1-carboxylate (L21n)

L21n was prepared using the same procedures as L21a. Chemical Formula: $C_{29}H_{25}FN_6O_2$.

Molecular Weight: 508.56. LC-MS, $[M + H]^+$ = 509.21 (calcd.) 509.34 (found). ^{1}H NMR (500 MHz, $CDCl_3$) δ 9.10 (s, 1H), 8.19 (d, *J* = 8.1 Hz, 2H), 7.74 (d, *J* = 8.1 Hz, 2H), 7.62 (d, *J* = 7.9 Hz, 2H), 7.47 (d, *J* = 7.9 Hz, 2H), 7.41 (t, *J* = 7.5 Hz, 1H), 7.22 (m, 1H), 7.10 (t, *J* = 7.5 Hz, 2H), 6.13 (s, 1H), 5.43 (s, 1H), 3.68 (s, 3H), 1.67 (q, 2H), 1.66 (d, 3H), 1.26 (q, 2H).

Synthesis of Compound - (R)-1-(4'-(5-((1-(2-fluorophenyl) ethyl) amino)-3H- [1,2,3] triazolo[4,5-d] pyrimidin-3-yl)-[1,1'-biphenyl]-4-yl) cyclopropane-1-carboxylic acid (L22n)

L22n was prepared using the same procedures as L22a. The crude product was purified through flash column chromatography (eluent gradient, 20% EtOAc in hexanes) to provide the final compound. A white solid product was obtained in 38% yield (30mg). Chemical Formula: $C_{28}H_{23}FN_6O_2$. Molecular Weight: 494.53. LC-MS, $[M + H]^+$ = 495.19 (calcd.) 495.26 (found). ^{1}H NMR (500 MHz, DMSO) δ 12.40 (s, 1H), 9.31 (s, 1H), 8.91 (d, 1H), 8.12 (d, *J* = 8.4 Hz, 2H), 7.85 (d, *J* = 8.4 Hz, 2H), 7.70 (d, *J* = 8.2 Hz, 2H), 7.47 (d, 3H), 7.27 (t, *J* = 8.2Hz, 2H), 7.16 (t, 1H), 5.34 (q, 1H), 1.54 (d, *J* = 6.9 Hz, 3H), 1.52 – 1.50 (q, *J* = 4.5 Hz, 2H), 1.21 (q, *J* = 4.5 Hz, 2H). Purity testing by HPLC (Acquisition method 65%-95% Acetonitrile 20 minutes) t_R = 10.9 minutes. Purity=96%.

Synthesis of Compounds L20o-L22o

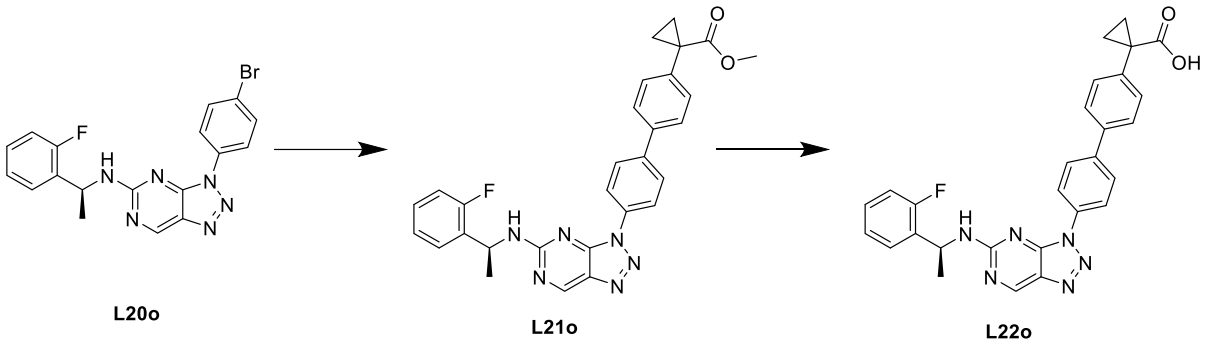

Synthesis of Compound - (S)-3-(4-bromophenyl)-N-(1-(2-fluorophenyl) ethyl)-3H-[1,2,3] triazolo[4,5-d] pyrimidin-5-amine (L20o)

L20o was prepared using the same procedures as L20a, but (S)-1-(2-fluorophenyl) ethan-1-amine was used in place of 2-methylpropan-2-amine. Chemical Formula: $C_{18}H_{14}BrFN_6$. Molecular Weight: 413.25. ^{1}H NMR (500 MHz, $CDCl_3$) δ 9.08 (s, 1H), 8.04 (d, *J* = 7.7 Hz, 2H), 7.64 (d, 2H), 7.38 (t, 1H), 7.23 (d, 1H), 7.10 (d, *J* = 7.7 Hz, 2H), 6.29 (s, 1H), 5.39 (s, 1H), 1.65 (d, 3H).

Synthesis of Compound - Methyl (S)-1-(4'-(5-((1-(2-fluorophenyl) ethyl) amino)-3H-[1,2,3] triazolo[4,5-d] pyrimidin-3-yl)-[1,1'-biphenyl]-4-yl) cyclopropane-1-carboxylate (L21o)

L21o was prepared using the same procedures as L21a. Chemical Formula: $C_{29}H_{25}FN_6O_2$. Molecular Weight: 508.56. LC-MS, $[M + H]^+$ = 509.20 (calcd.) 509.34 (found). ^{1}H NMR (500 MHz, $CDCl_3$) δ 9.10 (s, 1H), 8.19 (d, *J* = 8.2 Hz, 2H), 7.74 (d, *J* = 8.2 Hz, 2H), 7.62 (d, *J* = 7.9 Hz, 2H), 7.47 (d, *J* = 7.9 Hz, 2H), 7.41 (t, *J* = 7.4 Hz, 1H), 7.22 (m, 1H), 7.10 (t, *J* = 7.4 Hz, 2H), 6.12 (s, 1H), 5.43 (s, 1H), 3.68 (s, 3H), 1.68 (q, 2H), 1.66 (d, 3H), 1.26 (q, 2H).

Synthesis of Compound - (S)-1-(4'-(5-((1-(2-fluorophenyl) ethyl) amino)-3H- [1,2,3] triazolo[4,5-d] pyrimidin-3-yl)-[1,1'-biphenyl]-4-yl) cyclopropane-1-carboxylic acid (L22o)

L22o was prepared using the same procedures as L22a. The crude product was purified through flash column chromatography (eluent gradient, 20-30% EtOAc in hexanes) to provide the final compound. A white solid product was obtained in 37% yield (29mg). Chemical Formula: $C_{28}H_{23}FN_6O_2$. Molecular Weight: 494.53. LC-MS, $[M + H]^+$ = 495.19 (calcd.) 495.34 (found). ^{1}H NMR (500 MHz, DMSO) δ 12.41 (s, 1H), 9.31 (s, 1H), 8.91 (d, 1H), 8.12 (d, *J* = 8.4 Hz, 2H), 7.85 (d, *J* = 8.4 Hz, 2H), 7.70 (d, *J* = 7.6 Hz, 2H), 7.47 (d, 3H), 7.27 (t, *J* = 7.6 Hz, 2H), 7.16 (t, 1H), 5.34 (m, 1H), 1.54 (d, *J* = 6.8 Hz, 3H), 1.51 (q, *J* = 2.3 Hz, 2H), 1.21 (q, *J* = 2.3 Hz, 2H). Purity testing by HPLC (Acquisition method 65%-95% Acetonitrile 20 minutes) t_R = 10.9 minutes. Purity=99%.

Synthesis of Compounds L20p-L22p

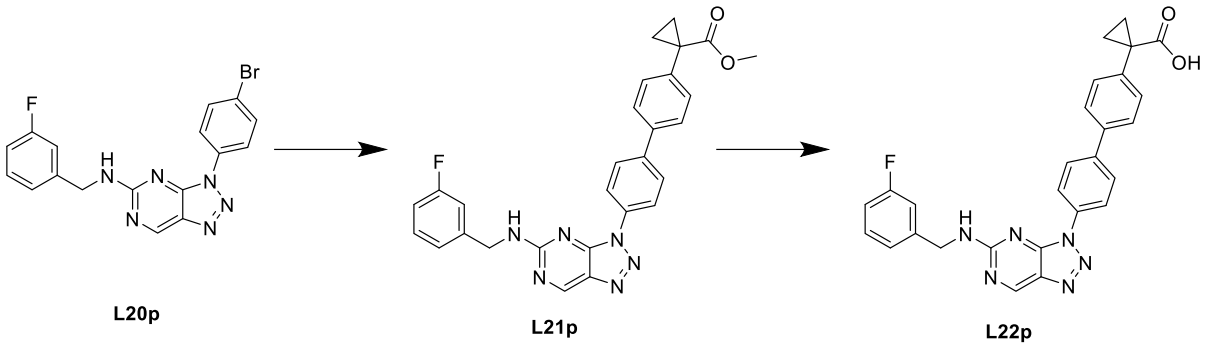

Synthesis of Compound - 3-(4-bromophenyl)-N-(3-fluorobenzyl)-3H-[1,2,3] triazolo[4,5-d] pyrimidin-5-amine (L20p)

L20p was prepared using the same procedures as L20a, but (3-fluorophenyl) methanamine was used in place of 2-methylpropan-2-amine. Chemical Formula: $C_{17}H_{12}BrFN_6$. Molecular Weight: 399.23. ^{1}H NMR (500 MHz, $CDCl_3$) δ 9.12 (s, 1H), 8.06 (d, *J* = 8.7 Hz, 2H), 7.66 (d, *J* = 8.7 Hz, 2H), 7.33 (m, 1H), 7.18 (d, 1H), 7.11 (d, 1H), 7.00 (t, 1H), 6.20 (s, 1H), 4.70 (s, 2H).

Synthesis of Compound - Methyl 1-(4'-(5-((3-fluorobenzyl) amino)-3H- [1,2,3] triazolo[4,5-d] pyrimidin-3-yl)-[1,1'-biphenyl]-4-yl) cyclopropane-1-carboxylate (L21p)

L21p was prepared using the same procedures as L21a. Chemical Formula: $C_{28}H_{23}FN_6O_2$. Molecular Weight: 494.53. LC-MS, $[M + H]^+$ = 495.19 (calcd.) 495.34 (found). ^{1}H NMR (500 MHz, $CDCl_3$) δ 9.14 (s, 1H), 8.21 (d, *J* = 8.5 Hz, 2H), 7.76 (d, *J* = 8.5 Hz, 2H), 7.60 (d, *J* = 8.1 Hz, 2H), 7.46 (d, *J* = 8.1 Hz, 2H), 7.33 (q, *J* = 7.7 Hz, 1H), 7.17 (dd, *J* = 7.6 Hz, 2H), 6.99 (t, *J* = 7.6 Hz, 1H), 6.13 (s, 1H), 4.74 (s, 2H), 3.67 (s, 3H), 1.66 (q, *J* = 4.0 Hz, 2H), 1.25 (q, *J* = 4.0 Hz, 2H).

Synthesis of Compound - 1-(4'-(5-((3-fluorobenzyl) amino)-3H- [1,2,3] triazolo[4,5-d] pyrimidin-3-yl)-[1,1'-biphenyl]-4-yl) cyclopropane-1-carboxylic acid (L22p)

L22p was prepared using the same procedures as L22a. The crude was purified by ACN/Water (65% / 35%) in prep-HPLC to provide the final compound. A light-grey solid product was obtained in 35% yield (26mg). Chemical Formula: $C_{27}H_{21}FN_6O_2$. Molecular Weight: 480.50. LC-MS, $[M + H]^+$ = 481.18 (calcd.) 481.25 (found). ^{1}H NMR (500 MHz, DMSO) δ 9.25 (s, 1H), 8.79 (s, 1H), 8.09 (d, *J* = 8.1 Hz, 2H), 7.82 (d, *J* = 8.1 Hz, 2H), 7.60 (d, *J* = 7.7 Hz, 2H), 7.38 (d, *J* = 7.7 Hz, 2H), 7.35 – 7.31 (m, 1H), 7.23 – 7.17 (m, 2H), 6.99 (t, 1H), 4.52 (d, *J* =

5.5 Hz, 2H), 1.40 (q, *J* = 2.4 Hz, 2H), 1.08 (q, *J* = 2.4 Hz,2H). Purity testing by HPLC (Acquisition method 75%-95% Acetonitrile 20 minutes) t_R = 9.3 minutes. Purity=97%.

Synthesis of Compounds L20q-L22q

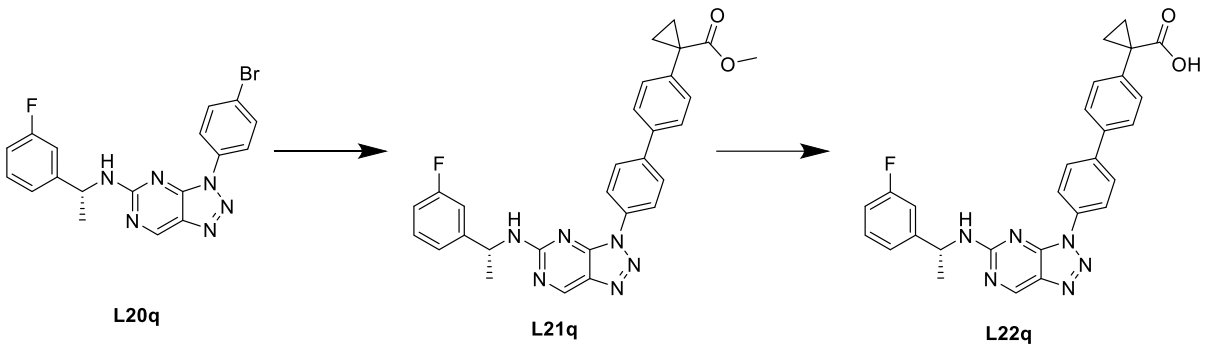

Synthesis of Compound - (R)-3-(4-bromophenyl)-N-(1-(3-fluorophenyl) ethyl)-3H-[1,2,3] triazolo[4,5-d] pyrimidin-5-amine (L20q)

L20q was prepared using the same procedures as L20a, but (R)-1-(3-fluorophenyl) ethan-1-amine was used in place of 2-methylpropan-2-amine. Chemical Formula: $C_{18}H_{14}BrFN_6$. Molecular Weight: 413.25. 1H NMR (500 MHz, CDCl3) δ 9.09 (s, 1H), 7.91 (s, J = 8.2 Hz, 2H), 7.63 (d, J = 8.2 Hz, 2H), 7.34 (d, 1H), 7.20 (d, 1H), 7.13 (d, 1H), 6.96 (t, 1H), 6.24 (s, 1H), 5.02 (s, 1H), 1.62 (d, 3H).

Synthesis of Compound - Methyl (R)-1-(4'-(5-((1-(3-fluorophenyl) ethyl) amino)-3H-[1,2,3] triazolo[4,5-d] pyrimidin-3-yl)-[1,1'-biphenyl]-4-yl) cyclopropane-1-carboxylate (L21q)

L21q was prepared using the same procedures as L21a. Chemical Formula: $C_{29}H_{25}FN_6O_2$.

Molecular Weight: 508.56. ^{1}H NMR (500 MHz, $CDCl_3$) δ 9.11 (s, 1H), 8.08 (s, *J* = 8.2 Hz, 2H), 7.73 (d, *J* = 8.2 Hz, 2H), 7.61 (d, *J* = 7.9 Hz, 2H), 7.47 (d, *J* = 7.9 Hz, 2H), 7.33 (d, 1H), 7.22 (d, 1H), 7.16 (d, 1H), 6.96 (t, 1H), 6.10 (s, 1H), 5.07 (s, 1H), 3.68 (s, 3H), 1.67 (q, *J* = 4.1 Hz, 2H), 1.63 (d, *J* = 6.9 Hz, 3H), 1.26 (q, *J* = 4.1 Hz, 2H).

Synthesis of Compound - (R)-1-(4'-(5-((1-(3-fluorophenyl) ethyl) amino)-3H- [1,2,3] triazolo[4,5-d] pyrimidin-3-yl)-[1,1'-biphenyl]-4-yl) cyclopropane-1-carboxylic acid (L22q)

L22q was prepared using the same procedures as L22a. The crude product was purified through flash column chromatography (eluent gradient, 20-30% EtOAc in hexanes) to provide the final

compound. A light-grey solid product was obtained in 33% yield (24mg). Chemical Formula: $C_{28}H_{23}FN_6O_2$. Molecular Weight: 494.53. LC-MS, $[M + H]^+$ = 495.19 (calcd.) 495.42 (found). ^{1}H NMR (500 MHz, DMSO) δ 12.39 (s, 1H), 9.30 (s, 1H), 8.84 (d, 1H), 8.11 (d, *J* = 8.4 Hz, 2H), 7.87 (d, *J* = 8.4 Hz, 2H), 7.68 (d, *J* = 7.9 Hz, 2H), 7.47 (d, *J* = 7.9 Hz, 2H), 7.44 – 7.39 (m, 1H), 7.31 (d, 2H), 7.03 (t, 1H), 5.05 (m, 1H), 1.53 (d, *J* = 7.1 Hz, 3H), 1.51 (q, *J* = 2.4 Hz, 2H), 1.21 (q, *J* = 2.4 Hz, 2H). Purity testing by HPLC (Acquisition method 65%-95% Acetonitrile 20 minutes) t_R = 10.8 minutes. Purity=97%.

Synthesis of Compounds L20r-L22r

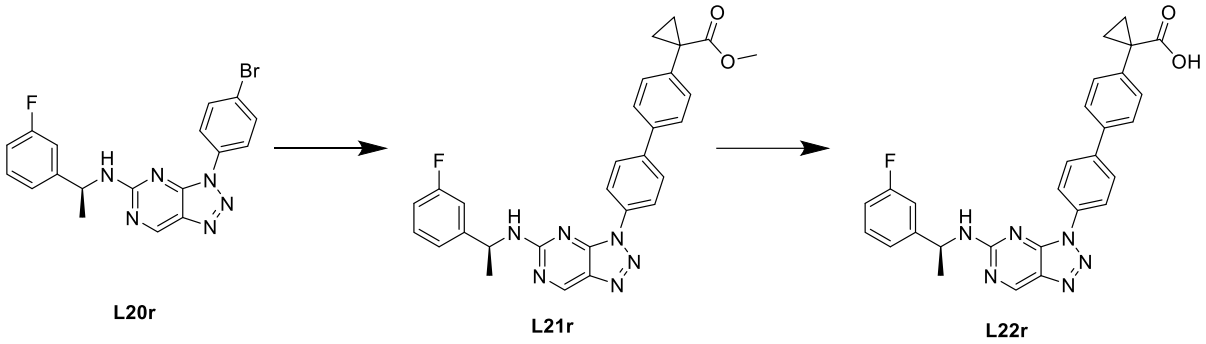

Synthesis of Compounds - (S)-3-(4-bromophenyl)-N-(1-(3-fluorophenyl) ethyl)-3H-[1,2,3] triazolo[4,5-d] pyrimidin-5-amine (L20r)

L20r was prepared using the same procedures as L20a, but (S)-1-(3-fluorophenyl) ethan-1-amine was used in place of 2-methylpropan-2-amine. Chemical Formula: $C_{18}H_{14}BrFN_6$. Molecular Weight: 413.25. ^{1}H NMR (500 MHz, $CDCl_3$) δ 9.09 (s, 1H), 7.92 (d, *J* = 8.2 Hz, 2H), 7.63 (d, *J* = 8.2 Hz, 2H), 7.34 (d, 1H), 7.20 (d, *J* = 7.7 Hz, 1H), 7.13 (d, 1H), 6.96 (t, 1H), 6.17 (s, 1H), 5.02 (s, 1H), 1.62 (d, 3H).

Synthesis of Compound - Methyl (S)-1-(4'-(5-((1-(3-fluorophenyl) ethyl) amino)-3H-[1,2,3] triazolo[4,5-d] pyrimidin-3-yl)-[1,1'-biphenyl]-4-yl) cyclopropane-1-carboxylate (L21r)

L21r was prepared using the same procedures as L21a. Chemical Formula: $C_{29}H_{25}FN_6O_2$.

Molecular Weight: 508.56. ^{1}H NMR (500 MHz, $CDCl_3$) δ 9.11 (s, 1H), 8.08 (s, *J* = 8.2 Hz, 2H), 7.73 (d, *J* = 8.2 Hz, 2H), 7.61 (d, *J* = 8.0 Hz, 2H), 7.47 (d, *J* = 8.0 Hz, 2H), 7.33 (q, 1H), 7.22 (d, 1H), 7.16 (d, 1H), 6.97 (t, 1H), 6.05 (s, 1H), 5.07 (s, 1H), 3.68 (s, 3H), 1.67 (q, *J* = 4.0 Hz, 2H), 1.63 (d, *J* = 6.9 Hz, 3H), 1.26 (q, *J* = 4.0 Hz, 2H).

Synthesis of Compound - (S)-1-(4'-(5-((1-(3-fluorophenyl) ethyl) amino)-3H- [1,2,3] triazolo[4,5-d] pyrimidin-3-yl)-[1,1'-biphenyl]-4-yl) cyclopropane-1-carboxylic acid (L22r)

L22r was prepared using the same procedures as L22a. The crude product was purified through flash column chromatography (eluent gradient, 20-30% EtOAc in hexanes) to provide the final compound. A white solid product was obtained in 40% yield (37mg). Chemical Formula: $C_{28}H_{23}FN_6O_2$. Molecular Weight: 494.53. LC-MS, $[M + H]^+$ = 495.19 (calcd.) 495.34 (found). ^{1}H NMR (500 MHz, DMSO) δ 12.41 (s, 1H), 9.31 (s, 1H), 8.86 (d, 1H), 8.12 (d, *J* = 8.5 Hz, 2H), 7.89 (d, *J* = 8.5 Hz, 2H), 7.69 (d, *J* = 8.1 Hz, 2H), 7.48 (d, *J* = 8.1 Hz, 2H), 7.41 (t, 1H), 7.34 – 7.30 (d, 2H), 7.04 (d, 1H), 5.06 (m, *J* = 6.8 Hz, 1H), 1.53 (d, 3H), 1.50 (q, *J* = 2.6 Hz, 2H), 1.21 (q, *J* = 2.6 Hz, 2H). Purity testing by HPLC (Acquisition method 65%-95% Acetonitrile 20 minutes) t_R = 11.1 minutes. Purity=98%.

Synthesis of Compounds L20s-L22s

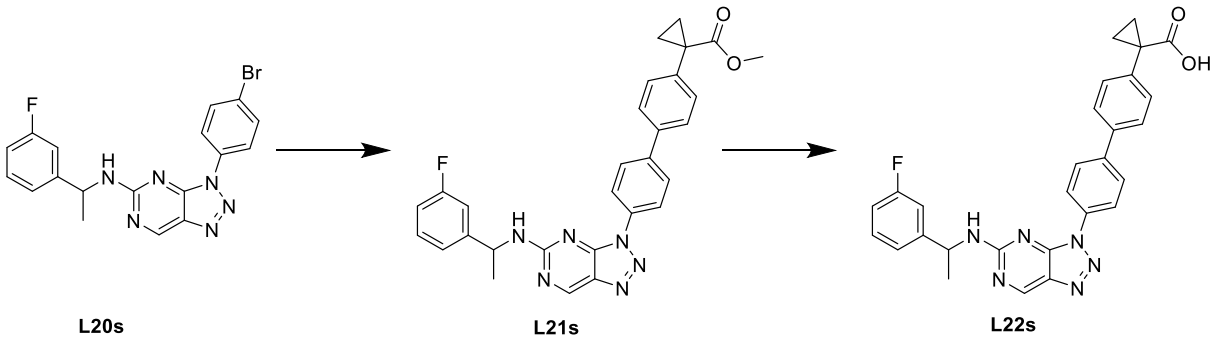

Synthesis of Compound - 3-(4-bromophenyl)-N-(1-(3-fluorophenyl) ethyl)-3H- [1,2,3] triazolo[4,5-d] pyrimidin-5-amine (L20s)

L20s was prepared using the same procedures as L20a, but 1-(3-fluorophenyl) ethan-1-amine was used in place of 2-methylpropan-2-amine. Chemical Formula: $C_{18}H_{14}BrFN_6$. Molecular Weight: 413.25. ^{1}H NMR (500 MHz, $CDCl_3$) δ 9.10 (s, 1H), 7.92 (d, *J* = 7.9 Hz, 2H), 7.63 (d, *J* = 7.9 Hz, 2H), 7.34 (d, 1H), 7.20 (d, 1H), 7.13 (d, 1H), 6.97 (t, 1H), 6.04 (s, 1H), 5.02 (s, 1H), 1.62 (d, 3H).

Synthesis of Compound - Methyl 1-(4'-(5-((1-(3-fluorophenyl) ethyl) amino)-3H- [1,2,3] triazolo[4,5-d] pyrimidin-3-yl)-[1,1'-biphenyl]-4-yl) cyclopropane-1-carboxylate (L21s)

L21s was prepared using the same procedures as L21a. Chemical Formula: $C_{29}H_{25}FN_6O_2$. Molecular Weight: 508.56. LC-MS, $[M + H]^+$ = 509.21 (calcd.) 509.34 (found). ^{1}H NMR (500 MHz, $CDCl_3$) δ 9.12 (s, 1H), 8.07 (d, *J* = 7.9 Hz, 2H), 7.74 (d, *J* = 8.1 Hz, 2H), 7.61 (d, *J* = 8.1 Hz, 2H), 7.47 (d, *J* = 7.9 Hz, 2H), 7.34 (m, 1H), 7.23 (d, 1H), 7.16 (d, 1H), 6.97 (t, 1H), 6.14 (s, 1H), 5.07 (q, 1H), 3.68 (s, 3H), 1.67 (q, *J* = 4.0 Hz, 2H), 1.63 (d, *J* = 6.9 Hz, 3H), 1.28 – 1.25 (q, *J* = 4.0 Hz, 2H).

Synthesis of Compound - 1-(4'-(5-((1-(3-fluorophenyl) ethyl) amino)-3H- [1,2,3] triazolo[4,5-d] pyrimidin-3-yl)-[1,1'-biphenyl]-4-yl) cyclopropane-1-carboxylic acid (L22s)

L22s was prepared using the same procedures as L22a. The crude was purified by ACN/Water (65% / 35%) in prep-HPLC to provide the final compound. A grey solid product was obtained in 26% yield (19mg). Chemical Formula: $C_{28}H_{23}FN_6O_2$. Molecular Weight: 494.53. LC-MS, $[M + H]^+$ = 495.19 (calcd.) 495.20 (found). ^{1}H NMR (500 MHz, DMSO) δ 9.24 (s, 1H), 8.77 (d, 1H), 8.05 (d, *J* = 8.5 Hz, 2H), 7.82 (d, *J* = 8.5 Hz, 2H), 7.61 (d, *J* = 7.6 Hz, 2H), 7.40 (d, *J* = 7.6 Hz, 2H), 7.34 (d, 1H), 7.27 – 7.21 (m, 2H), 6.96 (t, 1H), 4.98 (q, 1H), 1.46 (d, *J* = 6.9 Hz, 3H), 1.41 (q, 2H), 1.10 (q, 2H). Purity testing by HPLC (Acquisition method 65%-95% Acetonitrile 20 minutes) t_R = 15.6 minutes. Purity=97%.

Synthesis of Compounds L20t-L22t

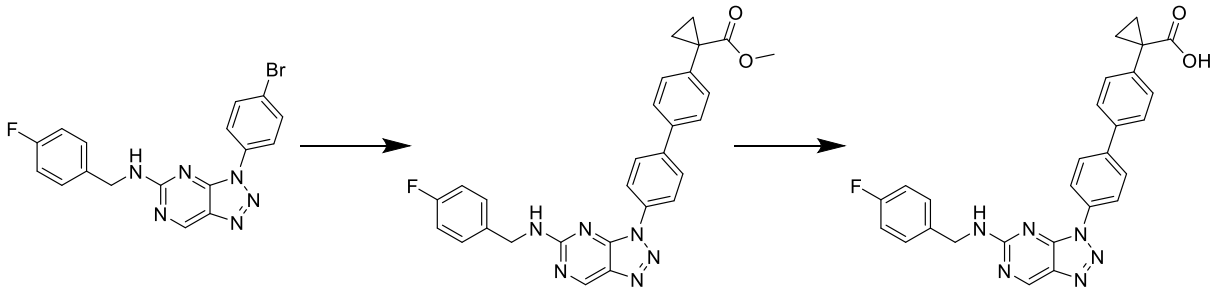

L20t L21t L22t

Synthesis of Compound - 3-(4-bromophenyl)-N-(4-fluorobenzyl)-3H- [1,2,3] triazolo[4,5-d] pyrimidin-5-amine (L20t)

L20t was prepared using the same procedures as L20a, but (4-fluorophenyl) methanamine was used in place of 2-methylpropan-2-amine. Chemical Formula: $C_{17}H_{12}BrFN_6$. Molecular

Weight: 399.23. ^{1}H NMR (500 MHz, $CDCl_3$) δ 9.11 (s, 1H), 8.10 (d, *J* = 8.9 Hz, 2H), 7.67 (d, *J* = 8.9 Hz, 2H), 7.36 (m, *J* = 8.6 Hz, 2H), 7.05 (t, *J* = 8.6 Hz, 2H), 6.10 (s, 1H), 4.68 (s, 2H).

Synthesis of Compound - Methyl 1-(4'-(5-((4-fluorobenzyl) amino)-3H- [1,2,3] triazolo[4,5-d] pyrimidin-3-yl)-[1,1'-biphenyl]-4-yl) cyclopropane-1-carboxylate (L21t)

L21t was prepared using the same procedures as L21a. Chemical Formula: $C_{28}H_{23}FN_6O_2$. Molecular Weight: 494.53. ^{1}H NMR (500 MHz, $CDCl_3$) δ 9.14 (s, 1H), 8.25 (d, *J* = 8.2 Hz, 2H), 7.76 (d, *J* = 8.2 Hz, 2H), 7.60 (d, *J* = 7.8 Hz, 2H), 7.46 (d, *J* = 7.8 Hz, 2H), 7.39 (d, *J* = 8.5 Hz, 2H), 7.05 (d, *J* = 8.5 Hz, 2H), 6.03 (s, 1H), 4.72 (s, 2H), 3.67 (s, 3H), 1.67 (q, 2H), 1.25 (q, 2H).

Synthesis of Compound - 1-(4'-(5-((4-fluorobenzyl) amino)-3H- [1,2,3] triazolo[4,5-d] pyrimidin-3-yl)-[1,1'-biphenyl]-4-yl) cyclopropane-1-carboxylic acid (L22t)

L22t was prepared using the same procedures as L22a. The crude product was purified through flash column chromatography (eluent gradient, 20-30% EtOAc in hexanes) to provide the final compound. A grey solid product was obtained in 27% yield (20mg). Chemical Formula: $C_{27}H_{21}FN_6O_2$. Molecular Weight: 480.50. LC-MS, $[M + H]^+$ = 481.18 (calcd.) 481.33 (found). ^{1}H NMR (500 MHz, DMSO) δ 9.29 (s, 1H), 8.18 (d, *J* = 8.0 Hz, 2H), 7.92 (d, *J* = 8.4 Hz, 2H), 7.70 (d, *J* = 7.3 Hz, 2H), 7.46 (d, *J* = 8.0 Hz,, 2H), 7.37 (d, *J* = 8.4 Hz, 2H), 7.19 (d, *J* = 8.7 Hz, 2H), 7.07 (d, *J* = 8.7 Hz, 2H), 6.82 (d, *J* = 7.3 Hz, 2H), 4.55 (s, 2H), 1.56 (m, *J* = 2.4 Hz, 2H), 1.30 (m, *J* = 2.4 Hz, 2H). Purity testing by HPLC (Acquisition method 65%-95% Acetonitrile 20 minutes) t_R = 10.9 minutes. Purity=95%.

Synthesis of Compounds L20v-L22v

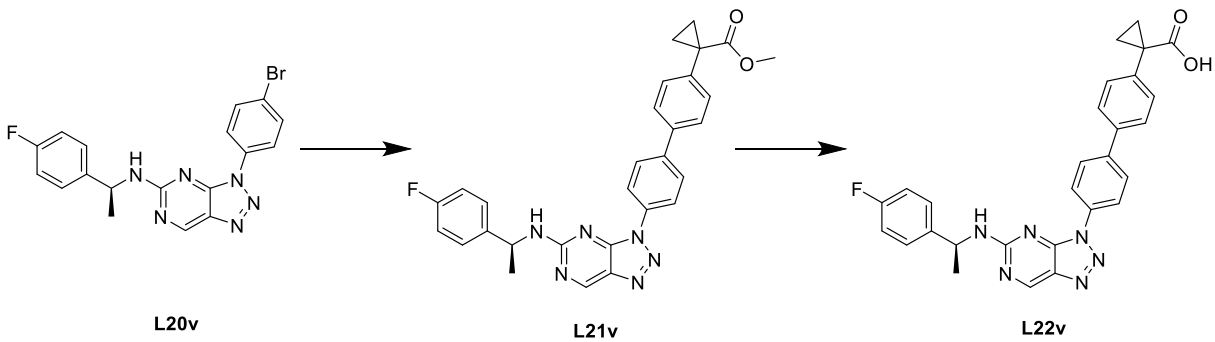

Synthesis of Compound - (S)-3-(4-bromophenyl)-N-(1-(4-fluorophenyl) ethyl)-3H- [1,2,3] triazolo[4,5-d] pyrimidin-5-amine (L20v)

L20v was prepared using the same procedures as L20a, but (S)-1-(4-fluorophenyl) ethan-1-amine was used in place of 2-methylpropan-2-amine. Chemical Formula: $C_{18}H_{14}BrFN_6$. Molecular Weight: 413.25. ^{1}H NMR (500 MHz, $CDCl_3$) δ 9.08 (s, 1H), 7.97 (d, *J* = 7.8 Hz, 2H), 7.63 (d, *J* = 8.4 Hz, 2H), 7.38 (d, *J* = 7.8 Hz, 2H), 7.05 (t, *J* = 8.4 Hz, 2H), 6.22 (s, 1H), 5.06 (s, 1H), 1.62 (d, 3H).

Synthesis of Compound - Methyl (S)-1-(4'-(5-((1-(4-fluorophenyl) ethyl) amino)-3H-[1,2,3] triazolo[4,5-d] pyrimidin-3-yl)-[1,1'-biphenyl]-4-yl) cyclopropane-1-carboxylate (L21v)

L21v was prepared using the same procedures as L21a. Chemical Formula: $C_{29}H_{25}FN_6O_2$.

Molecular Weight: 508.56. LC-MS, $[M + H]^+$ = 509.21 (calcd.) 509.30 (found). ^{1}H NMR (500 MHz, $CDCl_3$) δ 9.11 (s, 1H), 8.13 (d, 2H), 7.73 (d, 2H), 7.61 (d, *J* = 7.9 Hz, 2H), 7.47 (d, *J* = 7.9 Hz, 2H), 7.41 (m, *J* = 8.4 Hz, 2H), 7.05 (t, *J* = 8.4 Hz, 2H), 6.04 (s, 1H), 5.12 (s, 1H), 3.68 (s, 3H), 1.67 (q, 2H), 1.63 (d, 3H), 1.26 (q, 2H).

Synthesis of Compound - (S)-1-(4'-(5-((1-(4-fluorophenyl) ethyl) amino)-3H- [1,2,3] triazolo[4,5-d] pyrimidin-3-yl)-[1,1'-biphenyl]-4-yl) cyclopropane-1-carboxylic acid (L22v)

L22v was prepared using the same procedures as L22a. The crude product was purified through flash column chromatography (eluent gradient, 20-30% EtOAc in hexanes) to provide the final compound. A white solid product was obtained in 29% yield (27mg). Chemical Formula: $C_{28}H_{23}FN_6O_2$. Molecular Weight: 494.53. LC-MS, $[M + H]^+$ = 495.19 (calcd.) 495.26 (found). ^{1}H NMR (500 MHz, DMSO) δ 12.40 (s, 1H), 9.29 (s, 1H), 8.84 (d, *J* = 6.9 Hz, 1H), 8.14 (d, *J* = 8.4 Hz, 2H), 7.92 (d, *J* = 8.4 Hz, 2H), 7.72 (d, *J* = 7.9 Hz, 2H), 7.54 – 7.50 (d, *J* = 8.6 Hz, 2H), 7.47 (d, *J* = 7.9 Hz, 2H), 7.20 (d, *J* = 8.6 Hz, 2H), 5.09 – 5.04 (m, 1H), 1.52 (q, *J* = 3.2 Hz, 2H), 1.51 (d, 3H), 1.21 (q, *J* = 3.2 Hz, 2H). Purity testing by HPLC (Acquisition method 65%-95% Acetonitrile 20 minutes) t_R = 10.8 minutes. Purity=97%.

Synthesis of Compounds L23a-L25a

Synthesis of Compound - 5-(benzyloxy)-3-(4-bromophenyl)-3H- [1,2,3] triazolo[4,5-d] pyrimidine (L23a)

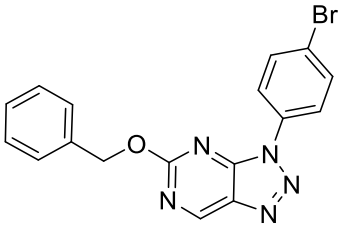

To a solution of 60% Sodium Hydride (NaH) in mineral oil (11mg, 1.75 equiv.) in DMF (5ml) was added benzyl alcohol (65 mg, 2.0 equiv.) dropwise. After stirring for 30 minutes, compound L19 (100mg, 1.0 equiv.) was added, and the solution was heated in a microwave at 110ºC. Upon cooling, the solution was partitioned between EtOAc and water. During work out, upon separation, the organic layer was washed further into water and brine, and dried over $MgSO_4$, concentrated and purified by chromatography column (eluent gradient, 5-10% EtOAc in hexanes) to afford Compound L23a (28 mg, 22% yield). Chemical Formula: $C_{17}H_{12}BrN_5O$. Molecular Weight: 382.22. LC-MS, $[M + H]^+$ = 384.03 (calcd.) 384.09 (found). ^1H NMR (500 MHz, $CDCl_3$) δ 9.38 (s, 1H), 8.10 (d, *J* = 5.8 Hz, 2H), 7.73 (d, *J* = 5.8 Hz, 2H), 7.52 (d, 2H), 7.30 (m, 3H), 5.58 (s, 2H).

Synthesis of Compound - Methyl 1-(4'-(5-(benzyloxy)-3H- [1,2,3] triazolo[4,5-d] pyrimidin-3-yl)-[1,1'-biphenyl]-4-yl) cyclopropane-1-carboxylate (L24a)

Compound L23a (101 mg, 0.24 mmol) was dissolved in 8 mL of a 1:3 mixture of H_2O:1,4-dioxane and the reflux condenser was prepared. The solution was heated to 80ºC, and Na_2CO_3 (54 mg, 0.515 mmol) was added to the solution. Compound L13 (99 mg, 0.31 mmol) was added to the solution, quickly followed by the addition of $Pd(dppf)Cl_2$ (18 mg, 0.1 mol%). The solution was bubbled with argon and then stirred for 10 hrs. The mixture was cooled and then filtered through diatomaceous earth and partitioned between EtOAc and brine. The organic phase was separated, dried over Na_2SO_4, filtered, and concentrated. The dried residue was adsorbed to silica and purified using flash silica gel column chromatography (eluent gradient, 5-10% EtOAc in hexanes) to afford Compound L24a (44mg, 39% of yield). Chemical Formula: $C_{28}H_{23}N_5O_3$. Molecular Weight: 477.52. LC-MS, $[M + H]^+$ = 478.19 (calcd.) 478.29 (found). ^1H NMR (500 MHz, $CDCl_3$) δ 9.40 (s, 1H), 8.25 (d, *J* = 8.5 Hz, 2H), 7.81 (d, *J* = 8.0 Hz, 2H), 7.62 (d, *J* = 8.5 Hz, 2H), 7.54 (d, *J* = 7.4 Hz, 2H), 7.48 (d, *J* = 8.0 Hz, 2H), 7.40 (t, *J* = 7.4 Hz,

2H), 7.35 (t, *J* = 7.4 Hz, 1H), 5.60 (s, 2H), 3.67 (s, 3H), 1.67 (q, *J* = 3.9 Hz, 2H), 1.26 (q, *J* = 3.9 Hz, 2H).

Synthesis of Compound - 1-(4'-(5-(benzyloxy)-3H- [1,2,3] triazolo[4,5-d] pyrimidin-3-yl)-[1,1'-biphenyl]-4-yl) cyclopropane-1-carboxylic acid (L25a)

Compound 24a (23 mg, 0.05 mmol) was dissolved in 2 mL of a prepared 1:3 mixture of H_2O: THF. Lithium hydroxide pellets (LiOH) (20 mg, 0.71 mmol) were added to the solution, and the solution was stirred overnight. The mixture was partitioned between EtOAc and brine, and the organic phase was separated, dried over Na_2SO_4, filtered, and concentrated. The residue was dissolved in a mixture of HPLC-grade acetonitrile (ACN) with 0.1% formic acid. The crude was purified by ACN/Water (65% / 35%) in prep-HPLC to provide the final compound L25a. A grey solid product was obtained in 17% yield (12mg). Molecular Weight: 463.50. LC-MS, $[M + H]^+$ = 464.17 (calcd.) 464.16 (found).

Synthesis of Compounds L23b-L23e

Synthesis of Compound - (R)-3-(4-bromophenyl)-5-(1-phenylethoxy)-3H- [1,2,3] triazolo[4,5-d] pyrimidine (L23b)

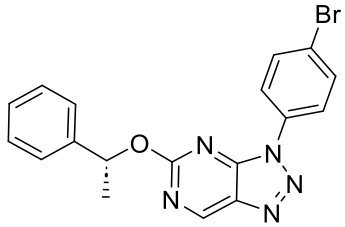

L23b was prepared using the same procedures as L23a, but (R)-1-phenylethan-1-ol was used in place of benzyl alcohol. Chemical Formula: $C_{18}H_{14}BrN_5O$. Molecular Weight: 396.25. LC-MS, $[M + H]^+$ = 398.04 (calcd.) 398.18 (found).

Synthesis of Compound - (S)-3-(4-bromophenyl)-5-(1-phenylethoxy)-3H- [1,2,3] triazolo[4,5-d] pyrimidine (L23c)

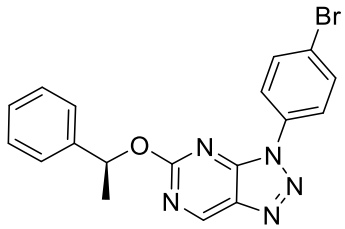

L23c was prepared using the same procedures as L23a, but (S)-1-phenylethan-1-ol was used in place of benzyl alcohol. Chemical Formula: $C_{18}H_{14}BrN_5O$. Molecular Weight: 396.25. LC-MS, $[M + H]^+$ = 398.04 (calcd.) 398.07 (found).

Synthesis of Compound - 3-(4-bromophenyl)-5-(1-(3-fluorophenyl) ethoxy)-3H-[1,2,3] triazolo[4,5-d] pyrimidine (L23d)

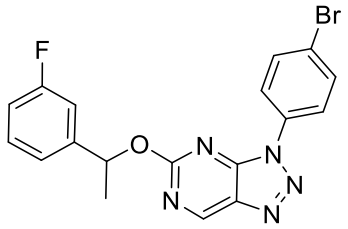

L23d was prepared using the same procedures as L23a, but 1-(3-fluorophenyl) ethan-1-olwas used in place of benzyl alcohol. Chemical Formula: $C_{18}H_{13}BrFN_5O$. Molecular Weight: 414.24. LC-MS, $[M + H]^+$ = 416.03 (calcd.) 416.23 (found).

Synthesis of Compound - 3-(4-bromophenyl)-5-(1-(4-fluorophenyl) ethoxy)-3H-[1,2,3] triazolo[4,5-d] pyrimidine (L23e)

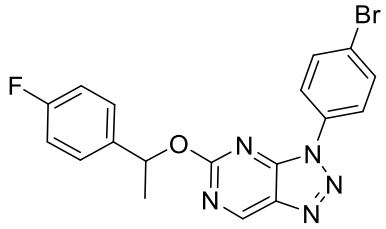

L23e was prepared using the same procedures as L23a, but 1-(4-fluorophenyl) ethan-1-ol was used in place of benzyl alcohol. Chemical Formula: $C_{18}H_{13}BrFN_5O$. Molecular Weight: 414.24. LC-MS, $[M + H]^+$ = 416.03 (calcd.) 416.20 (found).

Synthesis of compound - methyl 1-(4'-(5-chloro-3H-[1,2,3] triazolo[4,5-d]pyrimidin-3-yl)-[1,1'-biphenyl]-4-yl)cyclopropane-1-carboxylate (L26)

Compound L19 (250 mg, 0.82 mmol) was dissolved in 8 mL of a 1:3 mixture of H_2O:1,4-dioxane and the reflux condenser was prepared. The solution was heated to 80ºC, and Cs_2CO_3 (650 mg, 2.1 mmol) was added to the solution. Compound L13 (325 mg, 1.3 mmol) was added to the solution, quickly followed by the addition of $Pd(pph_3)Cl_2$ (57 mg, 0.2 mol%). The solution was bubbled with argon and then stirred for 10 hrs. The reaction mixture was monitored and confirmed by HPLC-MS. Chemical Formula: $C_{21}H_{16}ClN_5O_2$. Molecular Weight: 405.84. LC-MS, $[M + H]^+$ = 406.11 (calcd.) 406.18 (found).

3.6.4 Experimental Procedure and Results for the Third Series Compounds

Synthesis of Compounds L30i-L31i

Synthesis of Compound– N-benzyl-3-(4-(4,4,5,5-tetramethyl-1,3,2-dioxaborolan-2-yl) phenyl)-3H-[1,2,3] triazolo[4,5-d]pyrimidin-5-amine (L30i)

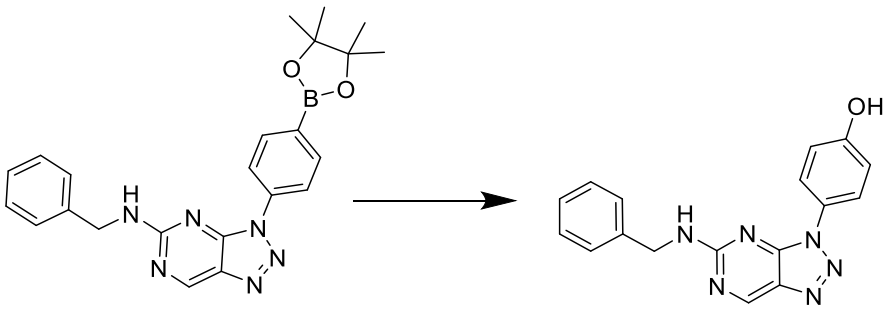

To a stirred solution of **L20i** (140 mg, 0.36 mmol) and bis(pinacolato)diboron (142 mg, 0.57 mmol) in 1,4-dioxane (7 mL) was added KOAc (81 mg, 0.9 mmol). The reaction mixture was degassed with Ar for 5 mins. 1,1′-Bis(diphenylphosphino)ferrocene-$Pd^{II}Cl_2$-toluene adduct (17 mg, 0.05 mmol) was added, and the reaction mixture was stirred at 90°C for 16 hrs under Ar and then cooled to r.t. The mixture was filtered through Celite and washed with EtOAc (50 mL); the combined organic filtrates were concentrated in vacuo. The residue was chromatographed (eluent gradient, 25% EtOAc in hexanes) to give L30i (95 mg, 65% yield) as a pale-yellow oily liquid. Chemical Formula: $C_{23}H_{25}BN_6O_2$. Molecular Weight: 428.30. LC-MS, $[M + H]^+$ = 429.22 (calcd.) 429.31 (found).

L31i - 4-(5-(benzylamino)-3H- [1,2,3] triazolo[4,5-d] pyrimidin-3-yl) phenol

To a solution of L30i (100 mg, 0.24 mmol) in a THF (10 mL) and water (2 mL) mixture was added $NaH_2BO_4H_2O$ (58 mg, 0.5 mmol). The reaction mixture was stirred at r.t. for 90 mins, then diluted with saturated aqueous NH_4Cl (50 mL), and extracted with EtOAc (2 × 50 mL). The combined organic extracts were dried (Na_2SO_4) and concentrated in vacuo. The crude product was chromatographed (eluent gradient, 30% EtOAc in hexanes) to give L31i (65 mg, 86% yield) as a white solid. Molecular Weight: 318.34. LC-MS, $[M + H]^+$ = 319.13 (calcd.) 319.11 (found). ^{1}H NMR (500 MHz, DMSO) δ 9.90 (s, 1H), 9.26 (s, 1H), 8.70 (s, 1H), 7.79 (d, *J* = 8.5 Hz, 2H), 7.39 (d, *J* = 7.2 Hz, 2H), 7.33 (t, *J* = 7.2 Hz, 2H), 7.23 (t, *J* = 7.2 Hz, 1H), 6.96 (d, *J* = 8.5 Hz, 2H), 4.53 (d, *J* = 5.7 Hz, 2H).

Synthesis of Compounds L30m-L31m

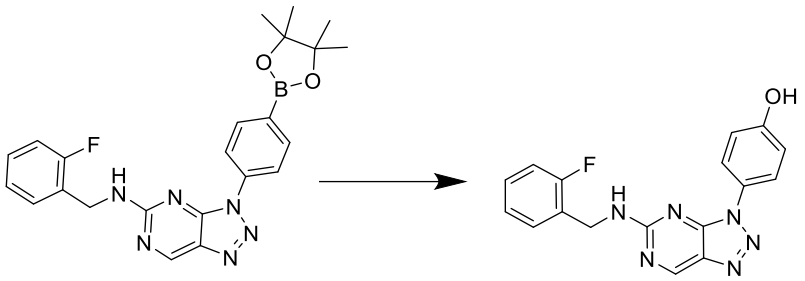

Synthesis of Compound - N-(2-fluorobenzyl)-3-(4-(4,4,5,5-tetramethyl-1,3,2-dioxaborolan-2-yl) phenyl)-3H-[1,2,3] triazolo[4,5-d]pyrimidin-5-amine (L30m)

L30m was prepared using the same procedures as L30i. Chemical Formula: $C_{23}H_{24}BFN_6O_2$. Molecular Weight: 446.29. LC-MS, $[M + H]^+$ = 447.21 (calcd.) 447.24 (found).

Synthesis of Compound - 4-(5-((2-fluorobenzyl) amino)-3H- [1,2,3] triazolo[4,5-d] pyrimidin-3-yl) phenol (L31m)

L31m was prepared using the same procedures as L31i. Chemical Formula: $C_{17}H_{13}FN_6O$. Molecular Weight: 336.33. LC-MS, $[M + H]^+$ = 337.12 (calcd.) 337.19 (found). ^{1}H NMR (500 MHz, DMSO) δ 9.31 (s, 1H), 7.84 (d, *J* = 8.4 Hz, 2H), 7.48 (s, 1H), 7.37 (m, 1H), 7.25 (t, 1H), 7.19 (t, 1H), 7.01 (d, *J* = 8.4 Hz, 2H), 4.62 (s, 2H).

Synthesis of Compounds L30p-L31p

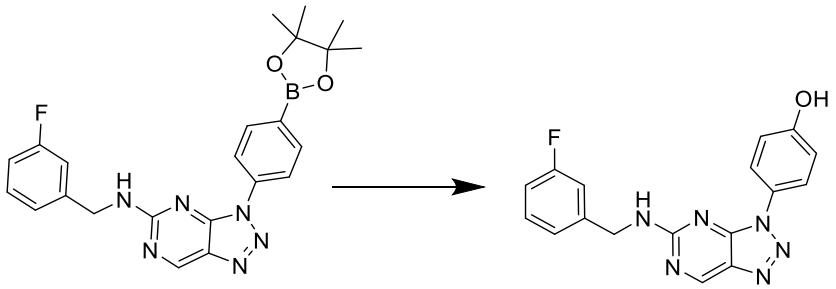

Synthesis of Compound - N-(3-fluorobenzyl)-3-(4-(4,4,5,5-tetramethyl-1,3,2-dioxaborolan-2-yl) phenyl)-3H- [1,2,3] triazolo[4,5-d] pyrimidin-5-amine (L30p)

L30p was prepared using the same procedures as L30i. Chemical Formula: $C_{23}H_{24}BFN_6O_2$. Molecular Weight: 446.29. LC-MS, $[M + H]^+$ = 447.21 (calcd.) 447.32 (found).

Synthesis of Compound - 4-(5-((3-fluorobenzyl) amino)-3H- [1,2,3] triazolo[4,5-d] pyrimidin-3-yl) phenol (L31p)

L31p was prepared using the same procedures as L31i. Chemical Formula: $C_{17}H_{13}FN_6O$. Molecular Weight: 336.33. LC-MS, $[M + H]^+$ = 337.12 (calcd.) 337.19 (found). ^1H NMR (500 MHz, DMSO) δ 9.31 (s, 1H), 7.82 (d, *J* = 8.4 Hz, 2H), 7.45 (s, 1H), 7.29(t, 2H), 7.11 (t, 1H), 7.01 (d, *J* = 8.4 Hz, 2H), 4.58 (s, 2H).

Synthesis of Compounds L30t-L31t

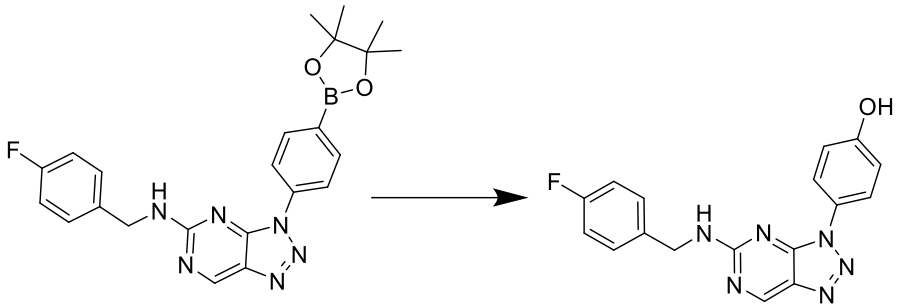

Synthesis of Compound - N-(4-fluorobenzyl)-3-(4-(4,4,5,5-tetramethyl-1,3,2-dioxaborolan-2-yl) phenyl)-3H-[1,2,3] triazolo[4,5-d]pyrimidin-5-amine (L30t)

L30t was prepared using the same procedures as L30i. Chemical Formula: $C_{23}H_{24}BFN_6O_2$. Molecular Weight: 446.29. LC-MS, $[M + H]^+$ = 447.21 (calcd.) 447.32 (found).

Synthesis of Compound - 4-(5-((4-fluorobenzyl) amino)-3H- [1,2,3] triazolo[4,5-d] pyrimidin-3-yl) phenol (L31t)

L31t was prepared using the same procedures as L31i. Chemical Formula: $C_{17}H_{13}FN_6O$. Molecular Weight: 336.33. LC-MS, $[M + H]^+$ = 337.12 (calcd.) 337.19 (found). ^1H NMR (500 MHz, DMSO) δ 9.91 (s, 1H), 9.26 (s, 1H), 8.69 (s, 1H), 7.79 (d, *J* = 8.8 Hz, 2H), 7.41 (d, *J* = 8.6 Hz, 2H), 7.15 (d, *J* = 8.8 Hz, 2H), 6.98 (d, *J* = 8.6 Hz, 2H), 4.51 (s, *J* = 5.4 Hz, 2H).

Synthesis of Compounds L35-L36

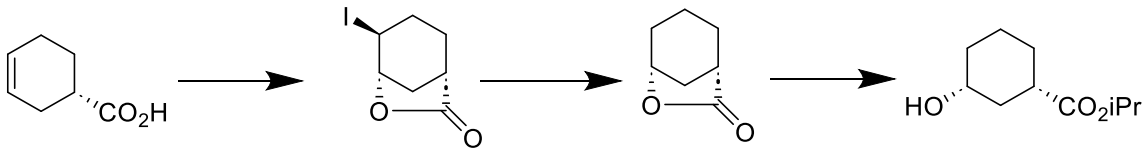

L34 **L35** **L36** **L37**

Synthesis of Compound - (1S,4S,5S)-4-iodo-6-oxabicyclo [3.2.1] octan-7-one (L35)

To a mixture of (S)-cyclohex-3-enecarboxylic acid L34 (500 mg, 3.96 mmol) in water (20 mL) was added $NaHCO_3$ (997 mg, 11.8 mmol) portionwise; the mixture was stirred until it became homogeneous. A solution of iodine (1107 mg, 4.36 mmol) and KI (3951mg, 23.8 mmol) in water (100 mL) was added (protected from light), and the reaction was stirred overnight in the dark. Water (100 mL) was added, and the mixture was extracted with CH_2Cl_2 (3 × 50 mL). The combined organic extracts were washed with aqueous10%$Na_2S_2O_3$(2×150 mL) and brine, dried ($MgSO_4$), and concentrated in vacuo to give crude iodolactone L35 (751 mg; 75% yield) as a white solid, which was used in the next step without further purification. Chemical Formula: $C_7H_9IO_2$. Molecular Weight: 252.05.

Synthesis of Compound - (1S,5R)-6-oxabicyclo [3.2.1] octan-7-one (L36)

Ar was bubbled through a needle to solution of L35 (252mg, 1mmol) in dry toluene (10ml) with AIBN (820 mg, 5 mmol) at room temperature for 10 mins. Then $(TMS)_3SiH$ (1240 mg, 5 mmol) was added, and the resultant mixture was stirred at 110ºC under Ar protection for 2 hrs. Then, the volatiles were removed, and the residue was purified by column chromatography (eluent gradient, 10-30% EtOAc in hexanes) to afford Compound L36 (84mg, 67% of yield). Chemical Formula: $C_7H_{10}O_2$. Molecular Weight: 126.16. LC-MS, $[M + H]^+$ = 127.08 (calcd.) 127.02 (found).

Synthesis of Compound - isopropyl (1S,3S)-3-hydroxycyclohexane-1-carboxylate (L37)

Acetyl chloride (101 mg, 1.3 mmol) was added portionwise to isopropanol (10 mL) at 0°C. The solution was allowed to warm to r.t. and stirred at r.t. for 30 mins. Compound L36 (200 mg, 1.07 mmol) was added, and the reaction was stirred overnight at r.t, after which it was concentrated in vacuo and then azeotroped with toluene. The residue was purified by column chromatography (eluent gradient, 20-50% EtOAc in hexanes) to afford Compound L37. Chemical Formula: $C_{10}H_{18}O3$. Molecular Weight: 186.25. LC-MS, $[M + H]^+$ = 187.13 (calcd.) 187.13 (found).

Chapter Four

Conclusions and Future Work

4.1 Conclusions

As of 2024, early diagnose and effective treatment of lung cancer remain significant challenges in Canada[7,8]. To address these challenges, this study focuses on the design, synthesis, and biological evaluation of novel small molecules with potential applications in lung cancer diagnosis and therapy[16,172,204]. The PAR2 and LPA1 receptors are attractive targets due to their elevated expression in lung cancer cell lines and their roles in cancer development and progression[172,207]. While several LPA1-targeting compounds, such as AZ3451 and RO6842262, have been reported in the literature, none have reached the market[99,101]. To facilitate the discovery of novel compounds, a multi-structure modification approach was employed to identify new molecular entities with improved pharmacological properties based on these reference compounds[35,221,237]. Structural modifications, including scaffold-hopping strategies and fluorine incorporation for fluorine-18 radiolabeling, have yielded promising candidates that not only target key receptors involved in cancer progression but also have potential therapeutic applications[233,237].

In **Chapter 2**, a library of 35 novel PAR2 antagonists was synthesized through structural modifications of AZ3451[99]. Functional evaluation of these compounds identified the potential of biased ligands that selectively modulate PAR2-dependent signaling pathways. Additionally, given the high expression of PAR2 in lung cancer, a fluorine-containing candidate, P1c, demonstrated high potency in β-arrestin recruitment assays, was selected for radiolabeling study. The successful synthesis of SPIAd iodonium (III) ylide precursor facilitates the development of a novel radiolabeled PAR2 ligand – [^{18}F]P1c for PET imaging[177]. Overall, the radiotracer [^{18}F]P1c holds great significance as a PET imaging agent capable of stabilizing specific PAR2 conformations may better capture the receptor's pathological state in disease conditions, making it an important step for precision imaging in cancer (**Fig. 4.1**).

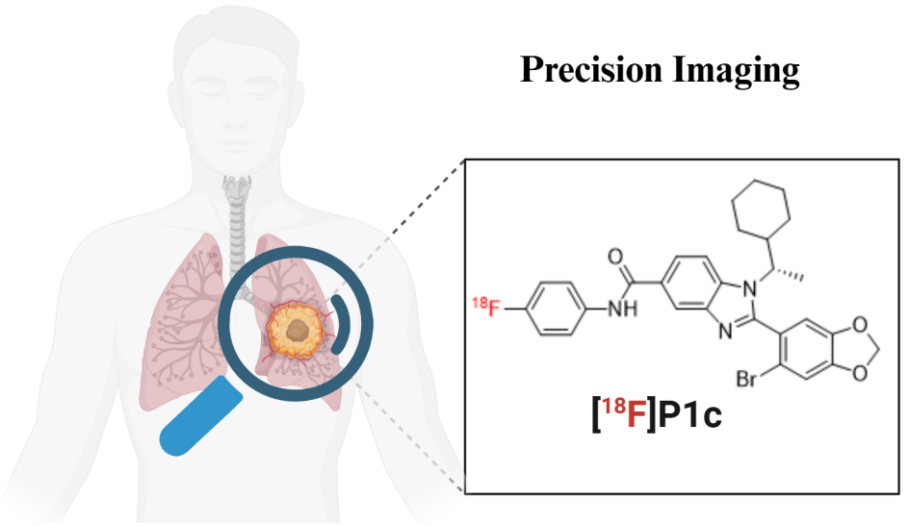

Figure 4.1. Radioligand [^{18}F]P1c holds the potential for precision imaging in cancer diagnosis.

In **Chapter 3**, three series of novel LPA1 antagonists were developed and synthesized, yielding a total of 24 synthesized compounds. The first series was derived from RO6842262, while the second was inspired by compound 12f, an anti-metastatic agent previously reported by our group[90,101]. Structural modifications, including scaffold hopping and molecular docking, were employed to optimize ligand-receptor interactions[237]. Preliminary cAMP signaling assays revealed that compound L22p exhibited an IC_{50} of 1.33 nM, indicating strong antagonistic activity (**Fig. 4.2**).

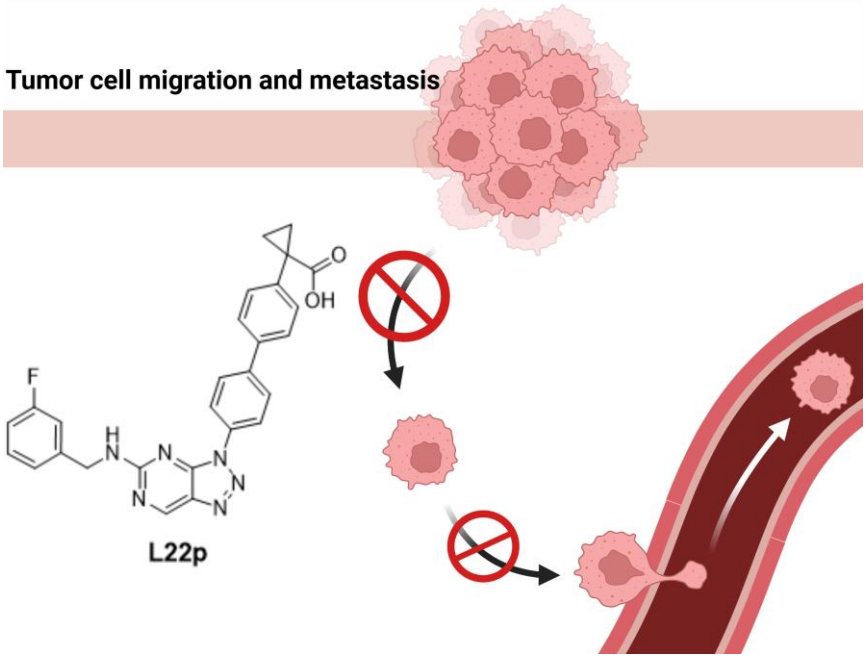

Figure 4.2. L22p holds promise as a LPA1 antagonist with anti-metastatic potential.

Moreover, given the high expression of LPA1 in cancer, a lead candidate from these two series will be further modified for iodonium (III) ylide precursor synthesis, enabling the development of a novel fluorine-18 radiolabeled LPA1 ligand for PET imaging applications[178].

4.2 Future Work

4.2.1 Development of Novel Biased Ligands for PAR2

The reference compound AZ3451 is a pan-inhibitor of PAR2-dependent G-protein coupling, while some of its analogs in **Chapter 2**, including AZ3451 derivatives P8 and P14, exhibit potential functional selectivity. Given that GPCRs adopt multiple conformations, regulating distinct signaling pathways, certain pathways may be preferentially activated in disease states. For example, selective inhibition of Gi/Go coupling could be therapeutically relevant in lung cancer by potentially suppressing tumor growth or metastasis.

To further characterize these analogs, Dr. Ramachandran's group will conduct duplicate assays, including calcium signaling and β-arrestin recruitment assays, to confirm the probe-dependent activity and functional selectivity of these compounds. Additionally, in ongoing work, Dr. Ramachandran's group is further evaluating all compounds presented in **Chapter 2** to investigate functional selectivity and biased signaling in PAR2-mediated G protein recruitment assay (Gαq/11, Gαi, and Gα12/13). The data obtained from these studies will be instrumental in guiding the rational design of next-generation AZ3451 derivatives with improved selectivity and therapeutic potential (**Fig. 4.3**).

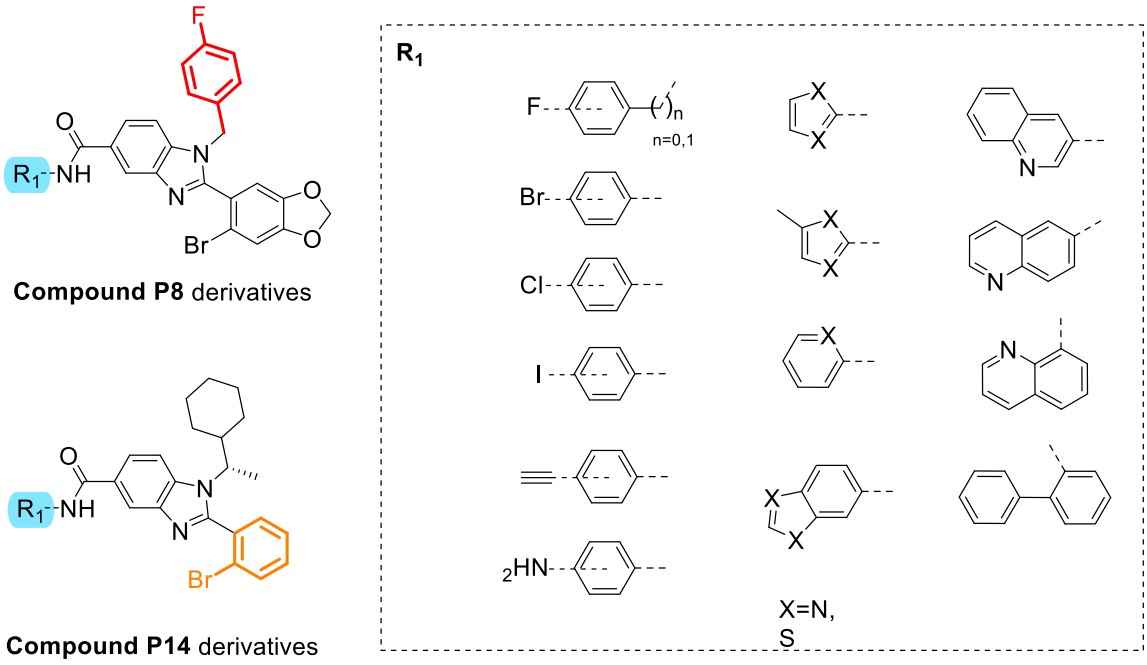

Figure 4.3. Structure of P8 and P14 derivatives with several examples of building blocks (R1).

4.2.2 Biological evaluation of novel LPA1 antagonists *in vitro* assays

As shown in **Figure 3.2**, LPA1 activation inhibits cAMP production. Therefore, blocking LPA1 activation with an LPA1 antagonist is expected to increase intracellular cAMP levels. To evaluate this effect, all three series of synthesized compounds presented in **Chapter 3** will be tested in our group using an *in vitro* cAMP assay with Chinese hamster ovary (CHO) cells.

In addition to the cAMP assay, these compounds will be evaluated for their effects on cell migration using a wound-healing assay in the MDA-MB-231 breast cancer cell line. LPA1 is overexpressed in many breast cancer cell lines relative to non-tumorigenic lines, and its activation promotes migration and invasion, implicating it in breast cancer metastasis. In the scratch assay, cells will be plated in 6-well plates and a wound introduced using a micropipette tip. After allowing time for migration, the extent of wound closure will be quantified to assess the effect of LPA1 antagonists on cell motility.

4.2.3 Employing the Boc Group for Amide Protection

After reviewing the literature on [^{18}F] radiolabeling, it was found that, in addition to optimizing reaction conditions, the hydrogen atom of the amide bond is a potential issue that can interfere with the radio-fluorination process, as discussed in **Chapter 2.4.2**[177,180]. The hydrogen atom of the amide group is a strong hydrogen bond donor. Under the basic conditions used in nucleophilic radio-fluorination with [^{18}F], it can form hydrogen bonds with fluoride ions (F^-),

effectively reducing the availability of [^{18}F] for the desired reaction by 'trapping' it. Additionally, the amide nitrogen can be deprotonated under strongly basic conditions, which could interfere with the fluorination reaction[177,180].

To address this issue, as shown in **Scheme 4.1 A-B**, the Boc (tert-butoxycarbonyl) protecting group is primarily used to protect the amide group during the synthesis of the SCIDY precursor for radio-labeling[180]. The Boc group minimizes interference by masking the amide group[177,180]. Additionally, the Boc group remains stable under the basic fluorination conditions and can be selectively removed using mild acidic conditions after radiolabeling[177,180]. The optimized radiolabeling process is currently under investigation.

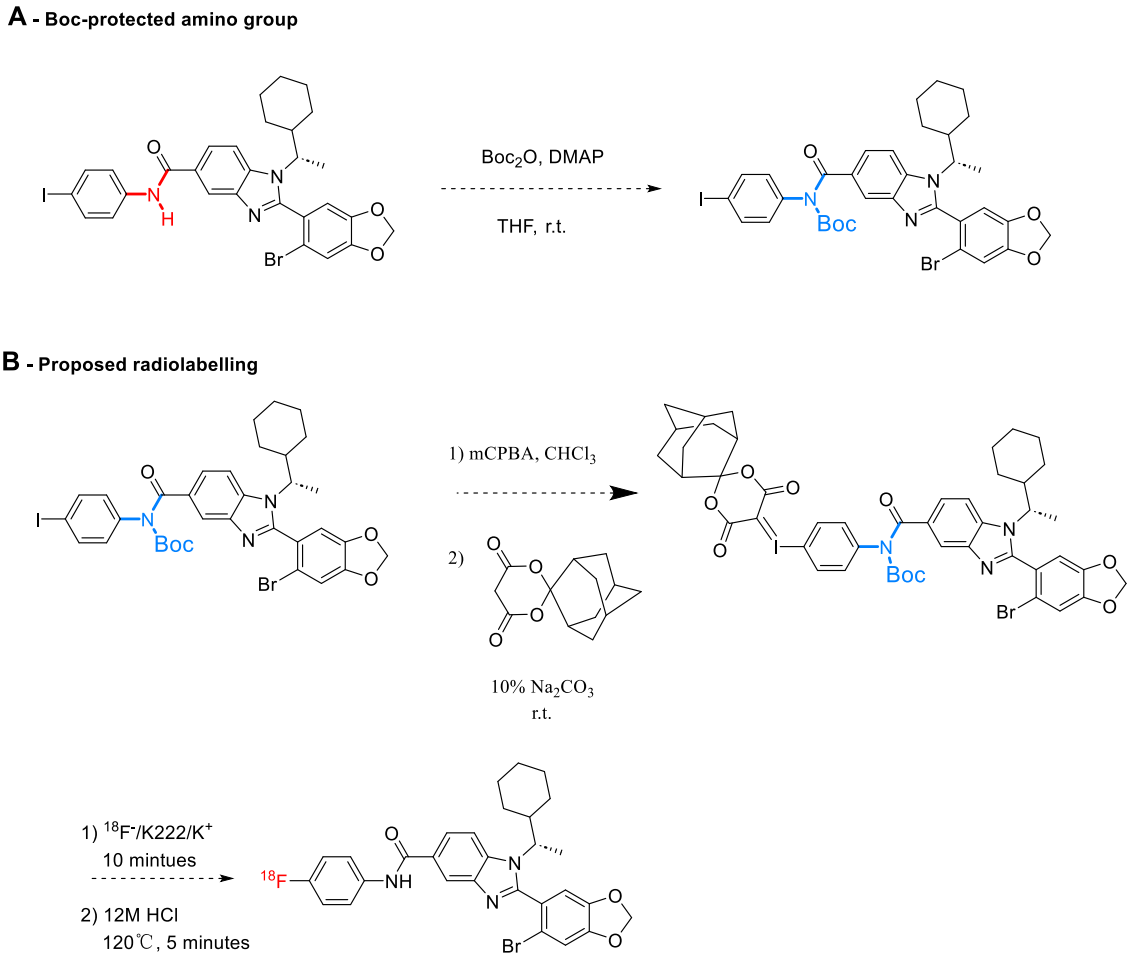

Scheme 4.1. Proposed synthetic scheme with Boc group for radiolabeling.

4.2.4 Modification of the Synthetic Scheme for Efficient ^{18}F-Labeling in 2nd Series

To date, the only reported LPA1 radiotracers are [^{11}C] BMT-136088 and [^{18}F] BMS-986327, both recently adapted as PET imaging agents in literature, primarily for imaging idiopathic pulmonary fibrosis (IPF)[90,246]. [^{11}C] BMT-136088 is a radiolabeled analogue of BMS-986020, employing a scaffold like Ki16425 (**Fig. 4.4**)[246]. Notably, no selectivity data has been presented for LPA1 over other LPARs[246]. This compound was evaluated *in vivo* using PET imaging in rhesus monkeys[246]. It is anticipated that [^{11}C] BMT-136088 will also support the clinical evaluation of BMS-986020, whose last clinical trial, a Phase 1 trial, was completed in 2015[195,246]. The other compound, [^{18}F] BMS-986327, announced by Bristol Myers Squibb Pharma, has no reported structure or selectivity data available in the literature[89,237]. This compound completed Phase 1 clinical trials in 2020[237].

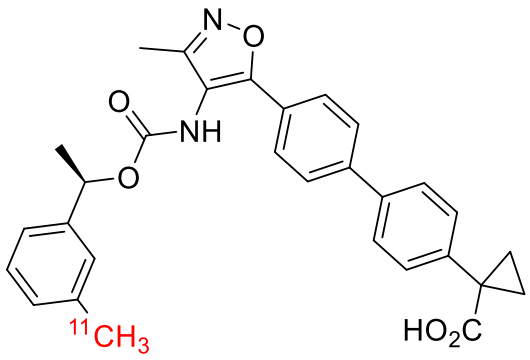

^{11}C-BMT-136088

Figure 4.4. Chemical structures of reported LPA1 radiotracer.

The SPIAd iodonium (III) ylide remains incorporated in this Chapter for ^{18}F-radiolabeling study[247]. However, as discussed in **Scheme 3.3**, the use of **Scheme 3.6** through Suzuki coupling reaction to generating the iodo-compound would prove to be ineffective (**Scheme 4.2-A**)[237]. Therefore, to produce the SPIAd iodonium (III) ylide for radiolabeled compounds, an alternate synthetic scheme is designed, and the alternative intermediate (compound L26) is synthesized and characterized (**Scheme 4.2-B**), the detailed results are available in **Chapter 3.5.3**.

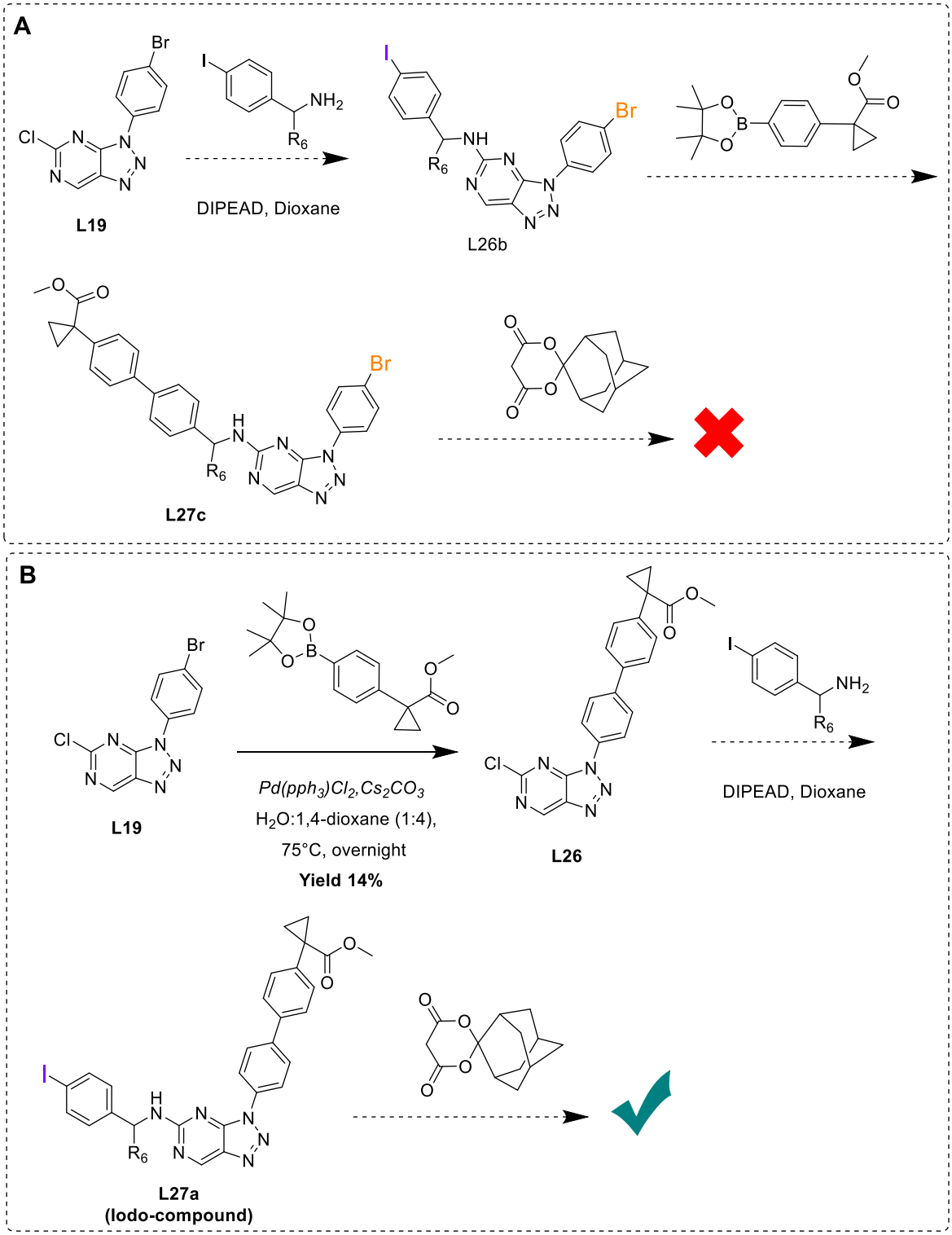

Scheme 4.2. A – Unwanted synthetic route for the preparation of SPIAd iodonium (III) ylide. B - Optimized alternative synthetic route for the preparation of SPIAd iodonium (III) ylide.

The alternate synthetic scheme enables the synthesis of iodine-containing final compounds while effectively avoiding undesired side products. However, during the Suzuki coupling reactions, chlorine on the intermediate may compete with bromine, resulting in the formation

of the corresponding ester product L26 in low yield (<15%)[237]. This competition reduces the efficiency of the reaction and complicates the process. Consequently, L26 is not considered a reliable intermediate for synthesizing the array of triazolo pyrimidine compounds in this series.

Given the radiolabeling issue mentioned in **Chapter 2.4.2** and the amine group in structure of L27a, a prospective strategy that protecting the amine group with a Boc group during radiolabeling would typically be necessary to prevent unwanted side reactions (**Scheme 4.3-A**)[180].

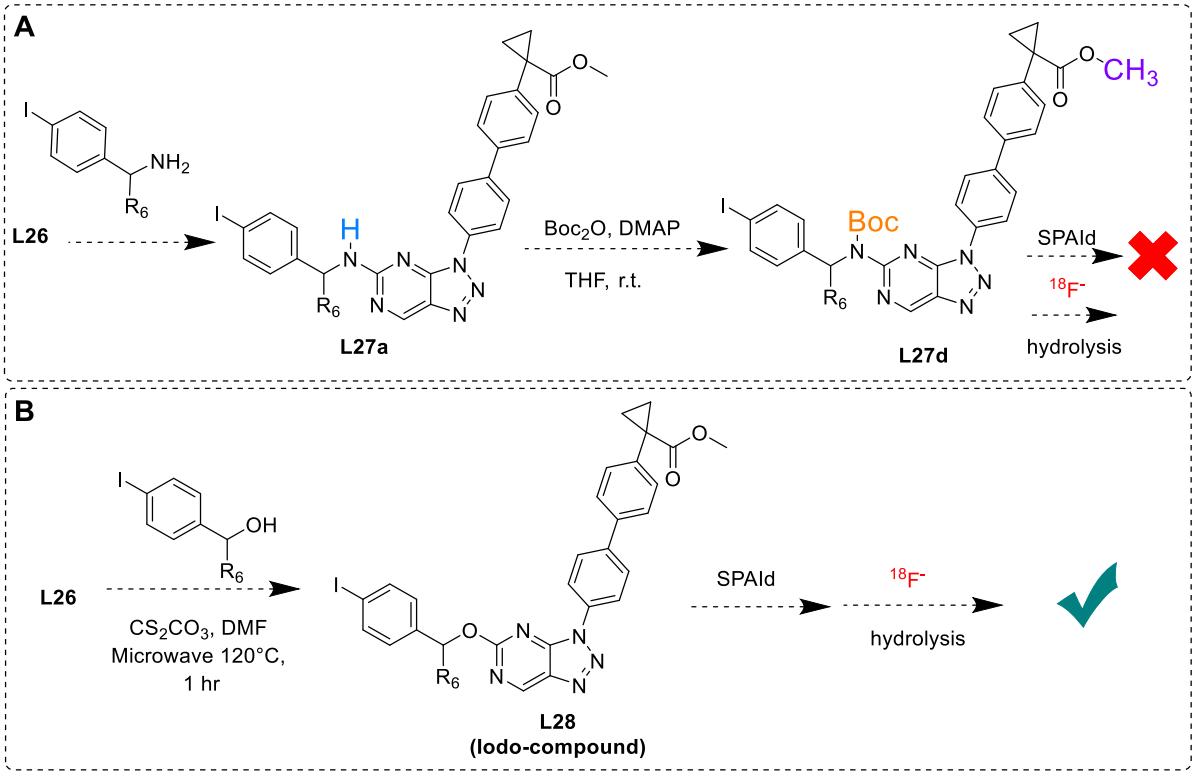

Scheme 4.3. (A) Hypothetical Boc-protected reaction of compound L27d with the R6 building block. (B) Proposed structure of Iodo-compound (L28) incorporating the R6 building block.

However, a post-radiolabeling Boc-deprotection step introduces an additional reaction, which is impractical given the time-sensitive nature of fluorine-18 radiolabeling. Besides the amine group, L27a also contains an ester group requiring hydrolysis after radiolabeling, further complicating the process and burdening its overall efficiency. Boc-deprotection requires acidic conditions, while ester hydrolysis typically occurs under basic conditions[180]. Although both reactions could theoretically occur under acidic conditions, acidic ester hydrolysis is significantly slower and less efficient. To streamline radiolabeling, employing the alcohol group to form the iodo-compound (L28) is a more efficient alternative (**Scheme 4.3-B**).

Based on the biological data in **Figure 3.18** of **Chapter 3.3**, a preliminary chemical structure can be proposed for the radiolabeling study. The radiolabeling strategy of possible building block (R6 group) of L28 is proposed in **Scheme 4.4**.

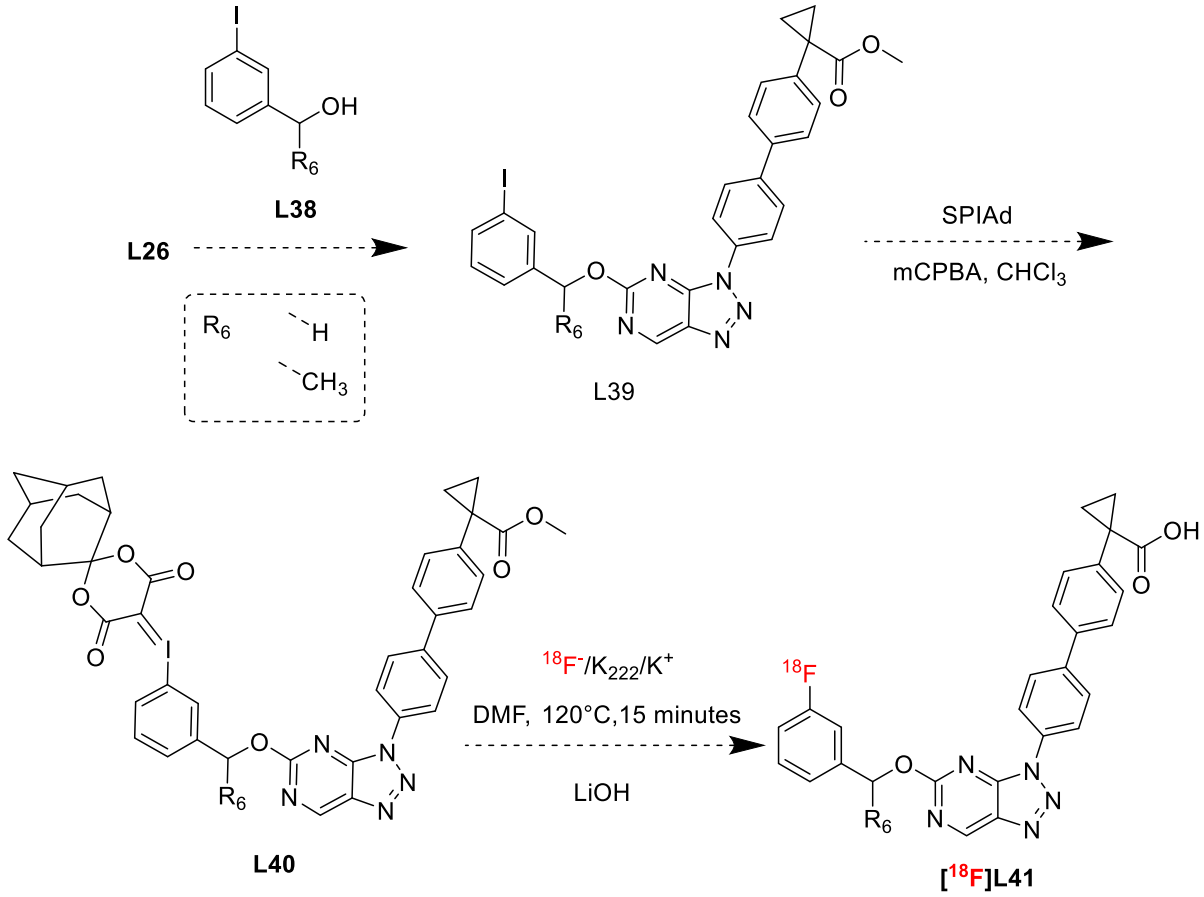

Scheme 4.4. Proposed radiolabeling scheme to produce ^{18}F-labeled compounds: production of the iodonium ylide species and subsequent one-pot reaction with ^{18}F and LiOH to yield the final 'hot' compound.

Reference

1 R. L. Siegel, A. N. Giaquinto, A. Jemal, *CA Cancer J Clin* **2024**, *74*, 12.

2 J. S. Brown, S. R. Amend, R. H. Austin, R. A. Gatenby, E. U. Hammarlund, K. J. Pienta, *Molecular Cancer Research* **2023**, *21*, 1142.

3 D. Hanahan, *Hallmarks of Cancer: New Dimensions*, American Association for Cancer Research Inc., **2022**.

4 D. Hanahan, R. A. Weinberg, The Hallmarks of Cancer Review evolve progressively from normalcy via a series of pre, **2000**.

5 J. C. A. Marshall, J. W. Collins, J. Nakayama, C. E. Horak, D. J. Liewehr, S. M. Steinberg, M. Albaugh, F. Vidal-Vanaclocha, D. Palmieri, M. Barbier, M. Murone, P. S. Steeg, *J Natl Cancer Inst* **2012**, *104*, 1306.

6 L. Hristova, M. Hakama, *Acta Oncologica, Supplement* **1997**, *36*.

7 Canadian Cancer Statistics 2024.

8 D. R. Brenner, A. Poirier, R. R. Woods, L. F. Ellison, J.-M. Billette, A. A. Demers, S. X. Zhang, C. Yao, C. Finley, N. Fitzgerald, N. Saint-Jacques, L. Shack, D. Turner, E. Holmes, Canadian Cancer Statistics Advisory Committee, *CMAJ* **2022**, *194*, E601.

9 L. A. Gaudette, E. M. Illing, G. B. Hill, *Health reports / Statistics Canada, Canadian Centre for Health Information = Rapports sur la santé / Statistique Canada, Centre canadien d'information sur la santé* **1991**, *3*, 107.

10 U. Advanced, M. Cancer, M. A. Cancer, B. Metastases, B. Metastases, L. Metastases, L. Metastases, M. Cancer, **2016**, 1.

11 R. J. Cersosimo, Lung cancer: A review.

12 A. A. Thai, B. J. Solomon, L. V. Sequist, J. F. Gainor, R. S. Heist, *Lung cancer*, Elsevier B.V., **2021**.

13 H. Rosling, **2009**, *2010*, 2.

14 W. D. Travis, *Pathology of Lung Cancer*, **2011**.

15 D. N. Haddad, K. L. Sandler, L. M. Henderson, M. P. Rivera, M. C. Aldrich, *Disparities in lung cancer screening: A review*, American Thoracic Society, **2020**.

16 M. B. Schabath, M. L. Cote, *Cancer Epidemiology Biomarkers and Prevention* **2019**, *28*, 1563.

17 C. Zappa, S. A. Mousa, *Transl Lung Cancer Res* **2016**, *5*, 288.

18 C. S. Dela Cruz, L. T. Tanoue, R. A. Matthay, *Lung Cancer: Epidemiology, Etiology, and Prevention*, **2011**.

19 R. G. Blasberg, *Mol Cancer Ther* **2003**, *2*, 335.

20 M. L. James, S. S. Gambhir, *Physiol Rev* **2012**, *92*, 897.

21 O. W. Brawley, B. S. Kramer, *Journal of Clinical Oncology* **2005**, *23*, 293.

22 L. P. Nguyen, R. A. Khan, S. Kang, H. Lee, J. I. Hwang, H. R. Kim, *ACS Omega* **2023**, *8*, 40375.

23 M. F. Kircher, H. Hricak, S. M. Larson, *Mol Oncol* **2012**, *6*, 182.

24 F. Pet, F. Pet, T. Fdg-, L. Sokoloff, D. Chiro, N. Institutes, F. Pet, F. Pet, U. States, F. Pet, T. Q. Although, 31.

25 I. Collins, P. Workman, *New approaches to molecular cancer therapeutics*, Nature Publishing Group, **2006**.

26 S. S. Gambhir, *Molecular imaging of cancer with positron emission tomography*, **2002**.

27 C. Ma, C. W. Lindsley, J. Chang, B. Yu, *Rational Molecular Editing: A New Paradigm in Drug Discovery*, American Chemical Society, **2024**.

28 B. K. Shoichet, S. L. McGovern, B. Wei, J. J. Irwin, *Curr Opin Chem Biol* **2002**, *6*, 439.

29 A. Gallamini, C. Zwarthoed, A. Borra, *Cancers (Basel)* **2014**, *6*, 1821.

30 M. M. Alauddin, Positron emission tomography (PET) imaging with 18F-based radiotracers Positron emission tomography (PET) imaging with F-based radiotracers, **2012**.

31 M. M. Alauddin, *Am J Nucl Med Mol Imaging* **2012**, *2*, 55.

32 M. E. Phelps, *Proc Natl Acad Sci U S A* **2000**, *97*, 9226.

33 M. E. Phelps, Positron emission tomography provides molecular imaging of biological processes, **1999**.

34 S. Jain, V. Chandra, P. Kumar Jain, K. Pathak, D. Pathak, A. Vaidya, *Arabian Journal of Chemistry* **2019**, *12*, 4920.

35 Y. MAO, **2021**.

36 A. S. Hauser, M. M. Attwood, M. Rask-Andersen, H. B. Schiöth, D. E. Gloriam, *Nat Rev Drug Discov* **2017**, *16*, 829.

37 J. Allingham, Brightening Up Brain Injuries: Design, Synthesis and Characterization of a PET Diagnostic Agent for Traumatic Brain Injuries, **2022**.

38 L. Zhang, Y. Li, C. Tian, R. Yang, Y. Wang, H. Xu, Q. Zhu, S. Chen, L. Li, S. Yang, *J Med Chem* **2024**, *67*, 754.

39 C. A. Lipinski, *Drug Discov Today Technol* **2004**, *1*, 337.

40 Y. Ma, F. Gao, *Advances of radiolabeled GRPR ligands for PET/CT imaging of cancers*, BioMed Central Ltd, **2024**.

41 D. K. Lam, D. Dang, J. Zhang, J. C. Dolan, B. L. Schmidt, *Journal of Neuroscience* **2012**, *32*, 14178.

42 G. J. Liao, A. S. Clark, E. K. Schubert, D. A. Mankoff, *Journal of Nuclear Medicine* **2016**, *57*, 1269.

43 M. S. Hofman, R. J. Hicks, *How We Read Oncologic FDG PET/CT*, BioMed Central Ltd., **2016**.

44 Production and use of PET radioisotopes Teacher resource. (2019).

45 P. Lind, I. Igerc, T. Beyer, P. Reinprecht, K. Hausegger, *Eur J Nucl Med Mol Imaging* **2004**, *31*.

46 J. Rong, A. Haider, T. E. Jeppesen, L. Josephson, S. H. Liang, *Radiochemistry for positron emission tomography*, Nature Research, **2023**.

47 M. Piel, I. Vernaleken, F. Rösch, *J Med Chem* **2014**, *57*, 9232.

48 X. Deng, J. Rong, L. Wang, N. Vasdev, L. Zhang, L. Josephson, S. H. Liang, *Angewandte Chemie* **2019**, *131*, 2604.

49 D. Zhao, Design, Synthesis, and Evaluation of Novel Aurora Kinase Inhibitors for Cancer Diagnosis and Therapy.

50 T. Huhtala, P. Poutiainen, J. Rytkönen, K. Lehtimäki, T. Parkkari, I. Kasanen, A. J. Airaksinen, T. Koivula, P. Sweeney, O. Kontkanen, J. Wityak, C. Dominiquez, L. C. Park, *EJNMMI Radiopharm Chem* **2019**, *4*.

51 S. Purser, P. R. Moore, S. Swallow, V. Gouverneur, *Chem Soc Rev* **2008**, *37*, 320.

52 E. P. Gillis, K. J. Eastman, M. D. Hill, D. J. Donnelly, N. A. Meanwell, *J Med Chem* **2015**, *58*, 8315.

53 P. E. Edem, E. J. L. Steen, A. Kjær, M. M. Herth, in *Late-Stage Fluorination of Bioactive Molecules and Biologically-Relevant Substrates*, Elsevier, **2018**, pp. 29–103.

54 O. Jacobson, D. O. Kiesewetter, X. Chen, *Fluorine-18 radiochemistry, labeling strategies and synthetic routes*, American Chemical Society, **2015**.

55 J. Swinson, *Pharmaceuticals* **2005**, 26.

56 N. A. Meanwell, *Fluorine and Fluorinated Motifs in the Design and Application of Bioisosteres for Drug Design*, American Chemical Society, **2018**.

57 M. Chassé, A. Pees, A. Lindberg, S. H. Liang, N. Vasdev, *Chemical Record* **2023**, *23*.

58 E. Salminen, A. Hogg, D. Binns, M. Frydenberg, R. Hicks, *Acta Oncol (Madr)* **2002**, *41*, 425.

59 J. Hou, M. S. Kovacs, S. Dhanvantari, L. G. Luyt, SUPPORTING INFORMATION Development of Candidates for PET Imaging of GHS-R1a in Disease: Design, Synthesis and Evaluation of Fluorine-bearing Quinazolinone Derivatives.

60 P. T. W. Cheng, R. F. Kaltenbach, H. Zhang, J. Shi, S. Tao, J. Li, L. J. Kennedy, S. J. Walker, Y. Shi, Y. Wang, S. Dhanusu, R. Reddigunta, S. Kumaravel, S. Jusuf, D. Smith, S. Krishnananthan, J. Li, T. Wang, R. Heiry, C. S. Sum, S. S. Kalinowski, C. P. Hung, C. H. Chu, A. V. Azzara, M. Ziegler, L. Burns, B. A. Zinker, S. Boehm, J.

Taylor, J. Sapuppo, K. Mosure, G. Everlof, V. Guarino, L. Zhang, Y. Yang, Q. Ruan, C. Xu, A. Apedo, S. C. Traeger, M. E. Cvijic, K. A. Lentz, G. Tirucherai, L. Sivaraman, J. Robl, B. A. Ellsworth, G. Rosen, D. A. Gordon, M. G. Soars, M. Gill, B. J. Murphy, *J Med Chem* **2021**, *64*, 15549.

61 B. Ting Kung, S. Mehdizadeh Seraj, M. Zirakchian Zadeh, C. Rojulpote, E. Kothekar, C. Ayubcha, K. Sing Ng, K. Kiu Ng, T. Kun Au-Yong, T. J. Werner, H. Zhuang, S. J. Hunt, S. Hess, A. Alavi, An update on the role of 18 F-FDG-PET/CT in major infectious and inflammatory diseases, **2019**.

62 R. Boellaard, R. Delgado-Bolton, W. J. G. Oyen, F. Giammarile, K. Tatsch, W. Eschner, F. J. Verzijlbergen, S. F. Barrington, L. C. Pike, W. A. Weber, S. Stroobants, D. Delbeke, K. J. Donohoe, S. Holbrook, M. M. Graham, G. Testanera, O. S. Hoekstra, J. Zijlstra, E. Visser, C. J. Hoekstra, J. Pruim, A. Willemsen, B. Arends, J. Kotzerke, A. Bockisch, T. Beyer, A. Chiti, B. J. Krause, *FDG PET/CT: EANM procedure guidelines for tumour imaging: version 2.0*, Springer Science and Business Media Deutschland GmbH, **2015**.

63 J. Cuaron, M. Dunphy, A. Rimner, *Front Oncol* **2013**, *2 JAN*.

64 J. P. Pijl, P. H. Nienhuis, T. C. Kwee, A. W. J. M. Glaudemans, R. H. J. A. Slart, L. C. Gormsen, *Limitations and Pitfalls of FDG-PET/CT in Infection and Inflammation*, W.B. Saunders, **2021**.

65 C. Bisschop, E. C. de Heer, A. H. Brouwers, G. A. P. Hospers, M. Jalving, *Rational use of 18F-FDG PET/CT in patients with advanced cutaneous melanoma: A systematic review*, Elsevier Ireland Ltd, **2020**.

66 C. Sprinz, M. Zanon, S. Altmayer, G. Watte, K. Irion, E. Marchiori, B. Hochhegger, *Sci Rep* **2018**, *8*.

67 Y. Mao, Design and Synthesis of Small Molecule Ligands Targeting Protease-Activated Receptor 2 as Potential Diagnostic and Therapeutic Agents, **2021**.

68 Y. Mao, Design and Synthesis of Small Molecule Ligands Targeting Protease-Activated Receptor 2 as Potential Diagnostic and Therapeutic Agents, **2021**.

69 R. Lappano, M. Maggiolini, *GPCRs and cancer*, **2012**.

70 M. Spillmann, L. Thurner, N. Romantini, M. Zimmermann, B. Meger, M. Behe, M. Waldhoer, G. F. X. Schertler, P. Berger, *Int J Mol Sci* **2020**, *21*, 1.

71 P. Jeffrey Conn, A. Christopoulos, C. W. Lindsley, *Nat Rev Drug Discov* **2009**, *8*, 41.

72 J. K. Archbold, J. L. Martin, M. J. Sweet, *Towards selective lysophospholipid GPCR modulators*, Elsevier Ltd, **2014**.

73 D. Wacker, R. C. Stevens, B. L. Roth, *How Ligands Illuminate GPCR Molecular Pharmacology*, Cell Press, **2017**.

74 P. Addis, U. Bali, F. Baron, A. Campbell, S. Harborne, L. Jagger, G. Milne, M. Pearce, E. M. Rosethorne, R. Satchell, D. Swift, B. Young, J. F. Unitt, *Key aspects of modern*

GPCR drug discovery, Society for Laboratory Automation and Screening (SLAS), **2024**.

75 B. Trzaskowski, D. Latek, S. Yuan, U. Ghoshdastider, A. Debinski, S. Filipek, *Curr Med Chem* **2012**, *19*, 1090.

76 J. Shonberg, R. C. Kling, P. Gmeiner, S. Löber, *Bioorg Med Chem* **2015**, *23*, 3880.

77 R. B. Clark, *Proc Natl Acad Sci U S A* **2013**, *110*, 5274.

78 C. W. Lindsley, *The top prescription drugs of 2012 globally: Biologics dominate, but small molecule CNS drugs hold on to top spots*, American Chemical Society, **2013**.

79 S. M. Lee, J. M. Booe, A. A. Pioszak, *Eur J Pharmacol* **2015**, *763*, 196.

80 P. K. Chaudhary, S. Kim, *An insight into gpcr and g-proteins as cancer drivers*, MDPI, **2021**.

81 S. Zhang, X. Wang, X. Gao, X. Chen, L. Li, G. Li, C. Liu, Y. Miao, R. Wang, K. Hu, *Radiopharmaceuticals and their applications in medicine*, Springer Nature, **2025**.

82 S. Thompson, M. R. Kilbourn, P. J. H. Scott, *ACS Cent Sci* **2016**, *2*, 497.

83 S. Krajewski, L. Steczek, K. Gotowicz, U. Karczmarczyk, J. Towpik, E. Witkowska-Patena, K. Łyczko, M. Mazur, P. Kozanecki, J. Włostowska, J. Knuuti, M. Dziuk, P. Garnuszek, C. Kozanecki, *EJNMMI Res* **2024**, *14*.

84 X. Chen, M. Hirano, R. A. Werner, M. Decker, T. Higuchi, *ACS Omega* **2018**, *3*, 10460.

85 J. Hou, M. S. Kovacs, S. Dhanvantari, L. G. Luyt, *J Med Chem* **2018**, *61*, 1261.

86 A. H. Bansode, N. Damuka, N. Bashetti, K. K. Gollapelli, I. Krizan, B. Bhoopal, M. Miller, S. K. Jv, C. T. Whitlow, D. McClain, T. Ma, M. J. Jorgensen, K. K. Solingapuram Sai, *J Med Chem* **2023**, *66*, 9120.

87 C. L. Charron, J. Hou, M. S. McFarland, S. Dhanvantari, M. S. Kovacs, L. G. Luyt, *J Med Chem* **2017**, *60*, 7256.

88 K. Wu, L. Xu, L. Cheng, *Comput Math Methods Med* **2021**, *2021*.

89 W. Liu, A. M. Hopkins, J. Hou, *The development of modulators for lysophosphatidic acid receptors: A comprehensive review*, Academic Press Inc., **2021**.

90 W. Liu, A. A. K. Mousa, A. M. Hopkins, Y. F. Wu, K. L. Thu, M. Campbell, S. J. Lees, R. Ramachandran, J. Hou, *ChemMedChem* **2024**, *19*.

91 F. Schaffner, H. H. Versteeg, A. Schillert, N. Yokota, L. C. Petersen, B. M. Mueller, W. Ruf, **2010**.

92 M. W. Majewski, D. M. Gandhi, R. Rosas, R. Kodali, L. A. Arnold, C. Dockendorff, *ACS Med Chem Lett* **2019**, *10*, 121.

93 C. Avet, C. Sturino, S. Grastilleur, C. Le Gouill, M. Semache, F. Gross, L. Gendron, Y. Bennani, J. A. Mancini, C. E. Sayegh, M. Bouvier, *Commun Biol* **2020**, *3*.

94 Y. Tang, Y. Chen, M. Yang, Q. Zheng, Y. Li, Y. Bao, *BMC Musculoskelet Disord* **2022**, *23*.

95 S. L. Pan, K. Y. Tao, J. H. Guh, H. L. Sun, D. Y. Huang, Y. L. Chang, C. M. Teng, *Shock* **2008**, *30*, 496.

96 X. Shi, B. Gangadharan, L. F. Brass, W. Ruf, B. M. Mueller, Protease-Activated Receptors (PAR1 and PAR2) Contribute to Tumor Cell Motility and Metastasis, **2004**.

97 A. Sidduri, D. C. Budd, M. E. Fuentes, T. Lambros, Y. Ren, V. Roongta, R. C. Schoenfeld, P. Gillespie, C. S. Stevenson, T. Truitt, Y. Qian, *Bioorg Med Chem Lett* **2014**, *24*, 4450.

98 M. Srikanth, W. S. Chew, T. Hind, S. M. Lim, N. W. J. Hay, J. H. M. Lee, R. Rivera, J. Chun, W. Y. Ong, D. R. Herr, *Eur J Pharmacol* **2018**, *841*, 49.

99 R. K. Y. Cheng, C. Fiez-Vandal, O. Schlenker, K. Edman, B. Aggeler, D. G. Brown, G. A. Brown, R. M. Cooke, C. E. Dumelin, A. S. Doré, S. Geschwindner, C. Grebner, N. O. Hermansson, A. Jazayeri, P. Johansson, L. Leong, R. Prihandoko, M. Rappas, H. Soutter, A. Snijder, L. Sundström, B. Tehan, P. Thornton, D. Troast, G. Wiggin, A. Zhukov, F. H. Marshall, N. Dekker, *Nature* **2017**, *545*, 112.

100 B. H. Rotstein, N. A. Stephenson, N. Vasdev, S. H. Liang, *Nat Commun* **2014**, *5*.

101 Y. Qian, M. Hamilton, A. Sidduri, S. Gabriel, Y. Ren, R. Peng, R. Kondru, A. Narayanan, T. Truitt, R. Hamid, Y. Chen, L. Zhang, A. J. Fretland, R. A. Sanchez, K. C. Chang, M. Lucas, R. C. Schoenfeld, D. Laine, M. E. Fuentes, C. S. Stevenson, D. C. Budd, *J Med Chem* **2012**, *55*, 7920.

102 H. Sun, G. Tawa, A. Wallqvist, *Classification of scaffold-hopping approaches*, **2012**.

103 O. Trott, A. J. Olson, *J Comput Chem* **2010**, *31*, 455.

104 P. T. W. Cheng, R. F. Kaltenbach, H. Zhang, J. Shi, S. Tao, J. Li, L. J. Kennedy, S. J. Walker, Y. Shi, Y. Wang, S. Dhanusu, R. Reddigunta, S. Kumaravel, S. Jusuf, D. Smith, S. Krishnananthan, J. Li, T. Wang, R. Heiry, C. S. Sum, S. S. Kalinowski, C. P. Hung, C. H. Chu, A. V. Azzara, M. Ziegler, L. Burns, B. A. Zinker, S. Boehm, J. Taylor, J. Sapuppo, K. Mosure, G. Everlof, V. Guarino, L. Zhang, Y. Yang, Q. Ruan, C. Xu, A. Apedo, S. C. Traeger, M. E. Cvijic, K. A. Lentz, G. Tirucherai, L. Sivaraman, J. Robl, B. A. Ellsworth, G. Rosen, D. A. Gordon, M. G. Soars, M. Gill, B. J. Murphy, *J Med Chem* **2021**, *64*, 15549.

105 L. R. Gardell, J. N. Ma, J. G. Seitzberg, A. E. Knapp, H. H. Schiffer, A. Tabatabaei, C. N. Davis, M. Owens, B. Clemons, K. K. Wong, B. Lund, N. R. Nash, Y. Gao, J. Lameh, K. Schmelzer, R. Olsson, E. S. Burstein, *Journal of Pharmacology and Experimental Therapeutics* **2008**, *327*, 799.

106 R. Ramachandran, F. Noorbakhsh, K. Defea, M. D. Hollenberg, *Targeting proteinase-activated receptors: Therapeutic potential and challenges*, **2012**.

107 N. Bunnett, K. DeFea, J. Hamilton, M. D. Hollenberg, R. Ramachandran, J. Trejo, *IUPHAR/BPS Guide to Pharmacology CITE* **2019**, *2019*.

108 M. N. Adams, R. Ramachandran, M. K. Yau, J. Y. Suen, D. P. Fairlie, M. D. Hollenberg, J. D. Hooper, *Structure, function and pathophysiology of protease activated receptors*, Elsevier Inc., **2011**.

109 A. Chandrabalan, R. Ramachandran, *Molecular mechanisms regulating Proteinase-Activated Receptors (PARs)*, Blackwell Publishing Ltd, **2021**.

110 D. M. Rosenbaum, S. G. F. Rasmussen, B. K. Kobilka, *The structure and function of G-protein-coupled receptors*, **2009**.

111 A. J. Venkatakrishnan, X. Deupi, G. Lebon, C. G. Tate, G. F. Schertler, M. Madan Babu, *Molecular signatures of G-protein-coupled receptors*, **2013**.

112 N. Bunnett, K. Defea, J. Hamilton, M. D. Hollenberg, R. Ramachandran, **2019**, 1.

113 M. K. Yau, L. Liu, D. P. Fairlie, *Toward drugs for protease-activated receptor 2 (PAR2)*, **2013**.

114 S. Kagota, K. Maruyama, J. J. McGuire, *Characterization and Functions of Protease-Activated Receptor 2 in Obesity, Diabetes, and Metabolic Syndrome: A Systematic Review*, Hindawi Limited, **2016**.

115 M. Z. Wojtukiewicz, D. Hempel, E. Sierko, S. C. Tucker, K. V. Honn, *Cancer and Metastasis Reviews* **2015**, *34*, 775.

116 M. A. Ayoub, J. P. Pin, *Front Endocrinol (Lausanne)* **2013**, *4*.

117 P. Guo, Y. Tai, M. Wang, H. Sun, L. Zhang, W. Wei, Y. K. Xiang, Q. Wang, *Gα12 and Gα13: Versatility in Physiology and Pathology*, Frontiers Media S.A., **2022**.

118 T. S. Sidhu, S. L. French, J. R. Hamilton, *Differential signaling by protease-activated receptors: Implications for therapeutic targeting*, MDPI AG, **2014**.

119 F. Gieseler, H. Ungefroren, U. Settmacher, M. D. Hollenberg, R. Kaufmann, *Proteinase-activated receptors (PARs) - Focus on receptor-receptor- interactions and their physiological and pathophysiological impact*, **2013**.

120 K. K. Kim, R. Turner, N. Khazan, A. Kodza, A. Jones, R. K. Singh, R. G. Moore, *PLoS One* **2020**, *15*.

121 G. Ma, C. Wang, B. Lv, Y. Jiang, L. Wang, *Archives of Medical Science* **2019**, *15*, 1147.

122 F. Guenther, M. F. Melzig, *Protease-activated receptors and their biological role - Focused on skin inflammation*, Blackwell Publishing Ltd, **2015**.

123 PAR2 induces migration and promotes in lung adenocarcinoma cells.

124 H. Ungefroren, D. Witte, B. H. Rauch, U. Settmacher, H. Lehnert, F. Gieseler, R. Kaufmann, *Proteinase-activated receptor 2 may drive cancer progression by facilitating TGF-β signaling*, MDPI AG, **2017**.

125 N. Qian, X. Li, X. Wang, C. Wu, L. Yin, X. Zhi, *Oncol Lett* **2018**, *16*, 1513.

126 J. R. Lindner, M. L. Kahn, S. R. Coughlin, G. R. Sambrano, E. Schauble, D. Bernstein, D. Foy, A. Hafezi-Moghadam, K. Ley, *The Journal of Immunology* **2000**, *165*, 6504.

127 N. N. Jimenez-Vargas, L. A. Pattison, P. Zhao, T. M. Lieu, R. Latorre, D. D. Jensen, J. Castro, L. Aurelio, G. T. Le, B. Flynn, C. K. Herenbrink, H. R. Yeatman, L. Edgington-Mitchell, C. J. H. Porter, M. L. Halls, M. Canals, N. A. Veldhuis, D. P. Poole, P. McLean, G. A. Hicks, N. Scheff, E. Chen, A. Bhattacharya, B. L. Schmidt, S. M. Brierley, S. J. Vanner, N. W. Bunnett, *Proc Natl Acad Sci U S A* **2018**, *115*, E7438.

128 M. Sébert, N. Sola-Tapias, E. Mas, F. Barreau, A. Ferrand, *Protease-Activated Receptors in the Intestine: Focus on Inflammation and Cancer*, Frontiers Media S.A., **2019**.

129 T. Kanke, H. Ishiwata, M. Kabeya, M. Saka, T. Doi, Y. Hattori, A. Kawabata, R. Plevin, *Br J Pharmacol* **2005**, *145*, 255.

130 O. Pierre, M. Fouchard, P. Buscaglia, N. Le Goux, R. Leschiera, O. Mignen, J. W. Fluhr, L. Misery, R. Le Garrec, *Cells* **2020**, *9*, 1.

131 Y. Li, H. Huang, X. Chen, N. Yu, X. Ye, L. Chen, Z. Huang, *Tissue Cell* **2022**, *79*.

132 W. Pao, J. Chmielecki, *Rational, biologically based treatment of EGFR-mutant non-small-cell lung cancer*, **2010**.

133 Treatment of Non-small Cell Lung Cancer with EGFR-mutations.

134 K. Xu, L. Wang, M. Lin, G. He, *Update on protease-activated receptor 2 in inflammatory and autoimmune dermatological diseases*, **2024**.

135 Y. Jiang, J. Lim, K. C. Wu, W. Xu, J. Y. Suen, D. P. Fairlie, *Br J Pharmacol* **2021**, *178*, 913.

136 Y. Jiang, X. Zhuo, X. Fu, Y. Wu, C. Mao, *Front Pharmacol* **2021**, *12*.

137 M. Shaikh, Y. Shinde, R. Pawara, M. Noolvi, S. Surana, I. Ahmad, H. Patel, *J Med Chem* **2022**, *65*, 1008.

138 F. Xu, X. Zhang, Z. Chen, S. He, J. Guo, L. Yu, Y. Wang, C. Hou, H. Ai-Furas, Z. Zheng, J. B. Smaill, A. V. Patterson, Z. M. Zhang, L. Chen, X. Ren, K. Ding, *J Med Chem* **2022**, *65*, 14032.

139 Y. Jiang, X. Zhuo, Y. Wu, X. Fu, C. Mao, *Biochim Biophys Acta Mol Cell Res* **2022**, *1869*.

140 J. R. Hamilton, J. Trejo, *Challenges and opportunities in protease-activated receptor drug development*, Annual Reviews Inc., **2017**.

141 M. K. Yau, L. Liu, J. Y. Suen, J. Lim, R. J. Lohman, Y. Jiang, A. J. Cotterell, G. D. Barry, J. Y. W. Mak, D. A. Vesey, R. C. Reid, D. P. Fairlie, *ACS Med Chem Lett* **2016**, *7*, 1179.

142 J. C. LeSarge, P. Thibeault, L. Yu, M. D. Childs, V. M. Mirka, Q. Qi, M. S. Fox, M. S. Kovacs, R. Ramachandran, L. G. Luyt, *Eur J Med Chem* **2023**, *246*.

143 R. Ramachandran, A. Eissa, K. Mihara, K. Oikonomopoulou, M. Saifeddine, B. Renaux, E. Diamandis, M. D. Hollenberg, Biological Chemistry, 421–427.

144 Q. Sun, Y. Wang, J. Zhang, J. Lu, *Sci Rep* **2017**, *7*.

145 Y. Wang, M. Lin, H. Weng, X. Wang, L. Yang, F. Liu, *Am J Obstet Gynecol* **2014**, *210*, 531.e1.

146 J. Y. Suen, G. D. Barry, R. J. Lohman, M. A. Halili, A. J. Cotterell, G. T. Le, D. P. Fairlie, *Br J Pharmacol* **2012**, *165*, 1413.

147 S. P.- Agonists, B. W. Lund, S. M. Bertozzi, E. A. Currier, J. Ma, V. Sherbukhin, E. S. Burstein, R. Olsson, S. Valley, V. Boule, **2008**, 5490.

148 Y. Jiang, M. K. Yau, J. Lim, K. C. Wu, W. Xu, J. Y. Suen, D. P. Fairlie, *Journal of Pharmacology and Experimental Therapeutics* **2018**, *364*, 246.

149 A. J. Kennedy, L. Sundström, S. Geschwindner, E. K. Y. Poon, Y. Jiang, R. Chen, R. Cooke, S. Johnstone, A. Madin, J. Lim, Q. Liu, R. J. Lohman, A. Nordqvist, M. Fridén-Saxin, W. Yang, D. G. Brown, D. P. Fairlie, N. Dekker, *Commun Biol* **2020**, *3*.

150 Kennedy, Protease-activated receptor-2 ligands reveal orthosteric and allosteric mechanisms of receptor inhibition.

151 A. Leggio, E. L. Belsito, G. De Luca, M. L. Di Gioia, V. Leotta, E. Romio, C. Siciliano, A. Liguori, *RSC Adv* **2016**, *6*, 34468.

152 P. Devi, S. M. Barry, K. M. Houlihan, M. J. Murphy, P. Turner, P. Jensen, P. J. Rutledge, *Sci Rep* **2015**, *5*.

153 A. De La Hoz, P. Prieto, Microwave-Assisted Green Organic Synthesis, **2016**.

154 E. Berrino, C. T. Supuran, *Advances in microwave-assisted synthesis and the impact of novel drug discovery*, Taylor and Francis Ltd, **2018**.

155 J. P. Tierney, P. Lidström, *Microwave Assisted Organic Synthesis i Microwave Assisted Organic Synthesis Edited*, **2007**.

156 C. Kramer, A. Ting, H. Zheng, J. Hert, T. Schindler, M. Stahl, G. Robb, J. J. Crawford, J. Blaney, S. Montague, A. G. Leach, A. G. Dossetter, E. J. Griffen, *J Med Chem* **2018**, *61*, 3277.

157 W. Jung, S. Goo, T. Hwang, H. Lee, Y. K. Kim, J. W. Chae, H. Y. Yun, S. Jung, *Pharmaceuticals* **2024**, *17*.

158 R. Wilcken, M. O. Zimmermann, A. Lange, A. C. Joerger, F. M. Boeckler, *Principles and applications of halogen bonding in medicinal chemistry and chemical biology*, American Chemical Society, **2013**.

159 Z. Xu, Z. Yang, Y. Liu, Y. Lu, K. Chen, W. Zhu, *J Chem Inf Model* **2014**, *54*, 69.

160 M. Balkenhohl, P. Knochel, *Recent Advances of the Halogen–Zinc Exchange Reaction*, Wiley-VCH Verlag, **2020**.

161 Y. Zhu, L. Chen, W. Hou, Y. Li, *Recent Progress in Nucleophilic Fluoride Mediated Fluorine-18 Labeling of Arenes and Heteroarenes*, Science Press, **2021**.

162 J. Jampilek, *Molecules* **2019**, *24*, 10.

163 M. M. Heravi, V. Zadsirjan, *RSC Adv* **2020**, *10*, 44247.

164 R. Guha, *Methods in Molecular Biology* **2013**, *993*, 81.

165 K. Banert, J. Seifert, *Organic Chemistry Frontiers* **2019**, *6*, 3517.

166 A. Buchler, U. S. Ismailani, N. MacMullin, F. Abdirahman, M. Adi, C. Bi, C. Jany, J. W. Keillor, B. H. Rotstein, *J Med Chem* **2023**, *66*, 6682.

167 S. Kumari, A. V. Carmona, A. K. Tiwari, P. C. Trippier, *Amide Bond Bioisosteres: Strategies, Synthesis, and Successes*, American Chemical Society, **2020**.

168 Q. Guan, S. Xing, L. Wang, J. Zhu, C. Guo, C. Xu, Q. Zhao, Y. Wu, Y. Chen, H. Sun, *Triazoles in Medicinal Chemistry: Physicochemical Properties, Bioisosterism, and Application*, American Chemical Society, **2024**.

169 G. R. Krow, R. Edupuganti, D. Gandla, F. Yu, M. Sender, P. E. Sonnet, M. J. Zdilla, C. Debrosse, K. C. Cannon, C. W. Ross, A. Choudhary, M. D. Shoulders, R. T. Raines, *Journal of Organic Chemistry* **2011**, *76*, 3626.

170 D. M. Heuberger, R. A. Schuepbach, *Protease-activated receptors (PARs): Mechanisms of action and potential therapeutic modulators in PAR-driven inflammatory diseases*, BioMed Central Ltd., **2019**.

171 EC50 and relative activity for 2f-LIGRL-NH 2 and trypsin in the presence of AZ3451 in CHO-hPAR2 cells.

172 E. Jin, M. Fujiwara, X. Pan, M. Ghazizadeh, S. Arai, Y. Ohaki, K. Kajiwara, T. Takemura, O. Kawanami, *Cancer* **2003**, *97*, 703.

173 W. Scholarship, J. C. LeSarge, S. Luyt, Design, Synthesis, and Evaluation of Novel Protease-Activated Design, Synthesis, and Evaluation of Novel Protease-Activated Receptor 2 (PAR2)-Targeting Imaging Agents for Cancer Receptor 2 (PAR2)-Targeting Imaging Agents for Cancer.

174 S. Lee, J. Xie, X. Chen, *Chem Rev* **2010**, *110*, 3087.

175 S. Haddadzadegan, F. Dorkoosh, A. Bernkop-Schnürch, *Oral delivery of therapeutic peptides and proteins: Technology landscape of lipid-based nanocarriers*, Elsevier B.V., **2022**.

176 M. A. Ayoub, J. P. Pin, *Front Endocrinol (Lausanne)* **2013**, *4*.

177 B. H. Rotstein, L. Wang, R. Y. Liu, J. Patteson, E. E. Kwan, N. Vasdev, S. H. Liang, *Chem Sci* **2016**, *7*, 4407.

178 B. H. Rotstein, L. Wang, R. Y. Liu, J. Patteson, E. E. Kwan, N. Vasdev, S. H. Liang, Supporting Information Mechanistic Studies and Radiofluorination of Structurally Diverse Pharmaceuticals with Spirocyclic Iodonium(III) Ylides, **2016**.

179 S. H. Liang, L. Wang, N. A. Stephenson, B. H. Rotstein, N. Vasdev, *Nat Protoc* **2019**, *14*, 1530.

180 U. S. Ismailani, A. Buchler, G. Farber, A. Pekošak, E. Farber, N. MacMullin, E. J. Suuronen, N. Vasdev, R. S. B. Beanlands, R. A. De Kemp, B. H. Rotstein, *ACS Chem Neurosci* **2021**, *12*, 4350.

181 M.-E. Lin, D. R. Herr, J. Chun, .

182 by Jerold Chun, T. Hla, S. Spiegel, W. Moolenaar, H. Mirendil, M. Lin, J. Chun, Lysophospholipid Receptors: Signaling and Biochemistry, First Edition, **2013**.

183 H. Xiang, Y. Lu, M. Shao, T. Wu, *Lysophosphatidic acid receptors: Biochemical and clinical implications in different diseases*, Ivyspring International Publisher, **2020**.

184 I. González-Gil, D. Zian, H. Vázquez-Villa, S. Ortega-Gutiérrez, M. L. López-Rodríguez, *The status of the lysophosphatidic acid receptor type 1 (LPA1R)*, Royal Society of Chemistry, **2015**.

185 Y. H. Lin, Y. C. Lin, C. C. Chen, *Lysophosphatidic acid receptor antagonists and cancer: The current trends, clinical implications, and trials*, MDPI, **2021**.

186 K. C. Tran, J. Zhao, *Lysophosphatidic Acid Regulates Rho Family of GTPases in Lungs*, Springer, **2021**.

187 J. E. Chrencik, C. B. Roth, M. Terakado, H. Kurata, R. Omi, Y. Kihara, D. Warshaviak, S. Nakade, G. Asmar-Rovira, M. Mileni, H. Mizuno, M. T. Griffith, C. Rodgers, G. W. Han, J. Velasquez, J. Chun, R. C. Stevens, M. A. Hanson, *Cell* **2015**, *161*, 1633.

188 B. S. Shea, A. M. Tager, Lysophospholipid Regulation of Lung Fibrosis.

189 Y. C. Yung, N. C. Stoddard, J. Chun, *LPA receptor signaling: Pharmacology, physiology, and pathophysiology*, American Society for Biochemistry and Molecular Biology Inc., **2014**.

190 L. H. M. Geraldo, T. C. L. de S. Spohr, R. F. do Amaral, A. C. C. da Fonseca, C. Garcia, F. de A. Mendes, C. Freitas, M. F. dosSantos, F. R. S. Lima, *Role of lysophosphatidic acid and its receptors in health and disease: novel therapeutic strategies*, Springer Nature, **2021**.

191 S. M. Schleicher, D. K. Thotala, A. G. Linkous, R. Hu, K. M. Leahy, E. M. Yazlovitskaya, D. E. Hallahan, *PLoS One* **2011**, *6*.

192 S. Dedoni, C. Camoglio, C. Siddi, M. Scherma, W. Fratta, P. Fadda, *Future Pharmacology* **2024**, *4*, 199.

193 X. Tang, M. G. K. Benesch, D. N. Brindley, *Role of the autotaxin–lysophosphatidate axis in the development of resistance to cancer therapy*, Elsevier B.V., **2020**.

194 by Jerold Chun, T. Hla, S. Spiegel, W. Moolenaar, H. Mirendil, M. Lin, J. Chun, Lysophospholipid Receptors: Signaling and Biochemistry, First Edition, **2013**.

195 B. E. Decato, D. J. Leeming, J. M. B. Sand, A. Fischer, S. Du, S. M. Palmer, M. Karsdal, Y. Luo, A. Minnich, *Respir Res* **2022**, *23*.

196 J. E. Chrencik, C. B. Roth, M. Terakado, H. Kurata, R. Omi, Y. Kihara, D. Warshaviak, S. Nakade, G. Asmar-Rovira, M. Mileni, H. Mizuno, M. T. Griffith, C. Rodgers, G. W. Han, J. Velasquez, J. Chun, R. C. Stevens, M. A. Hanson, *Cell* **2015**, *161*, 1633.

197 B. S. Shea, A. M. Tager, Lysophospholipid Regulation of Lung Fibrosis.

198 B. Mehić, L. Duranović Rayan, N. Bilalović, D. Dohranović Tafro, I. Pilav, *BMC Cancer* **2016**, *16*.

199 B. S. Shea, A. M. Tager, Lysophospholipid Regulation of Lung Fibrosis.

200 A. Chanakira, P. R. Westmark, I. M. Ong, J. P. Sheehan, *Gynecol Oncol* **2017**, *145*, 167.

201 R. Leblanc, O. Peyruchaud, *New insights into the autotaxin/LPA axis in cancer development and metastasis*, Academic Press Inc., **2015**.

202 D. C. Budd, Y. Qian, *Development of lysophosphatidic acid pathway modulators as therapies for fibrosis.*, **2013**.

203 Y. Ren, L. Guo, X. Tang, S. Apparsundaram, C. Kitson, J. Deguzman, M. E. Fuentes, L. Coyle, R. Majmudar, J. Allard, T. Truitt, R. Hamid, Y. Chen, Y. Qian, D. C. Budd, *Microvasc Res* **2013**, *85*, 59.

204 A. Gomez-Larrauri, P. Gangoiti, L. Camacho, N. Presa, C. Martin, A. Gomez-Muñoz, *Biomedicines* **2023**, *11*.

205 M. Pazhouhandeh, F. Samiee, T. Boniadi, A. F. Khedmat, E. Vahedi, M. Mirdamadi, N. Sigari, S. D. Siadat, F. Vaziri, A. Fateh, F. Ajorloo, E. Tafsiri, M. Ghanei, F. Mahboudi, F. Rahimi Jamnani, *Sci Rep* **2017**, *7*.

206 R. Ray, N. Jangde, S. K. Singh, S. Sinha, V. Rai, *Cell Communication and Signaling* **2020**, *18*.

207 C. Magkrioti, N. Oikonomou, E. Kaffe, M. A. Mouratis, N. Xylourgidis, I. Barbayianni, P. Megadoukas, V. Harokopos, C. Valavanis, J. Chun, A. Kosma, G. T. Stathopoulos, E. Bouros, D. Bouros, K. Syrigos, V. Aidinis, *Cancer Res* **2018**, *78*, 3634.

208 G. Mao, S. S. Smyth, A. J. Morris, *Journal of Biological Chemistry* **2019**, *294*, 14009.

209 M. C. Olianas, S. Dedoni, P. Onali, *Biochem Pharmacol* **2015**, *95*, 311.

210 M. Centonze, G. Di Conza, M. Lahn, I. Fabregat, F. Dituri, I. Gigante, G. Serino, R. Scialpi, L. Carrieri, R. Negro, E. Pizzuto, G. Giannelli, *Journal of Experimental and Clinical Cancer Research* **2023**, *42*.

211 A. Kazlauskas, *Lysophosphatidic acid contributes to angiogenic homeostasis*, Academic Press Inc., **2015**.

212 Y. Kihara, H. Mizuno, J. Chun, *Lysophospholipid receptors in drug discovery*, Academic Press Inc., **2015**.

213 H. Akasaka, F. K. Sano, W. Shihoya, O. Nureki, *Commun Biol* **2024**, *7*, 1444.

214 T. Sato, K. Sugimoto, A. Inoue, S. Okudaira, J. Aoki, H. Tokuyama, *Bioorg Med Chem Lett* **2012**, *22*, 4323.

215 M. W. Gill, B. J. Murphy, P. T. W. Cheng, L. Sivaraman, M. Davis, L. Lehman-McKeeman, *Toxicol Appl Pharmacol* **2022**, *438*.

216 B. P. Gaire, A. Sapkota, J. W. Choi, *Antioxidants* **2020**, *9*, 1.

217 T. J. Corte, L. Lancaster, J. J. Swigris, T. M. Maher, J. G. Goldin, S. M. Palmer, T. Suda, T. Ogura, A. Minnich, X. Zhan, G. S. Tirucherai, B. Elpers, H. Xiao, H. Watanabe, R. A. Smith, E. D. Charles, A. Fischer, *BMJ Open Respir Res* **2021**, *8*.

218 Corporate/Financial News CORPORATE NEWS DETAILS Bristol Myers Squibb's Investigational LPA1 Antagonist Reduces Rate of Lung Function Decline in Progressive Pulmonary Fibrosis Cohort of Phase 2 Study, **2023**.

219 M. Terakado, H. Suzuki, K. Hashimura, M. Tanaka, H. Ueda, H. Kohno, T. Fujimoto, H. Saga, S. Nakade, H. Habashita, Y. Takaoka, T. Seko, *ACS Med Chem Lett* **2016**, *7*, 913.

220 C. Lescop, C. Brotschi, J. T. Williams, C. P. Sager, M. Birker, K. Morrison, S. Froidevaux, S. Delahaye, O. Nayler, M. H. Bolli, *J Med Chem* **2024**, *67*, 2379.

221 J. E. Olsen, DEVELOPMENT OF SMALL MOLECULE LIGANDS TARGETING THE LYSOPHOSPHATIDIC ACID RECEPTOR 1 FOR PET IMAGING.

222 S. Singh Gujral, S. Khatri, P. Riyal, V. Gahlot, *Indo Global Journal of Pharmaceutical Sciences* **2012**, *02*, 351.

223 L. K. Rasmussen, B. C. Boren, V. V. Fokin, Org Lett 2007, 9, 5337.

224 L. K. Rasmussen, B. C. Boren, V. V. Fokin, *Org Lett* **2007**, *9*, 5337.

225 B. C. Boren, S. Narayan, L. K. Rasmussen, L. Zhang, H. Zhao, Z. Lin, G. Jia, V. V. Fokin, *J Am Chem Soc* **2008**, *130*, 8923.

226 J. R. Johansson, T. Beke-Somfai, A. Said Stålsmeden, N. Kann, *Ruthenium-Catalyzed Azide Alkyne Cycloaddition Reaction: Scope, Mechanism, and Applications*, American Chemical Society, **2016**.

227 L. K. Rasmussen, B. C. Boren, V. V. Fokin, *Org Lett* **2007**, *9*, 5337.

228 R. Hopson, P. Y. B. Lee, K. M. Hess, *J Chem Educ* **2018**, *95*, 641.

229 S. Munawar, A. F. Zahoor, S. Ali, S. Javed, M. Irfan, A. Irfan, K. Kotwica-Mojzych, M. Mojzych, *Mitsunobu Reaction: A Powerful Tool for the Synthesis of Natural Products: A Review*, MDPI, **2022**.

230 S. D. Lepore, Y. He, *Journal of Organic Chemistry* **2003**, *68*, 8261.

231 S. Munawar, A. F. Zahoor, S. Ali, S. Javed, M. Irfan, A. Irfan, K. Kotwica-Mojzych, M. Mojzych, *Mitsunobu Reaction: A Powerful Tool for the Synthesis of Natural Products: A Review*, MDPI, **2022**.

232 P. S. Humphries, Q. Q. T. Do, D. M. Wilhite, *Beilstein Journal of Organic Chemistry* **2006**, *2*.

233 M. J. Vainio, T. Kogej, F. Raubacher, J. Sadowski, *J Chem Inf Model* **2013**, *53*, 1825.

234 Y. Hu, D. Stumpfe, J. Bajorath, *Recent Advances in Scaffold Hopping*, American Chemical Society, **2017**.

235 C. Lamberth, *Ring Closure and Ring Opening as Useful Scaffold Hopping Tools in Agrochemistry*, American Chemical Society, **2023**.

236 S. Y. Ho, J. Alam, D. A. Jeyaraj, W. Wang, G. R. Lin, S. H. Ang, E. S. W. Tan, M. A. Lee, Z. Ke, B. Madan, D. M. Virshup, L. J. Ding, V. Manoharan, Y. S. Chew, C. B. Low, V. Pendharkar, K. Sangthongpitag, J. Hill, T. H. Keller, A. Poulsen, *J Med Chem* **2017**, *60*, 6678.

237 A. M. Hopkins, Design, Synthesis, and Evaluation of Novel Lysophosphatidic Acid Receptor-Targeting Small Molecules as Therapeutic and Diagnostic Agents.

238 A. Acharya, M. Yadav, M. Nagpure, S. Kumaresan, S. K. Guchhait, *Molecular medicinal insights into scaffold hopping-based drug discovery success*, Elsevier Ltd, **2024**.

239 WO2014135244A1

240 J. S. Swaney, C. Chapman, L. D. Correa, K. J. Stebbins, R. A. Bundey, P. C. Prodanovich, P. Fagan, C. S. Baccei, A. M. Santini, J. H. Hutchinson, T. J. Seiders, T. A. Parr, P. Prasit, J. F. Evans, D. S. Lorrain, *Br J Pharmacol* **2010**, *160*, 1699.

241 WO2015144799

242 M. T. Huggins, T. Kesharwani, J. Buttrick, C. Nicholson, *J Chem Educ* **2020**, *97*, 1425.

243 WO 2014113485A1

244 WO 20121492809

245 C. M. Stapleton, D. G. Mashek, S. Wang, C. A. Nagle, G. W. Cline, P. Thuillier, L. M. Leesnitzer, L. O. Li, J. B. Stimmel, G. I. Shulman, R. A. Coleman, *PLoS One* **2011**, *6*.

246 J. D. Gallezot, N. B. Nabulsi, D. Holden, S. F. Lin, D. Labaree, J. Ropchan, S. Najafzadeh, D. J. Donnelly, K. Cao, S. Bonacorsi, J. Seiders, J. Roppe, W. Hayes, Y. Huang, S. Du, R. E. Carson, *Journal of Nuclear Medicine* **2018**, *59*, 327.

247 Spirocyclic hypervalent iodine(III)-mediated radiofluorination supply information.

248 T. J. Corte, V. Cottin, M. K. Glassberg, M. Kreuter, T. Ogura, T. Suda, J. G. Goldin, E. Berkowitz, B. Elpers, S. Kim, G. S. Tirucherai, H. Watanabe, A. Fischer, T. M. Maher, BMS-986278, an Oral Lysophosphatidic Acid Receptor 1 (LPA1) Antagonist,

for Patients With Idiopathic Pulmonary Fibrosis: Results From a Phase 2 Randomized Trial.

249 C. Chatgilialoglu, J. Lalevée, *Recent applications of the (TMS) 3SiH radical-based reagent*, **2012**.

Appendix A - Characterization Data of Chapter 2

Results of Mass Spectroscopy and HPLC purity

AZ3451

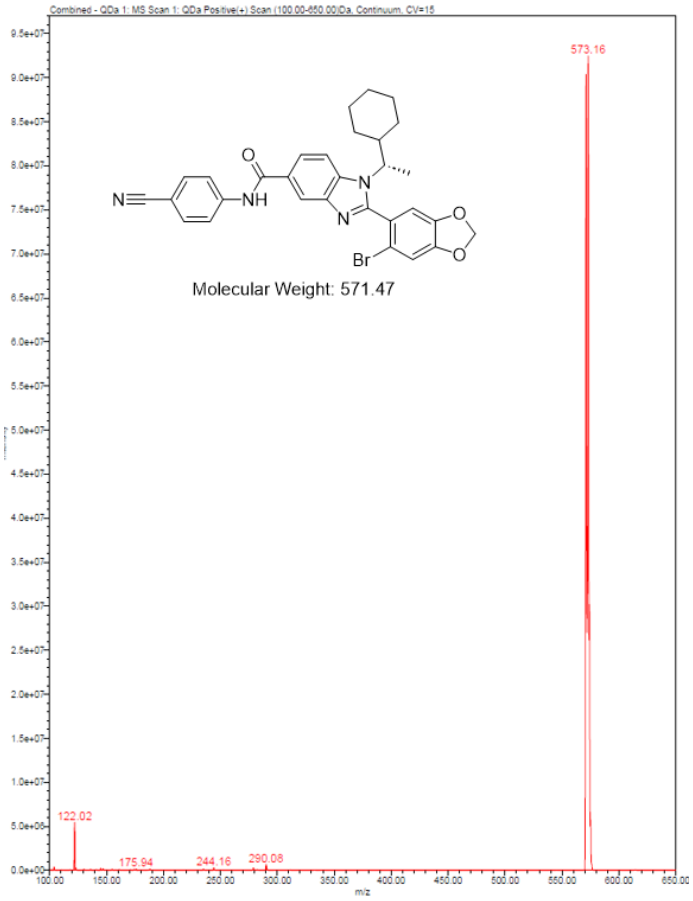

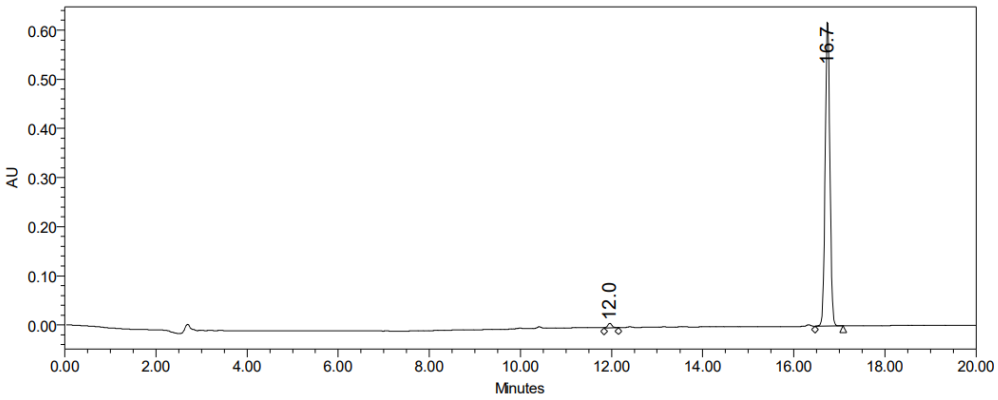

Channel: W2489 ChA; Processed Channel: W2489 ChA 254nm; Result Id: 2247; Processing Method: PM_Yang

Processed Channel Descr.: W2489 ChA 254nm

	Processed Channel Descr.	RT	Area	% Area	Height
1	W2489 ChA 254nm	11.963	58778	1.30	8797
2	W2489 ChA 254nm	16.741	4465103	98.70	622203

Compound P1c

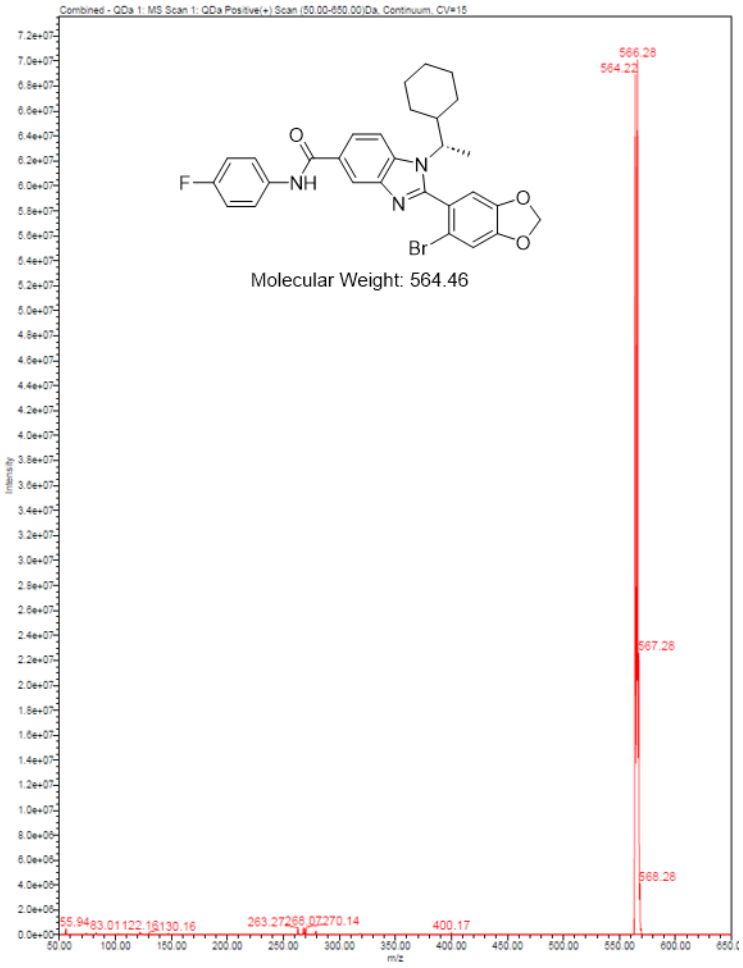

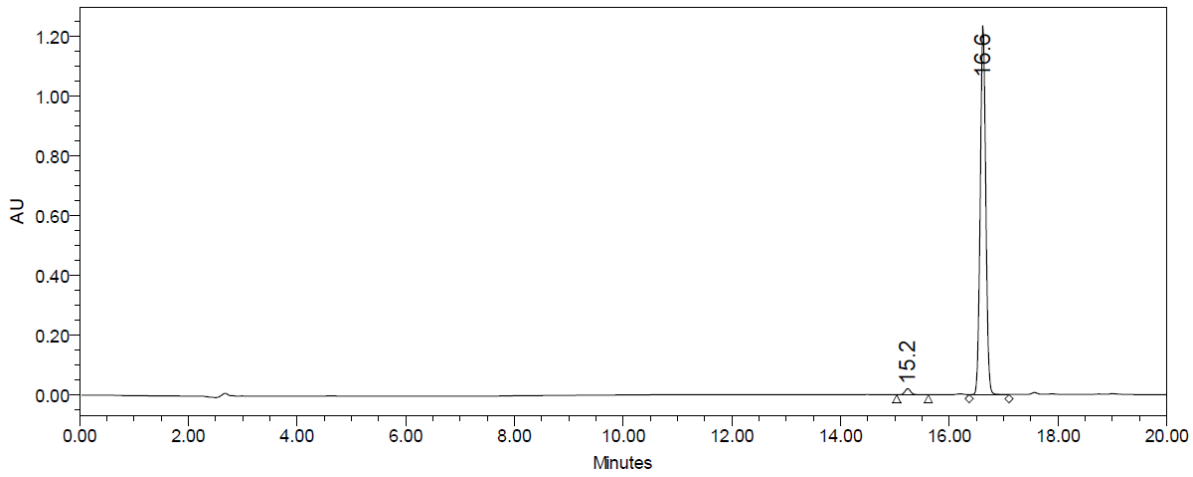

Channel: W2489 ChA; Processed Channel: W2489 ChA 254nm; Result Id: 24136; Processing Method: PM_Yang

Processed Channel Descr.: W2489 ChA 254nm

	Processed Channel Descr.	RT	Area	% Area	Height
1	W2489 ChA 254nm	15.236	150815	1.70	20456
2	W2489 ChA 254nm	16.621	8725009	98.30	1232536

Compound P1h.

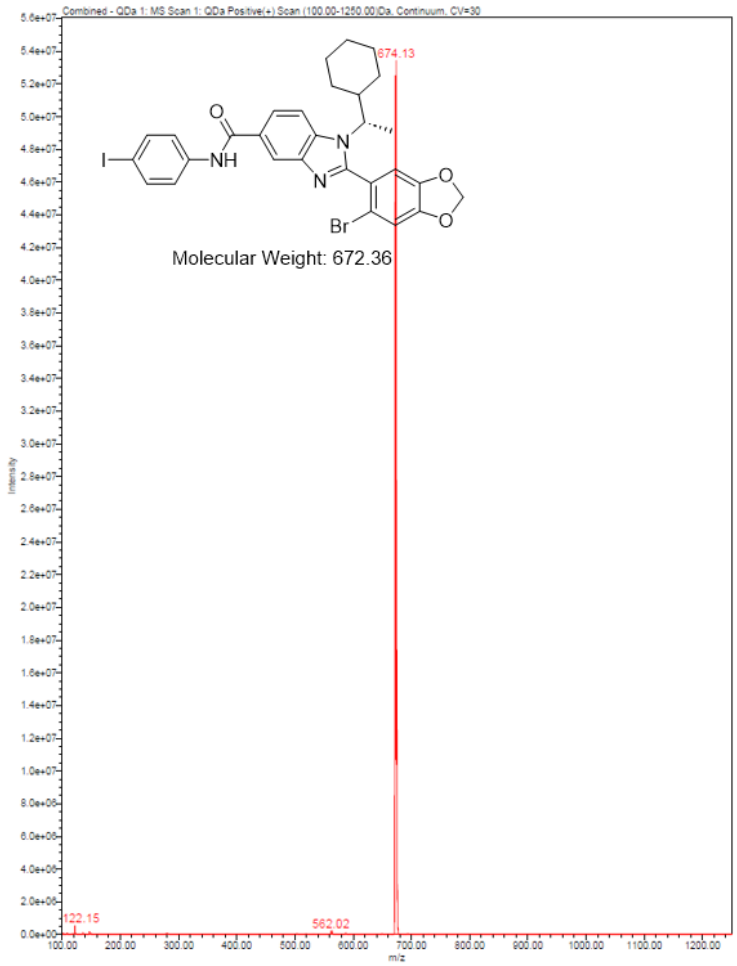

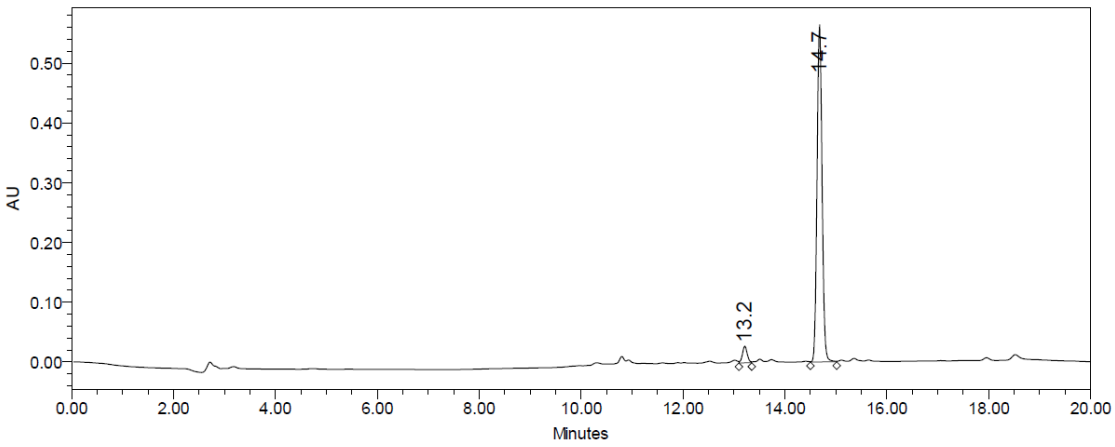

Channel: W2489 ChA; Processed Channel: W2489 ChA 254nm; Result Id: 23590; Processing Method: PM_Yang

Processed Channel Descr.: W2489 ChA 254nm

	Processed Channel Descr.	RT	Area	% Area	Height
1	W2489 ChA 254nm	13.215	181152	4.47	27708
2	W2489 ChA 254nm	14.681	3871295	95.53	562548

Compound P1k.

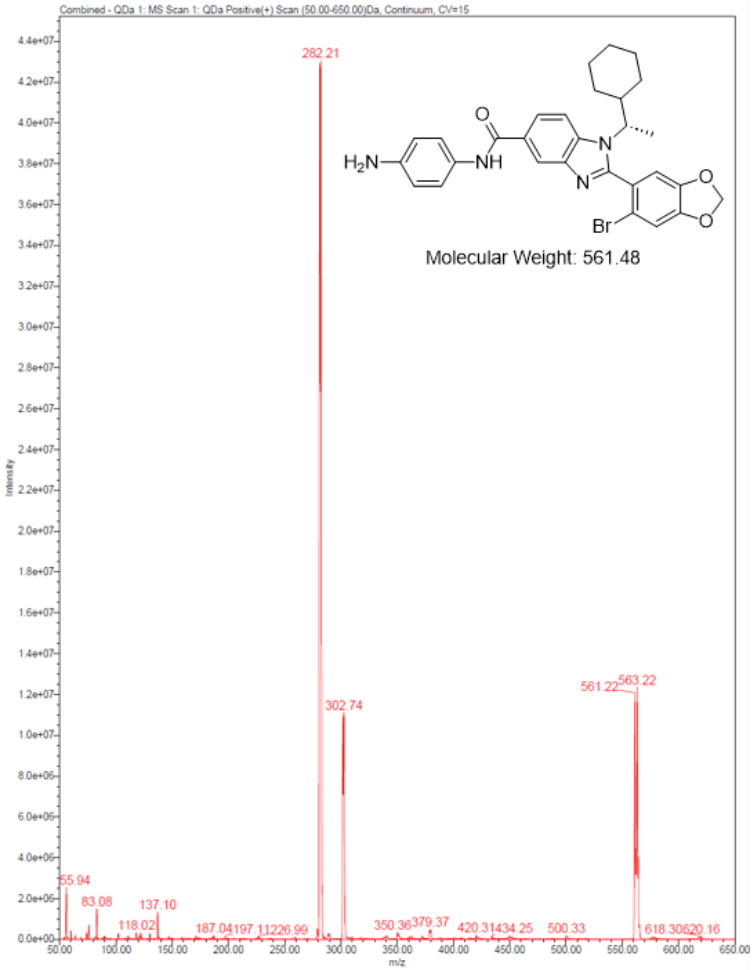

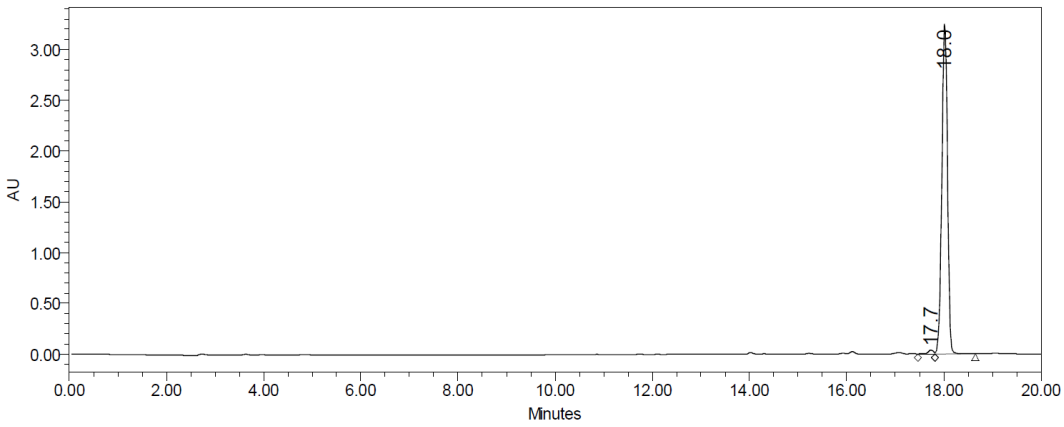

Channel: W2489 ChA; Processed Channel: W2489 ChA 254nm; Result Id: 11095; Processing Method: PM_Yang

Processed Channel Descr.: W2489 ChA 254nm

	Processed Channel Descr.	RT	Area	% Area	Height
1	W2489 ChA 254nm	17.736	282097	1.06	37785
2	W2489 ChA 254nm	18.020	26208079	98.94	3249103

Compound P1l.

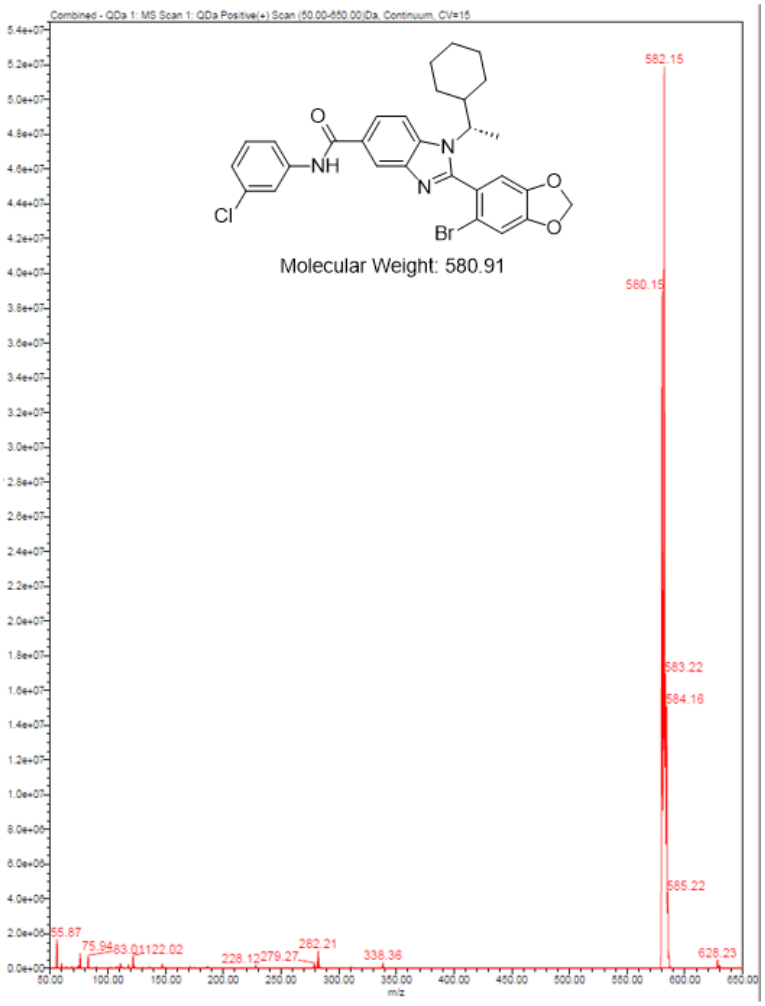

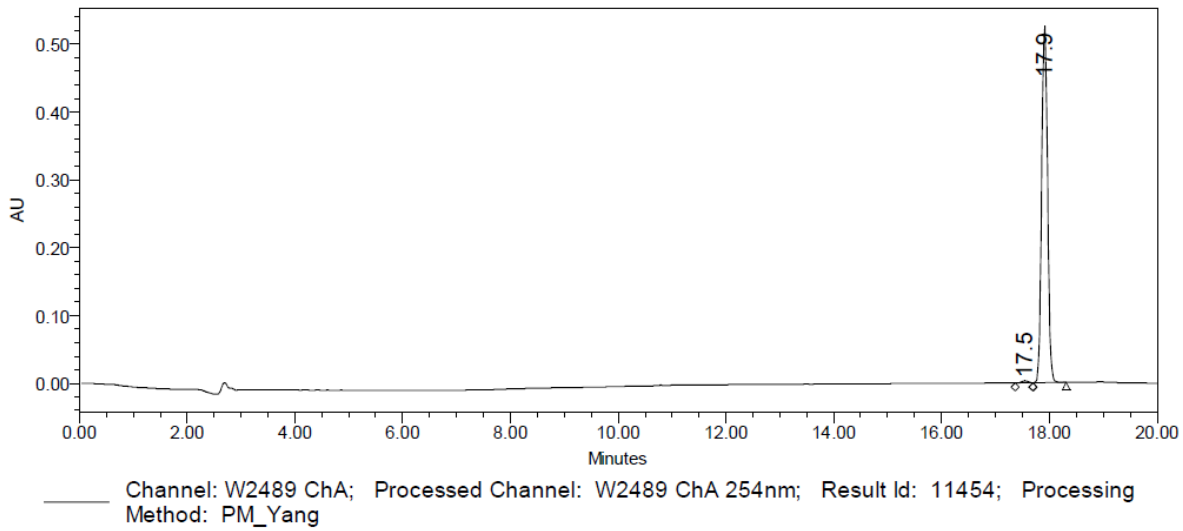

Channel: W2489 ChA; Processed Channel: W2489 ChA 254nm; Result Id: 11454; Processing Method: PM_Yang

Processed Channel Descr.: W2489 ChA 254nm

	Processed Channel Descr.	RT	Area	% Area	Height
1	W2489 ChA 254nm	17.547	27327	0.68	3191
2	W2489 ChA 254nm	17.914	3972570	99.32	524497

Compound P1m.

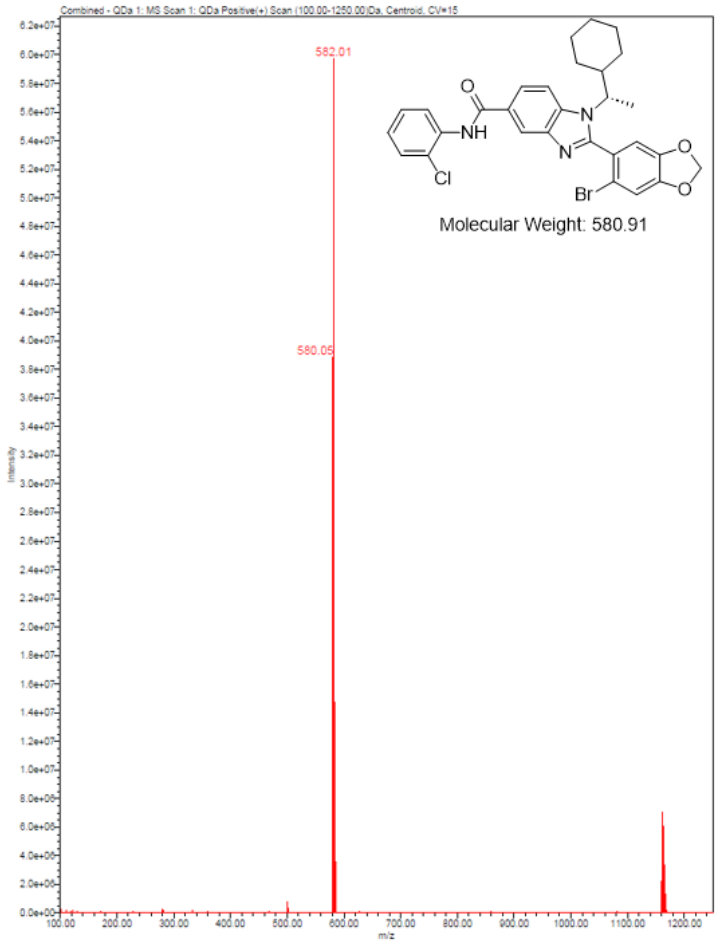

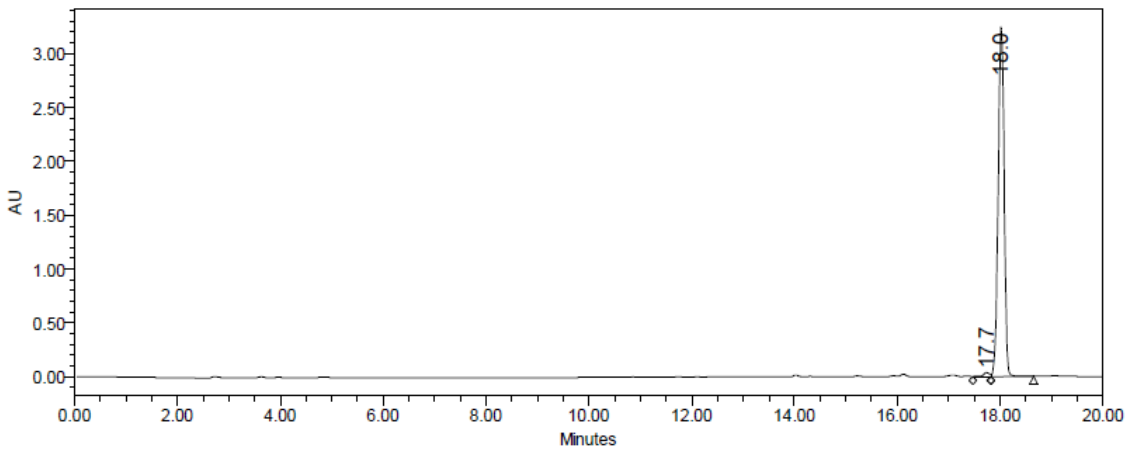

Channel: W2489 ChA; Processed Channel: W2489 ChA 254nm; Result Id: 11095; Processing Method: PM_Yang

Processed Channel Descr.: W2489 ChA 254nm

	Processed Channel Descr.	RT	Area	% Area	Height
1	W2489 ChA 254nm	17.736	282097	1.06	37785
2	W2489 ChA 254nm	18.020	26208079	98.94	3249103

Compound P1n.

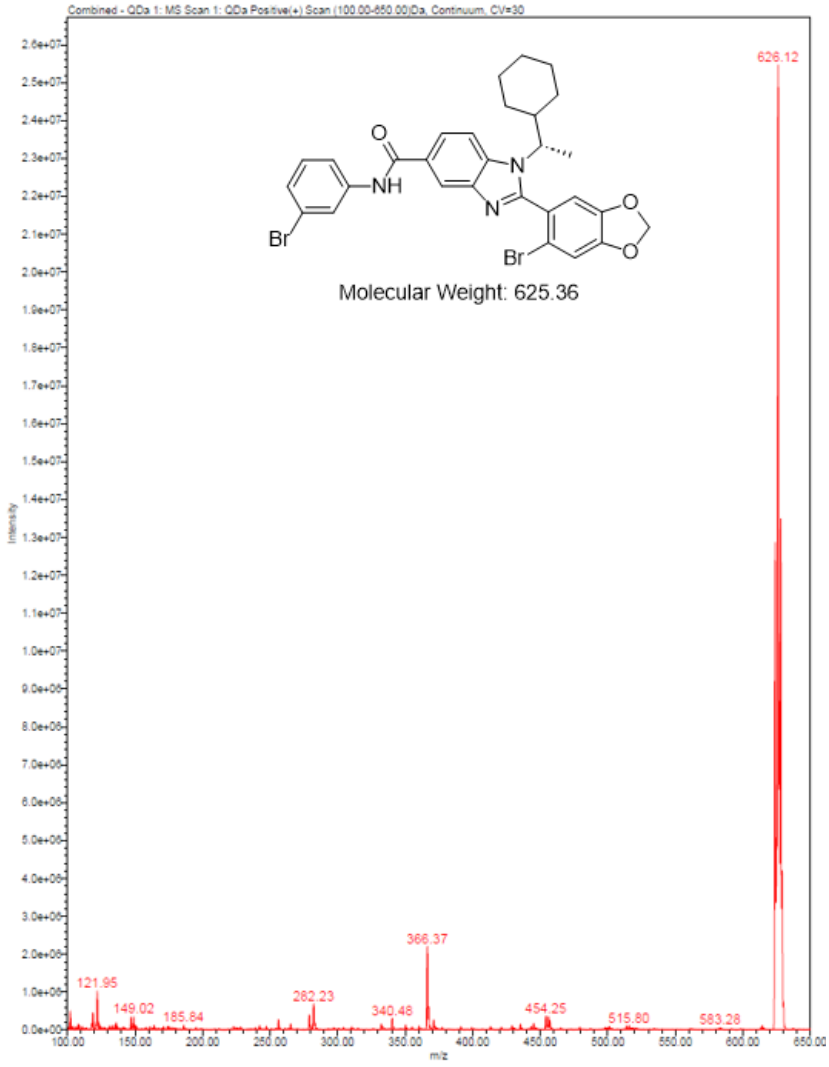

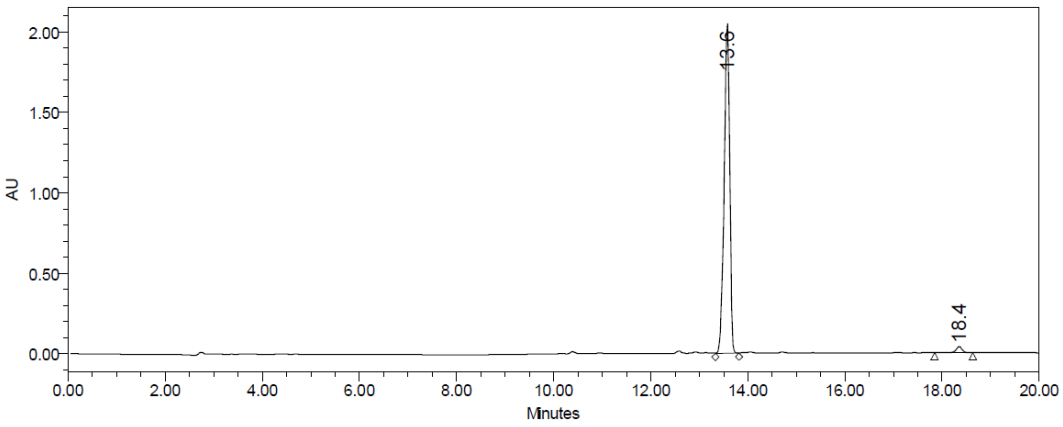

Channel: W2489 ChA; Processed Channel: W2489 ChA 254nm; Result Id: 11091; Processing Method: PM_Yang

Processed Channel Descr.: W2489 ChA 254nm

	Processed Channel Descr.	RT	Area	% Area	Height
1	W2489 ChA 254nm	13.578	16274758	97.94	2052216
2	W2489 ChA 254nm	18.354	341803	2.06	38582

Compound P2e.

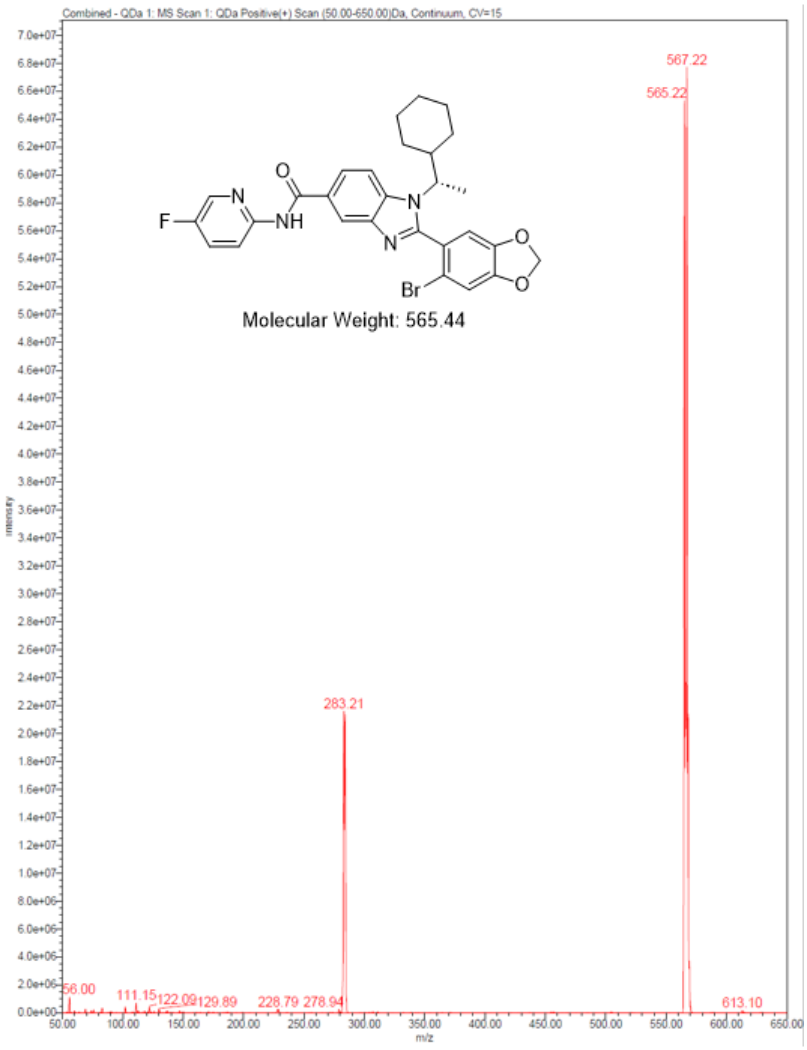

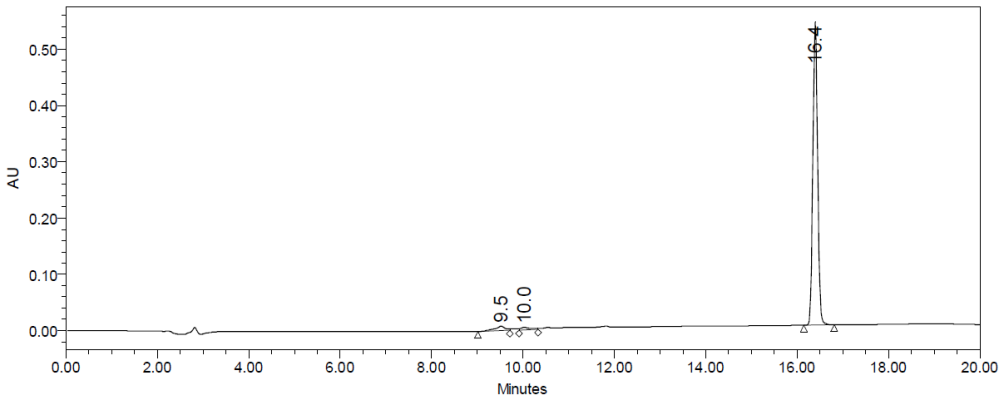

Channel: W2489 ChA; Processed Channel: W2489 ChA 254nm; Result Id: 13242; Processing Method: PM_Yang

Processed Channel Descr.: W2489 ChA 254nm

	Processed Channel Descr.	RT	Area	% Area	Height
1	W2489 ChA 254nm	9.530	125271	3.04	7958
2	W2489 ChA 254nm	10.038	64695	1.57	4273
3	W2489 ChA 254nm	16.400	3929587	95.39	536103

Compound P2f.

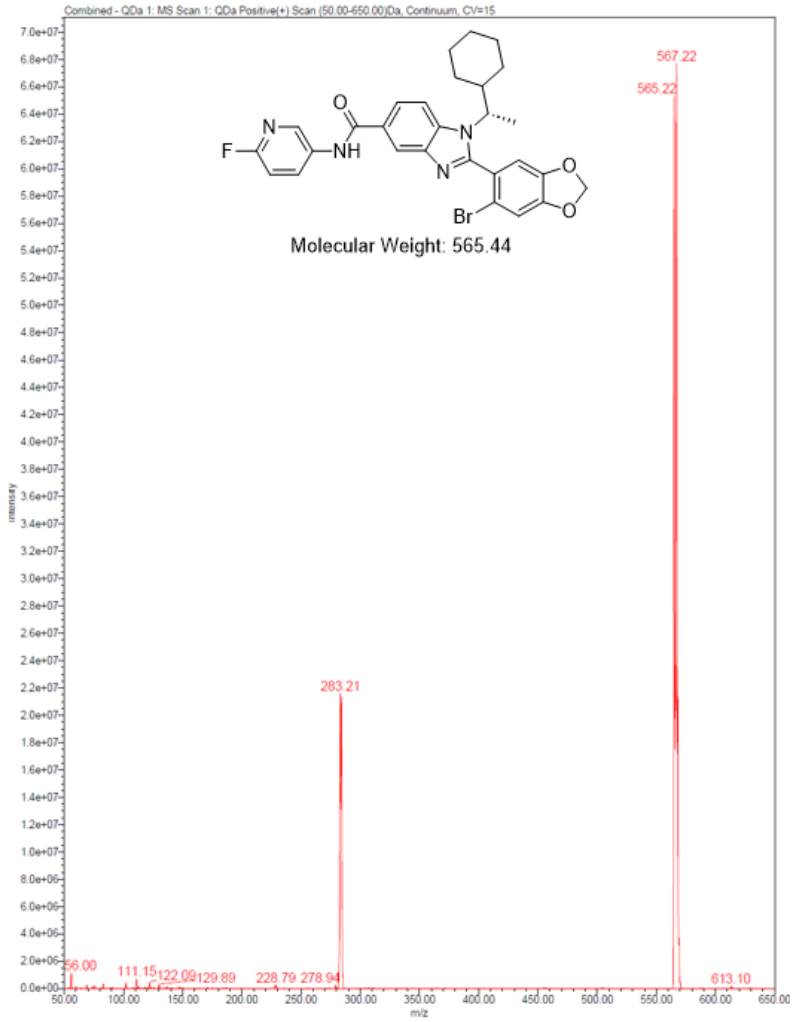

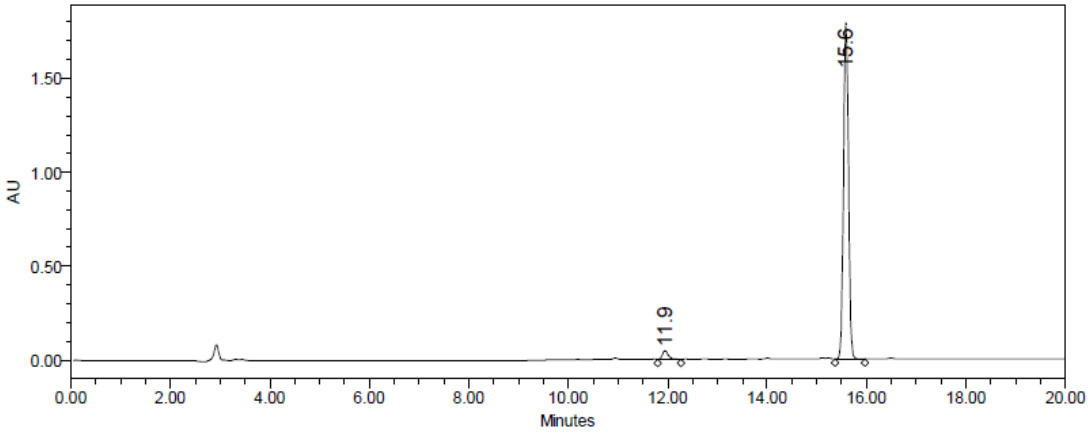

Channel: W2489 ChA; Processed Channel: W2489 ChA 254nm; Result Id: 12360; Processing Method: PM_Yang

Processed Channel Descr.: W2489 ChA 254nm

	Processed Channel Descr.	RT	Area	% Area	Height
1	W2489 ChA 254nm	11.944	372895	2.90	46125
2	W2489 ChA 254nm	15.585	12493723	97.10	1783305

Compound P2g.

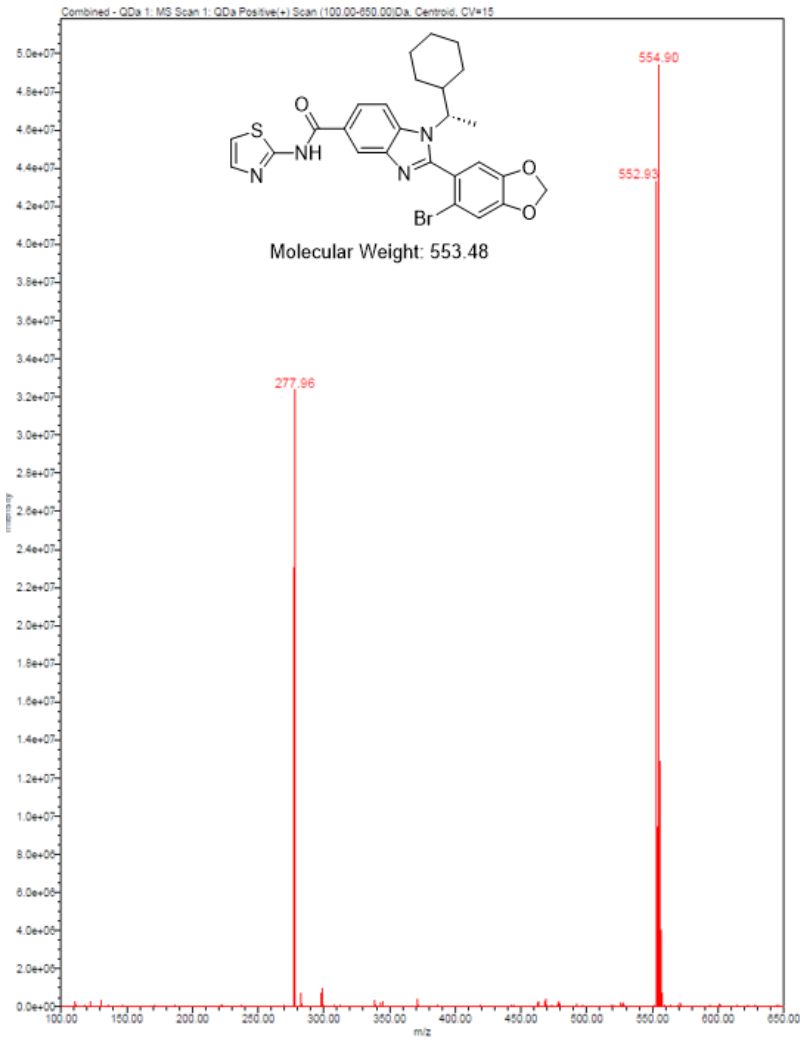

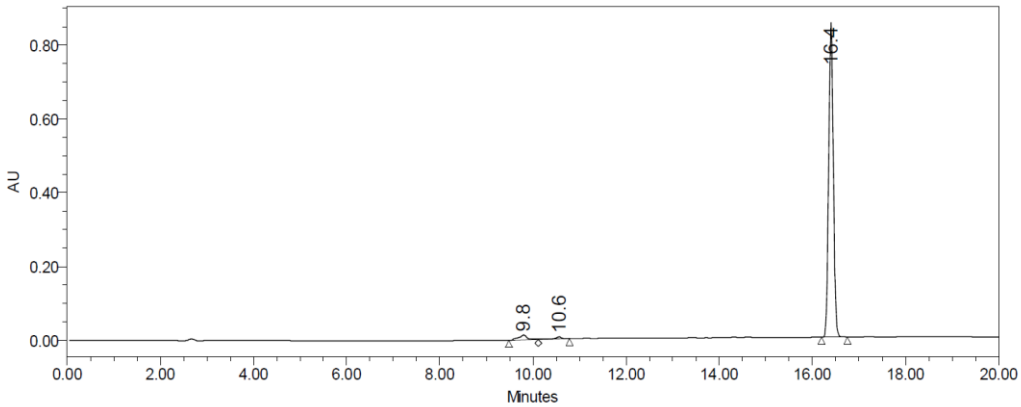

Channel: W2489 ChA; Processed Channel: W2489 ChA 254nm; Result Id: 16437; Processing Method: PM_Yang

Processed Channel Descr.: W2489 ChA 254nm

	Processed Channel Descr.	RT	Area	% Area	Height
1	W2489 ChA 254nm	9.800	185351	2.98	13649
2	W2489 ChA 254nm	10.562	70013	1.13	5660
3	W2489 ChA 254nm	16.400	5960071	95.89	849343

Compound P2h.

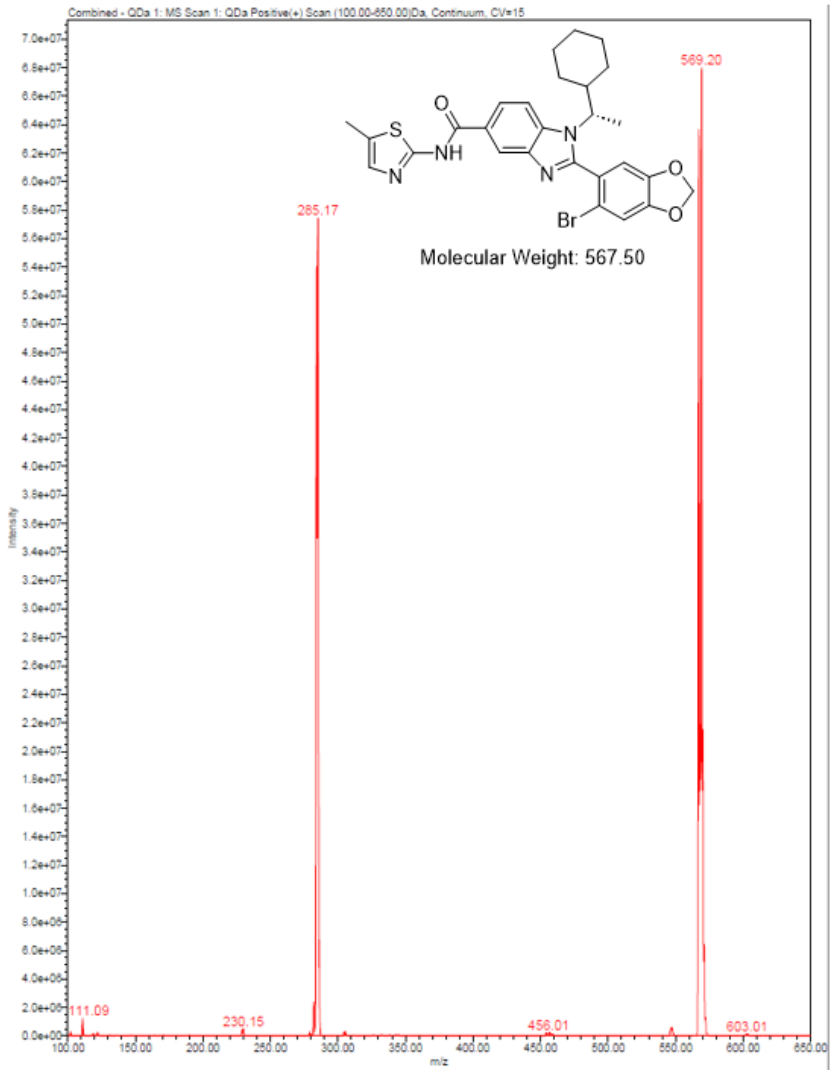

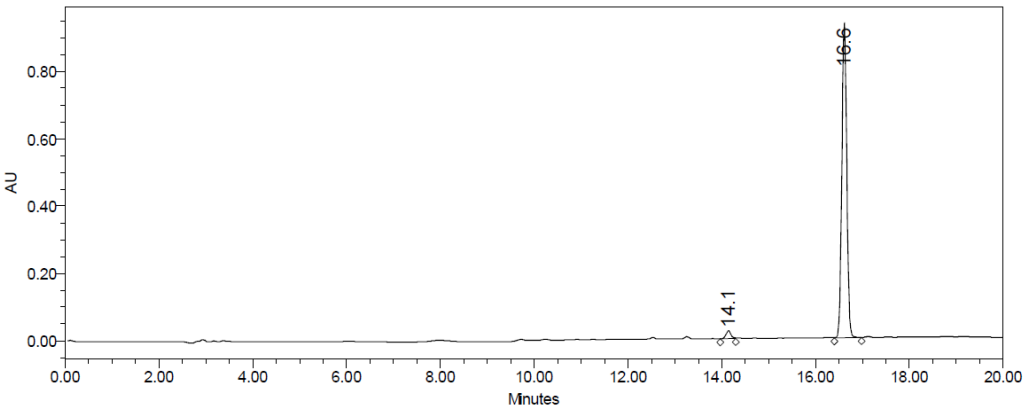

Channel: W2489 ChA; Processed Channel: W2489 ChA 254nm; Result Id: 11099; Processing Method: PM_Yang

Processed Channel Descr.: W2489 ChA 254nm

	Processed Channel Descr.	RT	Area	% Area	Height
1	W2489 ChA 254nm	14.143	166760	2.39	22470
2	W2489 ChA 254nm	16.615	6815530	97.61	932910

Compound P2i.

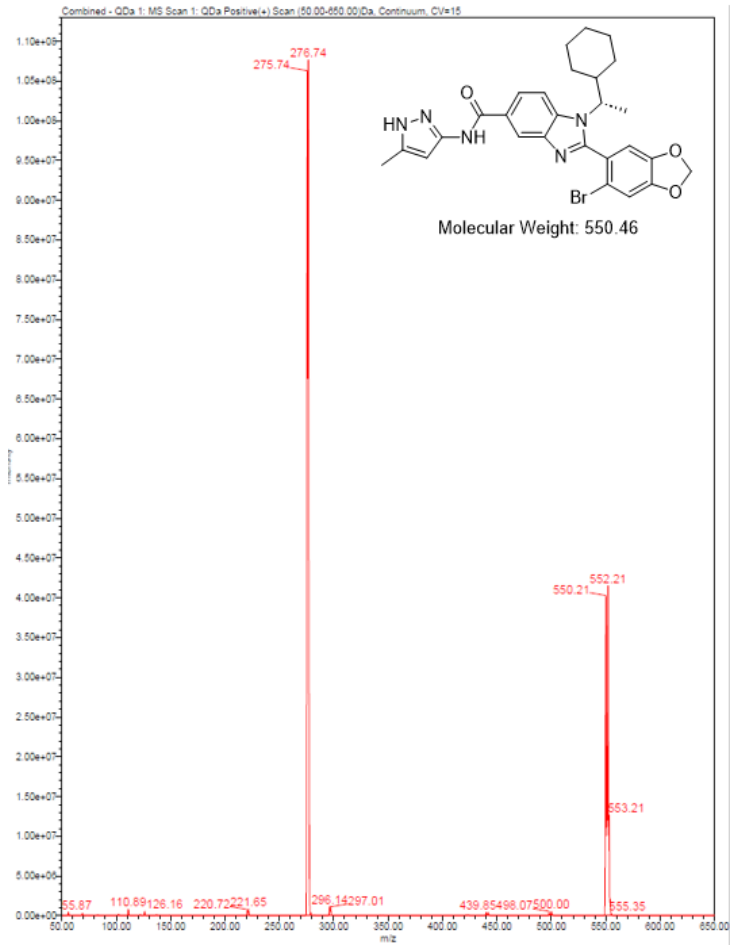

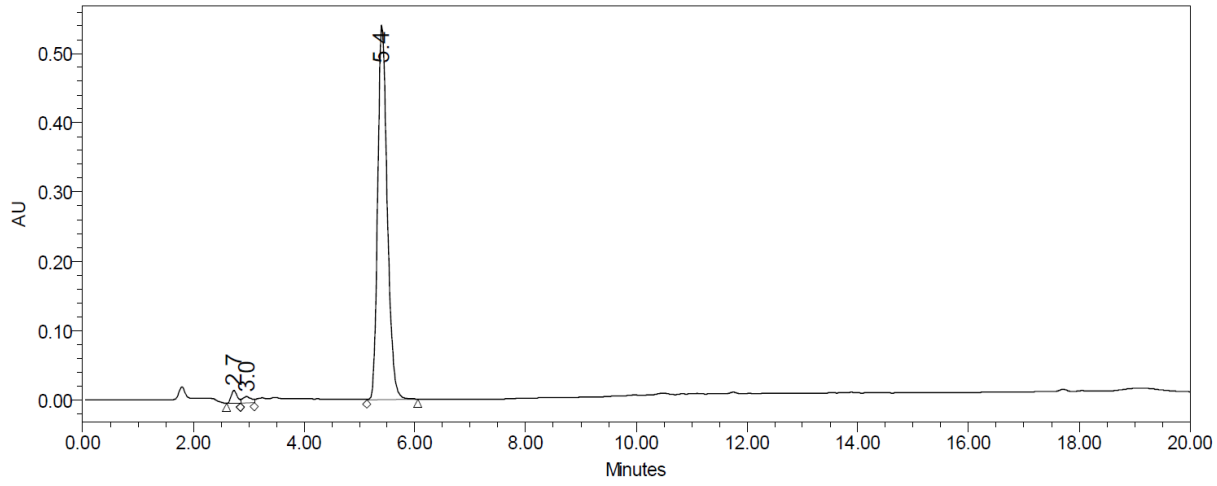

Channel: W2489 ChA; Processed Channel: W2489 ChA 254nm; Result Id: 16433; Processing Method: PM_Yang

Processed Channel Descr.: W2489 ChA 254nm

	Processed Channel Descr.	RT	Area	% Area	Height
1	W2489 ChA 254nm	2.734	137182	2.02	18365
2	W2489 ChA 254nm	2.963	100101	1.48	8783
3	W2489 ChA 254nm	5.404	6537573	96.50	541583

Compound P3f.

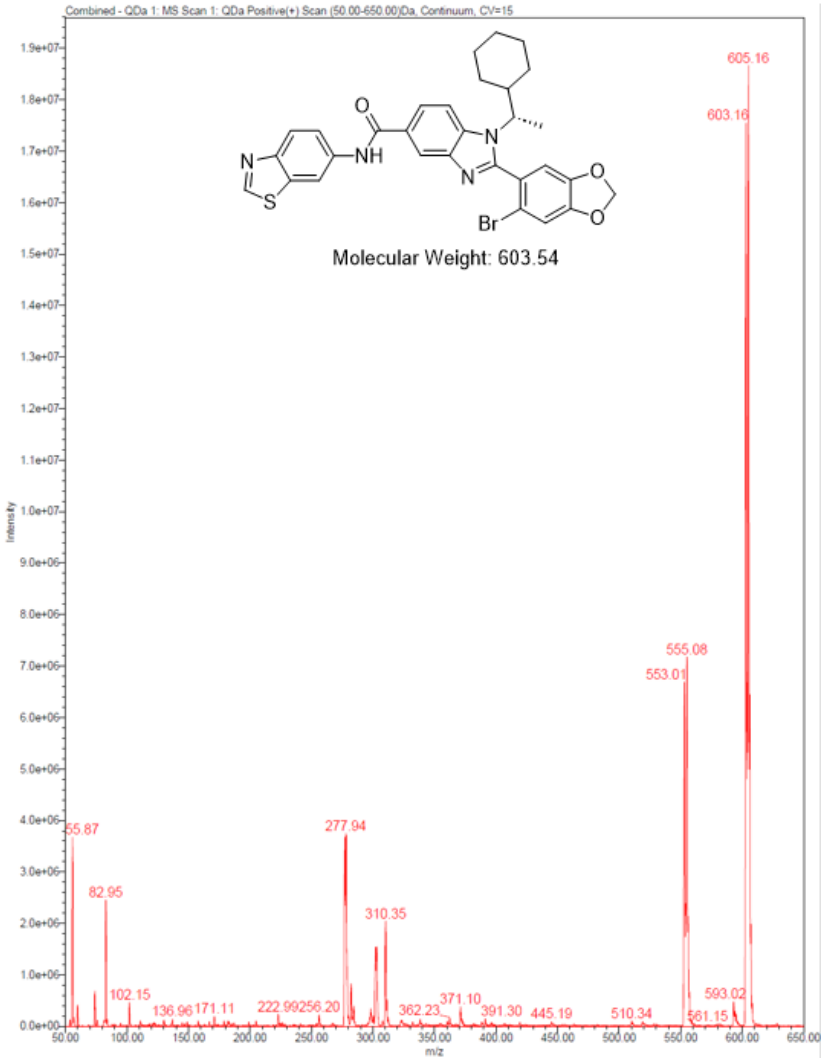

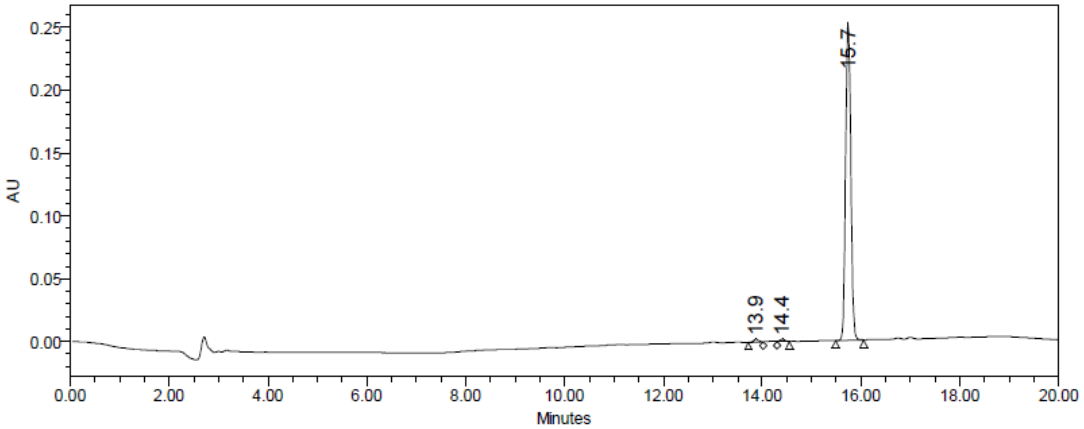

Channel: W2489 ChA; Processed Channel: W2489 ChA 254nm; Result Id: 11083; Processing Method: PM_Yang

Processed Channel Descr.: W2489 ChA 254nm

	Processed Channel Descr.	RT	Area	% Area	Height
1	W2489 ChA 254nm	13.874	16290	0.88	2340
2	W2489 ChA 254nm	14.404	12673	0.68	1880
3	W2489 ChA 254nm	15.738	1824190	98.44	252787

Compound P3g.

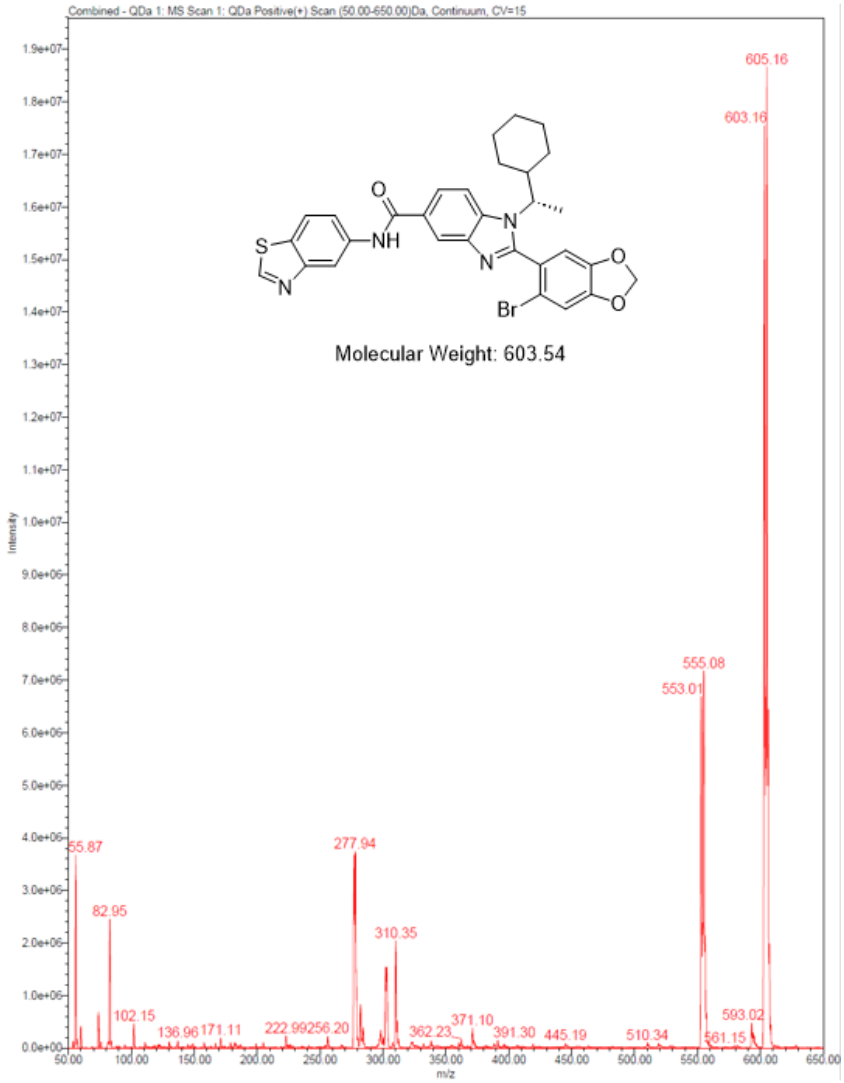

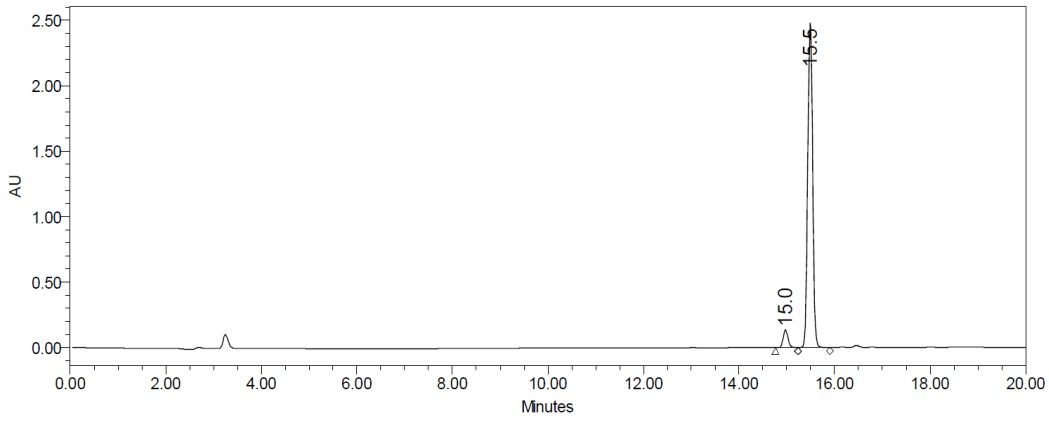

Channel: W2489 ChA; Processed Channel: W2489 ChA 254nm; Result Id: 16441; Processing Method: PM_Yang

Processed Channel Descr.: W2489 ChA 254nm

	Processed Channel Descr.	RT	Area	% Area	Height
1	W2489 ChA 254nm	14.973	957169	5.18	135038
2	W2489 ChA 254nm	15.490	17507260	94.82	2491351

Compound P3h.

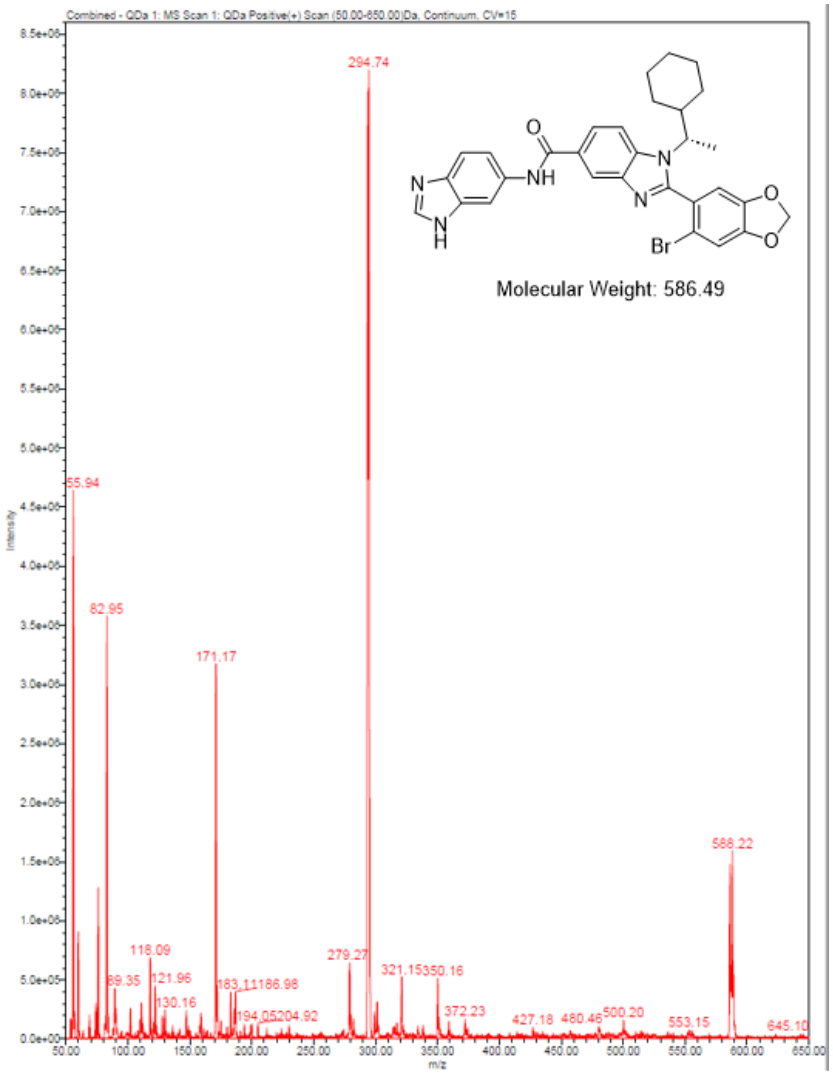

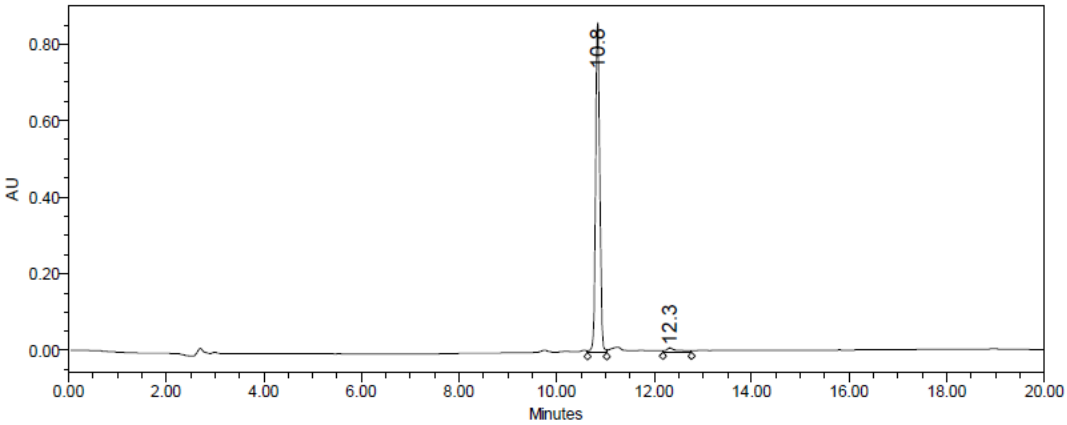

Channel: W2489 ChA; Processed Channel: W2489 ChA 254nm; Result Id: 11389; Processing Method: PM_Yang

Processed Channel Descr.: W2489 ChA 254nm

	Processed Channel Descr.	RT	Area	% Area	Height
1	W2489 ChA 254nm	10.844	5177340	96.17	864864
2	W2489 ChA 254nm	12.321	206064	3.83	11739

Compound P3i.

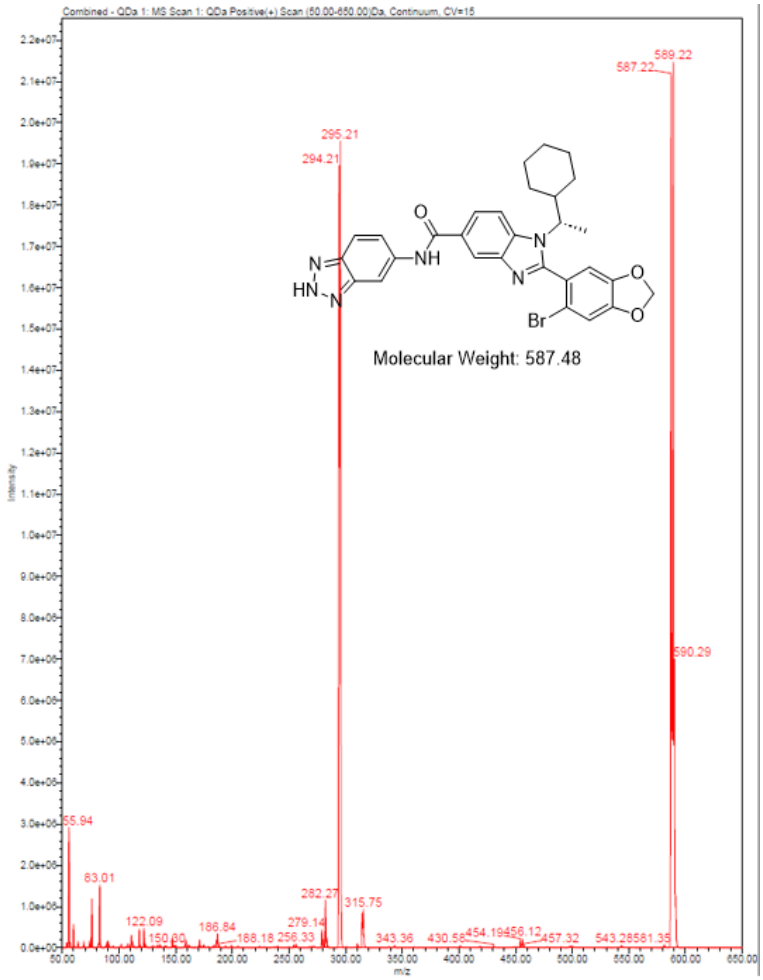

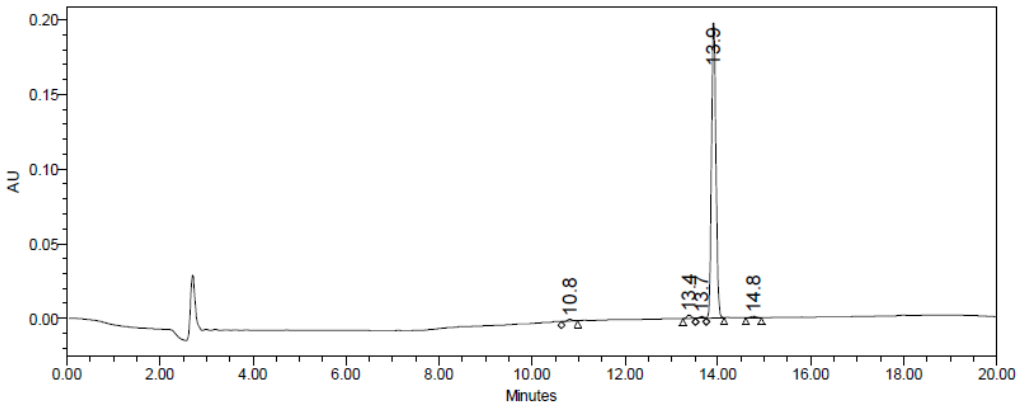

Channel: W2489 ChA; Processed Channel: W2489 ChA 254nm; Result Id: 11602; Processing Method: PM_Yang

Processed Channel Descr.: W2489 ChA 254nm

	Processed Channel Descr.	RT	Area	% Area	Height
1	W2489 ChA 254nm	10.816	8990	0.66	1468
2	W2489 ChA 254nm	13.380	15444	1.14	2389
3	W2489 ChA 254nm	13.654	8176	0.60	1231
4	W2489 ChA 254nm	13.909	1316295	97.01	199050
5	W2489 ChA 254nm	14.768	7934	0.58	1045

Compound P8.

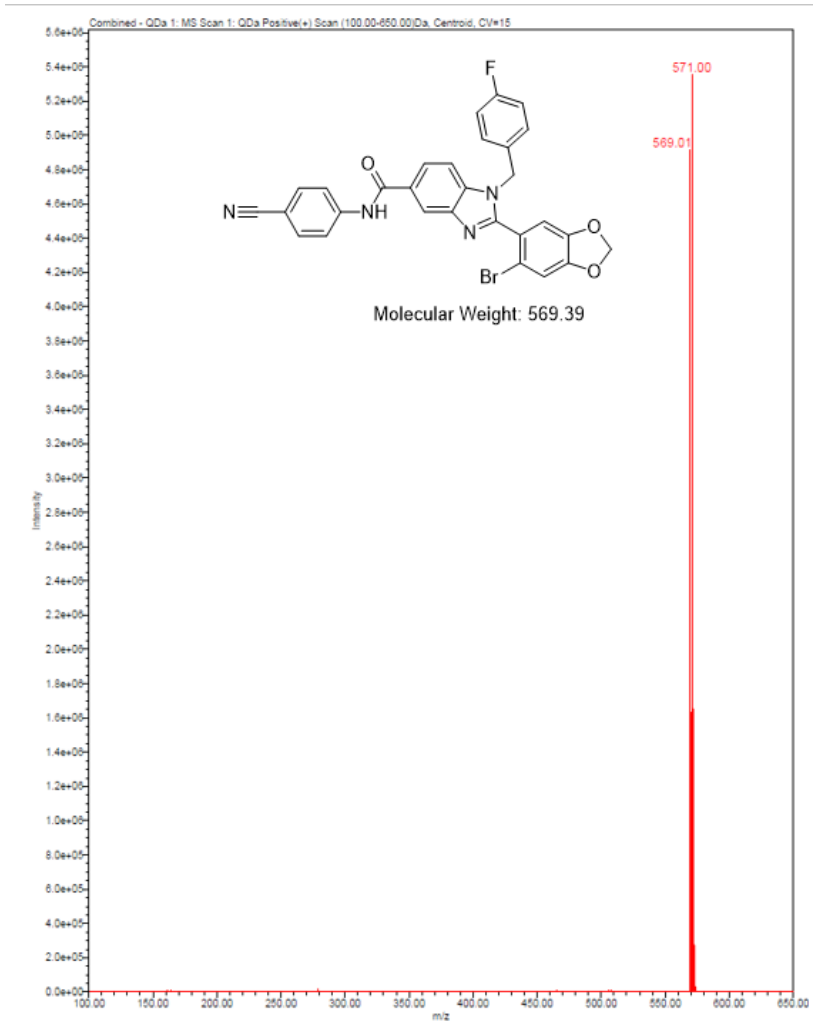

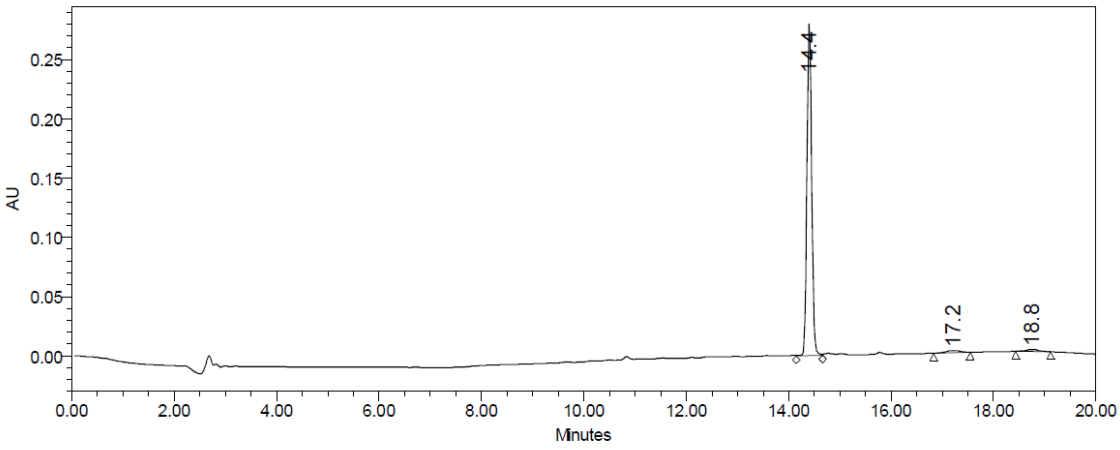

Channel: W2489 ChA; Processed Channel: W2489 ChA 254nm; Result Id: 11385; Processing Method: PM_Yang

Processed Channel Descr.: W2489 ChA 254nm

	Processed Channel Descr.	RT	Area	% Area	Height
1	W2489 ChA 254nm	14.403	1808405	96.47	278853
2	W2489 ChA 254nm	17.219	36903	1.97	1951
3	W2489 ChA 254nm	18.761	29179	1.56	1656

Compound P10.

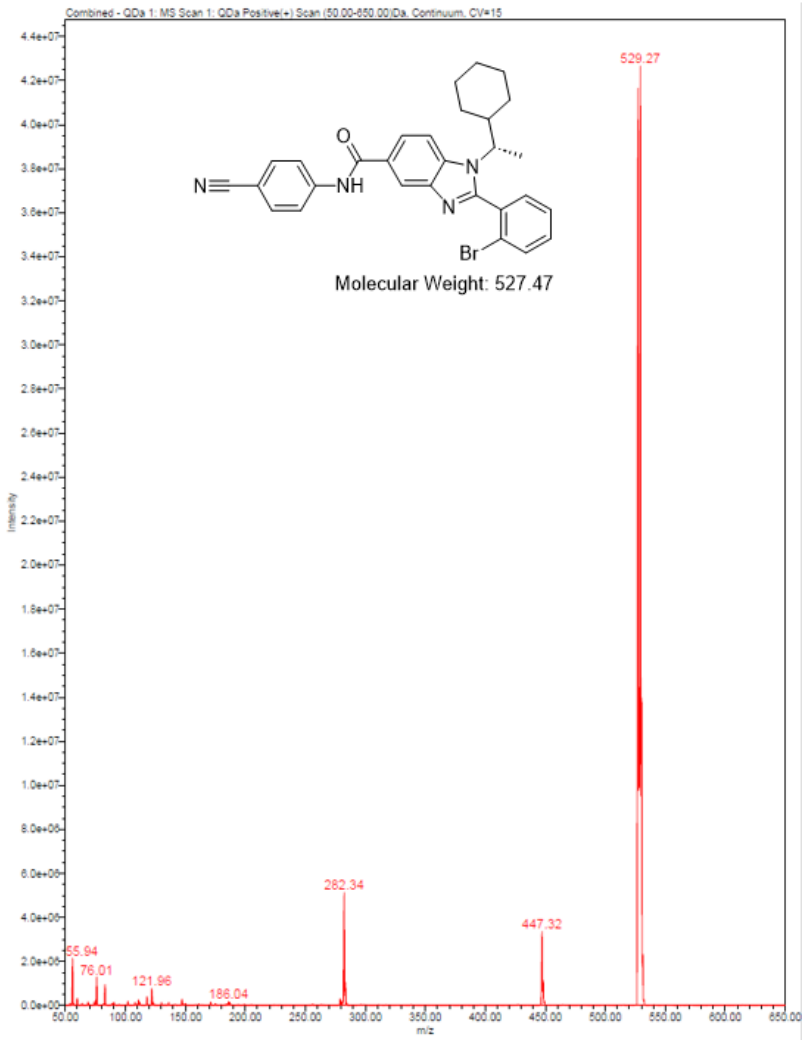

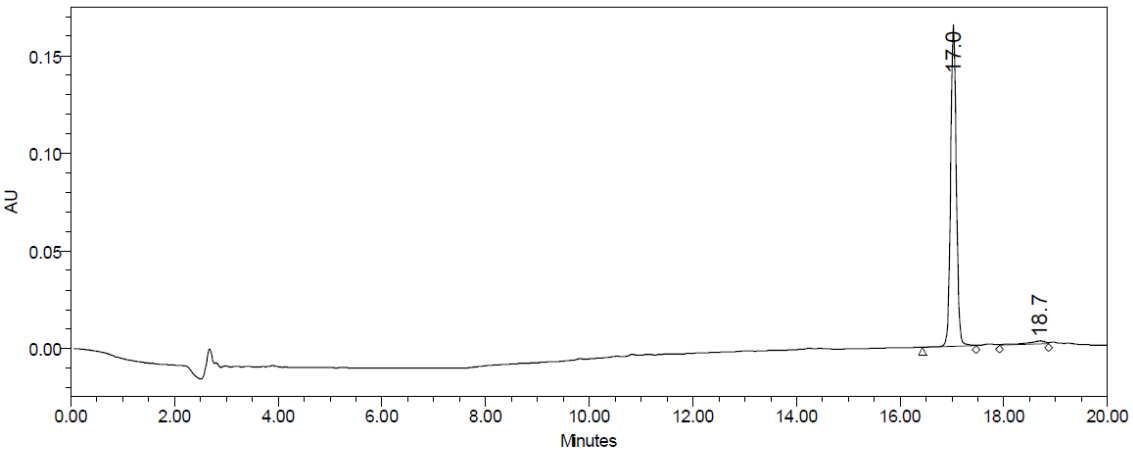

Channel: W2489 ChA; Processed Channel: W2489 ChA 254nm; Result Id: 11427; Processing Method: PM_Yang

Processed Channel Descr.: W2489 ChA 254nm

	Processed Channel Descr.	RT	Area	% Area	Height
1	W2489 ChA 254nm	17.029	1260010	96.79	164766
2	W2489 ChA 254nm	18.700	41748	3.21	1558

Compound P14.

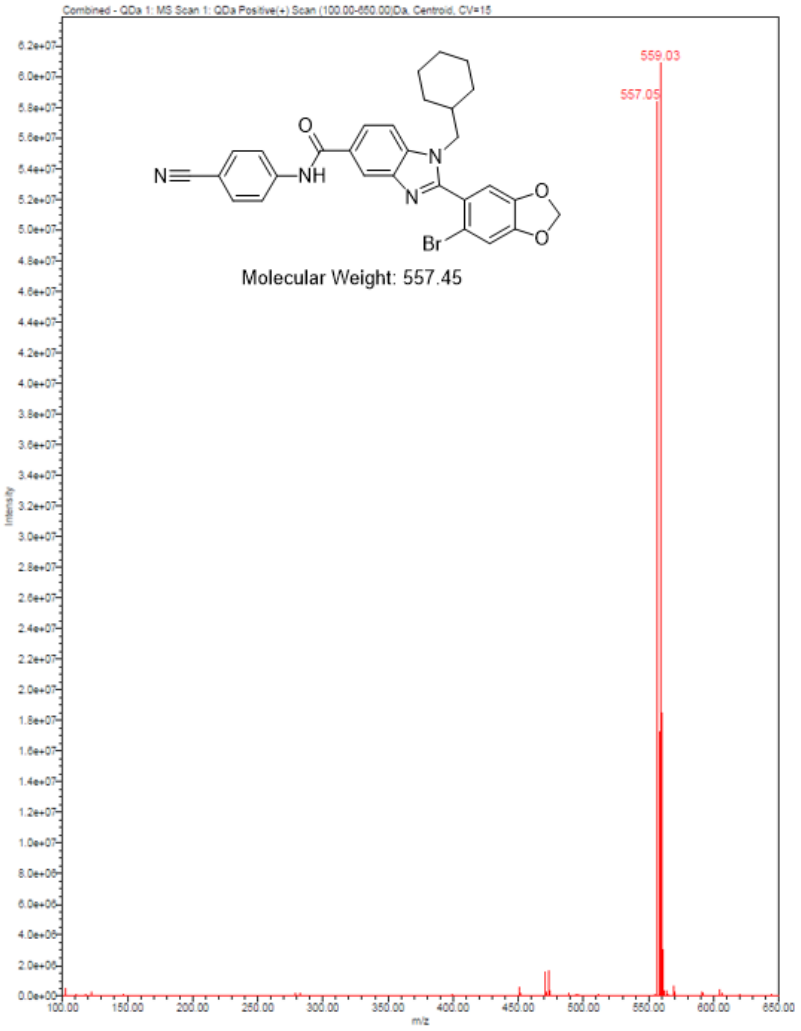

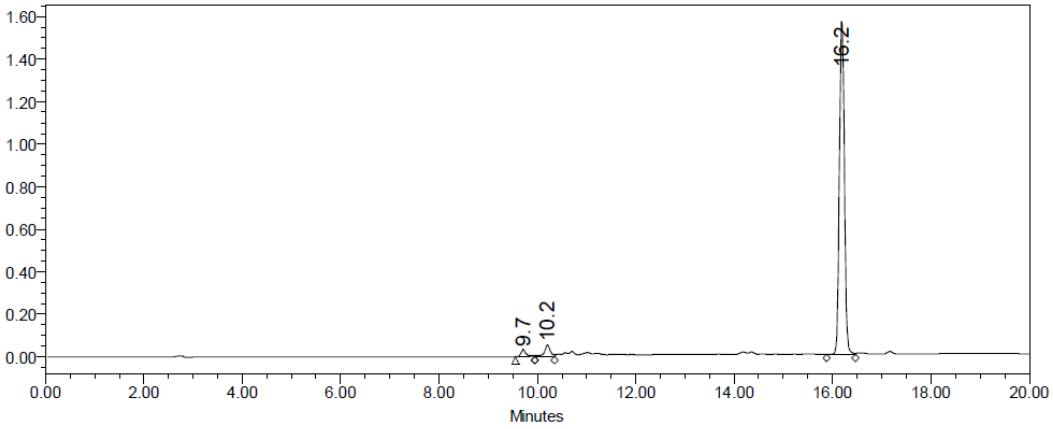

Channel: W2489 ChA; Processed Channel: W2489 ChA 254nm; Result Id: 11103; Processing Method: PM_Yang

Processed Channel Descr.: W2489 ChA 254nm

	Processed Channel Descr.	RT	Area	% Area	Height
1	W2489 ChA 254nm	9.714	254324	2.18	32775
2	W2489 ChA 254nm	10.205	453137	3.88	53631
3	W2489 ChA 254nm	16.190	10970059	93.94	1574216

Compound – Precursor

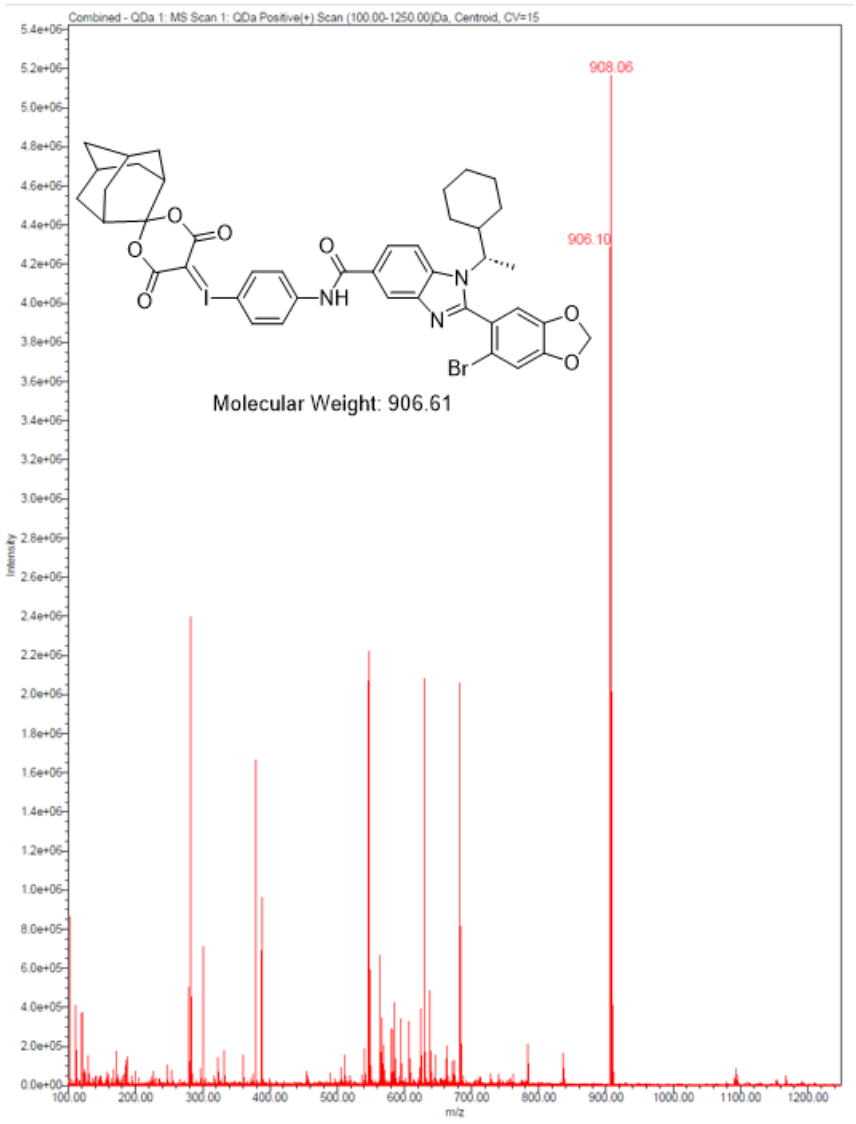

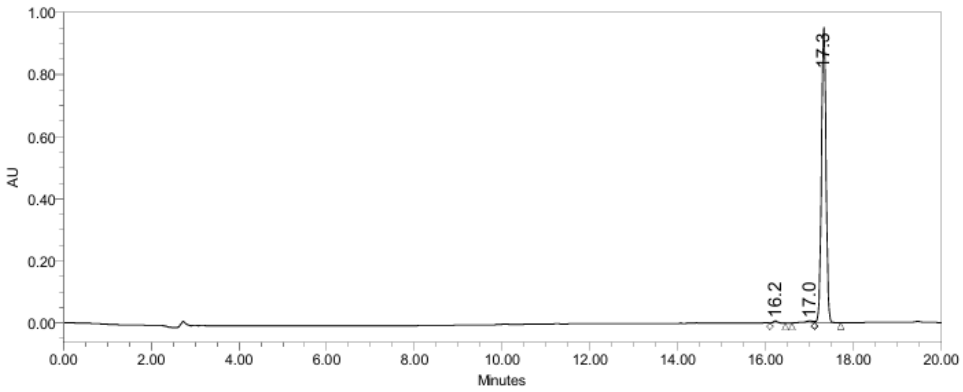

Channel: W2489 ChA; Processed Channel: W2489 ChA 254nm; Result Id: 2272; Processing Method: PM_Yang

Processed Channel Descr.: W2489 ChA 254nm

	Processed Channel Descr.	RT	Area	% Area	Height
1	W2489 ChA 254nm	16.227	44495	0.63	6301
2	W2489 ChA 254nm	17.012	86624	1.23	5666
3	W2489 ChA 254nm	17.328	6899255	98.13	954563

Spectrum of Proton-NMR (^{1}H-NMR)

AZ3451

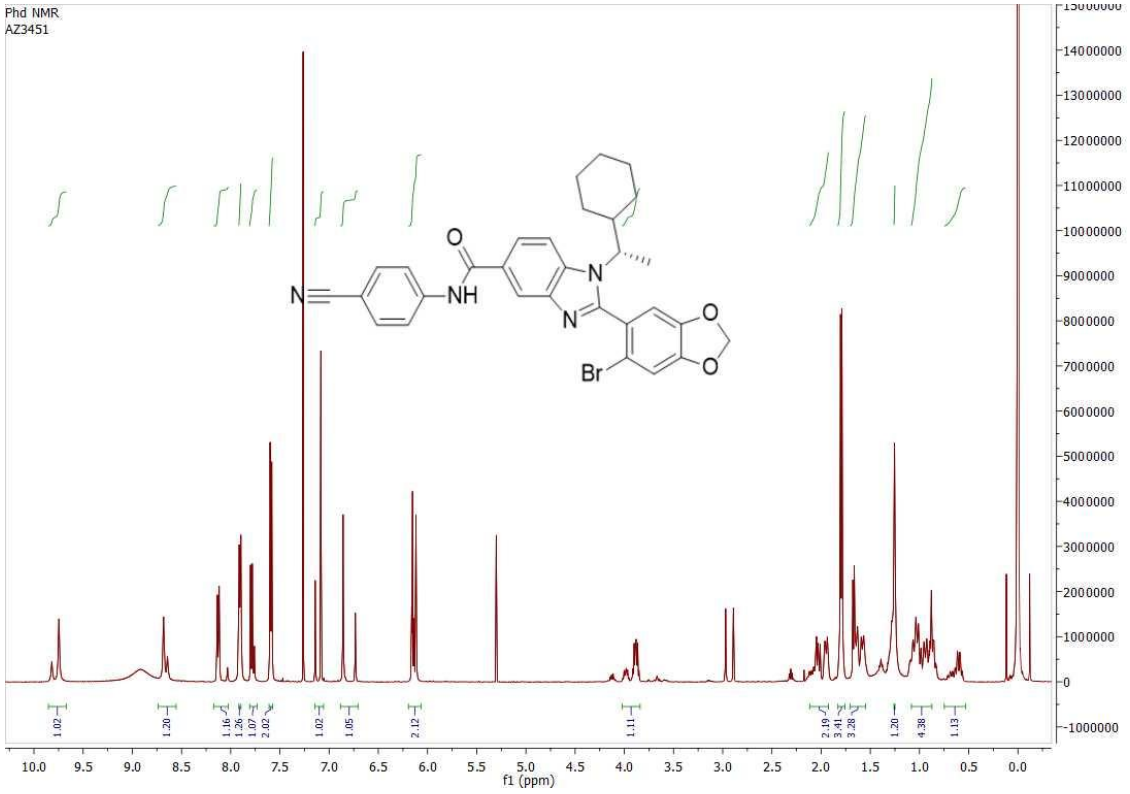

Compound P1c.

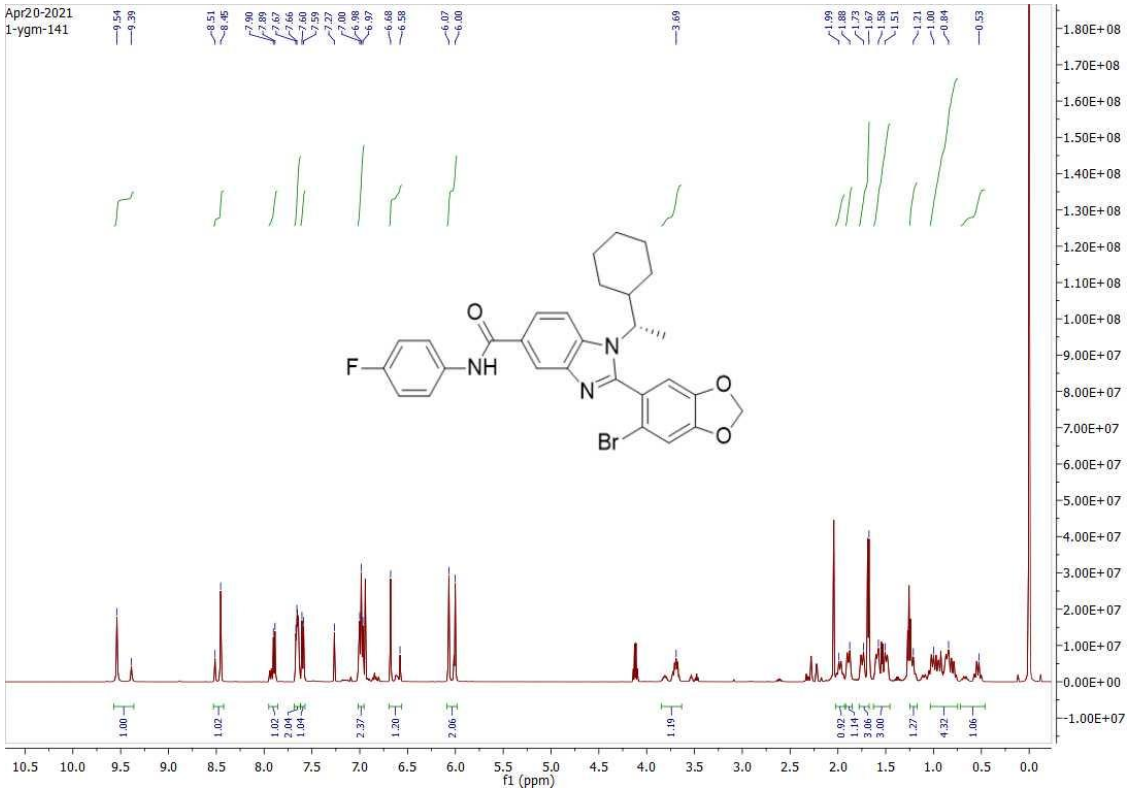

Compound P1d.

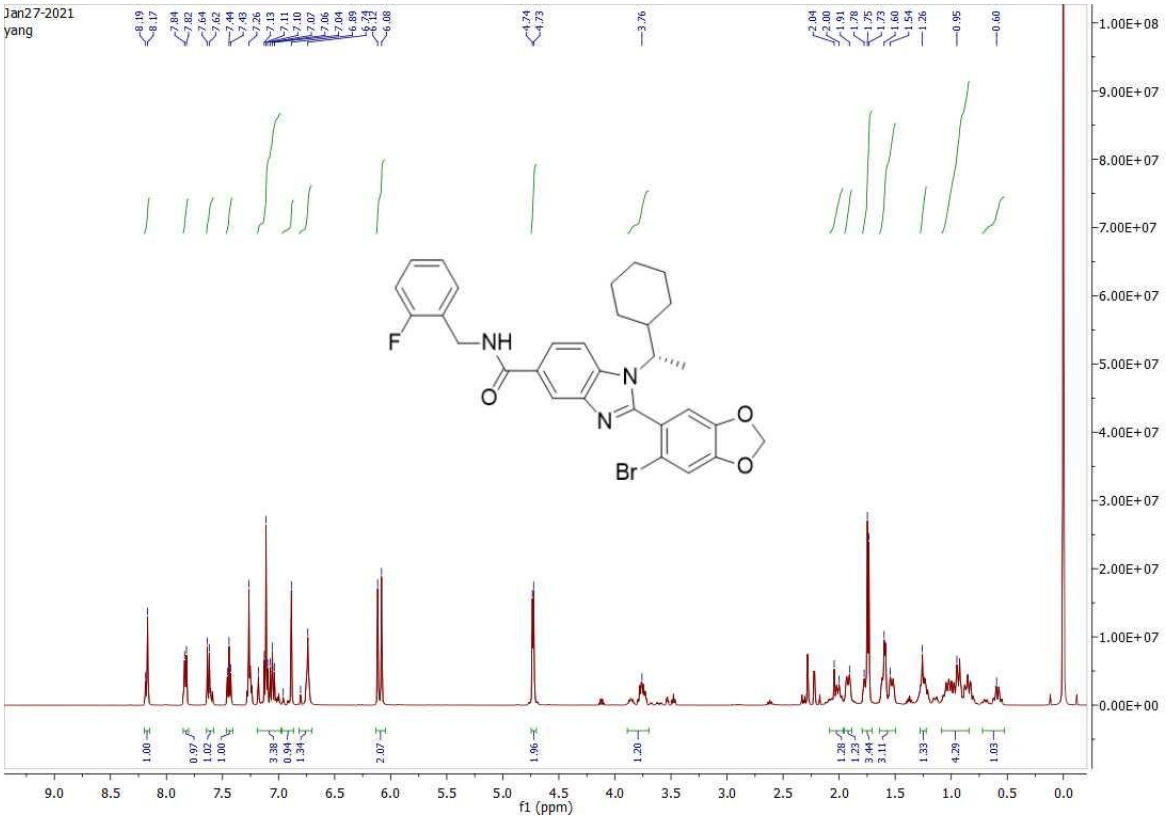

Compound P1e.

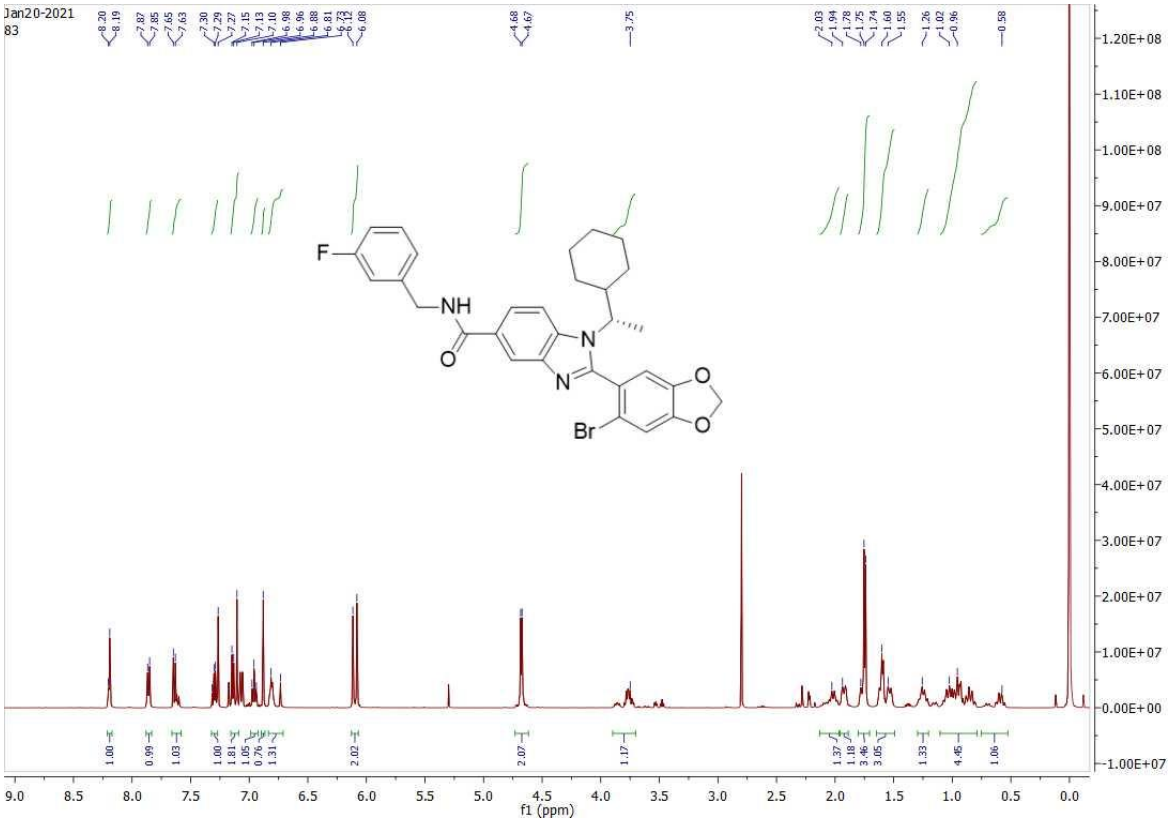

Compound P1f.

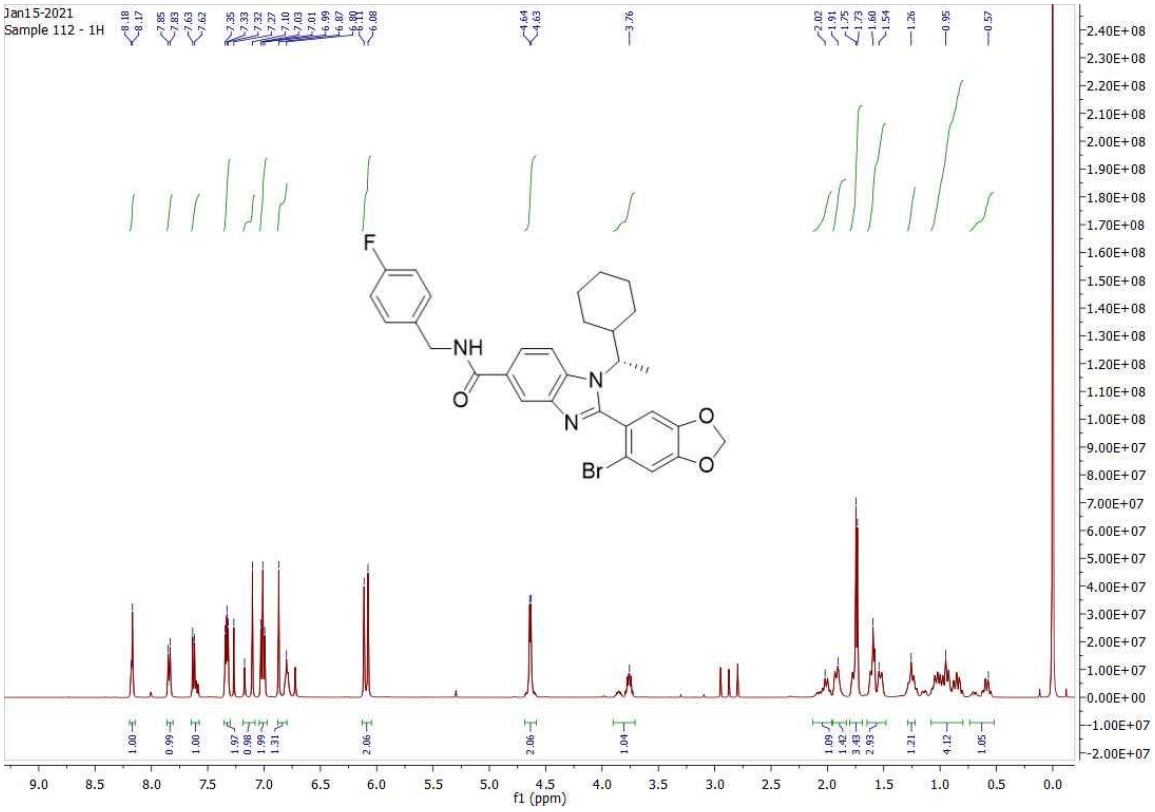

Compound P1h.

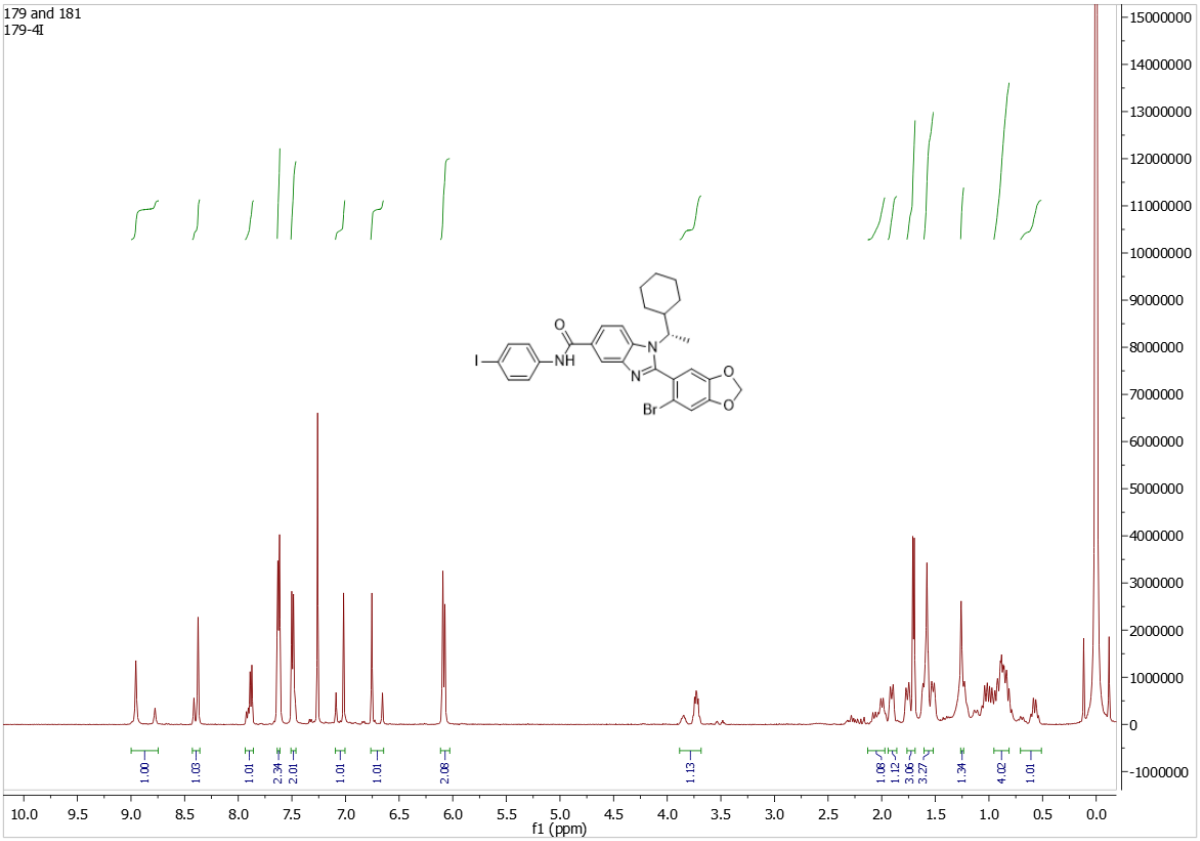

Compound P1k.

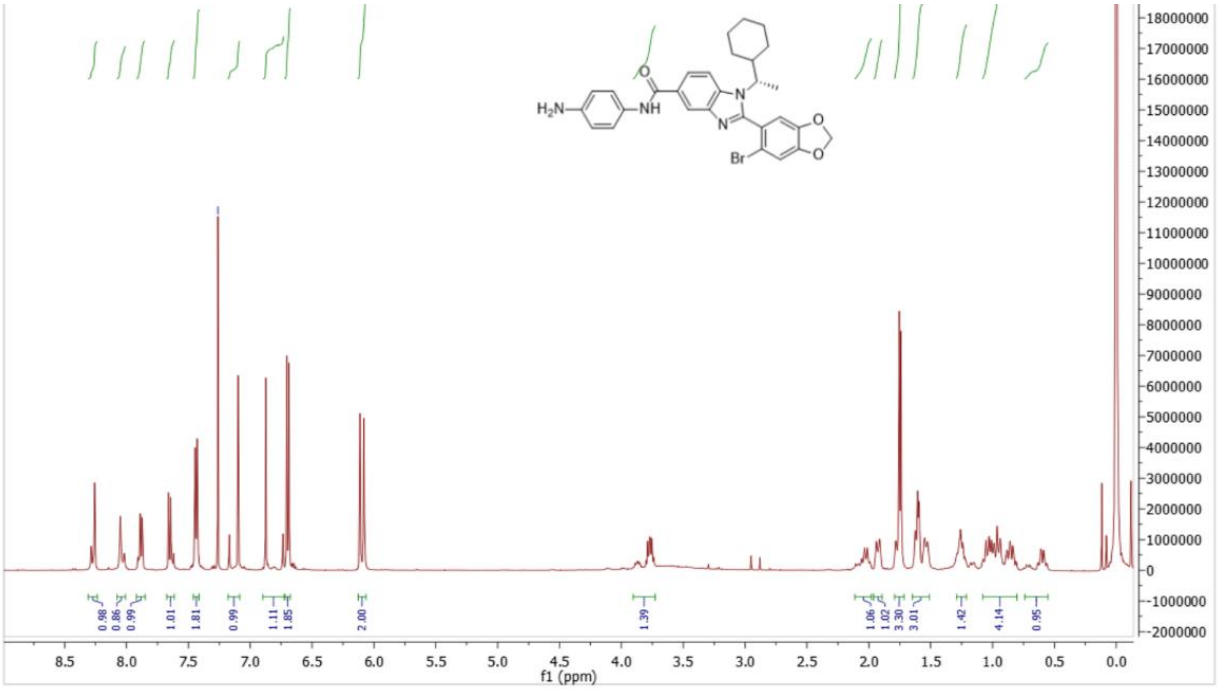

Compound P1l.

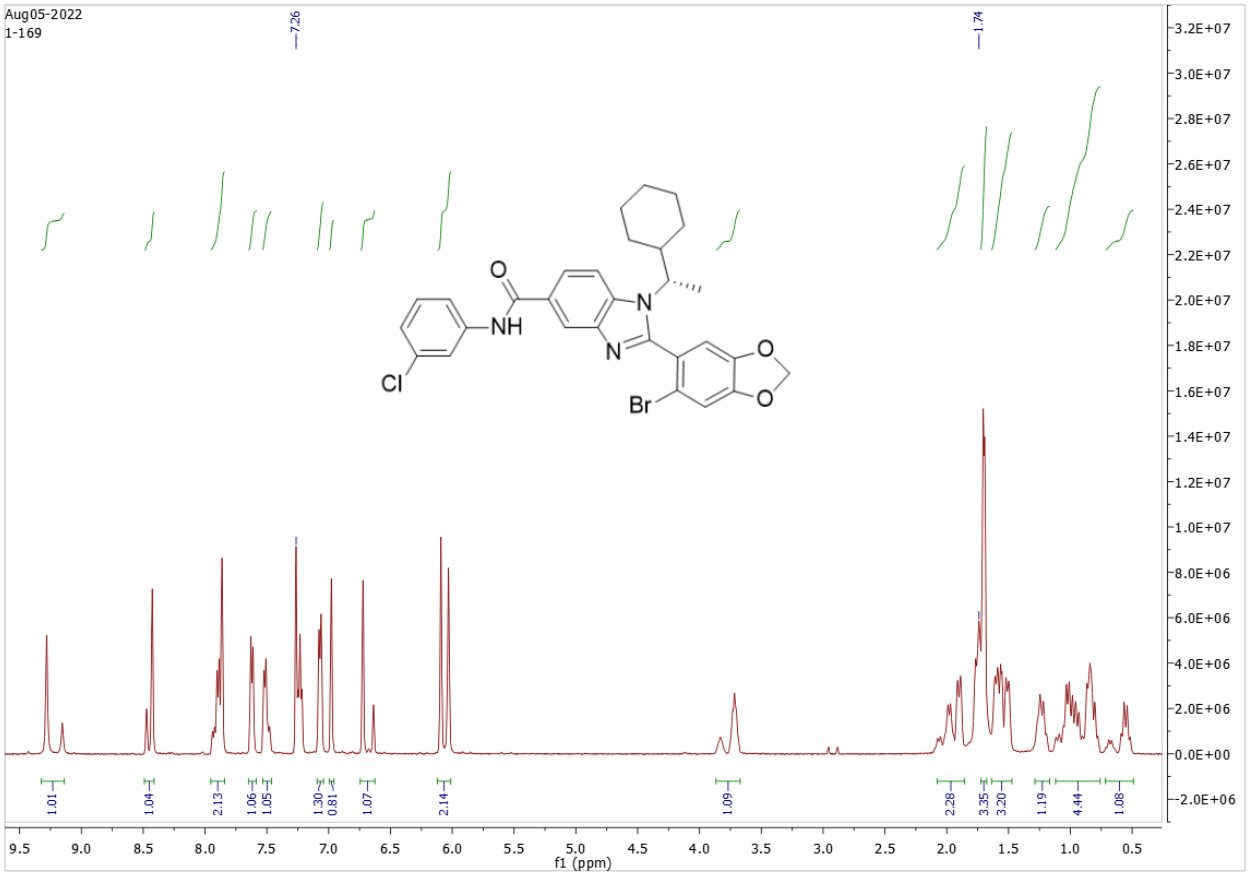

Compound P1m.

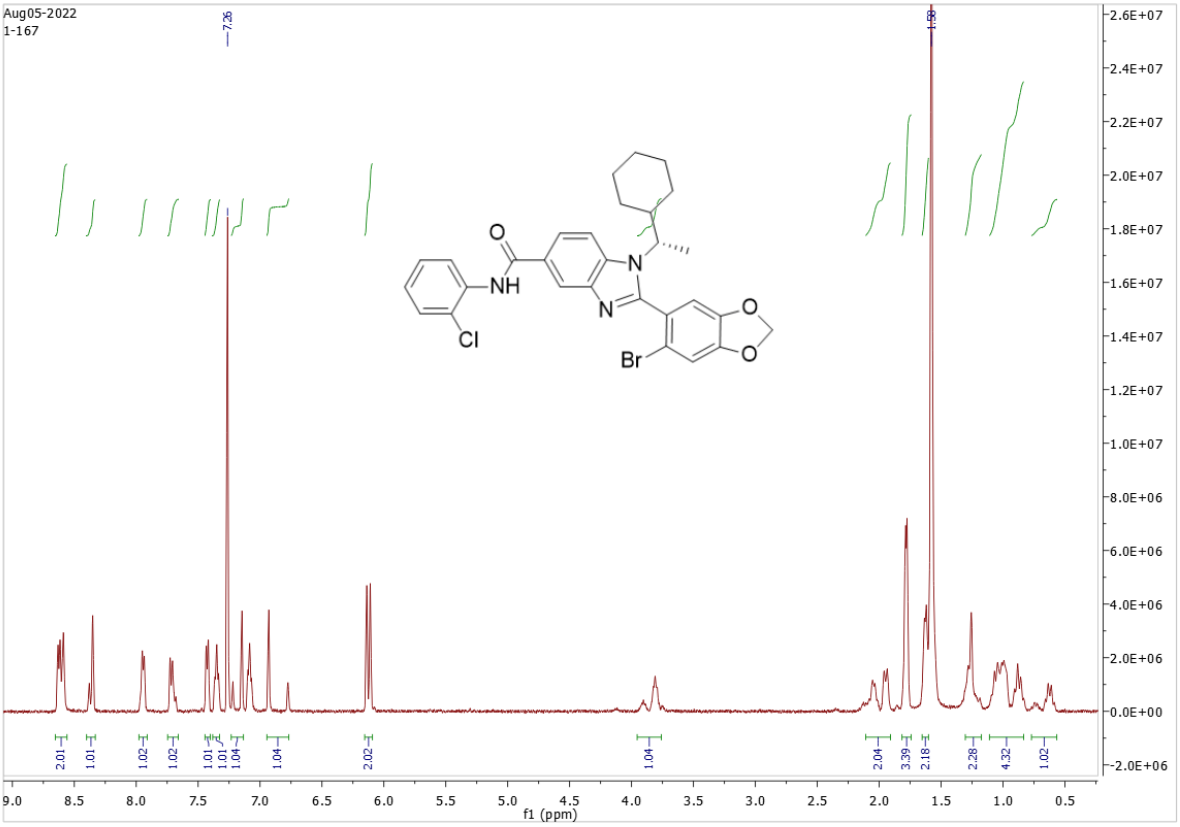

Compound P1n.

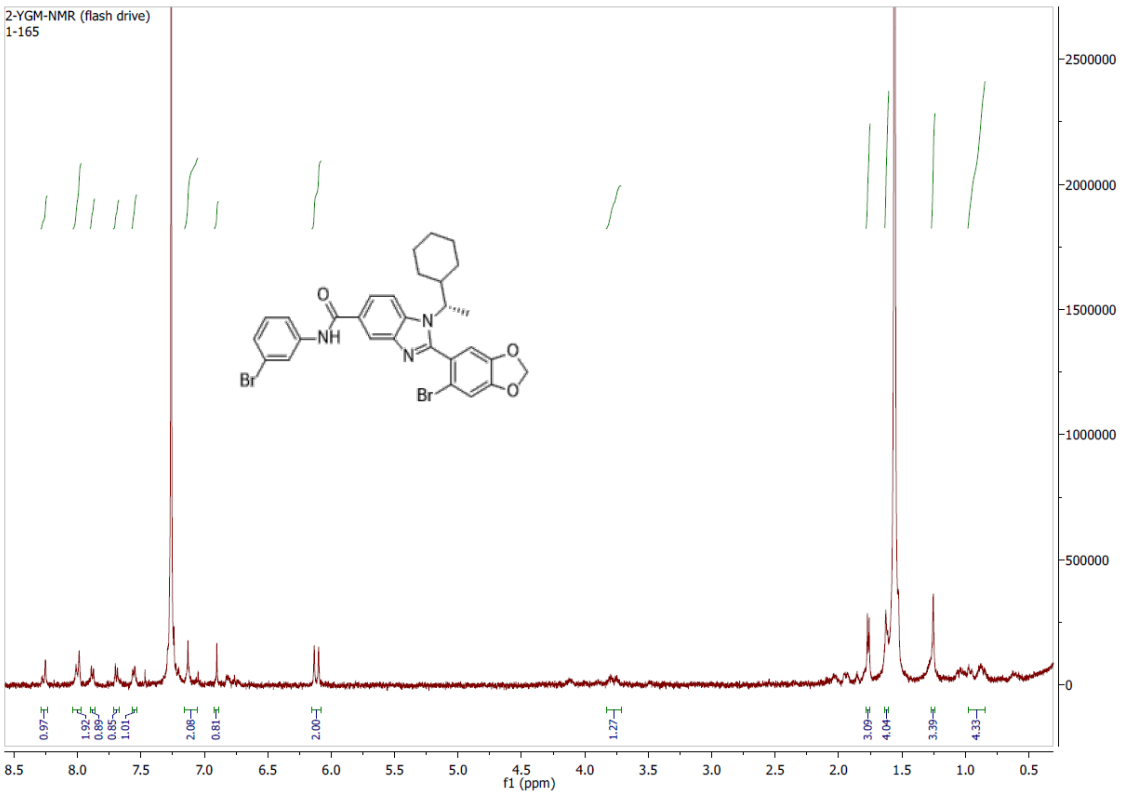

Compound P2e.

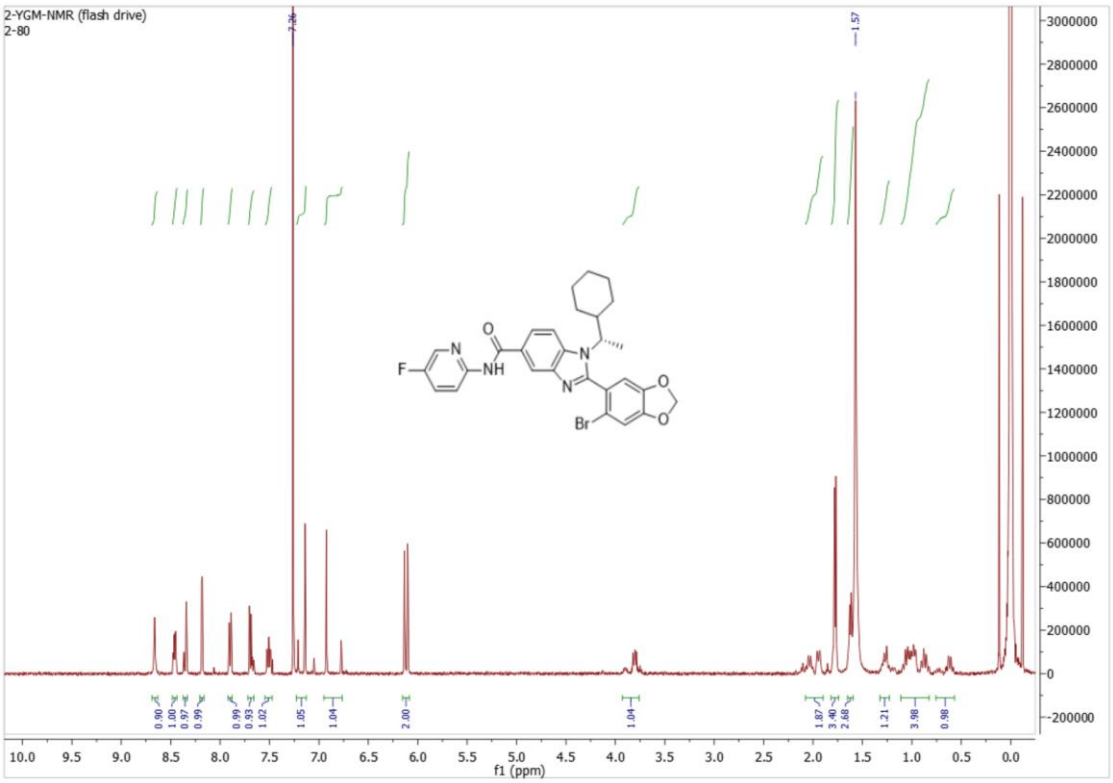

Compound P2f.

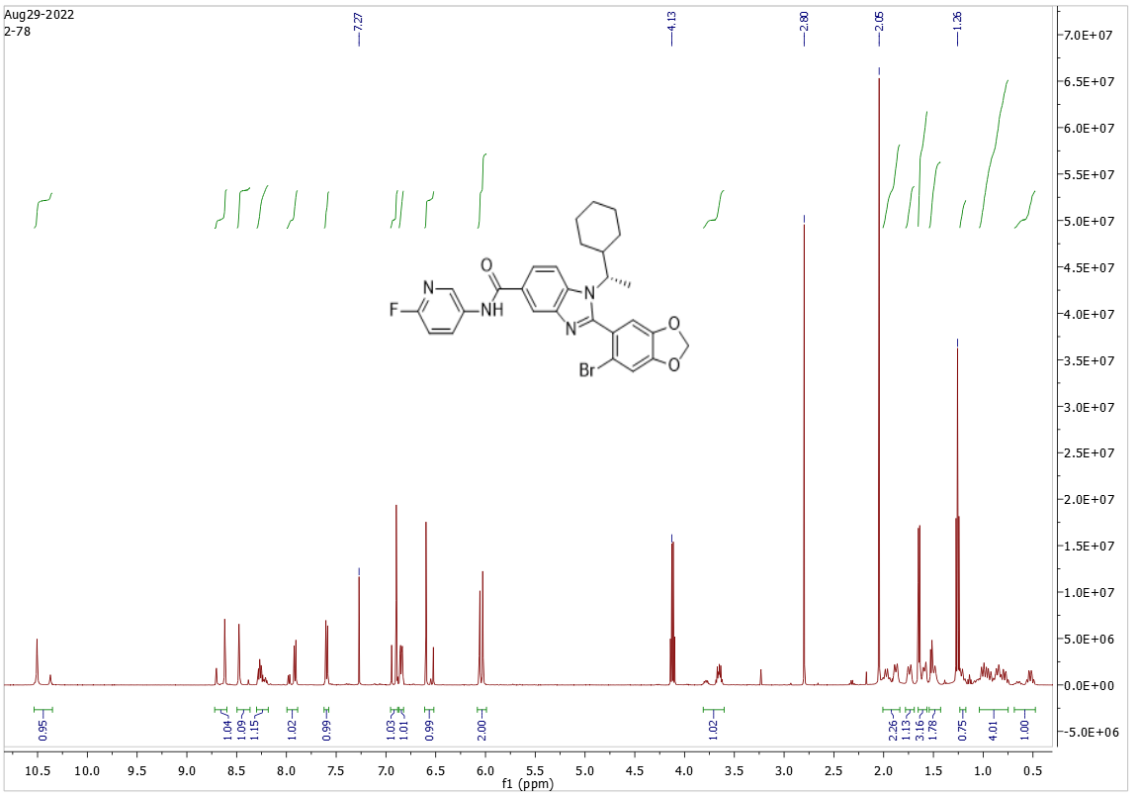

Compound P2g.

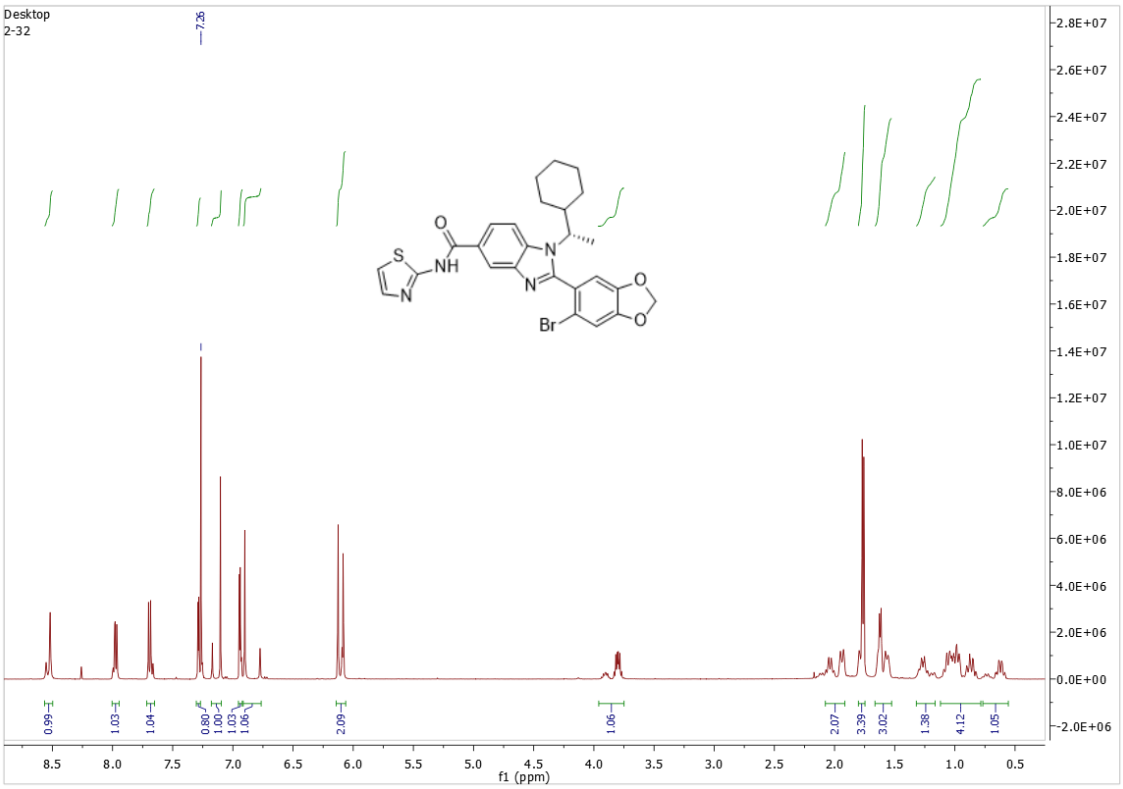

Compound P2h.

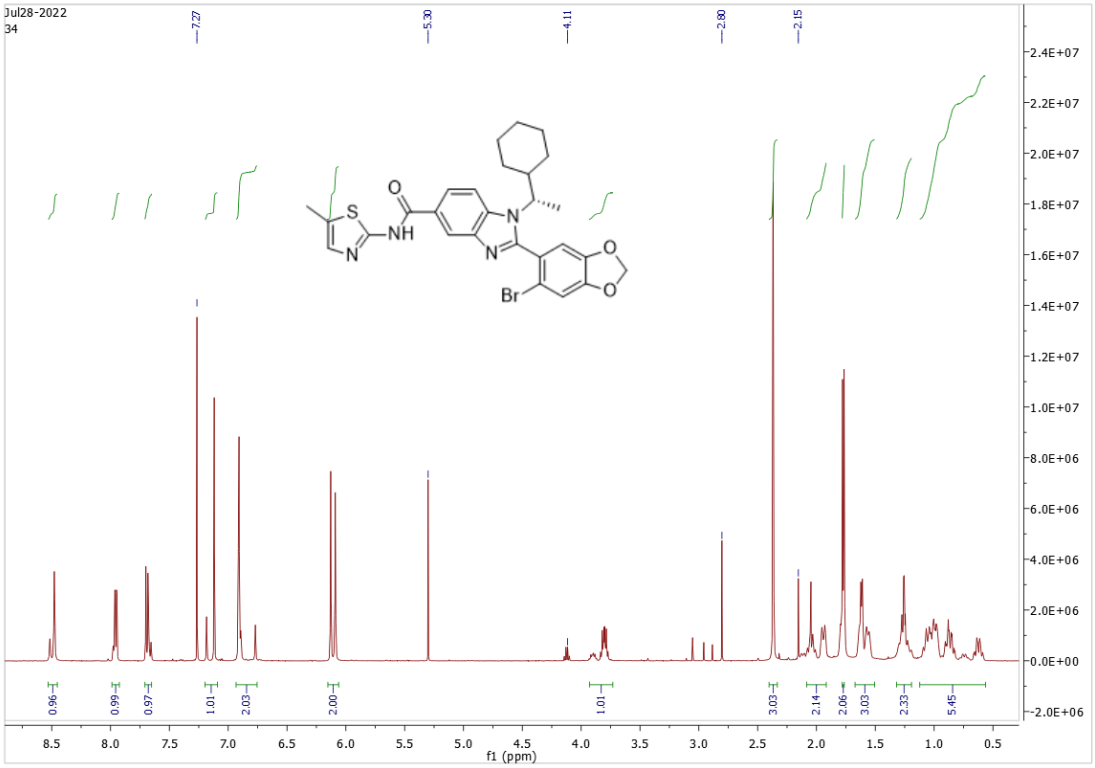

Compound P2i.

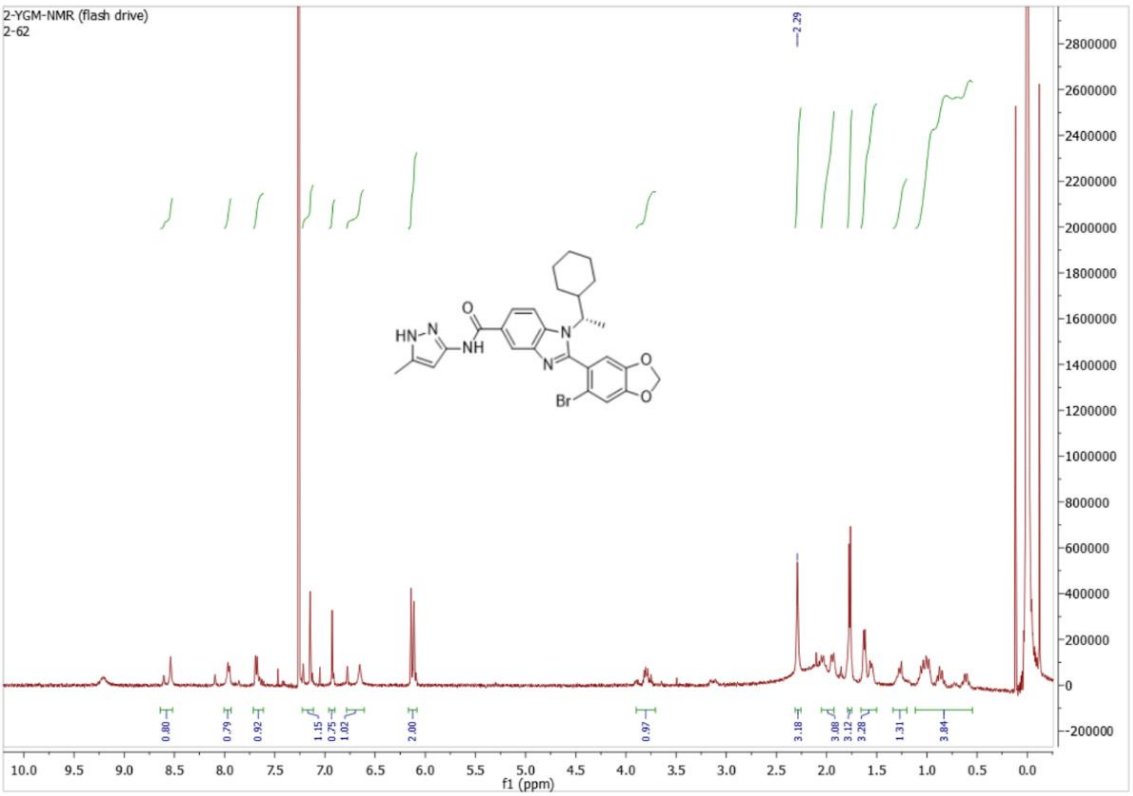

Compound P3f.

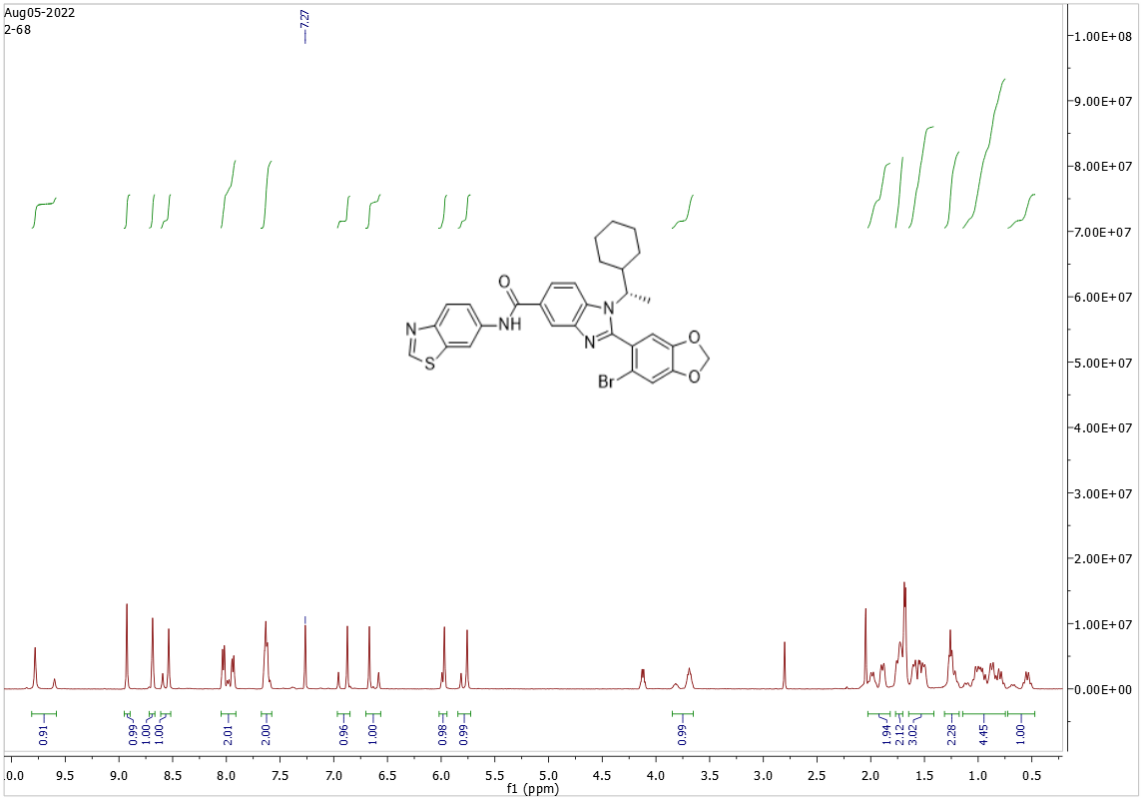

Compound P3g.

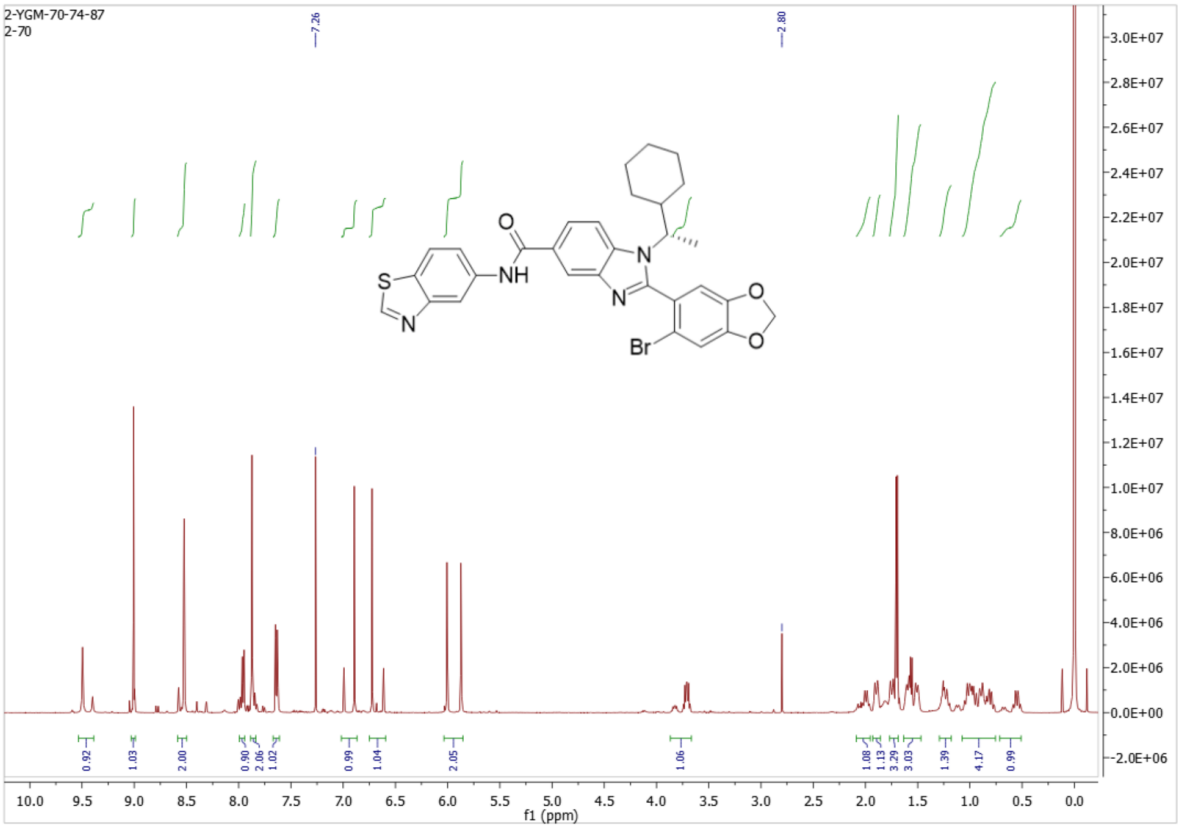

Compound P3h.

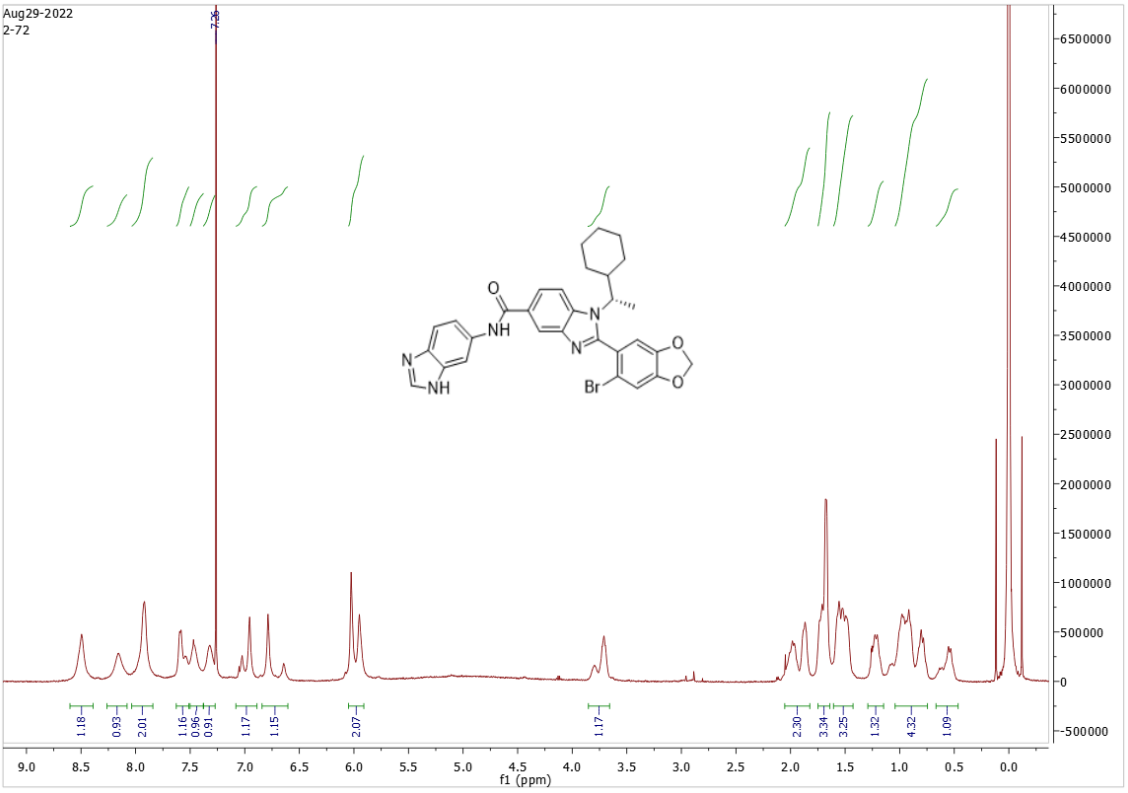

Compound P3i.

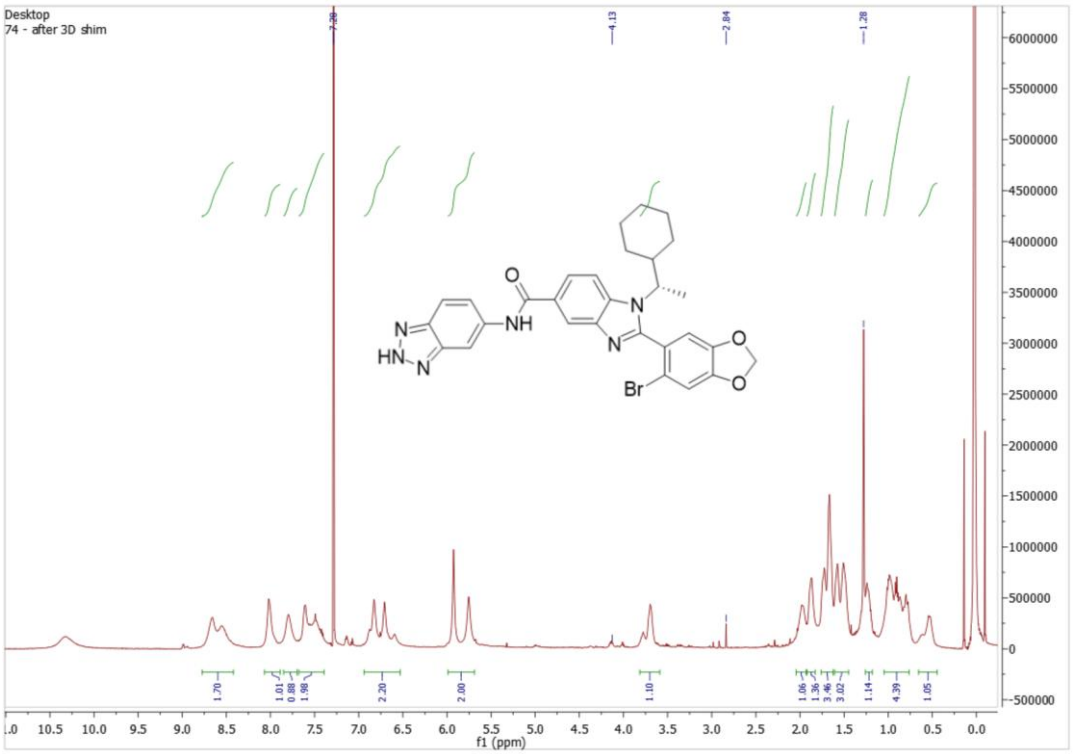

Compound P8.

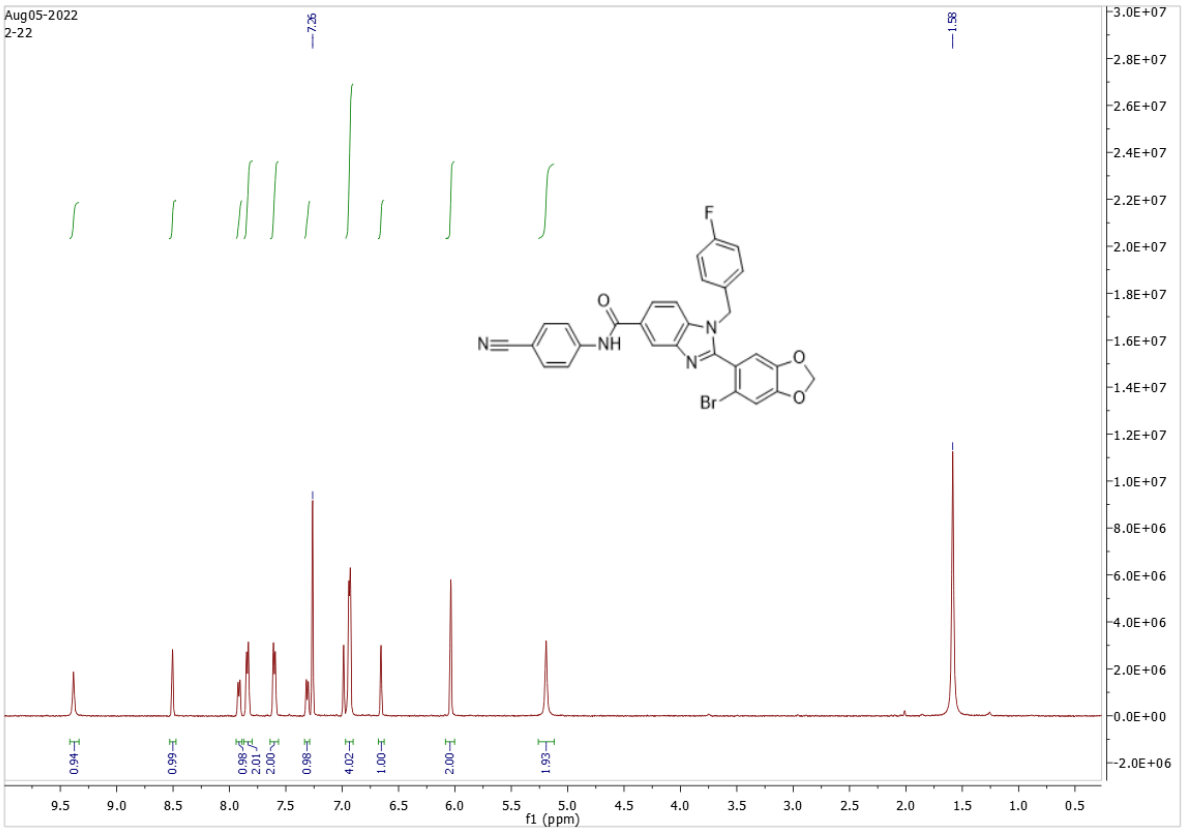

Compound P10.

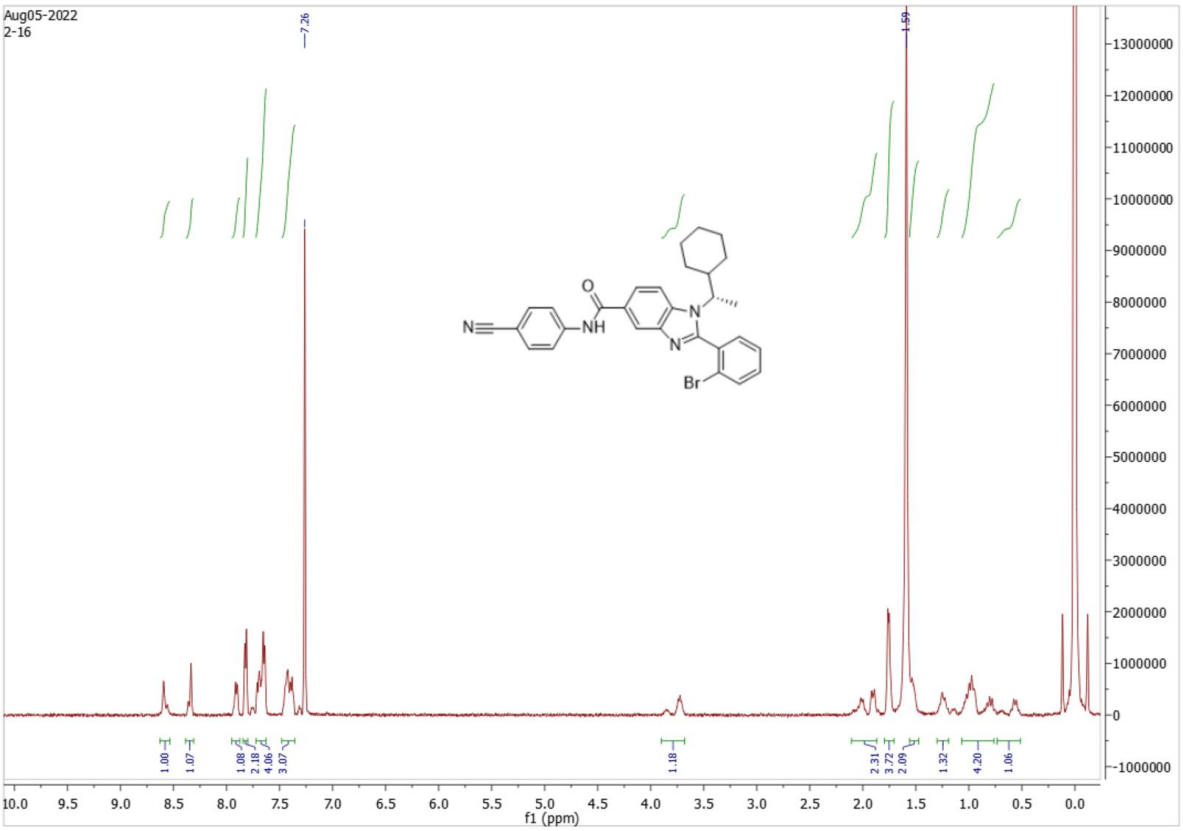

Compound P14.

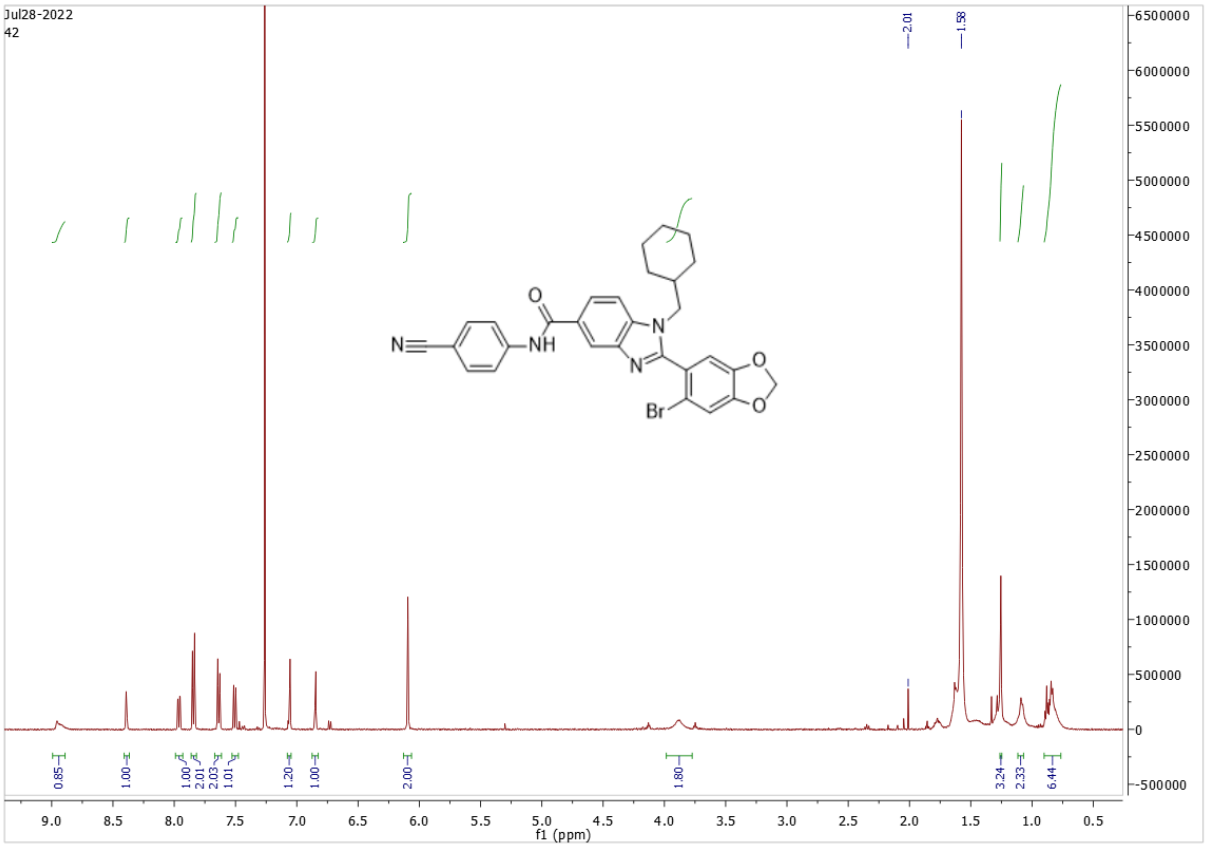

^{1}H-NMR - Precursor

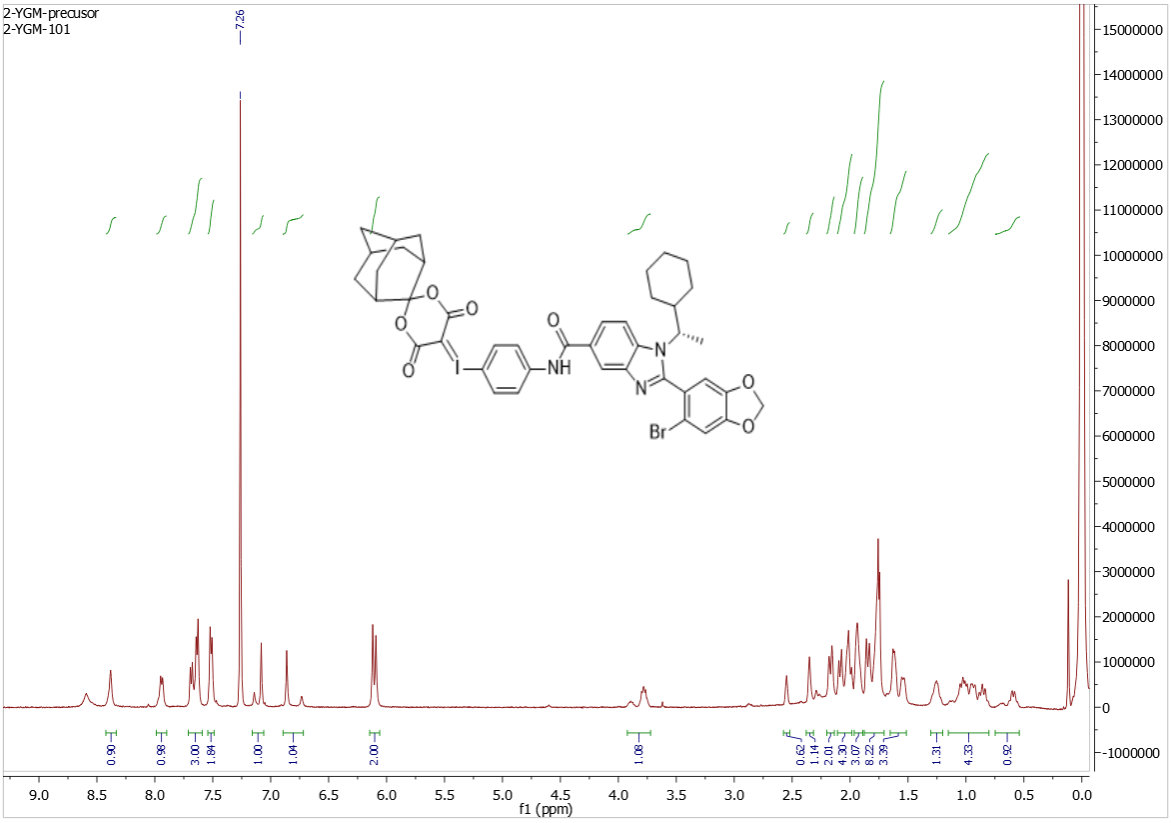

Appendix B - Characterization Data of Chapter 3 and Chapter 4

Results of Mass Spectroscopy and HPLC purity

Compound – **L8x**

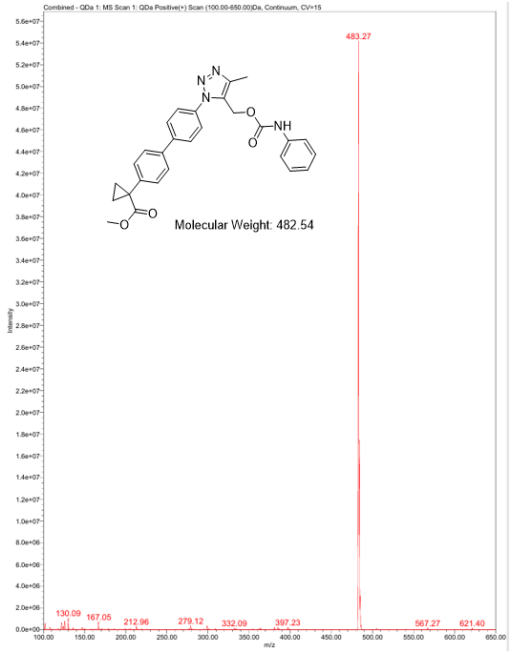

Compound - **L11y**

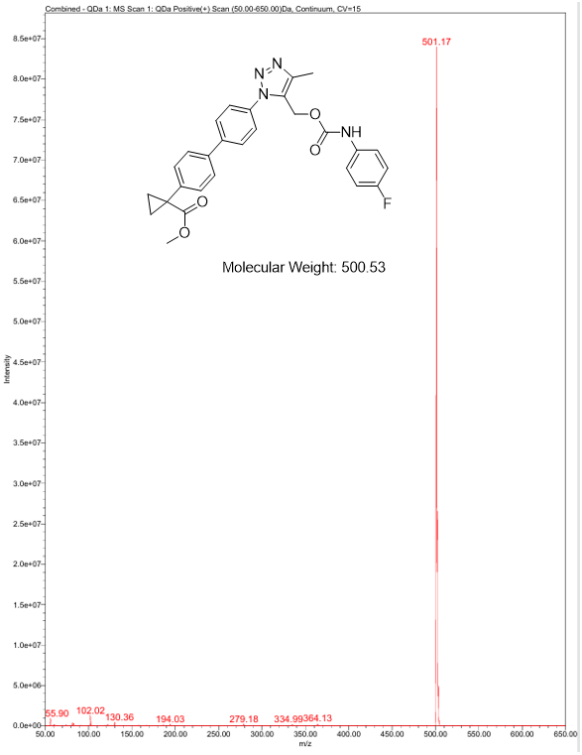

Compound - **L9x**

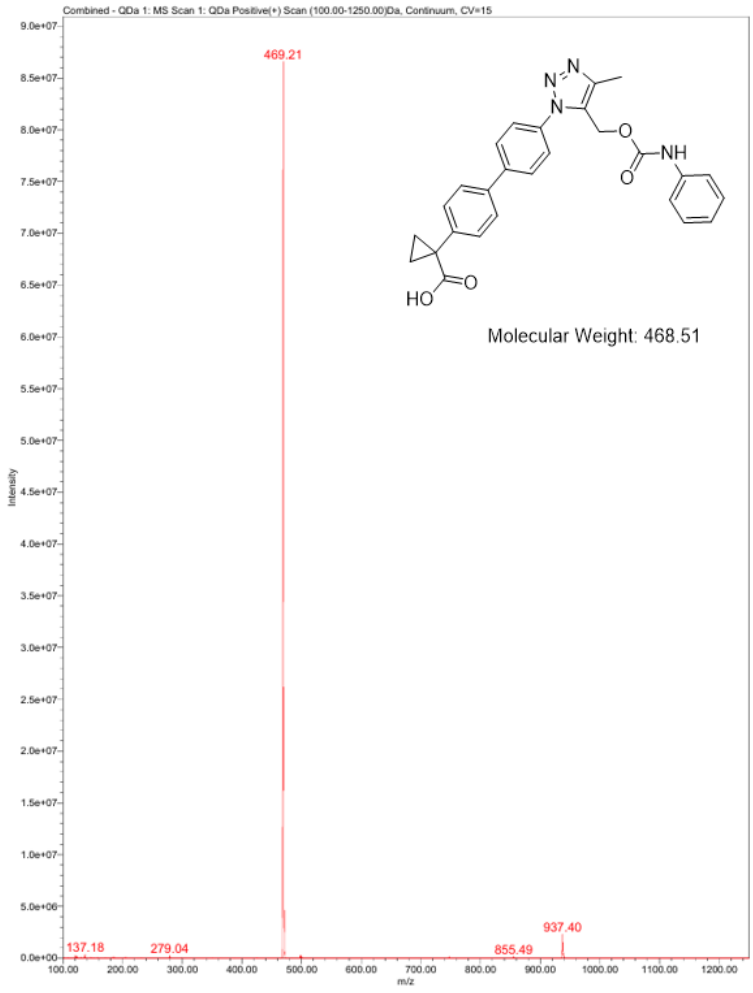

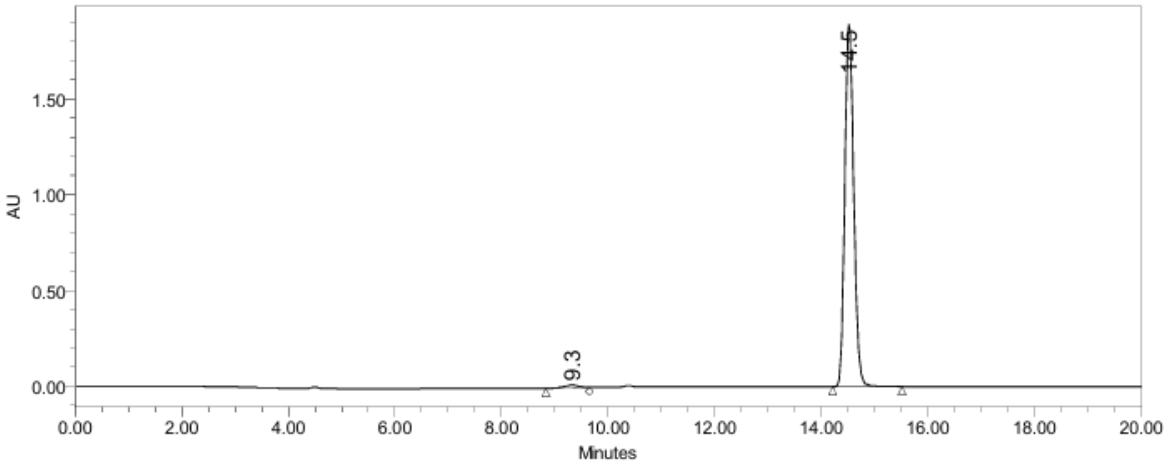

Channel: W2489 ChA; Processed Channel: W2489 ChA 254nm; Result Id: 46210; Processing Method: PM_Yang

Processed Channel Descr.: W2489 ChA 254nm

	Processed Channel Descr.	RT	Area	% Area	Height
1	W2489 ChA 254nm	9.331	268550	1.20	14736
2	W2489 ChA 254nm	14.520	22065572	98.80	1888020

Compound - **L12y**

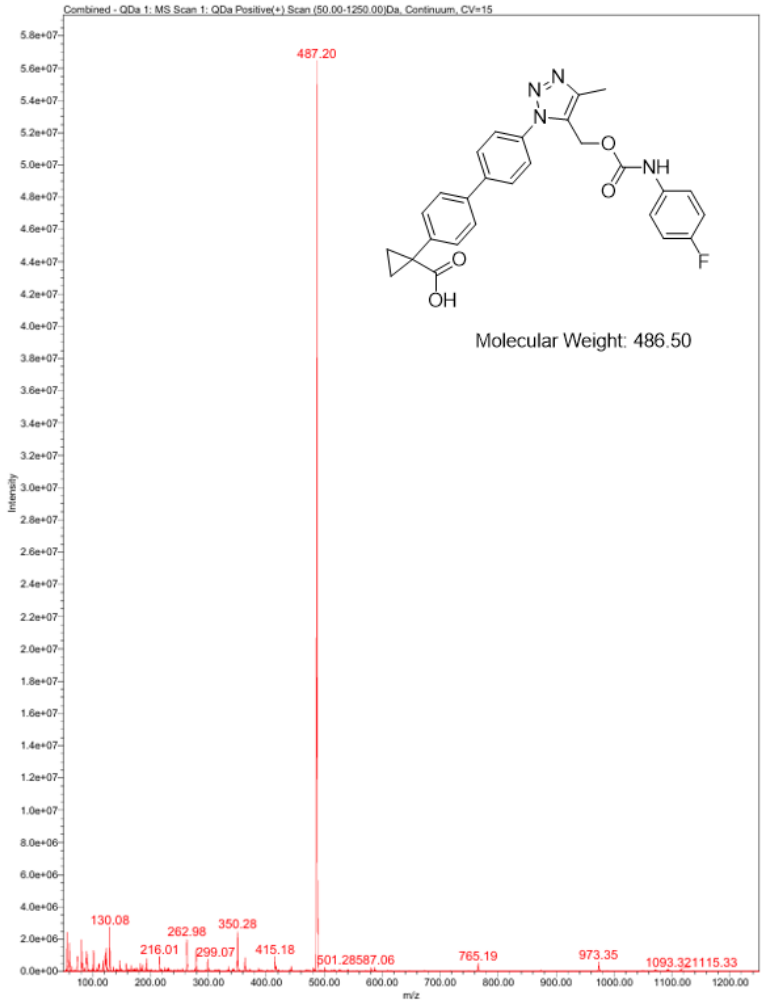

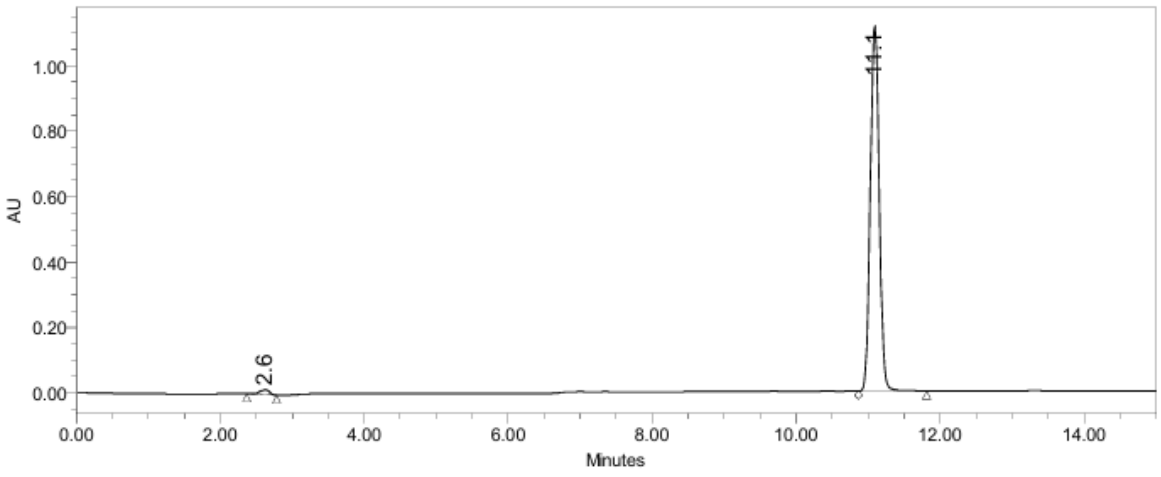

Channel: W2489 ChA; Processed Channel: W2489 ChA 254nm; Result Id: 40449; Processing Method: PM_Yang

Processed Channel Descr.: W2489 ChA 254nm

	Processed Channel Descr.	RT	Area	% Area	Height
1	W2489 ChA 254nm	2.626	140791	1.45	15102
2	W2489 ChA 254nm	11.094	9574619	98.55	1118889

Compound - **L14'**

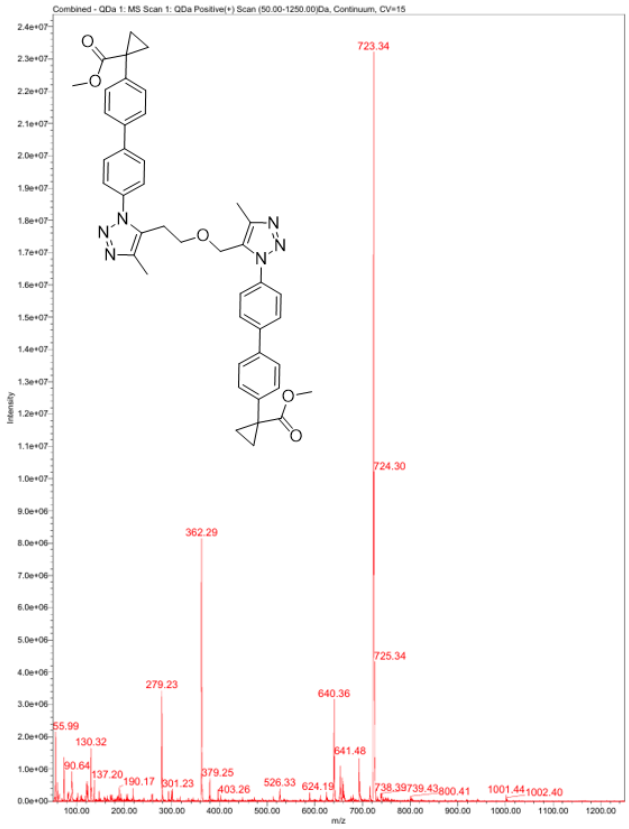

Compound **L20d**

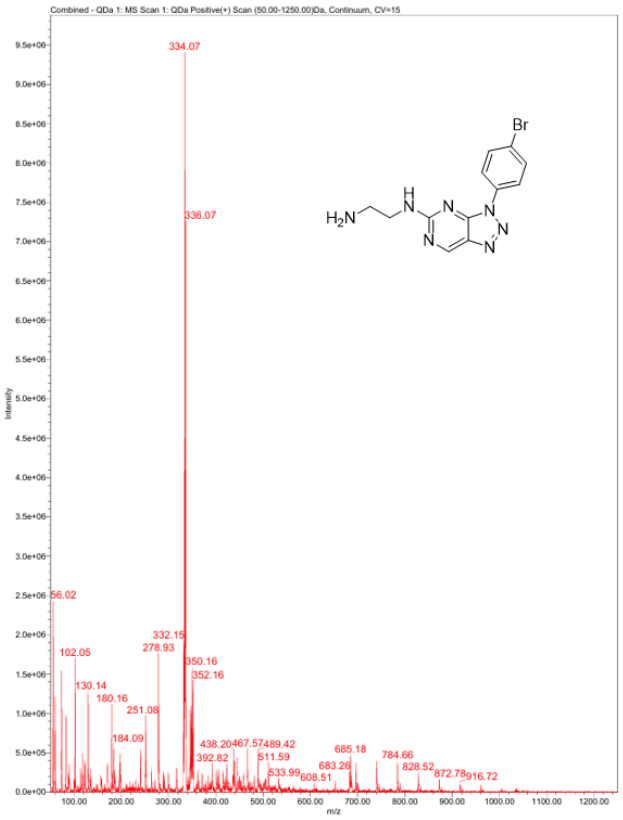

Compounds **L22a**

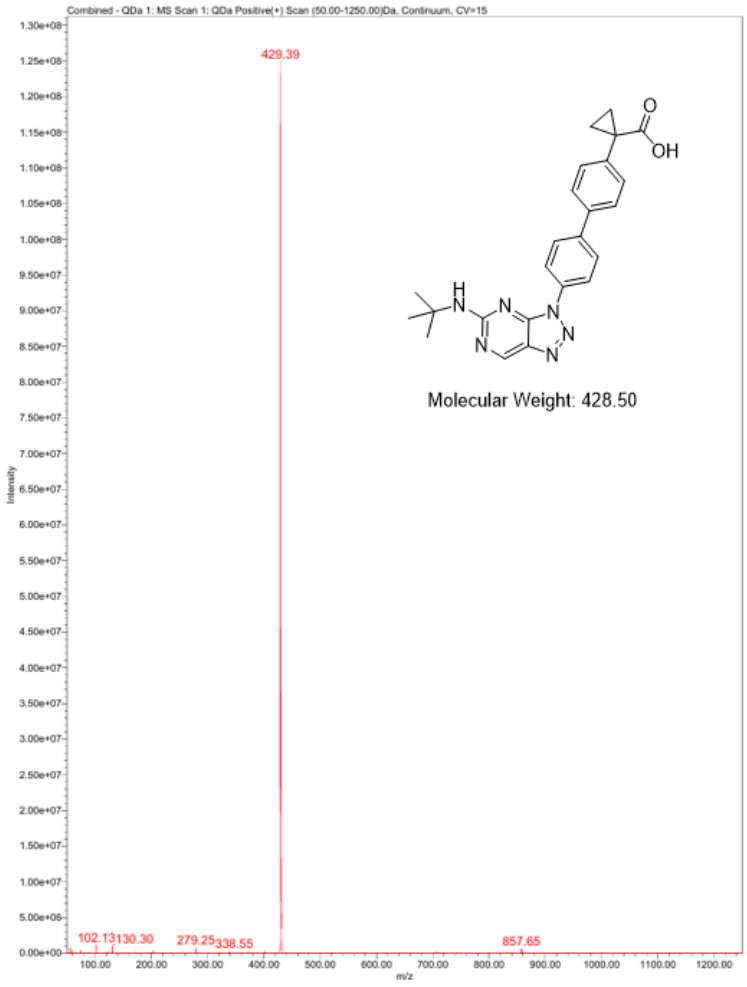

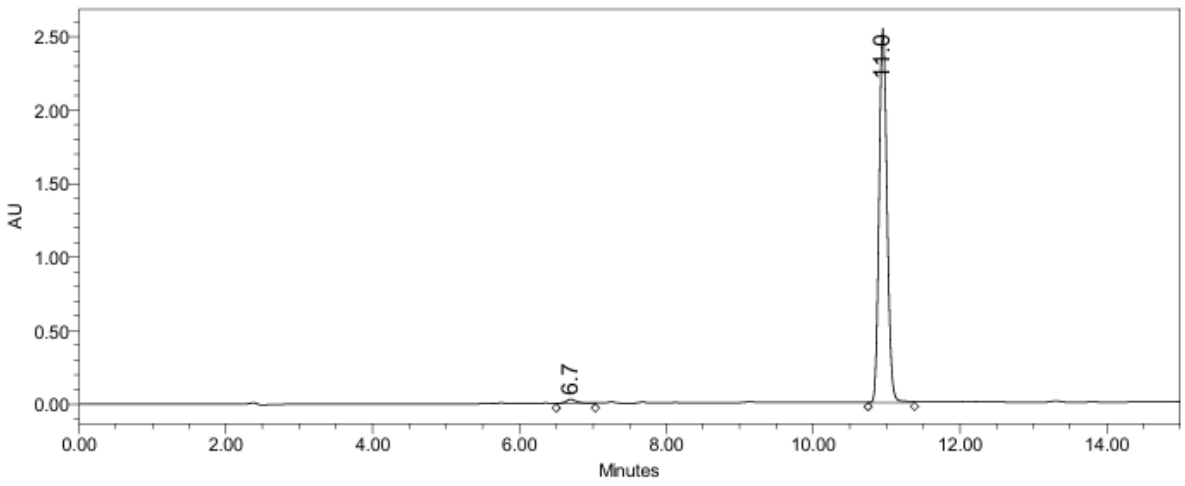

Channel: W2489 ChA; Processed Channel: W2489 ChA 254nm; Result Id: 53550; Processing Method: PM_Yang

Processed Channel Descr.: W2489 ChA 254nm

	Processed Channel Descr.	RT	Area	% Area	Height
1	W2489 ChA 254nm	6.698	370038	1.90	29506
2	W2489 ChA 254nm	10.951	19106604	98.10	2540535

Compound **L22b**

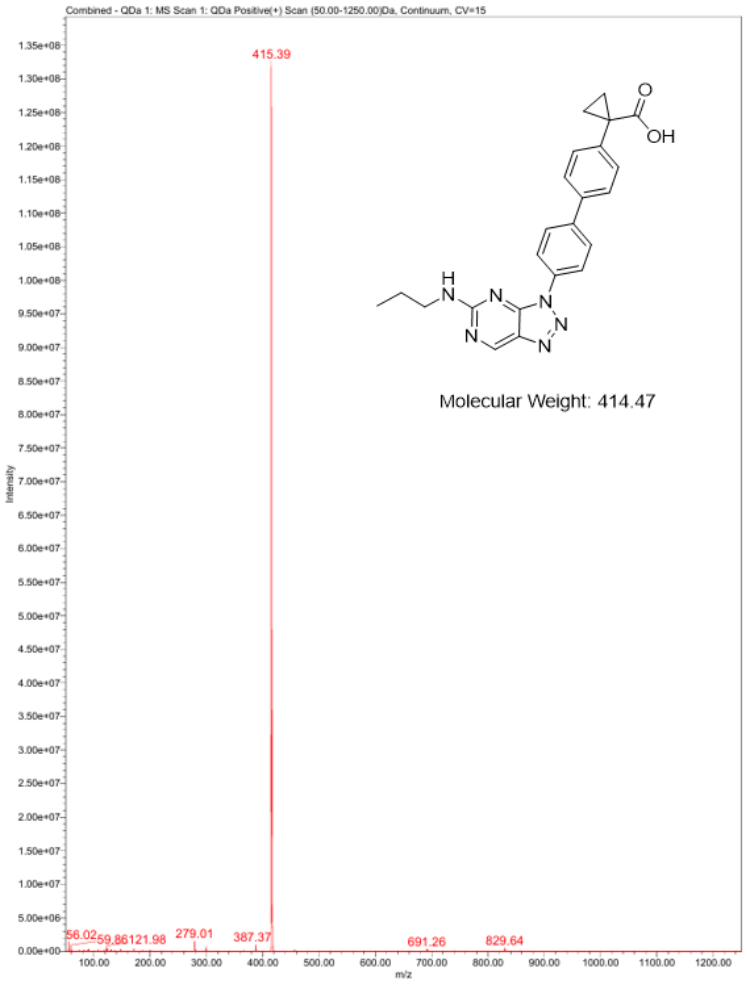

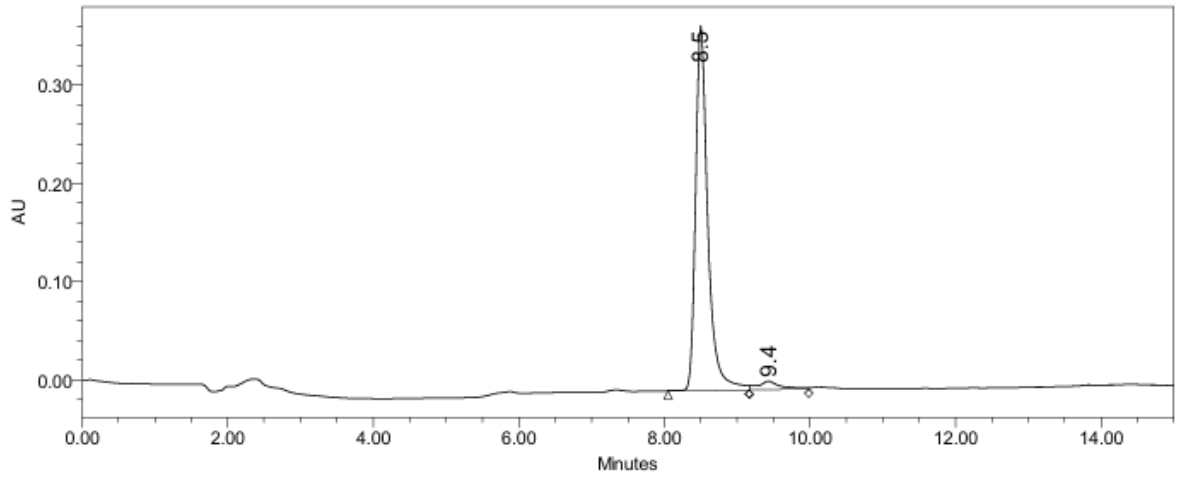

Channel: W2489 ChA; Processed Channel: W2489 ChA 254nm; Result Id: 54998; Processing Method: PM_Yang

Processed Channel Descr.: W2489 ChA 254nm

	Processed Channel Descr.	RT	Area	% Area	Height
1	W2489 ChA 254nm	8.501	4326901	95.72	370906
2	W2489 ChA 254nm	9.431	193572	4.28	8653

Compound **L22e**

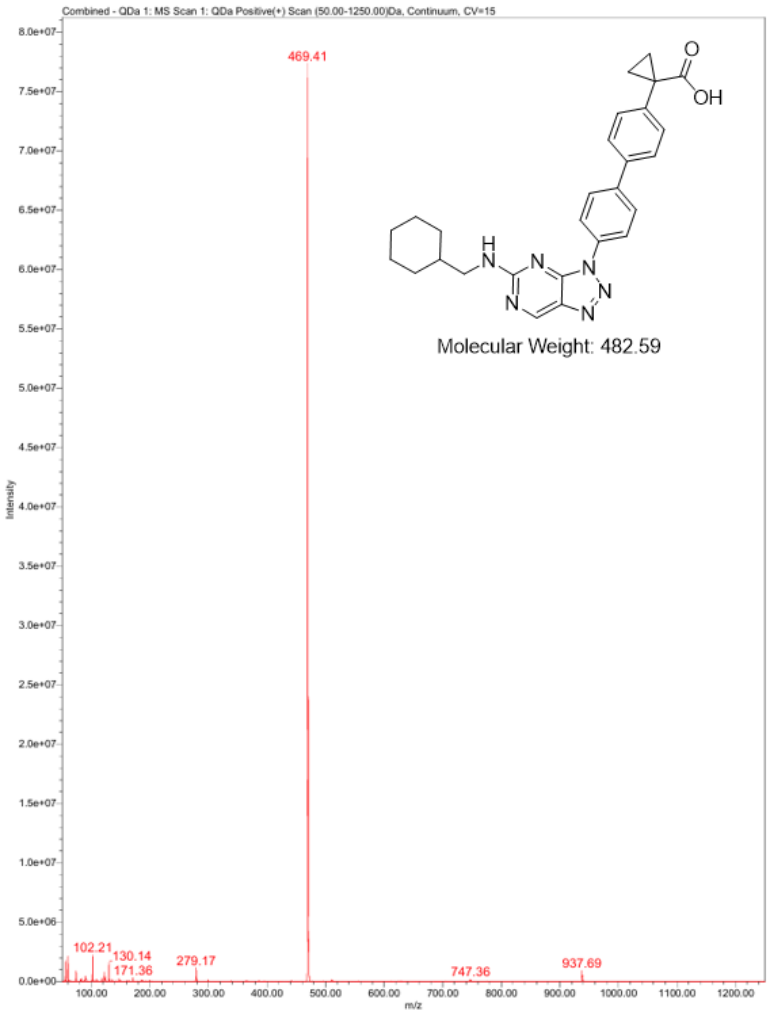

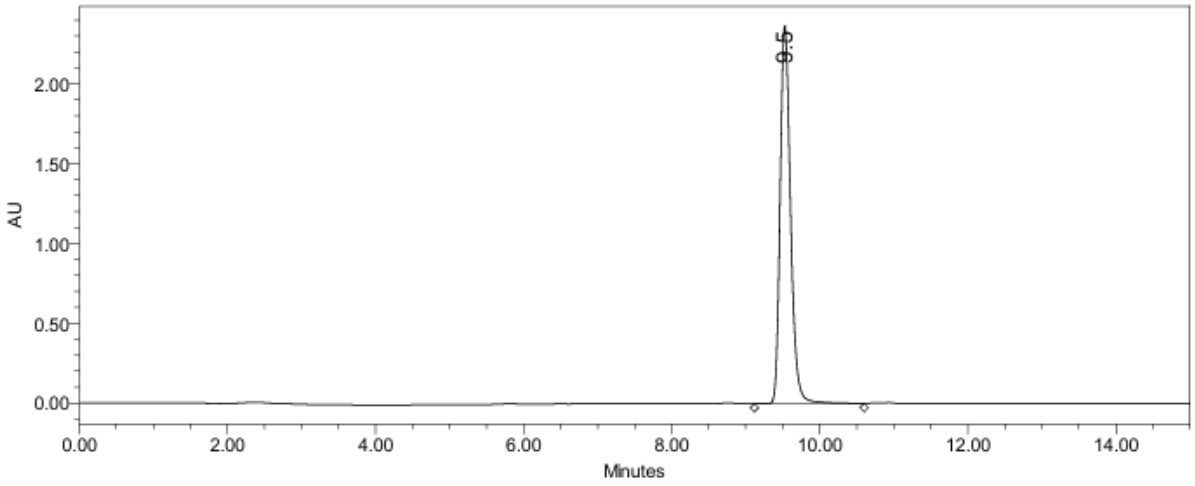

Channel: W2489 ChA; Processed Channel: W2489 ChA 254nm; Result Id: 55811; Processing Method: PM_Yang

Processed Channel Descr.: W2489 ChA 254nm

	Processed Channel Descr.	RT	Area	% Area	Height
1	W2489 ChA 254nm	9.528	23182281	100.00	2374984

Compound **L22f**

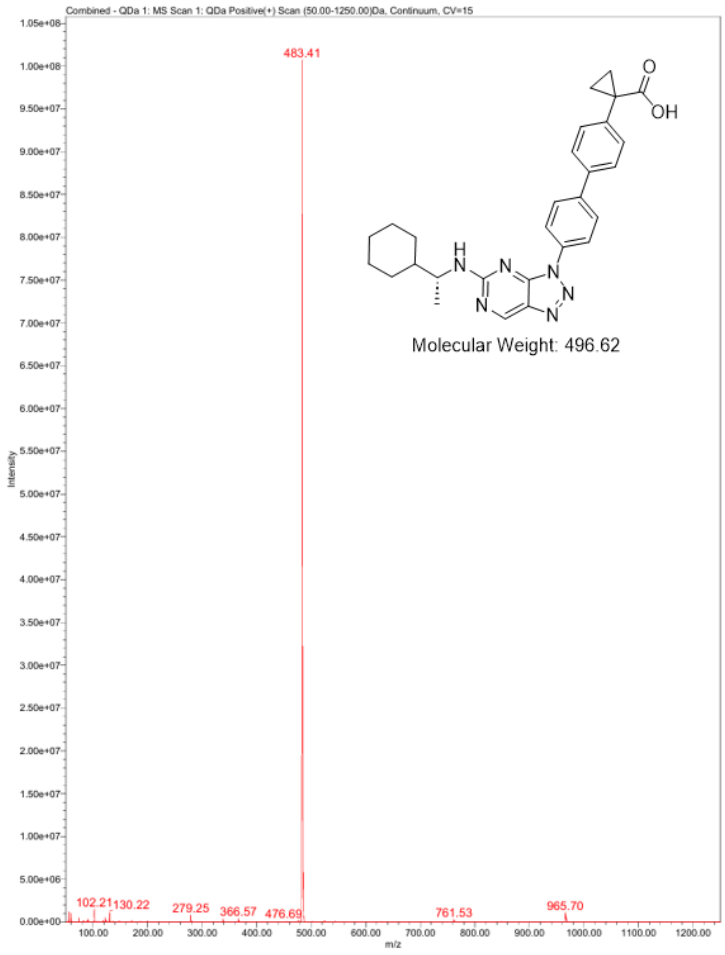

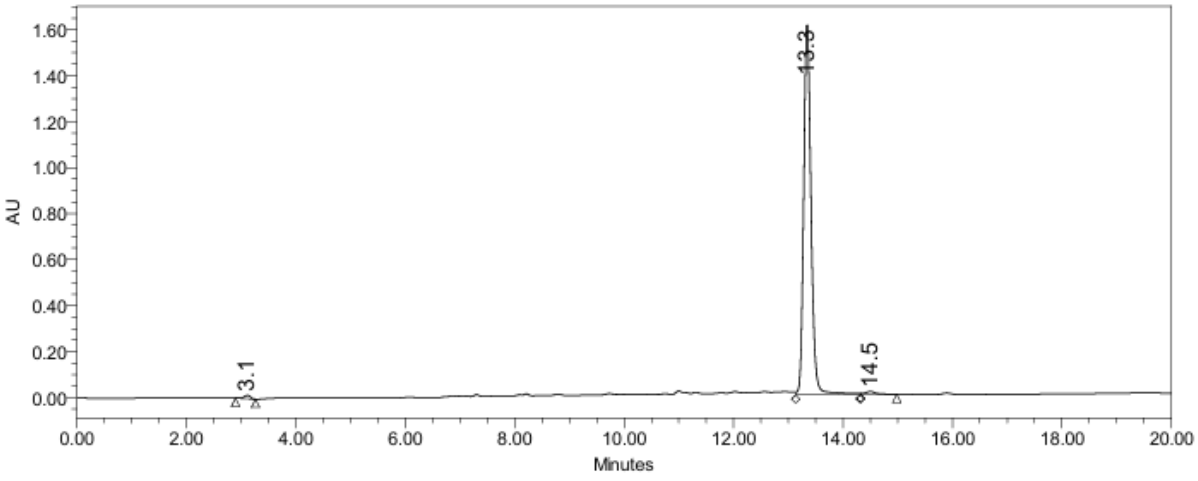

Channel: W2489 ChA; Processed Channel: W2489 ChA 254nm; Result Id: 53493; Processing Method: PM_Yang

Processed Channel Descr.: W2489 ChA 254nm

	Processed Channel Descr.	RT	Area	% Area	Height
1	W2489 ChA 254nm	3.120	116367	0.75	15103
2	W2489 ChA 254nm	13.343	15173711	98.11	1615451
3	W2489 ChA 254nm	14.499	176130	1.14	12426

Compound **L22h**

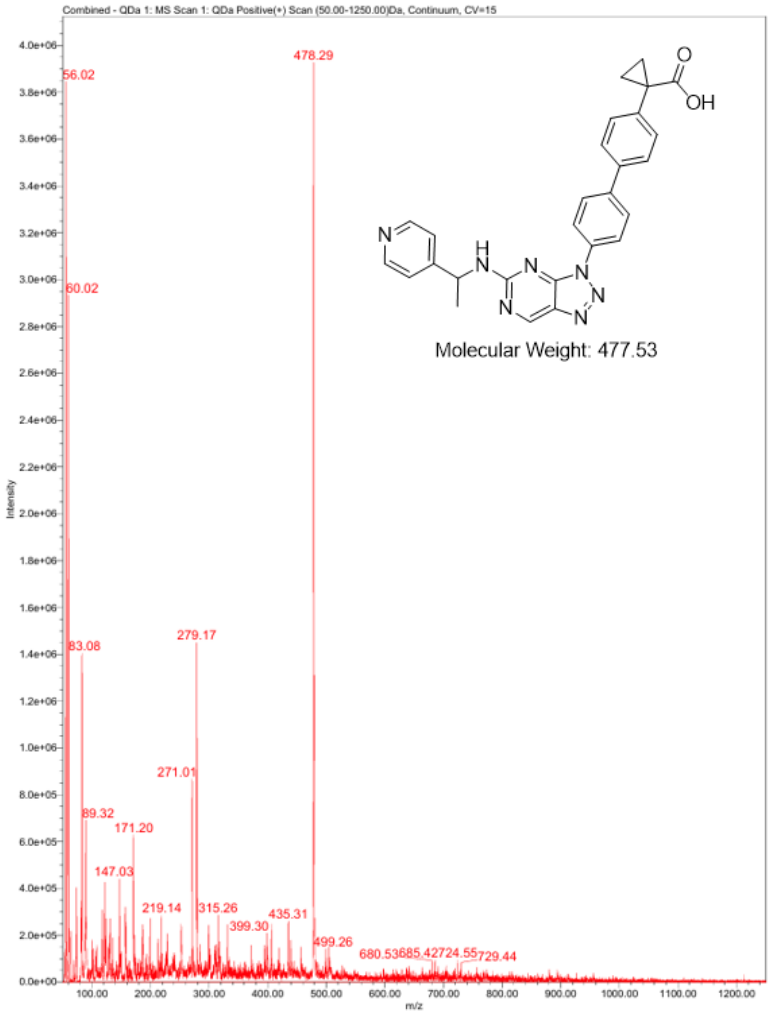

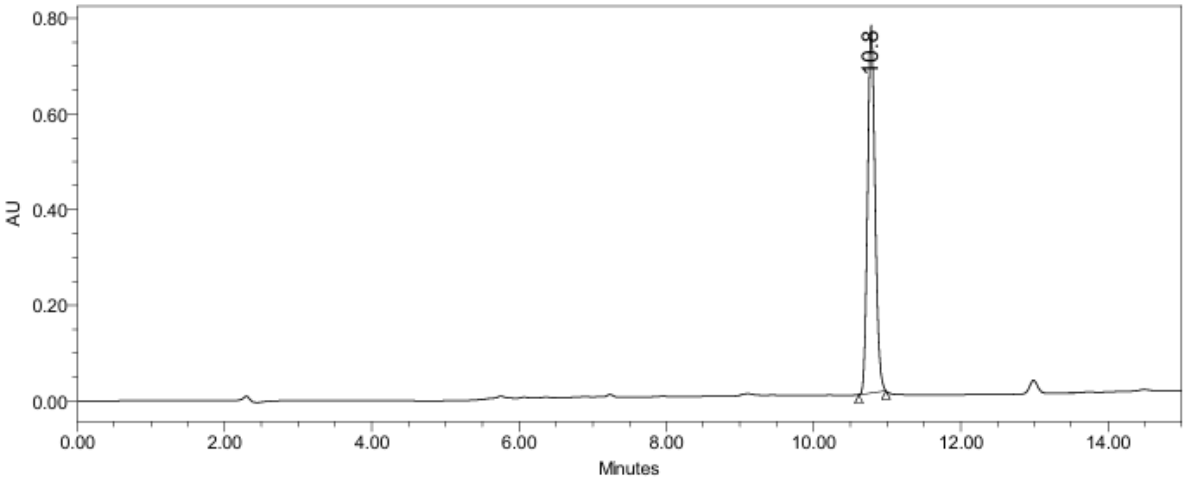

Channel: W2489 ChA; Processed Channel: W2489 ChA 254nm; Result Id: 56974; Processing Method: PM_Yang

Processed Channel Descr.: W2489 ChA 254nm

	Processed Channel Descr.	RT	Area	% Area	Height
1	W2489 ChA 254nm	10.784	5443973	100.00	766037

Compound **L22i**

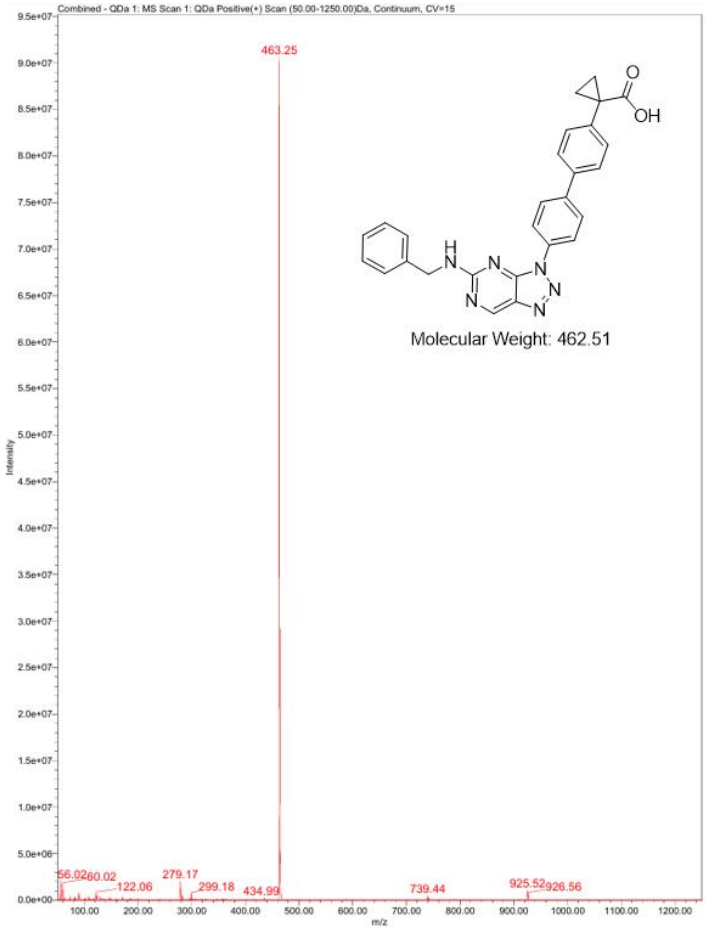

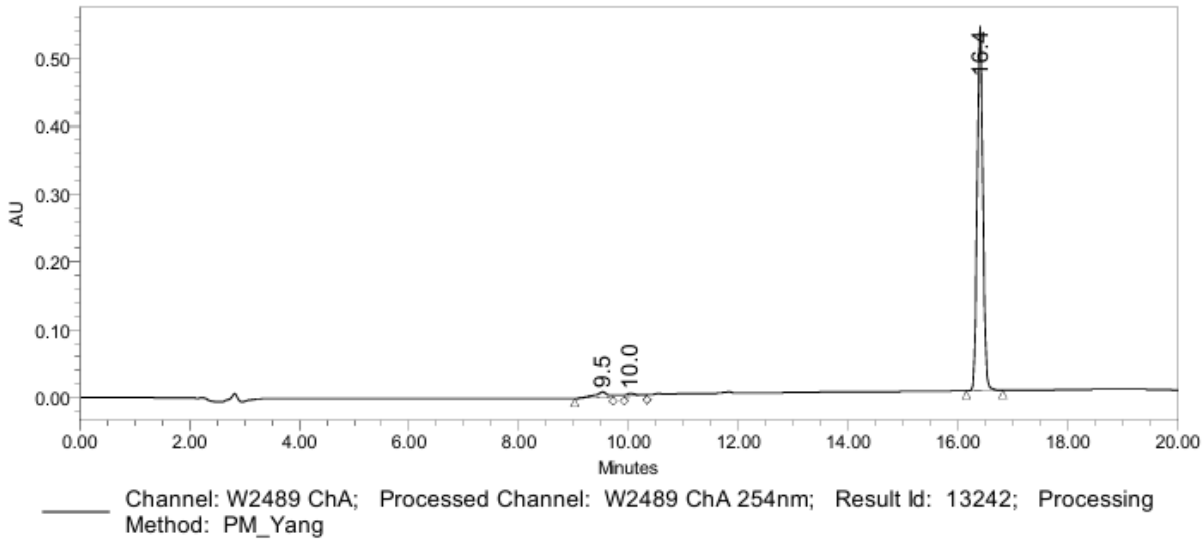

Channel: W2489 ChA; Processed Channel: W2489 ChA 254nm; Result Id: 13242; Processing Method: PM_Yang

Processed Channel Descr.: W2489 ChA 254nm

	Processed Channel Descr.	RT	Area	% Area	Height
1	W2489 ChA 254nm	9.530	125271	3.04	7958
2	W2489 ChA 254nm	10.038	64695	1.57	4273
3	W2489 ChA 254nm	16.400	3929587	95.39	536103

Compound **L22j**

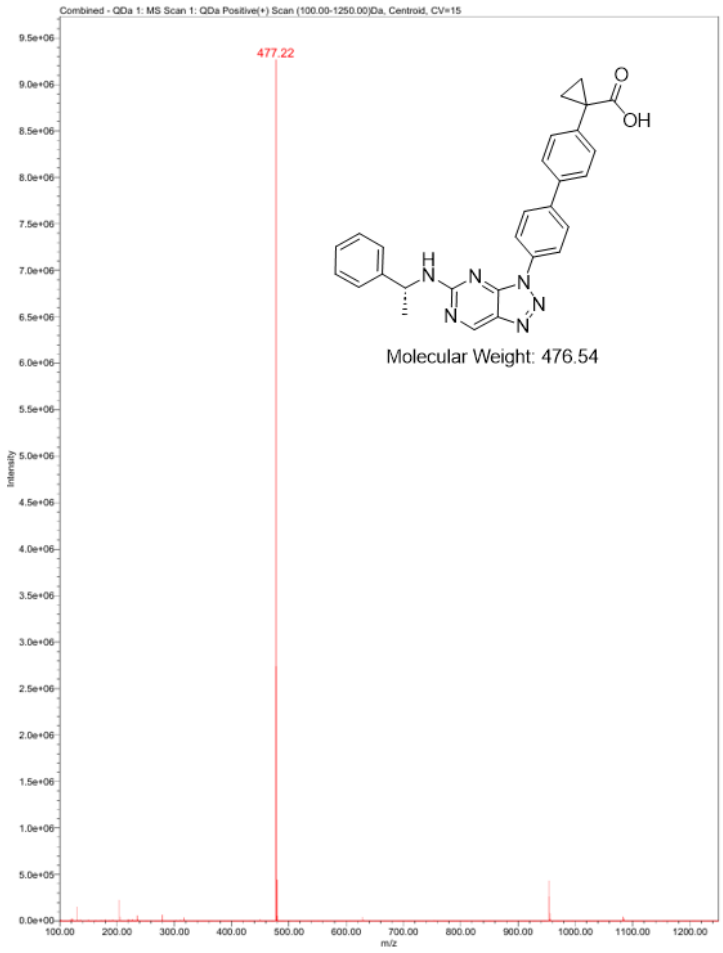

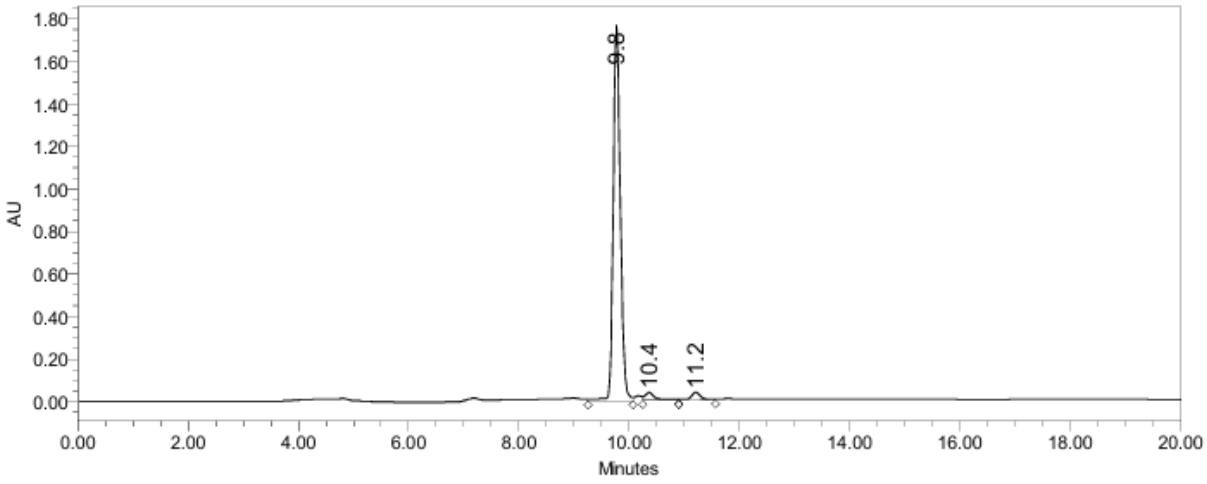

Channel: W2489 ChA; Processed Channel: W2489 ChA 254nm; Result Id: 50152; Processing Method: PM_Yang

Processed Channel Descr.: W2489 ChA 254nm

	Processed Channel Descr.	RT	Area	% Area	Height
1	W2489 ChA 254nm	9.771	15840513	94.61	1765683
2	W2489 ChA 254nm	10.363	481318	2.87	36124
3	W2489 ChA 254nm	11.208	421489	2.52	34549

Compound **L22k**

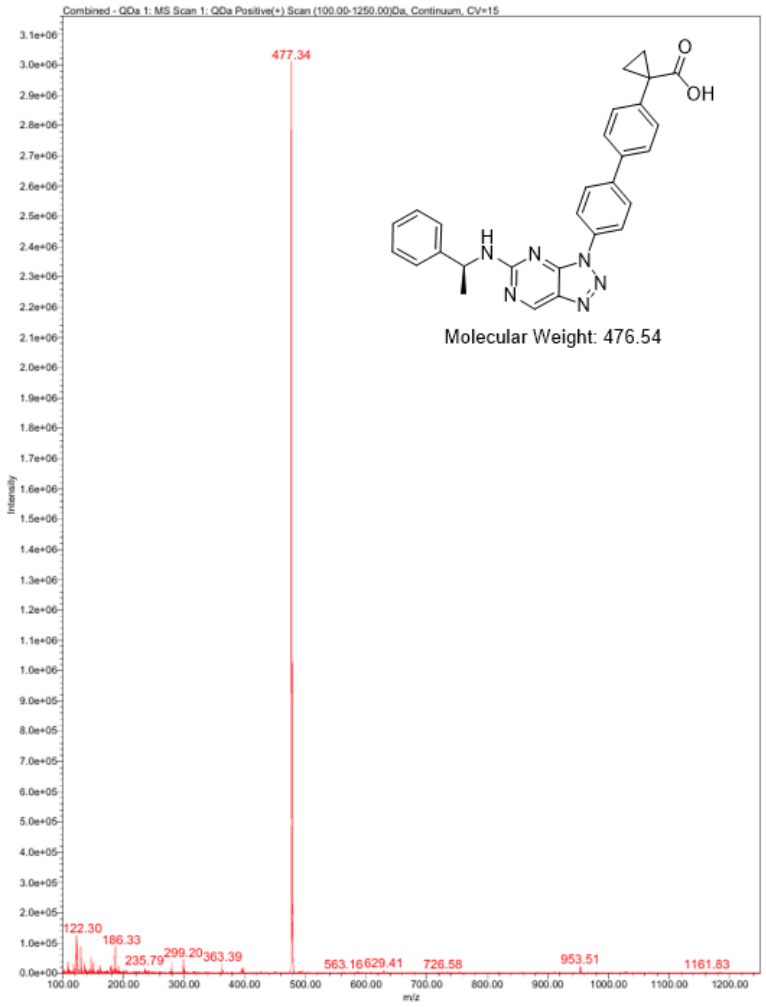

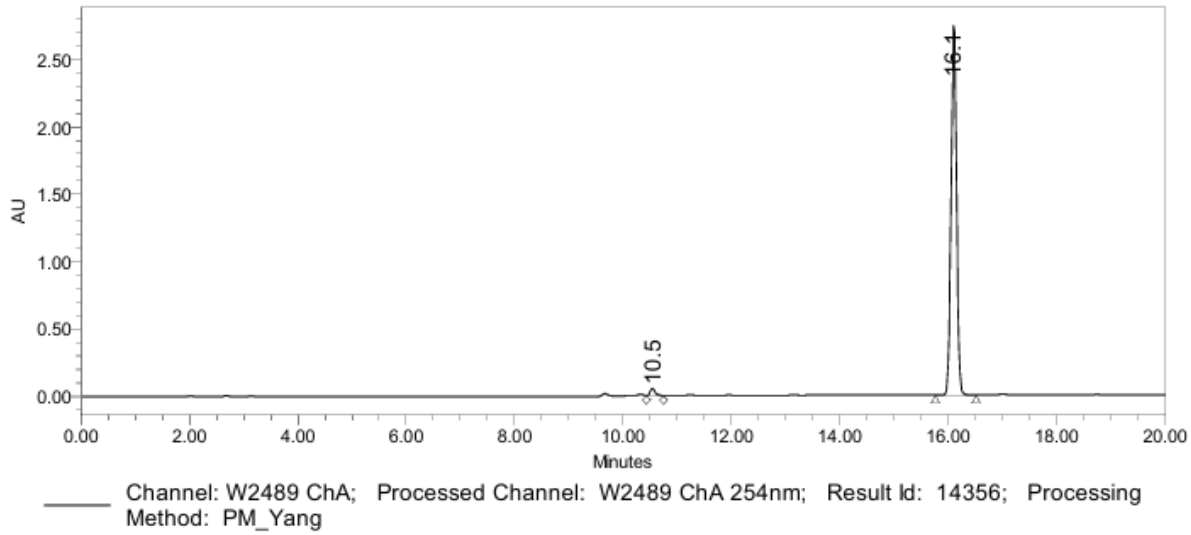

Processed Channel Descr.: W2489 ChA 254nm

	Processed Channel Descr.	RT	Area	% Area	Height
1	W2489 ChA 254nm	10.543	388143	1.96	57039
2	W2489 ChA 254nm	16.106	19435688	98.04	2748317

Compound **L22m**

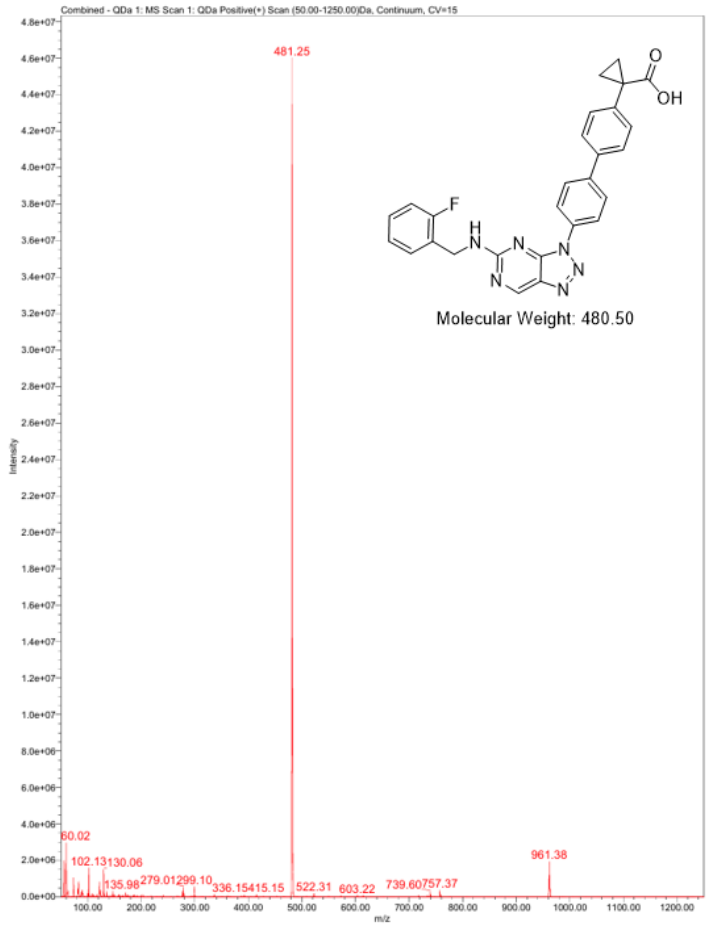

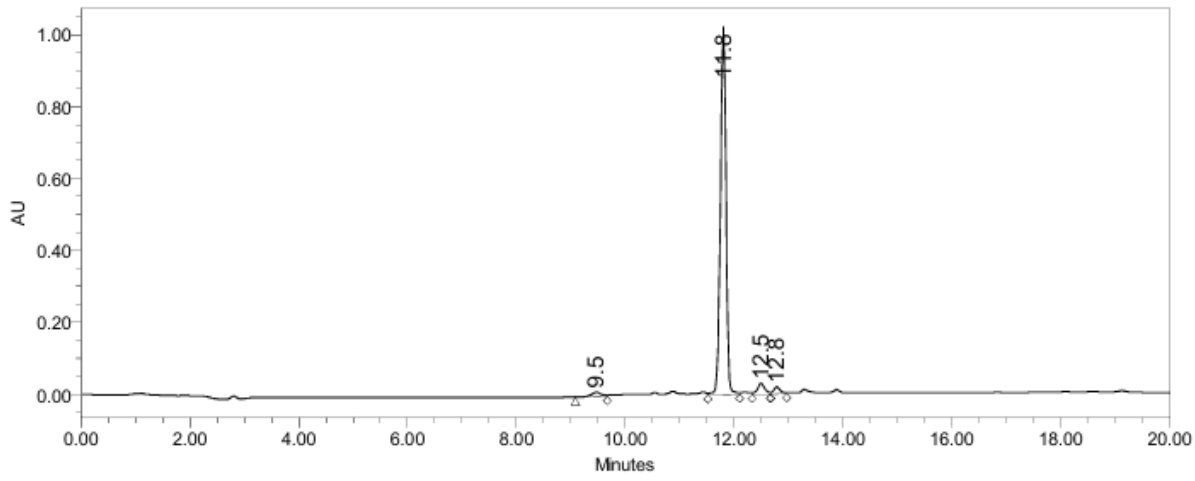

Channel: W2489 ChA; Processed Channel: W2489 ChA 254nm; Result Id: 14338; Processing Method: PM_Yang

Processed Channel Descr.: W2489 ChA 254nm

	Processed Channel Descr.	RT	Area	% Area	Height
1	W2489 ChA 254nm	9.476	172311	2.16	12747
2	W2489 ChA 254nm	11.802	7330283	92.06	1019050
3	W2489 ChA 254nm	12.492	288758	3.63	30874
4	W2489 ChA 254nm	12.785	171217	2.15	20198

Compound **L22n**

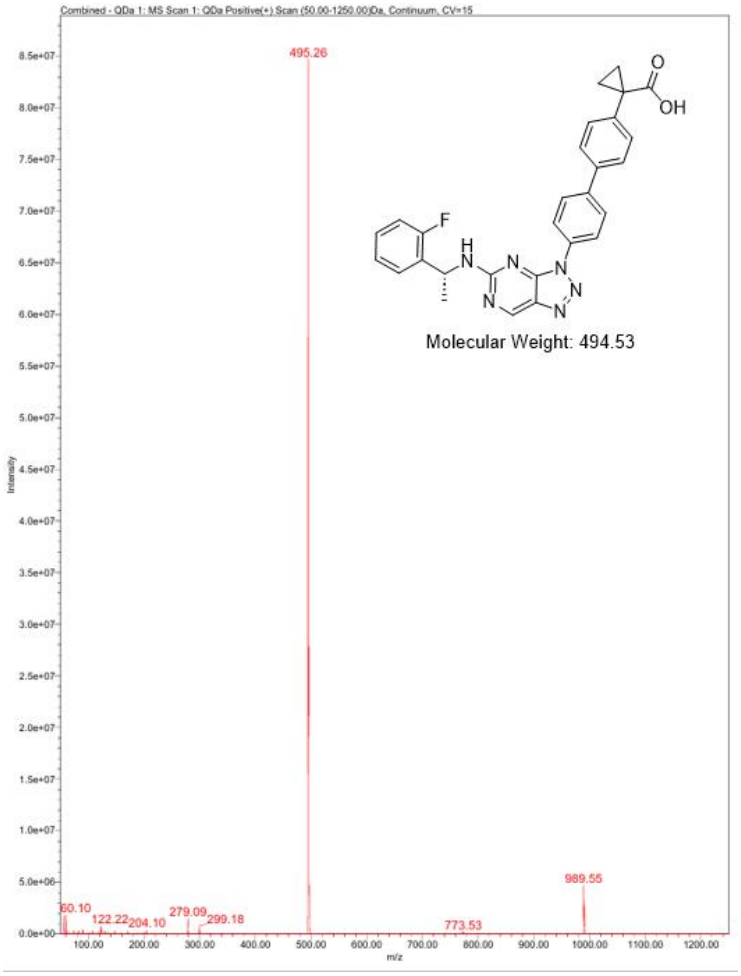

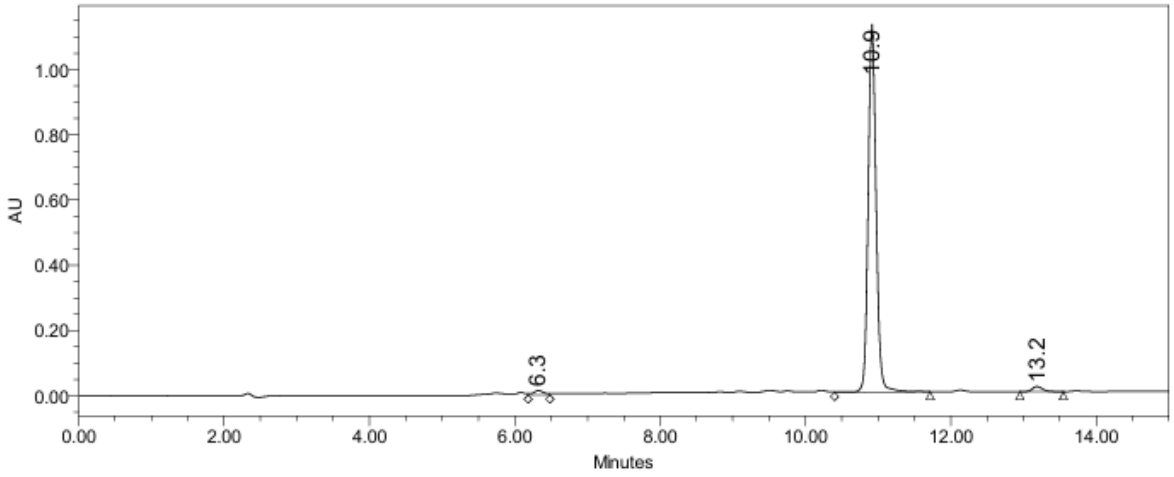

Channel: W2489 ChA; Processed Channel: W2489 ChA 254nm; Result Id: 54563; Processing Method: PM_Yang

Processed Channel Descr.: W2489 ChA 254nm

	Processed Channel Descr.	RT	Area	% Area	Height
1	W2489 ChA 254nm	6.327	142716	1.62	13974
2	W2489 ChA 254nm	10.916	8521567	96.66	1123479
3	W2489 ChA 254nm	13.185	151697	1.72	15949

Compound **L22o**

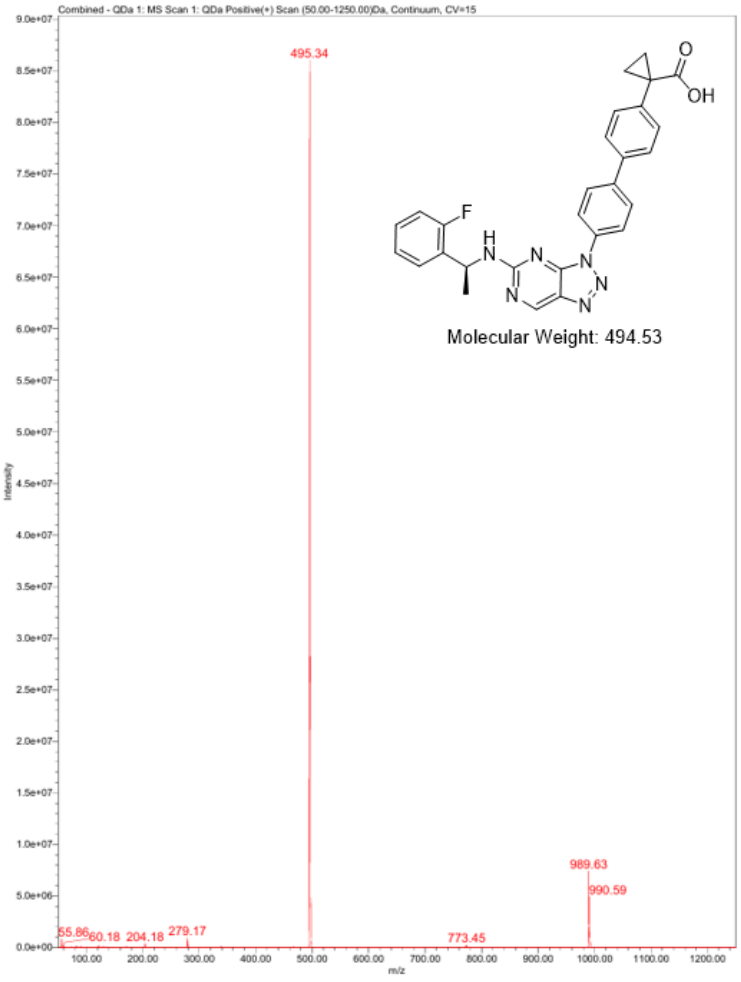

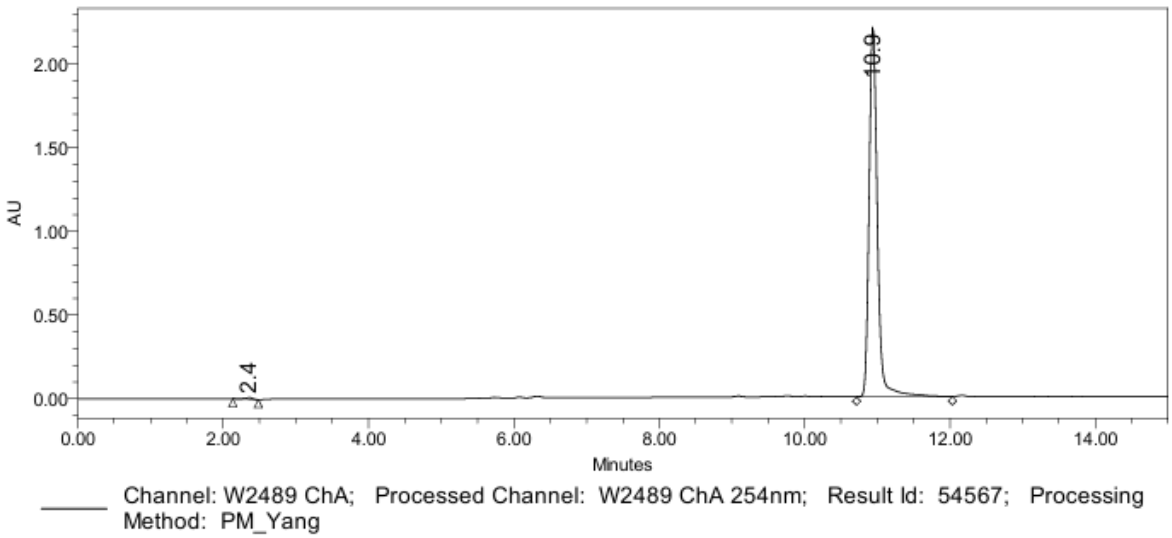

Channel: W2489 ChA; Processed Channel: W2489 ChA 254nm; Result Id: 54567; Processing Method: PM_Yang

Processed Channel Descr.: W2489 ChA 254nm

	Processed Channel Descr.	RT	Area	% Area	Height
1	W2489 ChA 254nm	2.360	70528	0.40	10097
2	W2489 ChA 254nm	10.940	17697626	99.60	2218931

Compound **L22p**

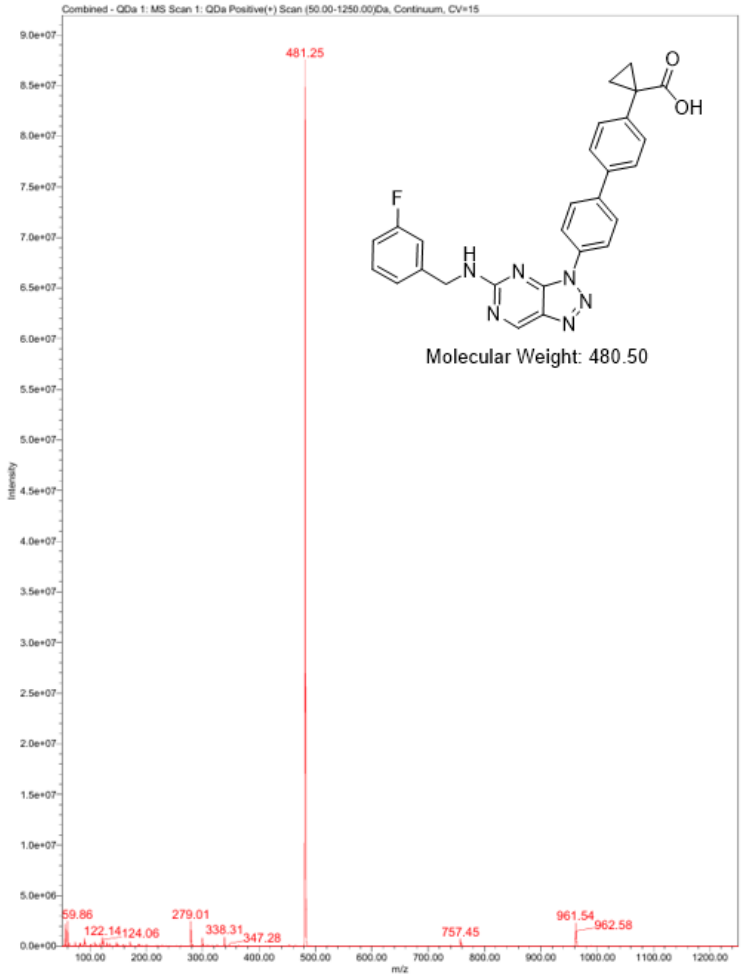

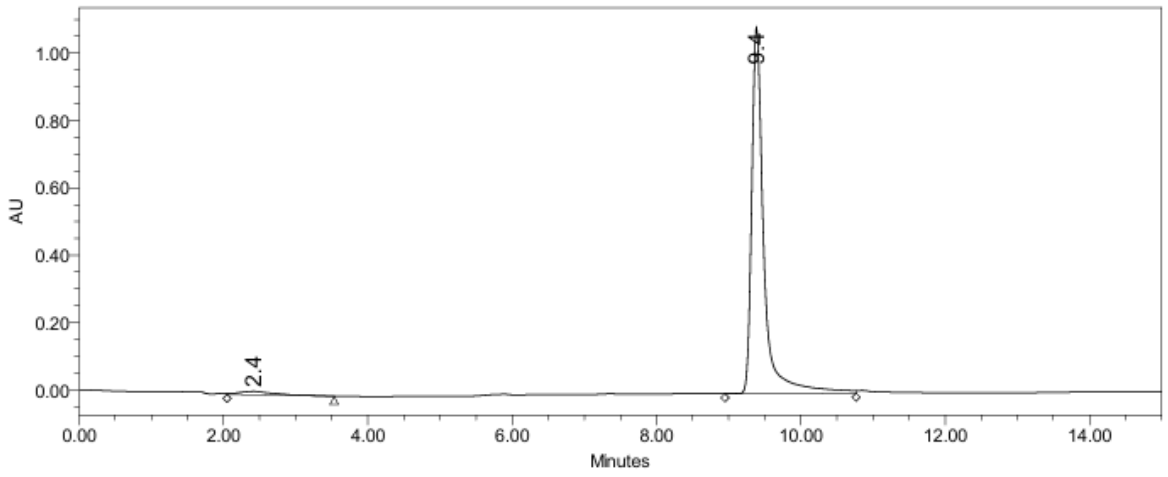

Channel: W2489 ChA; Processed Channel: W2489 ChA 254nm; Result Id: 54846; Processing Method: PM_Yang

Processed Channel Descr.: W2489 ChA 254nm

	Processed Channel Descr.	RT	Area	% Area	Height
1	W2489 ChA 254nm	2.417	337313	2.58	9943
2	W2489 ChA 254nm	9.387	12736191	97.42	1090172

Compound **L22q**

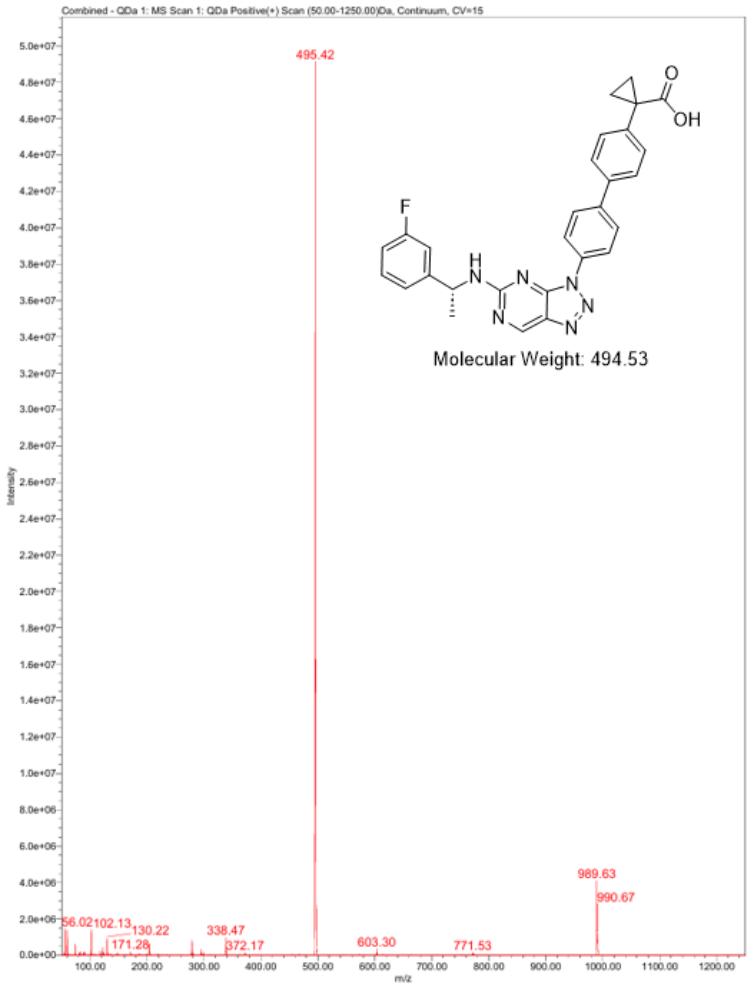

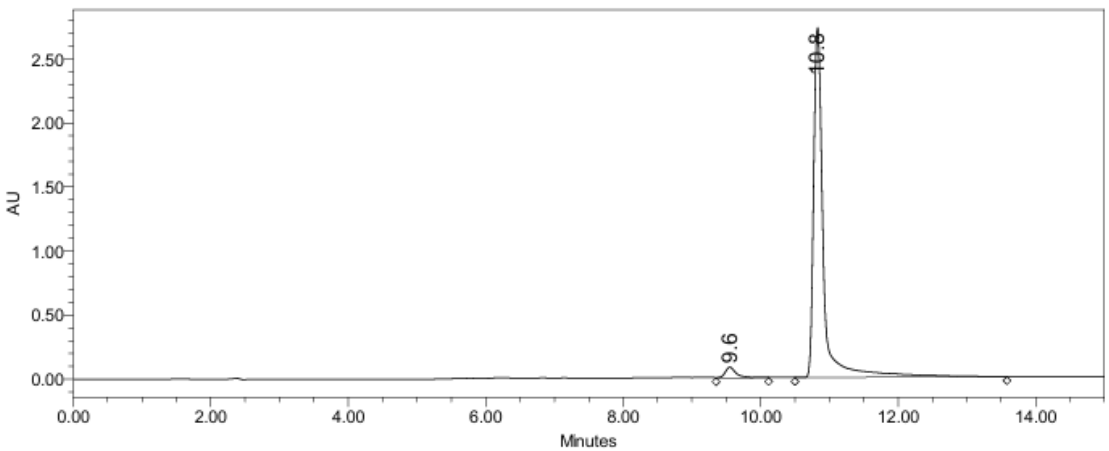

Channel: W2489 ChA; Processed Channel: W2489 ChA 254nm; Result Id: 54335; Processing Method: PM_Yang

Processed Channel Descr.: W2489 ChA 254nm

	Processed Channel Descr.	RT	Area	% Area	Height
1	W2489 ChA 254nm	9.552	936518	3.32	83547
2	W2489 ChA 254nm	10.828	27236769	96.68	2738596

Compound **L22r**

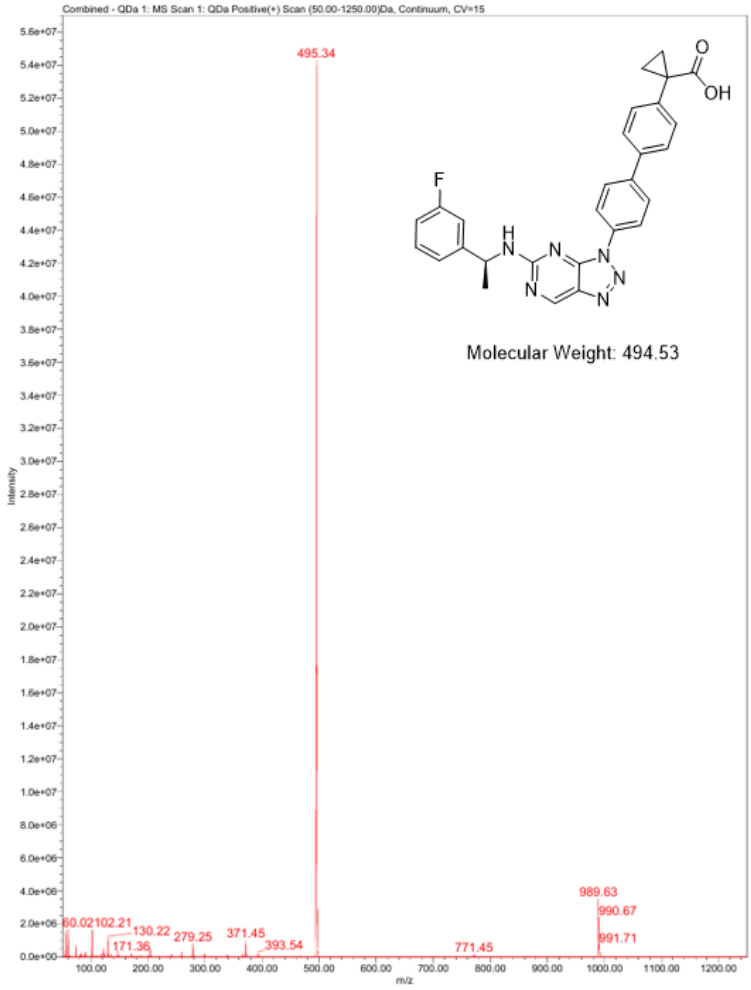

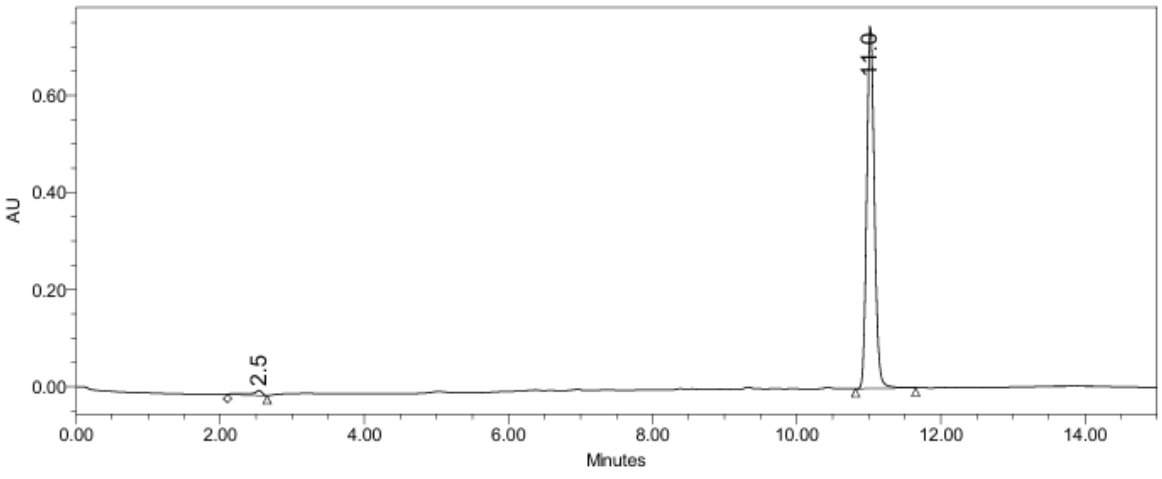

Channel: W2489 ChA; Processed Channel: W2489 ChA 254nm; Result Id: 54273; Processing Method: PM_Yang

Processed Channel Descr.: W2489 ChA 254nm

	Processed Channel Descr.	RT	Area	% Area	Height
1	W2489 ChA 254nm	2.536	115210	2.04	10210
2	W2489 ChA 254nm	11.023	5528859	97.96	748537

Compound **L22s**

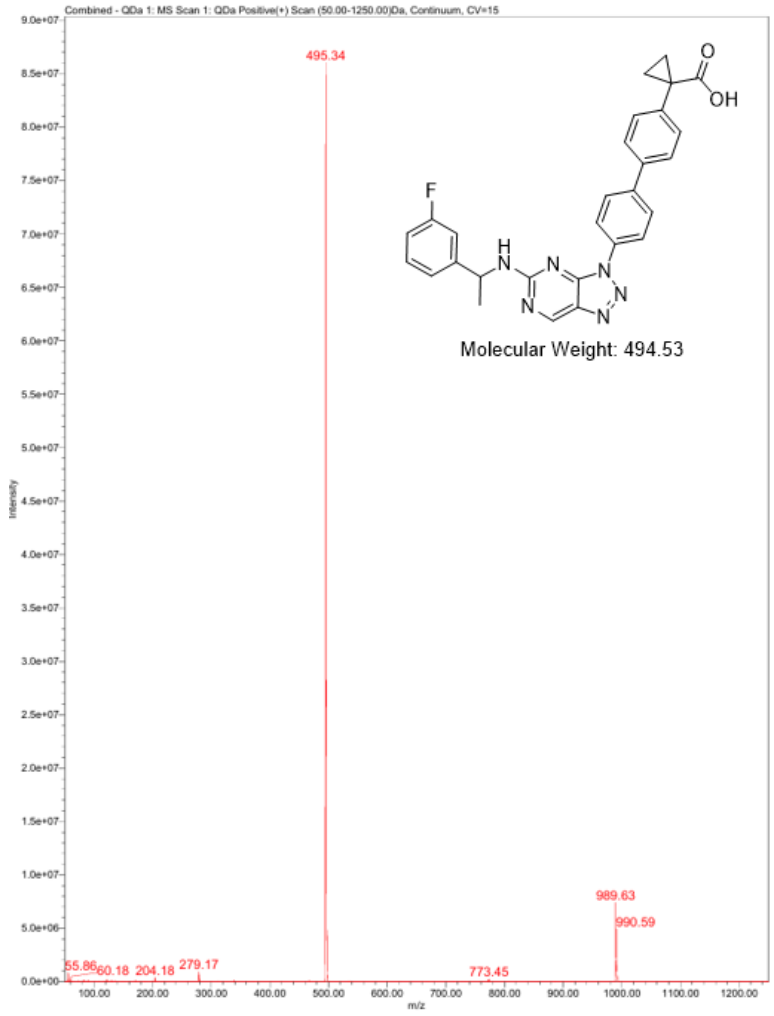

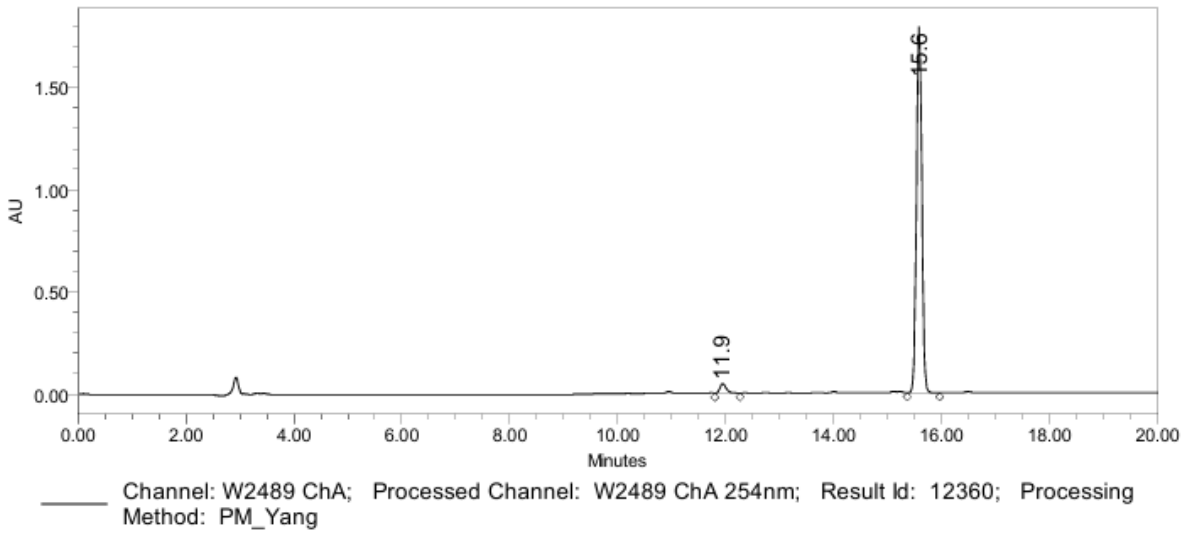

Channel: W2489 ChA; Processed Channel: W2489 ChA 254nm; Result Id: 12360; Processing Method: PM_Yang

Processed Channel Descr.: W2489 ChA 254nm

	Processed Channel Descr.	RT	Area	% Area	Height
1	W2489 ChA 254nm	11.944	372895	2.90	46125
2	W2489 ChA 254nm	15.585	12493723	97.10	1783305

Compound **L22t**

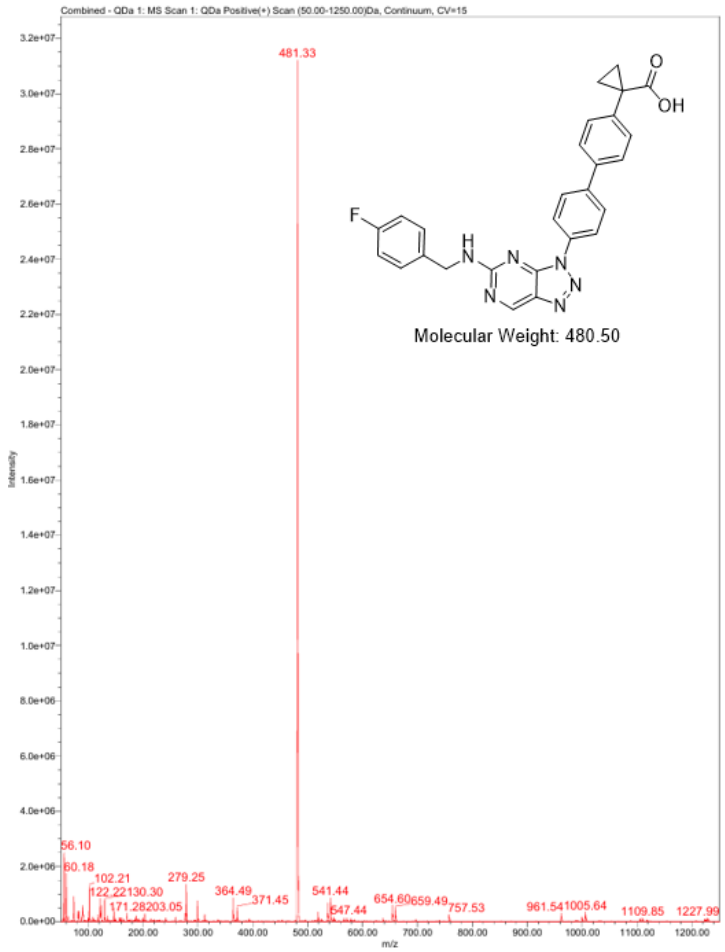

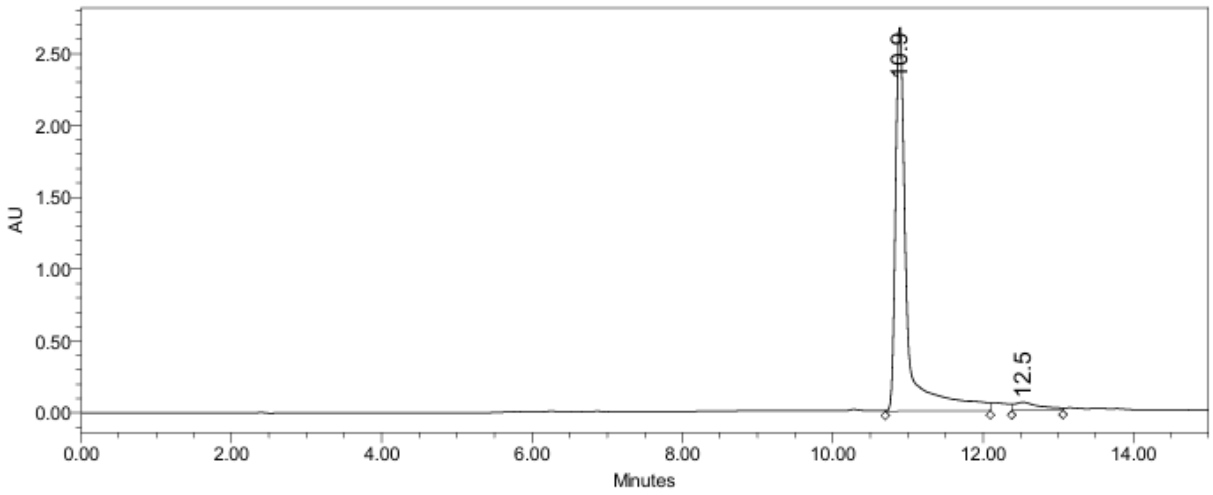

Channel: W2489 ChA; Processed Channel: W2489 ChA 254nm; Result Id: 54551; Processing Method: PM_Yang

Processed Channel Descr.: W2489 ChA 254nm

	Processed Channel Descr.	RT	Area	% Area	Height
1	W2489 ChA 254nm	10.893	28191504	95.12	2685785
2	W2489 ChA 254nm	12.534	1445562	4.88	57066

Compound **L22u**

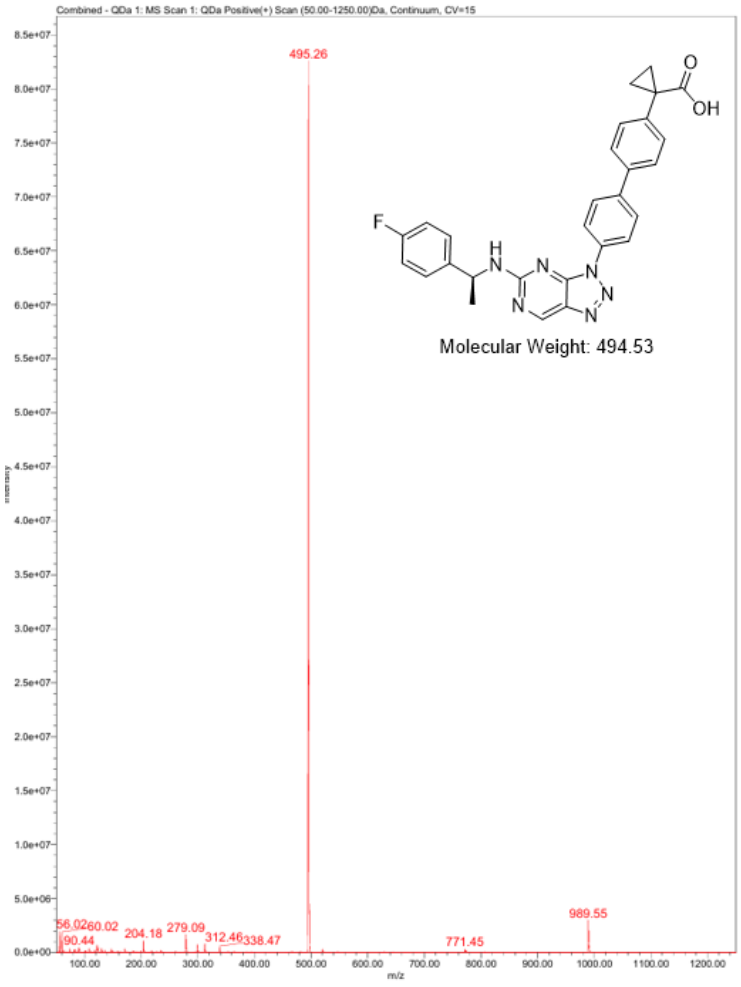

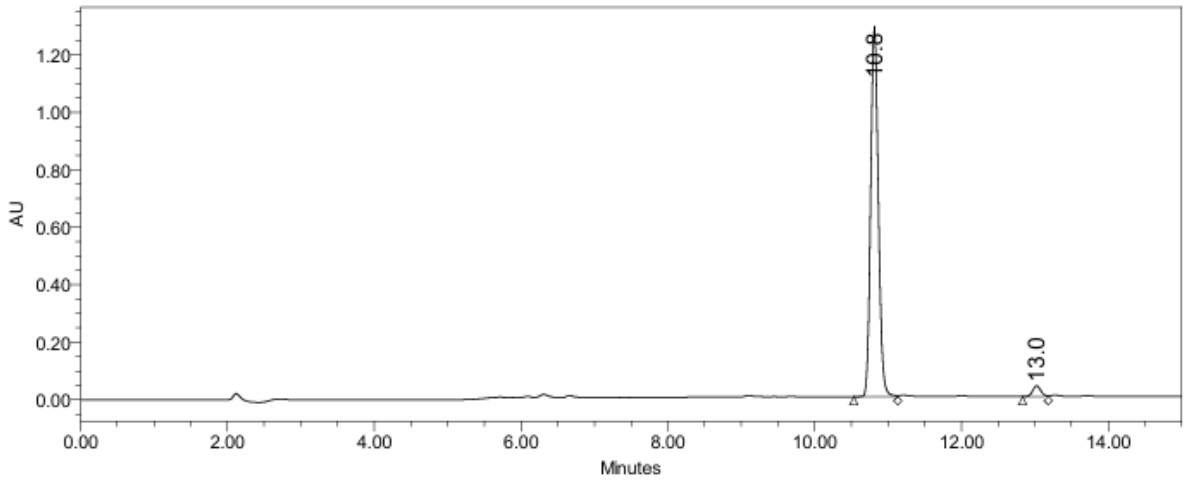

Channel: W2489 ChA; Processed Channel: W2489 ChA 254nm; Result Id: 54559; Processing Method: PM_Yang

Processed Channel Descr.: W2489 ChA 254nm

	Processed Channel Descr.	RT	Area	% Area	Height
1	W2489 ChA 254nm	10.814	9329592	97.03	1284896
2	W2489 ChA 254nm	13.025	285480	2.97	36888

Compound **L22c**

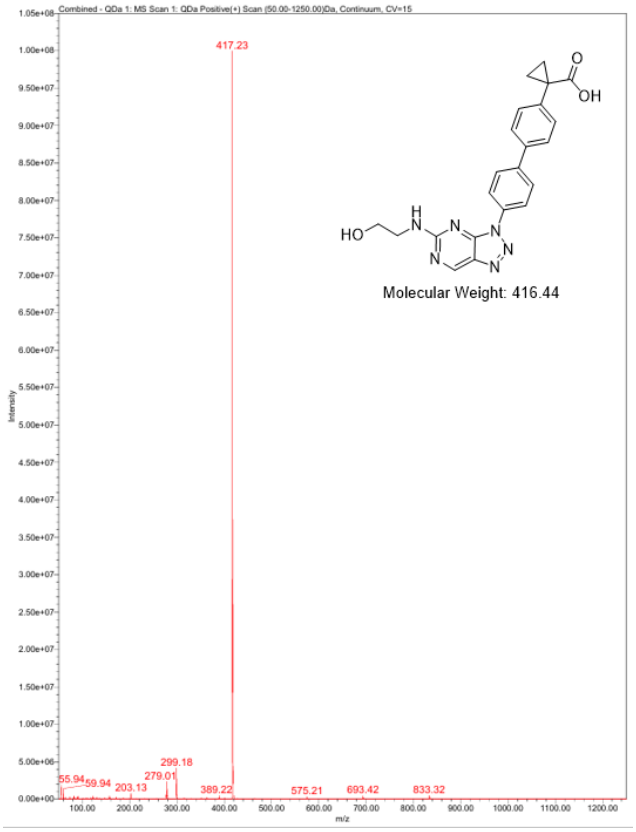

Compound **L22g**

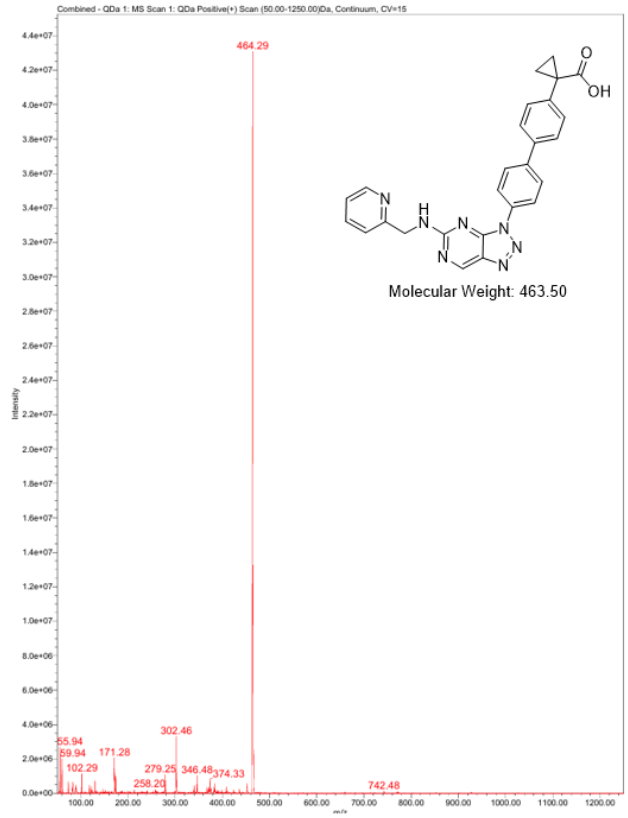

Compound **L22l**

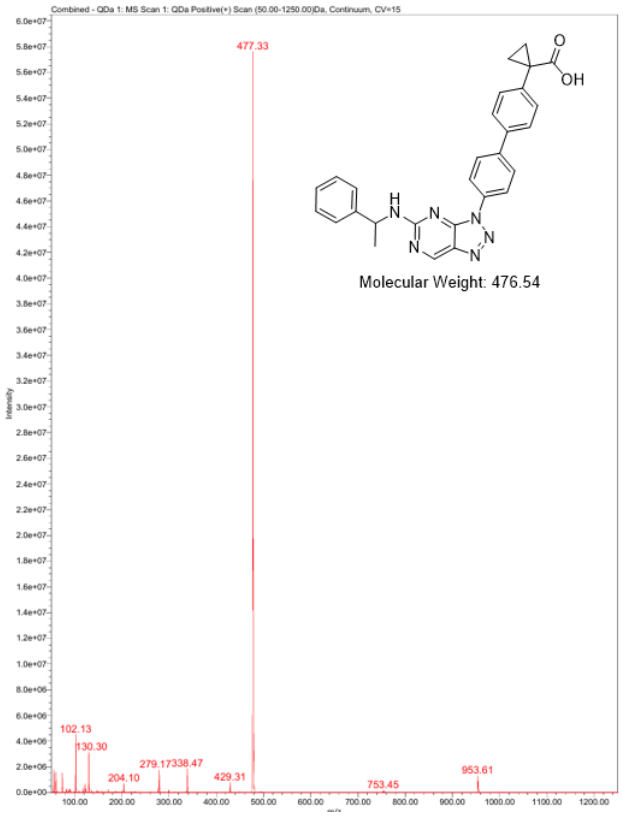

Compound **L24a**

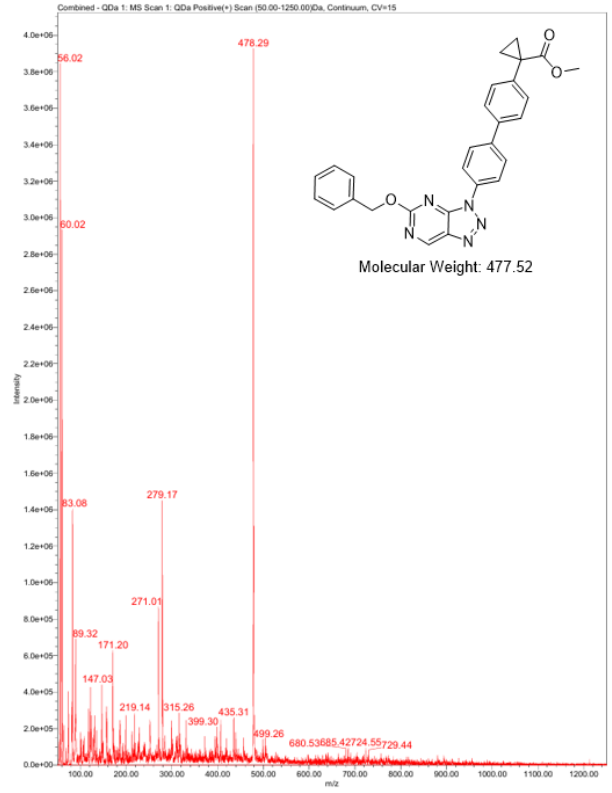

Compound **L25a**

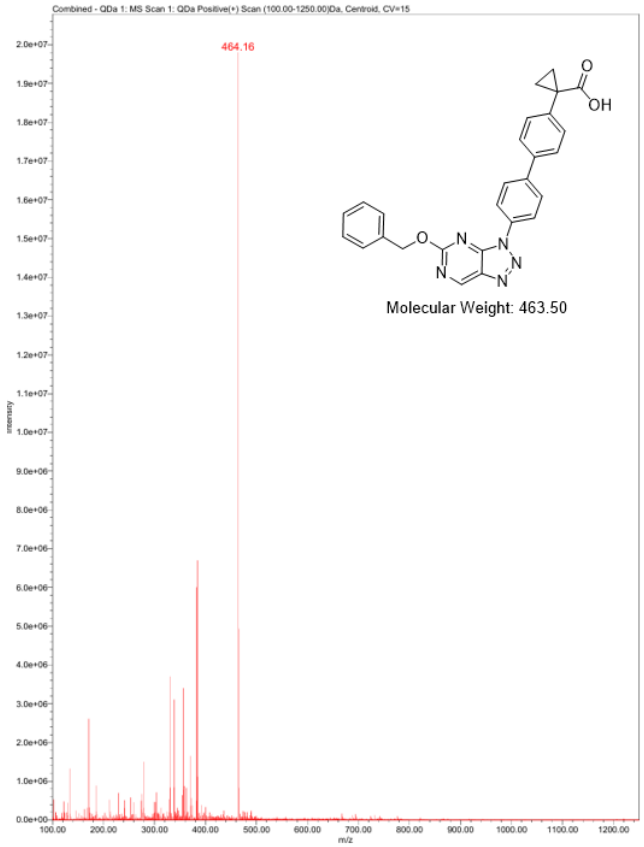

Compound **L26**

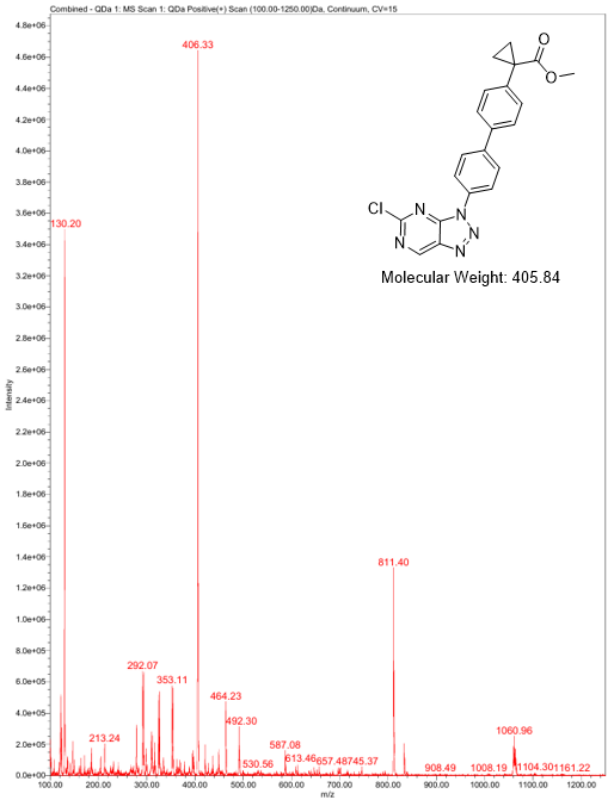

Spectrum of ^{1}H-NMR

Compound - **L11**

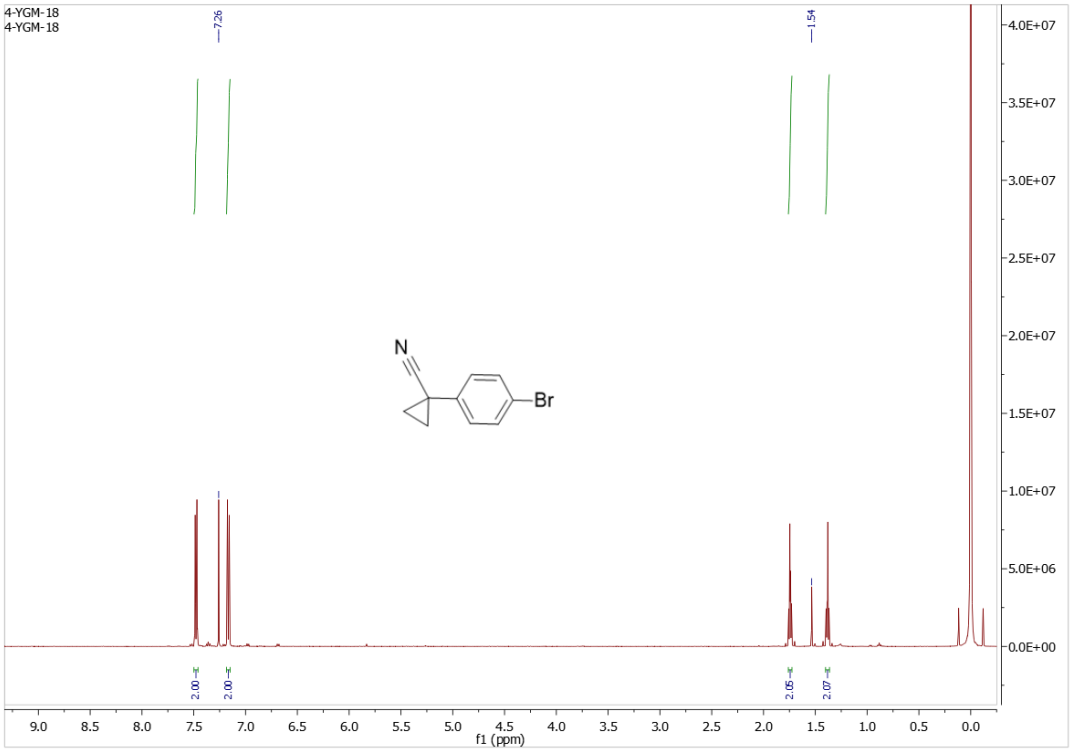

Compound - **L12**

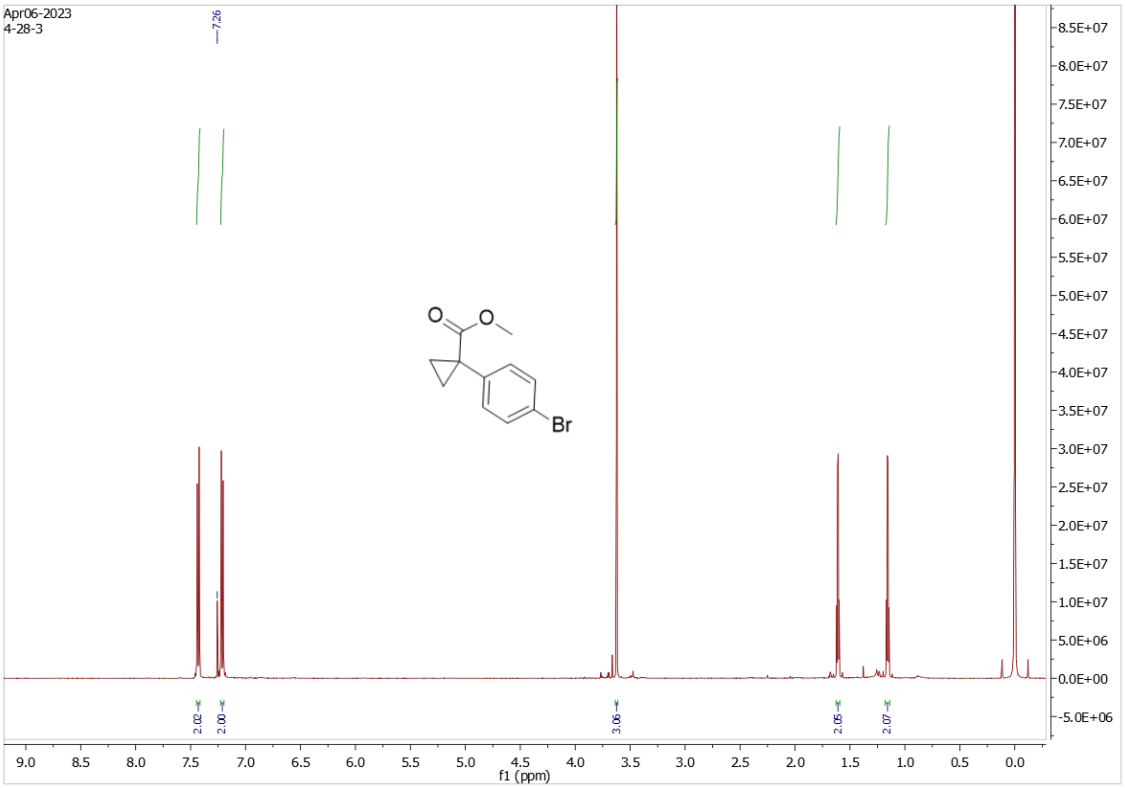

Compound - **L13**

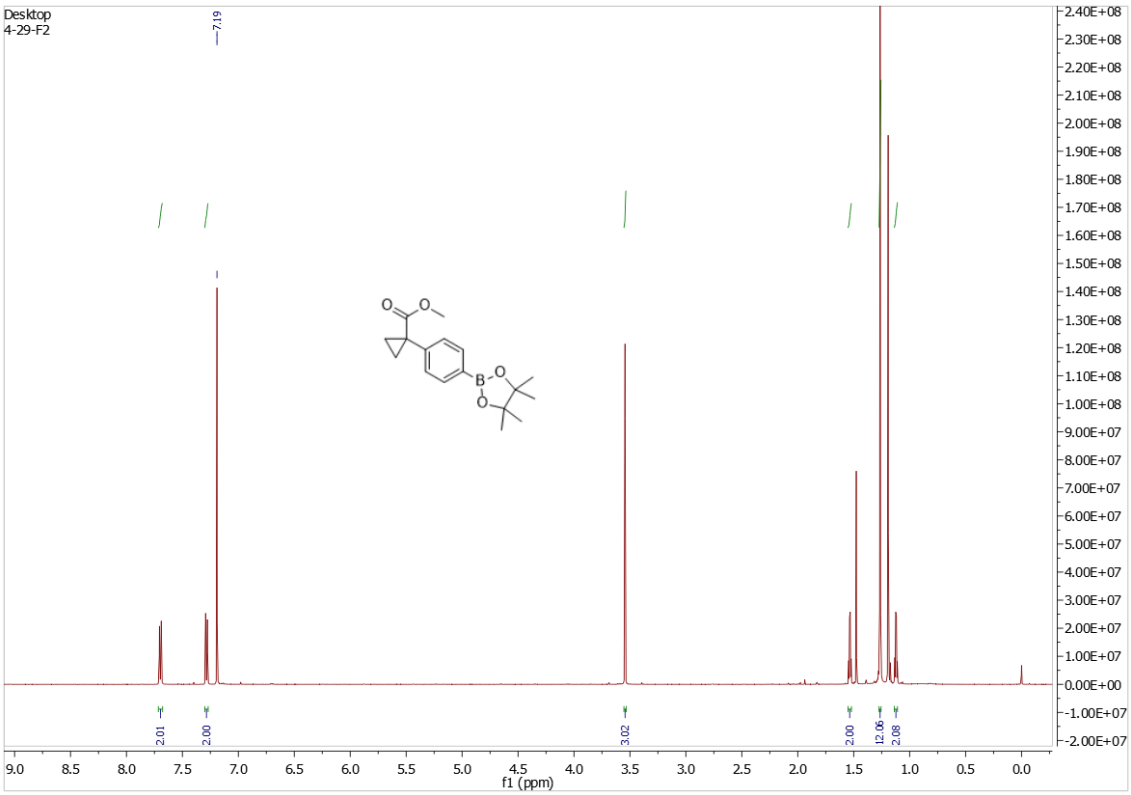

Compound -**L17**

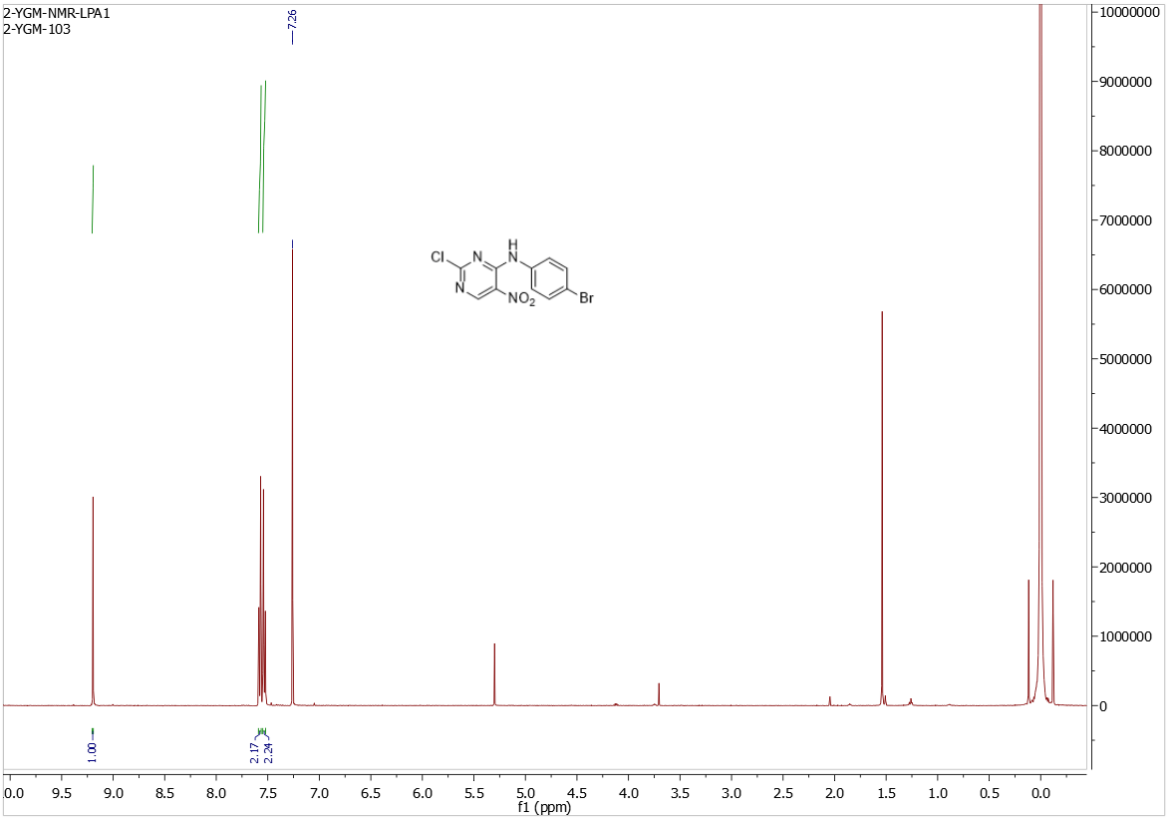

Compound - **L18**

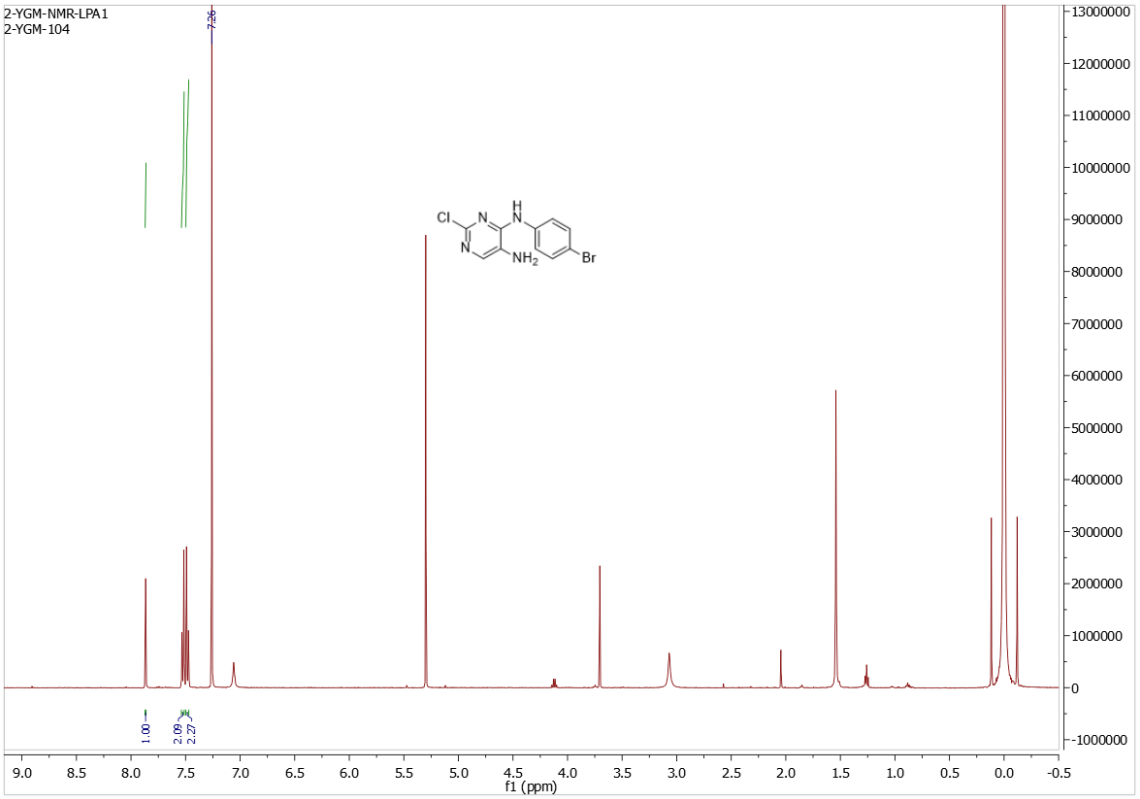

Compound - **L19**

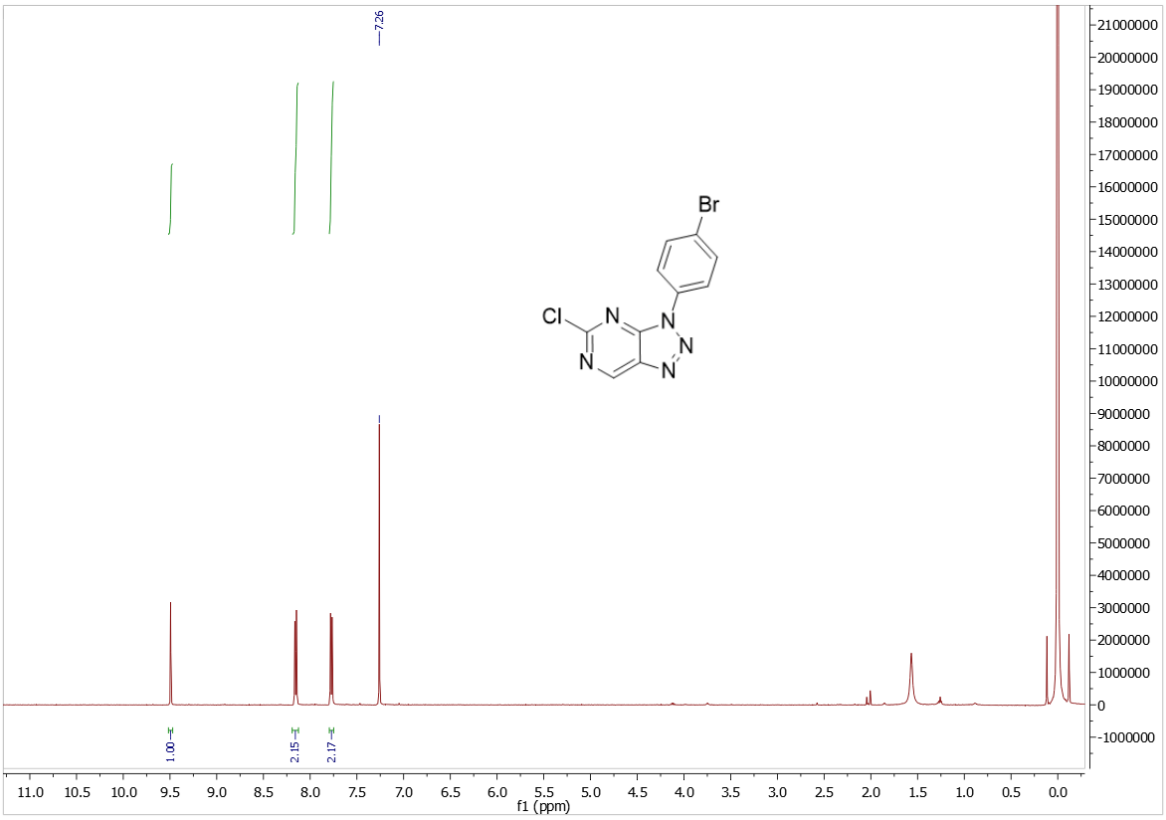

Compound **L20a**

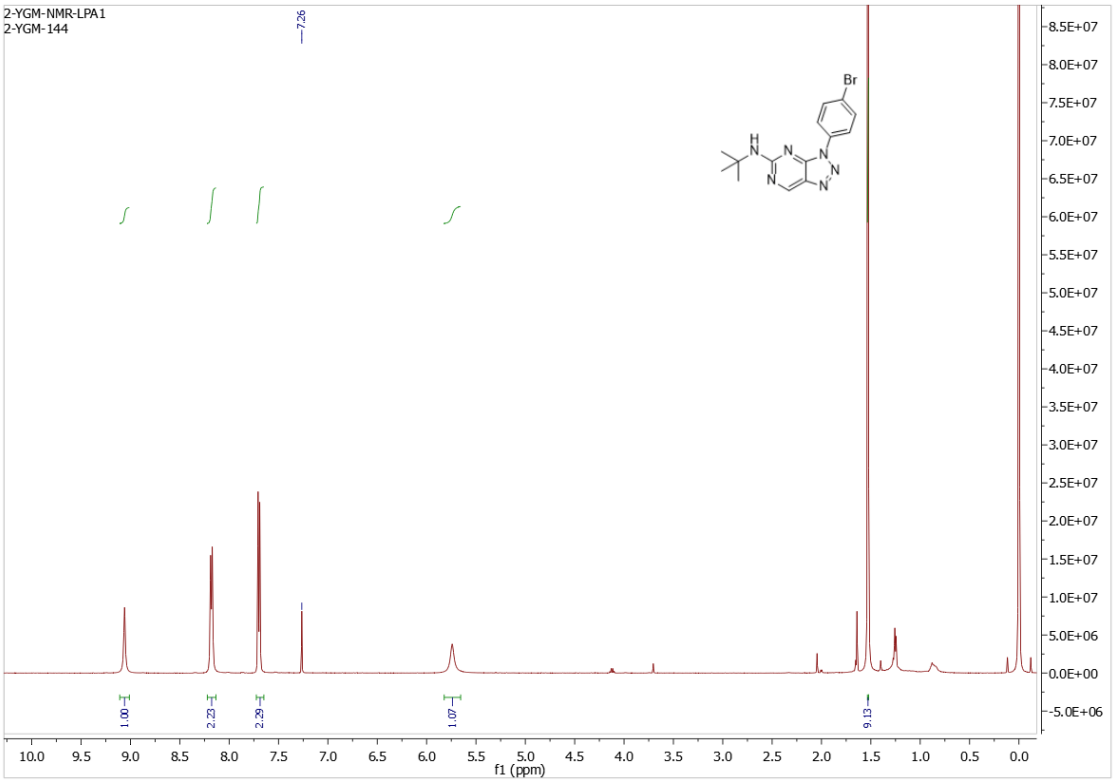

Compound **L20b**

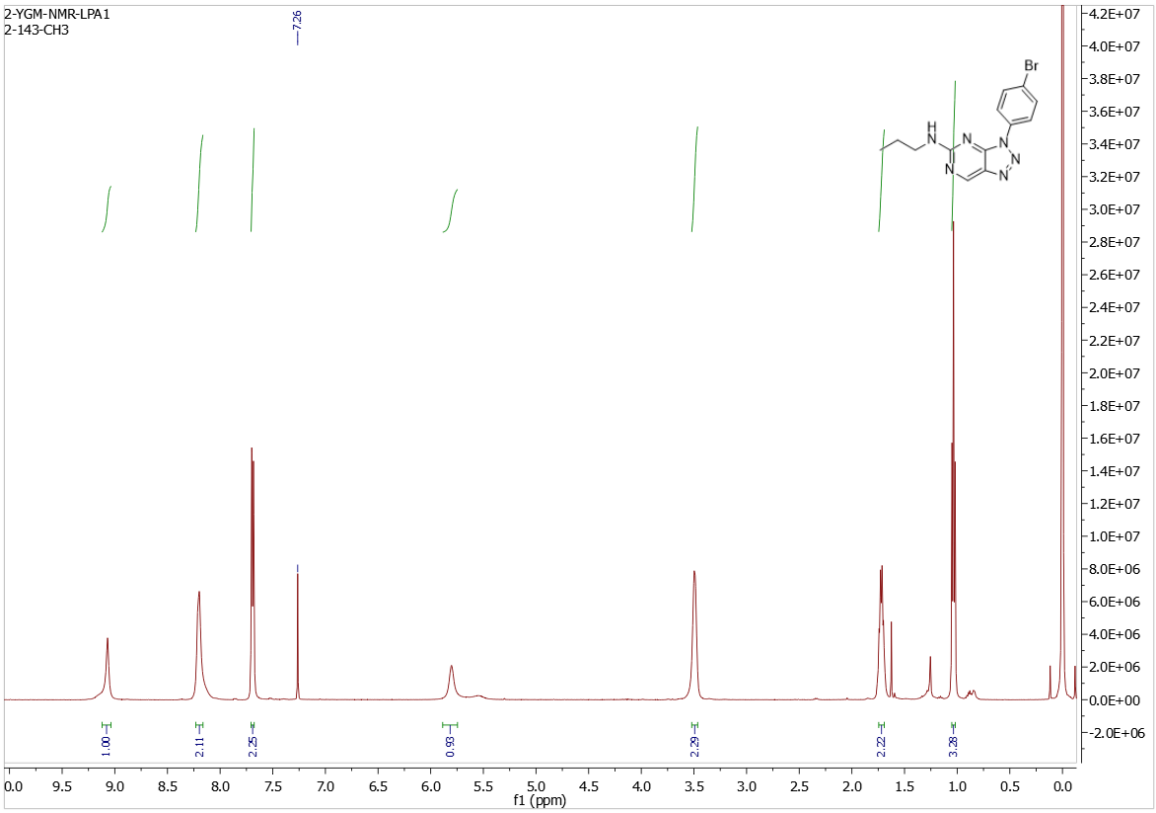

Compound **L20c**

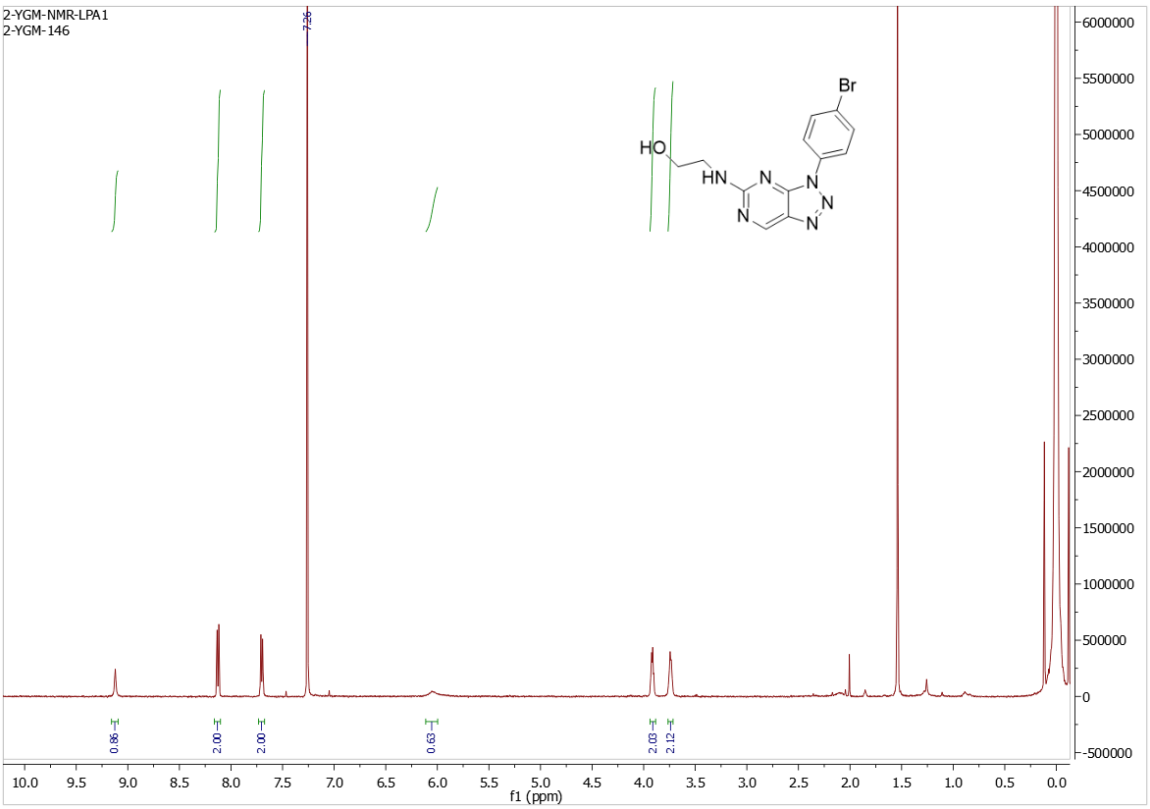

Compound **L20e**

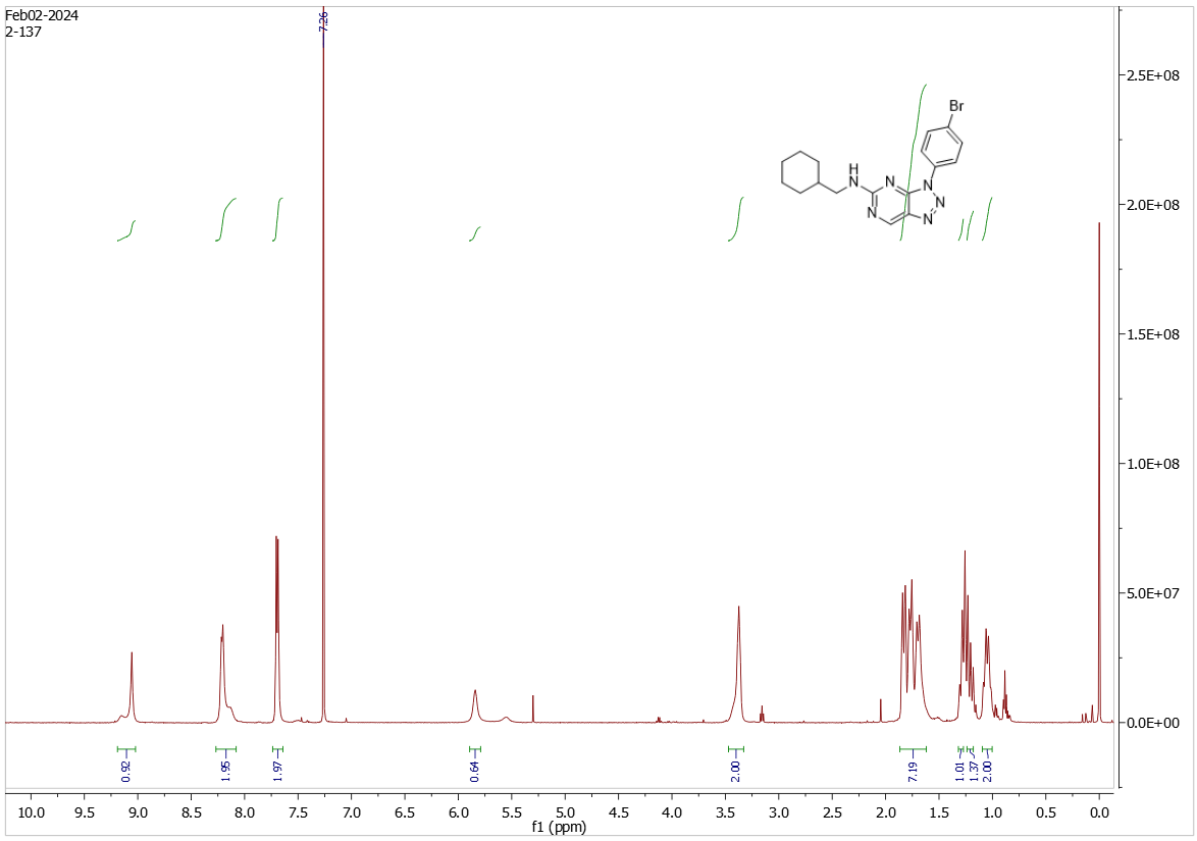

Compound **L20f**

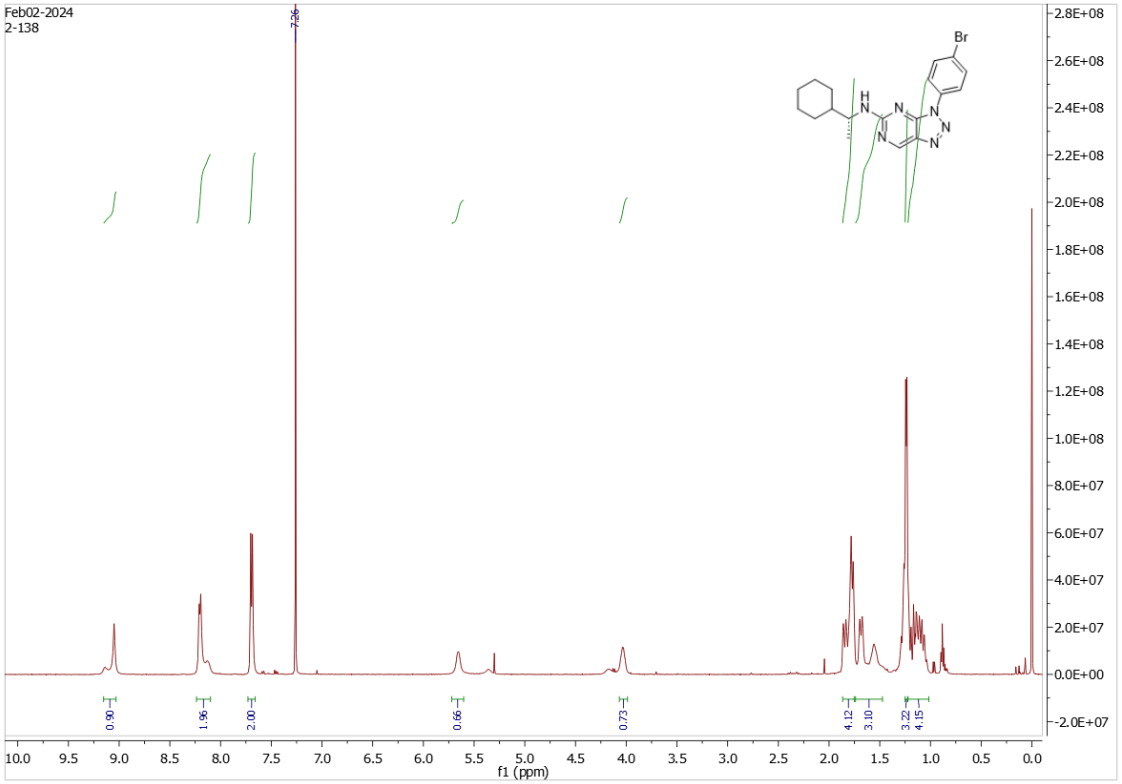

Compound **L20g**

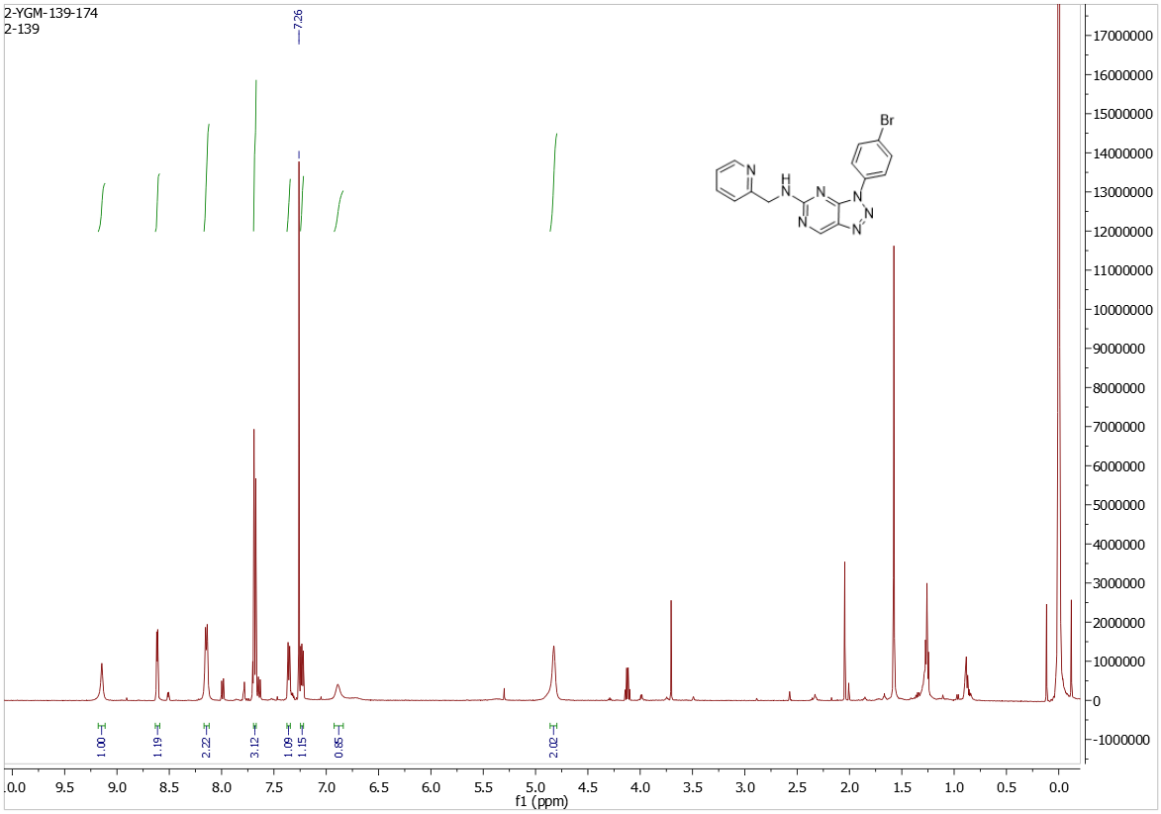

Compound **L20h**

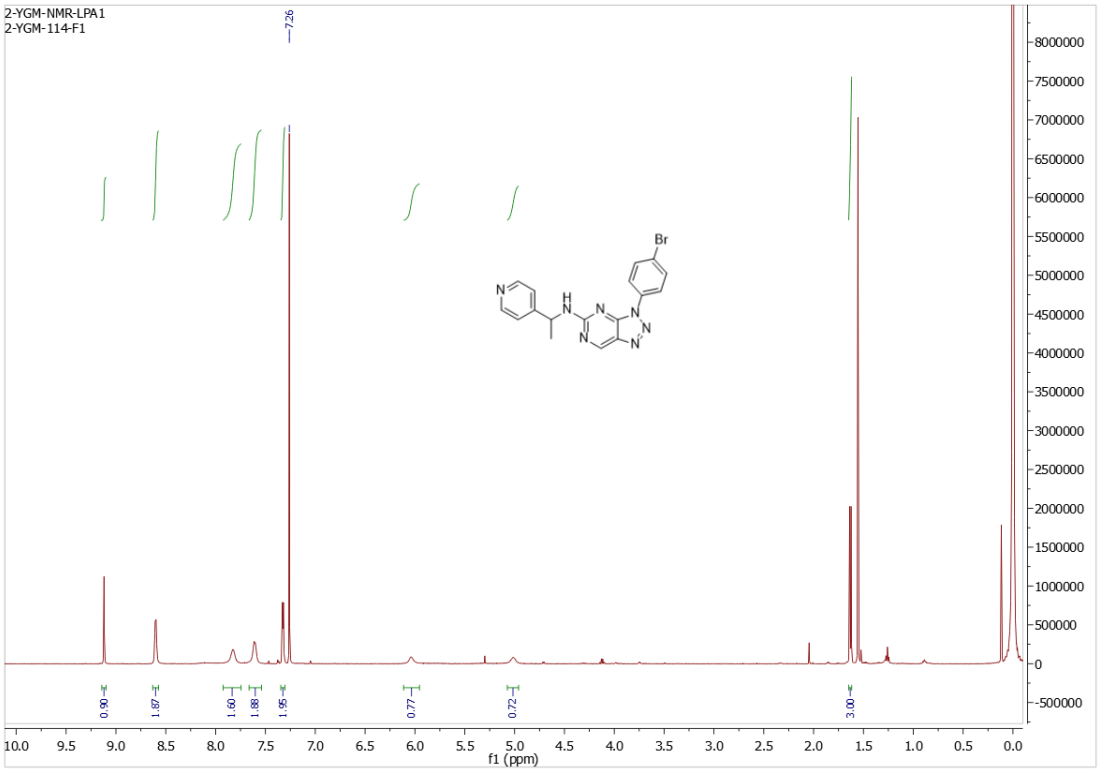

Compound **L20i**

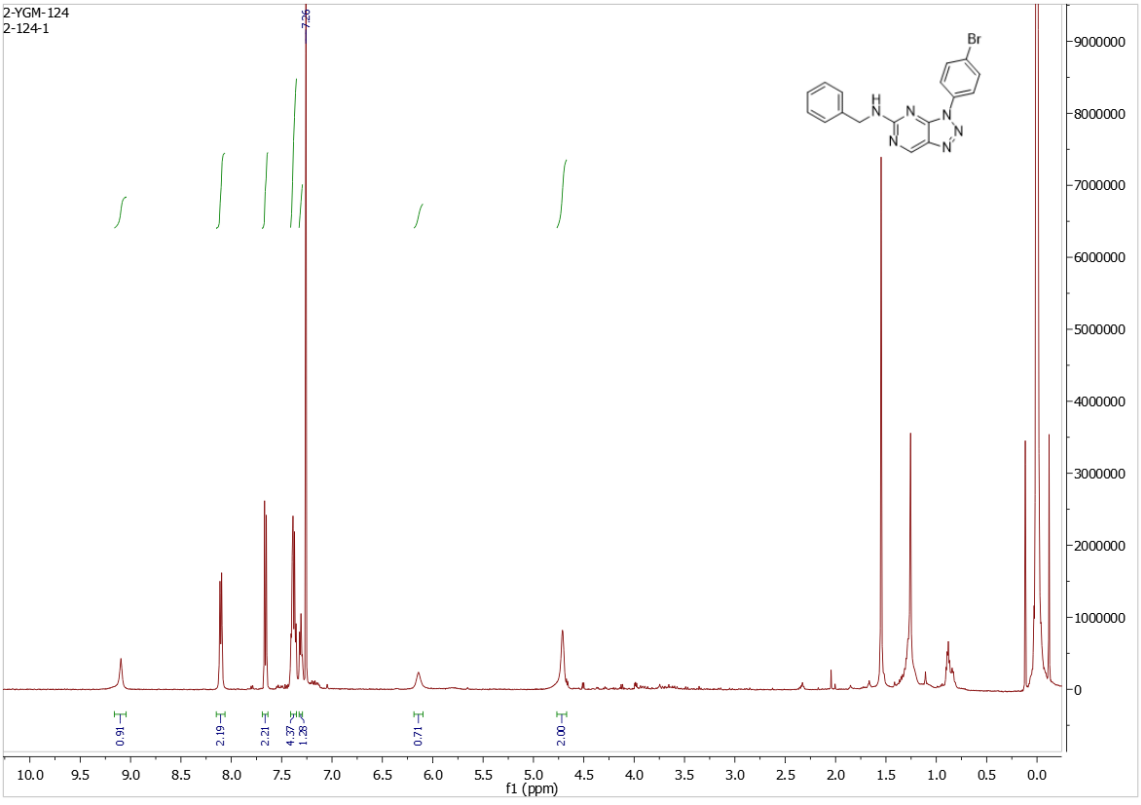

Compound **L20j**

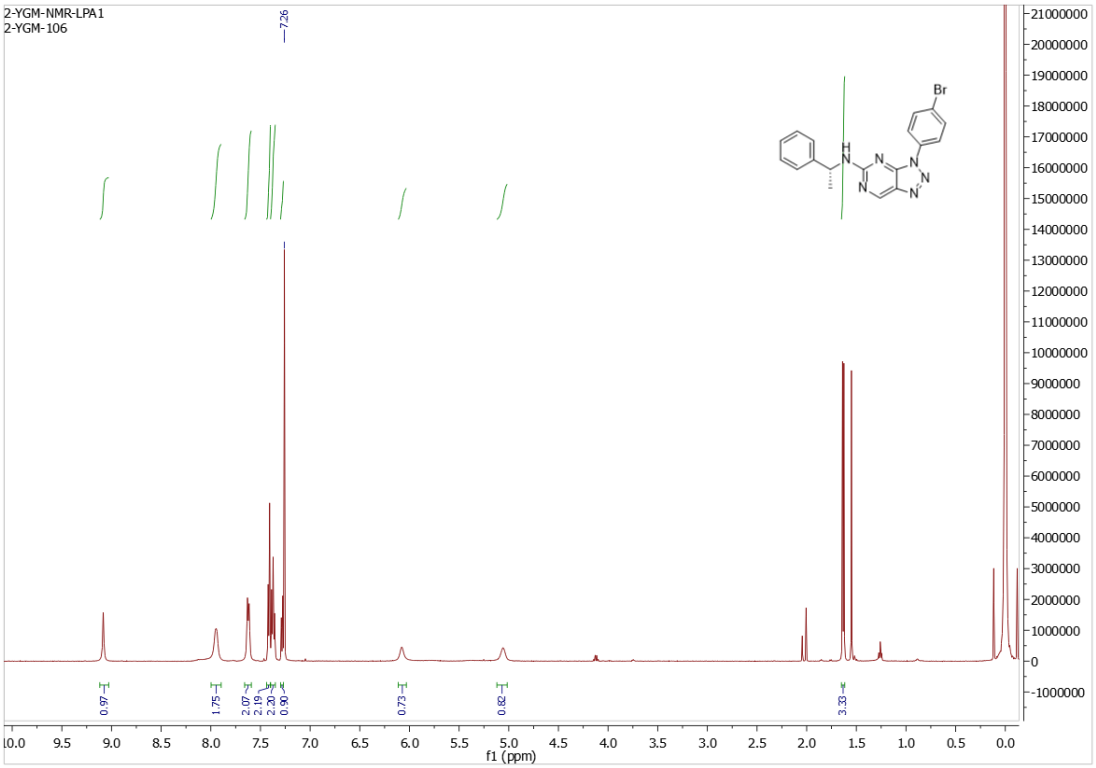

Compound **L20k**

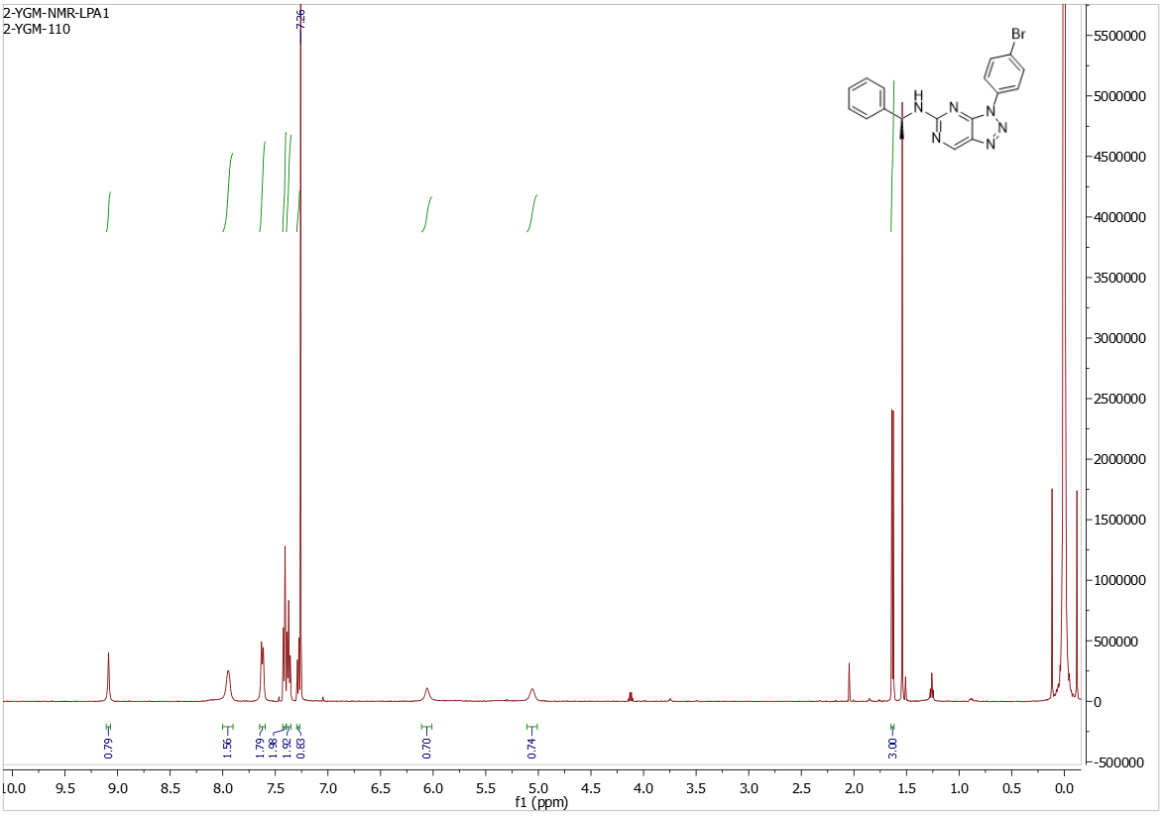

Compound **L20l**

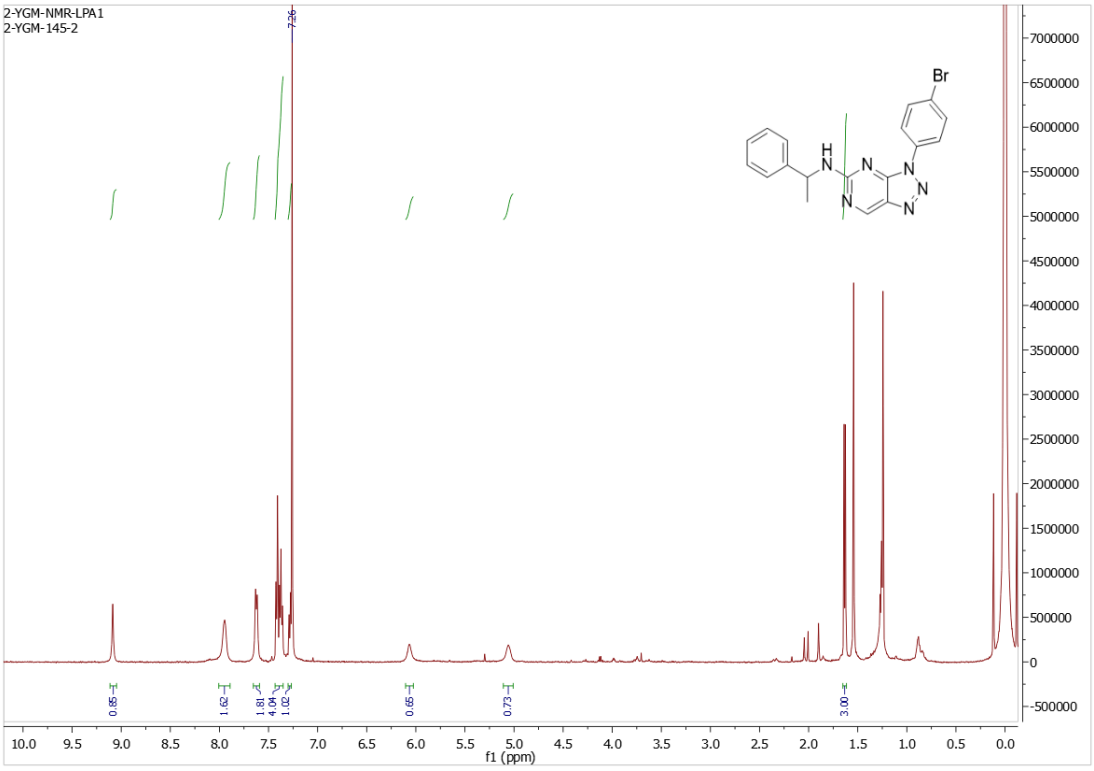

Compound **L20m**

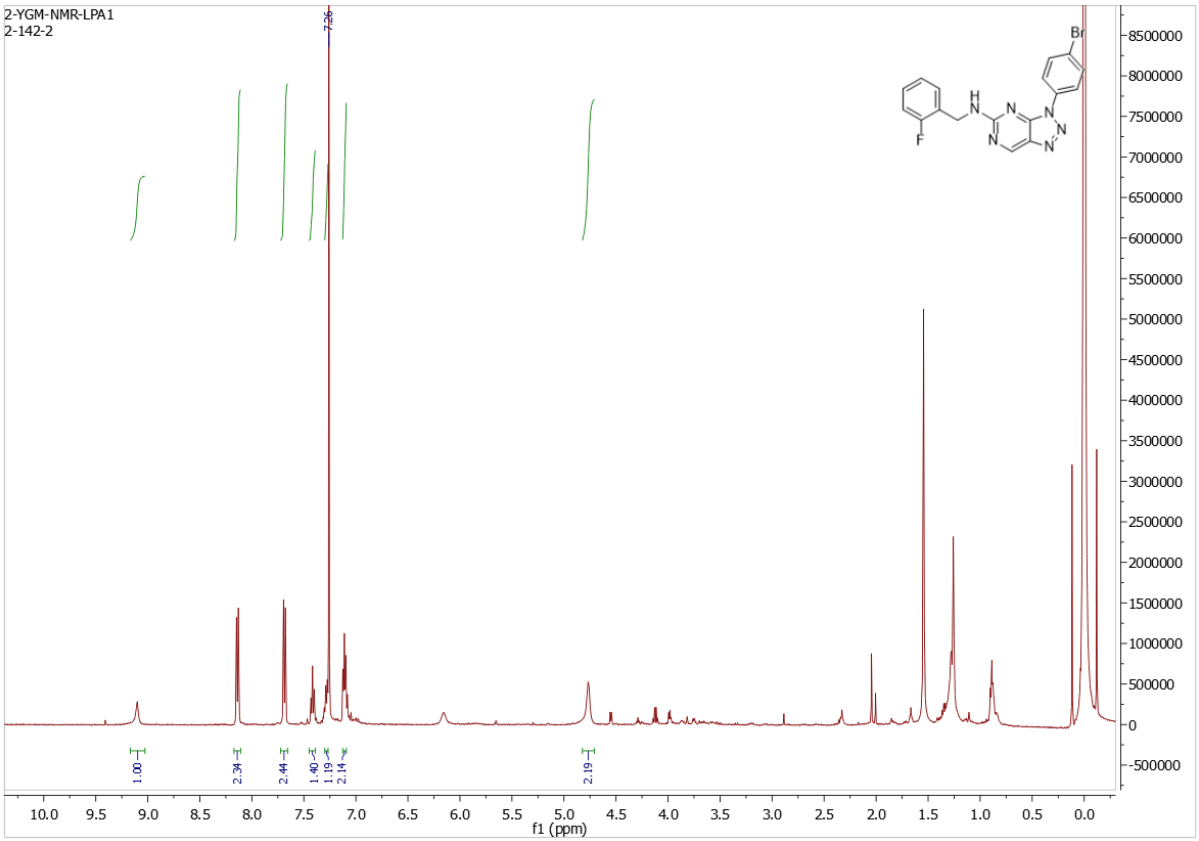

Compound **L20n**

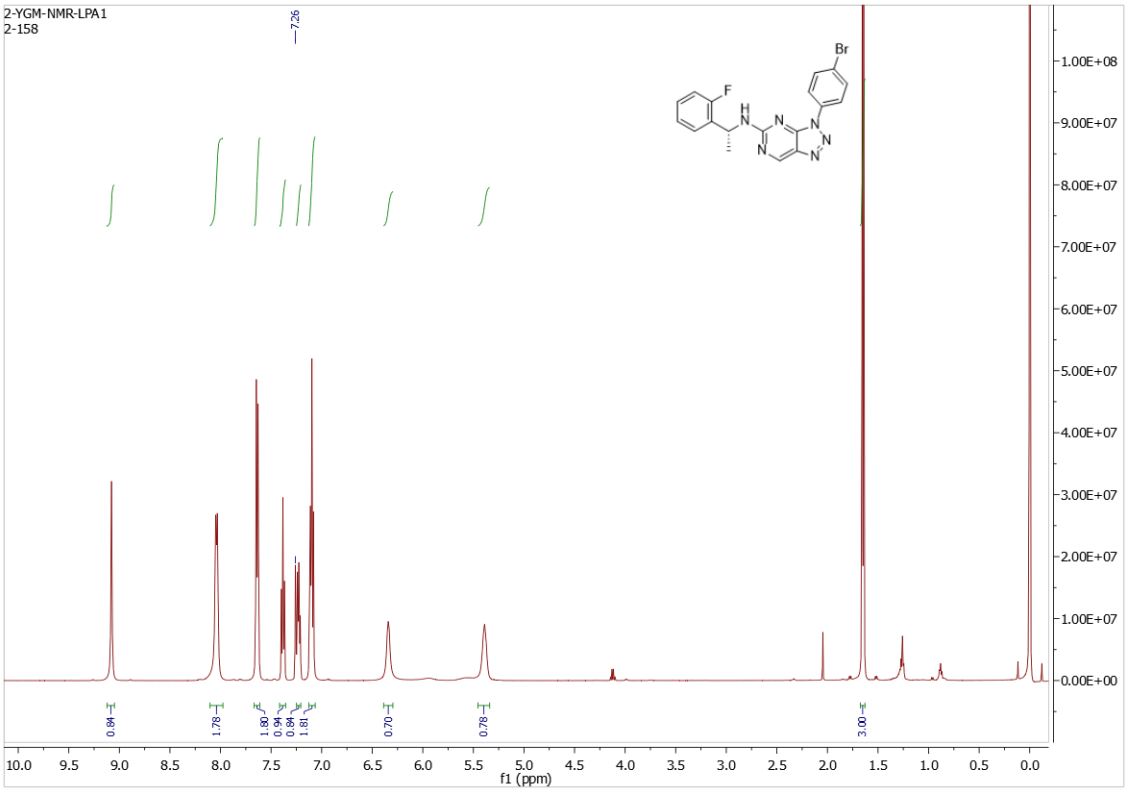

Compound **L20o**

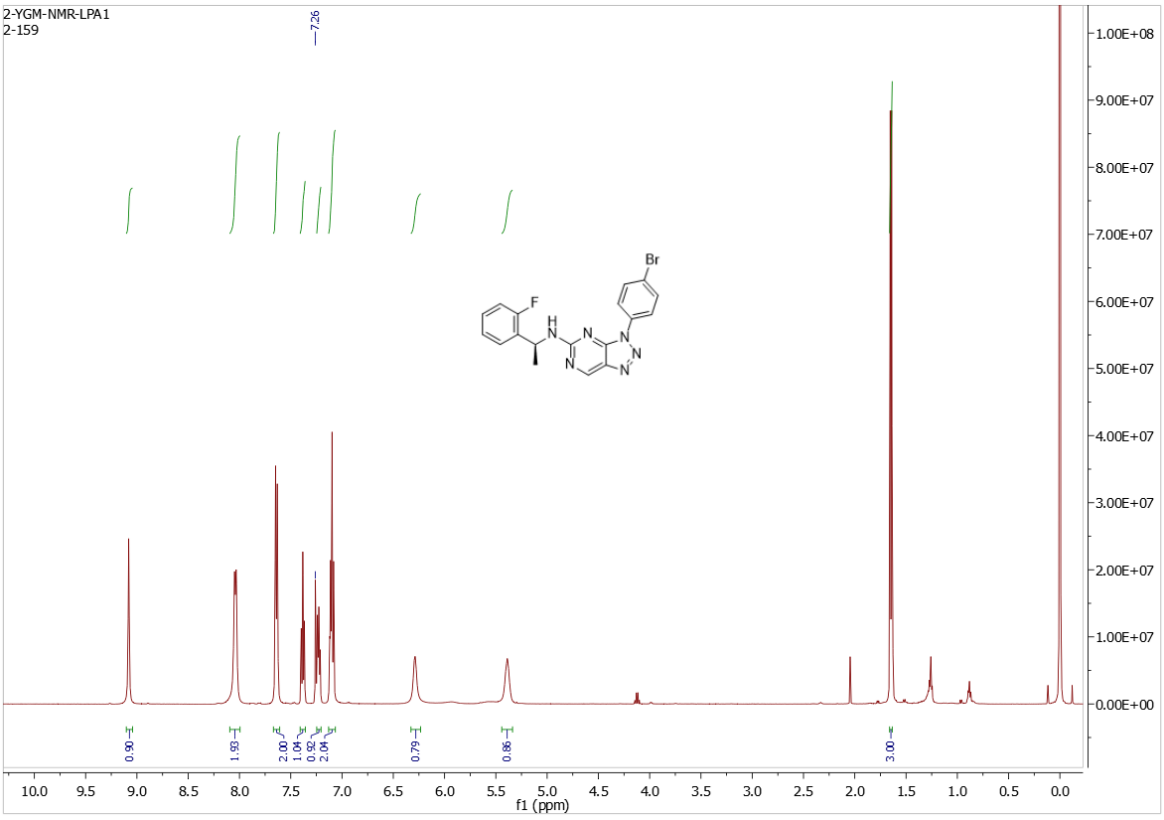

Compound **L20p**

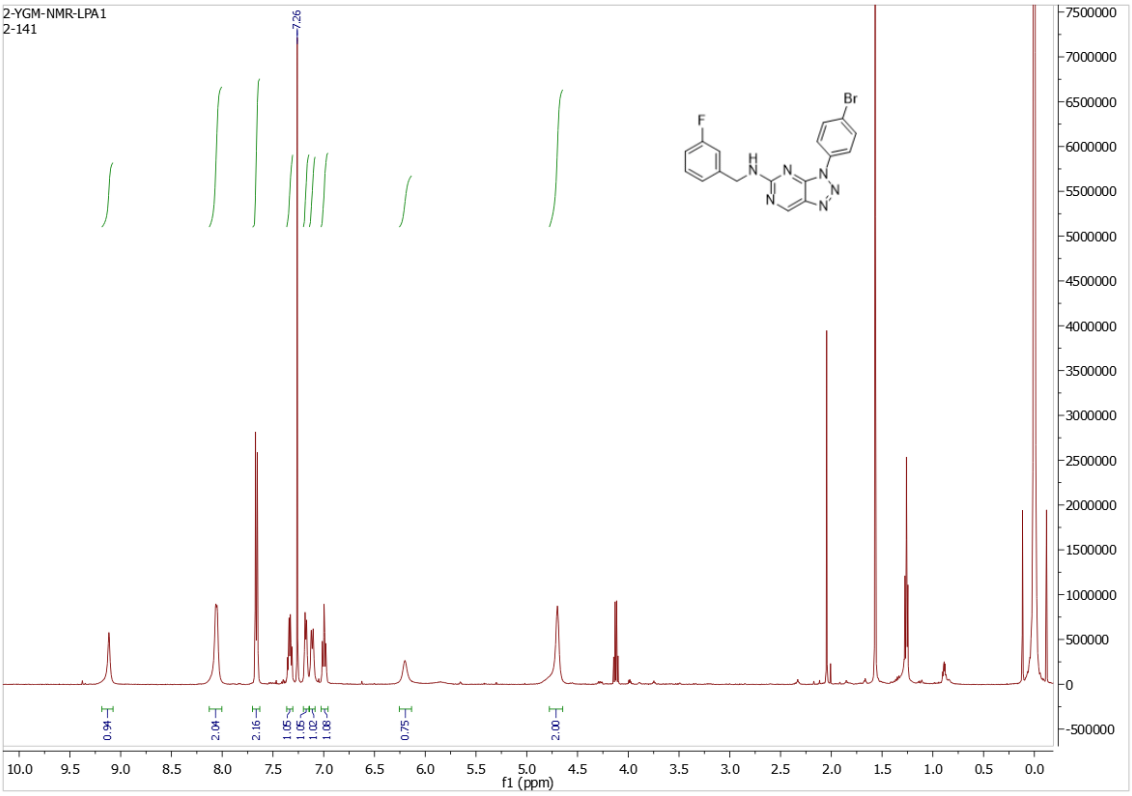

Compound **L20q**

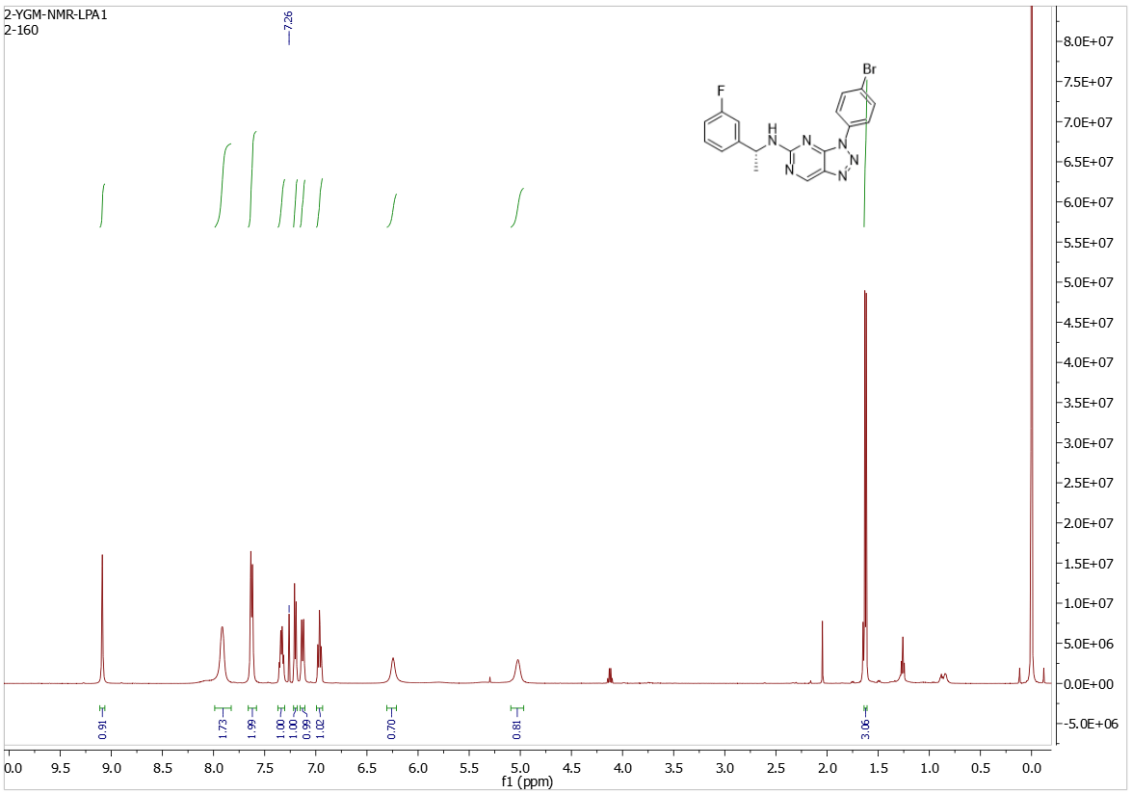

Compounds **L20r**

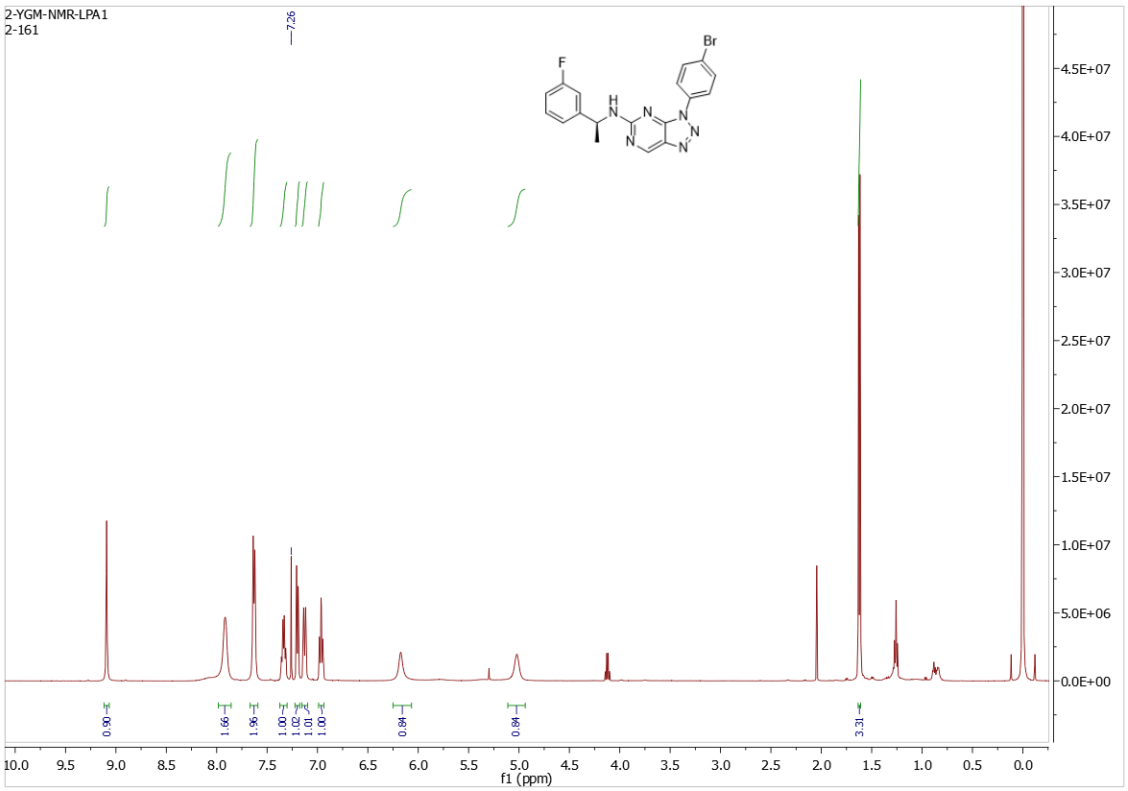

Compound **L20s**

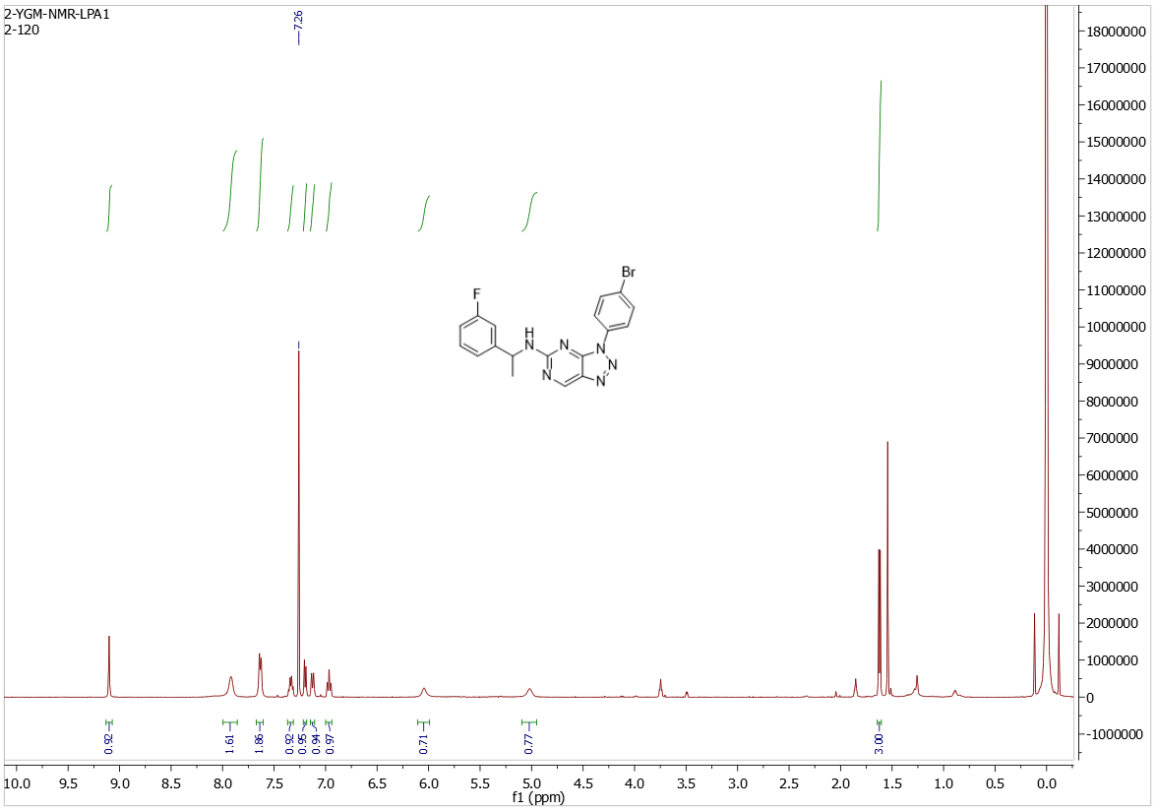

Compound **L20t**

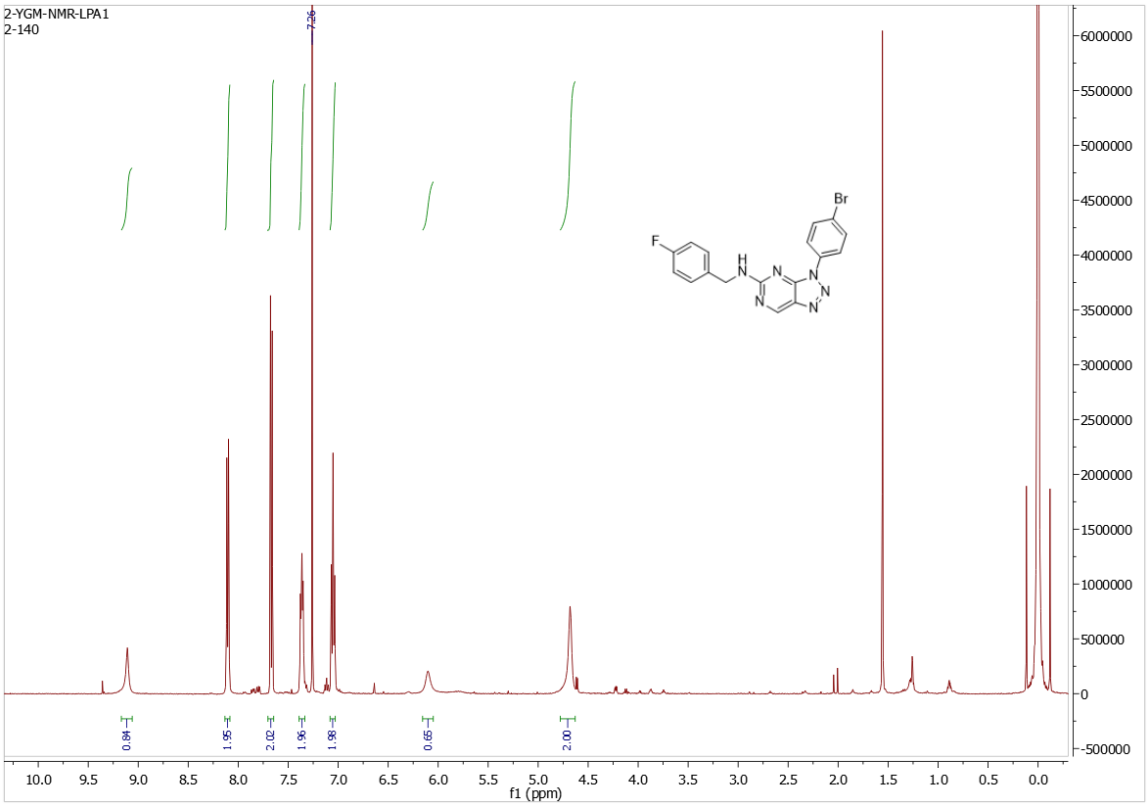

Compound **L20u**

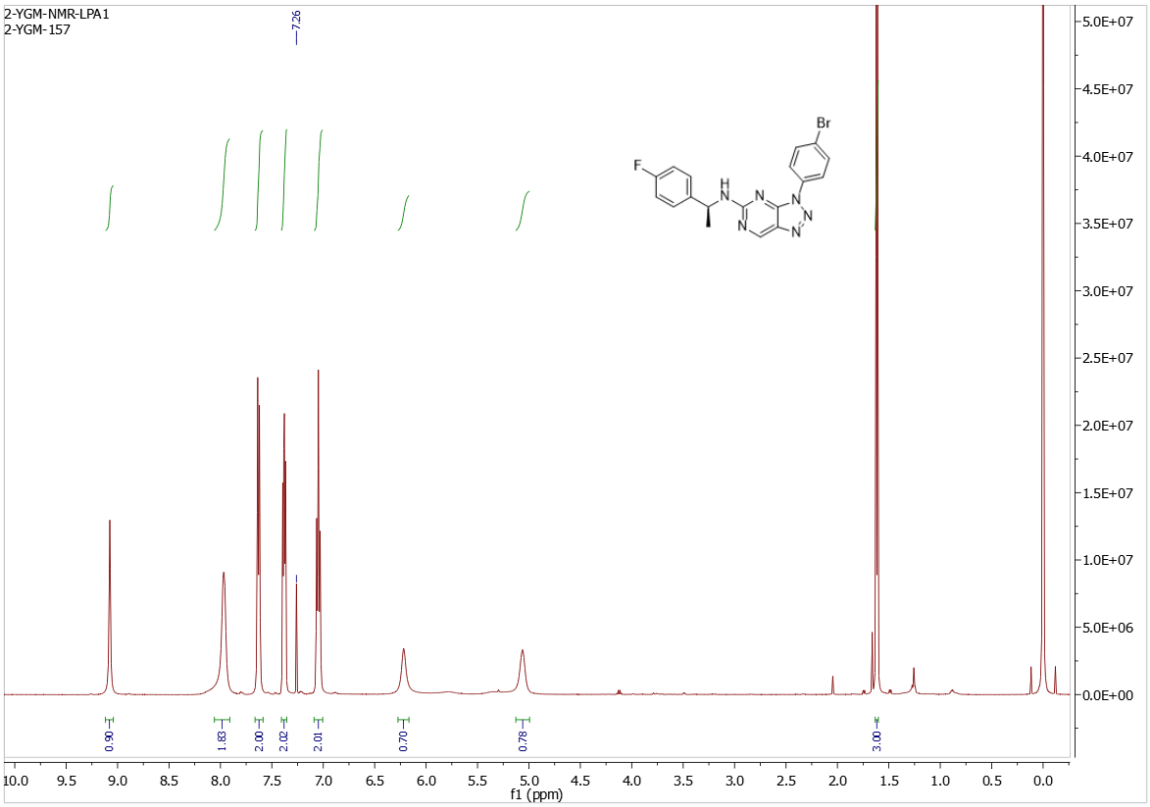

Compound **L21a**

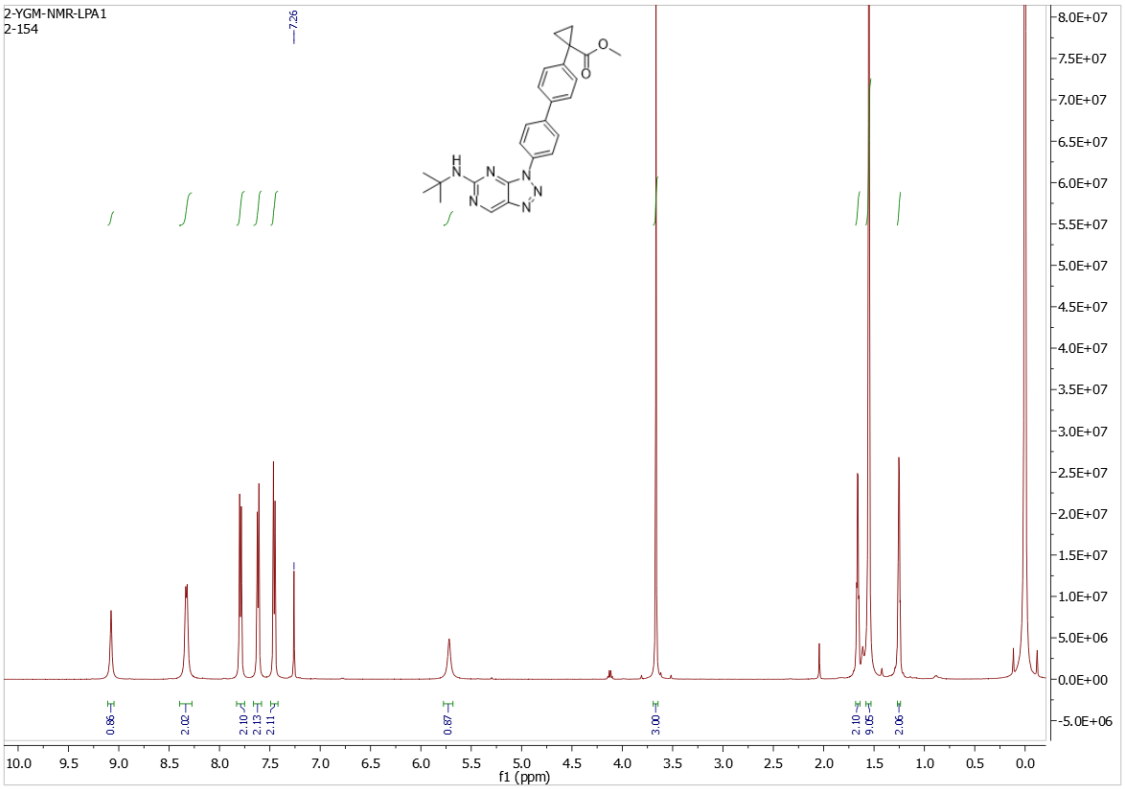

Compound **L21b**

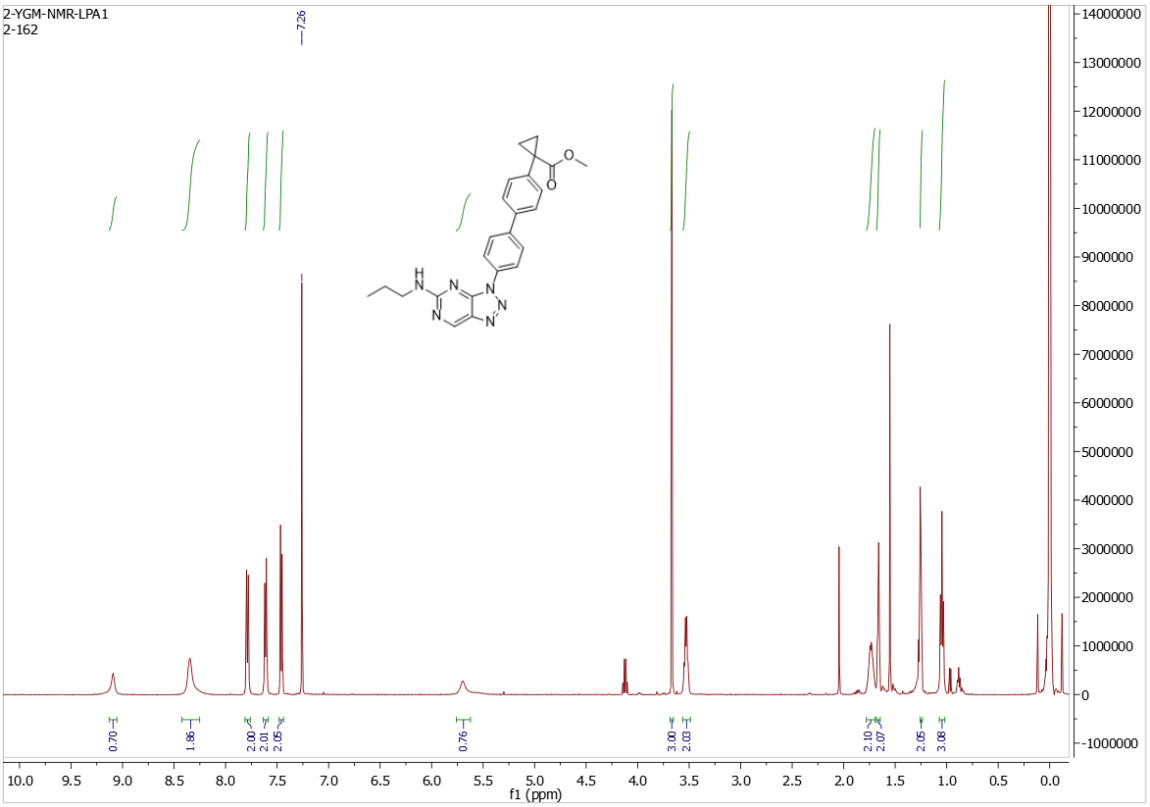

Compound **L21c**

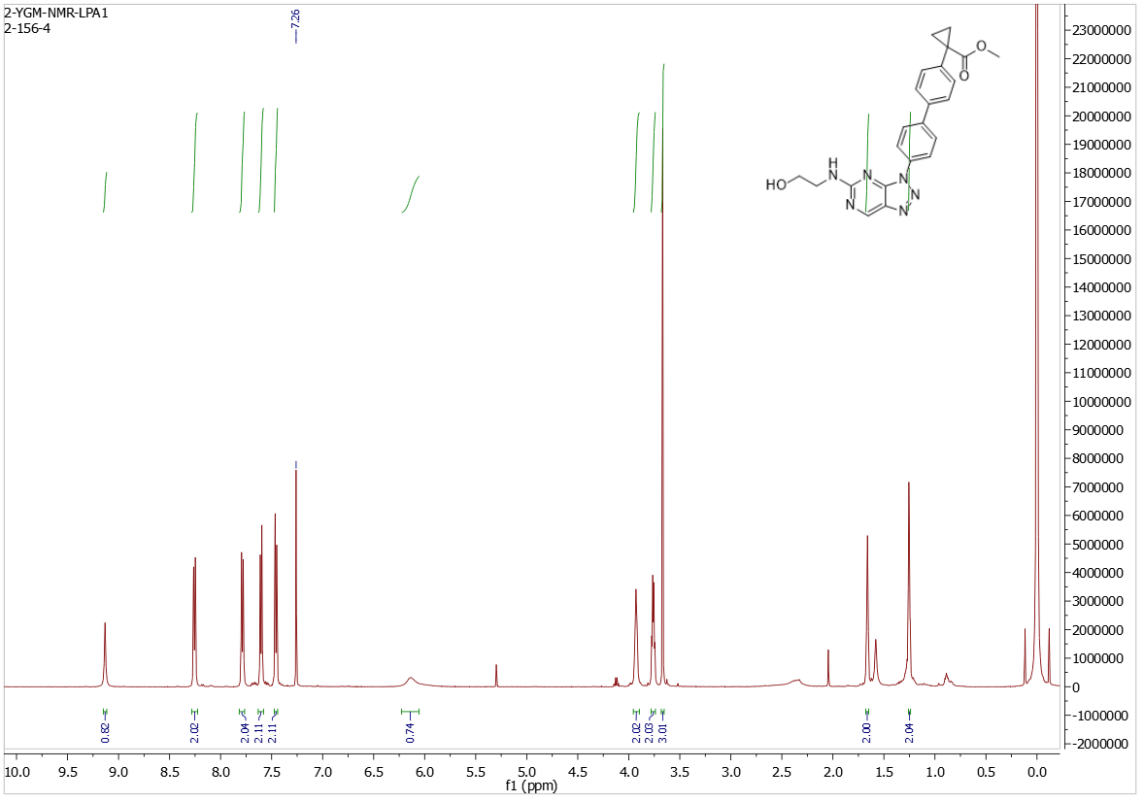

Compound **L21e**

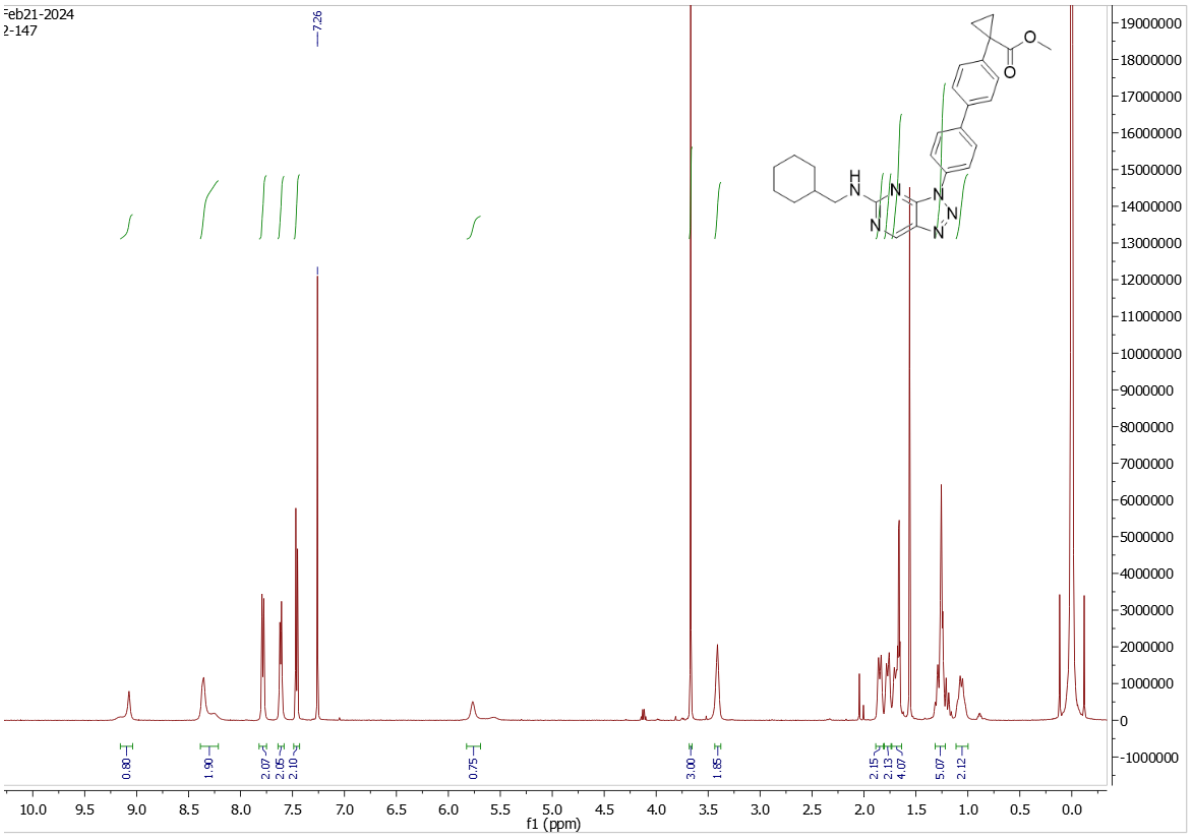

Compound **L21f**

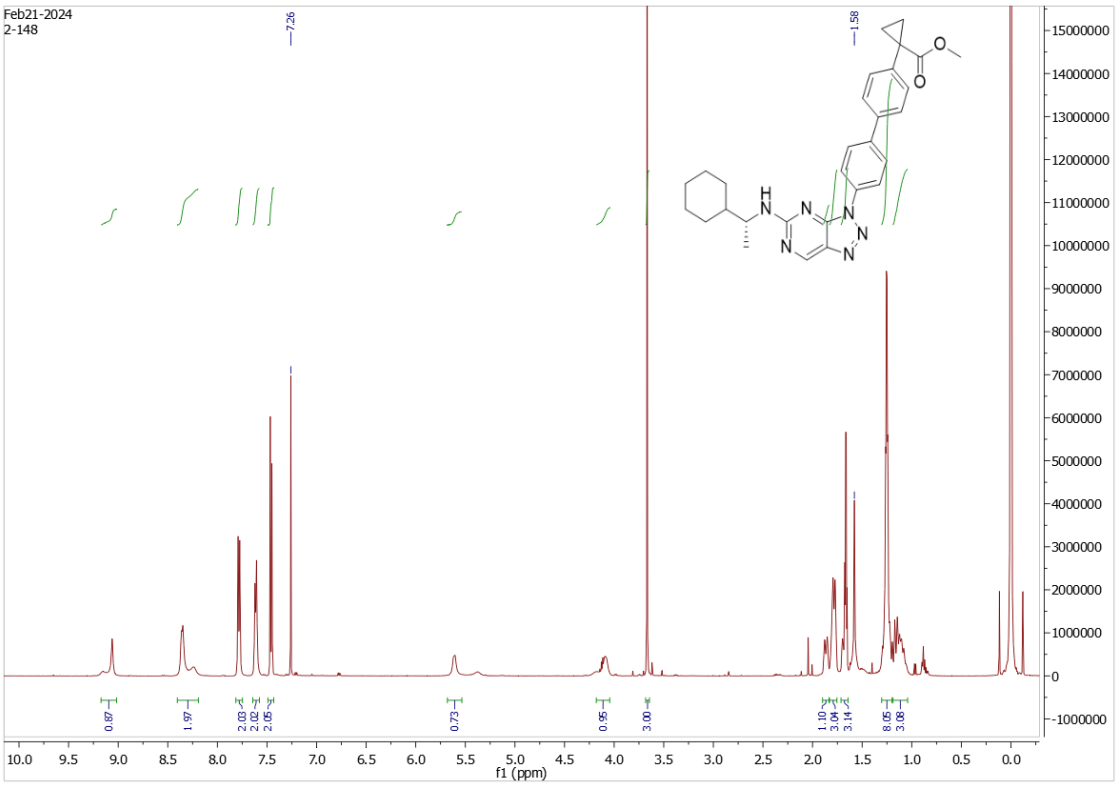

Compound **L21h**

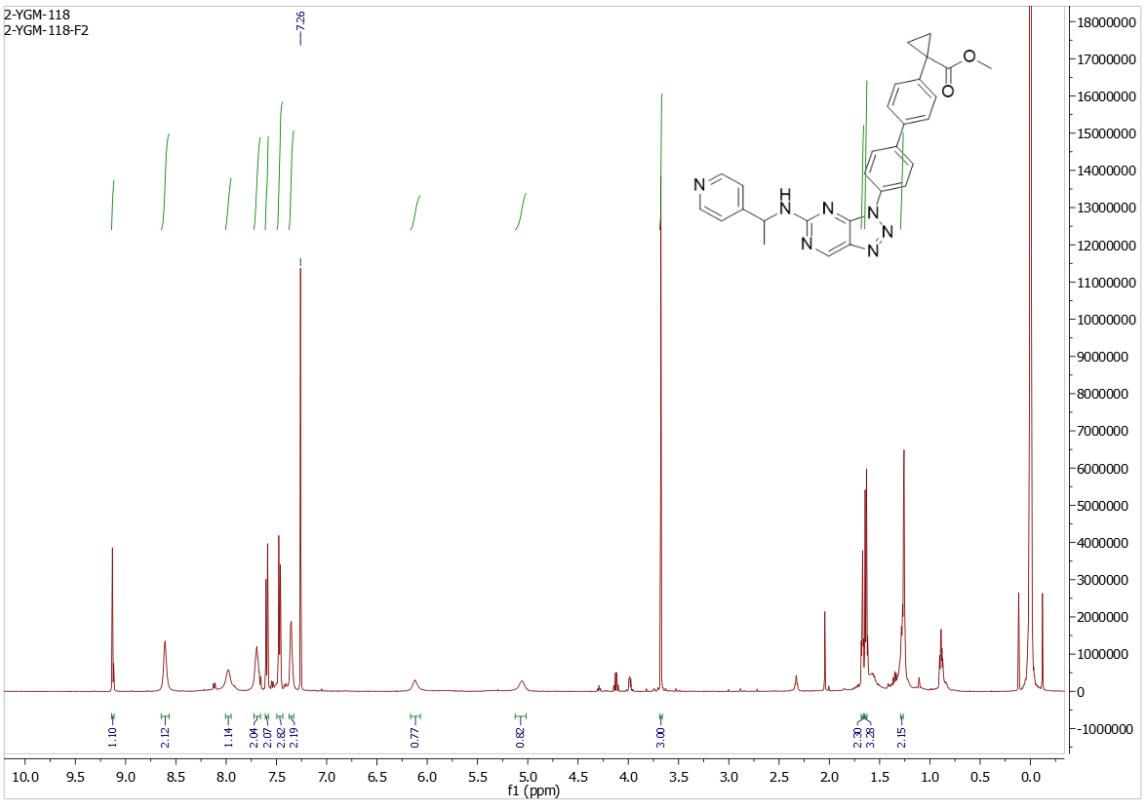

Compound **L21i**

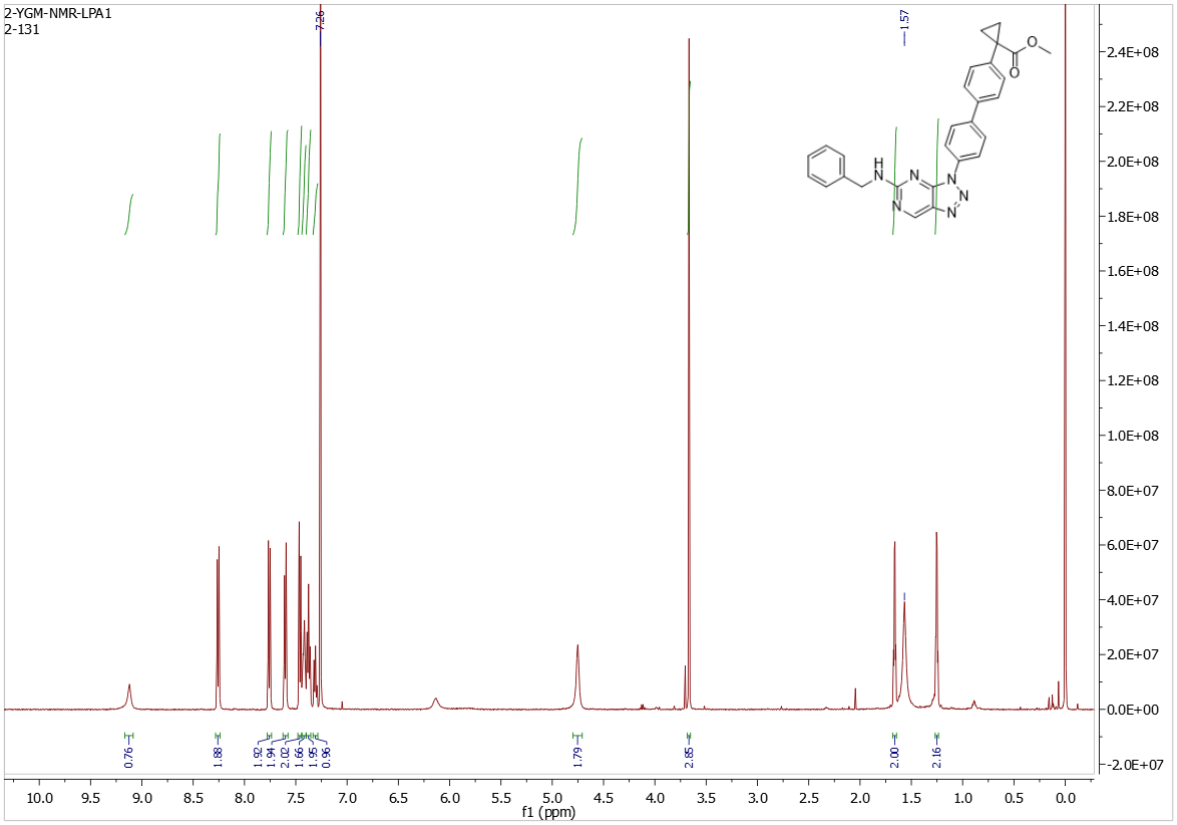

Compound **L21j**

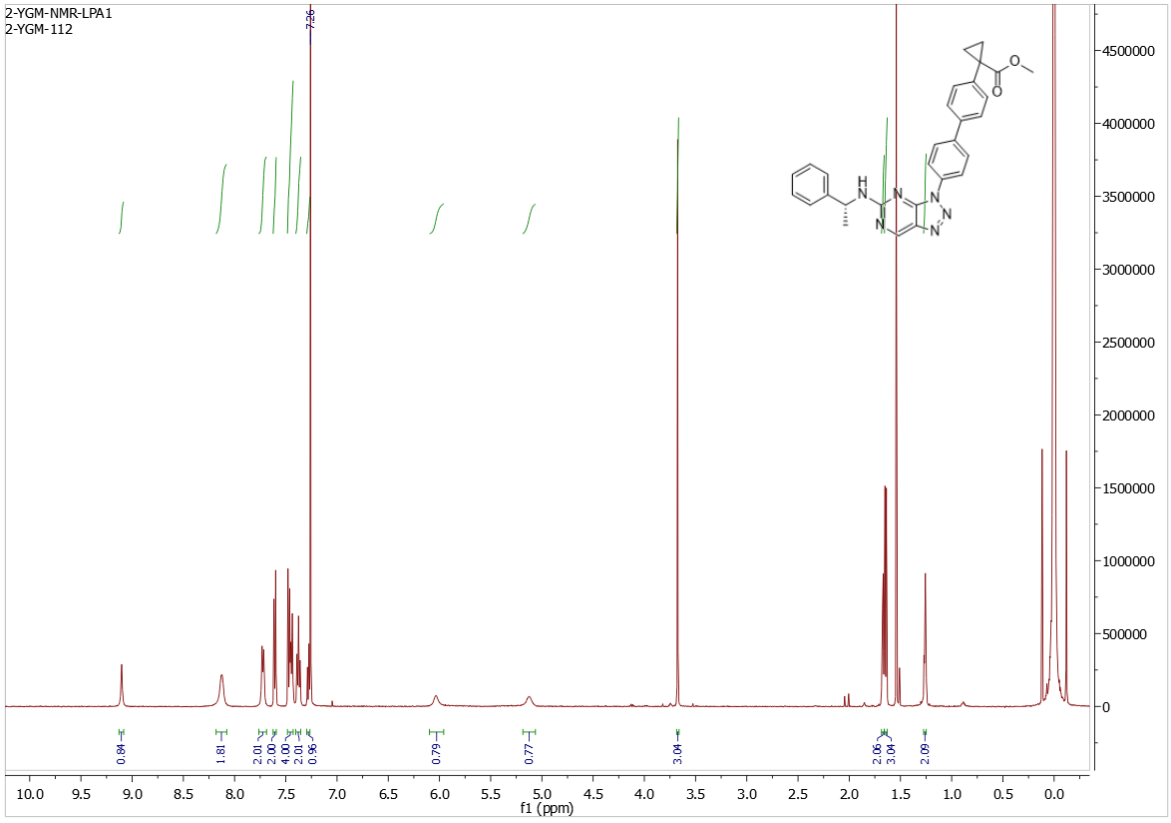

Compound **L21k**

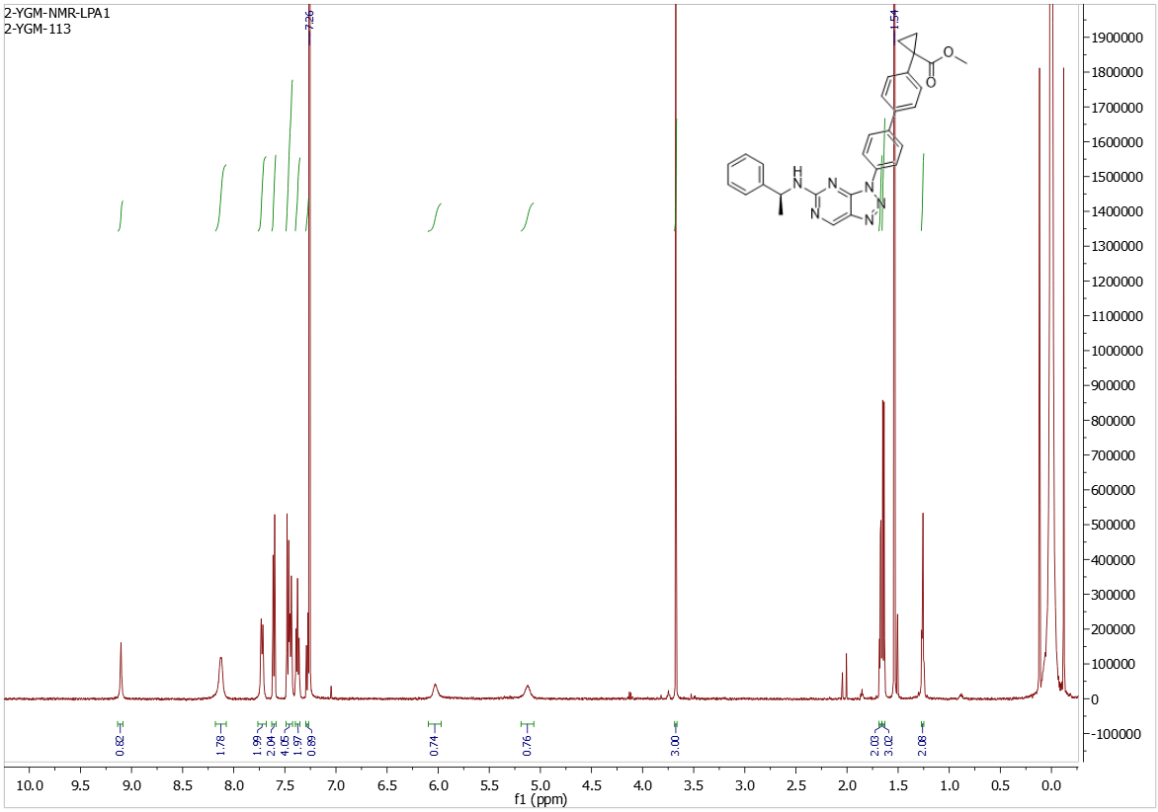

Compound **L21l**

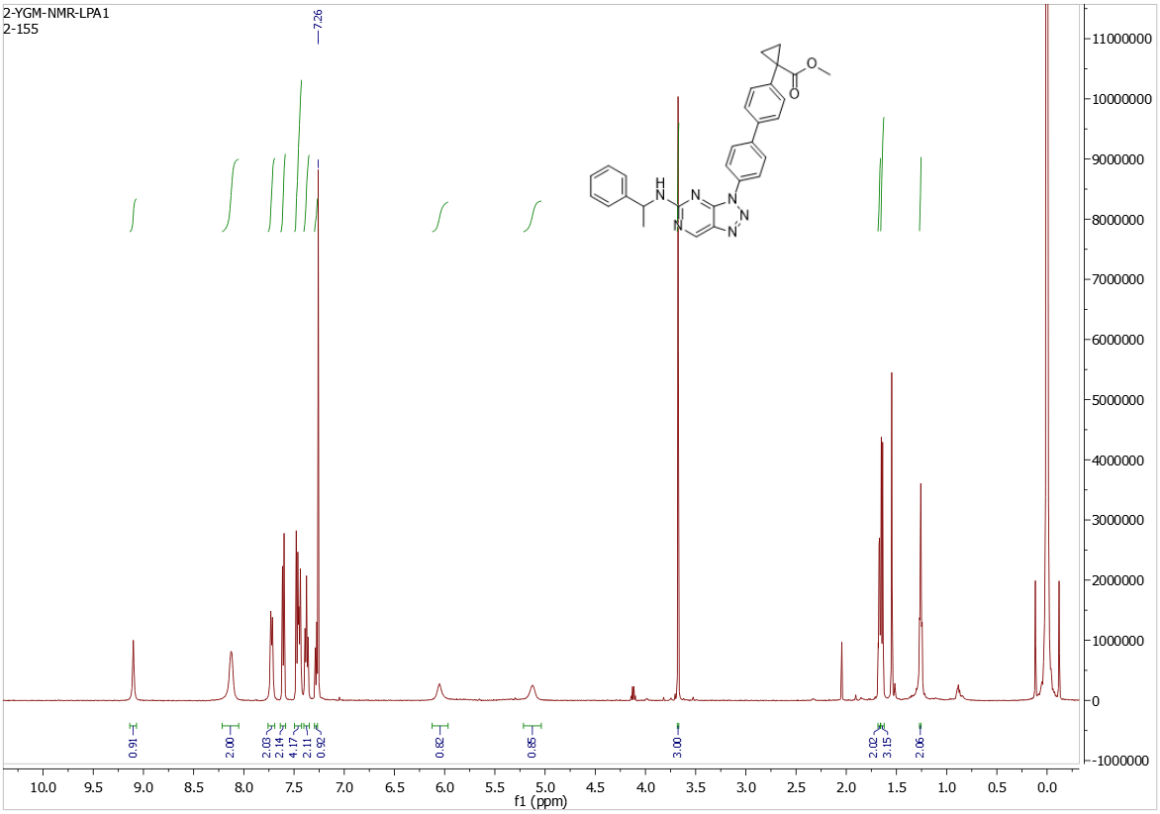

Compound **L21m**

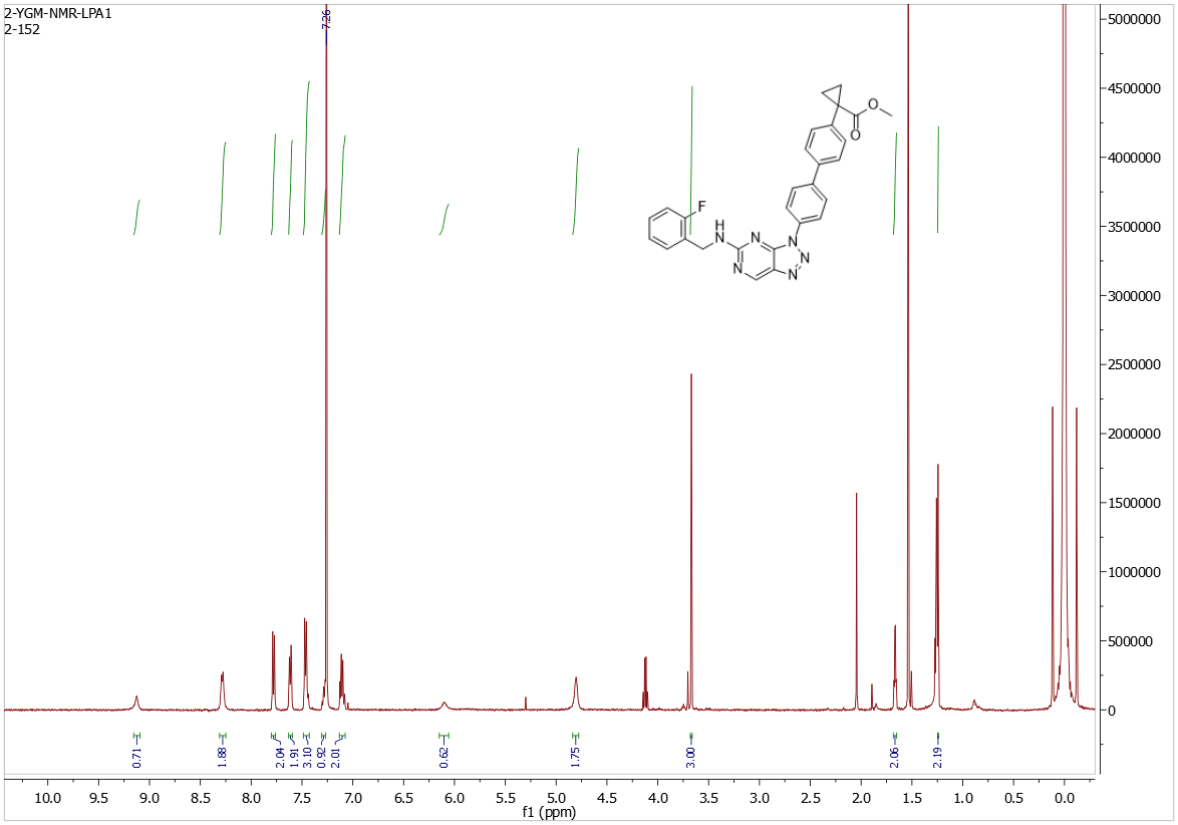

Compound **L21n**

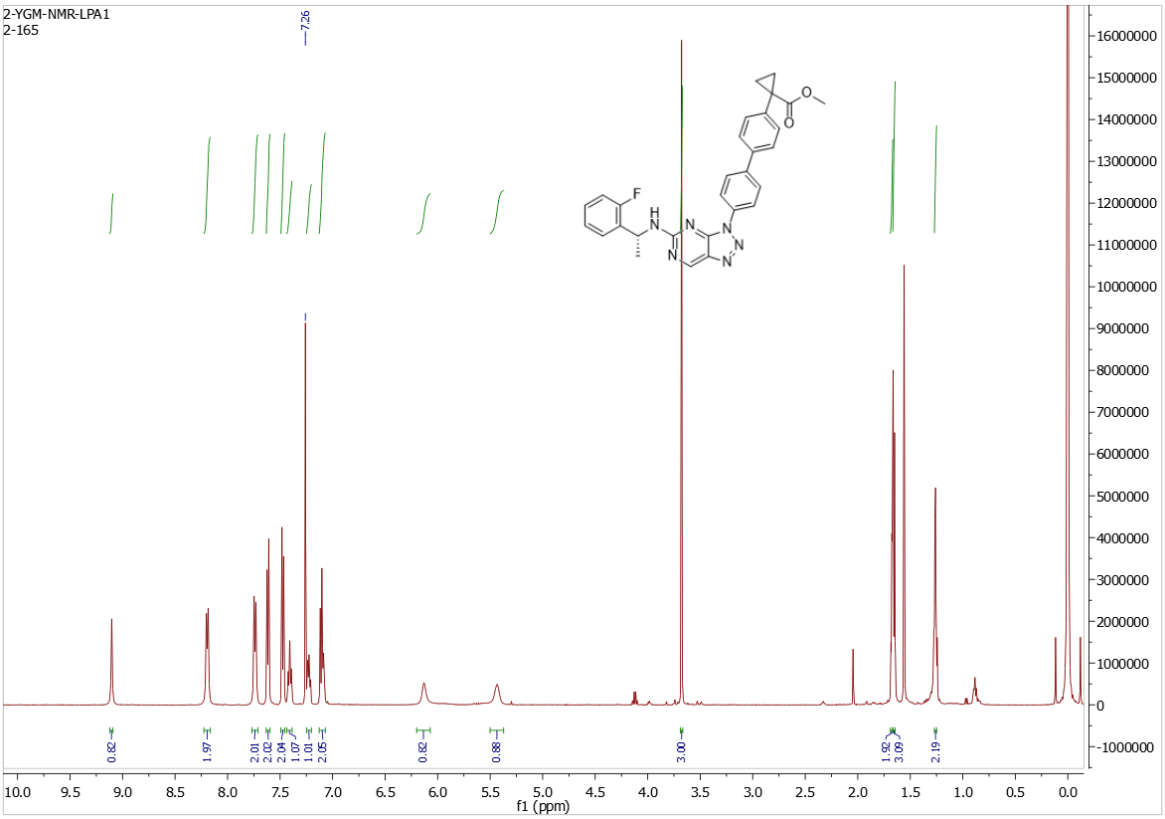

Compound **L21o**

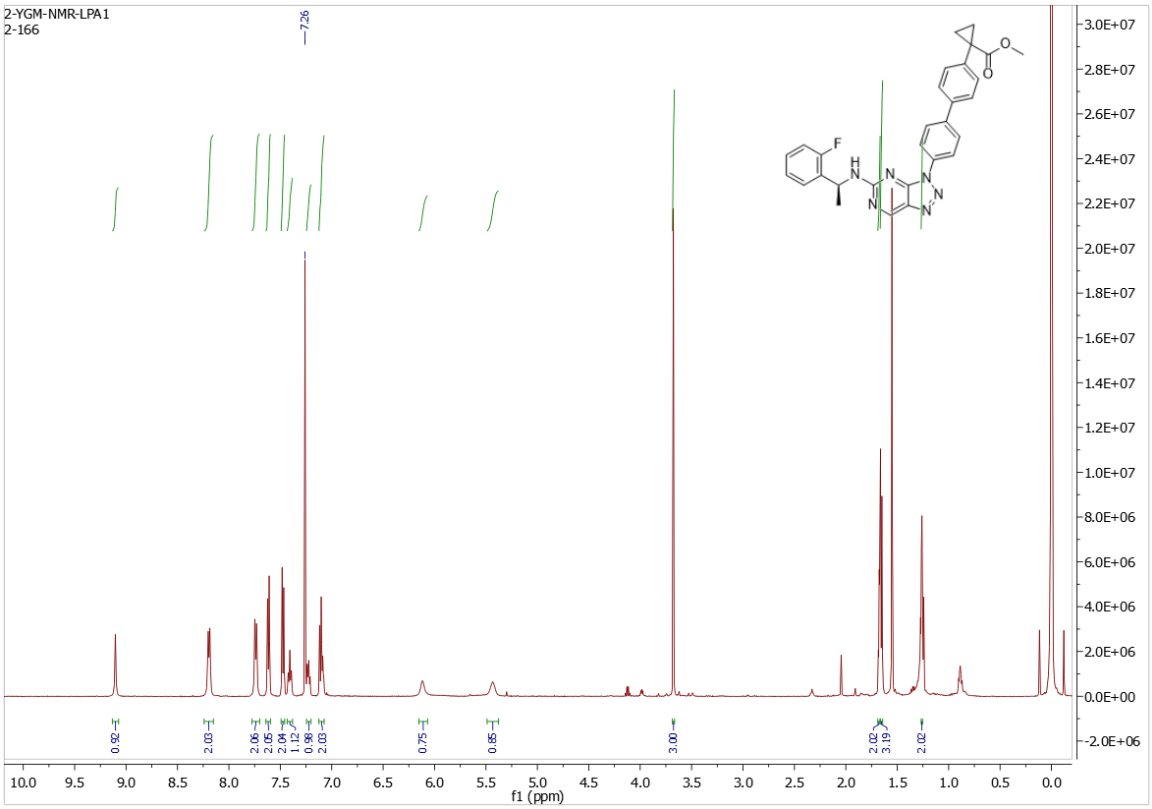

Compound **L21p**

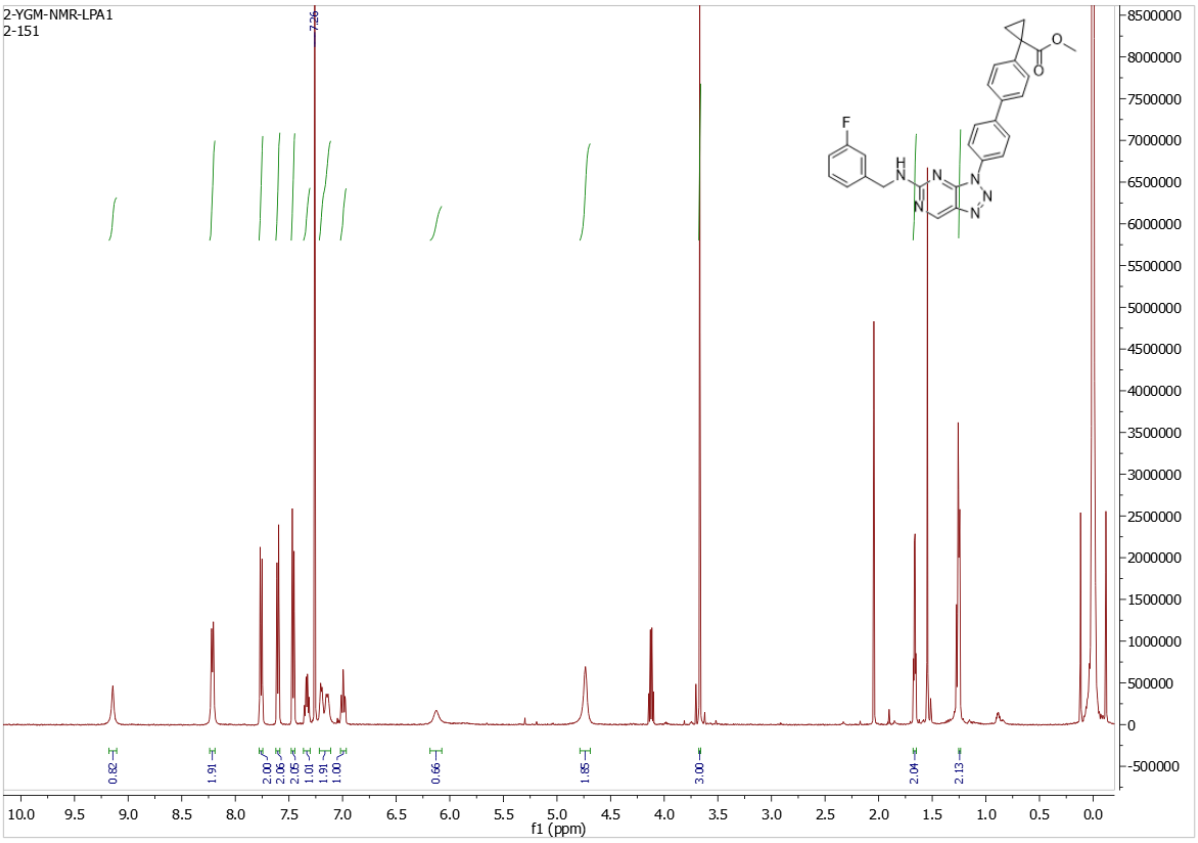

Compound **L21q**

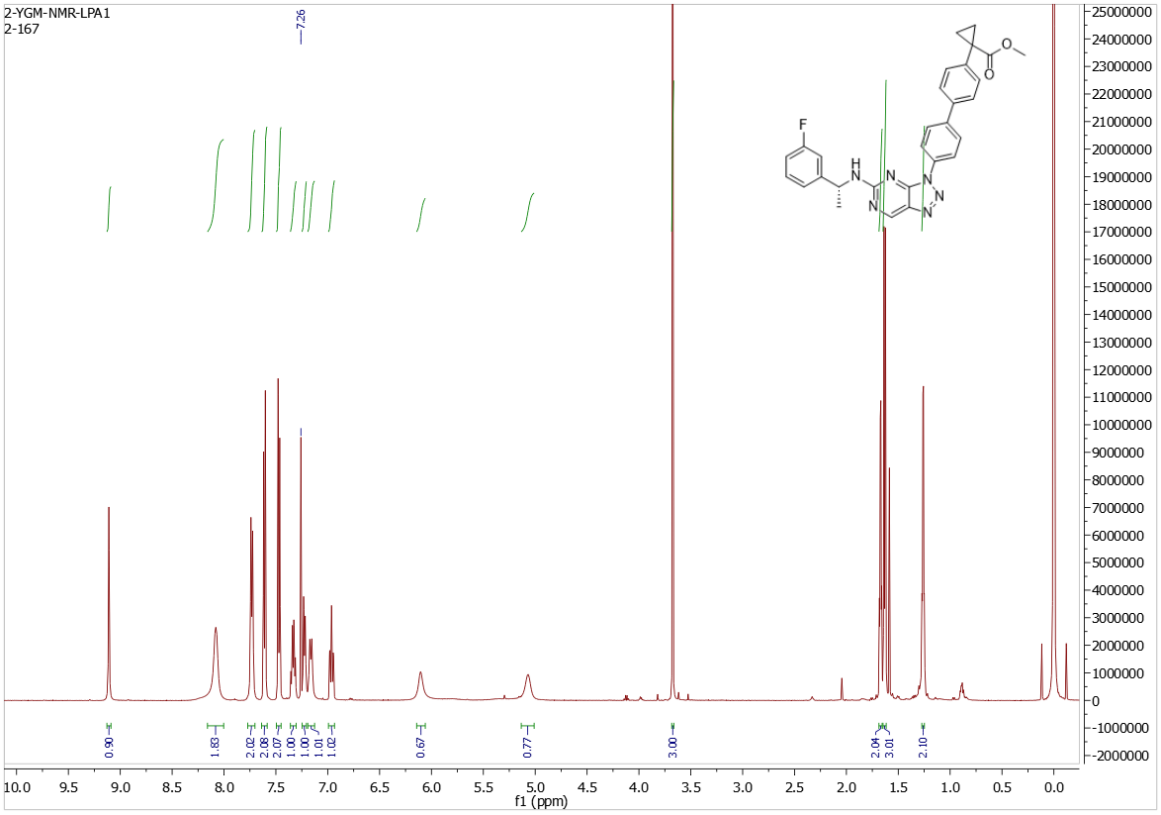

Compound **L21r**

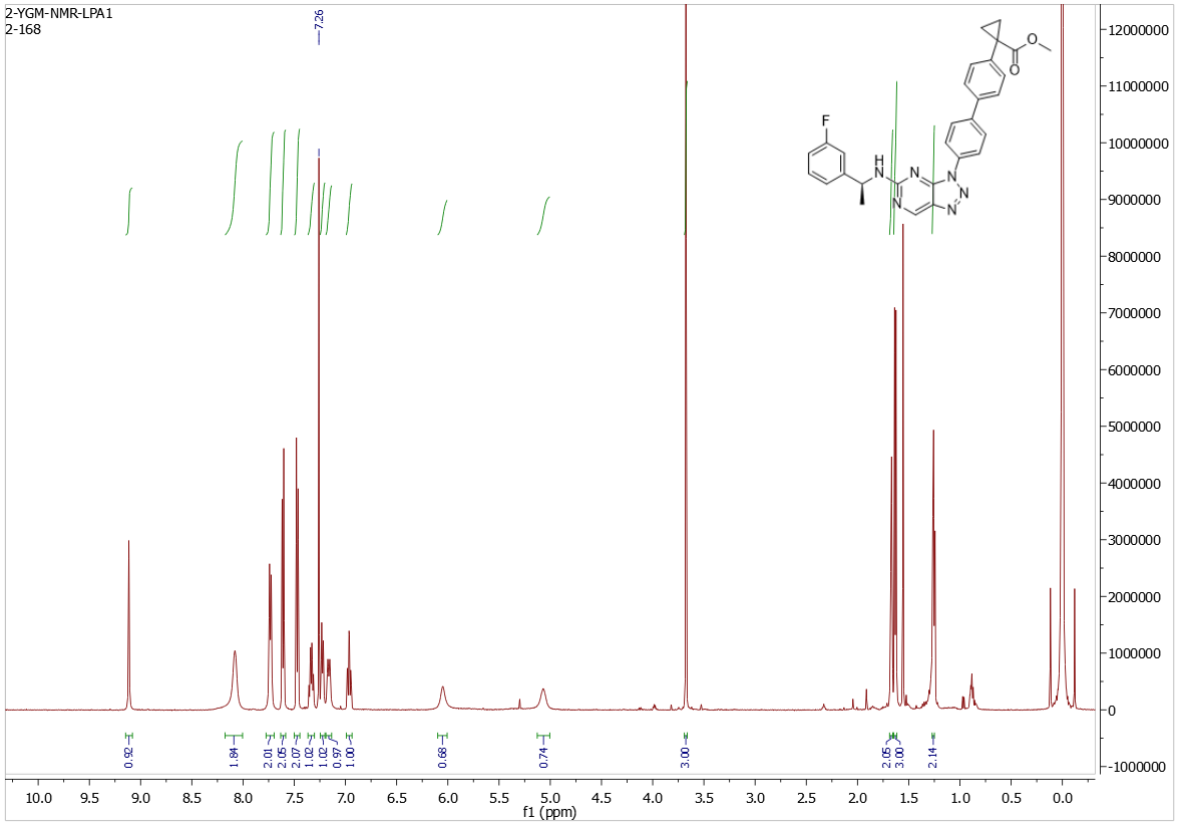

Compound **L21s**

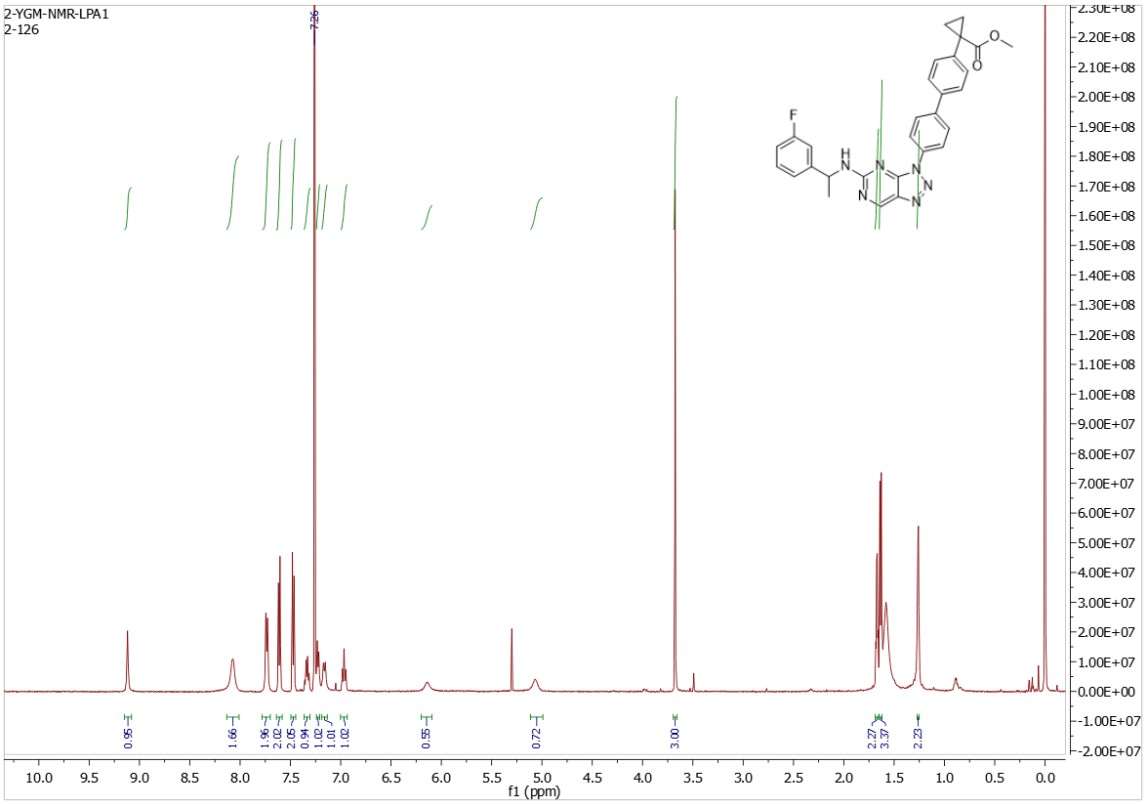

Compound **L21t**

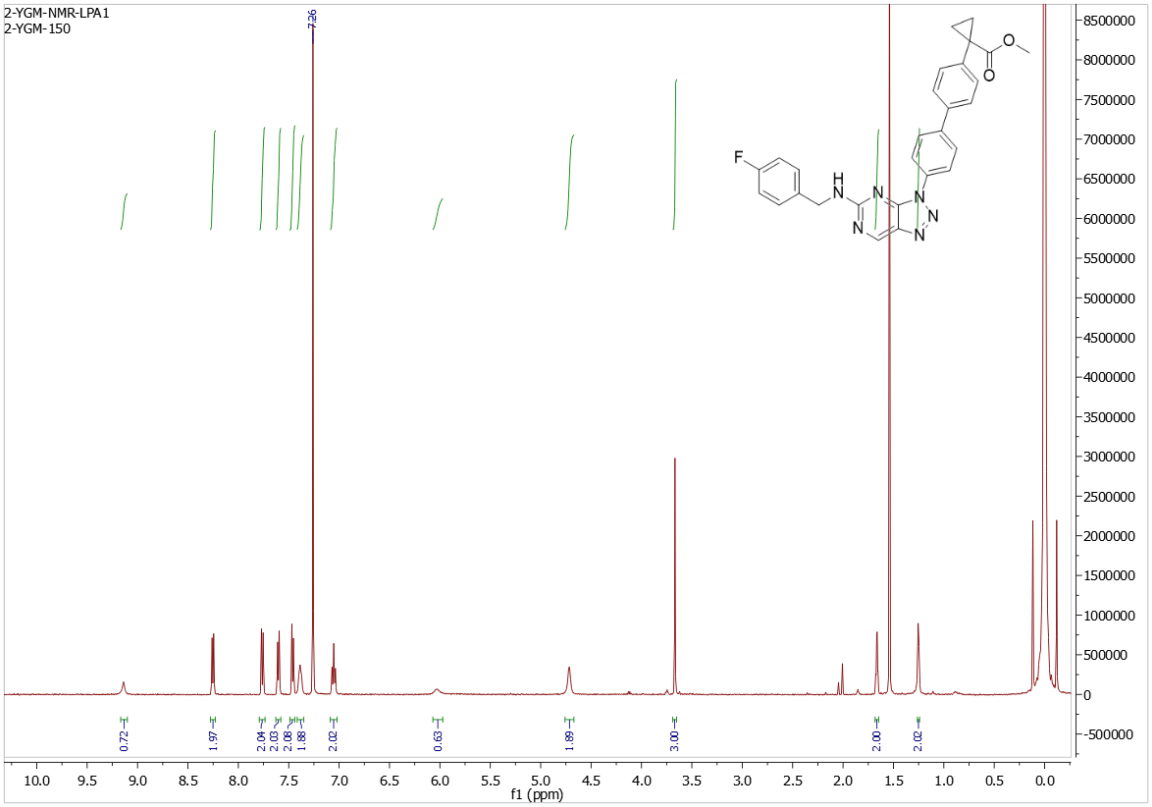

Compound **L21u**

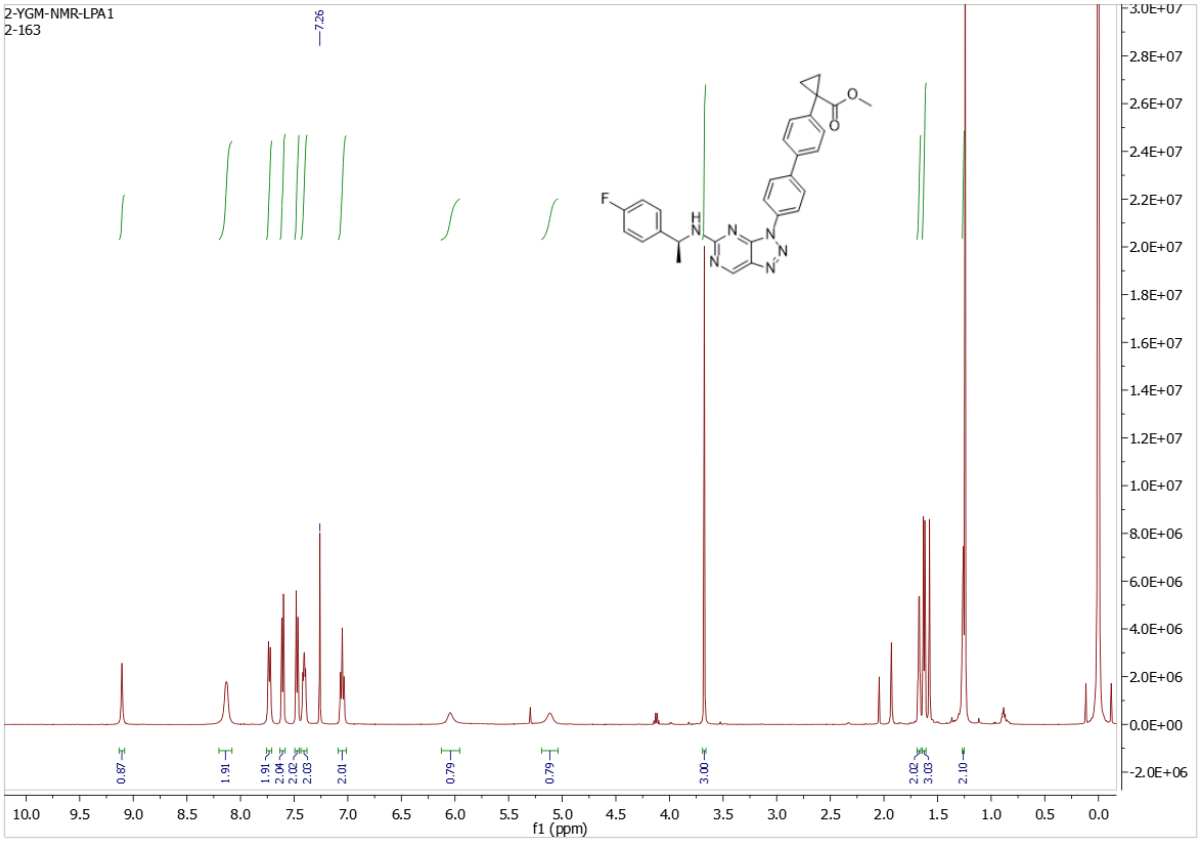

Compounds **L22a**

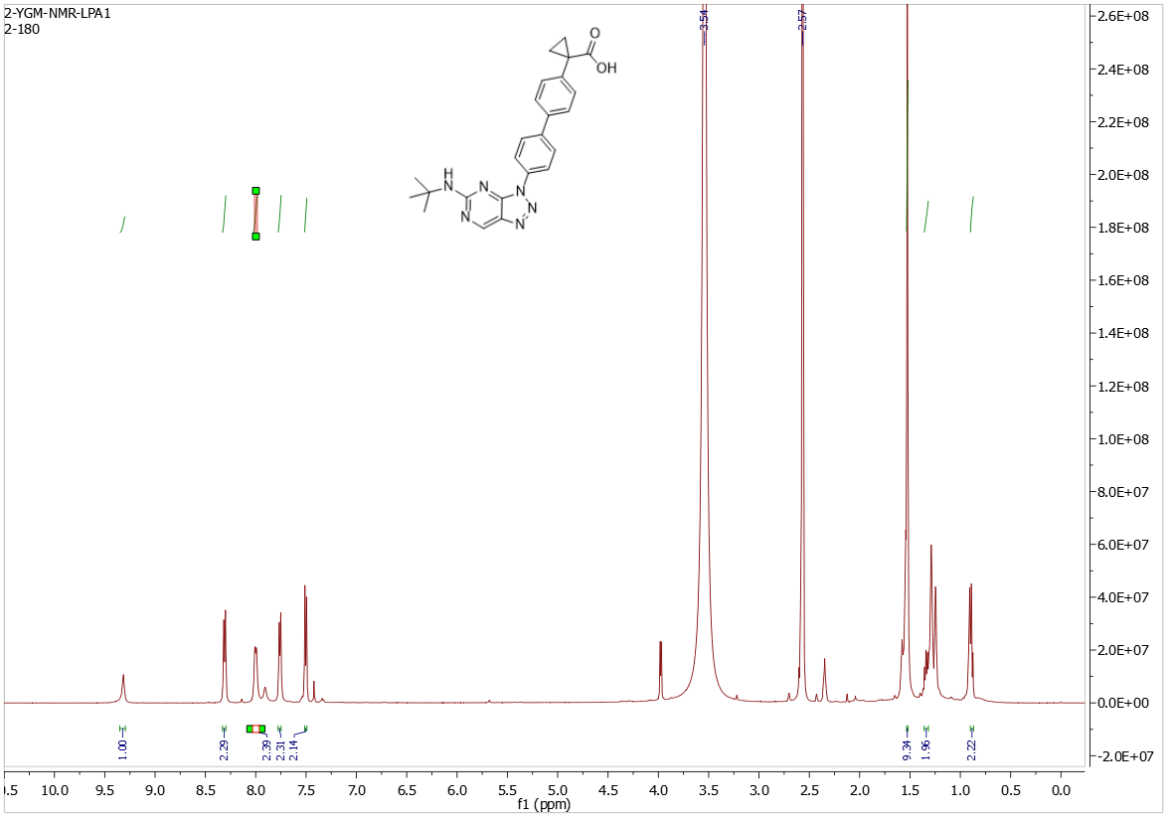

Compound **L22b**

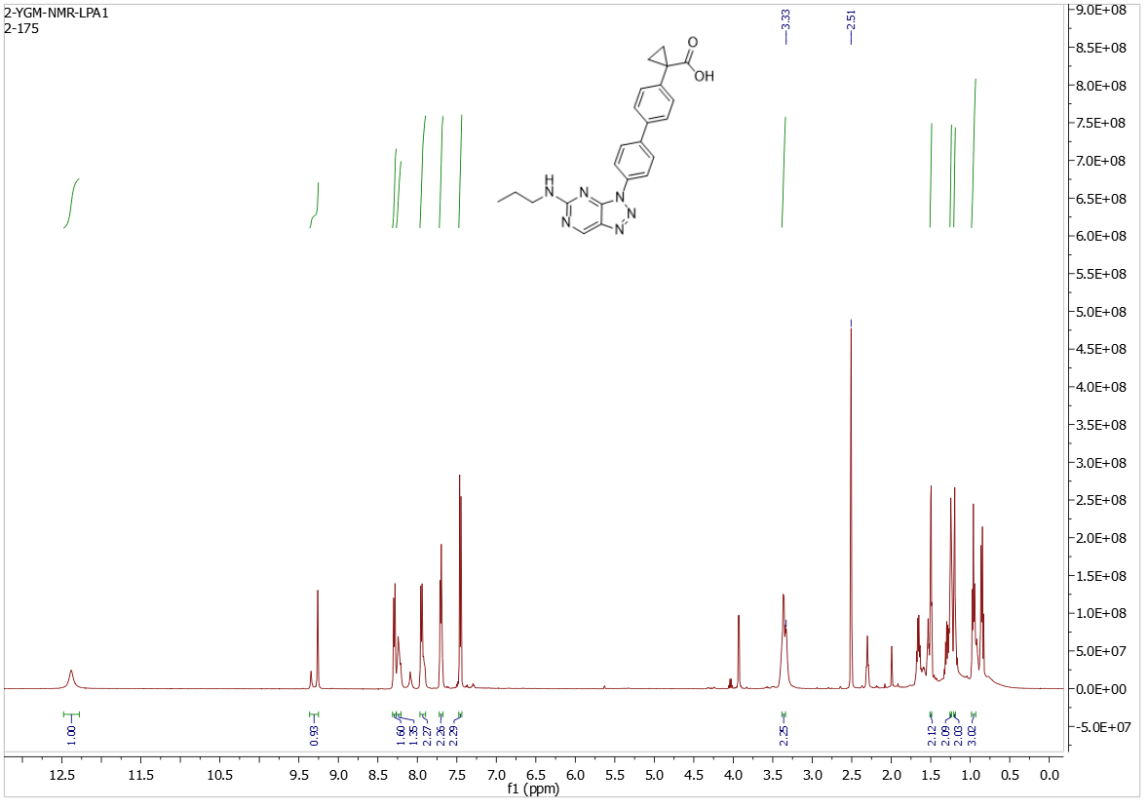

Compound **L22c**

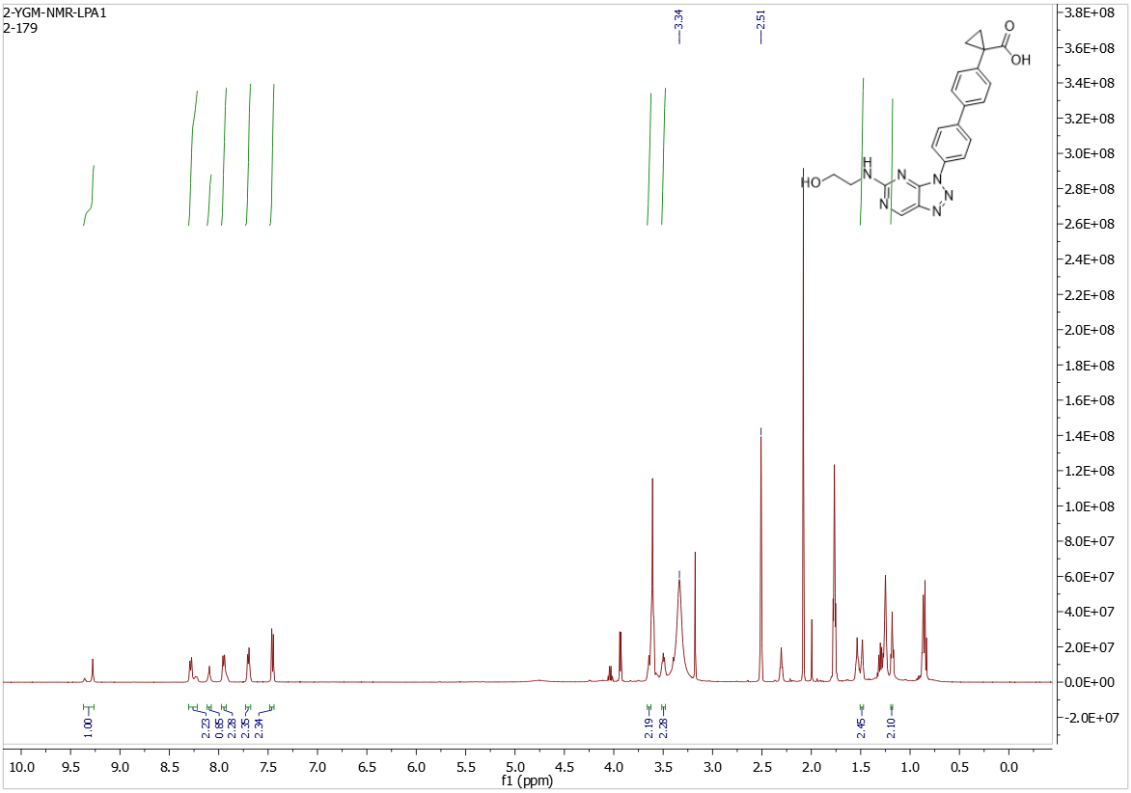

Compound **L22e**

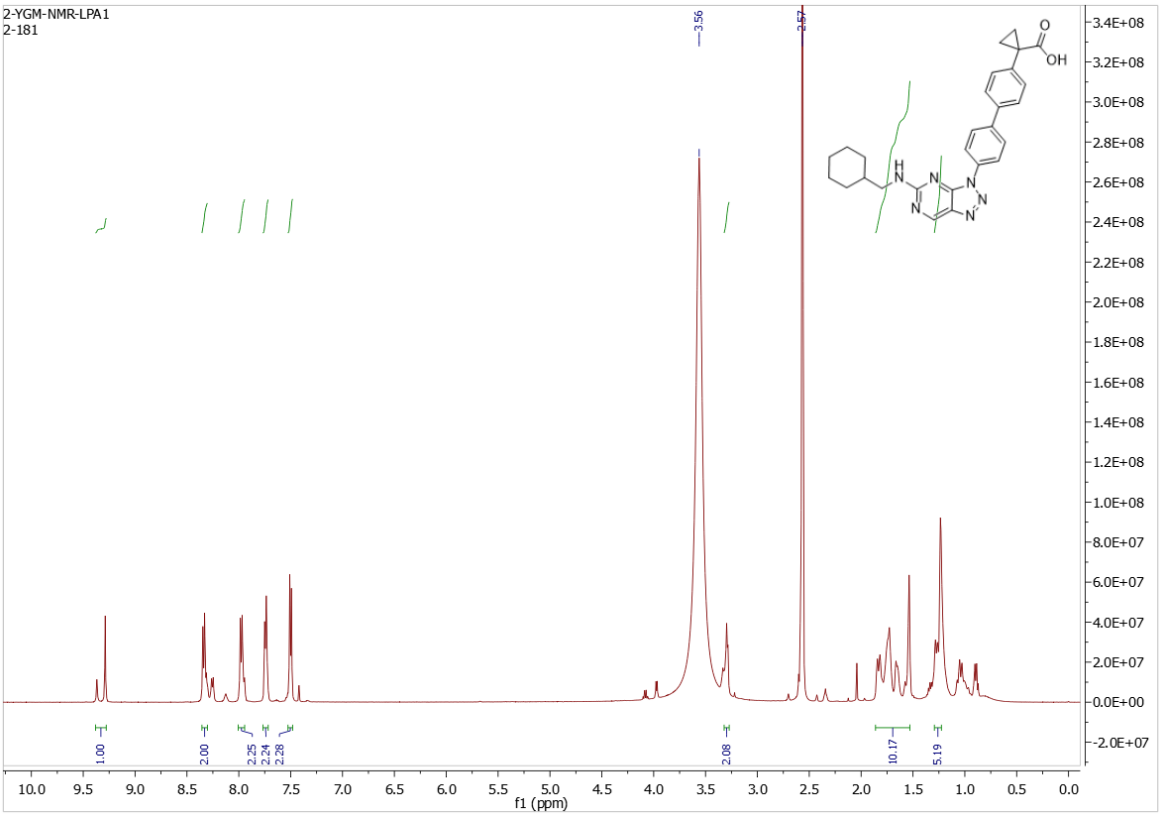

Compound **L22f**

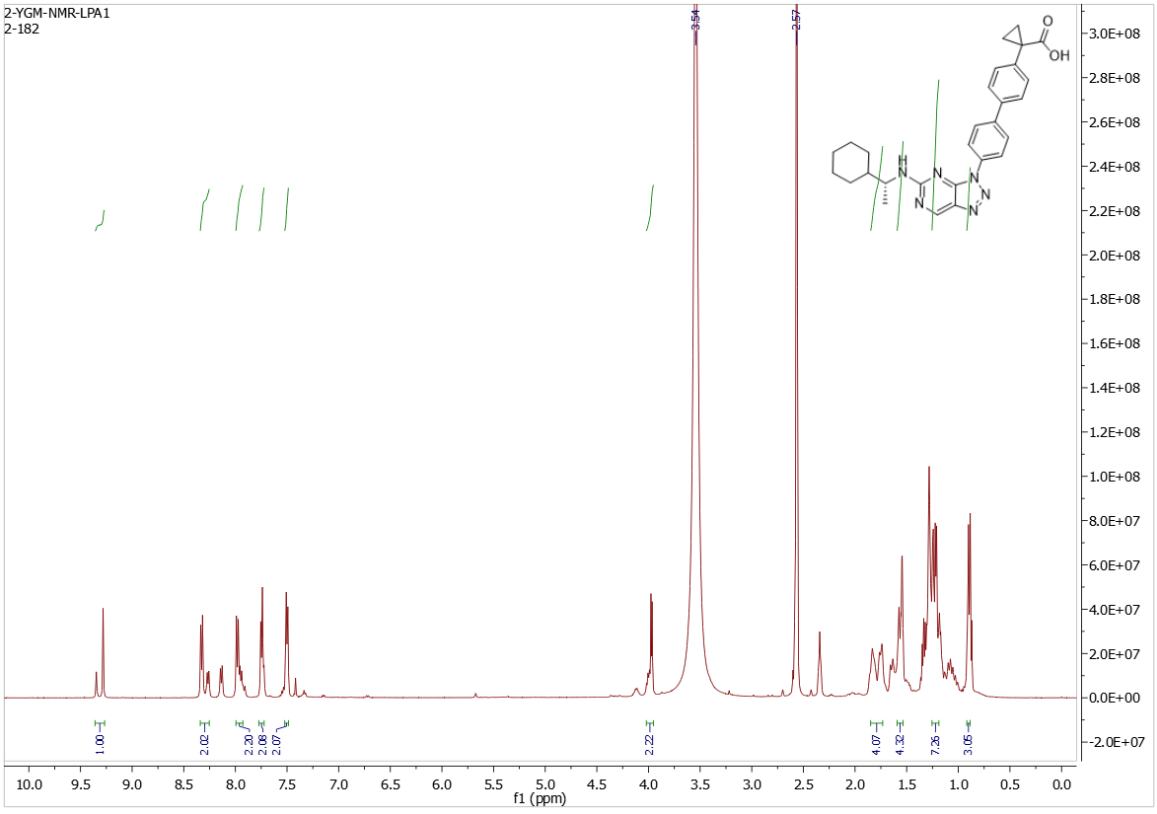

Compound **L22h**

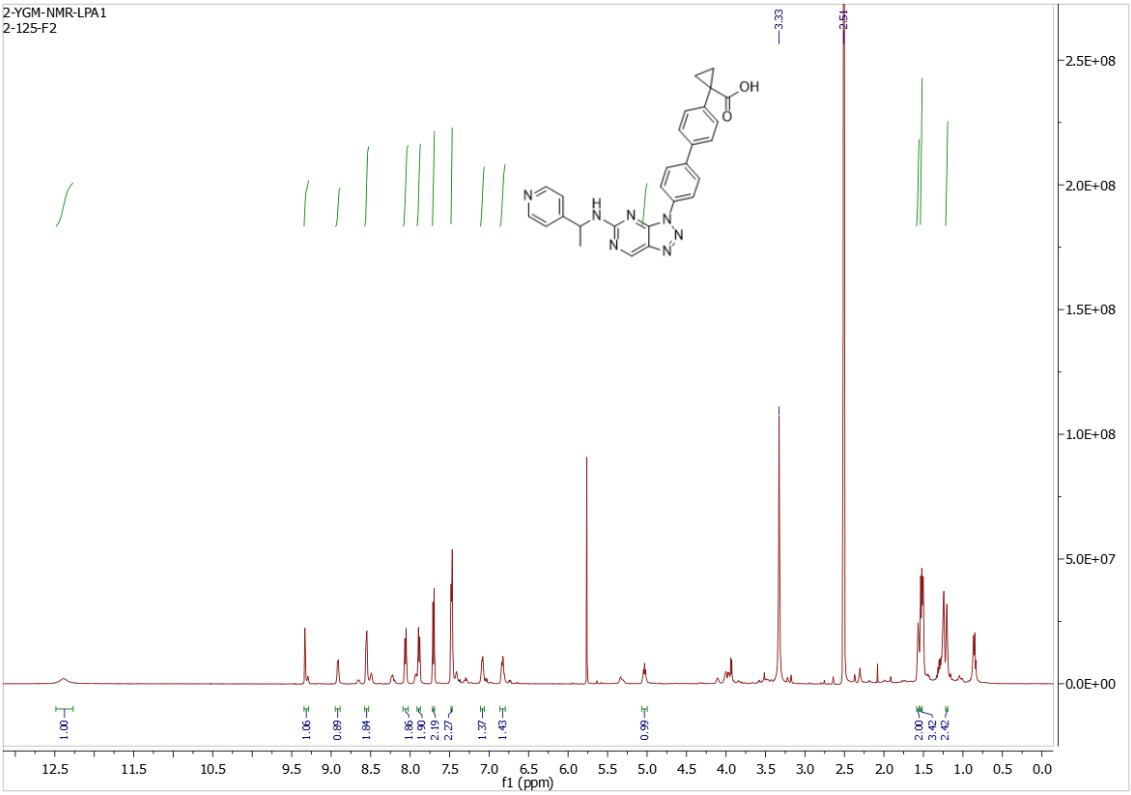

Compound **L22i**

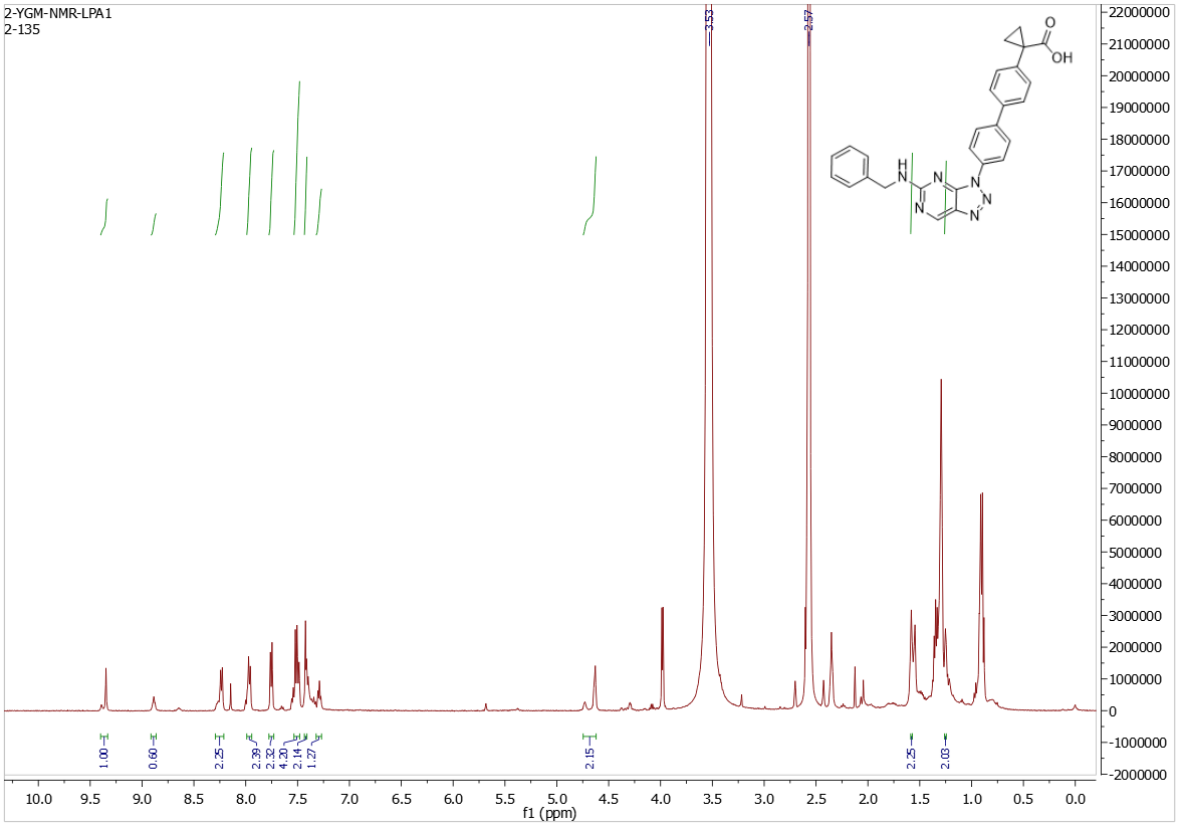

Compound **L22j**

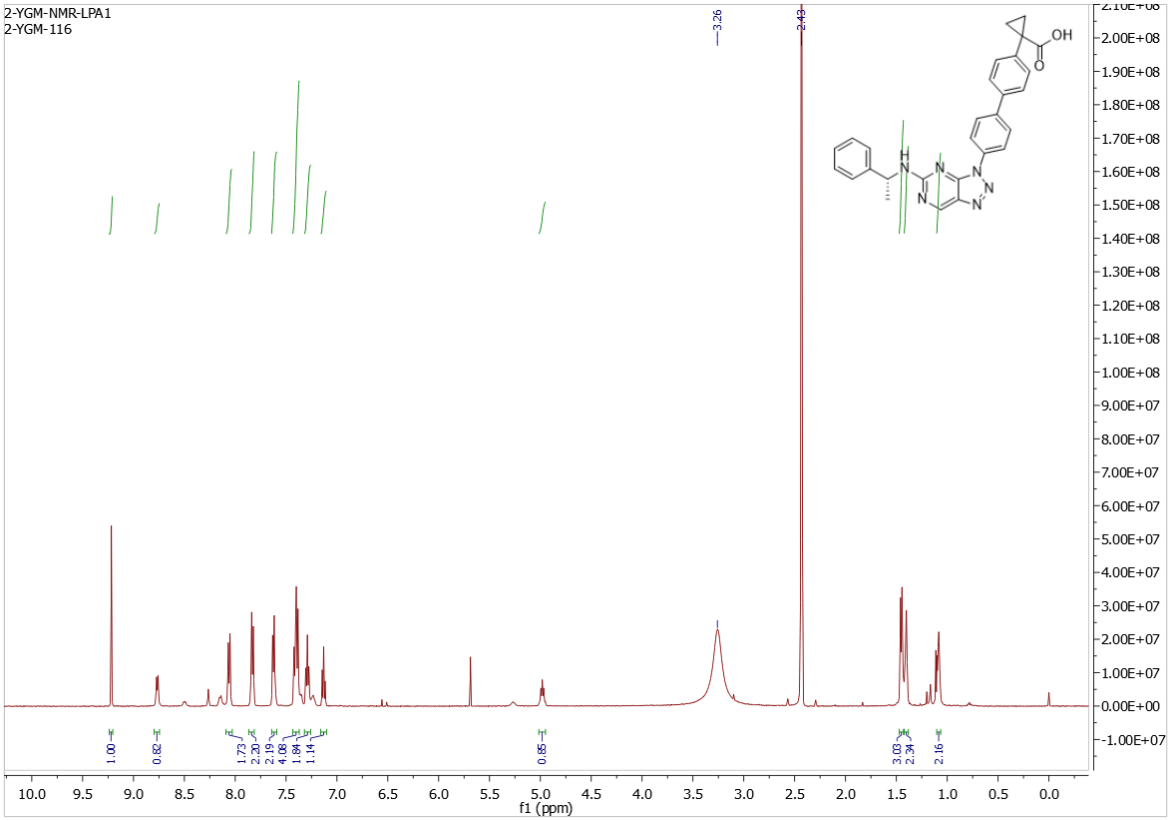

Compound **L22k**

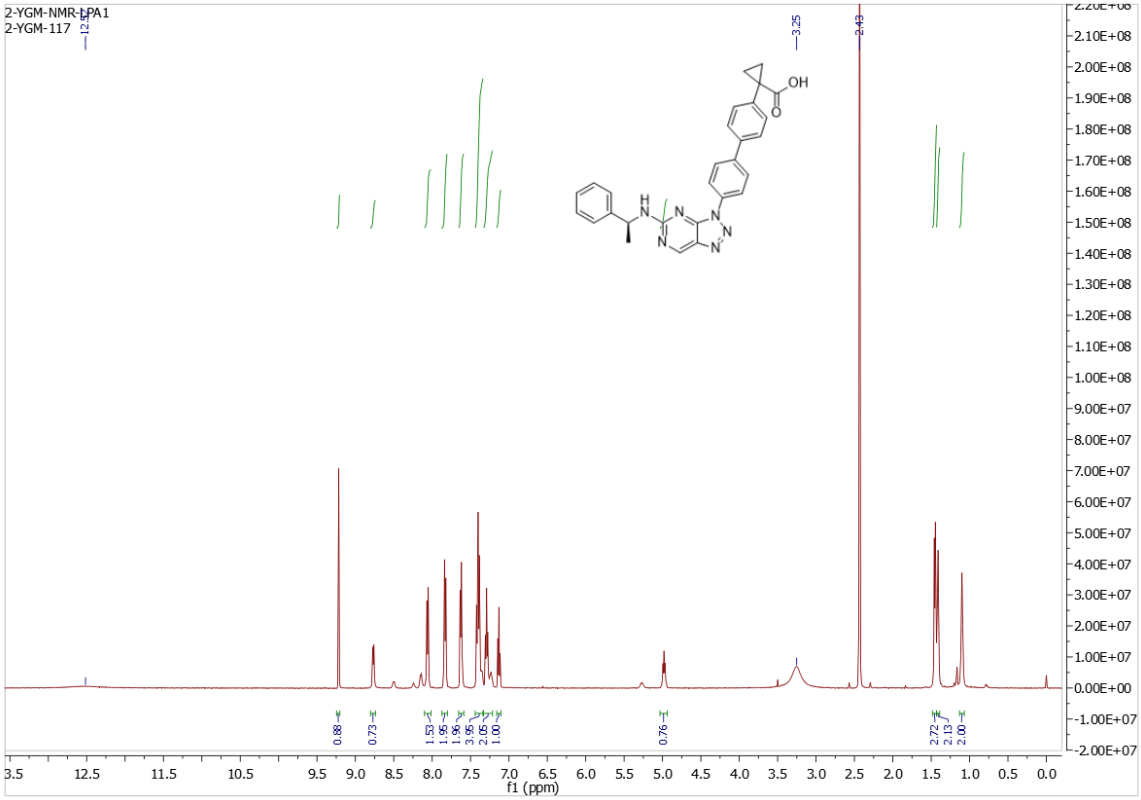

Compound **L22l**

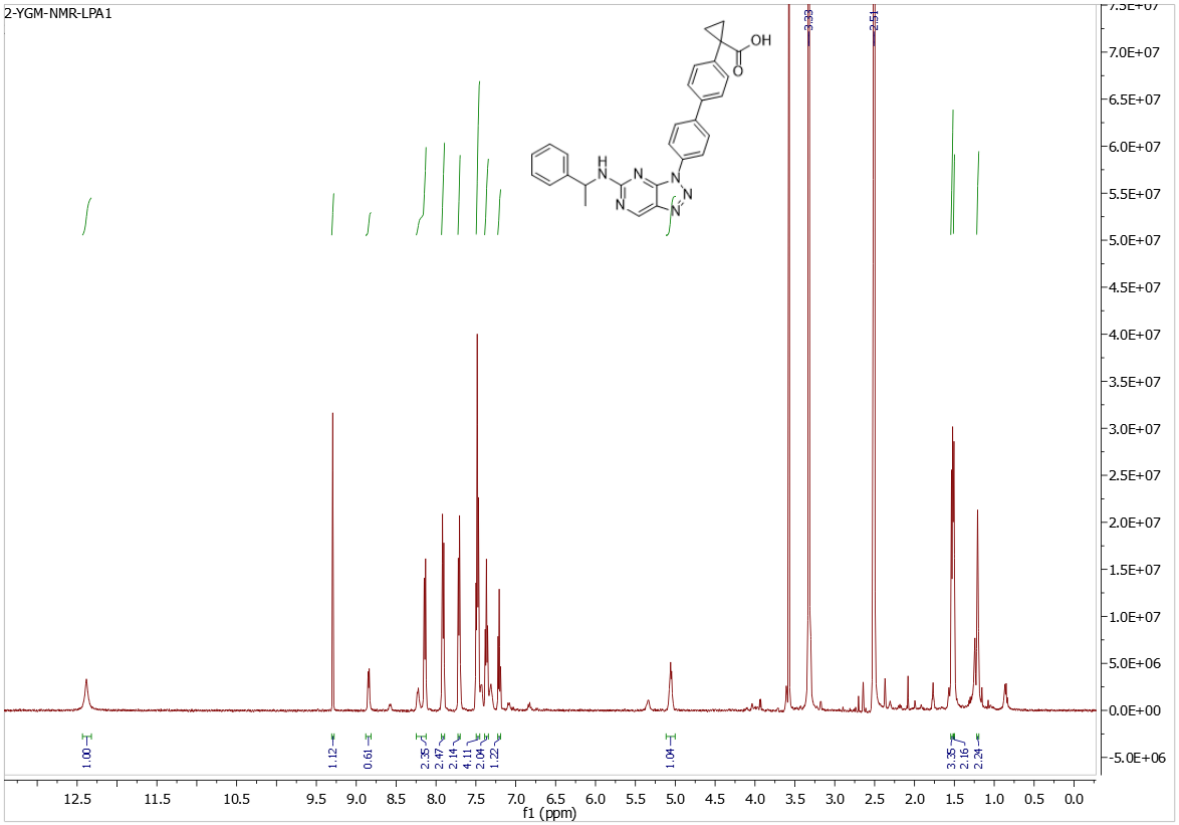

Compound **L22m**

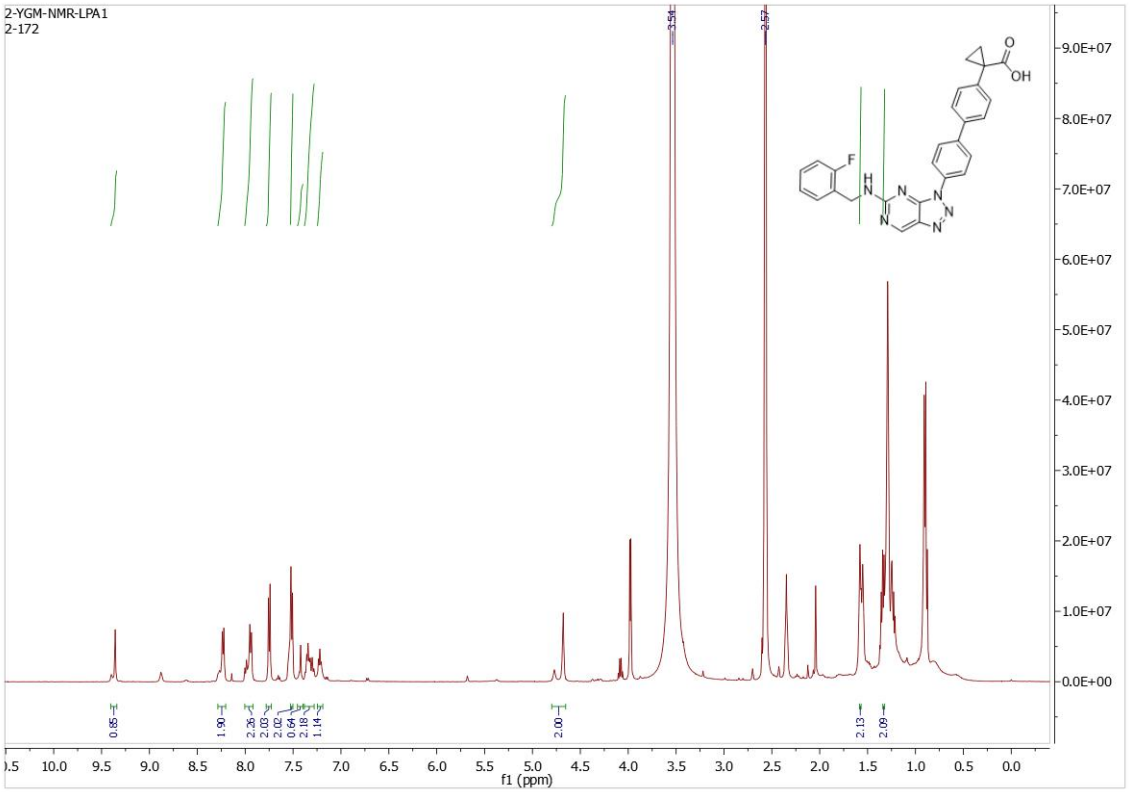

Compound **L22n**

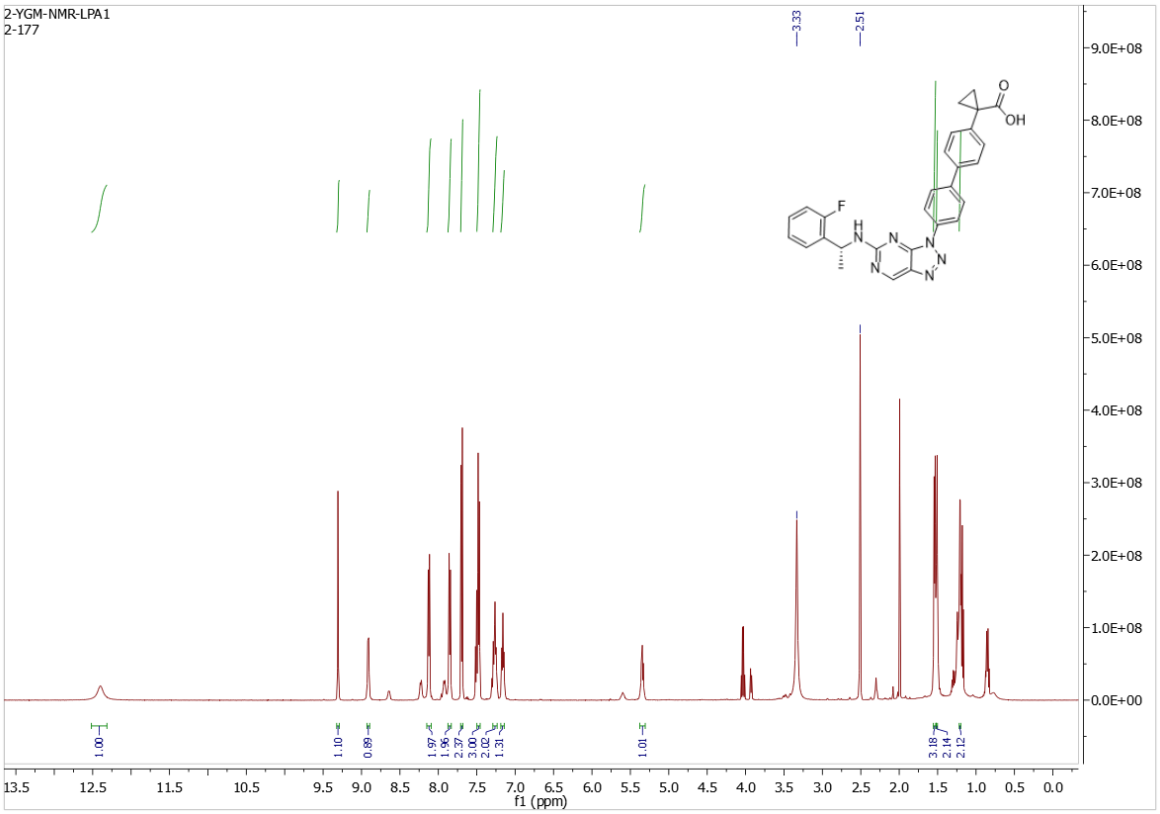

Compound **L22o**

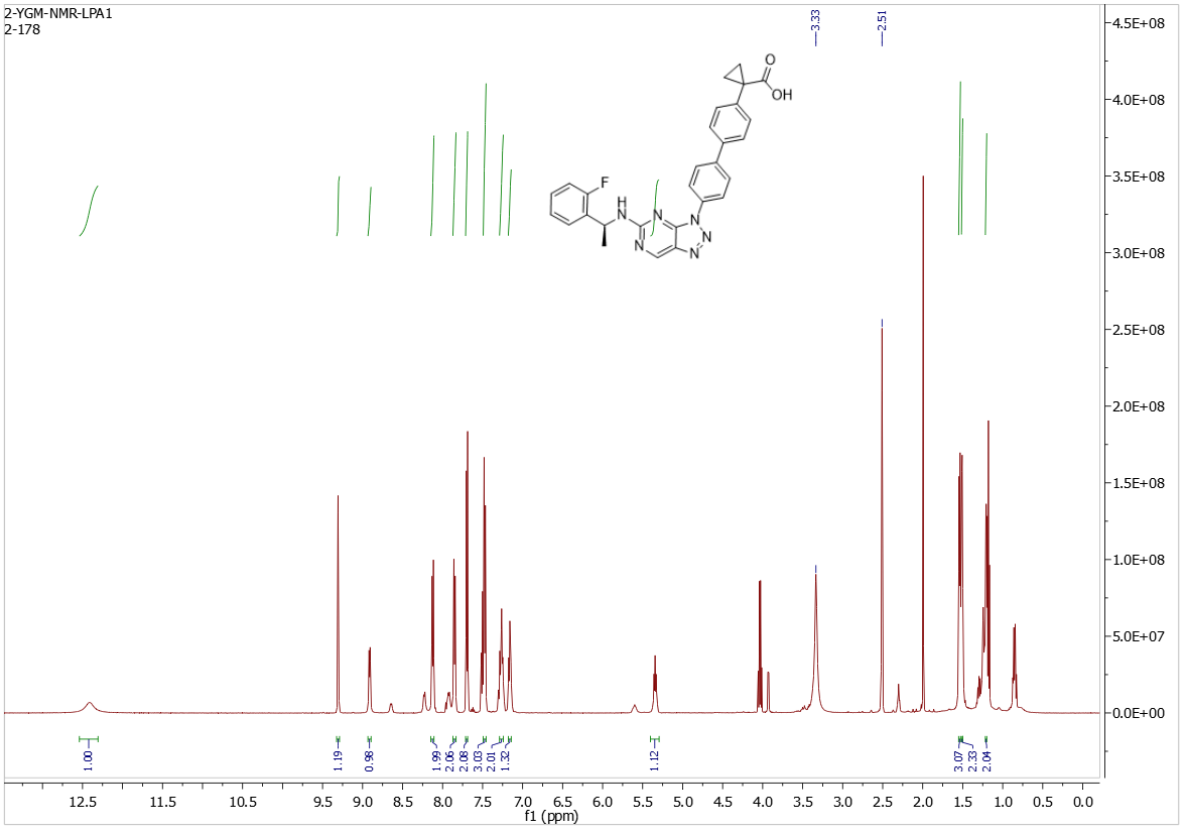

Compound **L22p**

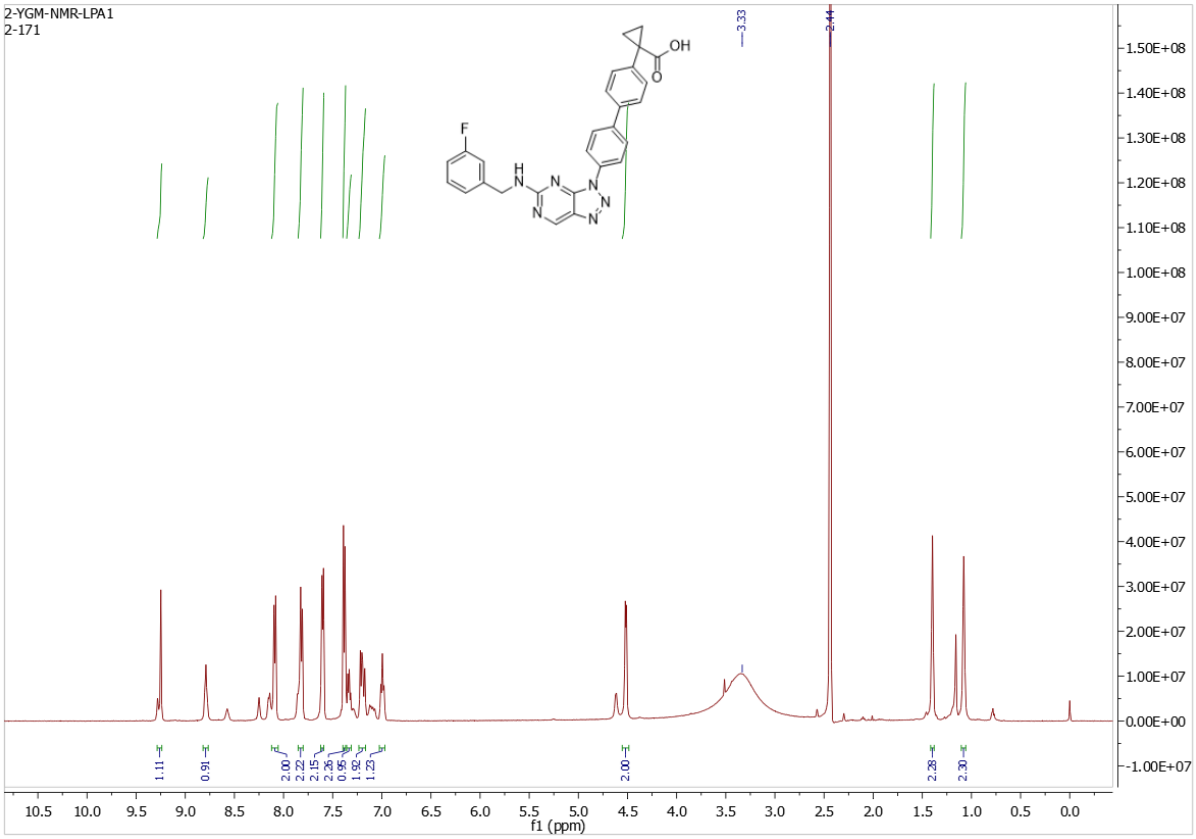

Compound **L22q**

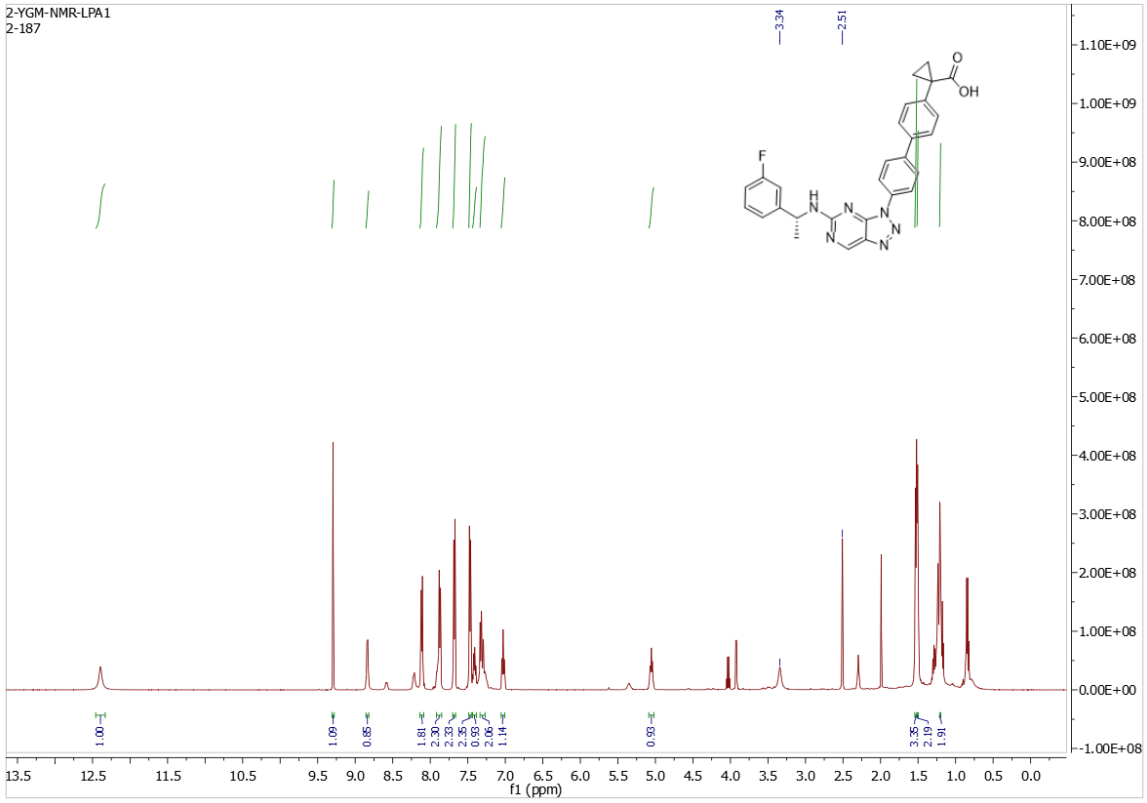

Compound **L22r**

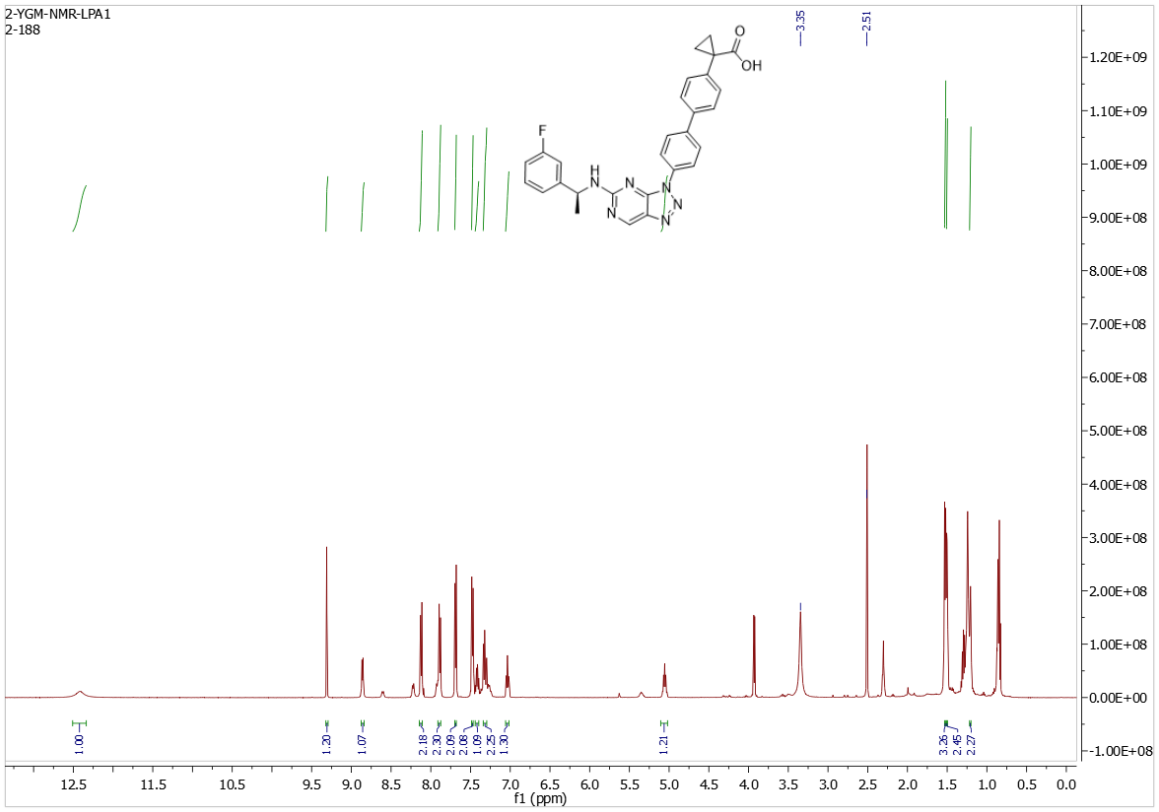

Compound **L22s**

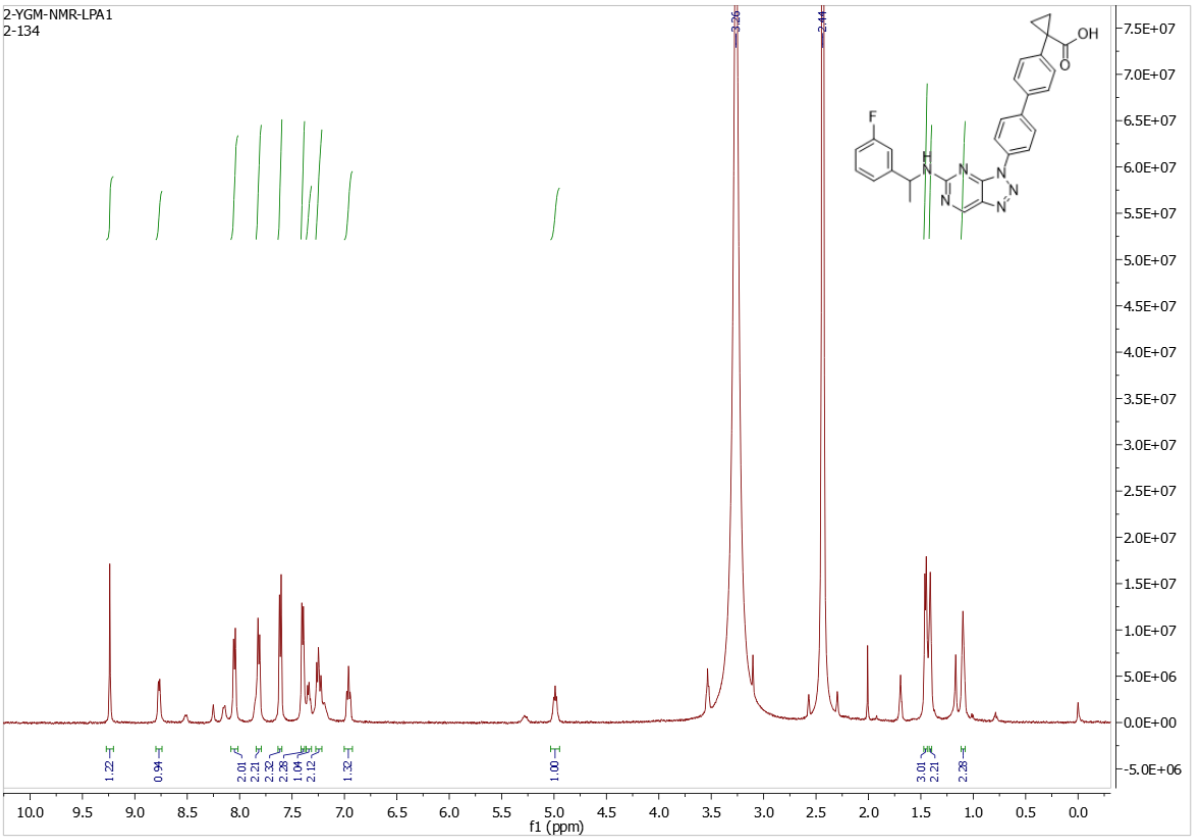

Compound **L22t**

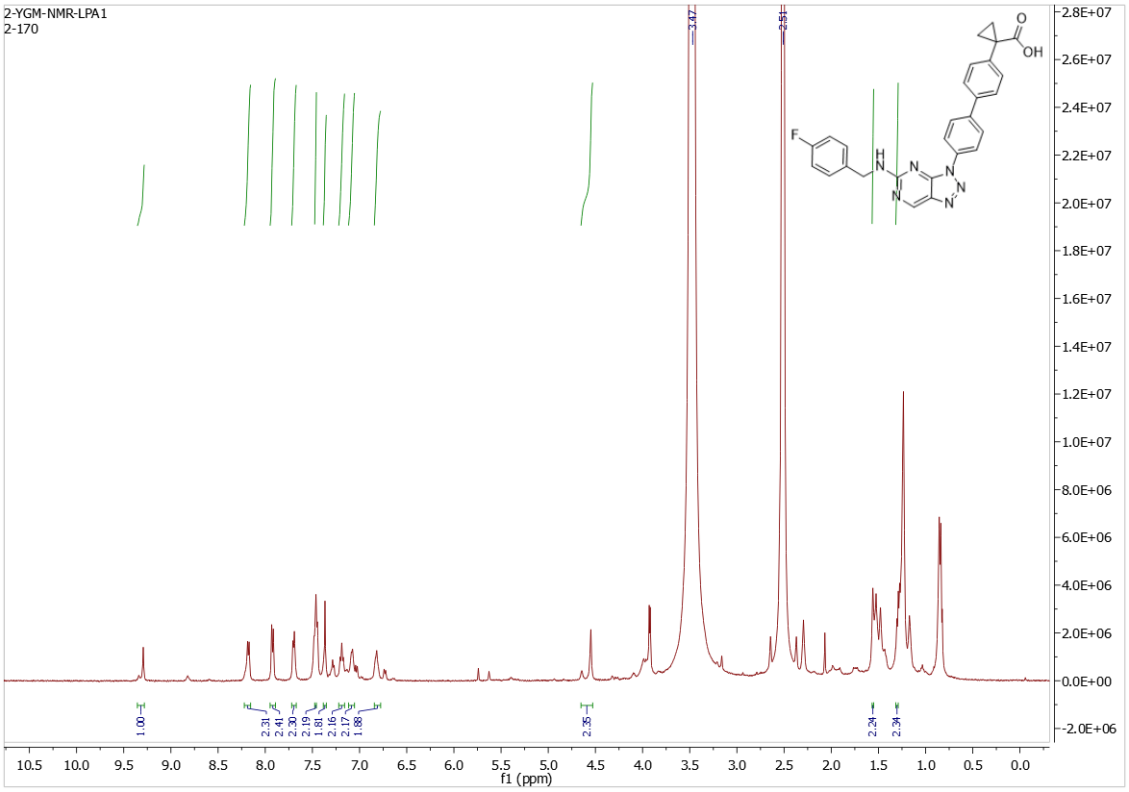

Compound **L22u**

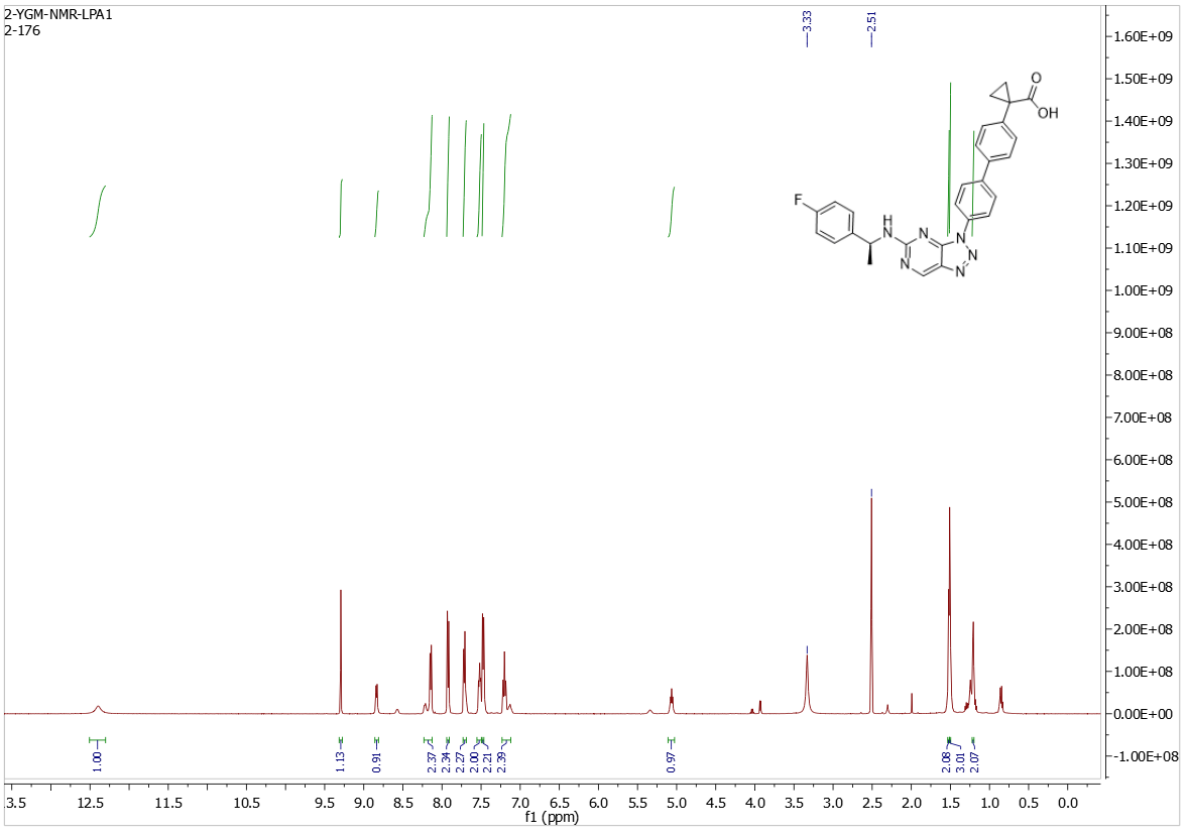

Compound **L23a**

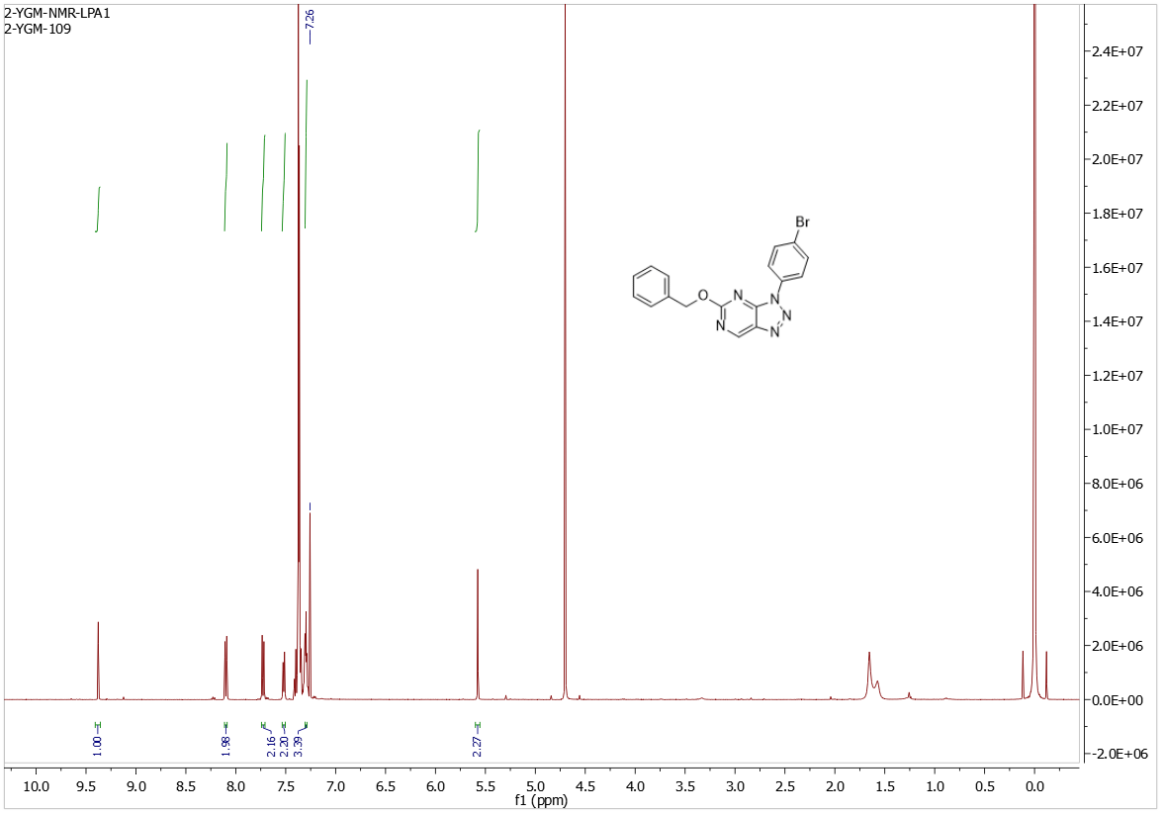

Compound **L24a**

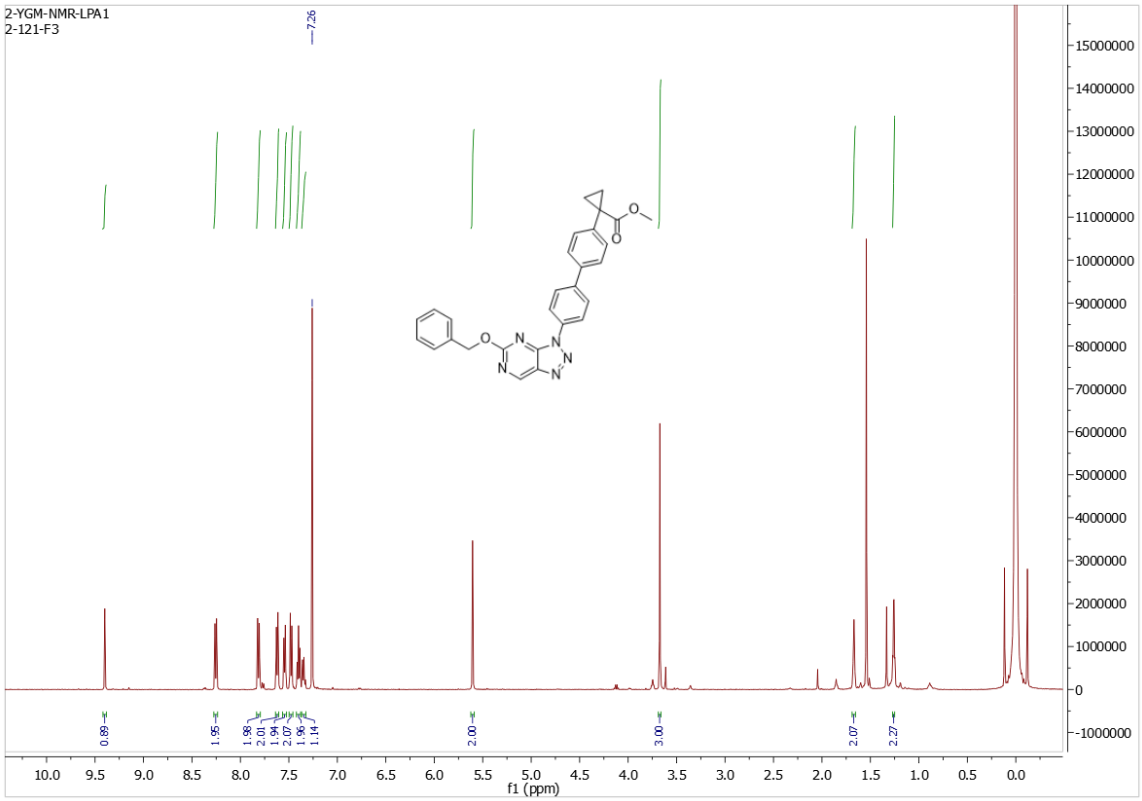

Compound **L31i**

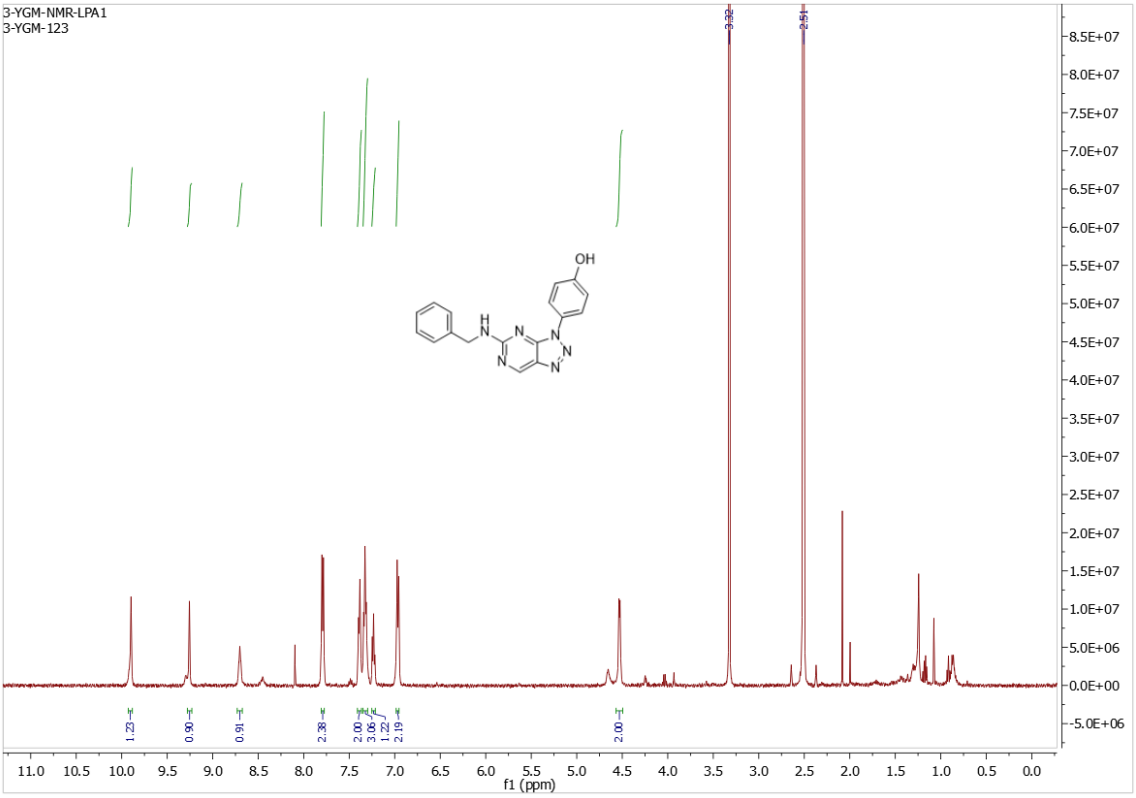

Compound **L31m**

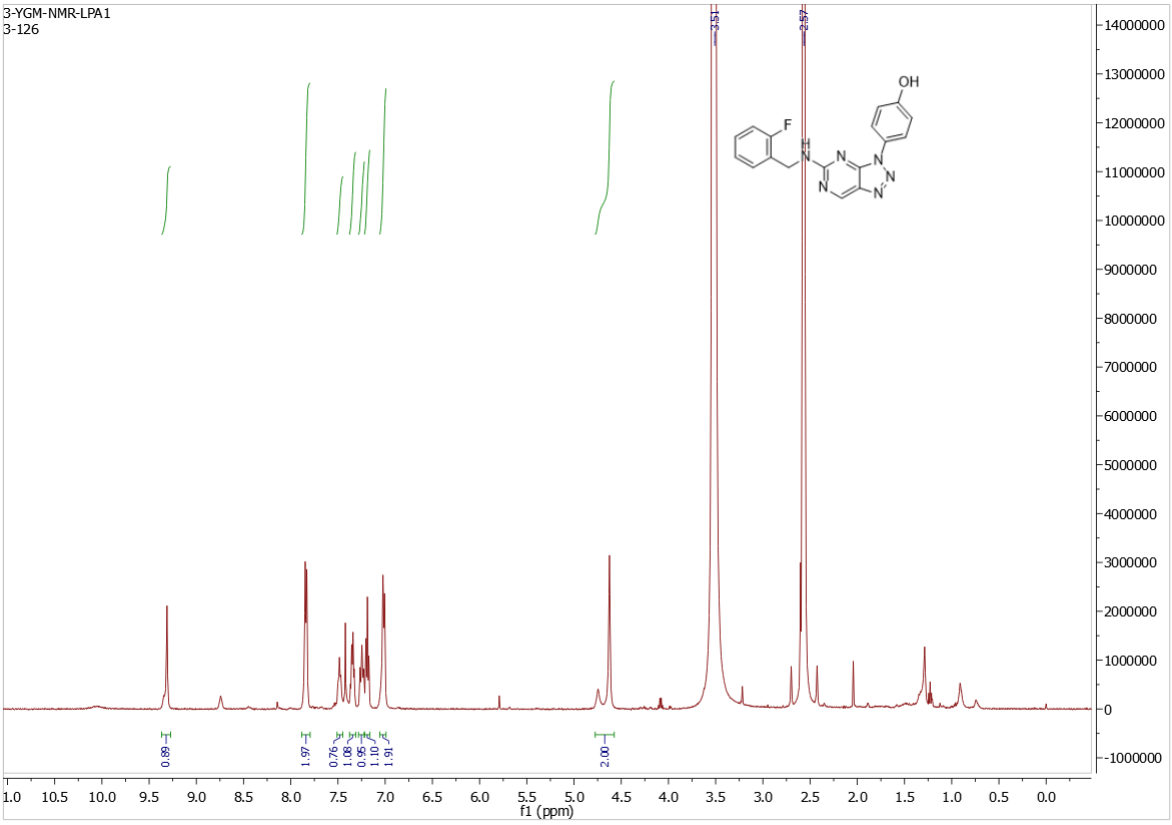

Compound **L31p**

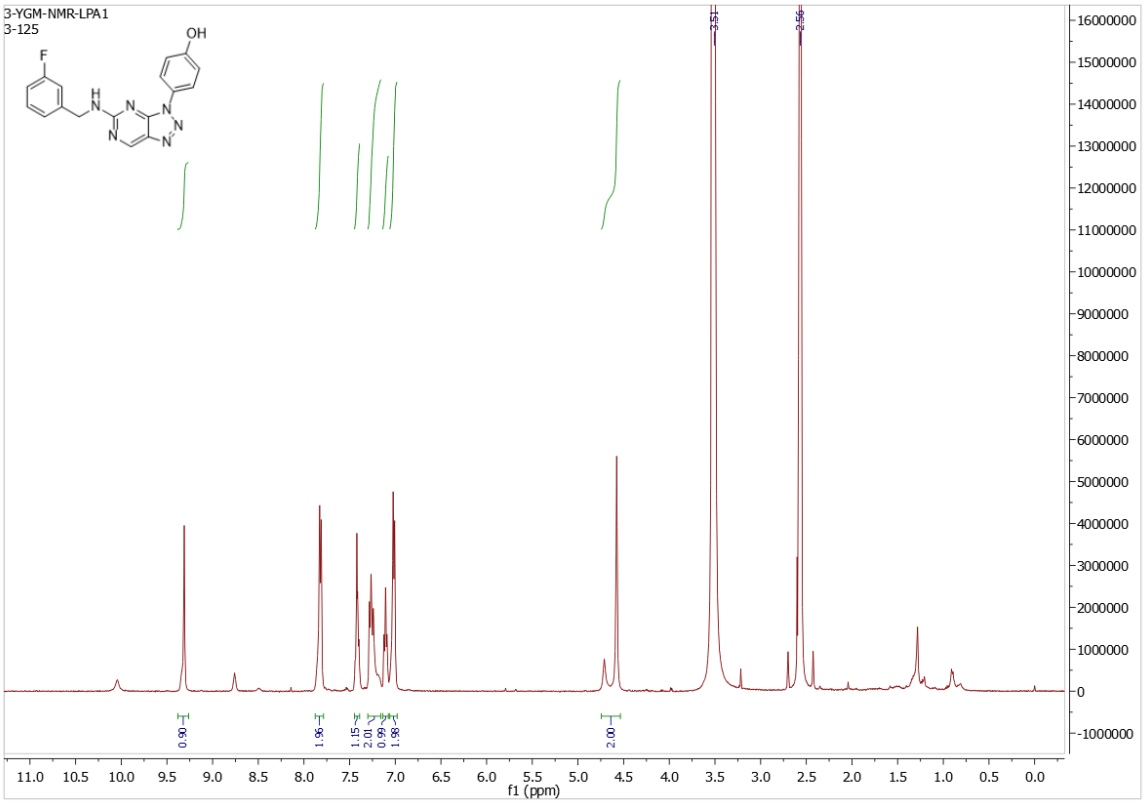

Compound **L31t**

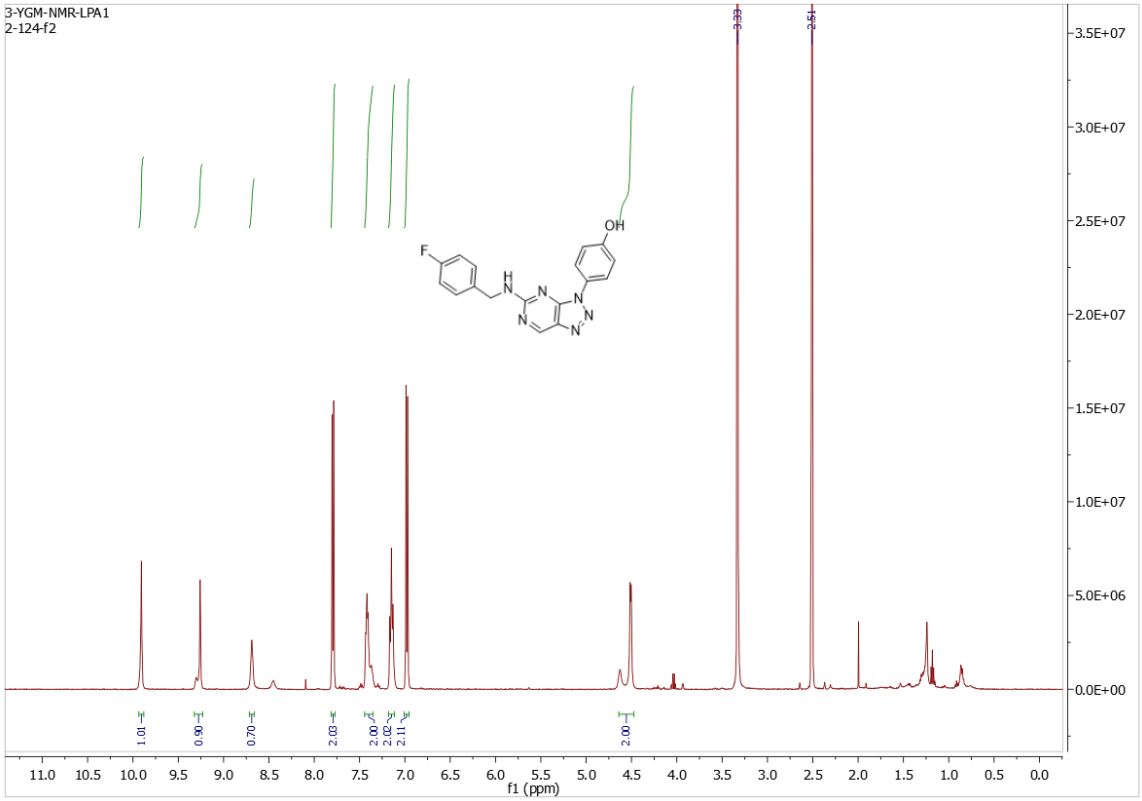

Compound **L35**

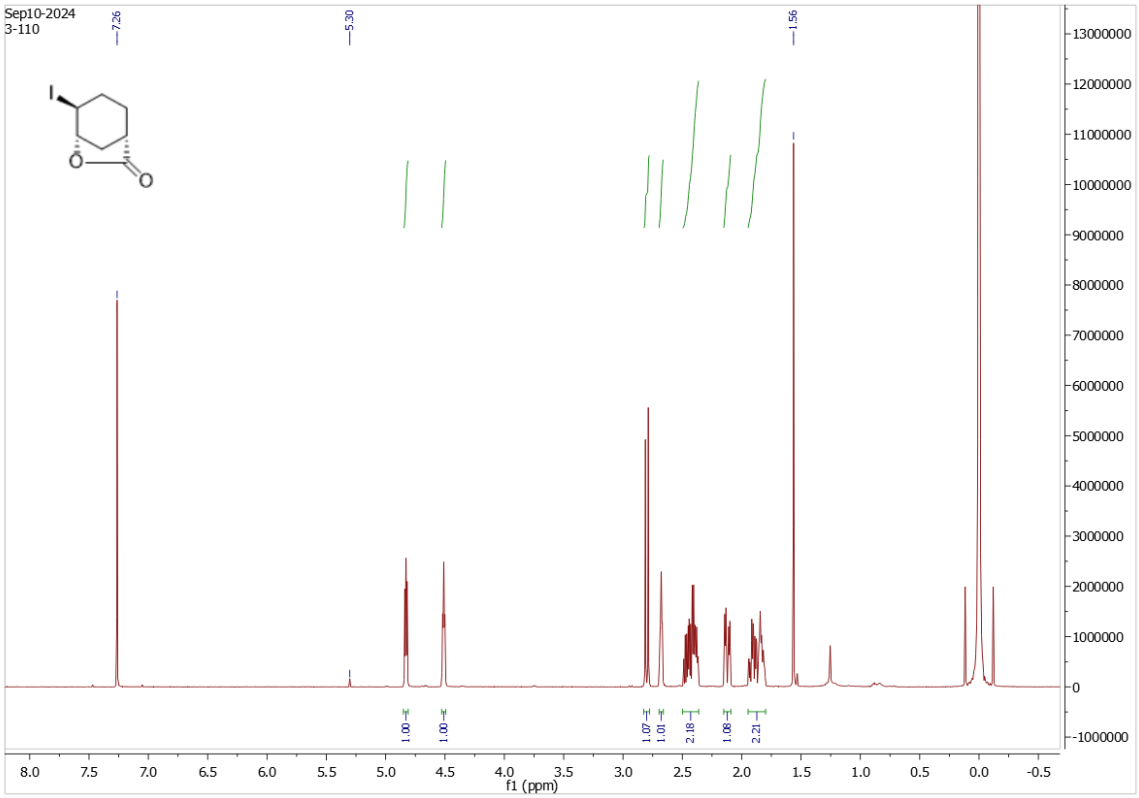

Appendix C

Dose-response curve of β-arrestin 1-Trypsin

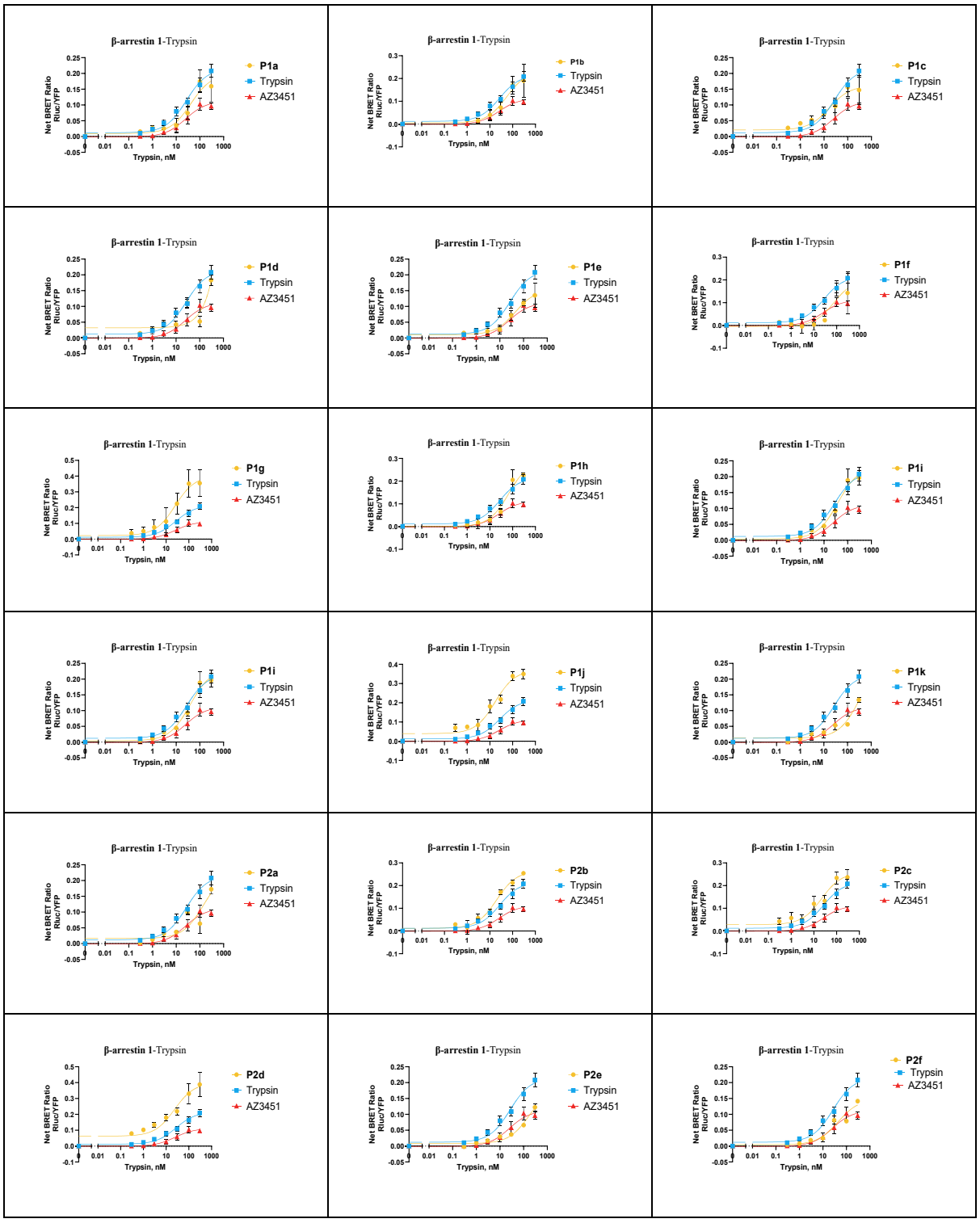

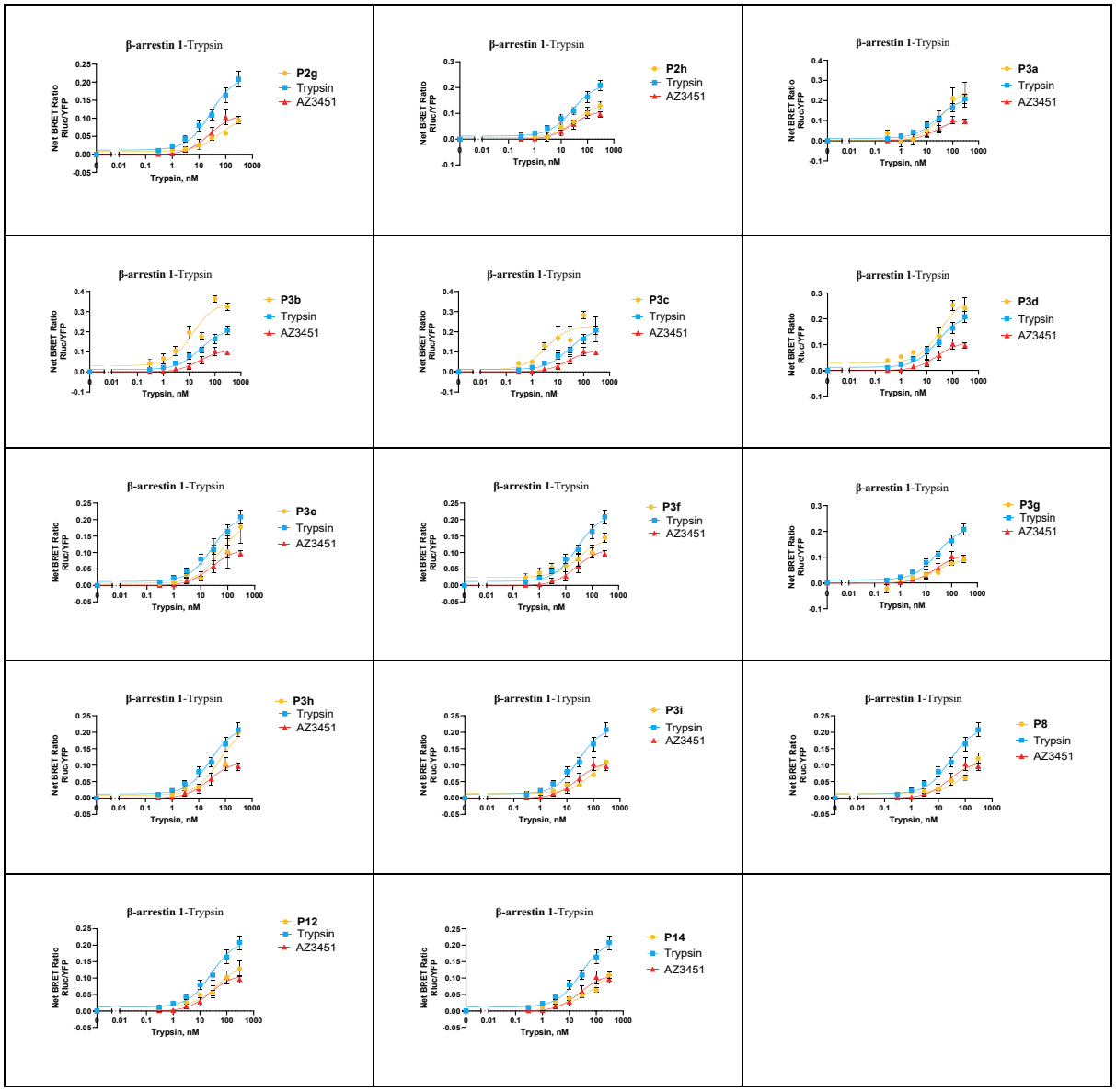

Dose-response curve of β-arrestin 2-Trypsin

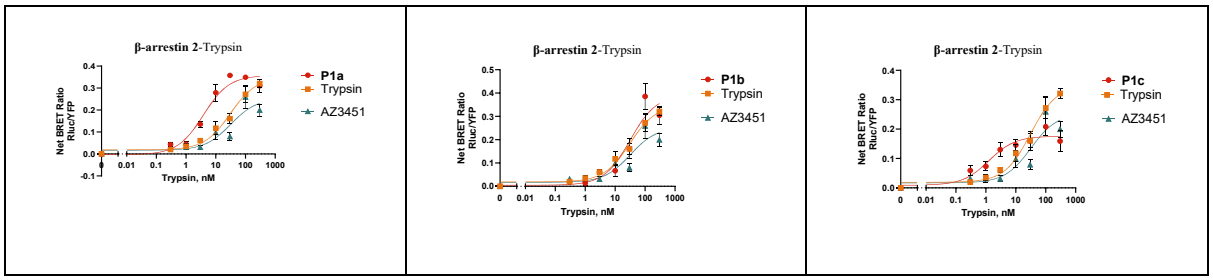

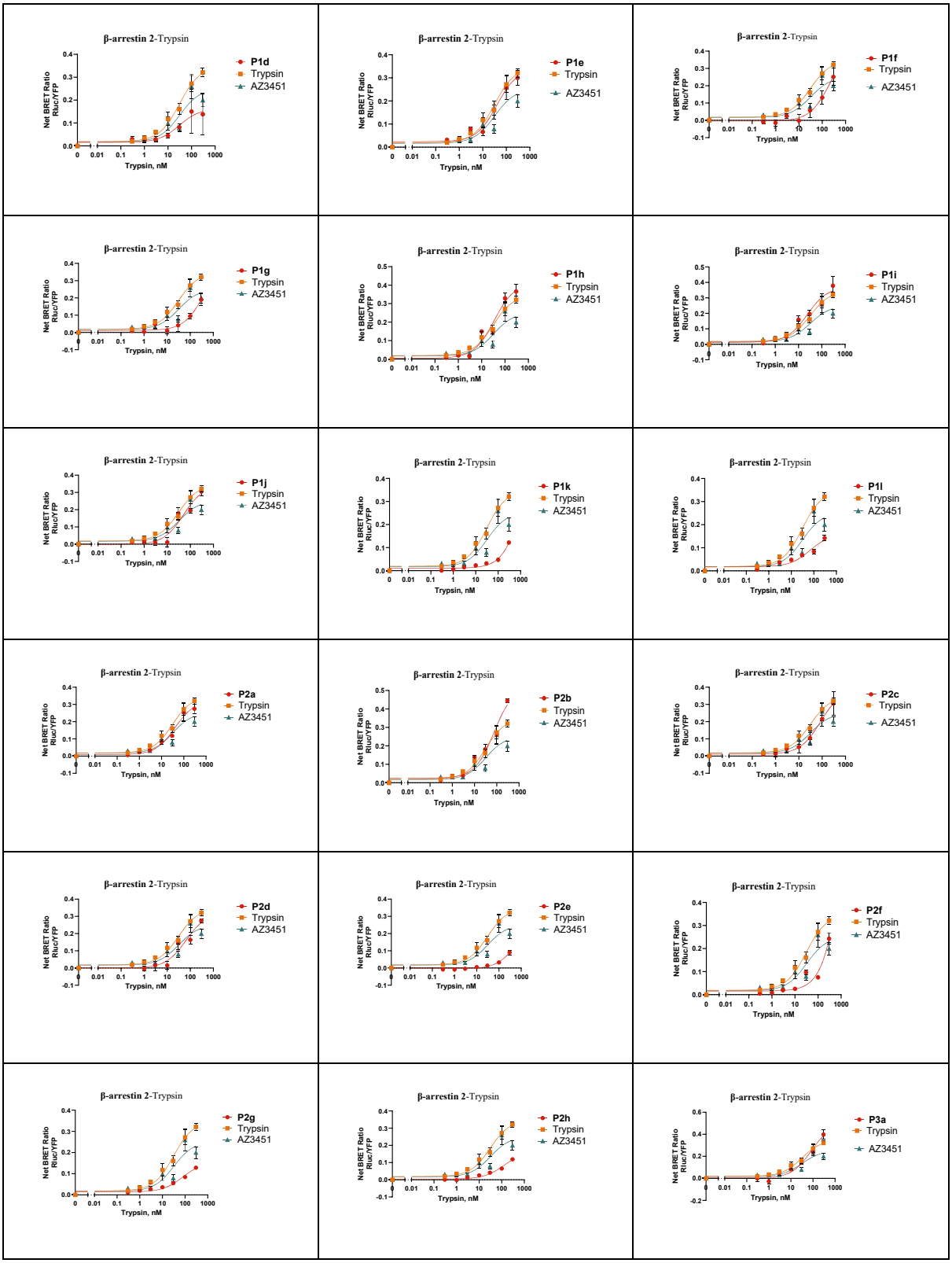
β-arrestin 2-Trypsin
P1d
Trypsin
AZ3451
β-arrestin 2-Trypsin
P1e
Trypsin
AZ3451
β-arrestin 2-Trypsin
P1f
Trypsin
AZ3451
β-arrestin 2-Trypsin
P1g
Trypsin
AZ3451
β-arrestin 2-Trypsin
P1h
Trypsin
AZ3451
β-arrestin 2-Trypsin
P1i
Trypsin
AZ3451
β-arrestin 2-Trypsin
P1j
Trypsin
AZ3451
β-arrestin 2-Trypsin
P1k
Trypsin
AZ3451
β-arrestin 2-Trypsin
P1l
Trypsin
AZ3451
β-arrestin 2-Trypsin
P2a
Trypsin
AZ3451
β-arrestin 2-Trypsin
P2b
Trypsin
AZ3451
β-arrestin 2-Trypsin
P2c
Trypsin
AZ3451
β-arrestin 2-Trypsin
P2d
Trypsin
AZ3451
β-arrestin 2-Trypsin
P2e
Trypsin
AZ3451
β-arrestin 2-Trypsin
P2f
Trypsin
AZ3451
β-arrestin 2-Trypsin
P2g
Trypsin
AZ3451
β-arrestin 2-Trypsin
P2h
Trypsin
AZ3451
β-arrestin 2-Trypsin
P3a
Trypsin
AZ3451
Net BRET Ratio Rluc/YFP
Trypsin, nM

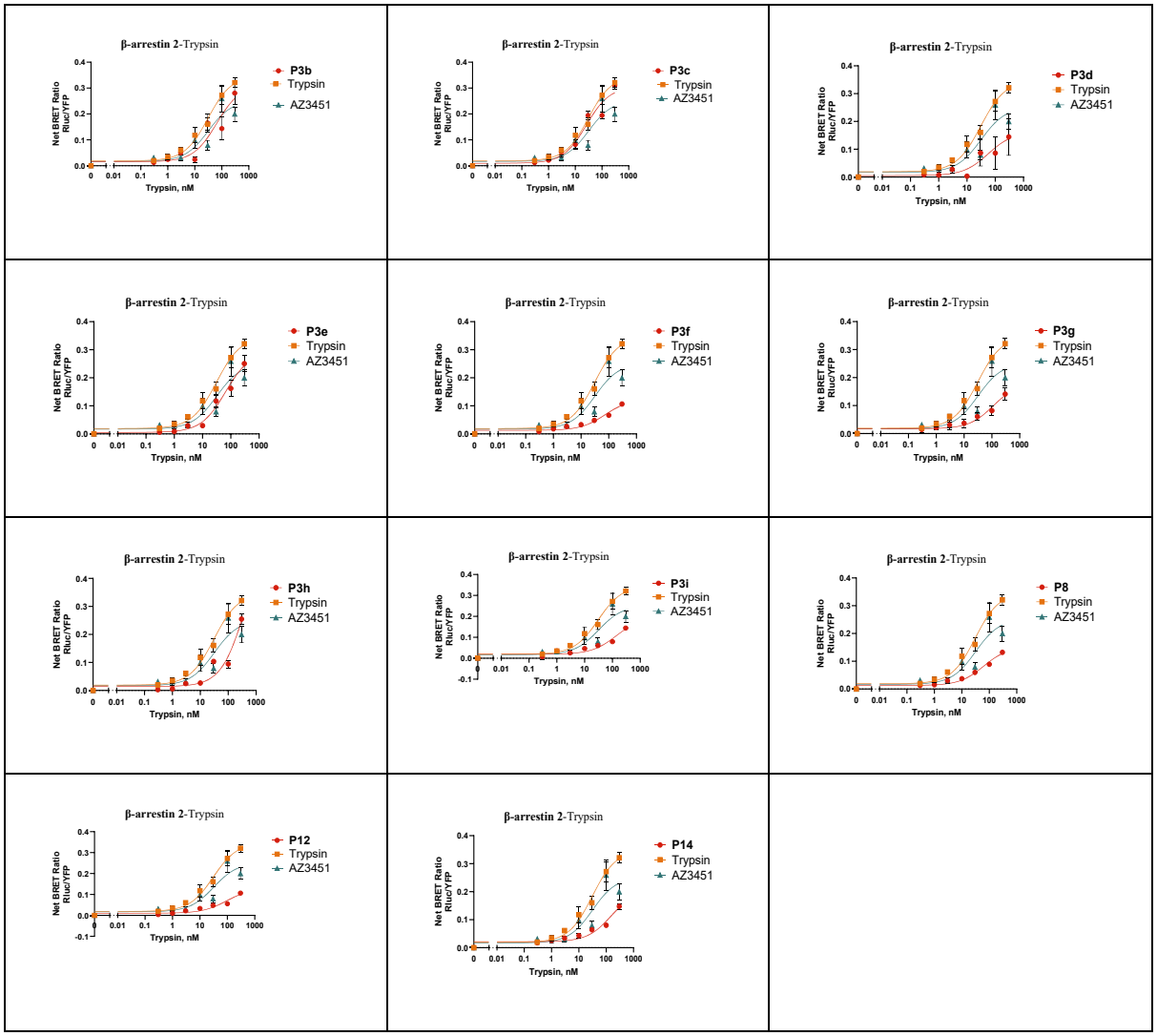

Dose-response curve of β-arrestin 1- SLIGRL-HN$_2$

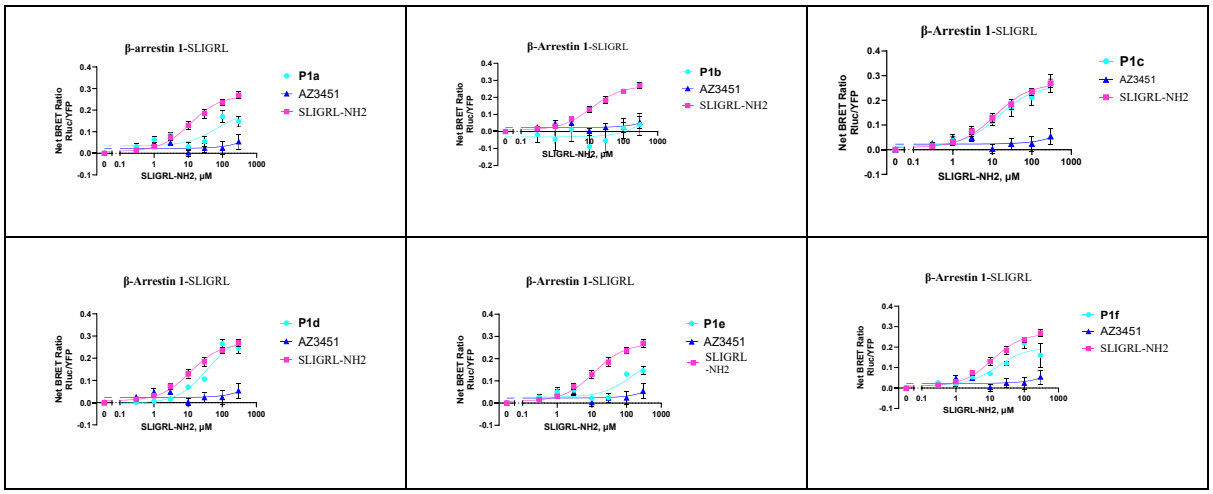

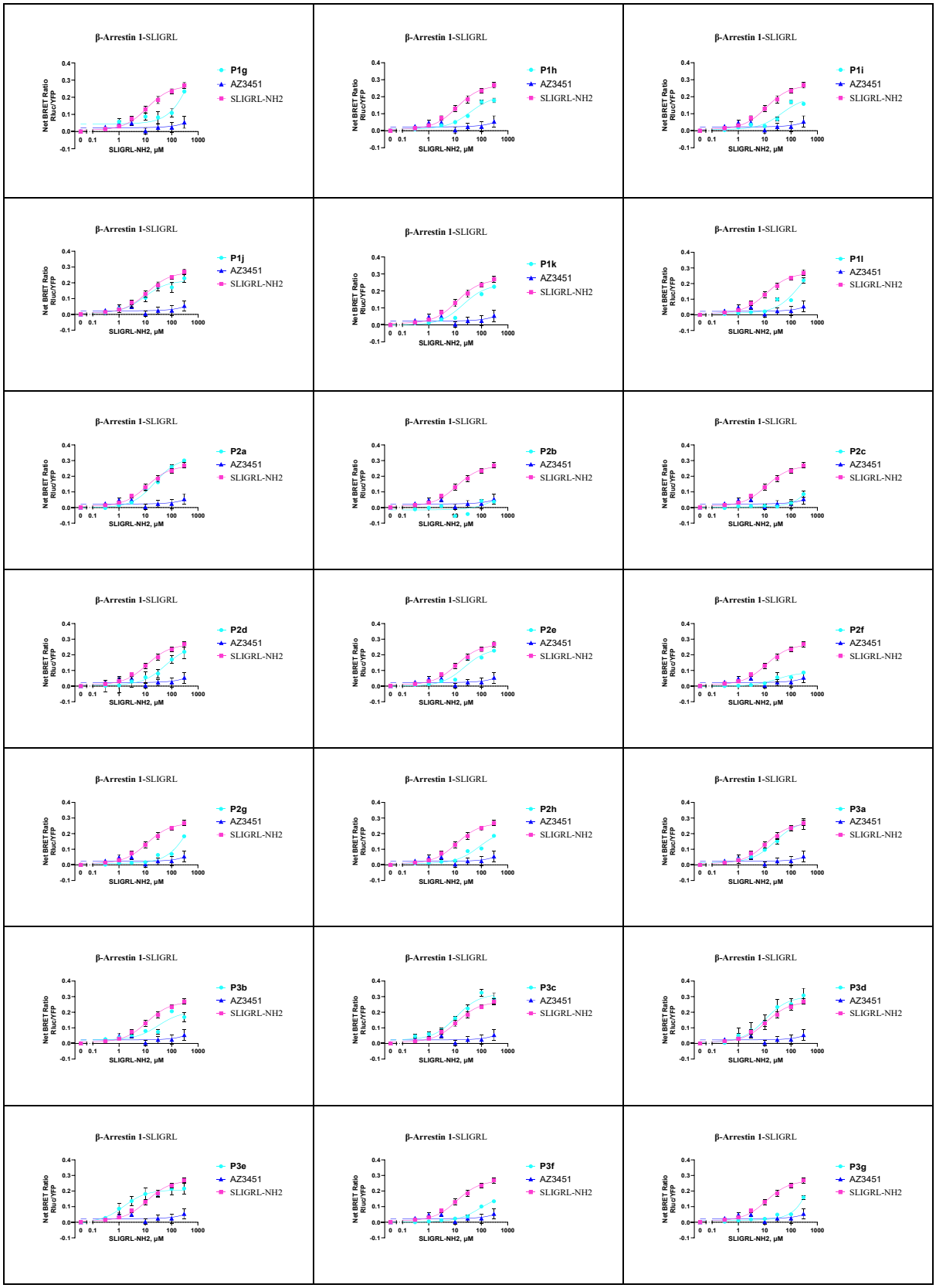
β-Arrestin 1-SLIGRL
Net BRET Ratio Rluc/YFP
SLIGRL-NH2, μM
P1g
AZ3451
SLIGRL-NH2
β-Arrestin 1-SLIGRL
Net BRET Ratio Rluc/YFP
SLIGRL-NH2, μM
P1h
AZ3451
SLIGRL-NH2
β-Arrestin 1-SLIGRL
Net BRET Ratio Rluc/YFP
SLIGRL-NH2, μM
P1i
AZ3451
SLIGRL-NH2
β-Arrestin 1-SLIGRL
Net BRET Ratio Rluc/YFP
SLIGRL-NH2, μM
P1j
AZ3451
SLIGRL-NH2
β-Arrestin 1-SLIGRL
Net BRET Ratio Rluc/YFP
SLIGRL-NH2, μM
P1k
AZ3451
SLIGRL-NH2
β-Arrestin 1-SLIGRL
Net BRET Ratio Rluc/YFP
SLIGRL-NH2, μM
P1l
AZ3451
SLIGRL-NH2
β-Arrestin 1-SLIGRL
Net BRET Ratio Rluc/YFP
SLIGRL-NH2, μM
P2a
AZ3451
SLIGRL-NH2
β-Arrestin 1-SLIGRL
Net BRET Ratio Rluc/YFP
SLIGRL-NH2, μM
P2b
AZ3451
SLIGRL-NH2
β-Arrestin 1-SLIGRL
Net BRET Ratio Rluc/YFP
SLIGRL-NH2, μM
P2c
AZ3451
SLIGRL-NH2
β-Arrestin 1-SLIGRL
Net BRET Ratio Rluc/YFP
SLIGRL-NH2, μM
P2d
AZ3451
SLIGRL-NH2
β-Arrestin 1-SLIGRL
Net BRET Ratio Rluc/YFP
SLIGRL-NH2, μM
P2e
AZ3451
SLIGRL-NH2
β-Arrestin 1-SLIGRL
Net BRET Ratio Rluc/YFP
SLIGRL-NH2, μM
P2f
AZ3451
SLIGRL-NH2
β-Arrestin 1-SLIGRL
Net BRET Ratio Rluc/YFP
SLIGRL-NH2, μM
P2g
AZ3451
SLIGRL-NH2
β-Arrestin 1-SLIGRL
Net BRET Ratio Rluc/YFP
SLIGRL-NH2, μM
P2h
AZ3451
SLIGRL-NH2
β-Arrestin 1-SLIGRL
Net BRET Ratio Rluc/YFP
SLIGRL-NH2, μM
P3a
AZ3451
SLIGRL-NH2
β-Arrestin 1-SLIGRL
Net BRET Ratio Rluc/YFP
SLIGRL-NH2, μM
P3b
AZ3451
SLIGRL-NH2
β-Arrestin 1-SLIGRL
Net BRET Ratio Rluc/YFP
SLIGRL-NH2, μM
P3c
AZ3451
SLIGRL-NH2
β-Arrestin 1-SLIGRL
Net BRET Ratio Rluc/YFP
SLIGRL-NH2, μM
P3d
AZ3451
SLIGRL-NH2
β-Arrestin 1-SLIGRL
Net BRET Ratio Rluc/YFP
SLIGRL-NH2, μM
P3e
AZ3451
SLIGRL-NH2
β-Arrestin 1-SLIGRL
Net BRET Ratio Rluc/YFP
SLIGRL-NH2, μM
P3f
AZ3451
SLIGRL-NH2
β-Arrestin 1-SLIGRL
Net BRET Ratio Rluc/YFP
SLIGRL-NH2, μM
P3g
AZ3451
SLIGRL-NH2

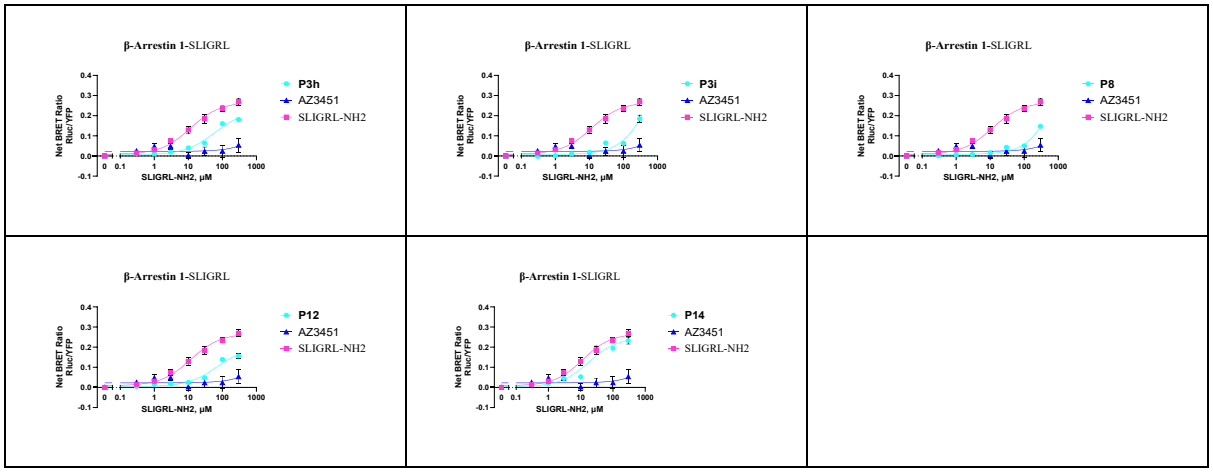

Dose-response curve of β-arrestin 2- SLIGRL-HN_2

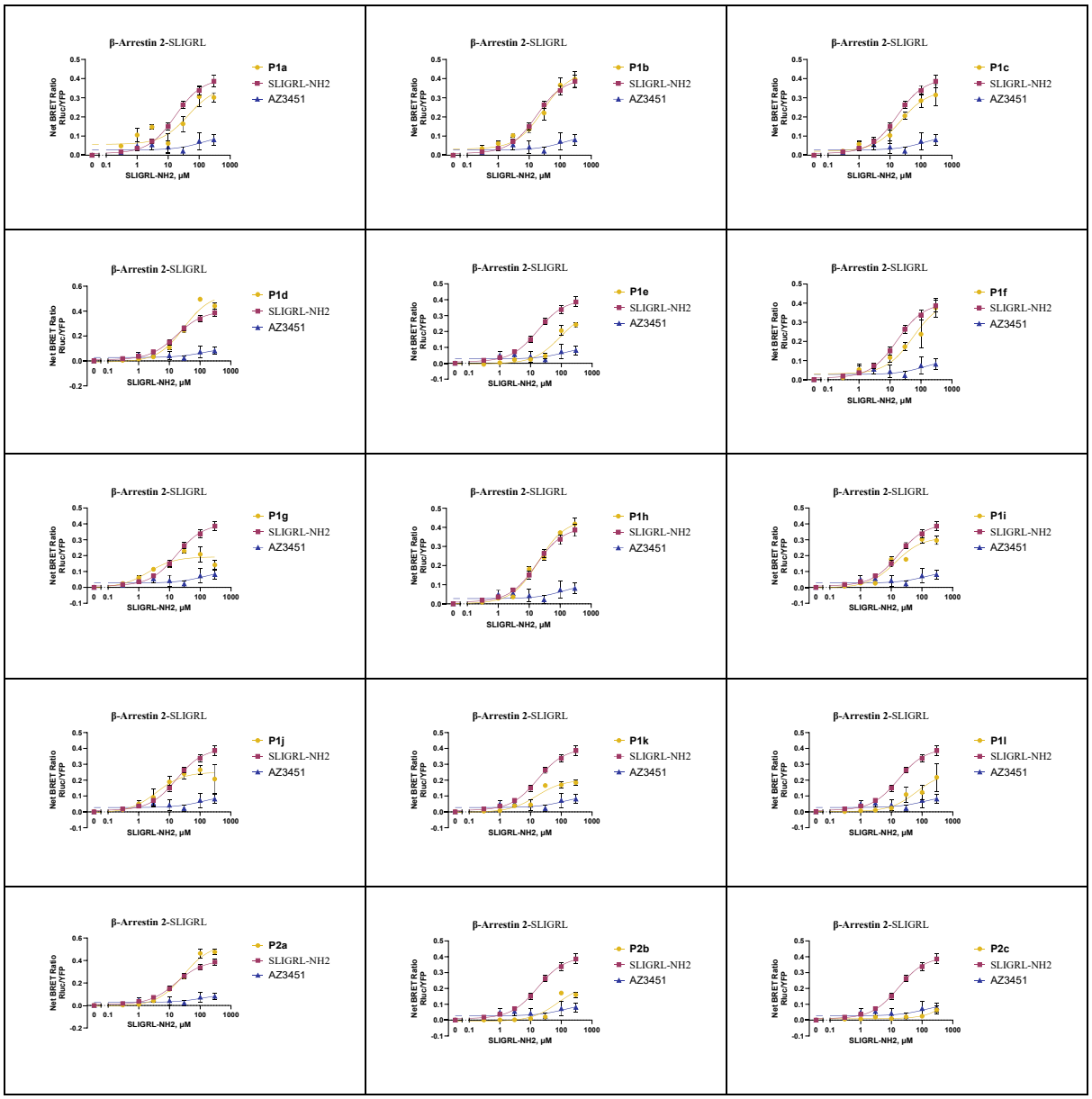

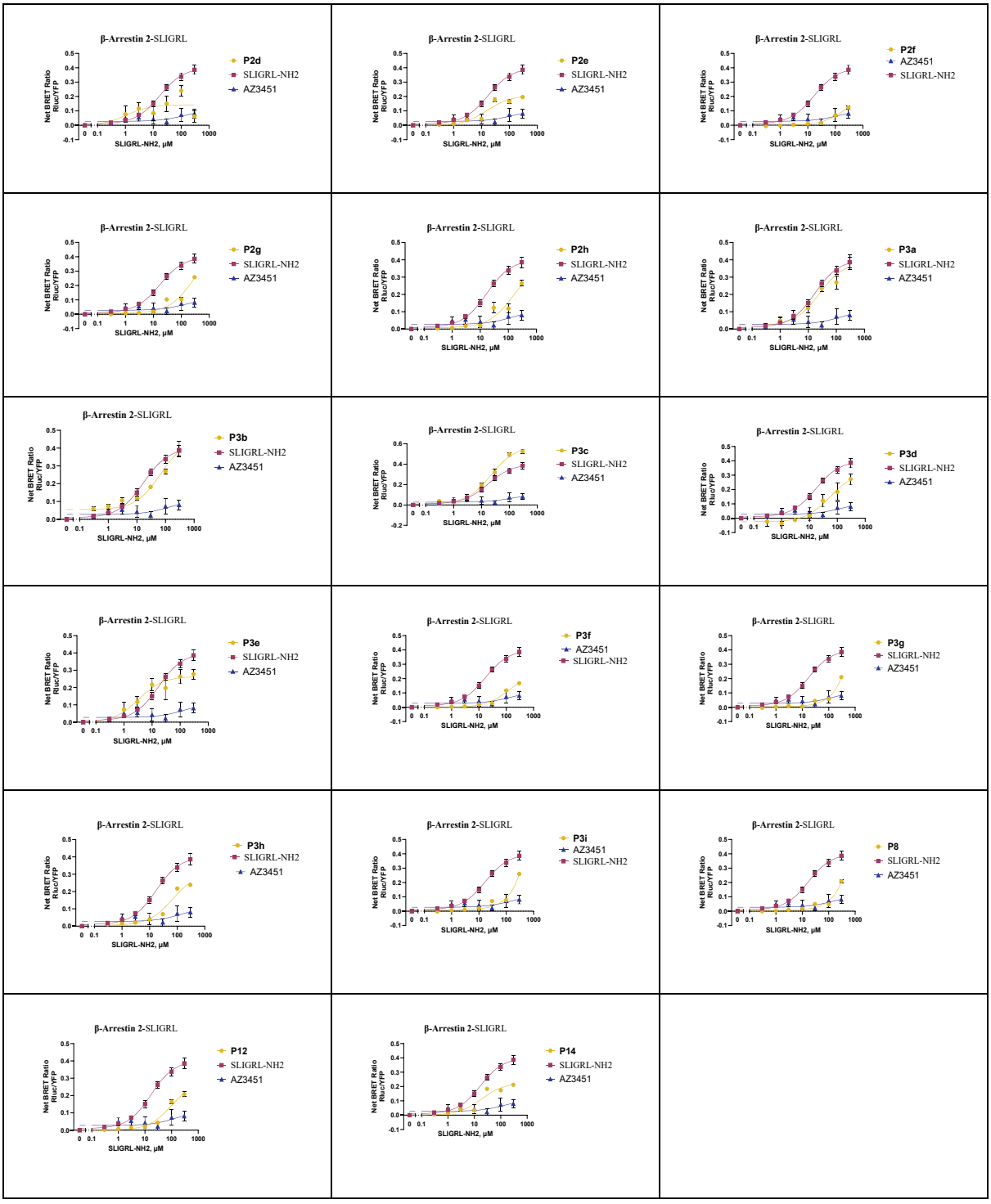
β-Arrestin 2-SLIGRL
Net BRET Ratio Rluc/YFP
SLIGRL-NH2, μM
P2d
SLIGRL-NH2
AZ3451
β-Arrestin 2-SLIGRL
Net BRET Ratio Rluc/YFP
SLIGRL-NH2, μM
P2e
SLIGRL-NH2
AZ3451
β-Arrestin 2-SLIGRL
Net BRET Ratio Rluc/YFP
SLIGRL-NH2, μM
P2f
AZ3451
SLIGRL-NH2
β-Arrestin 2-SLIGRL
Net BRET Ratio Rluc/YFP
SLIGRL-NH2, μM
P2g
SLIGRL-NH2
AZ3451
β-Arrestin 2-SLIGRL
Net BRET Ratio Rluc/YFP
SLIGRL-NH2, μM
P2h
SLIGRL-NH2
AZ3451
β-Arrestin 2-SLIGRL
Net BRET Ratio Rluc/YFP
SLIGRL-NH2, μM
P3a
SLIGRL-NH2
AZ3451
β-Arrestin 2-SLIGRL
Net BRET Ratio Rluc/YFP
SLIGRL-NH2, μM
P3b
SLIGRL-NH2
AZ3451
β-Arrestin 2-SLIGRL
Net BRET Ratio Rluc/YFP
SLIGRL-NH2, μM
P3c
SLIGRL-NH2
AZ3451
β-Arrestin 2-SLIGRL
Net BRET Ratio Rluc/YFP
SLIGRL-NH2, μM
P3d
SLIGRL-NH2
AZ3451
β-Arrestin 2-SLIGRL
Net BRET Ratio Rluc/YFP
SLIGRL-NH2, μM
P3e
SLIGRL-NH2
AZ3451
β-Arrestin 2-SLIGRL
Net BRET Ratio Rluc/YFP
SLIGRL-NH2, μM
P3f
AZ3451
SLIGRL-NH2
β-Arrestin 2-SLIGRL
Net BRET Ratio Rluc/YFP
SLIGRL-NH2, μM
P3g
SLIGRL-NH2
AZ3451
β-Arrestin 2-SLIGRL
Net BRET Ratio Rluc/YFP
SLIGRL-NH2, μM
P3h
SLIGRL-NH2
AZ3451
β-Arrestin 2-SLIGRL
Net BRET Ratio Rluc/YFP
SLIGRL-NH2, μM
P3i
AZ3451
SLIGRL-NH2
β-Arrestin 2-SLIGRL
Net BRET Ratio Rluc/YFP
SLIGRL-NH2, μM
P8
SLIGRL-NH2
AZ3451
β-Arrestin 2-SLIGRL
Net BRET Ratio Rluc/YFP
SLIGRL-NH2, μM
P12
SLIGRL-NH2
AZ3451
β-Arrestin 2-SLIGRL
Net BRET Ratio Rluc/YFP
SLIGRL-NH2, μM
P14
SLIGRL-NH2
AZ3451

Dose-response curve of calcium signaling assay (Trypsin-induced)

P1a

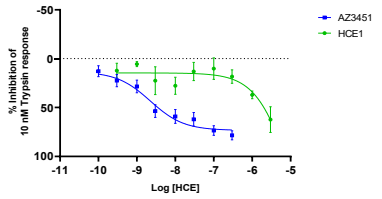

P1b

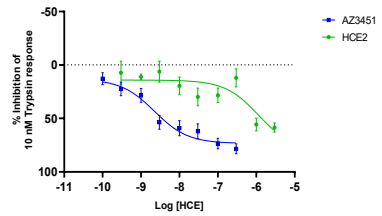

P1c

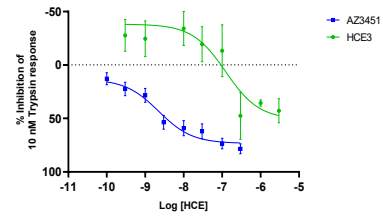

P1d

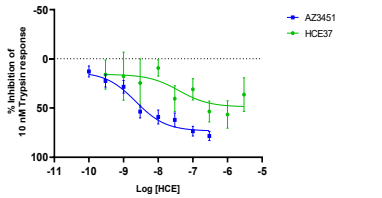

P1e

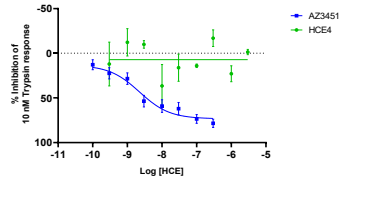

P1f

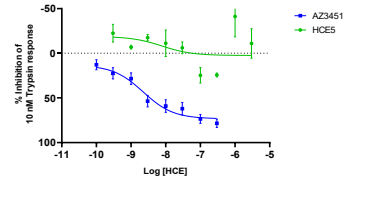

P1g

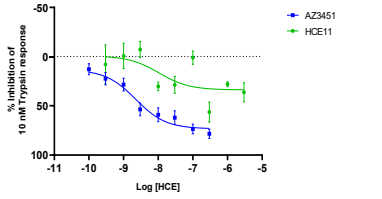

P2b

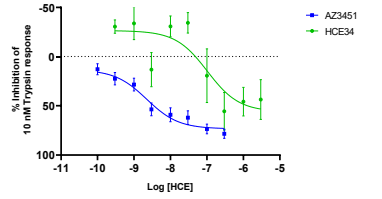

P2c

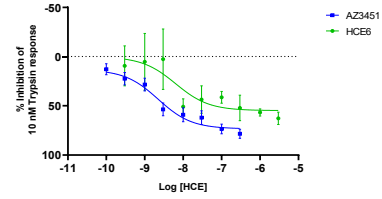

P3a

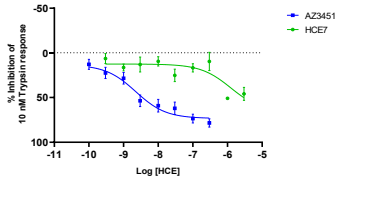

P3b

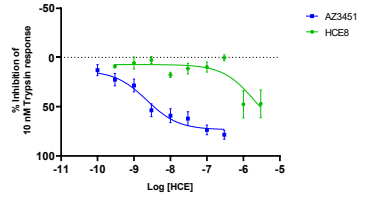

P3f

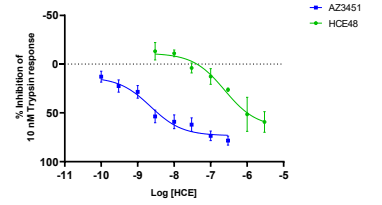

P3g

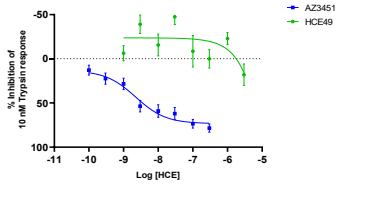

P8

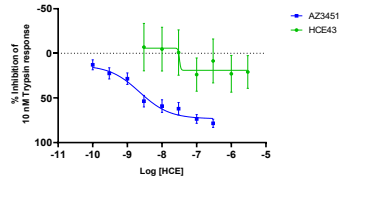

P12

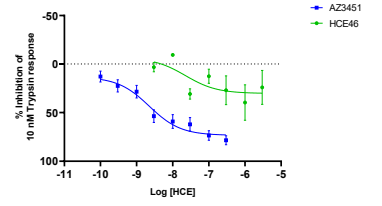

P14

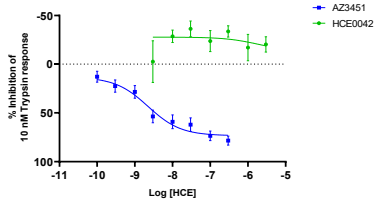

Dose-response curve of calcium signaling assay (SLIGRL-induced)

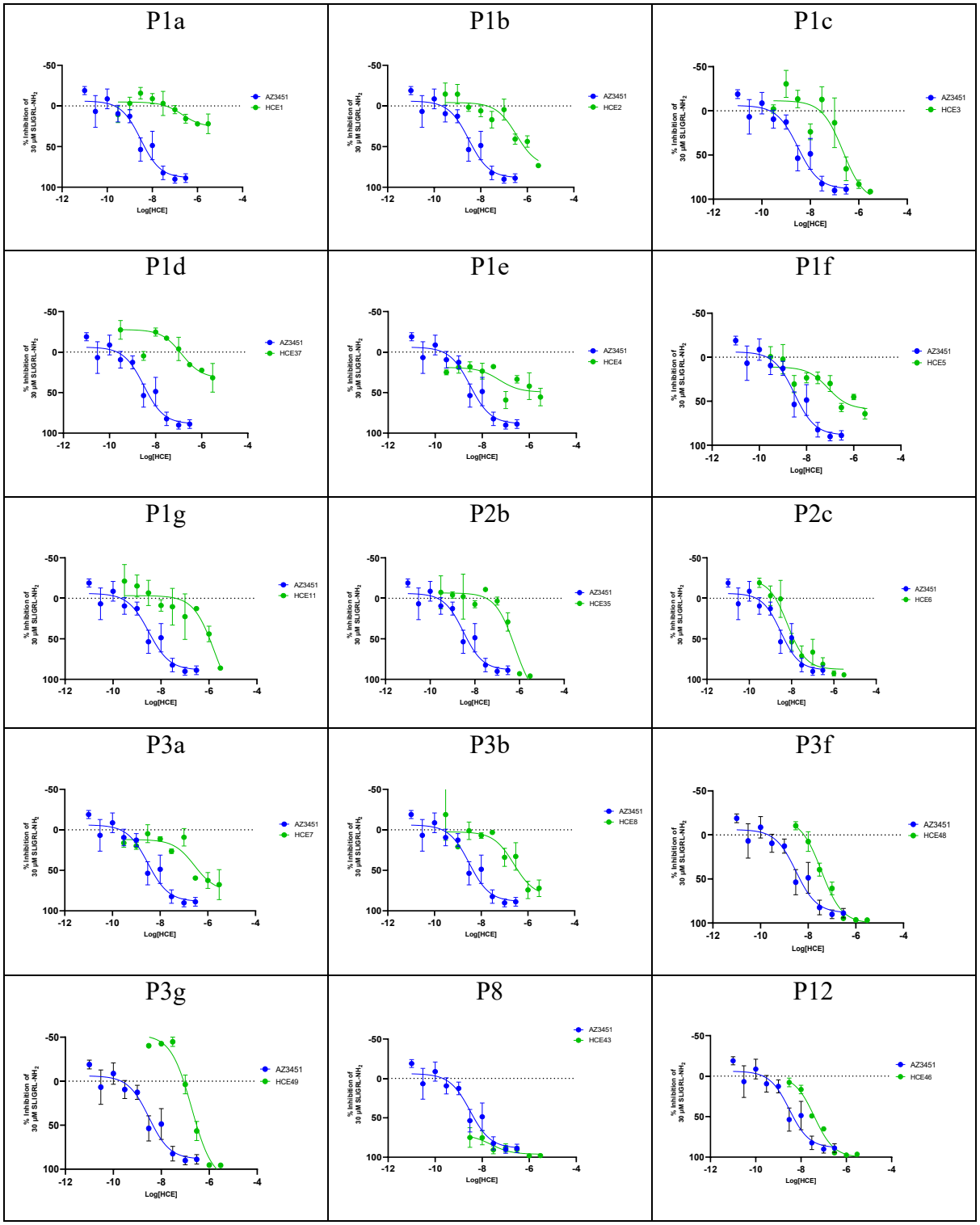

P14 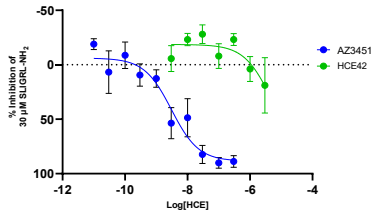 -50 0 50 100 -12 -10 -8 -6 -4 % Inhibition of 30 µM SLIGRL-NH2 Log[HCE] AZ3451 HCE42		